

Joint Congress of the Canadian Society for Mechanical Engineering and CFD Society of Canada

Proceedings of the 27th Annual Conference of the CFDSC

Société canadienne de



Society of Canada

June 2 – June 5, 2019

**Department of Mechanical and Materials Engineering
Western University
London, Ontario, Canada**



Message from the Co-Chairs of 27th Annual CFDSC Conference



On behalf of the Computational Fluid Dynamics Society of Canada (CFDSC), we welcome you to the 2019 Joint Congress of the Canadian Society for Mechanical Engineering and the CFD Society of Canada. This is the 27th Annual Conference of the CFDSC and marks the second time that the event has been hosted by Western University. Much of the event will be hosted within the newly-opened Amit Chakma Engineering Building, which is pursuing LEED® Platinum Certification for its sustainable design. A number of tours have been organized to showcase the state-of-the-art facilities at Western, including the



Fraunhofer Project Centre, the WindEEE Dome, and the Boundary Layer Wind Tunnel. We are excited for all of the conference participants to experience and enjoy the picturesque Western campus and all of its facilities.

We are very pleased to have had the opportunity to co-locate our conference with that of the Canadian Society for Mechanical Engineering (CSME). By combining the strengths of our two distinct events, we believe that we have created a technical program for the Joint Congress that is greater than the sum of its parts. We hope that this event will help foster further collaboration between the two Societies.

The Joint Congress features five plenary lectures from internationally-recognized distinguished speakers. The CFDSC speakers include Leigh Orf (University of Wisconsin) and Marcelo de Lemos (Instituto Tecnológico de Aeronáutica, Brazil). Dr. Orf will speak on his recent work involving petascale simulations of supercell thunderstorms and will discuss his latest hypothesis for tornado formation and their maintenance. Dr. de Lemos will be speaking about recent advances that have been made by his research group in numerical modelling of flow, heat, and mass transfer in heterogenous media. Both of these plenary lectures, as well as the three CSME-themes lectures, are sure to be fascinating. The CFDSC technical program includes 16 symposia with a total of 83 presentations from CFD researchers in all parts of Canada, as well as several other countries around the world. Additionally, we will feature several undergraduate posters and three-minute thesis talks.

We gratefully acknowledge the sponsors of the conference, including Bombardier, Delta Photonics, High Speed Imaging Inc., FLIR, Canadian Science Publishing and Western Engineering. Additionally, we thank all of the volunteers, session chairs, and the scientific committee for helping to make this event a success.

Sincerely,

Chris DeGroot

Co-Chair, CFDSC 2019 Conference

Chao Zhang

Co-Chair, CFDSC 2019 Conference



Congress Organizing Committee



Kamran Siddiqui
Chair
CSME International
Congress and Technical
Program
Western University



Christopher DeGroot
Co-Chair
CFDSC Annual
Conference
Western University



Chao Zhang
Co-Chair
CFDSC Annual
Conference
Western University



Ryan Willing
Communications Chair
Western University



Liying Jiang
Publications Chair
Western University



Remus Tutunea-Fatan
Exhibitions Chair
Western University

Plenary Speakers

Plenary Speaker (Sponsored by CFDSC)

Petascale Supercell Thunderstorm Simulations and New Hypothesis for Tornado Formation and Maintenance



Leigh Orf, PhD

Atmospheric scientist
Cooperative Institute for Meteorological Satellite Studies
University of Wisconsin

ABSTRACT

Each year tornadoes wreak devastation throughout the world. The United States experiences the highest frequency of thunderstorms that produce the strongest tornadoes, those ranked EF4 and EF5 on the Enhanced Fujita scale. Leigh Orf's current research focuses on the nature of these violently tornadic supercell thunderstorms primarily through the use of high resolution numerical modeling and visualization. In this presentation he will report on recent simulations of supercell thunderstorms conducted on the Blue Waters supercomputer, at up to 10 meter isotropic grid spacing. Simulations include violently tornadic supercells in two different environments based upon observations where real tornadoes formed. A new hypothesis for tornado formation and maintenance will be presented. In addition to presenting animations of highly resolved thunderstorms, the software and technology behind the simulations will be explained, with some discussion about the use of physical cloud models in wind engineering research.

BIOGRAPHY

Dr. Leigh Orf is an atmospheric scientist at the Cooperative Institute for Meteorological Satellite Studies at the University of Wisconsin. Leigh received his PhD in 1997 at the University of Wisconsin and was faculty at the University of North Carolina - Asheville and Central Michigan University before returning to the UW in 2015. His research focuses on the dangerous winds that occur in thunderstorms, primarily through the use of numerical models run on supercomputers to simulate entire thunderstorm clouds and their surrounding environment. He is primarily interested in the processes involved in the formation of downbursts and the genesis and maintenance of tornadoes. He has developed routines to manage and visualize, with very high fidelity, the tremendous of data produced in these simulations to provide new insight into the most dangerous storms.

Monday, June 3rd (1:00 pm – 2:00 pm), Ivey BMO Auditorium

Plenary Presentation (Sponsored by CFDSC)

Advances in Numerical Modelling of Flow, Heat, and Mass Transfer in Heterogeneous Media



Marcelo J.S. de Lemos, PhD, FASME

Professor

Departamento de Energia – IEME

Instituto Tecnológico de Aeronáutica – ITA

São José dos Campos, Brazil

ABSTRACT

Engineering and natural systems of practical relevance can be modelled as a porous structure through which a working fluid permeates. Engineering equipment design and environmental impact analyses can benefit from appropriate modeling of turbulent flow in permeable media. Turbulence models proposed for such heterogeneous media depend on the order of application of time and volume average operators. Two developed methodologies, following the two orders of integration, lead to different governing equations for the statistical quantities. This lecture reviews recently published methodologies to mathematically characterize turbulent transport in porous media. The concept of double-decomposition is discussed and models are classified in terms of the order of application of time and volume averaging operators, among other peculiarities. Thermal non-equilibrium between phases is discussed. For hybrid media, involving both a porous structure and a clear flow region, difficulties arise due to the proper mathematical treatment given at the interface. This lecture discusses numerical solutions for such hybrid medium. In addition, macroscopic forms of buoyancy terms are presented for both mean and turbulent fields. Cases reviewed include heat transfer in porous enclosures, cavities partially filled with porous material, moving bed systems, combustion in porous burners and double-diffusion effects in porous media.

BIOGRAPHY

Prof. de Lemos has obtained his PhD degree from Purdue University, USA. He spent a year as Assistant Professor at PUC-RJ in 1984, followed by two years as Resident Associate at Argonne National Laboratory, Illinois. In 1986, he joined the Aeronautical Institute of Technology -ITA in São José dos Campos, Brazil. He is Full Professor at ITA, founder and head of the Computational Transport Phenomena Laboratory -LCFT and the newly established Competence Center for Energy – CCE. He also serves as Head of the Department of Energy. Prof. de Lemos has set a new mathematical framework for novel treatment of turbulent flow, heat, and mass transfer through permeable media. He has published more than 370 articles in conference proceedings and journals in addition to ten book chapters and five books. He is member of the Honorary Editorial Advisory Boards of Int. J. Heat & Mass Transfer and Int. Comm. Heat & Mass Transfer, member of the Editorial Advisory Board of J. Porous Media and Editorial Board Member of Int. J. Dynamics of Fluids and Int. J. Applied Engineering Research. He has coordinated several joint research projects with DLR and Uni-Erlangen, Germany, and has delivered seminar lectures in Brazil, USA, Portugal, Tunis, Lebanon, Italy, France, Germany, South Korea, Romania, UAE and Japan. He is Consultant to Brazilian Education Ministry (CAPES), Brazilian National Research Council (CNPq) and São Paulo State Research Foundation (FAPESP). Prof. de Lemos is the Fellow of American Society of Mechanical Engineers –ASME.

Tuesday, June 4th (8:30 am – 9:30 am), Ivey BMO Auditorium

June 3, 2019 (Monday) - CFDCS TRACK

8:00 AM - 4:00 PM	Conference Registration (Amit Chakma Engineering Building Atrium)			
8:30 AM - 9:30 AM	CSME-CFDCS Congress Opening Ceremony Plenary Session (Ivey BMO Auditorium): "Artificial Knees: Can They Benefit from New Technologies?" Peter Walker (New York University)			
9:30 AM - 10:00 AM	Coffee Break (Amit Chakma Engineering Building Atrium)			
	Session L-1 (Large Eddy Simulation)	Session M-1 (Free Surface Flows)	Session N-1 (Heat and Mass Transfer I)	Session O-1 (Applications I)
	Session Chair: James McDonald	Session Chair: Olga Trichtchenko	Session Chair: Josuel Rogenski	Session Chair: Ronald Barron
	Room: SEB 1200	Room: SEB 2200	Room: SEB 2202	Room: SEB 3109
10:00 AM - 10:20 AM	Large Eddy Simulation Using the High-Order Flux Reconstruction Approach (Keynote Presentation) Brian Vermeire (Concordia University)	Computing Waves Under Ice Olga Trichtchenko (Western University); Emilian Parau (University of East Anglia)	Optimal Configuration Of Angled Rib Turbulators For Conjugate Heat Transfer Simulation Ramin Jalali (Sharif University of Technology); Masoud Darbandi (Sharif University of Technology); Ashkan Bagherzadeh (Sharif University of Technology); Gerry Schneider (University of Waterloo)	A Look Inside a Heart With Cardiomyopathy and Transcatheter Aortic Valve Replacement: An Image-Based Fluid-Structure Interaction Modeling Study Seyedvahid Khodaei; Reza Sadeghi; Ali Emadi; (McMaster University); Zahra Motamed (McMaster University, Massachusetts Institute of Technology)
10:20 AM - 10:40 AM		Simulations of Self-Propulsion Model Tests of a Fishing Vessel Using a Body-Force Method Coupled With a RANS Solver Md. Ashim Ali (Memorial University); Heather Peng (Memorial University); Wei Qui (Memorial University)	Natural Convective Heat Transfer From Two Parallel Thin Circular Vertically Spaced Axially Aligned Horizontal Isothermal Plates of Different Diameter Patrick Oosthuizen (Queen's University)	Patient-Specific Simulation of Coarctation Using Lattice Boltzmann Method and Lumped Parameter Modelling Reza Sadeghi (McMaster University); Seyedvahid Khodaei (McMaster University); Zahra Motamed (McMaster University, Massachusetts Institute of Technology)
10:40 AM - 11:00 AM	Analysis of High-Order Element Types for Implicit Large Eddy Simulation Carlos Pereira (Concordia University); Brian Vermeire (Concordia University)	Modelling Requirements for Dynamic Multiphase Ship Simulations Chunhui Liu (University of Waterloo); Xiaohua Wu (Royal Military College); Kevin McTaggart (DRDC); Jean-Pierre Hickey (University of Waterloo)	A Numerical Study of The Effect of Thin Horizontal and Vertical Adiabatic Side Extensions on Natural Convective Heat Transfer From a Downward Facing Heated Horizontal Isothermal Surface Patrick Oosthuizen (Queen's University); Jane Paul (Queen's University)	Validation of rhoCentralFoam for Numerical Modelling of Underexpanded Free Jets Impinging on Plates Peter Nielsen (Western University); Christopher DeGroot (Western University); Anthony Straatman (Western University)
11:00 AM - 11:20 AM	Stabilizing Filters for High-Order Implicit Large Eddy Simulation Mohsen Hamedji (Concordia University); Brian Vermeire (Concordia University)	Numerical Simulations of Two-Body Interaction in Waves Wei Meng (Memorial University); Heather Peng (Memorial University); Wei Qui (Memorial University)	Surrogate Model for Predicting Real-Time Airflow and Temperature Distributions in Data Centers Sahar Asgari (McMaster University); Peiyong Tsai (McMaster University); Ishwar Puri (McMaster University); Rong Zheng (McMaster University)	Evaluating Flocculation Strength Using CFD for Primary Wastewater Treatment Brooke Remler (Western University); Christopher DeGroot (Western University)
11:20 AM - 11:40 AM	Assessment of Error Estimators for Grid Adaptation for LES Application Yao Jiang (McGill University); Siva Nadarajah (McGill University)	Study of Inertial Coalescence of Droplets on a Solid Substrate Using Lattice Boltzmann Modelling Nilesh Pawar (IIT Delhi); Supreet Bahga (IIT Delhi); Sunil Kale (IIT Delhi); Sasidhar Kondarajji (IIT Bhubaneswar)	A Numerical Study Of Natural Convective Heat Transfer From A Two-Sided Circular Horizontal Isothermal Element Having A Linearly-Inclined Nonflat Surface Rafiq Manna (Queen's University); Patrick Oosthuizen (Queen's University)	Numerical investigation of the impact of Manufacturing Tolerances on Marine Propeller Performance Shanqin Jin (Memorial University); Ruosi Zha (Memorial University); Heather Peng (Memorial University); Wei Qui (Memorial University); David Hally (DRDC); Matthew Gauthier (DRDC); Bodo Gospodnetic (Dominis Engineering)
11:40 AM - 12:00 PM	Influence of Rib Height in a Rib-Roughened Square Duct on Turbulent Flow Using Large-Eddy Simulation Alex Czehryn (University of Manitoba); Vahid Mahmoodi (University of Manitoba); Bing-Chen Wang (University of Manitoba)	Performance Analysis of a Vertical Axis Hydrokinetic Turbines Array Bayram Mohamed (University of Calgary); Artem Korobenko (University of Calgary)	A Numerical Study of the Forced Convection Boiling of Nanofluid Refrigerant Diana Hernández; Mateo Arango; Fernando Toapanta-Ramos; Zulamita Zapata-Benabite; Cesar Nieto-Londoño; (Universidad Pontificia Bolivariana)	Numerical Modeling of a Freeze Desalination Process Ghobad Amini (American University of the Middle East); Jamal Jamal (American University of the Middle East)
12:15 PM - 1:00 PM	Lunch (Amit Chakma Engineering Building Atrium) and CSME Technical Committee Meetings			
1:00 PM - 2:00 PM	Plenary Session (Ivey BMO Auditorium): "Petascale Supercell Thunderstorm Simulations and New Hypothesis for Tornado Formation and Maintenance" Leigh Orf (University of Wisconsin)			
2:00 PM - 2:30 PM	Coffee Break (Amit Chakma Engineering Building Atrium)			
	Session L-2 (Algorithms)	Session M-2 (Environmental Flows)	Session N-2 (Heat and Mass Transfer II)	
	Session Chair: Brian Vermeire	Session Chair: Haltham Aboshosha	Session Chair: Gerry Schneider	
	Room: SEB 1200	Room: SEB 2200	Room: SEB 2202	
2:30 PM - 2:50 PM	Vorticity-Based Polynomial Adaptation for Moving and Deforming Domains Ramin Ghoreishi (Concordia University); Brian Vermeire (Concordia University)	Mixing In The Brazil Basin Kelly Ogden (Western University); Raffaele Ferrari (Massachusetts Institute of Technology)	Numerical Modeling of N-Heptane Injection and Combustion in the Ignition Quality Tester With ANSYS Forte Osama Hmood (Carleton University); Edgar Matida (Carleton University)	
2:50 PM - 3:10 PM	Deep Neural Networks for Non-Ideal Property Evaluation in Supercritical Flows Petro Junior Milan (Georgia Institute of Technology); Jean-Pierre Hickey (University of Waterloo); Zhaoyi Xu (Georgia Institute of Technology); Vigor Yang (Georgia Institute of Technology)	BIM-CFD Integrated Design Process Examples For Northern Architecture Muna Younis (Western University); Girma Bitsuamlak (Western University); Meseret Kahsay (Western University)	Soot Formation in a Steam-Introduced Kerosene Combustor Masoud Darbandi (Sharif University of Technology); Majid Ghalouzaideh (Sharif University of Technology); Gerry Schneider (University of Waterloo)	
3:10 PM - 3:30 PM	Investigation of Advection-Diffusion Problems and Simulations Using the Lattice Boltzmann Method and the ArrayFire Library for High-Performance Computing on GPU Michael Ho; Jesús Pérez; Sébastien Leclaire; Marcelo Reggio; Jean-Yves Trépanier; (Polytechnique Montréal)	A More Reliable Estimate For External Convective Heat Transfer Coefficient From Building Surfaces in an Urban-Setting Anwar Awol (Western University); Girma Bitsuamlak (Western University); Fitsum Tariku (British Columbia Institute of Technology)	CFD Modelling of Flow and Heat Transfer in a Thermosyphon Dwaipayan Sarker (Western University); Christopher DeGroot (Western University); Eric Savory (Western University)	
3:30 PM - 3:50 PM	Paired Explicit Runge-Kutta Schemes For Computational Aerodynamics Siavash Nasab (Concordia University); Brian Vermeire (Concordia University)	The Actuator Line Method For Wind Turbine Modelling Applied In A Variational Multi-Scale Framework Michael Ravensbergen (University of Calgary); Artem Korobenko (University of Calgary)	A New Framework For The Prediction Of Radiative Phenomena William Morin (University of Ottawa); James McDonald (University of Ottawa)	
3:50 PM - 4:10 PM	Improved Approximations For The Maximum-Entropy Fourteen-Moment Closure Of Gas Dynamics Fabien Giroux (University of Ottawa); James McDonald (University of Ottawa)	Flutter Instability of a Flat Plate Deforming With Large Amplitude to Align With the Fluid Flow Mohammad Tari (Polytechnique Montréal); Frederick Gosselin (Polytechnique Montréal); Eric Laurendeau (Polytechnique Montréal)	A Numerical Evaluation of Nanofluid Multiphase Flows for Different Micro-Heat Exchanger Geometries Daniel Bahamon (Universidad Pontificia Bolivariana); César Nieto-Londoño (Universidad Pontificia Bolivariana)	
4:15 PM - 4:35 PM	Undergraduate Poster 3-Minute Thesis Presentations (SEB 1200)			
5:00 PM - 7:30 PM	Various Tours (Meeting Point: Amit Chakma Engineering Building Atrium)			

June 4, 2019 (Tuesday) - CFDSC TRACK

8:00 AM - 4:00 PM	Conference Registration (Amit Chakma Engineering Building Atrium)		
8:30 AM - 9:30 AM	Plenary Session (Ivey BMO Auditorium): "Advances in Numerical Modelling of Flow, Heat, and Mass Transfer in Heterogeneous Media" Marcelo de Lemos (Instituto Tecnológico de Aeronáutica)		
9:30 AM - 10:00 AM	Coffee Break & CFDSC Undergraduate Poster Display (Amit Chakma Engineering Building Atrium)		
	Session L-3 (Porous Media)	Session M-3 (Turbulence I)	Session N-3 (Multiphase Flows I)
	Session Chair: Mahmoud Elhalwagy	Session Chair: BingChen Wang	Session Chair: Markus Bussmann
	Room: SEB 1200	Room: SEB 2200	Room: SEB 2202
10:00 AM - 10:20 AM	Airflow Balancing of a Produce Drying Chamber Using a Porous Media Approach (Keynote Presentation) Mahmoud Elhalwagy (Western University); Anthony Straatman* (Western University)	Mechanism For Transition To Turbulence in a Laminar Separation Bubble on an Airfoil (Keynote Presentation) Joshua Brinkerhoff (University of British Columbia)	Numerical Study of Atomization Mechanisms of Laminar Liquid Jets in High-Viscous Gaseous Crossflows Mohammad Hashemi (Concordia University); Mehdi Jadidi (Concordia University); Ali Dolatabadi (Concordia University)
10:20 AM - 10:40 AM			A Multi-Region CFD Model for Aircraft Ground Deicing by Liquid Spray Sami Emez (École de Technologie Supérieure); François Morency (École de Technologie Supérieure)
10:40 AM - 11:00 AM	Extension of Dynamic Heat and Mass Transfer Coupling to Turbulent Flow at Fluid/Porous Interfaces of Different Permeability Mahmoud Elhalwagy (Western University); Anthony Straatman (Western University)	Effect of Free-Stream Turbulence on Turbulent Boundary Layers From Flat Plates Ivia Magalhaes (Western University); Eric Savory (Western University)	Advances and Challenges in Simulation of LNG Behavior Inside a Tank Ehsan Tahmasebi (University of British Columbia); Aaron Stroda (University of British Columbia); Sai Pendli (University of British Columbia); Joshua Brinkerhoff (University of British Columbia)
11:00 AM - 11:20 AM	Modeling of Cathode Oxygen Transport in Polymer Electrolyte Membrane Fuel Cells Based on Measured Permeability and Effective Diffusivity Jian Zhao (University of Waterloo); Xianguo Li (University of Waterloo)	Application of Recurrence CFD to Study Mass Transport in Turbulent Vortex Shedding After a Cylinder Sanaz Abbasi (Johannes Kepler University); Thomas Lichtenegger (Johannes Kepler University)	Mass-Density-Based Model Using a Gaussian Moment Method for Polydisperse Multiphase Flow James McDonald (University of Ottawa); Jarod Ryan (University of Ottawa); Lucian Ivan (Canadian Nuclear Laboratories)
11:20 AM - 11:40 AM	Prediction of the Overall Performance of Catalyst-Coated Particulate Filters Using a Lattice Boltzmann-Based Model Igor Belot; David Vidal; François Bertrand; (Polytechnique Montréal); Martin Voitsmeier; Barry van Setten; Robert Greiner; (Umicore); Robert Hayes (University of Alberta)	Simulations of 3D Turbulent Flow Around a Circular Pier With a Splitter Plate Salar Kheshtgar (Concordia University); Samuel Li (Concordia University)	The Effects of Turbulent Models on Multiphase Flashing Flow Tarek Ngim (University of Alberta); Lei Li (University of Alberta); Carlos Lange (University of Alberta)
11:40 AM - 12:00 PM			
12:15 PM - 1:00 PM	Lunch and CFDSC Annual General Meeting (ACEB 1410)		
1:00 PM - 2:00 PM	Plenary Session (Ivey BMO Auditorium): "Advanced Materials for Energy Storage and Conversion: From Nano Scale to Single Atoms" Andy Sun (Western University)		
2:00 PM - 2:30 PM	Coffee Break & CFDSC Undergraduate Poster Display (Amit Chakma Engineering Building Atrium)		
	Session L-4 (Applications II)	Session M-4 (Turbulence II)	Session N-4 (Multiphase Flows II)
	Session Chair: Carlos Lange	Session Chair: Joshua Brinkerhoff	Session Chair: Bruno Blais
	Room: SEB 1200	Room: SEB 2200	Room: SEB 2202
2:30 PM - 2:50 PM	Numerical Investigation of the Thermodynamics Behaviors in the Central Downward Circular Tube of the 64-Element Canadian SCWR Fuel Bundle Huirui Han (Western University); Chao Zhang (Western University)	Numerical Study of Turbulent Heat Transfer of a Radially-Rotating Circular Pipe Flow (Keynote Presentation) Zhao-Ping Zhang (University of Manitoba); Bing-Chen Wang* (University of Manitoba); Dao-Qi Liu (Inner Mongolia University of Technology)	Application of a Piecewise Barotropic Equation of State in a Homogeneous Equilibrium Mixture (HEM) Cavitation Model Saeed Rahbarmanesh (University of British Columbia); Joshua Brinkerhoff (University of British Columbia); Ioannis Karathanassis (University of London); Manolis Gavaises (University of London)
2:50 PM - 3:10 PM	Permeability Tensor Orientation and its Effect on Resin Transfer Molding Anthony Sherratt (Western University); Christopher DeGroot (Western University); Anthony Straatman (Western University)		Modification of the CFD Model Based on the Bubble Size for the Three-Phase Flow in an Inverse Fluidized Bed Yunfeng Liu (Western University); Zeneng Sun (Western University); Chao Zhang (Western University); Jesse Zhu (Western University)
3:10 PM - 3:30 PM	CFD Investigation of Compressible Flow Effects on Performance Criteria of Inflow Control Devices Jean-Luc Olsen (University of Alberta); Matthew Miersma (University of Alberta); Carlos Lange (University of Alberta)	The Rod-Airfoil Problem: Capabilities and Limitations of Quasi-Two Dimensional Computations for Prediction of Near-Field Velocity Fluctuations Hanieh Param (University of Windsor); Jeffrey Defoe (University of Windsor)	CFD Simulation of Bubble Column Reactors in the Presence of Internals Glen Dsouza (Western University); Tuntun Gaurav (Western University); Chao Zhang (Western University); Anand Prakash (Western University)
3:30 PM - 3:50 PM	Oblique CFD Analysis of Open-Wheel Race Car With Circuit-Tailoring Shape Optimization Mark Lin (San Jose State University); Periklis Papadopoulos (San Jose State University)	Large Eddy Simulation of Turbulent Flow in Ice-Covered Channels Rui Zeng (Concordia University); Samuel Li (Concordia University)	CFD-PBM Study of Bubble Column Reactor Integrated with Mass Transfer Calculations Ahmed Khalil (Western University); Christopher DeGroot (Western University)
3:50 PM - 4:10 PM	Development of a Formula SAE Front Wing with an Emphasis on Additional Aerodynamic Devices Davin Jankovics (OUIT); Remon Pop-Iliev (OUIT); Ahmad Barari (OUIT)	Simulation of Shallow Open-Channel Flow Past a Vertical Cylinder Using IDDES-VOF Approach Subhadip Das; Vimaldoss Jesudhas; S. Abishek; Ram Balachandrar; Ronald Barron; (University of Windsor)	Numerical Study of Droplet Behavior Using Lattice Boltzmann Method Zhe Chen (University of Alberta); Alexandra Komrakova (University of Alberta)
4:10 PM - 4:30 PM	Computational Studies of the Aerodynamics of a Simplified Miata MX-5 Wing Yi Pao (OUIT); Remon Pop-Iliev (OUIT); Ghaus Rizvi (OUIT); Martin Agelin-Chaab (OUIT)	Hyperbolic Turbulence Models for Moment-Closure Solvers Chao Yan (University of Ottawa); James McDonald (University of Ottawa)	Novel Impeller Designs for Bioreactor Applications: CFD Analysis Of Shear Stress Sathuran Jegatheeswaran (Ryerson University); Farhad Ein Mozaafari (Ryerson University)
4:30 PM - 5:15 PM	NSERC Panel on Grants and Scholarships (Room: ACEB 1410)		
6:00 PM - 9:30 PM	Congress Banquet (Great Hall, Somerville House) Cash Bar (5:30 PM - 6:00 PM)		

June 5, 2019 (Wednesday) - CFDSC TRACK

CSME-CFDSC Congress Closing Ceremony Plenary Session (Ivey BMO Auditorium): "Resilient Manufacturing System" Ruxu Du (South China University of Technology)				
Coffee Break				
	Session L-5 (Aerodynamics)	Session M-5 (Particulate Flows)	Session N-5 (Non-Newtonian Flows)	
	Session Chair: Chris DeGroot	Session Chair: Alexandra Komrakova	Session Chair: Kelly Ogden	
	Room: SEB 1200	Room: SEB 2200	Room: SEB 3109	
8:30 AM - 9:30 AM				
9:30 AM - 10:00 AM				
10:00 AM - 10:20 AM	Unsteady Simulation of the Rotor Caradonna & Tung with SU2 Ahmed Mkaouer (École de Technologie Supérieure); François Morency (École de Technologie Supérieure)	Revisiting Solid-Liquid Mixing Through The Development Of An Open-Source CFD-DEM Model (Keynote Presentation) Bruno Blais (Polytechnique Montréal)	Numerical Simulation of the Forced Oscillations of a Wire in Newtonian and Shear-Thinning Fluids (Keynote Presentation) Cameron Hopkins (Western University); John de Bruyn* (Western University)	
10:20 AM - 10:40 AM	Numerical Simulation of Parallel Airfoil Vortex Interactions at Low Reynolds Number Using Detached-Eddy Simulation Nicholas Ogrodnik (Carleton University); Edgar Matida (Carleton University)			
10:40 AM - 11:00 AM	Hybrid Flow Control for Micro Aerial Vehicle Ali Esmâeili (Sharif University of Technology); Masoud Darbandi (Sharif University of Technology); Gerry Schneider (University of Waterloo)	Development of a CFD-DEM Model in Non Inertial Frame for Solid-Liquid Mixing Applications Bastien Delacroix (Polytechnique Montréal); Bruno Blais (Polytechnique Montréal); Louis Fradette (Polytechnique Montréal); François Bertrand (Polytechnique Montréal)	Stability Analysis Of Viscoplastic Fluids with Wall Slip Boundary Conditions Sayed Taghavi (Université Laval); Hossein Rahmani (Université Laval)	
11:00 AM - 11:20 AM	An Introduction to The Real Based Method for 3D Aerodynamic Analysis of the Insect Flyers at Low Reynolds Numbers Nasim Chitsaz (University of South Australia); Natania Yap (University of South Australia); Romeo Marian (University of South Australia); Javaan Chahl (University of South Australia)	Coupled CFD-DEM Model to Simulate Two-Particle Settlement in a Newtonian Fluid: A Grid Comparison Fatemeh Razavi (University of Alberta); Alexandra Komrakova (University of Alberta); Carlos Lange (University of Alberta)	Effect of Flow and Elasticity on Nematic Liquid Crystal Lubricants Arash Nikzad (University of British Columbia); Dana Grecov (University of British Columbia)	
11:20 AM - 11:40 AM	Numerical Study of Roundness Effect on Flow Around a Circular Cylinder Ran Wang (University of Windsor); Shaohong Cheng (University of Windsor)	Variational Data Assimilation Using a Polydisperse Gaussian Model for Short Range Atmospheric Dispersion Of Radionuclides François Forgues; James McDonald; (University of Ottawa); Volodymyr Korolevych; Luke Lebel; Lucian Ivan; (Canadian Nuclear Laboratories)	Analyzing the Effect of Rheology of Non-Newtonian Fluids in Gas Dispersion With a Coaxial Mixer Through Tomography and CFD Maryam Jamshidzadeh (Ryerson University); Farhad Ein-Mozaffari (Ryerson University); Ali Lothi (Ryerson University)	
11:40 AM - 12:00 PM	Large Eddy Simulation of Taylor-Couette Flow Mohammad Mohammadi (University of British Columbia); Joshua Brinkerhoff (University of British Columbia)	Numerical Solution of Multiphase Flow Using New High-Order Moment-Based Eulerian Methods Andr�e-Ann Dion Dallaire (University of Ottawa); Fran�ois Forgues (University of Ottawa); James McDonald (University of Ottawa); Lucian Ivan (Canadian Nuclear Laboratories)		
End of the CSME-CFDSC Congress 2019				

Authors Index (CFDSC Track)

Abbasi, Sanaz (Session M-3)
Agelin-Chaab, Martin (Session L-4)
Ali, Md. Ashim (Session M-1)
Amini, Ghobad (Session O-1)
Arango, Mateo (Session N-1)
Asgari, Sahar (Session N-1)
Awol, Anwar (Session M-2)
Bagherzadeh, Ashkan (Session N-1)
Bahamon, Daniel (Session N-2)
Bahga, Supreet (Session M-1)
Barari, Ahmad (Session L-4)
Belot, Igor (Session L-3)
Bertrand, François (Session L-3, M-5)
Bitsuamlak, Girma (Session M-2)
Blais, Bruno (Session M-5)
Brinkerhoff, Joshua (Session L-5, M-3, N-3, N-4)
Chahl, Javaan (Session L-5)
Chen, Zhe (Session N-4)
Cheng, Shaohong (Session L-5)
Chitsaz, Nasim (Session L-5)
Czehryn, Alex (Session L-1)
Dallaire, Andrée-Ann Dion (Session M-5)
Darbandi, Masoud (Session L-5, N-1, N-2)
de Bruyn, John (Session N-5)
Defoe, Jeffrey (Session M-4)
DeGroot, Christopher (Session L-4, N-2, N-4, O-1)
Delacroix, Bastien (Session M-5)
Dolatabadi, Ali (Session N-3)
Dsouza, Glen (Session N-4)
Ein-Mozaffari, Farhad (Session N-4, N-5)
Elhalwagy, Mahmoud (Session L-3)
Emadi, Ali (Session O-1)
Emez, Sami (Session N-3)
Esmaeili, Ali (Session L-5)
Ferrari, Raffaele (Session M-2)
Forgues, François (Session M-5)
Fradette, Louis (Session M-5)
Gaurav, Tuntun (Session N-4)
Gauthier, Matthew (Session O-1)
Gavaises, Manolis (Session N-4)
Ghafourizadeh, Majid (Session N-2)
Ghoreishi, Ramin (Session L-2)
Giroux, Fabien (Session L-2)
Gospodnetic, Bodo (Session O-1)
Gosselin, Frederick (Session M-2)
Grecov, Dana (Session N-5)
Greiner, Robert (Session L-3)
Hally, David (Session O-1)
Hamed, Mohsen (Session L-1)
Han, Huirui (Session L-4)
Hashemi, Mohammad (Session N-3)
Hayes, Robert (Session L-3)
Hernández, Diana (Session N-1)
Hickey, Jean-Pierre (Session L-2, M-1)
Hmood, Osama (Session N-2)
Ho, Michael (Session L-2)
Hopkins, Cameron (Session N-5)
Ivan, Lucian (Session M-5, N-3)
Jadidi, Mehdi (Session N-3)
Jalali, Ramin (Session N-1)
Jamali, Jamal (Session O-1)
Jamshidzadeh, Maryam (Session N-5)
Jankovics, Davin (Session L-4)
Jegatheeswaran, Sinthuran (Session N-4)
Jiang, Yao (Session L-1)
Jin, Shanqin (Session O-1)
Kahsay, Meseret (Session M-2)
Kale, Sunil (Session M-1)
Karathanassis, Ioannis (Session N-4)
Khalil, Ahmed (Session N-4)
Kheshtgar, Salar (Session M-3)
Khodaei, Seyedvahid (Session O-1)
Komrakova, Alexandra (Session M-5, N-4)
Kondaraji, Sasidhar (Session M-1)
Korobenko, Artem (Session M-1, M-2)
Korolevych, Volodymyr (Session M-5)
Lange, Carlos (Session L-4, M-5, N-3)
Laurendeau, Eric (Session M-2)
Lebel, Luke (Session M-5)
Leclaire, Sébastien (Session L-2)
Li, Lei (Session N-3)
Li, Samuel (Session M-3, M-4)
Li, Xianguo (Session L-3)
Lichtenegger, Thomas (Session M-3)
Lin, Mark (Session L-4)
Liu, Chunhui (Session M-1)
Liu, Dao-Qi (Session M-4)
Liu, Yunfeng (Session N-4)
Lohi, Ali (Session N-5)
Magalhaes, Ivian (Session M-3)

Authors Index (CFDSC Track)

Mahmoodi, Vahid (Session L-1)
Manna, Rafiq (Session N-1)
Marian, Romeo (Session L-5)
Matida, Edgar (Session L-5, N-2)
McDonald, James (Session L-2, M-4, M-5, N-2, N-3)
McTaggart, Kevin (Session M-1)
Meng, Wei (Session M-1)
Miersma, Matthew (Session L-4)
Milan, Petro Junior (Session L-2)
Mkaouar, Ahmed (Session L-5)
Mohamed, Bayram (Session M-1)
Mohammadi, Mohammad (Session L-5)
Morency, François (Session L-5, N-3)
Morin, William (Session N-2)
Motamed, Zahra (Session O-1)
Nadarajah, Siva (Session L-1)
Nasab, Siavash (Session L-2)
Nielsen, Peter (Session O-1)
Nieto-Londoño, Cesar (Session N-1, N-2)
Nigim, Tarek (Session N-3)
Nikzad, Arash (Session N-5)
Ogden, Kelly (Session M-2)
Ogrodnik, Nicholas (Session L-5)
Olsen, Jean-Luc (Session L-4)
Oosthuizen, Patrick (Session N-1)
Pao, Wing Yi (Session L-4)
Papadopoulos, Periklis (Session L-4)
Param, Hanieh (Session M-4)
Parau, Emilian (Session M-1)
Paul, Jane (Session N-1)
Pawar, Nilesh (Session M-1)
Pendli, Sai (Session N-3)
Peng, Heather (Session M-1, O-1)
Pereira, Carlos (Session L-1)
Pérez, Jesús (Session L-2)
Pop-Iliev, Remon (Session L-4)
Prakash, Anand (Session N-4)
Puri, Ishwar (Session N-1)
Qiu, Wei (Session M-1, O-1)
Rahbarimanesh, Saeed (Session N-4)
Rahmani, Hossein (Session N-5)
Ravensbergen, Michael (Session M-2)
Razavi, Fatemeh (Session M-5)
Reggio, Marcelo (Session L-2)
Remler, Brooke (Session O-1)
Rizvi, Ghaus (Session L-4)
Ryan, Jarod (Session N-3)
Sadeghi, Reza (Session O-1)
Sarkar, Dwaipayan (Session N-2)
Savory, Eric (Session M-3, N-2)
Schneider, Gerry (Session L-5, N-1, N-2)
Sherratt, Anthony (Session L-4)
Straatman, Anthony (Session L-3, L-4, O-1)
Stroda, Aaron (Session N-3)
Sun, Zeneng (Session N-4)
Taghavi, Sayed (Session N-5)
Tahmasebi, Ehsan (Session N-3)
Tari, Mohammad (Session M-2)
Tariku, Fitsum (Session M-2)
Toapanta-Ramos, Fernando (Session N-1)
Trépanier, Jean-Yves (Session L-2)
Trichtchenko, Olga (Session M-1)
Tsai, Peiying (Session N-1)
van Setten, Barry (Session L-3)
Vermeire, Brian (Session L-1, L-2)
Vidal, David (Session L-3)
Votsmeier, Martin (Session L-3)
Wang, Bing-Chen (Session L-1, M-4)
Wang, Ran (Session L-5)
Wu, Xiaohua (Session M-1)
Xu, Zhaoyi (Session L-2)
Yan, Chao (Session M-4)
Yang, Vigor (Session L-2)
Yap, Natania (Session L-5)
Younis, Muna (Session M-2)
Zapata-Benabithé, Zulamita (Session N-1)
Zeng, Rui (Session M-4)
Zha, Ruosi (Session O-1)
Zhang, Chao (Session L-4, N-4)
Zhang, Zhao-Ping (Session M-4)
Zhao, Jian (Session L-3)
Zheng, Rong (Session N-1)
Zhu, Jesse (Session N-4)

Technical Abstracts & Papers

Aerodynamics

Unsteady Simulation of the rotor Caradonna & Tung with SU2

Ahmed MKAOUAR
Mechanical engineering department
ETS
Montréal, Canada
Ahmed.mkaouar.1@ens.etsmtl.ca

François MORENCY
Mechanical engineering department
ETS
Montréal, Canada
Francois.Morency@etsmtl.ca

ABSTRACT

The numerical simulation of Helicopter rotor's flow field is still one of the most challenging aerodynamics problems due to the rotating flow and the complex geometry of the helicopter. Several experimental studies have been conducted resulting in a good validation database. However, the study of heat flux on the rotor remains unexamined. The distribution of heat transfer is needed to understand icing formation on rotor's blade. Rotor icing is considered among the most threaten weather condition for helicopter. One emerging method to solve the problem is the sliding mesh strategy. This method is a dynamic multizone mesh where the nodes move rigidly. Recently this capability has been added to the CFD tool SU2. The goal of my research is to calculate the distribution of Nusselt number on the rotor's blade. The aim of this work is to validate the study of unsteady flow on the Caradonna&Tung rotor with a sliding mesh. Upon validation, the study will deal with the variation of heat flux on the blades. The mesh is generated using ICEM-CFD. It is composed of two major zones. The first region rotates with the blades. The second region remains stationary and embodies the first one. The two grids slide past each other at a cylindrical interface. A nearest-neighbor approach ensures the communication between the two zones. The dual time stepping scheme is used for the unsteady simulation. First, an inviscid three-dimensional flow of the rotor in hover is calculated by solving Euler equations. A second study deals with the RANS equations. The results represent the variation of the pressure coefficient, lift, drag and torque with respect to the chordwise location for different positions among the blade spanwise. A comparison between the results and both numerical and experimental literature data is made in order to validate the study. Another comparison is made between the Euler and the RANS studies. The validation of the code with respect to literature allows the study to deal with heat transfer on the blades. Then the heat flux distribution will be evaluated.

Keywords: rotor, Cardonna&Tung, RANS, Euler, unsteady, sliding mesh, Nusselt.

Numerical Simulation of Parallel Airfoil Vortex Interactions at Low Reynolds Number using Detached-Eddy Simulation

Nicholas Ogrodnik, BEng

Department of Mechanical and Aerospace Engineering
Carleton University
Ottawa, Ontario
nick.ogrodnik@carleton.ca

Edgar A. Matida, PhD

Department of Mechanical and Aerospace Engineering
Carleton University
Ottawa, Ontario

ABSTRACT

The tip vortices generated from revolving rotorcraft blades can interact with the following advancing blade under certain flight conditions such as descending flight. When the axis of rotation of the vortex is parallel to the blade, additional vibrations, unsteady loads, and significant acoustic noise can be generated from the interaction of the vortex with the rotorcraft blades. This phenomenon is known as blade vortex interaction (BVI). Despite the common occurrence of BVIs, experimental BVI investigations of rotating helicopter blades are relatively complex. Straus et al. (1990) generated a vortex by pitching a NACA0018 airfoil approximately eight degrees during a period of fifteen milliseconds. This vortex advected and interacted with a NACA0012 airfoil (instrumented with 24 pressure taps) further downstream. The velocity distribution of the vortex was also measured using hotwire anemometry, along with the temporal variation of lift, momentum, and drag coefficients of two different BVIs: a clockwise and a counter-clockwise rotating vortex. Experiments were conducted in a low speed wind tunnel with a freestream velocity of 40 feet per second and Reynolds number of 375,000. In the present work, BVI numerical simulations were conducted using Detached Eddy Simulation (DES) to predict aerodynamic coefficients using the geometrical and experimental conditions by Straus et al. (1990). To replicate experimental conditions, a C-type grid was used with two tandem airfoils (NACA0018 and NACA0012) in a quasi-3D computational domain. The NACA0018 airfoil was pitched using mesh deformation to generate a vortex. The vortex is then advected downstream to interact with the NACA0012 airfoil. The preliminary results of the DES demonstrate similar lift and pressure coefficients as found by Straus et al. (1990). This CFD model can be used for the numerical prediction of BVI with a NACA0012 airfoil. By controlling characteristics such as miss distance, downstream distance, vortex rotation (i.e. clockwise or counterclockwise), vortex circulation strength and angle of attack, numerical results can demonstrate the effect of these factors on aerodynamic coefficients. Furthermore, a prediction of the impact of BVI on the aerodynamic performance of the rotorcraft blade and a further understanding of the conditions which cause the BVI phenomenon to occur is possible from this CFD model.

Numerical Study of Roundness Effect on Flow Around a Circular Cylinder

Ran Wang

Department of Civil and Environmental Engineering
University of Windsor
Windsor, Ontario, Canada
wang1hf@uwindsor.ca

Shaohong Cheng

Department of Civil and Environmental Engineering
University of Windsor
Windsor, Ontario, Canada
shaohong@uwindsor.ca

ABSTRACT

Increasing research effort has been dedicated to wind-induced vibrations of stay cables on cable-stayed bridges under no precipitation condition. Owing to the low lateral stiffness, low inherent damping and light mass, stay cables are sensitive to dynamic excitations such as wind. In typical bridge engineering practice, high-density polyethylene pipe is commonly used to shield a stay cable's steel strands from environmental impact. Thus, majority existing research modeled stay cable as a circular cylinder in various analytical, experimental, and numerical studies. However, the cross-sectional shape of a real stay cable is not always perfectly round. Its roundness could be affected by various factors including manufacturing precision, assembling processes, and deformations during shipping and storage.

Although aerodynamic behavior of a perfectly round circular cylinder has been extensively studied, such study on a circular cylinder having imperfect roundness is scarce. Results of a recent wind tunnel test suggested that the roundness of a circular cylinder could significantly affect the drag reduction when flow is in the critical Reynolds number regime, but details of the flow structure surrounding such a cylinder was not fully unveiled. Therefore, to have a deeper understanding of the mechanisms of wind-induced vibrations of dry stay cables on site, it is imperative to explore the aerodynamics of an imperfectly round circular cylinder and investigate the impact of roundness on its surrounding flow field.

In view of this, the current study aims at using delayed detached eddy simulation (DDES) implemented in Open source Field Operation and Manipulation (OpenFOAM) to investigate the three-dimensional flow structure in the near wake of a circular cylinder having imperfect roundness and the corresponding spatial distribution of the cross-flow force. The cross-sectional shape of the cylinder is formed by superimposing a sinusoidal curve on a circle. The control variable of roundness is defined as the ratio between the depth of groove, e , and the cylinder diameter, D . The computational grid has a cylindrical geometry (also known as O-type grid). The cylinder is located at the center of the computational domain whose diameter and length are respectively $40 D$ and $20 D$. Periodic boundary conditions are utilized to minimize the end effect. Spalding's law is applied to the turbulent kinematic viscosity to alleviate the extremely fine near-wall resolution near the cylinder surface. At the inflow plane, a turbulent inlet was adopted, of which the corresponding turbulence intensity was around 1%.

The simulation results of the perfectly round circular cylinder ($e/D = 0$), mainly the mean drag coefficient and the Strouhal number, are used to validate the developed numerical model due to the availability of rich literature data. Preliminary results of flow around a perfectly round circular cylinder in general agrees well with the literature data at a Reynolds number of 10000. Grids of other cases ($e/D = 1\%$, 2% , 3% , 4% , 5% , 10%) will be similar to that of the perfectly round circular cylinder. Next, the simulation results of the roundness case $e/D = 4\%$ will be compared with those of an existing experimental study, of which a circular cylinder of the same imperfect roundness was tested in the wind tunnel. Also, similarities and differences between the experimental and current numerical simulation results will be discussed. Then, aerodynamic response of cylinder in other roundness cases will be analyzed to study the roundness effect on the wind-induced behavior of an imperfectly round circular cylinder.

LARGE EDDY SIMULATION OF TAYLOR-COUETTE FLOW

Mohammad Haji Mohammadi

School of Engineering, University of British Columbia
Kelowna, Canada
mhajit@alumni.ubc.ca

Joshua Brinkerhoff

School of Engineering, University of British Columbia
Kelowna, Canada
Joshua.brinkerhoff@ubc.ca

ABSTRACT

The Taylor-Couette (TC) problem investigates the flow in the gap between two independently rotating coaxial cylinders. It is among the most investigated problems in fluid mechanics due to its geometrical simplicity and application to process technology. An exact analogy can be made between TC flow and the thermal Rayleigh-Bernard problem in which the dimensionless flux of angular velocity Nu_w , the Taylor number Ta , and the geometric Prandtl number in TC flow play the same role as the Nusselt number Nu , Rayleigh number Ra , and Prandtl numbers in Rayleigh-Bernard flow, respectively. The rich phenomenology of TC flow is divided into a parameter space defined by two control parameters (the rotation rates of the two cylinders) and two geometrical parameters (the cylinder radius ratio and the ratio of the cylinder length to the gap). The curved inner and outer walls with different rotational speeds pose a further complication, numerically and physically, to the TC flow. Investigating TC via numerical simulations can adopt a general curvilinear grid to resolve the difficulty of dealing with curved inner and outer walls. A great amount of literature has been dedicated for the global parameters calculations and their laws of scaling, including the torque, angular momentum transfer rate, and power. However, fewer works have been reported on the turbulence properties and detailed flow characteristic at higher Reynolds numbers. Moreover, very few works have been reported on large eddy simulation (LES) of the Taylor-Couette flows. As a result, the suitability of popular subgrid turbulence closure models within LES has not been thoroughly evaluated for highly-turbulent wall-bounded conditions with strong flow streamline curvature as appears in TC flows, all conditions that are likely to tax existing subgrid models. Rather, majority of the works on the turbulent Taylor-Couette flows have been carried out using direct numerical simulation (DNS), which in turn limit the maximum flow conditions achievable due to the high computational cost. This motivates us to conduct a series of LES studies of TC flow with the following objectives: (i) assess the suitability of the Germano dynamic subgrid model for resolving the turbulence behavior in TC flow; and (ii) characterize the nature of the turbulence both quantitatively in terms of turbulent statistics and qualitatively in terms of the existence and behavior of coherent flow structures.

An in-house computational code is employed to perform LES of TC flows. Body-fitted grids are used to discretize the computational domain. The code employs the partially-transformed equations in curvilinear coordinate to benefit from the flexibility of simulating flows in domains with non-uniform non-orthogonal computational cells. All the simulations are performed via LES in which a filtered form of the equations is employed to remove the length/time scales smaller than what can be resolved by the grid. In this approach, the subgrid stresses are modeled using the eddy viscosity model (dynamic Smagorinsky model) of Germano. The two-step fractional step method is used for coupling the pressure and velocity field and time integration of the equations. Krylov subspace methods are used to solve the resulting system of equations, for which the GMRES method is employed to solve the pressure correction Poisson equation and the Newton-Krylov method is used to solve for the implicit momentum equation.

Several test cases are considered to validate the accuracy and efficiency of our code, including two laminar test cases and three turbulent test cases corresponding to co-rotating, counter rotating and stationary outer cylinders. Excellent agreement is achieved with respect to analytical solutions and benchmark direct numerical simulation (DNS) results. Selected LES results are presented for a focused study with a large inner cylinder Reynolds number (Re_i) and a stationary outer cylinder. The aim is to use the LES results to characterize the instantaneous and time-averaged flow field, with a special focus on developing a mechanistic description of the turbulent dynamics in the TC flow. To this end, instantaneous results in terms of velocity and pressure fields and coherent vertical structures (isolated via the Q -criterion) will be presented and discussed. Also, the flow is time-averaged after the flow reaches statistically stationary turbulence, as monitored through the surrogate of kinetic energy of the filtered velocity field, dissipation rate and the pseudo Nusselt number for angular velocity, i.e. Nu_w . The spatio-temporally averaged results are presented in terms of time-averaged velocity and pressure field, budgets of the turbulence kinetic energy, and turbulent Reynolds stresses.

HYBRID FLOW CONTROL FOR MICRO AERIAL VEHICLE WITH PORTUBERANCE WING AND MORPHING SURFACE

Ali Esmaeili and Masoud Darbandi
Center of Excellence in Aerospace Systems,
Department of Aerospace Engineering,
Sharif University of Technology,
P.O. Box 11365-11155, Tehran, Iran
darbandi@sharif.edu

Gerry E. Schneider
Department of Mechanical and Mechatronics Engineering,
University of Waterloo,
Waterloo, Ontario, N2L 3G1, Canada
gerry.schneider@uwaterloo.ca

Abstract—This study presents new developments required for the fixed-wing MAVs, aiming to increase their aerodynamic performance and maneuverability. Since these small vehicles are restricted by the weight and space and since it is difficult to mount batteries inside them, their flight endurance and performance are decreased greatly. To overcome these weaknesses, the flow control techniques such as the passive and active controls would be effective on these small flying vehicles. Recently, a passive flow control solution inspired from the pectoral flippers of humpback whales. It can delay or mitigate out the aerodynamic stall arises. However, an inverse behavior has been found in pre-stall conditions with dropping down the lift coefficients due to the formation of laminar separation bubble (LSB) in the trough section of wing. In the current investigation, in an attempt to retrieve the lift-generation capabilities of the modified wing at pre-stall angles of attack, an active flow control method is designed and it is numerically simulated, making use of morphing plate specially on the area of the LSB position. The resulting hybrid flow control system proves its effectiveness, exhibiting complete suppression of the LSB at pre-stall, a delay in the occurrence of stall, and generalized lift enhancements irrespectively of the regime of operation.

Keywords—*micro air vehicles (MAV); hybrid control; laminarflow; separation bubble; morphing plate; CFD, numerical.*

I. INTRODUCTION

Recently, using leading edge tubercles on airfoils, wings, hydrofoils, fans and turbines have seen increased interests of scientists from different areas as a novel passive flow control technique. The original idea was inspired from a humpback whale flipper which is capable of performing acrobatic maneuvers, tight curves, high speed, banked turns as well as loops and rolls [1-3]. The morphology and placement of leading edge tubercles reveal that they enhance the lift to control the flow over the whale's flipper, and maintain lift at high angles of attack [4], consequently, delay stall [5]. These interesting abilities have attracted the aerodynamicists'

attention to use the same methodology in the real wings, especially in Micro Aerial Vehicles (MAV). Due to the small size and low velocities of MAVs, they operate in the low Reynolds number regime ($Re < 200,000$), viscous effects are dominant, which degrades lifting surfaces efficiency such as laminar separation, transition and reattachment and unsteady flow effects [6]. Various studies have demonstrated that implementing tubercles could help in reducing the current problems in the low Reynolds number flow region. Initial investigations focused on very specific high-aspect ratio tapered wings as an attempt to mimic a real whale flipper, both from the experimental [5] and computational points of view [7]. Even more recently, Particle Image Velocimetry (PIV) measurements have been carried out as well for different airfoil geometries [8-9], bringing additional insight about the physical mechanisms behind this type of flow control [10]. Parallel to the experimental attempts, numerical predictions of the flow around baseline and modified wings have lately been performed by employing various turbulence models [11-15]. In a nutshell, all of the previous studies indicate that the tubercle leading edge could manipulate the flow and finally delay the stall [16-18]. As shown in Fig. 1, a decrease in lift performance is, nevertheless, observed in pre-stall operation. However, these studies also identified the appearance of locally separated flow and forming a LSB on the suction side, even at relatively low incidences (i.e, pre-stall operation), not only as a consequence of the use of rather thick wing sections but namely resulting from the leading-edge modification. Then, the bubble changes the effective form of an airfoil section and subsequently, aerodynamic performance is degraded. Therefore, controlling the bubble would cause accomplished lead to a class of air vehicle aerodynamically very efficient.

Concerning the literature, the effectiveness of plasma actuator for a separated flow, as an active control device, has been demonstrated [19-20]. But a large actuator profile above the surface may inadvertently trip the flow causing premature separation or an early transition to turbulent flow, increasing the skin friction drag, making the plasma actuator ineffective [21] specially in the case of an MAV.

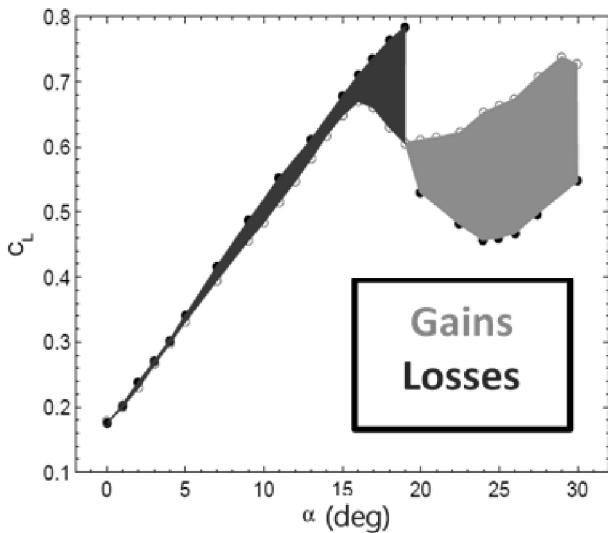


Figure 1. Gains and losses in lift characteristics for a finite-wing with a sinusoidal leading edge (SLE) operating at $Re = 140,000$, with respect to the baseline wing. Experimental data from [18].

Another traditional way to control the flow is blowing air jets inside the boundary layer where the flow would like to separate from the surface [22]. Control of flow over a NACA2415 airfoil which experiences an LSB at a transitional Reynolds number of 2×10^5 is computationally investigated using blowing or suction [23]. Moreover, an AFC via steady normal blowing has been employed at a Reynolds number of 6.4×10^4 on the NACA 643–618 airfoil and the blowing ratio was optimized by maximizing the lift coefficient with minimal power requirement [24]. Furthermore, a tangential blowing has been injected inside the bubble, which was appeared at the trailing edge, by [25]. To have a better efficient of air jets, a pulsating jet has been used to manipulate LSB [26]. However, this blowing actuator needs some equipment such as pump and tubes which increases the weight of MAVs inappropriately. In addition, zero-net-mass-flux injection devices have been recently developed to control the LSB [27], but mass injection into the bubble causes a strong mass imbalance affecting the shear layer entrainment characteristics [28]; consequently, these actuators have been identified as a potential practical means of applying the control strategy outlined in this paper.

In order to overcome the mentioned disadvantages appeared in MAVs application, micro flow control devices consist of morphing plate is being interested whereas a lot of investigations have been carried out on this subject, too. Therefore, a hybrid flow control is numerically investigated to control laminar separation bubble formed at the leading edge of a fixed-wing MAV prototype in the current study. The applied passive method which modifies the leading edge of the wing with a sinusoidal function inspired from nature is proposed to control stall phenomena. However, laminar boundary layer separates at the leading edge and the bubble appears on the pressure surface of the SLE wing at the pre-stall condition which is caused a reduction in the aerodynamic efficiency. Solving this inflection is one of the main objectives of this study and the only way is eliminating or controlling LSBs by

the morphing surface as an effective active control. The actuator surface can deform based on the pressure distribution on the separation area and the airfoil sectional shape is changed correctly.

II. NUMERICAL METHODOLOGY

A. Computational Meshes

A C-H-topology was selected to produce the computational meshes around the models. The far field boundary was set at a distance of $20c$ in upstream and downstream of the wing and $13c$ in the spanwise directions from the wing tip. In these simulations, a periodicity condition was imposed at the spanwise face boundaries of the computational domain. Finally, as the flow remained incompressible in all studied cases, a simple open boundary condition was used at the outflow section at a distance of $12c$, and no-slip conditions were applied to the wall surfaces of the wing. The domain extension was designed so that the inlet and outlet planes did not affect the flow over the wing vicinity.

To produce hexahedral elements in the mesh, the computational domain was split into four volumes. Each volume was meshed individually to have a desired cell density in the region; although it is a time-consuming process to mesh multiple volumes, doing so provided control over the mesh density. The cell quality is also important to ensure a good mesh, which is measured by the parameters equiskew and aspect ratio. The aspect ratio and equiskew of cells are maintained within the range throughout the domain. The leading edge protuberance induces more complexity to the mesh procedure with hexahedral elements near the surface of the wing. To avoid inverted cell volumes and high skewness, the least possible cell distance near the wall is applied while the maximum value of Y^+ was around 1 and the minimum requirement for DES model[29] was satisfied. Concerning the computational limits on the size of the grid, different numerical meshes were employed in the analysis of the flow around the wing. Then, the pressure coefficient distribution on the wing surface was compared for all the meshes and that mesh was kept unchanged irrespective of the turbulence model has been applied. As a consequence, the overall amounts of cells was 1.35×10^7 for aspect ratio 1.5 (Fig. 2).

B. Numerical Method

The computational procedure used a SIMPLE (Semi-Implicit Method for Pressure-Linked Equations) pressure-velocity coupling and a second-order accurate spatial discretization for the pressure. The QUICK (Quadratic Upwind Interpolation for Convective Kinematics) scheme was used in the discretization of momentum and turbulence equations.[30] However, the time integration was performed employing a second-order accurate implicit scheme to alleviate numerical stability restrictions. The time step used was 0.0025 s in all simulations. The model chord and the freestream velocity were fixed to 0.232 m and 8.815 m/s, respectively. It corresponds to a Reynolds number Re of $140,000$, within the typical range of operation of MAVs. In a

significant number of cases, the simulations had to be carried out for longer than 40 s in order to reach a stable (unsteady) behavior unaffected by initial transients. In this study, the model equation and the interactions between the flow and structure are carried out via writing suitable fluid-structure interaction (FSI) code.

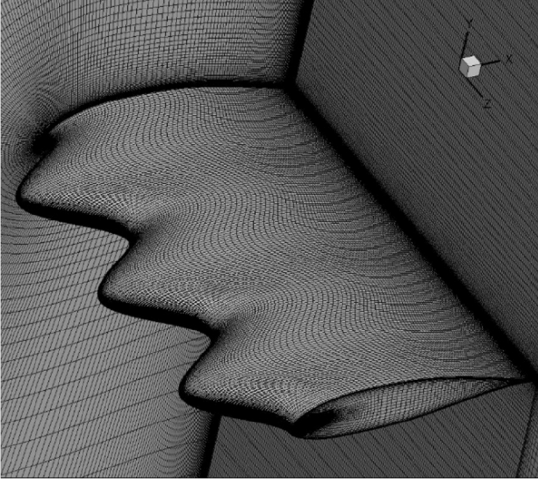


Figure 2. Illustration of the computational mesh for tubercle wing AR=1.5

C. Turbulence Modeling

Taking into account the geometry of the models and the selected Reynolds number, LES, and DNS (Direct Numerical Simulation) were deemed too computationally expensive and, therefore, were discarded. It was chosen DDES over unsteady RANS with different shielding function to find the best model for various conditions. DDES approach is known to perform better when massive separations occur,[31] which is expected to arise for the models operating at high angles of attack. Since the original Detached Eddy Simulation (DES) demonstrated an artificial separation which depends on the grid spacing and not the flow physics,[32] the switch zone from RANS to LES model could be protected by shielding functions. The resulting formulation was named Delayed option.[33] The mentioned method is a hybrid between LES and RANS, as it uses the latter to resolve the boundary layer. For this purpose, the selected turbulence model was the SST $k-\omega$. [32] The reason is twofold: firstly, because this modeling procedure can be coupled with transition prediction via a transport equation for intermittency; secondly, because of the superior performance of this model at reducing the mesh influence of the DDES limiter in the RANS boundary layer [31].

D. Validations

To check the degree of accuracy in the present CFD data, the aerodynamic coefficients are compared with the experimental data obtained by this study. The SLE wing model with AR=1.5 is chosen, and its lift (CL) and drag (CD) coefficients are compared with the experimental ones, as

shown in Fig. 3. The comparison demonstrates that the numerical results are in excellent agreement with those of experimental values. Usually, the CL values are easy to predict because they are mainly due to the pressure difference between the upper and lower surfaces of the wing. Typically, the CD values show poor agreement in turbulent flows since they are primarily caused by skin friction especially in high angle of attack. However, the values shown here have a good deal.

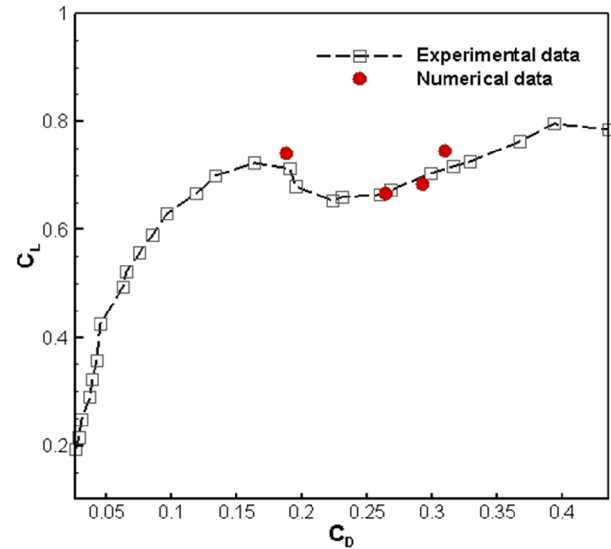


Figure 3. Polar comparison of lift and drag coefficients of modified wing between present numerical and experimental outputs [34] at AR=1.5.

E. Morphing geometry and model equation

More recently, the development of new actuation devices and material systems has enabled novel approaches to flow control still to be explored. These systems deform the surface of the airfoil to introduce disturbances into the flow. Additionally, they would no longer be a source of additional drag in the switched-off condition. Therefore, a thin, flexible macro-fiber composite (MFC) actuator is considered here to morph the surface of an airfoil at such low Reynolds number flow. When embedded in a surface or attached to flexible structures, such actuators provide a distributed force with little power consumption. These actuators are also very light and easy to integrate to the surface of an airfoil, thus maximizing their possible aerodynamic gains. MFC actuators consist of three main components: 1) a sheet of aligned piezoceramic fibers; 2) a pair of thin polymer films etched with a conductive electrode pattern; and 3) an adhesive matrix material. It is also noteworthy that these systems only provide very small deformation amplitudes, and they are very susceptible to the fluid loading and have a constant production of maximum deflection. In case of small deflections, the force and the corresponding shape of the beam can be approximated by using a Rayleigh-Ritz weighted residual method [35]. The force induced by the fluid flow is obtained from the pressure distribution and wall viscous shear stress by integration over the surface of the morphing surface. The spatially distributed

fluid force in each mesh cell is projected onto the mass normalized eigenfunctions, as follows:

$$f(t) = \int_{x=0}^L (f_p(x,t) + f_v(x,t)) \phi_r(x) dx \quad (1)$$

where $f_p(x,t)$ and $f_v(x,t)$ are the net pressure and viscous forces acting on the mentioned surface. Also $\phi_r(x)$ is the weighting function for the first-mode shape assumed to be:

$$\phi_r(x) = 1 - \cos\left(\frac{2\pi x}{L}\right) \quad (2)$$

In each time step, the fluid-induced force f is assumed constant and used in the solution of the structure equation. The force is applied to the center of beam and, as shown in Fig. 4, the deflection of each point (y) can be obtained by the following equation:

$$y(x) = \frac{fx}{48EI} (3L^2 - 4x^2) \quad (3)$$

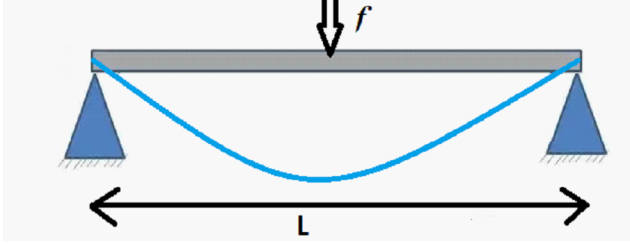


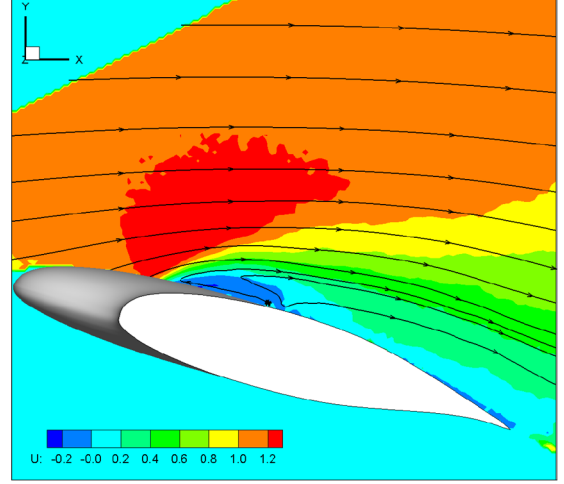
Figure 4. Hinted end beam used as a morphing geometry model.

III. RESULTS AND DISCUSSIONS

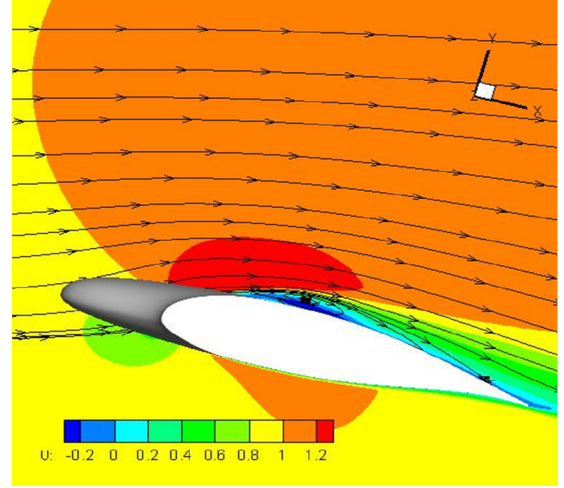
A. Effect of Leading Edge Modification

As Fig. 1 illustrated, sinusoidal leading edge modification has a positive effect in post-stall angles when compared to the baseline wing; but, the wing efficiency was damaged specially in pre-stall condition. Since a laminar separation bubble (LSB) was appeared on the suction side of SLE wing model at the trough cross-section based on Stereo PIV images in [34, 36], the numerical simulation is carried out in this study to obtain more details of flow field. As noted in previous study [37], RANS models have poor performance in the separated flow regions and otherwise, a high mesh resolution in wall-bounded flow would be required in resolved turbulence models such as LES which increases the computational costs. Then, a hybrid RANS/LES modeling is an attractive alternative approach to combine the advantages of both RANS and LES models. Therefore, IDDES model was introduced which combines WMLES and DDES models and the laminar separation bubble could correctly forecast by this approach, simulate a tiny reattached bubble and without any momentous trailing edge separation. To have a better comparison, the streamline contour plots of normalized x-velocity at the trough section of SLE wing were compared to the experimental one [34] at AOA=15°. Apparently, in Fig. 5, the IDDES model is able to generate a turbulent boundary layer over the upper surface, leading to

laminar separation at the leading edge. Furthermore, this model operated very well at the trailing edge, thus seemingly producing results that are closer to those obtained with Stereo PIV. In this figure, the ability of correctly reproducing an experimental operating condition characterized by capturing the laminar separation bubble on the wing can be seen as an adequate quality of the model and the same approach would be therefore used in the entire following cases.



(a)



(b)

Figure 5. Normalized time-averaged x-velocity obtained by stereo PIV measurement [34] and IDDES model around the tubercle wing at AOA=15 deg.

B. Active Flow Control System

The separated bubble alters the effective shape of SLE wing, and as a result of this, the accelerated flow area in the suction side would be smaller comparing with traditional wing model which influences on the aerodynamic coefficients. Honestly, the flow in the mentioned low Reynolds number is laminar and is dominated by viscous effects. Due to the low momentum, the flow could not move to downstream, and it

tends to separate before being turbulent. After laminar flow separation, the flow structure becomes sharply irregular, and under this circumstance, a transition phenomenon from laminar to turbulent occurs. Since the flow in the free stream is more energetic, the turbulent mixing process redeploys high-momentum fluid to the separated layer and then confronts to the adverse pressure gradient, and finally, the flow is squeezed to reattach. Moreover, some parameters such as Reynolds number, incidence angle, surface roughness, wing shape and free stream turbulence play a significant role on the dynamic of LSB; however, the balance between two competitors, high-momentum flow and adverse pressure gradient, defines the length of bubble. Therefore, morphing surface can modify the wing shape and depending on the pressure distribution on the wing surface, it is deformed and the separation bubble did not form as shown in Fig. 6. On the other word, LSB generates a low pressure area on the surface and the morphing surface deforms positively.

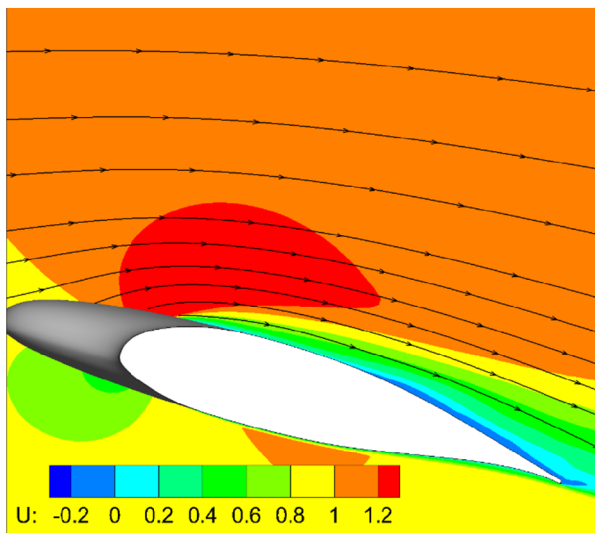


Figure 6. Normalized time-averaged x-velocity obtained by IDDES model around the tubercle wing with morphing actuator.

CONCLUSION

Numerical investigation of the flow over the finite tubercle wing in $AR=1.5$ was conducted at $Re=140,000$. Initially, the effect of leading edge shape modification of wing as a passive stall control was studied and the most important conclusion from passive control is that this modification has provided a better performance in post-stall condition because of appearing the superior streamwise vortices generated by the tubercles at the leading edge and as a result of this, the intensified momentum transport at peak and trough sections intend to maintain lift and preventing stall. In contrast, this passive control did not operate positively in pre-stall circumstances and the lift coefficient has a drop compared with the baseline wing. Comparison of the computed results with the experimental data on the SLE wing has also carried out which has effectively demonstrated a presence of laminar separation bubble as the main reason of this differences.

To solve the aforementioned discrepancies, an active flow control has been designed in this investigation, focusing on the effect of morphing surfaces on the topology of the flow and laminar separation bubble at low Reynolds number. Therefore, the actuator was established in the trough section of wing where the bubbles appear. Finally, the results demonstrated that the morphing surfaces had a substantial impact in pre-stall regimes such that the lift coefficient revived in these incidence angles.

REFERENCES

- [1] F. Fish and J. Battle, "Hydrodynamic design of the humpback whale flipper," *J. Morphol.*, vol. 225, no. 1, pp. 51–60, 1995.
- [2] C. Canning et al., "Population-level lateralized feeding behaviour in North Atlantic humpback whales, *Megaptera novaeangliae*," *Anim. Behav.*, vol. 82, no. 4, pp. 901–909, 2011.
- [3] F. E. Fish, L. E. Howle, and M. M. Murray, "Hydrodynamic flow control in marine mammals," *Integr. Comp. Biol.*, vol. 48, no. 6, pp. 788–800, Dec. 2008.
- [4] D. Miklosovic, M. Murray, and L. Howle, "Experimental evaluation of sinusoidal leading edges," *J. Aircr.*, vol. 44, no. 4, pp. 1404–1408, 2007.
- [5] D. S. Miklosovic, M. M. Murray, L. E. Howle, and F. E. Fish, "Leading-edge tubercles delay stall on humpback whale (*Megaptera novaeangliae*) flippers," *Phys. Fluids*, vol. 16, no. 5, p. L39, 2004.
- [6] M. Gad-el-Hak, *Flow control: passive, active, and reactive flow management*. Cambridge University Press, 2006.
- [7] H. Carreira Pedro and M. Kobayashi, "Numerical study of stall delay on humpback whale flippers," in 46th AIAA Aerospace Sciences Meeting and Exhibit, 2008.
- [8] M. Zhang, G. Wang, and J. Xu, "Aerodynamic control of low-Reynolds-number airfoil with leading-edge protuberances," *AIAA J.*, vol. 51, no. 8, pp. 1960–1971, 2013.
- [9] M. Zhang, G. Wang, and J. Xu, "Effect of humpback whale-like leading-edge protuberances on the low Reynolds number airfoil aerodynamics," *Fluid-Structure-Sound Interact.*, pp. 107–113, 2014.
- [10] N. Rostamzadeh and K. Hansen, "The formation mechanism and impact of streamwise vortices on NACA 0021 airfoil's performance with undulating leading edge modification," *Phys. Fluids*, vol. 26, no. 10, p. 107101, 2014.
- [11] P. Watts and F. Fish, "The influence of passive, leading edge tubercles on wing performance," in Proc. Twelfth Intl. Symp. Unmanned Untethered, 2001.
- [12] A. Dropkin, D. Custodio, C. W. Henoach, and H. Johari, "Computation of flow field around an airfoil with leading-edge protuberances," *J. Aircr.*, vol. 49, no. 5, pp. 1345–1355, Sep. 2012.
- [13] J. Favier, A. Pinelli, and U. Piomelli, "Control of the separated flow around an airfoil using a wavy leading edge inspired by humpback whale flippers," *Comptes Rendus Mécanique*, vol. 340, no. 1, pp. 107–114, 2012.
- [14] H. Arai, D. Yasuaki, N. Takuji, and M. Hidemi, "Numerical simulation around rectangular wings with wavy leading edge," *J. Japan Soc. Nav. Archit. Ocean Eng.*, vol. 12, pp. 33–41, 2010.
- [15] A. Malipeddi, N. Mahmoudnejad, and K. Hoffmann, "Numerical analysis of effects of leading-edge protuberances on aircraft wing performance," *J. Aircr.*, vol. 49, no. 5, pp. 1336–1344, 2012.
- [16] H. Johari, C. W. Henoach, D. Custodio, and A. Levshin, "Effects of leading-edge protuberances on airfoil performance," *AIAA Journal*, vol. 45, no. 11, pp. 2634–2642, 2007.
- [17] D. Custodio, C. W. Henoach, and H. Johari, "Aerodynamic characteristics of finite span wings with leading-edge protuberances," *AIAA J.*, vol. 53, no. 7, pp. 1878–1893, Jul. 2015.
- [18] J. L. E. Guerreiro and J. M. M. Sousa, "Low-Reynolds-number effects in passive stall control using sinusoidal leading edges," *AIAA J.*, vol. 50, no. 2, pp. 461–469, Feb. 2012.

- [19] M. Sato et al., "Mechanisms for laminar separated-flow control using dielectric-barrier-discharge plasma actuator at low Reynolds number," *Phys. Fluids*, vol. 27, no. 11, p. 117101, Nov. 2015.
- [20] M. G. De Giorgi, A. Ficarella, F. Marra, and E. Pescini, "Micro DBD plasma actuators for flow separation control on a low pressure turbine at high altitude flight operating conditions of aircraft engines," *Appl. Therm. Eng.*, vol. 114, pp. 511–522, 2017.
- [21] T. West and S. Hosder, "Numerical investigation of plasma actuator configurations for flow separation control at multiple angles of attack," 6th AIAA Flow Control Conf., 2012.
- [22] A. Farhadi, E. G. Rad, and H. Emdad, "Aerodynamic multi-parameter optimization of NACA0012 airfoil using suction/blowing jet technique," *Arab. J. Sci. Eng.*, pp. 1–9, Jul. 2016.
- [23] M. Genç and Ü. Kaynak, "Control of Flow Separation and Transition Point over an Aerofoil at Low Re Number using Simultaneous Blowing and Suction," in 19th AIAA Computational Fluid Dynamics, 2009.
- [24] N. O. Packard, M. P. Thake, C. H. Bonilla, K. Gompertz, and J. P. Bons, "Active control of flow separation on a laminar airfoil," *AIAA J.*, vol. 51, no. 5, pp. 1032–1041, May 2013.
- [25] P. Viswanath and K. Madhavan, "Control of trailing-edge separation by tangential blowing inside the bubble," *Aeronaut. J.*, vol. 108, no. 6, pp. 419–425, 2004.
- [26] Y. H. Choi and H. B. Kim, "Pulsating jet control for manipulating the separation bubble behind the fence," *J. Vis.*, vol. 13, no. 3, pp. 221–228, Aug. 2010.
- [27] O. Marxen, R. B. Kotapati, R. Mittal, and T. Zaki, "Stability analysis of separated flows subject to control by zero-net-mass-flux jet," *Phys. Fluids*, vol. 27, no. 2, p. 024107, Feb. 2015.
- [28] M. Jahanmiri, *Laminar Separation Bubble An overview on research works on characteristics, dynamics, and control of LSBs*. LAP LAMBERT Academic Publishing, 2013.
- [29] P. R. Spalart and C. Streett, "Young-person's guide to detached-eddy simulation grids," 2001.
- [30] J. Pereira and J. M. M. Sousa, "Finite volume calculations of self-sustained oscillations in a grooved channel," *J. Comput. Phys.*, vol. 106, no. 1, pp. 19–29, 1993.
- [31] M. Ilak, P. Schlatter, and S. Bagheri, "Bifurcation and stability analysis of a jet in cross-flow: onset of global instability at a low velocity ratio," *J. Fluid*, vol. 696, pp. 94–121, 2012.
- [32] F. Menter, M. Kuntz, and R. Langtry, "Ten years of industrial experience with the SST turbulence model," *Turbul. heat mass Transf.*, 2003.
- [33] P. R. Spalart, S. Deck, M. L. Shur, K. D. Squires, M. K. Strelets, and A. Travin, "A new version of detached-eddy simulation, resistant to ambiguous grid densities," *Theor. Comput. Fluid Dyn.*, vol. 20, no. 3, pp. 181–195, Jul. 2006.
- [34] A. Esmaili, H. E. C. Delgado, and J. M. M. Sousa, "Numerical simulations of low-Reynolds-number flow past finite wings with leading-edge protuberances," *J. Aircr.*, vol. 55, no. 1, pp. 226–238, Oct. 2018.
- [35] H. D. Akaydin, N. Elvin, and Y. Andreopoulos, "Energy harvesting from highly unsteady fluid flows using piezoelectric materials," *J. Intell. Mater. Syst. Struct.*, vol. 21, no. 13, pp. 1263–1278, Sep. 2010.
- [36] H. Delgado, A. Esmaili, and J. M. M. Sousa, "Stereo PIV measurements of low-aspect-ratio low-Reynolds-number wings with sinusoidal leading edges for improved computational modeling," in Proc 52st AIAA Aerospace Sciences Meeting, 2014.
- [37] A. Esmaili and J. M. M. Sousa, "Influence of wing aspect ratio on passive stall control at low Reynolds number using sinusoidal leading edges," in 29th Congress of the International Council of the Aeronautical Sciences, 2014.

An introduction to the real based method for 3D aerodynamic analysis of the insect flyers at low *Reynolds* numbers

Nasim Chitsaz^{1*}, Natania Yap¹, Romeo Marian¹ and Javaan Chahl^{1,2}

¹School of Engineering
 University of South Australia
 Adelaide, Australia
 nasim.chitsaz@mymail.unisa.edu.au

²Joint and Operations Analysis Division, Defence Science
 and Technology Group
 Adelaide, Australia

Abstract— The wings of a flying insect are corrugated with varying material and complexity which determine their aerodynamic performance and maneuverability during flight. The wing corrugations vary span-wise which make a complex 3D structure. This complexity raises a need to have a full three-dimensional reconstruction of the wing for aerodynamic analysis. However, 3D scanning methods like Micro-Computed Tomography and 3D laser scanning are destructive and expensive operations. This paper aims to present a new method for aerodynamic analysis of 3D corrugated wings. This method is an applied non-destructive photogrammetric method for simulating the wing structure including all the details and corrugations across the wing. The main aerodynamic parameters of the forewing (FW) of five species, such as maximum chord location, wing area and wing length are presented. Also, the three-dimensional computational fluid dynamics (CFD) was applied, and aerodynamics results were evaluated for five different species of insects with the same scale for the first time. The results show that by using the presented method, it is possible to measure the characteristics of bio-inspired 3D wings and distinguish the influence of the various corrugations on aerodynamic performance.

Keywords- *Aerodynamics performance; Bio-inspired; CFD; flying insect; 3D reconstruction*

Nomenclature

$b/2$	Wing semi-span
C_{max}	Maximum chord
$C_{max, L}$	Maximum chord location
$C_{min, tip}$	Tip chord
C_{mean}	Mean chord
α	Sweep angle

I. INTRODUCTION

Dragonflies are considered as a model for flapping wings of micro air vehicles (MAVs). In general, from more than 3600 known dragonfly species, only a few have been studied. There is a need to investigate the aerodynamic properties of different corrugation patterns of dragonfly species to optimise the flapping wings of MAVs. Recently, various aerodynamic analysis of insects' wings were investigated in different flight modes such as gliding [2] and hovering [3]. Insects can fly indoors and outdoors [4] at low Reynolds number [5]. Computational analysis is one of the methods to analyse the aerodynamics parameters and flow around the wing which leads to generation of lift and drag during flight. However, the aerodynamic performance of corrugated bio-inspired wings is still challenging due to the complexity of the wing structure, various profile and flapping flexible wing at low Reynolds number. Thereby, the different 3D reconstructed wing similar to the nature with all details and corrugation is yet necessary.

As shown in Fig. 1, the wing of most insects can be given familiar aeronautical parameter definitions. One of the important parameters is $b/2$ (half wingtip to half wingtip span) which is called wing semi-span [6]. Other parameters are the chord, which is the straight distance between leading edge (LE) [1] and trailing edge (TE), and the longest straight line from LE to TE is called "maximum chord" [1, 7].

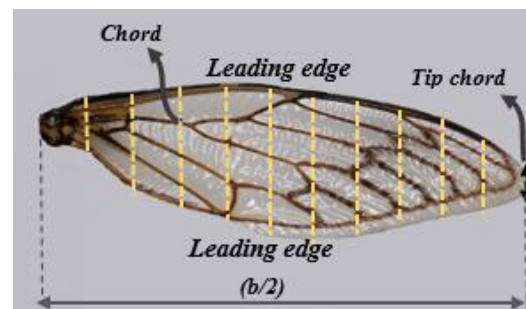


Figure 1 Aeronautical parameters of the wing

The aim of this paper is to provide the paper is to present the first aerodynamic analysis of 3D corrugated wings from multiple species and also a preliminary sizing of the main insect wing parameters, including wingspan, maximum/minimum chord length and their location. These parameters are exported from the solid model of five different insect wings by the new non-destructive 3D reconstructed methods that are required for optimisation of the next generation of corrugated bio-inspired flapping wings. Moreover, due to the effect of wing morphology on aerodynamic performance and maneuverability, computational analysis is conducted on five 3D reconstructed models.

II. MATERIAL AND METHODS

Fig. 2 shows the overall procedure of 3D corrugated wing model creation from a real insect specimen. There are three main steps including (1) taking multiple high-resolution photos of the insect, (2) creating the 3D reconstructed model and (3) 3D CAD model is prepared for both experimental and numerical analysis.

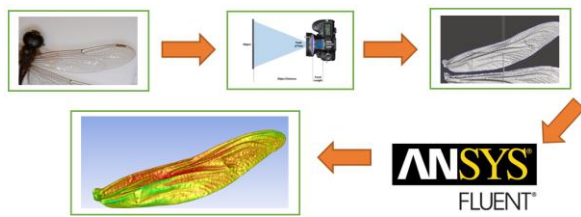


Figure 2 Real insect to the 3D corrugated wing structure

The non-destructive photogrammetry method is fast and cost-effective through using of a conventional digital camera (1). This method was used to create the three-dimensional corrugated wing model by taking up to 100 photos of each sample. Experimental analysis was performed on five selected categories of flying insect to demonstrate the ability of this method in computational analysis. According to the study, the five insects were selected from the insect collections of the South Australian Museum and South Australian Research and Development Institute (SARDI) Entomology Science Program.

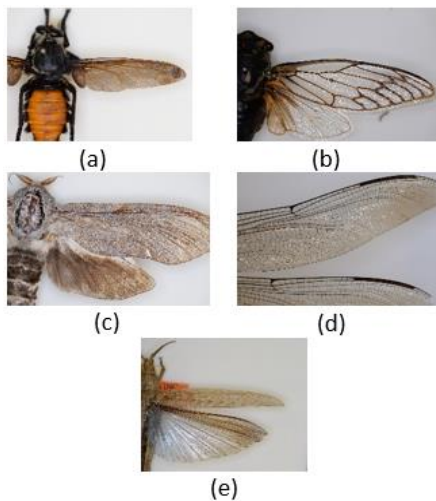


Figure 3 Different species representing different orders with various shape and dimension of the wing, a) Diptera, b) Hemiptera, c) Lepidoptera, d) Odonata and e) Orthoptera

The insects in this paper (Fig. 3) are from different species including Diptera, Hemiptera, Lepidoptera, Odonata and Orthoptera.

As shown in Fig. 3, four of the selected species have four wings rather than two wings. In this study, the main aerodynamic parameters for flapping wing were measured.

These parameters play an important role in flight performance and maneuverability of flying insects. Applying a laser scanner is another possible way to make a 3D model of the wing, but it is a time consuming and costly process rather than photogrammetry. Moreover, using a laser scanner may lead to destruction the wing (2) while photogrammetry is a non-destructive and accurate method. In this method, a high-resolution camera was installed above the object and automatically captured numerous photos by sliding along a single axis (Fig. 4). Then, commercial photogrammetry and 3D modelling software were used to reconstruct a 3D model of the wing, (3) and various formats were exported such as .stl, .ply formats. These 3D models were used for aerodynamics analysis. Fig.5 shows the 3D reconstruction process of the wing of Hemiptera. It is important to note that the generated 3D model can be edited as a term of the surface smoothness. In other words, it can be used for design and analysis of the wing with either corrugated section or smooth ones.



Figure 4 Camera set-up for photogrammetry analysis of the insect wings

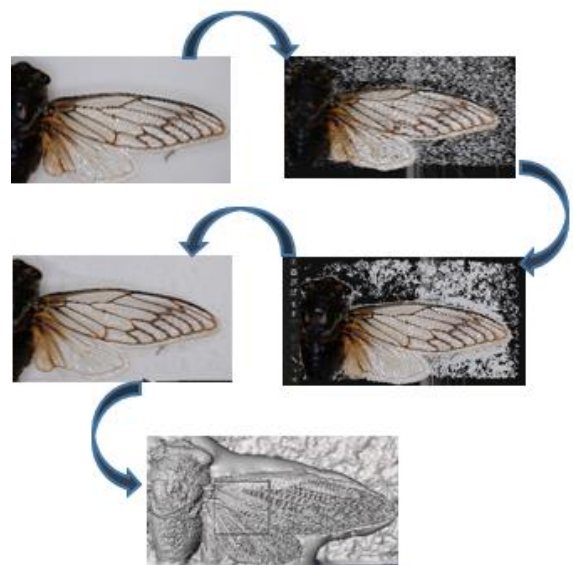


Figure 5 Three dimensional reconstruction process of Hemiptera FW

Table 1 Geometry parameters of corrugated FW of different flying insects

No	Superfamily	Family	FW geometry parameters (mm)				Non-dimensional ratio				
			$b/2$	C_{max}	$C_{max, L}$	C_{mean}	$2 \times C_{max}/b$	$2 \times C_{max} L/b$	$2 \times C_{mean}/b$	$2 \times C_{min, tip}/b$	AR
1	Diptera	Asilidae, Blepharotes coriarius (Wiedemann 1830)	34.44	9.66	13.37	6.68	0.28	0.39	0.19	0.01	10.3
2	Hemiptera	Cicadidae, Macrotristria sylvara (Distant 1901)	58.74	18.03	31.3	11.21	0.31	0.53	0.19	0.037	10.5
3	Lepidoptera	Cossidae, Xyleutes cinerus Tepp. (1936)	73.89	23.29	48.18	16.32	0.31	0.65	0.22	0.01	9.06
4	Odonata	Petaluridae, Petalura, Incentissima	84.77	16.24	49.67	12.65	0.19	0.59	0.15	0.01	13.3
5	Orthoptera	Orthoptera, Acrididae, Coryphistes ruricola	48.8	7.4	17.21	5.29	0.15	0.35	0.11	0.01	18.4

Table 1 shows the main geometrical aerodynamic parameters of the FW wings of the different five categories of superfamily derived by the photogrammetry method. It includes the basic aerodynamics parameters such as wing semi-span, maximum/minimum and mean chord length, maximum chord location and also non-dimensional ratio for FW. The maximum semi-span and chord length are around 85 mm 24 mm, respectively and the Aspect Ratio (AR) varies from 10 to 18 in this study.

III - COMPUTATIONAL ANALYSIS

In order to evaluate the feasibility of the presented 3D reconstructed method in aerodynamics analysis, the computational fluid dynamics is performed on the insects' 3D reconstructed wing. For this purpose, the 3D models of the corrugated wings consisting of irregular veins and complex details were imported to ANSYS Workbench and were analyzed with computational fluid dynamics. The commercial software ANSYS fluent 19 was used to demonstrate the pressure and velocity profiles of the wings.

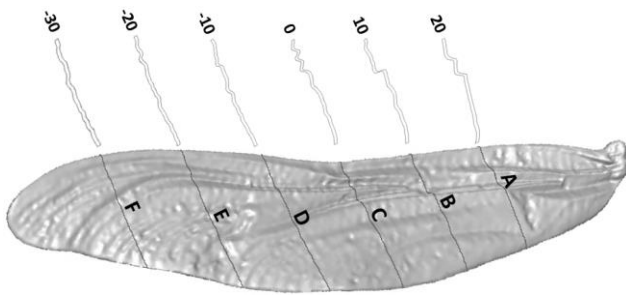


Figure 6 Corrugation patterns of the wing at six different sections

To get a better understanding of the effect of the corrugation on the aerodynamic performances of the wings, results were acquired at six different sections of the wings (-30, -20, -10, 0.0, 10 and 20 mm) as shown in Fig. 6. It can be seen that the

presented model can capture the corrugation patterns of the wings through the span of the wing. It is also evident that the root-to-mid sections have more corrugated patterns compared with the other half section. It is probably because of this fact that the root-to-half section takes part in a higher percentages of the lift production of the wing. However, more observations are required to validate this statement.

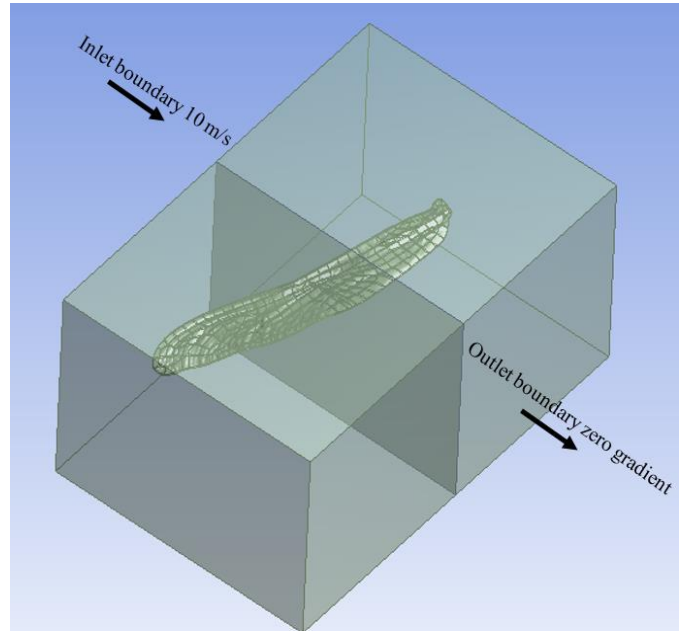


Figure 7 Boundary condition and fluid grid view of the Odonata 3D reconstructed wing

The 3D file was imported to SpaceClaim which is a solid modelling CAD software, and the geometry and mesh were developed. Due to the complexity of the 3D wing the high-performance, complicated meshes and many facets desktop PC including GPU (GeForce GTX 1080 Ti) was applied.

At this setting, the boundary conditions have been considered the same for all six corrugated wings. For this purpose, the non-slip wall boundary condition a rectangular fluid domain with the dimension of 20C, 60C and 30C was modelled (Fig. 6) at flight velocity of 10 m/s at the inlet and zero gradient pressure at the outlet. To solve the problem, the pressure based Navier-Stokes equation was used.

IV - RESULT AND DISCUSSION

Flow analysis around the structure of the wings was performed. Fig. 8 illustrates the pressure on the 3D corrugated Odonata Wing. In addition, Fig. 9 shows the pressure and velocity contours of the Odonata corrugated for a wing at six various sections of the wing. The flow recirculation zones in the corrugation valleys create turbulence. Indeed the flow separation vortices strapped in the peaks and valleys of the corrugated wing which lead to a reduction of flow separation and delayed onset of stall. So the corrugated aerofoil generated more lift to drag ratio and caused a delayed stall because of the suppression of flow separation.

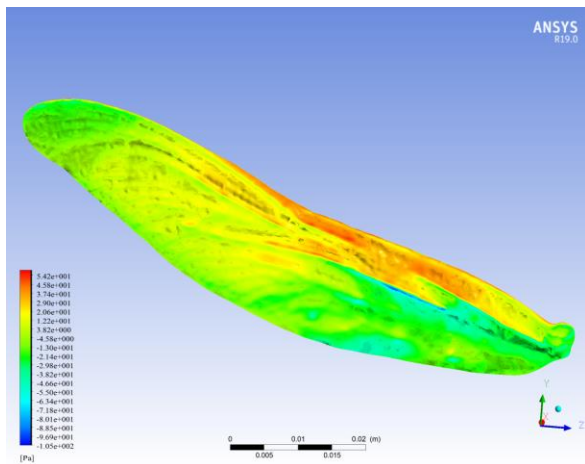


Figure 8 pressure contour on the 3D corrugated Odonata Wing

As a result, the aerofoil contour is transformed such that the flow patterns away from the immediate effect of the corrugations is smooth and representative of a conventional aerofoil for some sections (4).

Both changes in aerofoil through the span and also twist angle can affect the aerodynamic performance of the wing. Using our method relative angles span-wise across the wing as well as chord-wise aerofoil variations are preserved so our two dimensional approach considers the wing as it would be positioned in gliding flight. The location and the amount of C_p change through the sections considering twist angle is preserved.

For example, the maximum coefficient of pressure (C_p) at section *C* (mid-span) is 1.4 which has been placed at 41% of the chord from the leading edge.

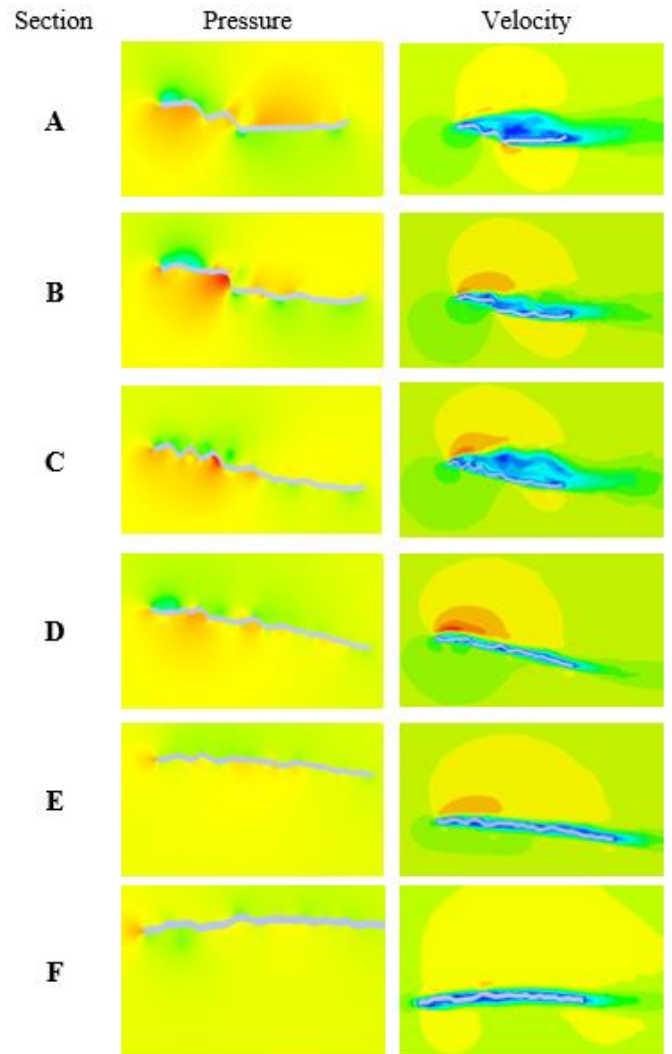


Figure 9 Pressure and vorticity contours at 10 m/s for the five wing cross-sections of Odonata

It is interesting to note that the less corrugated sections at *E* and *F* show patterns of velocity and pressure contours that are more similar to conventional aerofoils. Flow disturbance far from the wing surface is more visible in sections *A*, *B* and *C* due to the effect of both the corrugations and twist variations.

The same results for section *C* of all five species have been illustrated in Fig. 10. The presented model can capture the effect of corrugation pattern changes through the span length of the wing.

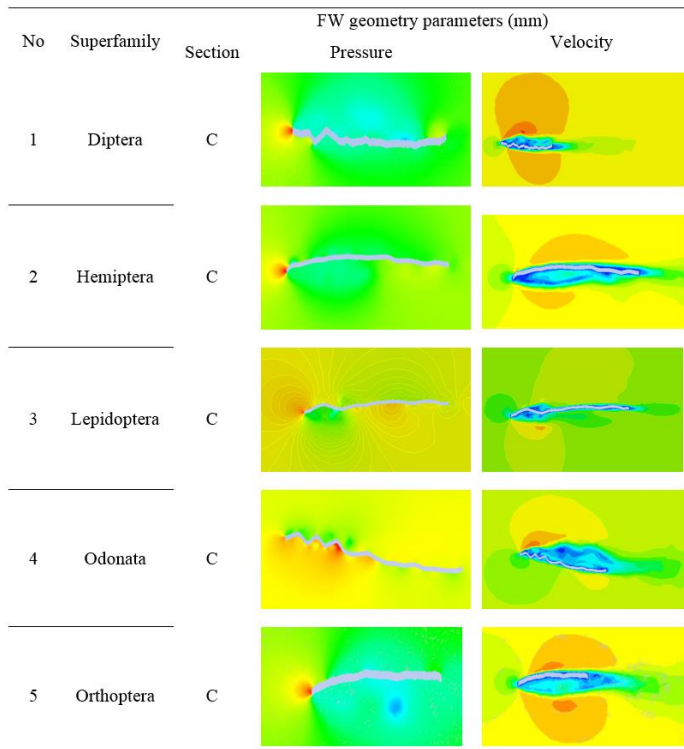


Figure 10 Pressure and velocity contours of five different superfamilies at C section of xy plane

V -CONCLUSIONS

In this paper, a new methodology was presented that allows the efficient capture of exotic aerodynamic surface shapes from collections of flying insects, with the hope of achieving a deeper understanding of biological wing design. The work flow from capture of the data to computational fluid dynamic analysis was executed leading to a series of CFD analysis. This method is non-destructive and can apply to any type of insect wings living or dead. Further work is required in model validation, both per sample and for the method. In addition the wings are analysed while resting and not loaded by aerodynamic forces, and it is possible that substantial changes may occur due to torsional and bending loads. Deeper analysis

of the membrane and vein structure is required to perform a more complete aerostructural analysis.

ACKNOWLEDGMENT

We would like to thank the South Australian Museum, Adelaide and Mr Kym Perry from the South Australian Research and Development Institute (SARDI) Entomology Science Program for granting access to their collections of insects used in this study. The first author is the recipient of the William T. Southcott Scholarship from the University of South Australia.

REFERENCES

- [1] Sun, X., X. Gong, and D. Huang, A review on studies of the aerodynamics of different types of maneuvers in dragonflies. *Archive of Applied Mechanics*, 2017. 87(3): p. 521-554.
- [2] Chen, Y. and M. Skote, Gliding performance of 3-D corrugated dragonfly wing with spanwise variation. *Journal of Fluids and Structures*, 2016. 62: p. 1-13.
- [3] Xie, C.-M. and W.-X. Huang, Vortex interactions between forewing and hindwing of dragonfly in hovering flight. *Theoretical and Applied Mechanics Letters*, 2015. 5(1): p. 24-29.
- [4] De Croon, G., et al., Design, aerodynamics, and vision-based control of the Delfly. *International Journal of Micro Air Vehicles*, 2009. 1(2): p. 71-97.
- [5] Khurana, M. and J. Chahl. Optimization of the leading edge segment of a corrugated wing. in *SPIE Smart Structures and Materials+ Nondestructive Evaluation and Health Monitoring*. 2014. International Society for Optics and Photonics.
- [6] Hefler, C., H. Qiu, and W. Shyy, Dragonflies Utilize Flapping Wings Phasing and Spanwise Characteristics to Achieve Aerodynamic Performance. *arXiv preprint arXiv:1612.05353*, 2016.
- [7] Gaurav, S., Investigation of Fluid Flow and Aerodynamic Performance of a Corrugated Dragonfly Wing section: A Review. 2016.
- [8] McQuaid, G., P. Millar, and D. Woodward. Use of 3D modeling to assess pothole growth. in *6th International Conference on Bituminous Mixtures and Pavements*, Thessaloniki, Greece. 2015. Taylor & Francis Group London.
- [9] Eren, G., et al., Scanning from heating: 3D shape estimation of transparent objects from local surface heating. *Optics express*, 2009. 17(14): p. 11457-11468.
- [10] Oniga, E., M. Macovei, and A. Negrila, Accuracy Assessment of a 3D Model Reconstructed from Images Acquired with a Low-Cost UAV. 2017, *Modern Technologies for the 3rd Millennium (23-24 March, 2017-Oradea, Romania)*.
- [11] Khurana, M. and J. Chahl. A computational fluid dynamic study of a bioinspired corrugated aerofoil for micro air vehicles. in *AIAC15: 15th Australian International Aerospace Congress*. 2013. Australian International Aerospace Congress.

Algorithms

Investigation of advection-diffusion problems and simulations using the lattice Boltzmann method and the ArrayFire library for high-performance computing on GPU

Michel Ho, Jesús García Pérez, Sébastien Leclaire, Marcelo Reggio & Jean-Yves Trépanier

Department of Mechanical Engineering
Polytechnique Montréal
Montreal, Canada
michel.ho@polymtl.ca

ABSTRACT

The lattice Boltzmann method (LBM) is an efficient numerical method to solve numerous problems, such as multiphase flows [1], compressible flows [2] as well as melting and solidification problems [3,4] among others. Its simple algorithm makes the LBM easy to implement for fluid flow simulations with complex geometries and boundary conditions [5,6]. Besides, each computational node has a local behavior regarding macroscopic quantities, making the LBM suitable for parallel computing [7,8].

Along these lines, the ArrayFire [9] library offers several tools for parallel computing on CPU and/or GPU using C/C++ programming language. Unlike other high-performance approaches which may need some thorough learning and programming skills (e.g. OpenCL and CUDA), implementing ArrayFire codes is straightforward with few changes to the basic C++ paradigm. Thus, it allows great computing potential and portability with few programming efforts.

LBM simulations of different advection-diffusion test cases are performed and various results are shown. Comparisons are made between CPU and GPU simulations to evaluate the speedup provided by using the ArrayFire library. The results lead to interesting prospects for large scale simulations with appealing computing performance.

I. REFERENCES

- [1] L. Chen, K. Q., A. Robinson, Y.-L. He et W.-Q. Tao, «Pore-scale modeling of multiphase reactive transport with phase transitions and dissolution-precipitation processes in closed systems,» *Physical Review E*, 2013.
- [2] A. F. Di Rienzo, P. Asinari, E. Chiavazzo, N. I. Prasianakis et J. Mantzaras, «Lattice Boltzmann model for reactive flow simulations,» *Europhysics Letters*, 2012.
- [3] C. Huber, A. Parmigiani, B. Chopard, M. Manga et O. Bachmann, «Lattice Boltzmann model for melting with natural convection,» *International Journal of Heat and Fluid Flow*, pp. 1469-1480, 2008.
- [4] D. Chatterjee et S. Chakraborty, «A hybrid lattice Boltzmann model for solid-liquid phase transition in presence of fluid flow,» *Physics Letters A*, pp. 359-367, 2006.
- [5] D. Gao, Z. Chen et L. Chen, «A thermal lattice Boltzmann model for natural convection in porous media under local thermal non-equilibrium conditions,» *International Journal of Heat and Mass Transfer*, vol. 70, pp. 979-989, 2014.
- [6] Q. Liu et H. Y.-L., «Double multiple-relaxation-time lattice Boltzmann model for solid-liquid phase change with natural convection in porous media,» *Physica A*, vol. 438, pp. 94-106, 2015.
- [7] S. Blair, C. Albing, A. Grund et A. Jocksch, «Accelerating an MPI Lattice Boltzmann code using OpenACC,» chez Proceedings of the Second Workshop on Accelerator Programming using Directives, Austin, 2015.
- [8] V. Heuveline, M. J. Krause et J. Latt, «Towards a hybrid parallelization of lattice Boltzmann methods,» *Computers & Mathematics with Applications*, pp. 1071-1080, 2009.
- [9] P. Yalamanchili, U. Arshad, Z. Mohammed, P. Garigipati, P. Entschew, B. Kloppenborg, J. Malcolm et J. Melonakos, «ArrayFire - A high performance software library for parallel computing with an easy-to-use API. Atlanta: AccelerEyes,» 2015. [En ligne]. Available: <https://github.com/arrayfire/arrayfire>.

VORTICITY-BASED POLYNOMIAL ADAPTATION FOR MOVING AND DEFORMING DOMAINS

Ramin Ghoreishi

Department of Mechanical, Industrial, and Aerospace
 Engineering
 Concordia University
 Montreal, QC, Canada
 ramin.ghoreishi@concordia.ca

Brian C. Vermeire

Department of Mechanical, Industrial, and Aerospace
 Engineering
 Concordia University
 Montreal, QC, Canada
 brian.vermeire@concordia.ca

ABSTRACT

In this paper, a p-adaptive method is presented to solve the Arbitrary Lagrangian-Eulerian (ALE) Navier-Stokes equations. Adaptation is performed based on a non-dimensional vorticity indicator. The complete adaptation framework will be explained in detail in the final paper, only a brief summary is presented herein. We begin by computing the maximum non-dimensional vorticity magnitude on any element according to

$$\kappa_n = \max_{1 \leq i \leq n_q} \bar{\omega}_{n,i}, \quad \bar{\omega}_{n,i} = \frac{|\omega_{n,i}| \Delta x_{\max,n}}{U} \quad (1)$$

where $\omega_{n,i}$ is the vorticity at quadrature point i on element n , $\Delta x_{\max,n}$ is the maximum mesh dimension, n_q is the number of quadrature points on the element, and U is the freestream velocity. We then define the solution polynomial degree on element n based on its maximum non-dimensional vorticity magnitude. Following this approach, elements with large vorticity magnitudes relative to the effective mesh resolution are adapted to higher-degree polynomials, increasing their resolving power.

To illustrate the performance of this strategy, four cases have been studied. Two cases of cross-flow over oscillatory circular cylinders with $Re = 500$ and $Re = 100$, $M_\infty = 0.1$, with coordinates of center of cylinder defined as $x = 0$ and $y(t) = A \sin(2\pi ft)$, where A and f are the amplitude and frequency of the cylinder oscillation. A case of dynamic stall to NACA0012 airfoil undergoing heaving and pitching motions at a low Reynolds number of $Re = 1000$, with $M_\infty = 0.1$, pitching motion of $\alpha(t) = \alpha_0 + \Delta a \sin(2\pi ft + \varphi)$ around the aerodynamic center, and heaving motion of $y(t) = A \sin(2\pi ft)$, where α_0 is the initial/mean angle of attack, Δa is the oscillation amplitude, and φ is the phase shift between the heaving and pitching motions. Finally, a case of a vertical axis wind turbine containing two NACA0012 blades. Time integration is carried out with the classical RK_{44} scheme for all simulations. This adaptation strategy is verified and compared in terms of accuracy and computational cost considering functional targets, namely lift and drag coefficients, of the adaptive k1-k5 and uniform k5 simulations. Computational cost is determined by calculating the total number of degrees of freedom (DoF) of both adaptive and uniform simulations.

Fig. 1 illustrates the polynomial degree for the five-level adaptive simulation. It is verified that the algorithm successfully indicates the location of elements with large vorticity magnitude relative to their element size, leading to refinement of these elements while keeping the degrees of freedom low in elements with smaller vorticity magnitude. The result is a sufficiently accurate, yet more efficient simulation. In fact, it is verified that the adaptive simulation needs almost 4 times less number of DoF than the uniform k5 simulation.

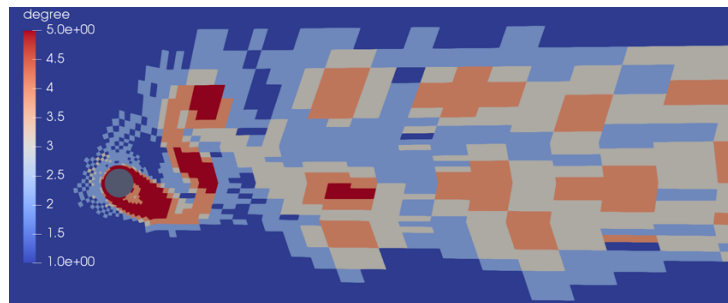


Figure 1 Polynomial adaptation distribution for five-level adaptive computation (k1 – k5) based on vorticity magnitude indicator for cross-flow oscillatory cylinder.

PAIRED EXPLICIT RUNGE-KUTTA SCHEMES FOR COMPUTATIONAL AERODYNAMICS

Siavash Hedayati Nasab

Department of Mechanical and Aerospace Engineering
Concordia University
Montreal, Canada
Siavash.hedayati@concordia.ca

Brian C. Vermeire

Department of Mechanical and Aerospace Engineering
Concordia University
Montreal, Canada
Brian.vermeire@concordia.ca

ABSTRACT

A wide range of practical applications require the solution of locally-stiff systems of equations such as Navier-Stokes and Euler equations. The solution of such systems using an explicit approach such as the popular explicit Runge-Kutta schemes, often proves impractical. Numerical stiffness implies prohibitively small time-steps to be taken to maintain stability, even if only a part of the computational domain is stiff. Implicit schemes typically are used to overcome such limitations. However, implicit approaches are relatively expensive for a global system of linear and nonlinear equations since they require higher storage and higher computational time. Recent work on Implicit-Explicit (IMEX) Runge-Kutta schemes have attracted attention using an implicit scheme in the stiff region and an explicit scheme in non-stiff part. However, these schemes significantly increase the complexity of a solver and still require the solution of a reduced local system of linear or nonlinear equations. While, explicit methods have the disadvantage of being only conditionally stable, they also have several appealing properties. Explicit methods are often preferred due to their simplicity of implementation and suitability for modern core-hardware architecture. Previous work on suitability of explicit Runge-Kutta methods has focused on optimizing their region of absolute stability for large number of steps. In this work, we propose a general formulation for the solution of locally stiff systems of equations, Paired Explicit Runge-Kutta schemes. In fact, these schemes have arbitrarily large numbers of stages with different number of active stages in different regions of the domain which result in different stability polynomial with different absolute stability regions.

In this Paper we introduce a family of third-order Paired Explicit Runge-Kutta (P-ERK) schemes with application to computational aerodynamics. This (P-ERK) approach allows Runge-Kutta schemes with a large number of derivative evaluations and large regions of absolute stability to be used in the stiff parts of the domain, such as the boundary layer, while schemes with relatively few derivatives evaluations are used in non-stiff parts to reduce computational cost. Importantly, different P-ERK schemes with different numbers of derivative evaluations can be chosen based on local stiffness requirements and seamlessly paired with one another. In other words, in a third-order P-ERK scheme with “s” number of stages and “e” number of active stages, we have “e” coefficients in stability polynomial where 3 of them are constraint by order conditions and “e-3” of them can be used for optimization. Hence as we increase “e” we have more coefficients to optimize and larger region of absolute stability that can be used in stiff regions. We demonstrate that P-ERK schemes obtain their designed order of accuracy using the advection equations with arbitrary combination of schemes. Then we demonstrate that P-ERK schemes can achieve speedup factors in excess of 5x for aerodynamics simulations including wall-resolved Large Eddy Simulation (LES) of flow over low Reynolds number airfoils.

Then, we demonstrate the utility of P-ERK schemes in combination with high-order unstructured spatial schemes. For example, for a flow over an airfoil SD7003 with an angle of attack of 8° and with $Ma=0.2$ and $Re=60,000$ and ratio of specific heat of $\gamma=1.4$ the P-ERK_{16,16,2}, P-ERK_{16,12,2}, P-ERK_{16,8,2}, P-ERK_{16,4,2}, P-ERK_{16,3,2} and P-ERK_{16,2,2} scheme for the stiff to non-stiff regions, respectively, has shown a speedup of 4.48x in runtime. Figure 1 is a picture of this simulation using aforementioned second-order family of P-ERK schemes.

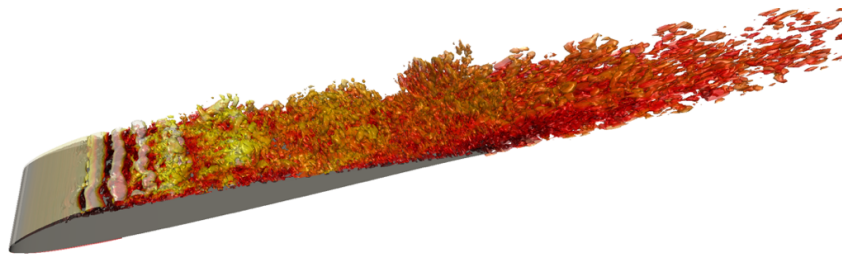


Figure 1 Simulation over SD7003 Airfoil using P-ERK schemes

Deep Neural Networks for Non-Ideal Property Evaluation in Supercritical Flows

Petro Junior Milan, Zhaoyi Xu and Vigor Yang

School of Aerospace Engineering
Georgia Institute of Technology
Atlanta, GA, USA
vigor.yang@aerospace.gatech.edu

Jean-Pierre Hickey

Department of Mechanical and Mechatronics Engineering
University of Waterloo
Waterloo, ON, Canada

ABSTRACT

Many propulsion devices such as liquid rocket engines and gas turbines operate under transcritical or supercritical conditions, where the real fluid properties must be taken into account to model the thermodynamic non-idealities and transport anomalies. The use of such complex non-ideal state equations is prohibitively expensive and can account for a significant portion of the total computation time in a given numerical simulation [1]. To alleviate the situation, a deep neural network (DNN)-based strategy [2] is proposed for an efficient real fluid property evaluation. The training and validation datasets for the DNN consist of thermodynamic and transport properties that span the thermophysical region of interest. The weights and biases are obtained using the back-propagation method with the Adam optimization algorithm. The rectified linear unit (ReLU) activation function is used in the hidden layers. The proposed DNN-based technique is implemented and tested in a fully-compressible, two-dimensional, large eddy simulation of supercritical turbulent mixing of liquid oxygen and gaseous methane flows around a splitter-plate. A Smagorinsky eddy viscosity model is used for turbulence closure. The operating pressure is 10 MPa, which is about twice the value of the critical pressure of oxygen (5.04 MPa), and the characteristic Reynolds number is $1.5 \cdot 10^5$. The thermodynamic properties, including density, enthalpy and specific heats, along with their partial derivatives, are evaluated according to fundamental thermodynamic theories and the modified Soave-Redlich-Kwong equation of state. Transport properties, including thermal conductivity and dynamic viscosity, are estimated according to Chung's method, which is based on the extended corresponding-state principle. Binary mass diffusivity is obtained by Fuller's empirical correlation for low-pressure values combined with the Takahashi's correction to account for high-pressure effect. The computational mesh consists of 1.2 million cells. The numerical framework employs a finite-volume methodology along with a preconditioned dual time-stepping technique [3], which allows an all Mach number formulation. In the model problem under consideration, the pressure fluctuation is very small compared to its mean value in the flowfield. Thus, only temperature and mass fraction of oxygen are chosen as inputs for the DNN. Numerical results using the DNN model are compared against a benchmark case, where the real fluid properties are computed in a brute-force manner. The accuracy, efficiency and memory requirement of the proposed DNN-based approach for real fluid property evaluation will be analyzed, and conclusions will be drawn accordingly.

ACKNOWLEDGMENT

This work is funded by the Air Force Office of Scientific Research (AFOSR) under Grant No. FA9550-18-1-0216. The first author gratefully acknowledges funding from the Natural Sciences and Engineering Research Council of Canada (NSERC) for financial support.

REFERENCES

- [1] X. Wang, H. Huo, U. Unnikrishnan and V. Yang, A Systematic Approach to High-Fidelity Modeling and Efficient Simulation of Supercritical Fluid Mixing and Combustion, *Combustion and Flame* 195 (2018) 203-215.
- [2] I. Goodfellow, Y. Bengio and A. Courville, *Deep Learning*, MIT Press (2016).
- [3] H. Meng and V. Yang, A Unified Treatment of General Fluid Thermodynamics and Its Application to a Preconditioning Scheme, *Journal of Computational Physics* 189 (2003) 277-304.

Improved Approximations for the Maximum-Entropy Fourteen-Moment Closure of Gas Dynamics

Fabien Giroux and James M^cDonald

*Department of Mechanical Engineering, University of Ottawa,
161 Louis Pasteur, Ottawa, Ontario, Canada, K1N 6N5*

Email: *fgiro059@uottawa.ca*

ABSTRACT

This work is focused on the improvement of an approximation for the fourteen-moment model from the kinetic theory of gases. This model is the third member of the maximum-entropy moment closures hierarchy. The fourteen-moment equations are a hyperbolic treatment of viscous compressible flows including heat transfer. This closure can be seen as a hyperbolic alternative to the Navier-Stokes equations and, as this model is derived from the kinetic theory of gases, it has the ability to offer solutions for situations in which the flow departs from local thermodynamic equilibrium, where the Navier-Stokes equations lose physical validity. Unfortunately, the distribution function associated with this model is expressed as an exponential of a fourth-order polynomial. Such functions cannot be integrated in closed form, making it impossible to integrate the closing fluxes of the model. In previous work, by M^cDonald and Torrilhon [11], an approximation was developed for the closing fluxes. In this previous work, a robustly hyperbolic model for a one-dimensional gas is given, however the extension to three-dimensions is not as robust and the model loses hyperbolicity for some realizable states. The current work demonstrates an improvement to the previous model that stays closer to the maximum entropy goal.

1 INTRODUCTION

The numerical treatment of fluid-flow problems by a purely first-order hyperbolic model brings many advantages. The requirement to only evaluate first derivatives means an extra order of spacial accuracy is often available for a given stencil. It has also been demonstrated that the solution of viscous flow problems using a purely hyperbolic treatment can produce

solutions that are far less sensitive to grid quality [10]. Lower-quality grids are often necessary for the discretization of practical domains with complex geometry.

The hyperbolic model considered in this work is in the maximum-entropy family of moment closures from the kinetic theory of gases [4, 9, 12]. This technique leads to a set of fourteen first-order partial-differential equations (PDEs) that describe the evolution of an expanded solution vector. The resulting model has the potential to produce accurate predictions for fluid flows that exist both in and out of local thermodynamic equilibrium with and without heat transfer. Previous work done by M^cDonald and Torrilhon [11] showed that this model yields very accurate results for one-dimensional gases.

The distribution function associated with this model is the exponential of a fourth-order polynomial. Since this type of function cannot be integrated in closed form, it is impossible to obtain a closed form expression for the closing fluxes by simply integrating the distribution function to recover the moments of the solution vector. To avoid this problem, approximations to the closing fluxes are used.

The goal of the present work is the development and implementation of an improved approximation to the fourteen-moment model for a three-dimensional gas with an axisymmetric distribution function of particle velocities.

2 KINETIC THEORY

The kinetic theory of gases starts from the knowledge that a gas is comprised of a huge number of particles. Rather than tracking individual particles, a distribution function, $\mathcal{F}(x_i, v_i, t)$, is defined that reflects the prob-

ability of finding particles at a given location, x_i , and time, t , having a velocity, v_i . The time evolution of \mathcal{F} is governed by the Boltzmann equation [3, 2, 5],

$$\frac{\partial \mathcal{F}}{\partial t} + v_i \frac{\partial \mathcal{F}}{\partial x_i} + \frac{\partial (a_i \mathcal{F})}{\partial v_i} = \frac{\delta \mathcal{F}}{\delta t}. \quad (1)$$

Here, a_i is the acceleration of gas particles due to external forces and is taken to be zero in the present work. The term on the right-hand side of the equation, $\delta \mathcal{F} / \delta t$, is the Boltzmann collision operator representing the time rate of change of the distribution function produced by binary inter-particle collisions. This term involves a multi-dimensional integral over both velocity space and solid angle and can, in most cases, be challenging to evaluate. Fortunately, for many engineering applications, the detailed evaluation of the collision operator can be avoided by utilizing simplifying approximations such as the relaxation-time BGK model, as first proposed by Bhatnagar *et al.* [1]. In this relaxation-time model, the collision operator is replaced by a source term

$$\frac{\delta \mathcal{F}}{\delta t} = -\frac{\mathcal{F} - \mathcal{M}}{\tau}, \quad (2)$$

where \mathcal{M} is the well-known Maxwell-Boltzmann distribution—the equilibrium solution to the Boltzmann equation towards which the non-equilibrium solution is relaxing—and τ is a characteristic relaxation time for the collision processes.

Traditional “macroscopic” properties of the gas are obtained through moment relations. This is done by multiplying the distribution function by a velocity-dependent weight, $W(v_i)$, and integrating over all velocity space. For example, if the gas-particle mass, m , is chosen as the weight, the corresponding velocity moment is the fluid mass density, given by

$$\rho = \int_{-\infty}^{\infty} m \mathcal{F}(x_i, v_i, t) d^3 v = \langle m \mathcal{F} \rangle. \quad (3)$$

The momentum density is related to the moment, $\langle m v_i \mathcal{F} \rangle = \rho u_i$. Here, u_i is the average (or bulk) velocity of the gas particles at a point, x_i , and time, t . This allows for the definition of the “random” velocity as the difference between a particle velocity and the average, $c_i = v_i - u_i$. Other moments that are important in this work are

$$\begin{aligned} U_{ij} &= \langle m v_i v_j \mathcal{F} \rangle, & P_{ij} &= \langle m c_i c_j \mathcal{F} \rangle, \\ Q_{ijk} &= \langle m c_i c_j c_k \mathcal{F} \rangle, & R_{ijkl} &= \langle m c_i c_j c_k c_l \mathcal{F} \rangle, \\ S_{ijklm} &= \langle m c_i c_j c_k c_l c_m \mathcal{F} \rangle, \end{aligned} \quad (4)$$

where U_{ij} is the total second-order moment and P_{ij} is an anisotropic pressure tensor. This tensor is the negative of the fluid stresses and is related to the deviatoric

(viscous) stress tensor, τ_{ij} as

$$\tau_{ij} = \delta_{ij} p - P_{ij}, \quad (5)$$

where $p = P_{ii}/3$ is the thermodynamic pressure.

3 THE MAXIMUM-ENTROPY HIERARCHY OF MOMENT CLOSURES

With the BGK collision operator, the Boltzmann equation is mathematically relatively simple. However, it is very high dimensional. It exists in three spacial dimensions, three dimensions of velocity space, plus time. The direct numerical solution of this equation is prohibitively expensive for most practical problems.

Fortunately, the huge amount of detail given by the distribution function is rarely required. It is the moments of the gas that are of interest. Evolution equations for a given moment can be obtained by taking velocity moments of the Boltzmann equation,

$$\frac{\partial}{\partial t} \langle W \mathcal{F} \rangle + \frac{\partial}{\partial x_i} \langle v_i W \mathcal{F} \rangle = -\frac{1}{\tau} [\langle W \mathcal{F} \rangle - \langle W \mathcal{M} \rangle]. \quad (6)$$

Unfortunately, this technique cannot lead to a closed system of PDEs. This is because the time evolution of any moment always depends on the spacial divergence of a moment of one higher order.

One way to obtain a closed system is through the technique of moment closure [6]. This is accomplished by prescribing an assumed form for the distribution function, \mathcal{F} . This assumed form must have the same number of free parameters as there are unknown moments in the system. These parameters are chosen such that the moment relations, such as those in Eqs. (3) and (4), are satisfied. Higher-order moments, present only in the flux terms, can then be directly integrated and automatically become functions of lower moments through the assumed form.

One particularly promising technique for the selection of an assumed form is based on an entropy-maximization principle [4, 9, 12]. In this technique, one chooses \mathcal{F} to be that which maximizes the entropy, while remaining consistent with known moments. This leads to distribution functions of the form

$$\mathcal{F}_{\text{M.E.}} = e^{\boldsymbol{\alpha} \mathbf{W}^T}, \quad (7)$$

where $\boldsymbol{\alpha}$ is a row vector containing the free parameters and \mathbf{W} is a row vector containing all the velocity weights of the closure. Such maximum-entropy closures have many desirable mathematical properties, including a proof of hyperbolicity of the resulting PDEs.

4 THE CAVEAT OF THE FOURTEEN-MOMENT MODEL

The lowest-order member of the maximum-entropy hierarchy is a five-moment system that leads to the compressible Euler equations for a monatomic gas. The next member is a ten-moment system that provides a hyperbolic treatment for a viscous adiabatic gas. These two first members are generated using the following vectors of generating weights,

$$\mathbf{W}_5 = [1, v_i, v_i v_i] \quad (8)$$

$$\mathbf{W}_{10} = [1, v_i, v_i v_j]. \quad (9)$$

This choice leads to distribution functions that are exponentials of second-order polynomials. The two first members of this hierarchy therefore have distribution function that can be integrated in closed form. This means closing fluxes can also be integrated and the model PDEs take simple forms.

The third member of the maximum-entropy hierarchy is the fourteen-moment model, which provides a hyperbolic treatment for a viscous gas with heat transfer. It is the simplest member of the hierarchy offering a treatment for the heat transfer. The velocity weights associated with its distribution function are

$$\mathbf{W}_{14} = [1, v_i, v_i v_j, v_i v_j v_j, v_i v_i v_j v_j], \quad (10)$$

which leads to a distribution function that is the exponential of a fourth-order polynomial. As opposed to the two previous members of the hierarchy, the fourteen-moment member does not have a distribution function that can be integrated in closed form.

The resulting system of moment equations can be written as,

$$\frac{\partial \mathbf{U}}{\partial t} + \frac{\partial \mathbf{F}_{x_k}}{\partial x_k} = -\frac{1}{\tau} [\mathbf{U} - \mathbf{U}_{\mathcal{M}}], \quad (11)$$

where the solution and flux vector can be written as

$$\mathbf{U} = \begin{bmatrix} \rho \\ \rho u_i \\ \rho u_i u_j + P_{ij} \\ \rho u_i u_j u_k + u_i P_{jk} + 2u_j P_{ij} + Q_{ijj} \\ \rho u_i u_j u_k + 2u_i u_j P_{jk} + 4u_i u_j P_{ij} + 4u_i Q_{ijj} + R_{ijj} \end{bmatrix}, \quad (12)$$

$$\mathbf{F}_{x_k} = \begin{bmatrix} \rho u_k \\ \rho u_i u_k + P_{ik} \\ \rho u_i u_j u_k + u_i P_{jk} + u_j P_{ik} + u_k P_{ij} + Q_{ijk} \\ \rho u_i u_j u_k + u_i u_k P_{jj} + 2u_i u_j P_{jk} + 2u_j u_k P_{ij} + u_j u_j P_{ik} + u_i Q_{kjj} + u_k Q_{ijj} + 2u_j Q_{ijk} + R_{ijjk} \\ \rho u_i u_j u_k + 2u_i u_j u_k P_{jj} + 4u_i u_j u_k P_{jk} + 4u_i u_j u_k P_{ij} + 2u_i u_i Q_{jjk} + 4u_i u_k Q_{ijj} + 4u_i u_j Q_{ijk} + 4u_i R_{ijjk} + u_k R_{ijj} + S_{ijjk} \end{bmatrix}. \quad (13)$$

The vector, $\mathbf{U}_{\mathcal{M}}$, in Eq. (11) contains the local equilibrium state that corresponds to the moments in \mathbf{U} .

In order to close this system it is needed to have an expression for Q_{ijk} , R_{ijkk} and S_{ijjkk} . These expression is normally obtained by integrating the distribution function. In the case of the fourteen-moment it is impossible to simply integrate an expression for the closing flux let alone integrate to recover the agreeing free parameters. Although it is possible to numerically solve the entropy-maximization problem, yielding the free parameters and further integrate to recover the closing fluxes, this method would be prohibitively expensive. It is more suitable to obtain an approximation to these closing fluxes that is fast to compute and that must preserve the hyperbolicity of the system.

5 REALIZABILITY OF THE FOURTEEN MOMENT MODEL AND MAPPING OF REALIZABLE SPACE

To determine what region of the closure is physically realizable, a Hamburger moment problem is performed [7]. This is done by defining a matrix

$$\mathbf{Y} = \langle m \mathbf{M} \mathbf{M}^T \mathcal{F} \rangle = \begin{bmatrix} \rho & 0 & 0 & 0 & P_{ii} \\ 0 & P_{xx} & P_{xy} & P_{xz} & Q_{xii} \\ 0 & P_{xy} & P_{yy} & P_{yz} & Q_{yii} \\ 0 & P_{xz} & P_{yz} & P_{zz} & Q_{zii} \\ P_{ii} & Q_{xii} & Q_{yii} & Q_{zii} & R_{ijj} \end{bmatrix}, \quad (14)$$

where $\mathbf{M} = [1, v_x, v_y, v_z, \mathbf{v}^2]$. A necessary condition for physical realizability is that the matrix must be positive definite. The positive definiteness is insured when

$$R_{ijj} \geq Q_{kii} (P^{-1})_{kl} Q_{ljj} + \frac{P_{ii} P_{jj}}{\rho}. \quad (15)$$

Although this is only a necessary condition, experience suggest that this does cover all of physical realizability [11].

Junk has shown that there is a subspace where no maximum-entropy distribution function exists that corresponds to the moment state [8]. For the fourteen-moment model the Junk subspace is given by

$$Q_{ijj} = 0 \quad R_{ijj} > \frac{2P_{ji} P_{ij} + P_{ii} P_{jj}}{\rho}. \quad (16)$$

The fourteen moment distribution function collapses down to the ten-moment closure on the boundary of the Junk subspace.

In order to facilitate the construction of an approximation, a variable, σ , is defined to map the phase space in

a parabolic manner. The variable, σ , transitions from $\sigma = 0$ when at the Junk subspace to $\sigma = 1$ when at the physical realizability boundary. It is defined as

$$\sigma = \frac{[2P_{ij}P_{ji} + P_{ii}P_{jj} - \rho R_{iijj}]}{4P_{ij}P_{ji}} \quad (17)$$

$$+ \frac{\sqrt{[2P_{ij}P_{ji} + P_{ii}P_{jj} - \rho R_{iijj}]^2 + 8\rho P_{mn}P_{nm}Q_{kii}(P^{-1})_{kl}Q_{ljj}}}{4P_{ij}P_{ji}}.$$

In building an affordable approximation to the true maximum-entropy model, the objective is to use the values of the closing fluxes at $\sigma = 0$ and $\sigma = 1$ and to interpolate for any interior values of σ .

6 APPROXIMATION OF CLOSING FLUXES

The derivation in the following section is shown in more details by McDonald and Torrilhon [11]. It is possible to obtain information on the closing fluxes when $\sigma = 0$ since they are the one of the Gaussian distribution. The closing moment R_{ijkk} can be simply integrated while, for Q_{ijk} and S_{ijjkk} , the derivative is obtained and used instead. This is because the values of these two latest moments at the Gaussian level is zero.

The derivative of Q_{ijk} near the Gaussian level is

$$\frac{\partial Q_{ijk}}{\partial Q_{mnn}} = \left[2P_{il}(P^2)_{jk} + 2P_{kl}(P^2)_{ij} + 2P_{jl}(P^2)_{ik} \right] B_{lm}^{-1} = K_{ijkm}, \quad (18)$$

where

$$B_{lm} = 2P_{lm}(P^2)_{\alpha\alpha} + 4(P^3)_{lm}. \quad (19)$$

Therefore it is possible to approximate the value of this moment at the Gaussian level with the following expression.

$$Q_{ijk} = K_{ijkm}Q_{mnn} \quad (20)$$

As mentioned the moment R_{ijkk} at the Gaussian level can simply be integrated analytically leading to

$$R_{ijkk} = \frac{1}{\rho} (P_{ij}P_{kk} + 2P_{ik}P_{kj}). \quad (21)$$

Finally, in a similar way to the Q_{ijk} moment, the derivative of S_{ijjkk} at the Gaussian level is found to be

$$\begin{aligned} \frac{\partial S_{ijjkk}}{\partial Q_{mnn}} &= \frac{1}{\rho} \left[2P_{il}(P_{\alpha\alpha})^3 + 12P_{il}(P^3)_{\alpha\alpha} + 14(P^2)_{\alpha\alpha}(P^2)_{il} \right. \\ &\quad + 20P_{\alpha\alpha}(P^3)_{il} + 20(P^4)_{il} - 2(P^2)_{\alpha\alpha}P_{\beta\beta}P_{il} \\ &\quad \left. - 6(P_{\alpha\alpha})^2(P^2)_{il} \right] B_{lm}^{-1} \\ &= W_{im}, \end{aligned} \quad (22)$$

from which it is possible to approximate the value of this moment as

$$S_{ijjkk} = W_{im}Q_{mnn}. \quad (23)$$

On the physical realizability boundary, when $\sigma = 1$, the distribution function shows that all particles exist on a sphere in velocity space. This offers many advantages as the domain of existence is now limited. By changing the bulk velocity of the distribution function through a Galilean transformation it is possible to shift the sphere so that it is centered in velocity space. This new bulk velocity can be expressed as

$$\hat{u}_j = -\frac{1}{2}(P^{-1})_{ij}Q_{ikk}. \quad (24)$$

The fact that particles only exist on a sphere on the physical realizability boundary proves to be useful as higher order contracted moments can be related to lower order moments by taking any \hat{v}^2 out of the integral. For example,

$$\hat{U}_{ii} = \langle m\hat{v}^2 \mathcal{F} \rangle = \hat{v}^2 \langle m\mathcal{F} \rangle = \hat{v}^2 \rho, \quad (25)$$

where \hat{v} is the radius of the sphere.

Since R_{ijkk} and S_{ijjkk} are contracted moments it is possible to use this trick in order to express them on the realizability boundary. The moments are then found to be

$$R_{ijkk} = Q_{ijl}(P^{-1})_{lm}Q_{mkk} + \frac{P_{ij}P_{kk}}{\rho} \quad (26)$$

$$S_{ijjkk} = P_{kn}^{-1}P_{lm}^{-1}Q_{npp}Q_{mjj}Q_{ikl} + 2\frac{P_{jj}Q_{ikk}}{\rho}. \quad (27)$$

With expressions for R_{ijkk} and S_{ijjkk} at both the Gaussian level and the realizability boundary, it is possible to fit an approximation for these closing fluxes as a function of σ .

$$R_{ijkk} = \frac{1}{\sigma}Q_{ijl}(P^{-1})_{lm}Q_{mkk} + \frac{2(1-\sigma)P_{ik}P_{kj} + P_{ij}P_{kk}}{\rho} \quad (28)$$

$$\begin{aligned} S_{ijjkk} &= \frac{1}{\sigma^2}P_{kn}^{-1}P_{lm}^{-1}Q_{npp}Q_{mjj}Q_{ikl} + 2\sigma^{\frac{3}{5}}\frac{P_{jj}Q_{ikk}}{\rho} \\ &\quad + (1-\sigma^{\frac{3}{5}})W_{im}Q_{mnn} \end{aligned} \quad (29)$$

Unfortunately, Q_{ijk} is not a contracted moment and therefore the manipulation shown in Eq. 25 cannot be applied in order to find a closed form expression at the realizability boundary. This means that an accurate closed form approximation for Q_{ijk} cannot be found for all of realizable space. Since both R_{ijkk} and S_{ijkk} are function of Q_{ijk} , it is indispensable to find an approximation in order to close the system. In a previous study, McDonald and Torrilhon used the linear extrapolation of Q_{ijk} from the Gaussian level as an approximation over all realizable space [11]. This leads to an approximation that is relatively poor for all closing fluxes due to their dependence on Q_{ijk} .

7 EXACT VALUE FOR Q_{ijk} ON THE REALIZABILITY BOUNDARY

The focus of this work is to obtain an improved approximation for the closing flux Q_{ijk} by using a technique to evaluate it at the realizability boundary. Since R_{ijkk} and S_{ijkk} also depends on Q_{ijk} it is crucial to find an appropriate approximation describing this closing flux. For the present work, a model for one space dimension is studied. This means that any moments associated with weights that are odd functions of v_y or v_z will be zero. The only member of Q_{ijk} that must be fit is Q_{xxx} and the distribution function will remain axisymmetric about the x axis.

As mentioned, at the realizability boundary all particles are present on a sphere. It is possible to center that sphere in velocity space by simply changing the bulk velocity. By non-dimensionalization, it is possible to force the radius of the sphere to be of 1. The axisymmetric distribution function for a three-dimensional gas can be expressed as

$$\mathcal{F} = e^{a_0 + a_x v_x + a_{xx} v_x^2 + 2a_{yy} v_y^2 + a_{xii} v_x v^2 + a_{iij} v^4}. \quad (30)$$

Since the distribution is only non-zero on a sphere having a radius of 1, it is possible to rewrite the distribution function as

$$\mathcal{F} = e^{a + b v_x + c v_x^2}, \quad (31)$$

where,

$$a = a_0 + a_{yy} + a_{iij} \quad b = a_x + a_{xii} \quad c = a_{xx} - a_{yy}. \quad (32)$$

Since this distribution function is an exponential of a second order polynomial, it is then possible to integrate it analytically. The following moments are ob-

tained.

$$\langle m\mathcal{F} \rangle = \hat{U}_0 = \frac{\pi^{\frac{3}{2}} e^{-\frac{ab^2}{4c}} \left(\operatorname{erf}\left(\frac{b-2c}{2\sqrt{-c}}\right) - \operatorname{erf}\left(\frac{b+2c}{2\sqrt{-c}}\right) \right)}{\sqrt{-c}} \quad (33)$$

$$\langle m v_x \mathcal{F} \rangle = \hat{U}_x = \frac{2\pi e^{a+c} (e^b - e^{-b}) - b\hat{U}_0}{2c} \quad (34)$$

$$\langle m v_x v_x \mathcal{F} \rangle = \hat{U}_{xx} = \frac{2\pi e^{a+c} (e^b + e^{-b}) - \hat{U}_0 - b\hat{U}_x}{2c} \quad (35)$$

Due to the complexity of these equations, the relations cannot be inverted to solve for a , b , and c . Instead, a Newton search is performed in order to recover the coefficients. Once the values of the coefficients are found it is possible to compute \hat{U}_{xxx} analytically

$$\hat{U}_{xxx} = \frac{b\hat{U}_0 + (2c-2)\hat{U}_x - b\hat{U}_{xx}}{2c}. \quad (36)$$

It is important to mention that this yields the exact value for U_{xxx} at the realizability boundary. The exact closing fluxes at the boundary are therefore obtained. This process is many orders of magnitudes cheaper than directly solving the entropy-maximization problem for the coefficients in Eq. (30) as the integrals no longer need to be evaluated numerically.

8 IMPROVED APPROXIMATION FOR Q_{ijk} IN ALL REALIZABLE SPACE

Similarly as for R_{ijkk} and S_{ijkk} , it is now possible to build an approximation for the closing flux, Q_{ijk} , using its expression at the Gaussian level and its value at the realizability boundary. The idea is now to extrapolate a value for Q_{ijk} from the values at both points and further approximate the closing flux across all realizable states.

It has been found that a much improved model for Q_{xxx} can be found by first building an extrapolation for $\left(\frac{Q_{xxx}}{Q_{xii}}\right)$ from the Gaussian level, $\sigma = 0$. Then producing a second extrapolation from the limits of physical realizability, $\sigma = 1$. The final approximation is proposed as a blending of these two extrapolations.

The value for Q_{ijk} at the Gaussian level, where $\sigma = 0$, can be obtained from Eq. (20). It is used to extrapolate the closing flux Q_{ijk} into moment space from its value at the Gaussian level as

$$\left(\frac{Q_{xxx}}{Q_{xii}}\right)_G = 1 - \left(1 - \left(\frac{Q_{xxx}}{Q_{xii}}\right)_{\sigma=0}\right) e^{\left(-\frac{1}{0.125+3.2\sigma^{1.5}} \frac{Q_{xii}^2}{P_{xx}}\right)}, \quad (37)$$

where \tilde{Q}_{xii} and \tilde{P}_{xx} are the non-dimensional heat transfer and pressure.

Similarly, it is possible to extrapolate the closing flux, Q_{ijk} , anywhere in moment space from its value at the realizability boundary where $\sigma = 1$ as

$$\left(\frac{Q_{xxx}}{Q_{xii}}\right)_B = 1 - \left(1 - \left(\frac{Q_{xxx}}{Q_{xii}}\right)_{\sigma=1}\right) e^{\left(\left(\frac{1}{3.325} - \frac{1}{0.125+3.2\sigma^{1.5}}\right) \frac{Q_{xii}^2}{P_{xx}}\right)} \quad (38)$$

The value for the closing flux Q_{ijk} is then proposed to be a blending between these function, and gives

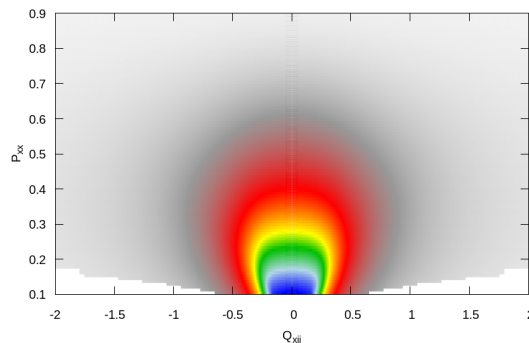
$$\frac{Q_{xxx}}{Q_{xii}} = \sigma^{\frac{1}{2}} \left(\frac{Q_{xxx}}{Q_{xii}}\right)_B + (1 - \sigma^{\frac{1}{2}}) \left(\frac{Q_{xxx}}{Q_{xii}}\right)_G \quad (39)$$

This yields an accurate value for the closing flux Q_{xxx} everywhere in realizable moment space.

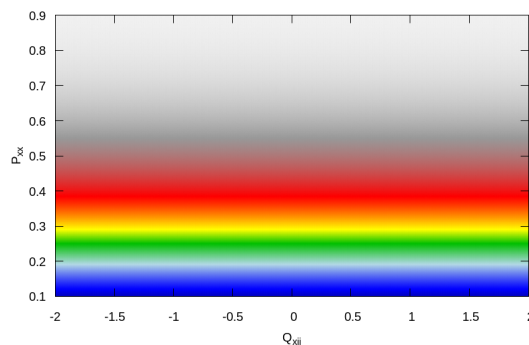
The huge improvement in the value of this moment is demonstrated in Figure 1. First, Figure 1(a) shows the ratio, $\left(\frac{Q_{xxx}}{Q_{xii}}\right)$, predicted by the true maximum-entropy closure in a non-dimensional moment space where $\rho = 1$, $u_i = 0$, $P_{ii} = 1$ and $\sigma = 0.55$. In this plot, non-dimensional heat flux is on the horizontal axis and P_{xx} is on the vertical axis. This is the target of the new fit. Figure 1(b) shows the prediction of the closing flux using the procedure proposed in [11]. It is clear to see that this is a poor fit. Unfortunately, this poor fit feeds into the closing expressions for both R_{ijjj} and S_{ijjjkk} , thus spoiling the whole closure.

Figure 1(c) shows the improved new fit. Clearly, this result is much improved. The closing flux now accurately follows all the trends of the true maximum-entropy flux and recovers the proper limiting behaviour as the magnitude of the heat flux tends to infinity.

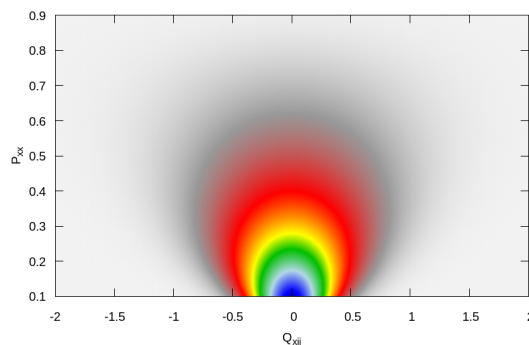
Finally, the hyperbolicity of the proposed approximation is investigated and compared to the previously proposed closure. It is found that the new approximation, although not globally hyperbolic, features a great improvement compared to the original fit. Figure 2 shows the maximum ratio of the imaginary part over the real part of the eigenvalues of the flux Jacobian for all points with $\sigma = 0.55$. The new fit features a smaller area where it loses hyperbolicity and the amplitude of the complex parts of the system eigenvalues is also lower than it is for the original fit. In fact, the imaginary part is at most around 15% of the real part of the eigenvalue. As σ increases and decreases, the area



(a) Maximum Entropy exact flux

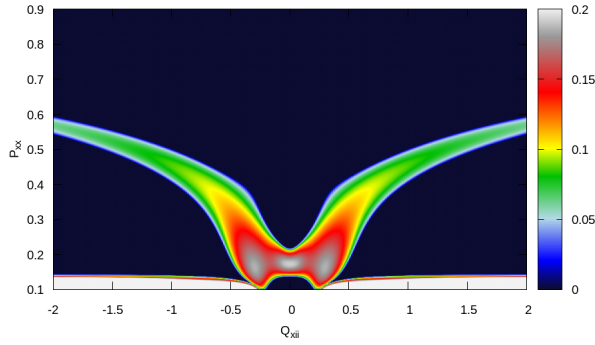


(b) Original fit

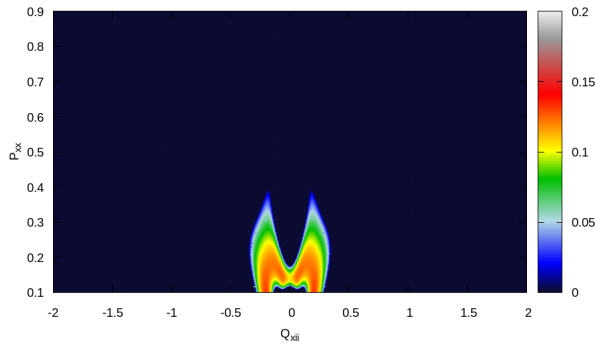


(c) New proposed fit

Figure 1: Closing flux $\left(\frac{Q_{xxx}}{Q_{xii}}\right)$ for $\sigma = 0.55$ and non-dimensionalized such that $\rho = 1$ and $P_{xx} + P_{yy} + P_{zz} = 1$.



(a) Original fit



(b) New proposed fit

Figure 2: Maximum ratio of imaginary over real part of eigenvalues at $\sigma = 0.55$.

of non-hyperbolicity becomes smaller. The new model is still not globally hyperbolic, but is much closer using the improved approximation for Q_{xxx} .

9 CONCLUSION

A new approximation for the axisymmetric maximum-entropy fourteen-moment closure is obtained. This approximation offers a much closer fit than the original approximation and presents a stronger hyperbolicity over all moment space.

Future work includes the improvement of the fit in order to obtain global hyperbolicity. An approximation for the full three-dimensional maximum-entropy fourteen-moment closure conserving global hyperbolicity is to be obtained.

REFERENCES

- [1] P. L. Bhatnagar, E. P. Gross, and M. Krook. A model for collision processes in gases. I. small amplitude processes in charged and neutral one-component systems. *Physical Rev.*, 94(3):511–525, 1954.
- [2] J. M. Burgers. *Flow Equations for Composite Gases*. Academic Press, New York, 1969.
- [3] S. Chapman and T. G. Cowling. *The Mathematical Theory of Non-Uniform Gases*. Cambridge University Press, Cambridge, 1960.
- [4] W. Dreyer. Maximization of the entropy in non-equilibrium. *Journal of Physics A: Mathematical and General*, 20:6505–6517, 1987.
- [5] T. I. Gombosi. *Gaskinetic Theory*. Cambridge University Press, Cambridge, 1994.
- [6] H. Grad. On the kinetic theory of rarefied gases. *Commun. Pure Appl. Math.*, 2:331–407, 1949.
- [7] H. L. Hamburger. Hermitian transformations of deficiency-index (1,1), jacobian matrices, and undetermined moment problems. *Amer. J. Math.*, 66:489–552, 1944.
- [8] M. Junk. Domain of definition of Levermore’s five-moment system. *J. Stat. Phys.*, 93(5/6):1143–1167, 1998.
- [9] C. D. Levermore. Moment closure hierarchies for kinetic theories. *J. Stat. Phys.*, 83:1021–1065, 1996.
- [10] J. G. McDonald, J. S. Sachdev, and C. P. T. Groth. Application of Gaussian moment closure to micro-scale flows with moving and embedded boundaries. *AIAA J.*, 52:1839–1857, 2014.
- [11] J. G. McDonald and M. Torrilhon. Affordable robust moment closures for CFD based on the maximum-entropy hierarchy. *J. Comput. Phys.*, 251:500–523, 2013.
- [12] I. Müller and T. Ruggeri. *Extended Thermodynamics*. Springer-Verlag, New York, 1993.

Applications

Evaluating floc strength using CFD for primary wastewater treatment

Brooke Remler

Department of Mechanical and Materials Engineering
 Western University, London, Canada
 bremler@uwo.ca

Christopher DeGroot

Department of Mechanical and Materials Engineering
 Western University, London, Canada
 cdegroo5@uwo.ca

ABSTRACT

Improving primary treatment operations while minimizing energy usage is a top tier concern for wastewater treatment plants (WWTP) [1]. Flocculation has been proven to enhance removal during primary filtration [1]; if the flocs can survive the transport network. Flocculation involves aggregating destabilized colloids into larger particles facilitating easier removal through settling or membrane filtration [2]. Floc strength was measured using an established method reported in [2] where the floc size prior, during, and post breakage was measured with a Malvern Mastersizer 2000. The flocculated mixture for experiments is prepared using municipal wastewater taken from Pottersburg WWTP London Ontario Canada, using Kamira Solutions 40% FeCl₃ (destabilizing coagulant) and FLOPAM EMF 140CT heavy weight cationic polymer (flocculant). Flocs are grown, and later broken, through a two-stage injection process in a JLT series flocculator. The larger the floc size post breakage, the stronger the floc. Breakage conditions are represented by velocity gradients, commonly referred to as G-values or G . G for experiments were determined by conducting CFD on common geometries in transport networks at WTP. Specifically, a 90° short elbow and a butterfly valve. In a mixing vessel, G is a function of the kinematic viscosity (ν) and turbulent eddy dissipation rate (ϵ) [2]. Through CFD it was found that G in pipe geometries is a function of fluid velocity and the pressure gradient along a streamline. CFD allows for G to be determined along streamlines highlighting local maximums, their frequency, and magnitudes.

The floc strength factor (SF) and floc recovery factor (RF) are two common methods for characterizing floc strength. SF represents a floc's resistance to breakage, RF represents a floc's regrowth ability. D50 values from a current experiment can be found in Fig. 1. For a growth G of 50s⁻¹ SF and RF were 88.51% and 41.58%. For a growth G to 75s⁻¹ SF and RF decreased to 84.56% and 25.88% respectively. The breakage G of 500s⁻¹ was the same for both growth trials. The results shown in Fig. 1 indicate that the G at which the flocs are formed has an impact on the floc strength, with a lower G resulting in greater floc strength. Previous works have outlined that floc breakage is irreversible [2], which can be seen in Figure 1. Regardless of the growth G once polymer is added the flocs grow to approximately the same size. Understanding the range of G within a transport network is vital to ensuring floc integrity is preserved in order to achieve removal targets. This work can contribute to the development of a flocculation process model to optimize removal during primary treatment and improve pipe network design to promote floc strength.

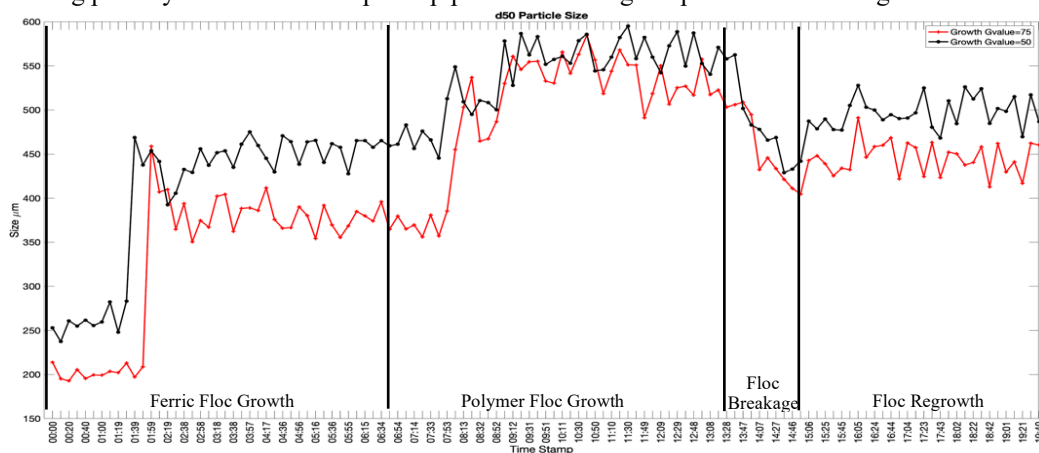


Figure 1: d50 particle size with different growth G

References:

- [1] T. Hey, J. Väänänen, N. Heinen, J. la Cour Jansen, and K. Jönsson, "Potential of combining mechanical and physicochemical municipal wastewater pre-treatment with direct membrane filtration," *Environ. Technol. (United Kingdom)*, vol. 38, no. 1, pp. 108–115, 2017.
- [2] A. N. Jones and J. Bridgeman, "Investigating the characteristic strength of flocs formed from crude and purified Hibiscus extracts in water treatment," *Water Res.*, vol. 103, pp. 21–29, 2016.

CFD INVESTIGATION OF COMPRESSIBLE FLOW EFFECTS ON PERFORMANCE CRITERIA OF INFLOW CONTROL DEVICES

Jean-Luc Olsen, Matthew Miersma, Carlos F. Lange
Dept. of Mechanical Engineering
University of Alberta
Edmonton, Canada

ABSTRACT

Inflow control devices (ICDs) are used in steam assisted gravity drainage (SAGD) wells to increase their efficiency in extracting oil from deep oil reservoirs. Previous work from our group used CFD to improve upon the common criteria used to compare ICD nozzle designs by characterizing how flow rate and fluid viscosity affect pressure drop through an ICD. The present work consists of modeling additional physics to include the effects of temperature and compressible flow to the nozzle criteria.

ANSYS CFX software was previously used to model steady state, adiabatic, incompressible flow of constant property fluid through complex 3D nozzle geometries inside wells at various flow rates and fluid viscosities. Various nozzle designs, including straight nozzle, channel, and modified Tesla diode, were modeled while including the relatively much larger surrounding well components. A mixture of structured and unstructured mesh with inflation layers is used to refine the area surrounding the ICDs. Laminar to slightly turbulent flow occurs in the open area upstream of the ICD, which becomes fully turbulent when passing through the relatively constricted devices, and is shot as a jet into an inner pipe where large vortices form. A two-equation SST turbulence model is used to model the separating flow in the device. These simulations found a quadratic relationship between fluid velocity and pressure drop through an ICD, and a linear relationship between viscosity and pressure drop. The strength of these relationships changes for each ICD design, and new criteria were developed based on regression models of the pressure drop as a function of either fluid velocity or viscosity to quantify the effect of each variable on ICD performance.

To study the effects of compressibility on the pressure drop at flow rates above a Mach number of 0.3, an ideal gas model was used in the present study, as well as a total energy model that includes the transport of enthalpy and effects from kinetic energy. These models allow for changes in fluid temperature and density to be captured.

The inclusion of compressible effects resulted in higher predicted pressure drops than incompressible, constant property simulations. The increase in pressure drop is larger for higher flow rates. These results show the importance of including compressible effects when numerically calculating pressure drop through an ICD. These simulations are also providing knowledge that could lead to a method for quantifying the effects of phase change and flashing on pressure drop through an ICD.

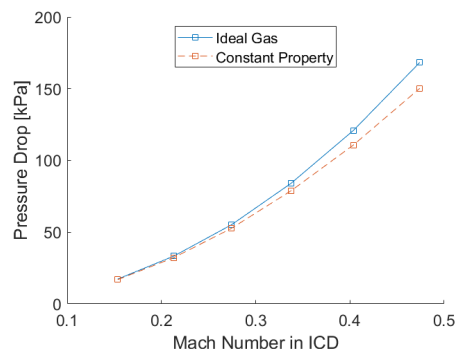


Figure 1 Straight nozzle ICD design, quadratic relationship between pressure drop and Mach number.

NUMERICAL INVESTIGATION OF THE IMPACT OF MANUFACTURING TOLERANCES ON MARINE PROPELLER PERFORMANCE

Shanqin Jin, Ruosi Zha, Heather Peng and Wei Qiu*
 Department of Ocean and Naval Architectural
 Engineering
 Memorial University
 St. John's, NL, Canada
 * Email: qiuw@mun.ca

David Hally and Matthew Gauthier
 DRDC Atlantic
 Dartmouth, NS, Canada

 Bodo Gospodnetic
 Dominis Engineering
 Ottawa, ON, Canada

ABSTRACT

The majority of marine propellers manufactured today are hand- or robotic finished from castings which are rough machined using Computer Numerical Control (CNC). Blade edges and tips, the most sensitive parts of a propeller's geometry, are made to conform to templates of their required form using manual grinding. Manual grinding of propeller surfaces introduces inaccuracies and deviations from design, which could lead to degradation of propeller performance in terms of cavitation, noise and efficiency. Manufacturing tolerances for new propellers for commercial ships are specified by ISO 484 standards. With the maturation of modern flow solvers, it is now possible to test the performance penalties caused by small manufacturing defects on propeller that comply with ISO 484.

The effects of a small flat defect on the surface of a blade section, representing a poorly hand-finished propeller section, on cavitation inception were studied using 2-D steady RANS solvers. Numerical simulations were carried out for the modified NACA 66 section with and without defects near the leading edge (LE) at $Re=3.0 \times 10^7$. Convergence studies were performed to examine the sensitivity of solutions to domain size, grid distribution, y^+ , grid aspect ratio. Various turbulence models, including the standard $k-\epsilon$, standard $k-\omega$, SST $k-\omega$ and Spalart-Allmaras model, were applied and their effects on the solutions were studied, especially for the cases with the largest manufacturing defects. The cavitation buckets in terms of minimum pressure coefficient were compared for the modified NACA sections with and without defects at a range of angles of attack.

RESULTS

Cavitation buckets in terms of minimum pressure coefficients, $-C_{P_{MIN}}$, are compared for the base foil (without defect) and three foils with defects, denoted as D1, D2 and D3, where D1 has the longest flat defect and D3 has the smallest defect, at angles of attack, α , from -4° to 4° . It can be clearly observed that the defects have significant effects on the minimum pressure coefficients. The longer flat defect leads to more significant effect on the cavitation bucket.

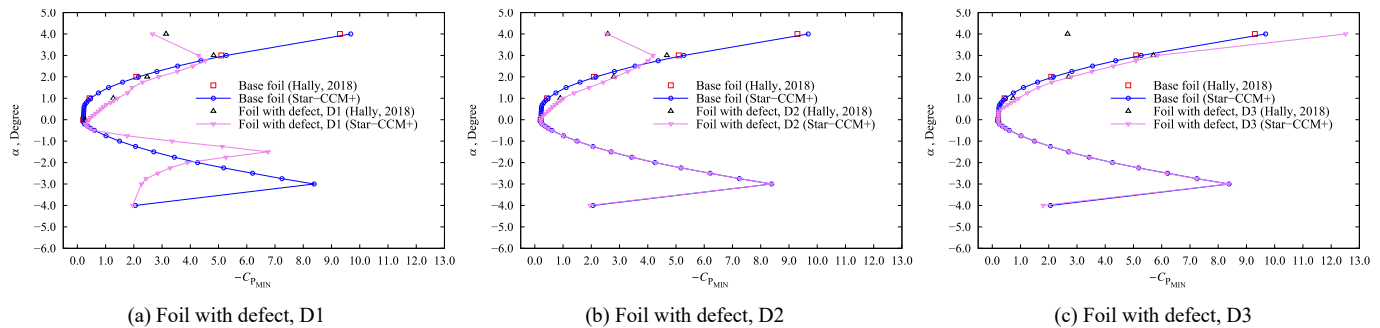


Figure 1: Cavitation buckets for the base foil and the foils with defect

Oblique CFD Analysis of Open-wheel Race Car with Circuit-Tailoring Shape Optimization

Mark Lin

Department of Aerospace Engineering
San Jose State University
San Jose, USA
Mark.Lin@SJSU.edu

Periklis Papadopoulos

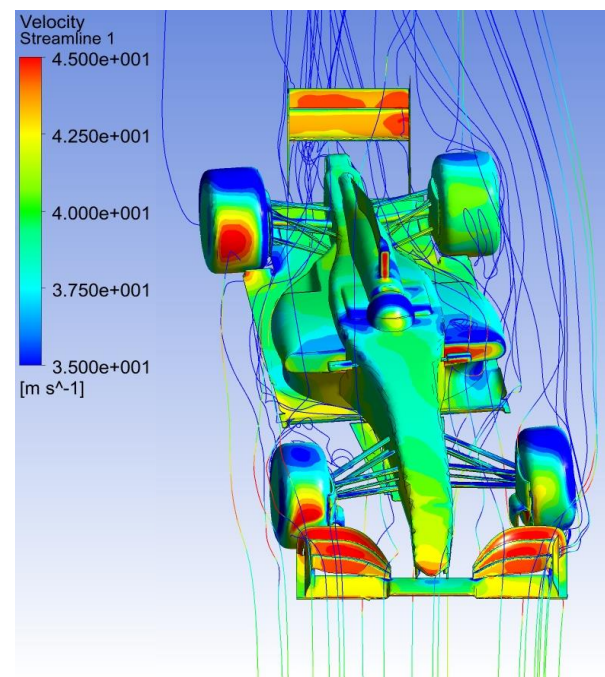
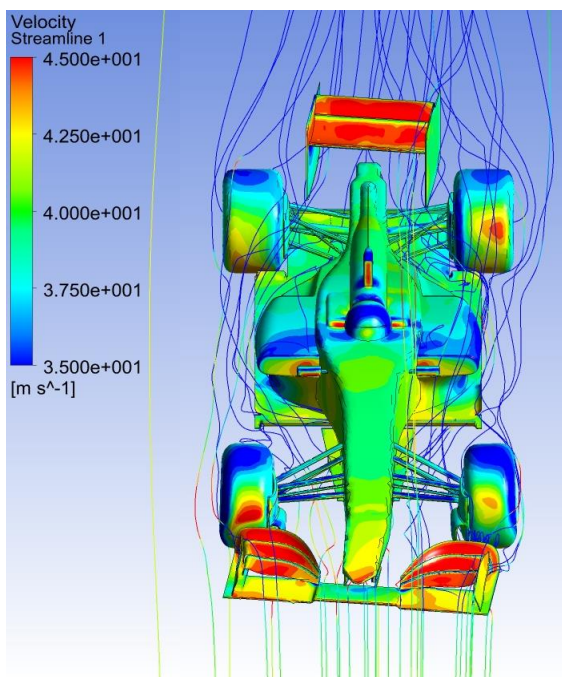
Department of Aerospace Engineering
San Jose State University
San Jose, USA
Periklis.Papadopoulos@SJSU.edu

ABSTRACT

In this paper, an oblique CFD simulation of an open-wheel race car is presented. The example case presented has the free-stream coming in at 7.5° incident angle-of-attack in the yaw angle, which simulates the aerodynamic performance of the car as it is turning. This type of oblique analysis is useful in road-circuit racing as oppose to oval-track racing because in road-circuit racing the numerous turns the vehicle must take will determine the overall lap time the vehicle can achieve. Downforce generated by the front, rear wing as well as the undercarriage diffuser is calculated. By varying the oblique angle of incidence and computing the downforce generated, an optimal design of the front and rear wing configuration can be determined for any given road-circuit, whether it's a high-speed circuit or a multi-corner tight and twisty circuit.

In addition to a complete car analysis, CFD results of 4 front wings from different eras of Formula 1 are presented for historical comparison. The drag and the lift coefficients of these 4 wings (with front wheels added to the model) are calculated using the drag and lift forces predicted by CFD. A comparison is made between the wings from different eras and a progression of the wing design is shown. Depending on the number of righthand turns versus left hand turns, a tailored, biased wing concept is proposed. This design approach is aimed to provide a continuum of different aerodynamic wings to cover a near symmetrical circuit to a left-turn only circuit as in IndyCars.

The CFD analysis is carried out using ANSYS Fluent and its pros and cons in prediction accuracy are discussed in this paper. The work was done at San Jose State University under the guidance of Professor Papadopoulos of the Aeronautical Engineering Department.



Permeability Tensor Orientation and Its Effect on Resin Transfer Molding

Anthony Sherratt, Christopher DeGroot, Anthony Straatman
Mechanical and Materials Engineering
Western University
London, Canada
asherra@uwo.ca, cdegroo5@uwo.ca, astraatman@eng.uwo.ca

ABSTRACT

Due to their high strength specific properties, carbon fiber reinforced polymers (CFRP) are gaining significant interest in the automotive sector [1]. Given the drive in the automotive sector to continually reduce the overall production costs of its components, a subset of liquid composite molding, resin transfer molding (RTM), is gaining significant headway due to its high automation potential [1]. To produce an RTM part, first, a sheet of carbon fiber is draped into a rigid mold. The mold is then closed, and resin is injected at high pressure, infiltrating the carbon fiber. After infiltration, the resin is left to cure after which the part is removed and passed onto trimming. To further reduce the overall cost and manufacturing time, numerous finite element and computational fluid dynamics models are being developed to optimize operational parameters such as inlet pressure/flow rate, outlet and vent location and resin/mold temperature. The macroscopic flow in the RTM process can be considered to be a flow through a porous region (i.e. the carbon fiber sheet), which is modelled using Darcy's law. Darcy's law states that the volume averaged velocity is proportional to the permeability tensor, the kinematic viscosity of the resin and the pressure gradient in the cavity [1]. In the RTM simulation, it is common to specify a constant permeability tensor throughout the domain (i.e. assuming a constant fiber volume fraction). However, during draping the fiber tows are distorted, which results in a non-uniform fiber volume fraction and therefore a non-isotropic permeability. Also, there is little mention of the method of orienting the permeability tensor in the computational domain, as it is highly dependent on the fiber orientation, which again has a significant effect on the flow front progression given the large difference in the permeability value parallel and normal to the fiber tows.

The current study will investigate the effect of the permeability tensor using a custom version of the open source CFD software OpenFOAM®. This will be done through two methods: (i) assuming a constant and varying permeability tensor orientation throughout the domain and (ii) varying the fiber volume fraction using a sinusoidal distribution with 3 frequency variations, an example of which can be seen in Fig. (1). For the constant permeability orientation case, the parallel component will be directed in the x-direction, the normal in the y- and z-directions. For the varying permeability tensor orientation case, the parallel component will be oriented with the fiber direction and the normal direction as the result of averaging the normal vectors of the closest top and bottom faces of the part. Finally, the third component will be the result of the cross product of the parallel and normal vectors. The value of the permeability tensor components will be calculated using the model developed by Gebart, who found that the permeability parallel and normal to the fiber tow directions is related to the fiber volume fraction and fitting parameters based on the tow bundle type [2]. Results of the six cases presented will be compared as follows: (i) the total filling time, (ii) the rate on infusion over time and (iii) the final volume fraction of resin within the domain. The result will show a comprehensive study showing the importance of the permeability tensor, its magnitude and its orientation in RTM mold filling simulations.

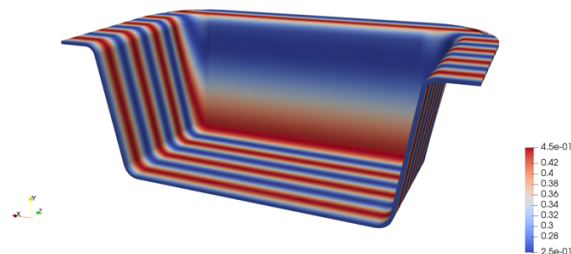


Figure 1: Figure showing the 3D domain and the sinusoidal distribution of fiber volume fraction.

- [1] J. Seuffert, L. Kärger, and F. Henning, "Simulating Mold Filling in Compression Resin Transfer Molding (CRTM) Using a Three-Dimensional Finite-Volume Formulation," *J. Compos. Sci.*, vol. 2, no. 23, 2018.
- [2] B. R. Gebart, "Permeability of Unidirectional Reinforcements for RTM," *Swedish Inst. Compos.*, vol. 26, no. 8, pp. 1100–1133, 1992.

NUMERICAL MODELING OF A FREEZE DESALINATION PROCESS

Ghobad Amini, Jamal Jamali

College of Engineering and Technology, American University of the Middle East, Kuwait
 ghobad.amini@aum.edu.kw, jamal.jamali@aum.edu.kw

Abstract—The freezing process of saltwater inside a cylindrical container is analyzed numerically. The solution is based on the interface capturing volume-of-fluid method allowing the simulation of the phase change with enthalpy-porosity technique. The numerical results are validated against the measurements for different salt concentration values.

Keywords-component; numerical modeling; enthalpy-porosity method; freeze desalination

I. INTRODUCTION

Solidification phenomena are widely encountered in numerous industries including food conservation, oil engineering, and seawater desalination [1-2]. The principle of freeze desalination process is based on water solidification phenomena, where the growing small ice crystal lattice prevents the inclusion of any solutes [3]. Therefore, during ice crystal formation, salts are rejected by the nature of the ice crystal lattice, which is formed by pure water. The main advantage of freeze desalination technology compared to other heat desalination processes is its lower energy consumption; since the latent heat of freezing is one-seventh of the latent heat of evaporation. As desalination capacity is rising worldwide, enhancing the freeze desalinate technology can improve the economics of the energy systems.

The formation of ice has experimentally been investigated by several researchers. However, the salt separation process has been studied numerically rarely. The challenge within this kind of numerical problems, the so-called Stefan problems, is prescribing the moving liquid-solid interface induced by the phase change and dealing with variable fluid properties induced by thermal evolution [3-4].

For modeling the freezing process, normally an enthalpy-porosity technique is used. In this method, the liquid fraction is defined associated with each cell in the domain. The interface is captured by a volume-of-fluid (VOF) function which represents the volume fraction occupied by the liquid volume. and its implementation is done by a source term in the energy equation. In order to simulate the phase change, the isothermal VOF method is extended by the energy conservation to solve for the temperature in the material as done by Rosler et al. [4-5] and is adapted to the liquid freezing phenomena in the current work. At the interface, one can consider a mushy zone modeled as a “pseudo” porous medium in which the porosity decreases

from 1 to 0 as the material freezes. The well-known enthalpy-porosity method [8] assumes the solid and mushy region to behave like a porous medium. In this method the solid phase is fixed to the numerical grid by introducing a Darcy type source term to the momentum conservation equation.

In the current work, for faster and stable convergence, the enthalpy-porosity method is extended by a continuous enthalpy function which allows the solution of the energy conservation equation without updating [4-5]. The simulations of freezing phase change are performed in the open source flow solver OpenFOAM and results are compared with experimental measurement of saltwater freezing in a cylindrical container.

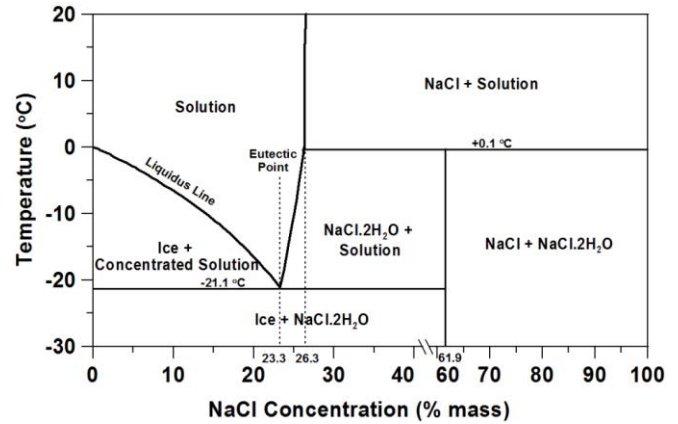


Fig.1. Phase diagram of saltwater

II. GOVERNING EQUATIONS

In a two-dimensional domain, for a fluid with density ρ and thermal conductivity k , the energy equation reads as,

$$\frac{\partial(\rho h)}{\partial t} + u \frac{\partial(\rho h)}{\partial x} + v \frac{\partial(\rho h)}{\partial y} = k \Delta T \quad (1)$$

where u and v are velocity in x and y directions, respectively. The specific enthalpy h consists the specific sensible enthalpy h_s and latent heat of freezing L as,

$$h = h_s + L(T) = \int_{T_{ref}}^T c dT + \alpha L \quad (2)$$

where c is the specific heat capacity and α is the volume of fluid fraction defined as the volume of liquid phase divided by the total volume of the computational cell. For non-isothermal freezing, the liquid fraction α is described by a linear function ranging from zero in the solid to one in the liquid phase as,

$$\alpha = \begin{cases} 1 & T > T_l \\ \frac{T - T_s}{T_l - T_s} & T_s < T < T_l \\ 0 & T < T_s \end{cases} \quad (3)$$

where T_s and T_l are liquid and solid temperature at the interface, respectively. Using (1) and (2) the energy conservation equation for phase change process is obtained as,

$$\frac{\partial(\rho c T)}{\partial t} + u \frac{\partial(\rho c T)}{\partial x} + v \frac{\partial(\rho c T)}{\partial y} = k \Delta T + S_t \quad (4)$$

in which source term S_t is,

$$S_t = -L \left(\frac{\partial(\rho \alpha)}{\partial t} + u \frac{\partial(\rho \alpha)}{\partial x} + v \frac{\partial(\rho \alpha)}{\partial y} \right) \quad (5)$$

Based on (4), the freezing is accounted for by a source term in the energy conservation equation which adds the latent heat of freezing according to the temperature in the fluid [4-5]. We note that at the interface $T = T_{freeze}$ which account for the isothermal nature of the phase change. As there is no velocity in the solid region, the convective transport in the frozen part will be suppressed.

The coupling between the liquid fraction and the energy conservation equation requires an iterative solution procedure, updating the liquid fraction every iterative sweep. Therefore, numerically, small density meshes and small time steps are required to accurately capture the liquid-solid interface. To improve the computational time efficiency of such simulations, Rosler et al. [4-5] introduced an error function for the evaluation of the liquid volume fraction for fast distinction between liquid/ mushy and solid regions. Basically, application of a continuous liquid fraction would allow its direct substitution into the energy conservation equation. The liquid fraction can be described by an error function as,

$$\alpha = 0.5(1 + \text{erf}(4(T - T_s)/(T_l - T_s))) \quad (6)$$

with the freezing temperature T_{freeze} equal to the arithmetic mean between T_l and T_s multiplied by a concentration factor as,

$$T_{freeze} = 0.5(T_l + T_s)(1 - sC_0) \quad (7)$$

Where C_0 is the initial salt concentration and s is a parameter obtained from the slope of the liquidus line in the phase diagram of saltwater (Fig. 1). Substituting (6) to (5), the source term of energy conservation equation takes form of one which is not a function of the liquid fraction α .

The conservation equation for mass reads as,

$$\frac{\partial u}{\partial x} + \frac{\partial v}{\partial y} = 0 \quad (8)$$

and the momentum conservation equations in x and y directions are,

$$\frac{\partial(\rho u)}{\partial t} + u \frac{\partial(\rho u)}{\partial x} + v \frac{\partial(\rho u)}{\partial y} = -\frac{\partial p}{\partial x} + \mu \Delta u + S_{xm} \quad (9)$$

$$\frac{\partial(\rho v)}{\partial t} + u \frac{\partial(\rho v)}{\partial x} + v \frac{\partial(\rho v)}{\partial y} = -\frac{\partial p}{\partial y} + \mu \Delta v + S_{ym} + S_b$$

where p is pressure and μ is viscosity. The source terms are derived from the Carman- Kozeny equations [4-6] for flow in porous media as,

$$S_{xm} = -D_c \frac{(1 - \alpha)^2}{\alpha^3 + \varepsilon} u \quad (10)$$

$$S_{ym} = -D_c \frac{(1 - \alpha)^2}{\alpha^3 + \varepsilon} v$$

where D_c represents the permeability of porous media in the mushy zone. It can be seen from (10) that in the liquid phase, the porosity function and thus the Darcy type source term turn to zero. Approaching the solid phase, the liquid fraction turns to zero. To avoid division by zero in the solid phase, a small numerical constant ε is introduced [4-5].

The source term S_b in the second equation of (9) is the buoyancy source term using the Boussinesq approximation,

$$S_b = \rho g [1 - \max(\beta, (T - T_s))] \quad (11)$$

with the volume expansion coefficient β and the gravitational force g . Finally, it is noted that the material properties $\varphi = \{c, \rho, k\}$ in the above equations are calculated as,

$$\varphi = \alpha \varphi_l + (1 - \alpha) \varphi_s \quad (12)$$

In the next section, the above introduced model is implemented into the open source computational fluid dynamics software OpenFOAM and results will be obtained accordingly.

III. PROBLEM DEFINITION AND NUMERICAL SOLUTION

Starting from initial conditions, the OpenFOAM solver calculates the energy equation. Based on the calculated temperature field, the error function describing the VOF equation are determined. Subsequently, the interface is updated by moving to a new position. A new conservation equation for the pressure is derived from the equations of conservation of mass and momentum. The pressure equation is solved for the pressure in the solution domain, coincidentally satisfies the mass conservation. The momentum equation is coupled with this newly introduced pressure equation and vice versa and hence solved by a suited pressure-velocity coupling (PISO-SIMPLE) scheme. This scheme iteratively corrects a first so-called momentum predictor solution by some corrector steps [4-6].

Convective and enthalpy-porosity based solidification solvers are implemented in OpenFOAM. Due to the considerable variations in density during freezing, the convection in the liquid phase has been taken into account. The flow is laminar since the Reynolds number, computed from the maximal velocity value, is very low.

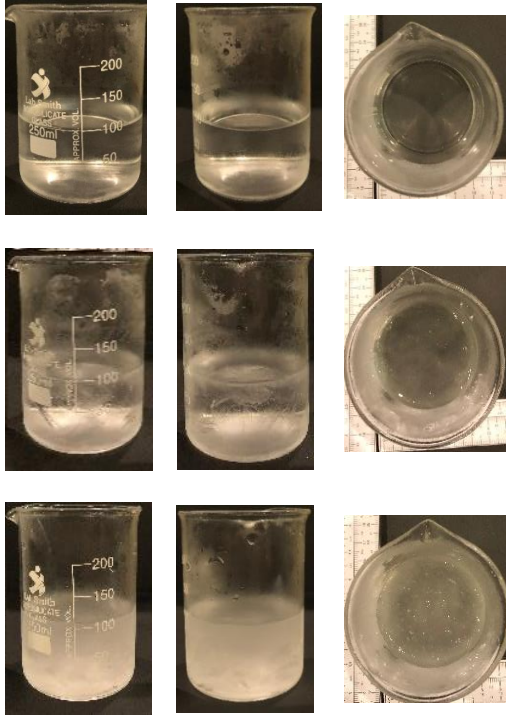


Fig. 2. Samples of freezing saltwater (concentration 5%); the first row at $t=30$ min, the middle row at $t=50$ min, and the third row at $t=90$ min.

The numerical method is used to investigate the water freezing process in a cylindrical container of diameter 62 mm and height 33 mm (Fig. 2). The container used in experiments is initially filled up with pure water at temperature $T=21^{\circ}\text{C}$ and slowly cooled down by a coolant flowing around its external surface at $T=-19^{\circ}\text{C}$. Due to the symmetry of the problem, a 2D model has been designed to reproduce the

experimental results. For the sake of simplicity, the thickness of the enclosure and its free surface effects have been ignored in the numerical simulations. Figure 3 illustrates the simulation domain and boundary conditions based on the experiments.

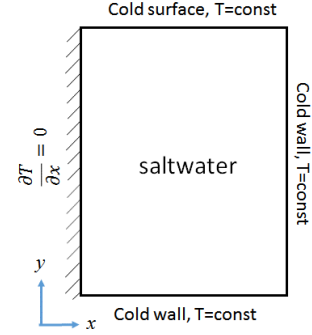


Fig. 3. Schematic diagram of the numerical problem

After performing a mesh sensitivity analysis, the simulation domain of $X = 31$ mm radius and $Y = 16.5$ mm height, is divided into 124×66 hexahedral cells. In addition, the time step is chosen so that the critical courant number remained less than 1 in each computational cell.

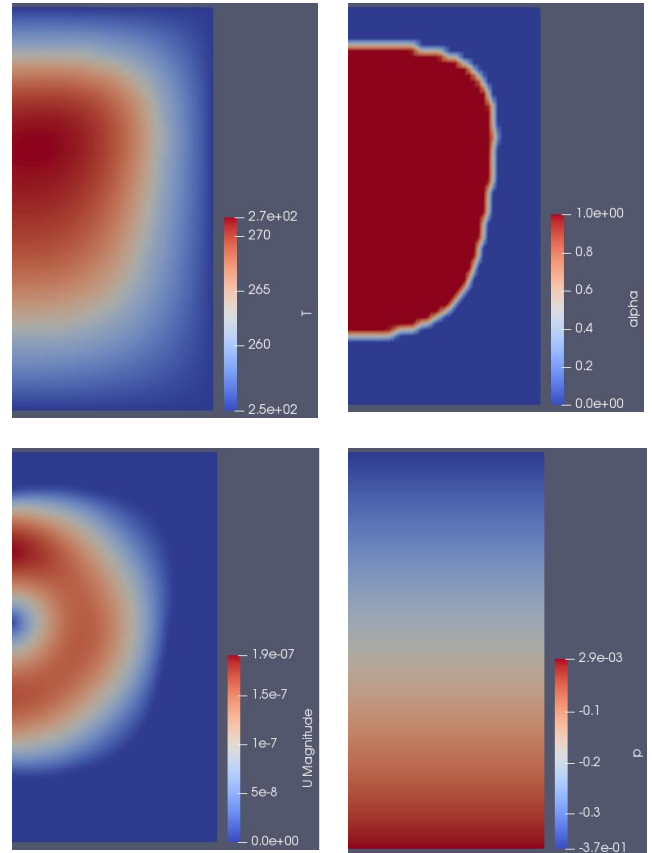


Fig. 4. Contours of flow-field parameters for 5% saltwater at $t=68$ min (temperature T , liquid volume fraction α , velocity magnitude U , and pressure p).

IV. RESULTS AND DISCUSSION

To validate the numerical method, the freezing of pure and salt water with different concentrations (5% and 20%) are measured experimentally. Fig. 4 shows the contours of scalar temperature, liquid volume fraction, velocity magnitude, and pressure for 5% saltwater at $t=68$ min. To study the freezing process, a beaker is filled by 100 ml water. The temperature is measured at time intervals of 10 minutes up to the full freezing of the content of the beaker. The volume of ice is calculated by measuring the volume of the water left in the beaker and results are compared with those of the numerical solution as shown in Fig. 5. Although a good agreement is obtained, discrepancies are clearly visible when salt concentration is increased.

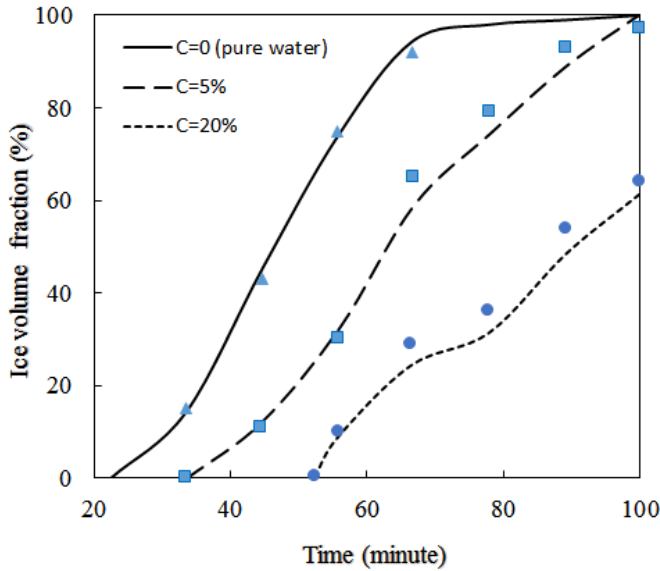


Fig. 5. Variation of ice volume fraction by time at different salt concentrations

(lines: curve-fitted experimental measurements, symbols: numerical results).

The comparison shows that the extended enthalpy-porosity method with continuous liquid fraction is capable to simulate desalinate freezing processes properly. The discrepancies to the experiment can be due to the three dimensional effects in the test enclosure and the assumption of non-temperature dependent physical properties (other than density) in the simulation.

REFERENCES

- [1] M.S. Rahman and M. Ahmed, "Freezing-melting process and desalination: review of present status and future prospects." *Int. J. Nuclear Desalination*, vol. 2, pp. 253–264, 2007.
- [2] P.M. Williams, M. Ahmad, B.C. Conolly, and D.L. Oatley-Radcliffe, "Technology for freeze concentration in the desalination industry" *Desalination*, vol. 356, pp. 314–327, 2011.
- [3] H. Jayakody, R. Al-Dadah, and S. Mahmoud, "Computational fluid dynamics investigation on indirect contact freeze desalination" *Desalination*, vol. 420, pp. 21–33, 2017.
- [4] F. Rosler and D. Bruggemann, "Shell-and-tube type latent heat thermal energy storage: numerical analysis and comparison with experiments" *Heat Mass Transfer*, vol. 47, pp. 1027–1033, 2011.
- [5] R.R. Kasibhatla, A. Konig-Haagen, F. Rosler, and D. Bruggemann, "Numerical modeling of melting and settling of an encapsulated PCM using variable viscosity" *Heat Mass Transfer*, vol. 53, pp. 1735–1744, 2017.
- [6] A.C. Bourdillon, P.G. Verdin, and C.P. Thompson, "Numerical simulations of water freezing process in cavities and cylindrical enclosures" *Applied Thermal Engineering*, vol. 75, pp. 839–855, 2015.
- [7] T. Michalek and T.A. Kowalewski, "Simulations of the water freezing process – numerical benchmarks" *Task Quarterly*, vol. 7(3), pp. 389–408, 2003.
- [8] V.R. Voller and C. Prakash, "A fixed grid numerical modeling methodology for convection-diffusion mushy region phase-change problems" *Int J Heat Mass Transf*, vol 30, pp. 1709-1719, 1987.

Patient-specific simulation of coarctation using lattice Boltzmann method and lumped parameter modelling

Reza Sadeghi^{1*}, Seyedvahid Khodaei¹, Zahra Keshavarz Motamed^{1,2}

1. Department of Mechanical Engineering, McMaster University, Hamilton, ON, Canada

2. Institute for Medical Engineering and Science, Massachusetts Institute of Technology, Cambridge, MA, USA

* sadeghir@mcmaster.ca

Abstract— Despite advancement in surgical/interventional procedures in coarctation of the aorta, life expectancy remained reduced due to the short- and long-term morbidity. The source of morbidity can be elucidated due to the presence of the adverse fluid mechanics resulting in degeneration of the vascular wall. Indeed, turbulent and disturbed flow strongly influence vascular pathogenesis and the disease progression. Accurate hemodynamics assessment in coarctation of the aorta have been of particular interest. In this study, we have developed computational fluid dynamics approach (based on Lattice Boltzmann method) and lumped parameter modelling to model a mild coarctation of the aorta. For verification, we compared velocity magnitude and pressure drop in a mild coarctation resulted from Lattice Boltzmann method vs. finite volume method. Findings of this study suggest that there are very good qualitative and quantitative agreements between Lattice Boltzmann method and finite volume method results. Lattice Boltzmann method, a computationally rather inexpensive and fast, can be considered as an alternative to the conventional computational fluid dynamics approaches to quantify blood flow dynamics.

Keywords: *Coarctation; Lattice Boltzmann method; Lumped parameter modelling; Turbulent modeling, Large Eddy simulation*

I. INTRODUCTION

Cardiovascular diseases are the leading causes of death in developed countries. Coarctation of the aorta (COA), a narrowing of the aorta distal to the left subclavian artery, is one of the most common and serious congenital cardiovascular problems. The hemodynamic severity and clinical manifestations of COA vary from asymptomatic mild narrowing of the aorta to severe obstruction with heart failure, aneurysms, aortic rupture and shock [1].

The sources of morbidity can be explained based on abnormal flow patterns and bio-mechanical forces, often categorized by turbulent flow, leading to the development and progression of cardiovascular diseases. Blood flow

quantification can be greatly useful for diagnosis in such patients.

To quantify blood flow structure, the Lattice Boltzmann Method (LBM) has attracted much attention in engineering and science as it is a simple and fast computational tool. Compared with traditional computational methods such as FVM and FEM, LBM has numerous advantages including easy parallelizing and programming [2]. Since it is not necessary to solve the Poisson equation for the pressure field, LBM can be much faster than common CFD methods [3]. Furthermore, the standard LBM is an explicit solver, thus LBM has intrinsic promising platforms for parallel processing [4].

The simplest form of LB equations (LBE) is based on Bhatnagar-Gross-Krook (BGK) approximation with single relaxation time (SRT) [5]. Recently, a vast range of research has been done in multiphase flow, heat transfer and turbulent flows by LBM. Most of the time, blood flow in the cardiac system follows a turbulent regime. Most common Lattice Boltzmann Turbulent modelling is based on Eddy-viscosity scheme which is similar to classical turbulence modelling for the Navier Stokes equations. The underlying equations in the Eddy-viscosity approach is based on turbulent collision time [6, 7]. These equations are usually solved with additional Finite difference (FD) schemes. In order to eliminate this additional computational effort, another numerical approach based on the subgrid scale (SGS) model was proposed [8-10]. Due to the complex geometry of the cardiac system and quadratic mesh shape of LBM, the mesh resolution of geometry has to be very high. In order to avoid the high-resolution domain, several solutions were proposed including, Immersed Boundary Methods (IBM) [11], non-uniform mesh grids [11] and extrapolation methods [12].

We have developed a computational fluid dynamics framework based on Lattice Boltzmann method and lumped parameter model to quantify fluid dynamic of coarctation. The former explicitly model the turbulent fluid flow domain, while the latter compute the flow boundary conditions.

II. METHODS

A. NUMERICAL STRATEGY

Under pathophysiological conditions, the blood flow becomes transitional to turbulent distally. Approaches based on the Reynolds-averaged Navier-Stokes (RANS) equations are the most prevalent to model but with noticeable limitations to model pulsatile flows [13]. Direct numerical simulations (DNS) are tax computing resources and are restricted to low Reynolds numbers. Large eddy simulation (LES) approach, which lies between DNS and RANS, is a technique well suited for the computational modelling of turbulent vascular flows with a high potential in modelling the physiological low-Reynolds transitional flows. Though the traditional LES modelling has allowed modelling of turbulence, it is still computationally expensive [14]. To compensate this, here we have developed a fast computational fluid dynamic (using LES-Smagorinsky modelling) and lumped parameter modelling framework. This patient-specific framework uses clinically measured hemodynamic input parameters in patients as well as 3-dimensional models reconstructed using CT images obtained in those patients (Fig. 1-a,b).

The computational domain was divided into blocks with uniform meshes that were processed by separate processors for parallelization purposes (Fig. 1-c). Time-dependent velocity at the ascending aorta and time-dependent pressure at the descending aorta were obtained from lumped parameter modelling (Fig. 2) and applied as the transient boundary conditions [14]. In order to suppress the undesired pressure fluctuation, a smooth startup phase was added to velocity inlet condition. Moreover, a nonslip Bouzidi boundary condition was considered at the walls. Fluid-structure interaction of wall was neglected. Keshavarz Motamed et al. [14, 15] showed that rigid wall assumption for the aorta is realistic. Patients with COA are usually hypertensive and characterized by reduced systemic compliance. The message passing model (MPI) is used on a computer with 64 GB RAM and 12 CPU cores (2.9 GHz). CPU time for our cases was on average around 2 hours. Blood was assumed to be Newtonian and incompressible fluid with a dynamic viscosity of 0.004 Pa·s and a density of 1050 kg/m³.

B. LATTICE BOLTZMANN METHOD

The simplest version of LBM is based on BGK (Bhatnagar, Gross and Krook) approximation. The discretized form of Boltzmann equation based on BGK approximation is [16]:

$$f_{\alpha}(x + e_{\alpha}\delta t, t + \delta t) - f_{\alpha}(x, t) = -\frac{1}{\tau}(f_{\alpha}(x, t) - f_{\alpha}^{eq}(x, t)) \quad (1)$$

Where f_{α} denotes distribution function, Maxwell-Boltzmann distribution function (f_{α}^{eq}) is defined as follows:

$$f_{\alpha}^{eq} = w_{\alpha}\rho\left[1 + \frac{e_{\alpha}\cdot u}{c_s^2} + \frac{(e_{\alpha}\cdot u)^2}{2c_s^4} - \frac{(u\cdot u)}{2c_s^2}\right] \quad (2)$$

Here, $\{e_{\alpha}|\alpha = 0, \dots, 18\}$ are the set of 19-discrete lattice direction vectors known as D3Q19 defining a local neighborhood of a three-dimensional grid points and w_{α} is a constant weighting coefficient that can be found in the literature [3].

Single relaxation time (τ) is a constant based on the BGK approach. For turbulent flow, the value of single relaxation time can be found in the literature [17]. The turbulence modelling that was utilized in the current article is based on the Explicit original Smagorinsky approach. The main idea is a superposition of the molecular kinematic viscosity ν_{mol} and a turbulent viscosity ν_{turb} related to the length scale or lattice size.

Equilibrium distribution function must satisfy the conservation of mass and momentum [18]. Therefore, hydrodynamic density (ρ) and macroscopic velocity (u) are conserved and determined by the following equations:

$$\rho = \sum_{\alpha=0}^{\alpha=18} f_{\alpha}^{eq} = \sum_{\alpha=0}^{\alpha=18} f_{\alpha} \quad (3)$$

$$\rho u = \sum_{\alpha=0}^{\alpha=18} f_{\alpha}^{eq} e_{\alpha} = \sum_{\alpha=0}^{\alpha=18} f_{\alpha} e_{\alpha} \quad (4)$$

An interpolation technique proposed by Bouzidi et al. [12] was used to represent boundaries of inclined and complicated shape.

Smagorinsky turbulent model is coupled with BGK-LBM numerical modelling in order to stabilize complex turbulent aorta fluid flow domain. For treating complex geometry, we utilized the second order accuracy method which is proposed by Bouzidi et al. [12].

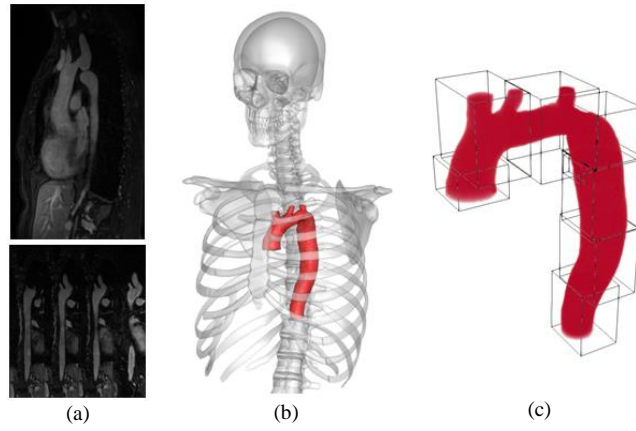


Figure 1. (a) CT scan Images and (b) Reconstructed 3-dimensional geometry in a patient with mild coarctation using computed tomography (CT). Geometries were used for investigating hemodynamics using computational fluid dynamics and lumped parameter modelling (c) Multiblock voxelization for a patient-specific geometry. Blocks are distributed between computer processor units in order to parallelize the simulation.

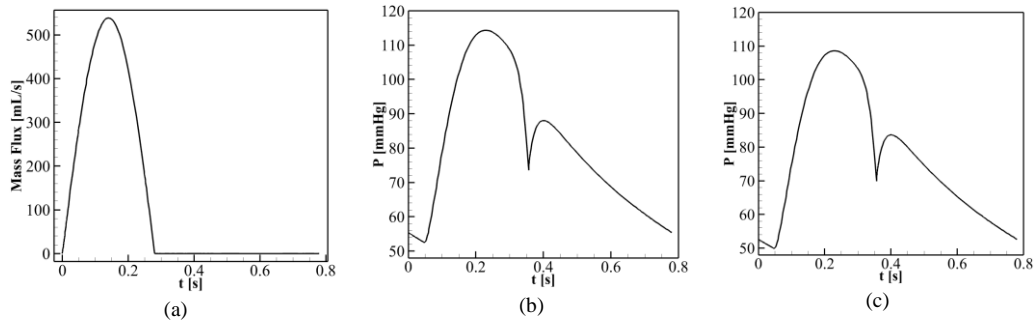


Figure 2. Pulsatile (a) inlet mass flow rate (b) inlet pressure and (c) outlet pressure waveforms (spline interpolation information is provided based on lumped parameter modelling).

III. RESULTS

In order to show mesh independency, the calculations were performed in three-dimensional lattice systems of 3915595, 8123432, 17012326 and 35342332 mesh numbers corresponding to, M1, M2, M3 and M4, respectively. The quantitative comparison of the pressure drops through a moderate coarctation of the aorta shown in Table 1. Based on the Table 1, a good trade-off between the accuracy and computational costs is mesh M2. Consequently, we will use this mesh in the remainder of the manuscript.

Table I. computed values for time-averaged pressure drop and maximum value of pressure drop during a cardiac cycle for different mesh resolutions (M1, M2, M3 and M4)

Case	Mesh number	Peak Pressure drop [mmHg]	Average Pressure drop [mmHg]	Time [minutes]
M1	3915595	26.6	4.3	66
M2	8123432	13.7	2.3	142
M3	17012326	13.8	2.4	315
M4	35342332	11.3	2.3	688

Computations were performed using computational fluid dynamics open source OpenLB, based on Lattice Boltzmann method and OpenFOAM (version 5.0), based on finite volume. The flow structures resulted from FVM and LBM solvers were compared (refer to Figure 3 for one example). Results show that the velocity magnitude distribution is quite similar for both methods within that specific plane.

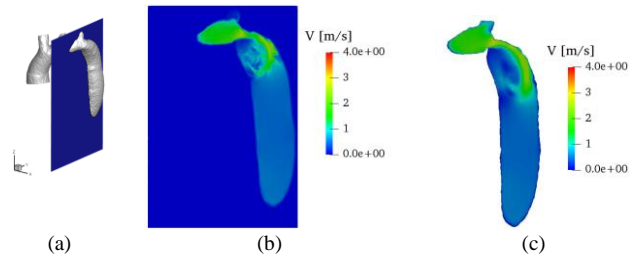


Figure 3. Comparison of the velocity magnitude in both LBM and FVM approaches for the same plan. Dynamic one equation eddy-viscosity model (dynamicKEqn) is used for LES simulation in OpenFoam (version 5.0), PISO solver is also used to solve transient Newtonian incompressible Navier-Stokes equations. The solution marched in time with a time step of e^{-5} s.

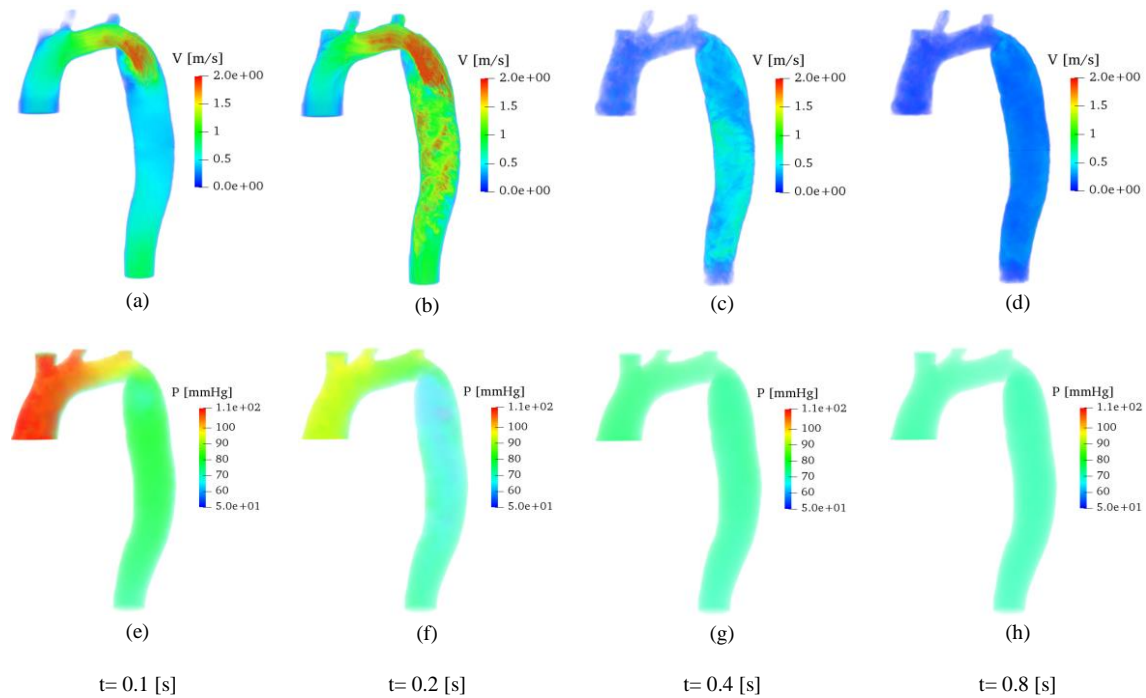


Figure 4. (a, b, c, d) Volume-rendered velocity magnitude and (e, f, g, h) Volume-rendered pressure magnitude during the cardiac cycle (systole, mid-to-late systole diastole)

Figure 4 shows the time-evolving velocity magnitude during cardiac cycle, showing a high eccentric jet downstream of coarctation during systole which later be diminished during diastole. This Figure also shows pressure magnitude contours at different times during a cardiac cycle - The presence of coarctation induces an increase in the pressure drop at the neck of the COA. This is very important since wall rupture and collapse are caused by the high-pressure gradient, which is caused by high flow velocity.

Figure 5 shows spatial pressure drop uncertainty analysis in before and after coarctation regions at different times during a cardiac cycle. This gives a range of potential pressure drop values that the cardiac catheter may have measured due to the unknown position of catheterization. In fact, this pressure drop must be compensated by the left ventricle (by increasing the left ventricle stroke work). This condition can rapidly affect the pumping action of the heart and can progress to heart failure.

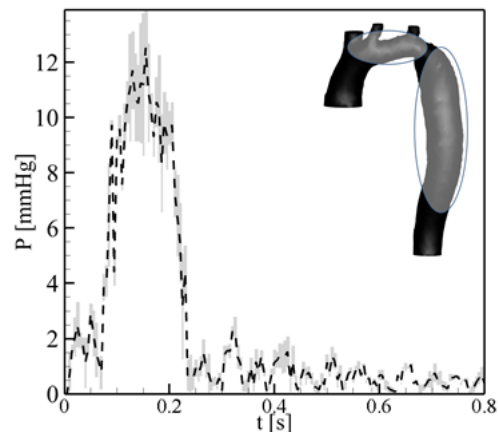


Figure 5. Uncertainty analysis for calculated pressure drops in a mild coarctation during a cardiac cycle.

ACKNOWLEDGMENT

This work was supported in part by NSERC Discovery Grant (RGPIN-2017-05349).

REFERENCES

- [1] P. S. Rao, "Coarctation of the aorta," *Current cardiology reports*, vol. 7, pp. 425-434, 2005.
- [2] R. Sadeghi, M. Shadloo, M. Hopp-Hirschler, A. Hadjadj, and U. Niekem, "Three-dimensional lattice Boltzmann simulations of high density ratio two-phase flows in porous media," *Computers & Mathematics with Applications*, 2018.
- [3] R. Sadeghi, M. Safdari Shadloo, M. Y. Abdollahzadeh Jamalabadi, and A. Karimipour, "A three-dimensional lattice Boltzmann model for numerical investigation of bubble growth in pool boiling," *International Communications in Heat and Mass Transfer*, vol. 79, pp. 58-66, 2016.
- [4] R. Sadeghi and M. Shadloo, "Three-dimensional numerical investigation of film boiling by the lattice Boltzmann method," *Numerical Heat Transfer, Part A: Applications*, vol. 71, pp. 560-574, 2017.
- [5] P. L. Bhatnagar, E. P. Gross, and M. Krook, "A model for collision processes in gases. I. Small amplitude processes in charged and neutral one-component systems," *Physical review*, vol. 94, p. 511, 1954.
- [6] S. Succi, G. Amati, and R. Benzi, "Challenges in lattice Boltzmann computing," *Journal of statistical physics*, vol. 81, pp. 5-16, 1995.
- [7] O. Filippova, S. Succi, F. Mazzocco, C. Arrighetti, G. Bella, and D. Hänel, "Multiscale lattice Boltzmann schemes with turbulence modeling," *Journal of Computational Physics*, vol. 170, pp. 812-829, 2001.
- [8] M. Krafczyk, J. Tölke, and L.-S. Luo, "Large-eddy simulations with a multiple-relaxation-time LBE model," *International Journal of Modern Physics B*, vol. 17, pp. 33-39, 2003.
- [9] H. Yu, S. S. Girimaji, and L.-S. Luo, "DNS and LES of decaying isotropic turbulence with and without frame rotation using lattice Boltzmann method," *Journal of Computational Physics*, vol. 209, pp. 599-616, 2005.
- [10] S. Hou, J. Sterling, S. Chen, and G. Doolen, "A lattice Boltzmann subgrid model for high Reynolds number flows," *arXiv preprint comp-gas/9401004*, 1994.
- [11] X. He, L.-S. Luo, and M. Dembo, "Some progress in lattice Boltzmann method. Part I. Nonuniform mesh grids," *Journal of computational Physics*, vol. 129, pp. 357-363, 1996.
- [12] M. h. Bouzidi, M. Firdaouss, and P. Lallemand, "Momentum transfer of a Boltzmann-lattice fluid with boundaries," *Physics of fluids*, vol. 13, pp. 3452-3459, 2001.
- [13] R. Mittal, S. Simmons, and H. Udaykumar, "Application of large-eddy simulation to the study of pulsatile flow in a modeled arterial stenosis," *Journal of biomechanical engineering*, vol. 123, pp. 325-332, 2001.
- [14] Z. Keshavarz-Motamed, F. R. Nezami, R. A. Partida, K. Nakamura, P. V. Staziaki, E. Ben-Assa, *et al.*, "Elimination of transcoarctation pressure gradients has no impact on left ventricular function or aortic shear stress after intervention in patients with mild coarctation," *JACC: Cardiovascular Interventions*, vol. 9, pp. 1953-1965, 2016.
- [15] Z. Keshavarz-Motamed, E. R. Edelman, P. K. Motamed, J. Garcia, N. Dahdah, and L. Kadem, "The role of aortic compliance in determination of coarctation severity: lumped parameter modeling, in vitro study and clinical evaluation," *Journal of biomechanics*, vol. 48, pp. 4229-4237, 2015.
- [16] A. A. Mohamad, *Lattice Boltzmann method: fundamentals and engineering applications with computer codes*: Springer Science & Business Media, 2011.
- [17] P. Nathen, D. Gaudlitz, M. Krause, and J. Kratzke, "An extension of the Lattice Boltzmann Method for simulating turbulent flows around rotating geometries of arbitrary shape," in *21st AIAA Computational Fluid Dynamics Conference. American Institute of Aeronautics and Astronautics*, 2013.
- [18] M. Sukop, "DT Thorne, Jr. Lattice Boltzmann Modeling Lattice Boltzmann Modeling," 2006.

A look inside a heart with cardiomyopathy and transcatheter aortic valve replacement: An imaged-based fluid-structure interaction modeling study

Seyedvahid Khodaei^{1*}, Reza Sadeghi¹, Ali Emadi^{1,2}, Zahra Keshavarz Motamed^{1,3}

1. Department of Mechanical Engineering, McMaster University, Hamilton, ON, Canada
2. Department of Electrical and Computer Engineering, McMaster University, Hamilton, ON, Canada
3. Institute for Medical Engineering and Science, Massachusetts Institute of Technology, Cambridge, MA, USA

* Khodae@mcmaster.ca

Abstract— Transcatheter aortic valve replacement (TAVR) is a minimally invasive device for patients with valvular disease. It was shown that while many patients experience a significant improvement after TAVR intervention, for others the situation worsens significantly. Blood flow quantification can be greatly useful for accurate and early diagnosis of cardiovascular diseases. Despite its importance, little is known regarding the changes in the left ventricle flow patterns induced by hypertrophic and restrictive cardiomyopathy and TAVR. For this purpose, we have developed an imaged-based fluid-structure interaction (FSI) method based on clinically measured hemodynamic metrics and imaging in patients who underwent TAVR. In healthy situation, the blood entering the left ventricle through the mitral valve forms a vortex that minimizes energy dissipation, prevents blood stagnation and optimizes pumping efficiency. Our findings show that cardiomyopathy and TAVR alter this optimized blood flow. Moreover, not only wall thickening of left ventricle tissue increases the magnitude of the pressure during diastole, but also tissue fibrosis has a major impact on blood flow dynamic in the left ventricle. Findings of this study showed the restricted motion of left ventricle (known as restrictive cardiomyopathy) as well as reduced systemic compliance can lead to considerable increase in blood pressure.

Keywords: Fluid-structure interaction (FSI), Hemodynamics, Cardiomyopathy, TAVR, Left ventricle, Aortic stenosis

I. INTRODUCTION

Heart, a fundamental part of the cardiovascular system, is responsible for pumping blood and distributing oxygen throughout the entire body. Due to its complex structure, the cardiovascular system must work in a synchronized fashion to provide enough blood for the body. Heart failure is a major cause of mortality in patients with cardiovascular diseases. Common causes of heart failure include hypertension, valvular heart disease, coronary artery disease, heart attack and cardiomyopathy.

Cardiomyopathy Originally defined as myocardial diseases of unknown cause by Goodwin in 1961 [1]. Cardiomyopathies are a collection of diseases of the left ventricle caused by alterations in ventricular tissue. Cardiomyopathy can be categorized to three groups: dilated cardiomyopathy, hypertrophic cardiomyopathy and restrictive cardiomyopathy. More recently, cardiomyopathy has been classified into four subgroups based on morphology, including hypertrophic, dilated, restrictive and arrhythmogenic cardiomyopathy [2]. *Among the different types of cardiomyopathy, the restrictive and hypertrophic cardiomyopathies are known to cause diastolic dysfunction* [2].

Restrictive cardiomyopathy is a disease that results in impaired filling of left ventricle, although systolic function remains normal [3]. The left ventricle muscle tissue becomes rigid, decreasing the ability of the left ventricle to expand and fill with blood during the diastole phase. Although in the early stages of disease, the pumping ability of the ventricle may be normal during systole phase, there is a significant disorder during diastole phase which makes it harder for the ventricle to get enough blood. This situation results in significant increase in the left ventricle pressure while non-significant increase in the left ventricle volume [3].

Hypertrophic cardiomyopathy is a genetically determined disease identified by an increase in left ventricle wall thickness, named left ventricular hypertrophy. Usually this is diagnosed by echocardiography or cardiac magnetic resonance imaging [1,4].

Generally, cardiomyopathies are diagnosed only in the absence of coronary artery disease, valvular disease, hypertension or other identifiable causes. However, some recent studies have reported patients with concomitant cardiomyopathy and aortic stenosis. The combination of aortic stenosis (AS) and asymmetrical septal hypertrophy has been noted in about 10% of patients with AS undergoing surgery [5–7]. There are several case reports of aortic stenosis together

with hypertrophic cardiomyopathy [8–10] and other configurations of cardiomyopathies [11].

Until recently, the only possible choice for high-risk patients with valvular disease was surgical replacement of the valve. This procedure has a high mortality rate. Transcatheter aortic valve replacement (TAVR) is a growing alternative therapeutic intervention for patients with symptomatic severe aortic stenosis especially in whom conventional surgical aortic valve replacement is deemed unfeasible due to pre-existing illness or high risk of postoperative mortality [12,13].

Despite the widespread usage of TAVR, there is a scarcity of a quantitative understanding of the interplay between pre-existing ventricular pathologies, and post-TAVR recovery. Further studies are needed to elucidate the relationship between valvular diseases, left ventricle remodeling and TAVR. Effective quantification hinges on quantification of the blood flow dynamics inside the left ventricle.

Numerical simulation is a useful non-invasive method to investigate the heart function in cardiovascular diseases. Computational fluid dynamics has been used for years to study blood flow in the left ventricle [14–18]. However, due to the nature of heart tissue and its interaction with blood flow, fluid-structure interaction (FSI) is the most comprehensive tool for such study that takes into the account both the effect of fluid (blood flow) and solid (tissue). Such simulations present formidable mathematical and computational challenges - modeling must incorporate the motion of fluid and the motion of vessel wall, persistent pulse-driven changes in flow as well as in pressure and the mechanical interactions of other concomitant cardiovascular diseases.

Except precise solution of the governing equations, Blood flow computational modeling in cardiovascular pathophysiology requires patients-specific image analysis, model reconstruction, boundary condition and material property selection. There have been reported several FSI studies exploring the filling phase of the left ventricle [19,20], and numerical simulations of cardiomyopathy [21–23]. However, these studies are associated with idealized and simplified geometries, boundary conditions and etc.

The aim of this study was to understand and to quantify the flow structure in the left ventricle using fluid-structure interaction method in a patient with severe hypertrophic and restrictive cardiomyopathy who subsequently received TAVR. For this purpose, we have developed a custom designed imaged-based computational mechanics method based on clinically measured hemodynamic metrics and imaging in patients who underwent TAVR.

II. MATERIALS AND METHODS

A. Geometry

Geometry of the left ventricle and the heart valves are obtained using computed tomography (CT) and echocardiography images of an 86 years old male patient. This patient has received TAVR since suffering from severe aortic stenosis. Figure 1 shows significant thickening of the left ventricle wall. In addition, echocardiography images show that left ventricle is restricted.

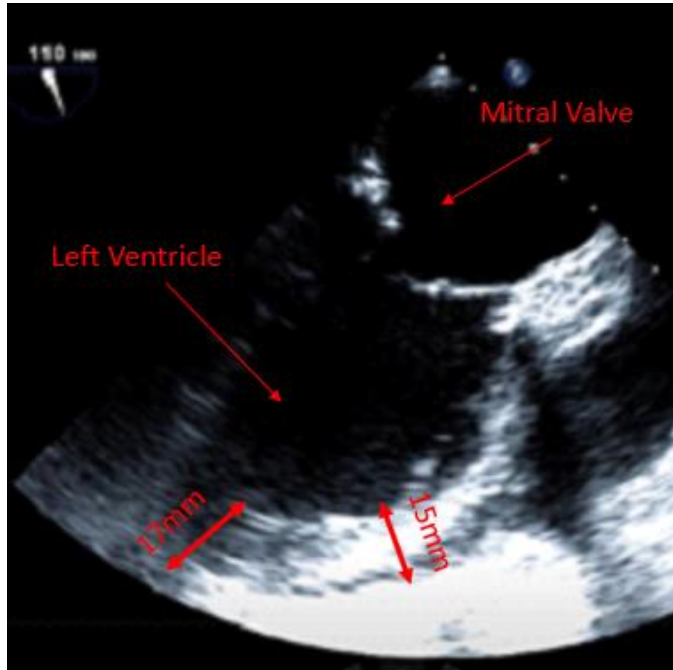


Figure 1. Echo image of the left ventricle in a patient with cardiomyopathy who received TAVR (Apical 2- chamber view)

CT images for the patient and the process of segmentation has been shown in Figure 2. We used CT images from the patient to segment and reconstruct the 3D geometries of the left ventricle using ITK-SNAP software [24], an open source 3D image processing and model generation software package. Same as echocardiography images, we observed a major thickening of the left ventricle wall in CT images (Figures 2 and 3).

B. Governing Equations

1) Fluid Governing Equations

Blood flow was modeled as an incompressible Newtonian viscous fluid and flow was assumed to be laminar, transient and pulsatile due to the nature of blood flow in cardiovascular system. Therefore, continuity and momentum equations are presented as:

$$\oint_s (n \cdot v) ds = 0 \quad (1)$$

$$\int_{\nabla} \frac{\partial v}{\partial t} d\nabla + \oint_s v [n \cdot v] ds = \frac{1}{\rho} \oint_s n \cdot [\mu \nabla v] ds - \frac{1}{\rho} \int_{\nabla} \nabla p d\nabla \quad (2)$$

where n is the normal vector to the surface S , V is the fluid velocity, μ is the fluid dynamic viscosity, P is the blood pressure and ρ is the fluid density. Due to the deformation of the fluid-solid interface, momentum equation (2) should be written in the form of Arbitrary Lagrangian-Eulerian (ALE):

$$\int_{\nabla} \frac{\partial v}{\partial t} d\nabla + \oint_s n \cdot (v - v_s) v ds = \frac{1}{\rho} \oint_s n \cdot [\mu \nabla v] ds - \frac{1}{\rho} \int_{\nabla} \nabla p d\nabla \quad (3)$$

$$\frac{d}{dt} \int_{\nabla} d\nabla = \oint_s n \cdot v_s ds \quad (4)$$

where V_s is the velocity of surface. Also, the relationship between the rate of change of the volume and the velocity of surface is according to the geometric conservation law (equation 4). Density of blood was assumed to be 1060 kg/m³ with the dynamic viscosity of 0.003 Pa s.

2) Solid Governing Equations

According to the linear momentum conservation law in the total Lagrangian form, deformation of elastic and compressible solid can be written as:

$$\int_{V_0} \rho_0 \frac{\partial}{\partial t} \left(\frac{\partial u}{\partial t} \right) dV = \oint_{s_0} n \cdot (\Sigma \cdot F^T) ds + \int_{V_0} \rho_0 b dV \quad (5)$$

in which the subscript 0 describes the undeformed configuration and u is the displacement vector. F is the deformation gradient tensor and can be described as:

$$F = I + (\nabla u)^T \quad (6)$$

where I is the second order Identity tensor. Also, Σ in eq. (5) is the second Piola-Kirchhoff stress tensor and can be explained through Cauchy stress tensor (σ) as:

$$\sigma = \frac{1}{\det F} F \cdot \Sigma \cdot F^T \quad (7)$$

Using St. Venant-Kirchhoff constitutive material model, Σ can be explained through isotropic Hooke's law:

$$\Sigma = 2\mu E + \lambda \text{tr}(E) I \quad (8)$$

where μ and λ are the Lamé's constants (related to the Young's modulus and Poisson's ratio of material). E is the Green-Lagrangian strain tensor and is defined as:

$$E = \frac{1}{2} [\nabla u + (\nabla u)^T + \nabla u \cdot (\nabla u)^T] \quad (9)$$

C. Boundary Condition

1) FSI Boundary condition

The fluid and solid models were coupled by kinematic and dynamic conditions. To satisfy the kinematic condition, the velocity and displacements must be continuous across the interface:

$$u_{f,i} = u_{s,i} \quad (10)$$

$$V_{f,i} = V_{s,i} \quad (11)$$

where subscripts i , s and f indicate the interface, solid and fluid regions respectively. To satisfy the dynamic condition, the forces at the interface must be in equilibrium:

$$n_i \cdot \sigma_{f,i} = n_i \cdot \sigma_{s,i} \quad (12)$$

The Dirichlet-Neumann procedure at the interface indicates that fluid domain was solved for a given velocity/displacement and solid was solved for a given traction.

The partitioned approach was used in which traction was calculated at the fluid side of interface and applied as a traction boundary condition at the solid side of the interface.

The fluid and solid domain are depicted in Figure 4 as well as FSI boundary with various thicknesses of the left ventricle tissue in the patient.

D. Numerical Method

The computational domain is split into finite number of tetrahedral elements for both solid and fluid. The discretized fluid model with a moving tetrahedral mesh consists of the discretized momentum and pressure equation. The system of equations governing the FSI problem are solved using Finite Volume Method which is quite well-known in CFD and is raising attention also in solid mechanics [25].

In the solid model, the second-order FV discretization of the integral conservation equation is used to transform surface integrals into sums of face integrals. Afterwards, the face and volume integrals are approximated by second-order accurate mid-point rule.

The open-source package foam-extend [26] is used in this study, implementing interface Quasi-Newton-Implicit Jacobian Least-Squares (IQN-ILS) [27] as the coupling algorithm to couple discretized fluid and solid governing equations.

The moving boundary (interface) is controlled using dynamic mesh methodology which is updated with the movement of the solid boundary. This method is based on Laplace equation using the cell-centered FV method. A lumped-parameter model simulating the function of the left side of the heart was used for imposing boundary conditions [28].

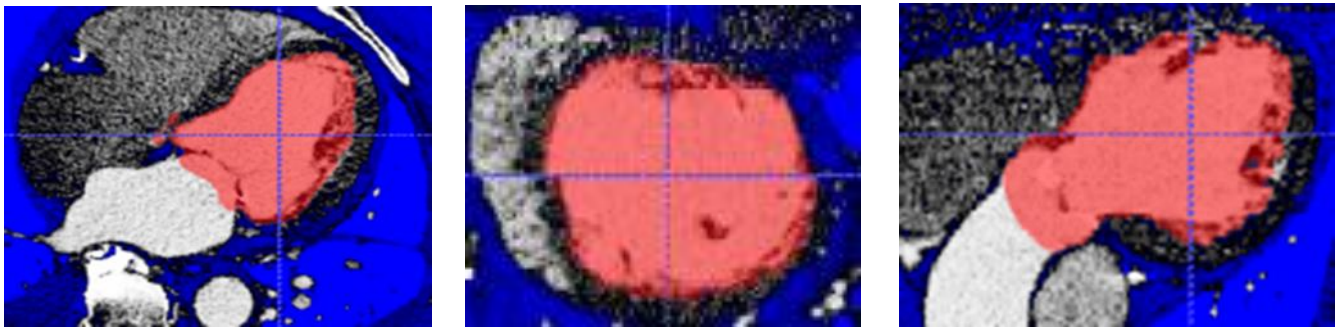


Figure 2. Computed tomography image segmentation

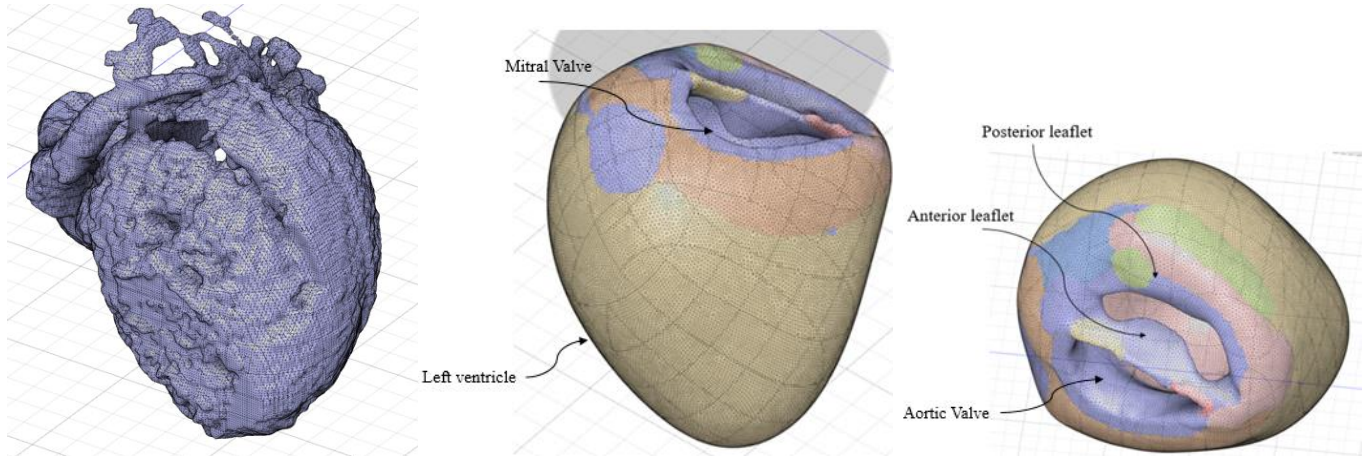


Figure 3. Different views of of the reconstructed model using computed tomography images

III. RESULTS AND DISCUSSION

In this study, an imaged-based FSI computational model of the left ventricle in a patient with cardiomyopathy and TAVR was presented. Simulations started at the end of systole, thus the mitral valve was fully opened (left ventricle and mitral valve geometries were reconstructed at the end of systole). Simulations were performed for three different Young's modulus of 1, 10 and 100 Mpa (Figure 6; A to C, respectively) to investigate the effect of the increase in the left ventricle wall stiffness. Also, the Poisson's ratio is the same for all three cases and is equal to 0.49.

Instantaneous streamlines of the flow during diastole (Figure 6) show that as the wall motion becomes restricted, the flow is less scattered across the left ventricle and is more focused at the apex of the left ventricle.

More importantly, the values of pressure are significantly different for these three different cases. As the tissue gets stiffer, the pressure value increases, and the left ventricle wall allows less expansion during diastole phase. At early diastole phase, the pressure increases from 0.03249 Mpa to 0.1102 Mpa and 0.3427 Mpa (A to C, respectively). This means once the Young's modulus increases to a considerable value, the pressure value inside the left ventricle increases significantly.

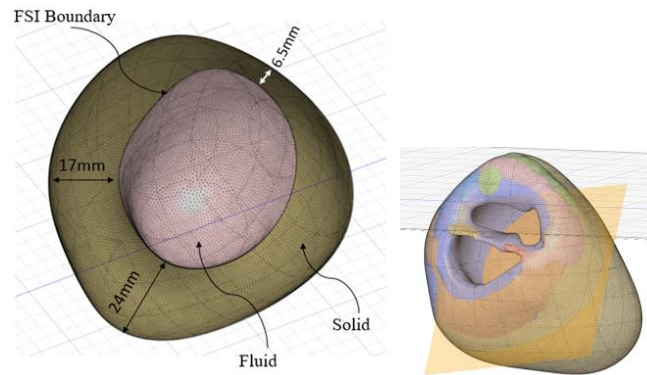


Figure 4. Fluid and solid boundaries representation of geometry (cross-section plane in right side)

Although patient-specific material property quantification is still a challenge, above mentioned results delineate the importance of considering restricted motion of left ventricle wall based on changes that could occur in patient's tissue (e.g., calcification and fibrosis). Moreover, since in different types of cardiomyopathy, different parts of the left ventricle will be affected, local stiffening occur for the left ventricle tissue also should be investigated to assess left ventricle blood pressure.

ACKNOWLEDGMENT

This work was supported in part by NSERC Discovery Grant (RGPIN-2017-05349).

REFERENCES

- [1] Goodwin JF, Gordon H, Hollman A, Bishop MB. Clinical aspects of cardiomyopathy. *British Medical Journal* 1961;1:69.
- [2] Cecchi F, Tomberli B, Olivotto I. Clinical and molecular classification of cardiomyopathies. *Global Cardiology Science and Practice* 2012;2012:4.
- [3] Kushwaha SS, Fallon JT, Fuster V. Restrictive cardiomyopathy. *New England Journal of Medicine* 1997;336:267–276.
- [4] Gersh BJ, Maron BJ, Bonow RO, Dearani JA, Fifer MA, Link MS, et al. 2011 ACCF/AHA guideline for the diagnosis and treatment of hypertrophic cardiomyopathy: a report of the American College of Cardiology Foundation/American Heart Association Task Force on practice guidelines developed in collaboration with the American Association for Thoracic Surgery, American Society of echocardiography, American Society of nuclear Cardiology, Heart Failure Society of America, Heart Rhythm Society, Society for Cardiovascular Angiography and Interventions, and Society of Thoracic Surgeons. *Journal of the American College of Cardiology* 2011;58:e212–e260.
- [5] Panza JA, Maron BJ. Valvular aortic stenosis and asymmetric septal hypertrophy: diagnostic considerations and clinical and therapeutic implications. *European Heart Journal* 1988;9:71–76.
- [6] Laskey WK, Kussmaul WG. Subvalvular gradients in patients with valvular aortic stenosis: prevalence, magnitude, and physiological importance. *Circulation* 2001;104:1019–1022.
- [7] Kayalar N, Schaff HV, Daly RC, Dearani JA, Park SJ. Concomitant septal myectomy at the time of aortic valve replacement for severe aortic stenosis. *The Annals of Thoracic Surgery* 2010;89:459–464.
- [8] Ramamurthi A, Aker EM, Pandian NG. A case of aortic stenosis and hypertrophic cardiomyopathy. *Echocardiography* 2012;29:1261–1263.
- [9] Ishimura M, Takayama M, Saji M, Takamisawa I, Umemura J, Sumiyoshi T, et al. A case of hypertrophic obstructive cardiomyopathy with aortic stenosis. *Journal of Cardiology Cases* 2014;9:129–133.
- [10] Vanichsarn C, Siegel RJ. Fool me once, fool me twice: hypertrophic cardiomyopathy with aortic stenosis. *The American Journal of Medicine* 2015;128:1076–1079.
- [11] Shenouda J, Silber D, Subramaniam M, Alkhatib B, Schwartz RK, Goncalves JA, et al. Evaluation and management of concomitant hypertrophic obstructive cardiomyopathy and valvular aortic stenosis. *Current Treatment Options in Cardiovascular Medicine* 2016;18:17.
- [12] Leon MB, Smith CR, Mack MJ, Makkar RR, Svensson LG, Kodali SK, et al. Transcatheter or surgical aortic-valve replacement in intermediate-risk patients. *New England Journal of Medicine* 2016;374:1609–1620.
- [13] Vy P, Auffret V, Badel P, Rochette M, Le Breton H, Haigron P, et al. Review of patient-specific simulations of transcatheter aortic valve implantation. *International Journal of Advances in Engineering Sciences and Applied Mathematics* 2016;8:2–24.
- [14] Peskin CS, McQueen DM. A three-dimensional computational method for blood flow in the heart I. Immersed elastic fibers in a viscous incompressible fluid. *Journal of Computational Physics* 1989;81:372–405.
- [15] Domenichini F, Pedrizzetti G, Baccani B. Three-dimensional filling flow into a model left ventricle. *Journal of Fluid Mechanics* 2005;539:179–198.
- [16] Vierendeels JA, Riemslag K, Dick E, Verdonck PR. Computer simulation of intraventricular flow and pressure gradients during diastole. *Journal of Biomechanical Engineering* 2000;122:667–674.
- [17] Saber NR, Gosman AD, Wood NB, Kilner PJ, Charrier CL, Firmin DN. Computational flow modeling of the left ventricle based on in vivo MRI data: initial experience. *Annals of Biomedical Engineering* 2001;29:275–283.
- [18] Khodaei S, Fatouree N, Nabaei M. Numerical simulation of mitral valve prolapse considering the effect of left ventricle. *Mathematical Biosciences* 2017;285:75–80.
- [19] Cheng Y, Oertel H, Schenkel T. Fluid-structure coupled CFD simulation of the left ventricular flow during filling phase. *Annals of Biomedical Engineering* 2005;33:567–576.
- [20] Watanabe H, Sugiura S, Kafuku H, Hisada T. Multiphysics simulation of left ventricular filling dynamics using fluid-structure interaction finite element method. *Biophysical Journal* 2004;87:2074–2085.
- [21] Baccani B, Domenichini F, Pedrizzetti G, Tonti G. Fluid dynamics of the left ventricular filling in dilated cardiomyopathy. *Journal of Biomechanics* 2002;35:665–671.
- [22] Domenichini F, Pedrizzetti G. Intraventricular vortex flow changes in the infarcted left ventricle: numerical results in an idealised 3D shape. *Computer Methods in Biomechanics and Biomedical Engineering* 2011;14:95–101.
- [23] Watanabe H, Sugano T, Sugiura S, Hisada T. Finite element analysis of ventricular wall motion and intra-ventricular blood flow in heart with myocardial infarction. *JSME International Journal Series C Mechanical Systems, Machine Elements and Manufacturing* 2004;47:1019–1026.
- [24] Yushkevich PA, Piven J, Hazlett HC, Smith RG, Ho S, Gee JC, et al. User-guided 3D active contour segmentation of anatomical structures: significantly improved efficiency and reliability. *Neuroimage* 2006;31:1116–1128.
- [25] Cardiff P, Demirdžić I. Thirty years of the finite volume method for solid mechanics. *ArXiv Preprint ArXiv:181002105* 2018.
- [26] Weller HG, Tabor G, Jasak H, Fureby C. A tensorial approach to computational continuum mechanics using object-oriented techniques. *Computers in Physics* 1998;12:620–631.
- [27] Degroote J, Bathe K-J, Vierendeels J. Performance of a new partitioned procedure versus a monolithic procedure in fluid–structure interaction. *Computers & Structures* 2009;87:793–801.
- [28] Keshavarz-Motamed Z, Nezami FR, Partida RA, Nakamura K, Staziaki PV, Ben-Assa E, et al. Elimination of transcoarctation pressure gradients has no impact on left ventricular function or aortic shear stress after intervention in patients with mild coarctation. *JACC: Cardiovascular Interventions* 2016;9:1953–1965.

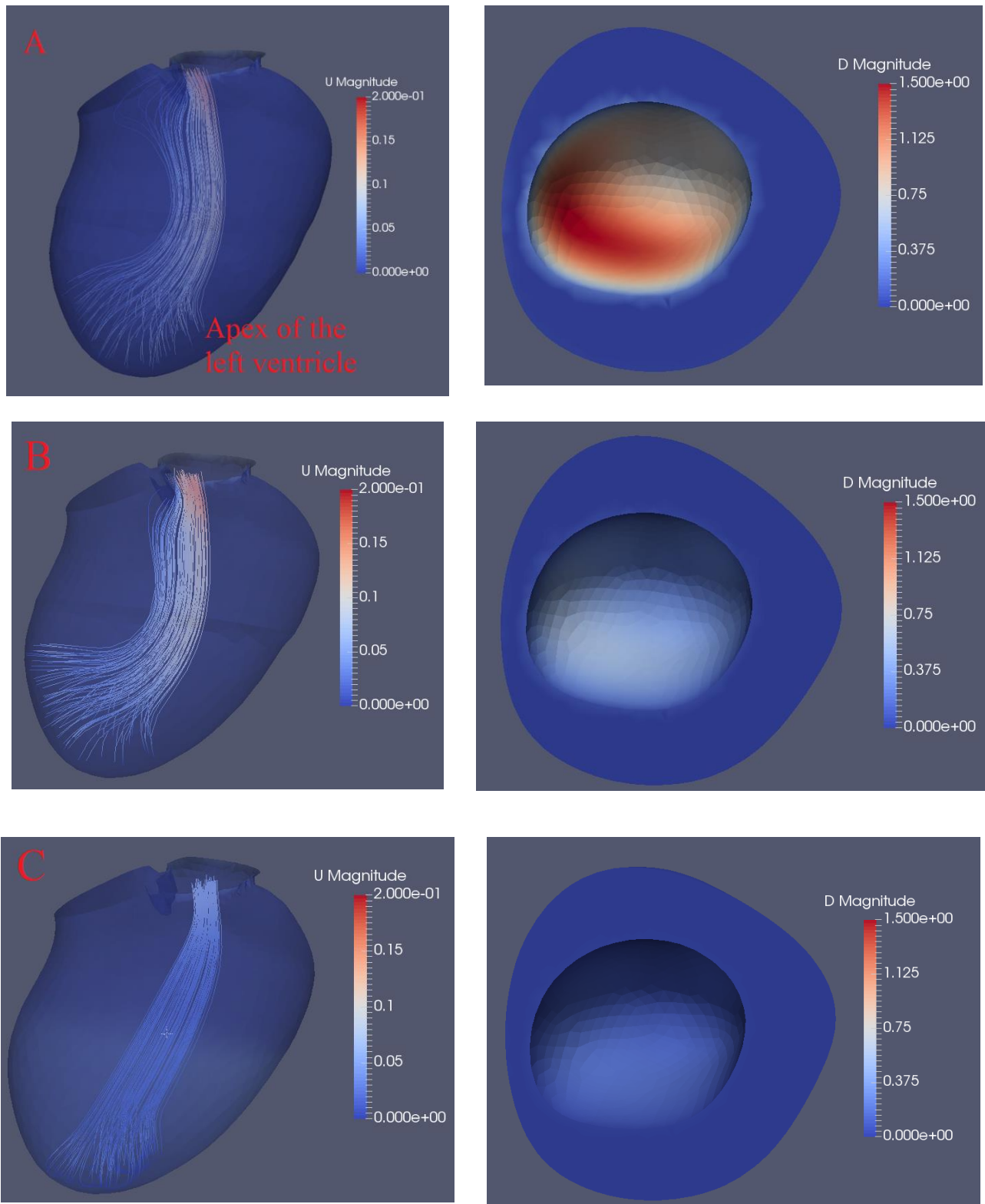


Figure 5. Velocity of fluid domain (m/s) (on the left column) and left ventricle tissue displacements (mm) for different material properties ($E=1, 10$ and 100 Mpa from A to C, respectively) during diastole.

Numerical Investigation of the thermodynamics behaviors in the Central Downward Circular Tube of the 64-element Canadian SCWR Fuel Bundle

Huirui Han and Chao Zhang
Mechanical and Materials Engineering
Western University
London, Canada
czhang@eng.uwo.ca

Abstract— The supercritical water-cooled reactor was proposed as one of the Generation IV nuclear systems. Despite many studies on supercritical water in circular channels have been conducted before, only very few studies on the fluid flow and heat transfer process in coolant channels of the supercritical water-cooled reactors have done. In this study, the thermo-hydraulic behaviors of the water in the coolant channel of the 64-element Canadian Supercritical water-cooled reactor are predicted by computational fluid dynamics (CFD) simulations using the software ANSYS FLUENT. The results show that the secondary flow appears at the inner coolant channel, and the high vorticity enhances the heat transfer between the wall and the supercritical water.

Keywords-*Supercritical water-cooled reactor; thermo-hydraulic; CFD; secondary flow; vorticity*

I. INTRODUCTION

The supercritical water-cooled reactor (SCWR) was proposed as one of the Generation IV nuclear reactors, which is the only one using the supercritical water as coolant. The proposed SCWR configuration is shown in Fig.1 [1]. Canadian supercritical water-cooled reactor concept is based on the design of the typical CANDU reactor. The moderator for the reactor is still heavy water, while the coolant is light water. Because of the single-phase coolant, steam separators and steam generators are not needed. Since the configuration of the SCWR is relatively simple, the heat loss can be decreased and the thermal efficiency can be around 44% [2]. Although SCWRs have these advantages, there are still challenges. The supercritical water experiences a dramatic thermophysical properties change near the pseudo-critical point, which can be seen in Fig.2. The pseudo-critical point is where the specific heat of the water has the peak value under a specific pressure above the critical point. Because of the strong properties change of the supercritical water around the pseudocritical point, especially density and specific heat, heat transfer deterioration in the channel is easy to happen.

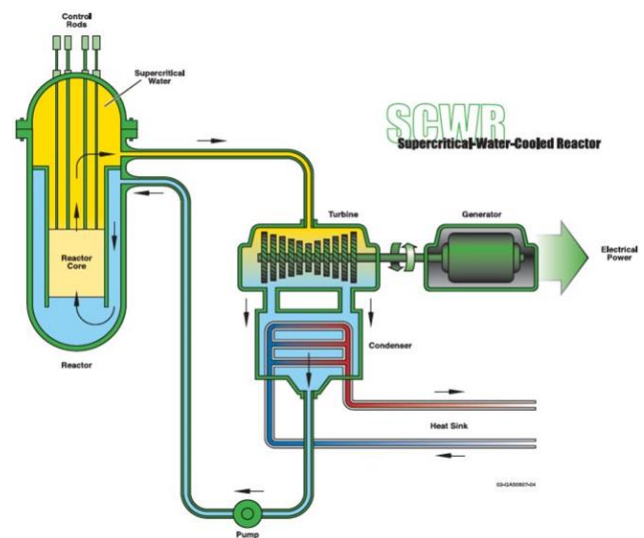
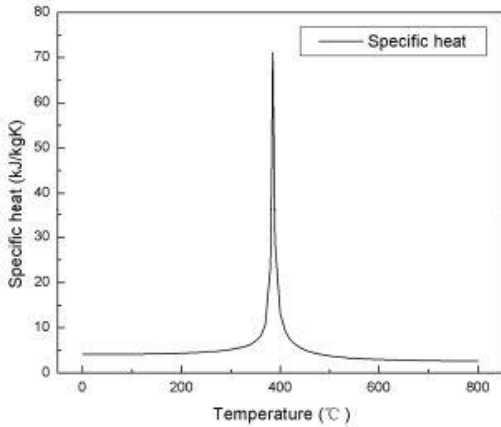


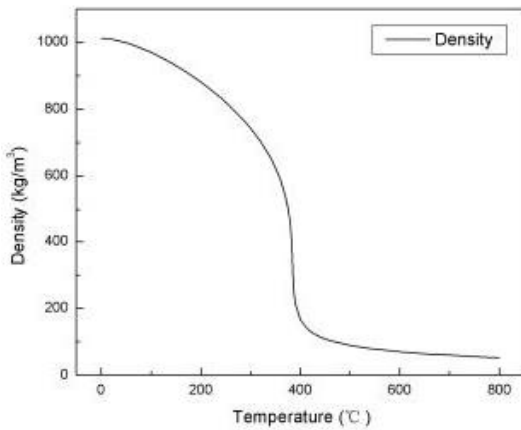
Figure1. Proposed supercritical water-cooled reactor configuration [1]

Only very limited experimental studies were carried out for the heat transfer and flow phenomenon of supercritical fluids because of the experiment environment restrictions. Xi et al. [3] did an investigation on the supercritical water flow between two heated parallel channels. Both inlet mass flow rate and outlet temperature oscillations were observed. Verma et al. [4] carried out the experiments using a scaled test facility of AHWR (Advanced Heavy Water Reactor) rod bundle. The effect of the spacer on the turbulent mixing rate in subchannels was investigated. The results showed that the turbulent mixing rate increased with the increase in the average Reynolds number.

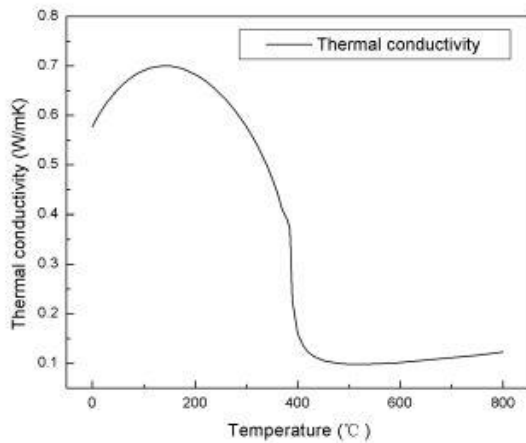
Until now, Canadian SCWR is still in conceptual design stage and no experimental data are available. Numerical method is highly recommended to predict the characteristics of fluid flow and heat transfer in reactor fuel bundles when there are no experimental data.



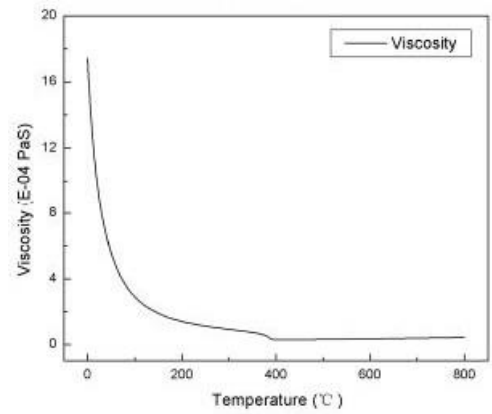
(a) Specific heat



(b) Density



(c) Thermal conductivity



(d) Viscosity

Figure2 Thermohydraulic properties of the water under $p=25\text{MPa}$

The numerical studies for the flow in rod bundles have been conducted by several researchers. Azih et al. [5] studied the convective heat transfer of supercritical fluids without gravity, and obtained the effects of Reynolds number, boundary layer and other factors on heat transfer. Zeng et al. [6] also conducted computational fluid dynamics simulation in circle channel. The gravity and thermal expansion acceleration effects were included in the turbulence model used in the subcritical fluid flow simulation. Zhang et al. [7] proposed a new supercritical fluid flow model to better deal with the physical instability properties of the supercritical fluid around the pseudo-critical point. Zhang et al. [8] simulated heat transfer and flow of supercritical water in a 37-element horizontal arranged SCWR under steady state condition and found that the anisotropic turbulent model, the Reynolds stress model, behaves much better than the isotropic model in predicting the cladding surface temperature. Rohit [9] also simulated heat transfer of supercritical water in circle channels using different turbulence models. The results were compared with the respective experimental data to validate the numerical model. However, these previous researchers mainly investigated either the supercritical water flows in circle channels or based on a simplified geometry of CANDU fuel bundle. The current design of the Canadian SCWR is shown in Fig.3 [10]. The coolant flows downward first in the circle tube, then flows upward in the fuel rods region. The cross-section view of the fuel bundle evolution of the Canadian SCWR is illustrated in Fig.4. The cross-section area of the inner coolant tube is enlarged gradually to reduce the cladding surface temperature of the fuel rod. There is still lack of the investigation of the thermo-hydraulic behaviors of the supercritical water in the inner coolant tube of 64-element fuel bundle. Therefore, in this work, the fluid flow and heat transfer phenomenon in the inner coolant tube under the full load condition will be investigated. And the Computational Fluid Dynamics (CFD) simulations are carried out by ANSYS FLUENT 19.1.

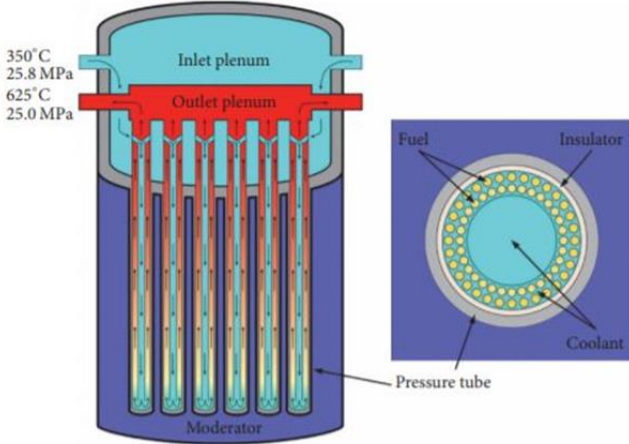


Figure 3. Canadian supercritical water-cooled reactor

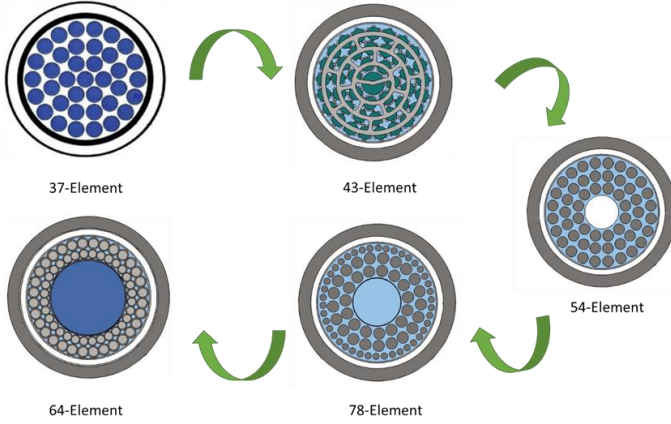


Figure 4. Cross-section view of the Canadian supercritical water-cooled reactor fuel bundle

II. GOVERNING EQUATIONS AND NUMERICAL MODELS

The simulation of the inner downward coolant flow in the circular tube of the 64-element Canadian SCWR fuel bundle is carried out under the full load condition, which is shown in Table 1. The properties of the water under 25 MPa are from Wagner [11]. The computational domain and the cross-section view of the mesh constructed used in the simulation are illustrated in Fig. 5.

Table 1 Specifications of the inner circular tube

Center tube radius/mm	46
Center tube wall thickness/mm	1
Center tube length/mm	5000
Center tube inlet temperature/Celsius	350

The governing equations for the three-dimensional steady flow are conservations of mass, momentum and energy:

$$\frac{\partial}{\partial x_i} (\rho \bar{u}_i) = 0 \quad (1)$$

$$\frac{\partial}{\partial x_j} (\rho \bar{u}_i \bar{u}_j) = -\frac{\partial \bar{p}}{\partial x_i} + \frac{\partial}{\partial x_j} \left(\mu \frac{\partial u_i}{\partial x_j} - \rho \overline{u_i' u_j'} \right) + \rho g_i \quad (2)$$

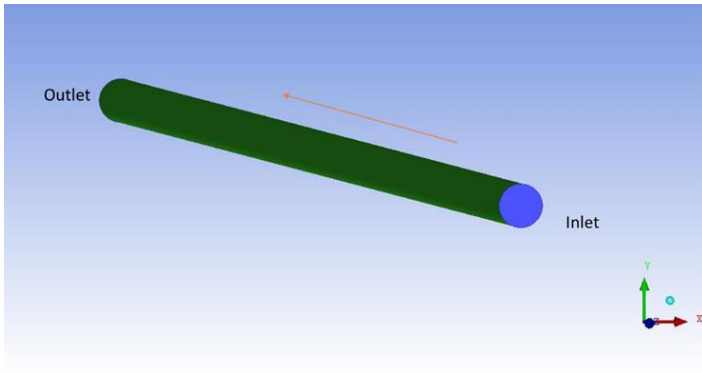
$$\frac{\partial}{\partial x_i} (\bar{u}_i \rho c_p T) = \frac{\partial}{\partial x_i} \left[\left(\lambda + \frac{c_p \mu_t}{Pr_t} \right) \frac{\partial T}{\partial x_i} \right] + \Phi \quad (3)$$

Here, u is the velocity, T is the temperature, μ is the dynamic viscosity, ρ is the density, λ is the thermal conductivity, c_p is the specific heat, μ_t is the turbulent viscosity, and Pr_t is the turbulent Prandtl number. Previously, Zhang et al. [8] found that the simulation results using the Reynolds stress model (RSM) can give a better agreement with the experimental data. Therefore, the RSM with the enhanced wall treatment is used in study and the transport equation of the RSM can be found from [12]. Gravity, thermal effects, buoyancy effects, and viscous heating are all included. The SIMPLEC scheme is chosen and the second order upwind is chosen for the spatial discretization. The convergence criteria for the continuum, momentum, energy and turbulent parameters are all set as 10^{-6} . Based on the grid independence tests, which are shown in Table 2, 8,184,000 nodes mesh is used for the simulation. Mesh near the wall is refined so that the non-dimensional distance to the wall is approximately 1. The boundary conditions for the simulation are as follows:

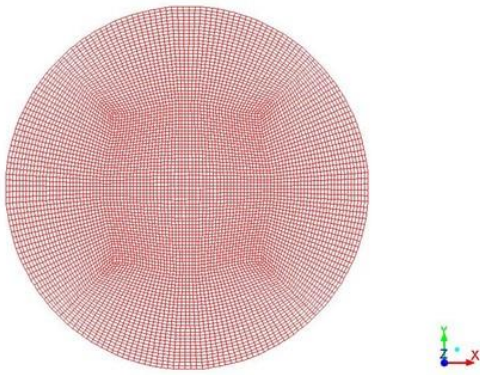
Inlet: The inlet mass flow rate is 3.929 kg/s, and the inlet temperature is 623.15 K (350 °C). Turbulent intensity and hydraulic diameter are specified based on the operation parameters of Canadian SCWR design [13].

Outlet: Outflow,

Wall: Smooth wall with no-slip condition. Heat flux is 879,931.2W/m² and the wall thickness is 1mm [14].



(a) Computational domain



(b) Cross-section view of the mesh

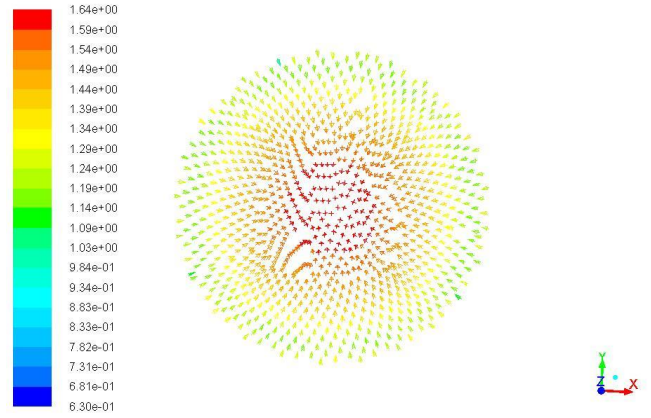
Figure 5. Computational domain and mesh of the inner central tube

Table 2 Grid independent tests

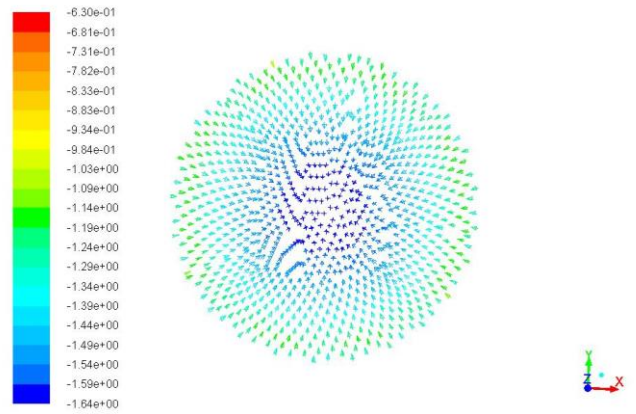
Mesh	Coarse	Medium	Fine
Nodes	2728000	4092000	8184000
Outlet bulk temperature(K)	661.84	652.77	656.13
Difference (%)		1.37	0.51
Outlet velocity magnitude (m/s)	1.3228	1.3801	1.3995
Difference (%)		4.33	1.41

III. RESULTS AND DISCUSSIONS

Fig.6 shows the outlet velocity vectors colored by the velocity magnitude of the supercritical water and the outlet velocity in the z-direction at the inner coolant channel. The velocity vectors colored by vorticity magnitude of the supercritical water at the outlet is presented in Fig.7. It is observed that the secondary flow occurs in the central coolant tube, and there is a big increase in the vorticity magnitude from the center to the wall.



(a) Velocity



(b) Velocity in the z direction

Figure 6. Outlet velocity vector of the supercritical water colored by the magnitude (m/s)

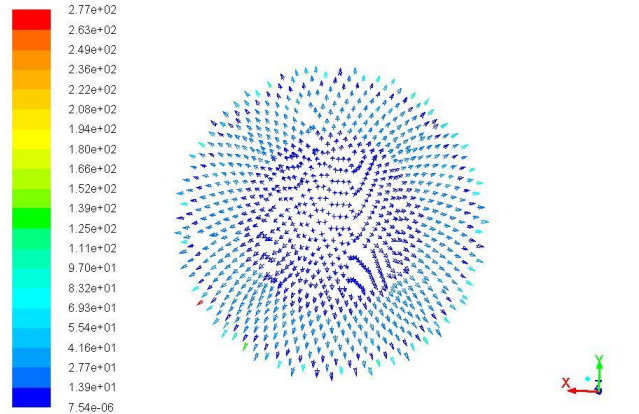


Figure 7. Velocity vectors colored by vorticity magnitude of at the outlet

The outlet bulk temperature of the supercritical water at the central tube is shown in Fig. 8. The temperature of the supercritical water along the wall is not evenly distributed. Comparing Fig. 7 and Fig. 8, it can be seen that higher

temperature appears at the higher vorticity location. The high vorticity caused by the secondary flow which enhances the heat transfer between the wall and the supercritical water.

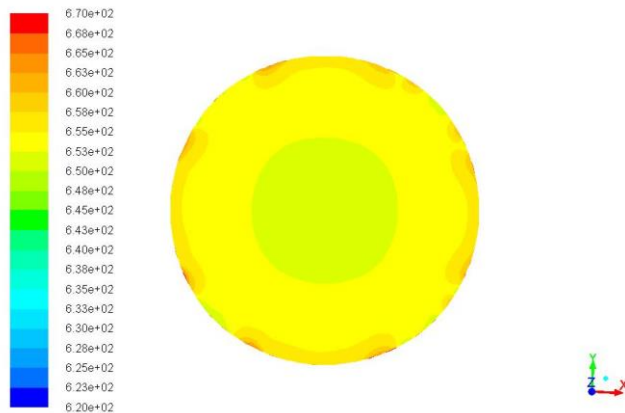


Figure 8. Contour of outlet static temperature

IV. CONCLUSIONS

In this study, the fluid flow and heat transfer characteristics of the supercritical water in the center coolant tube of the 64-element Canadian SCWR are investigated. The results show that the secondary flow appears in the central channel. And the strong vorticity enhances the heat transfer between the wall and coolant. The outlet bulk temperature of the supercritical water at the central coolant tube in the multi-rod channel is 656.13 K (382.98°C). The temperature has experienced the most drastic change at the pseudocritical point. Since the supercritical water will be transported to the outer region with multiple fuel rods, further numerical simulations will be performed in the future for fuel rod bundle region in order to study the cladding surface temperature limitations.

ACKNOWLEDGMENT

This work was supported by the NSERC Discovery grant.

REFERENCES

- [1] USNERAC, A Technology Roadmap for Generation IV Nuclear Energy Systems. Retrieved from The U.S.DOE nuclear energy research advisory committee and the generation IV international forum,2002.
- [2] C. K. Chowand, H. F. Khartabil. Conceptual fuel channel designs for CANDU-SCWR. *Journal of Nuclear Engineering and Technology*, 40:139-146,2007.
- [3] X. Xi, Z. Xiao, X. Yan, Y. Li, and Y. Huang, An experimental investigation of flow instability between two heated parallel channels with supercritical water, *Nuclear Engineering and Design*, pp. 171-181,2014.
- [4] S.K. Verma, S.L. Sinha, and D.K. Chandraker, Experimental investigation of effect of spacer on single phase turbulent mixing rate on simulated subchannel of Advanced Heavy Water Reactor, *Annals of Nuclear Energy*, pp. 186-195,2017.
- [5] Azih C, Brinkerhoff J R, Yaras M I. Direct numerical simulation of convective heat transfer in a zero pressure gradient boundary layer with supercritical water. *Journal of Thermal Science*, 21(1): 49–59,2012.
- [6] X. K. Zeng, Y. L. Li, X Yan, et al. CFD method application in supercritical water cooled reactor thermohydraulic research. *Journal of Nuclear Engineering*, 34(2): 114–120,2013.
- [7] Y F Zhang, H X Li, L X Li, et al. A new model for studying the density wave instabilities of supercritical water flows in tubes. *Journal of Applied Thermal Engineering*,75:397-409,2015.
- [8] Y. N. Zhang, C. Zhang, J. Jiang, Numerical simulation of heat transfer of supercritical water in SCWR, 17th Annual Conference of the CFD Society of Canada, Ottawa, Canada, 2009
- [9] R. V. Maitri, G. Dutta, C. Zhang and J. Jiang. Numerical Analysis of the Deterioration of Heat Transfer Phenomenon in Supercritical Water Flow in Circular Tubes Using Different Turbulence Models. 22nd Annual Conference of the CFD Society of Canada, Toronto, Canada, 2014
- [10] Yetisir M, Hamilton H, Xu R, et al. Fuel Assembly Concept of the Canadian Supercritical Water-Cooled Reactor. *ASME. ASME J of Nuclear Rad Sci.* 2017;4(1):011010-011010-7. doi:10.1115/1.4037818.
- [11] W. Wagner, A. Kruse, *Properties of Water and Steam: The Industrial Standard IAPWS-IF 97 for the Thermodynamic Properties and Supplementary Equations for Other Properties*, Springer, New York ,1998.
- [12] 14.0 ANSYS fluent theory guide. ANSYS inc, 2011
- [13] Yetisir M, Hamilton H, Xu R, et al. Fuel Assembly Concept of the Canadian Supercritical Water-Cooled Reactor. *ASME. ASME J of Nuclear Rad Sci.* 2017;4(1):011010-011010-7. doi:10.1115/1.4037818.
- [14] Frederic Salaun and David R. Novog, “Analysis of Control Rod Drop Accidents for the Canadian SCWR Using Coupled 3-Dimensional Neutron Kinetics and Thermal Hydraulics,” *Science and Technology of Nuclear Installations*, vol. 2018, Article ID 1706590, 17 pages, 2018. <https://doi.org/10.1155/2018/1706590>.

DEVELOPMENT OF A FORMULA SAE FRONT WING WITH AN EMPHASIS ON ADDITIONAL AERODYNAMIC DEVICES

Davin Jankovics, Martin Agelin-Chaab, Ahmad Barari

Faculty of Engineering and Applied Science
University of Ontario Institute of Technology
Oshawa, Canada

davin.jankovics@uoit.ca, martin.agelin-chaab@uoit.ca, ahmad.barari@uoit.ca

Abstract—This paper presents a new application framework for the design of a Formula SAE car front wing based on the addition of certain aerodynamic devices. High performance motorsports require the extensive use of aerodynamics to compete at the top level, and the front wing is one of the most important elements. The selection of a base airfoil including dimensions and placement was detailed and the additional performance of wing endplates, gurney flaps, twisted wing, and multiple elements were examined. Computer simulations were carried out to evaluate the performance of the proposed aerodynamic system. This paper demonstrates the enhancements provided by these devices, leading to a more effective front wing.

Keywords—*Computational Fluid Dynamics; CFD; Automotive Engineering; Formula SAE; Design Optimization*

I. INTRODUCTION

Aerodynamic development is perhaps the single most important driving factor for high performance automobiles. However, the addition of aerodynamic devices to cars is not an exact science, and there is considerable room to design an effective solution that is customized for a specific geometry. The student competition Formula SAE in particular sets very few restrictions on the design of these devices [1], so teams are motivated to implement the most effective solutions. Beyond different airfoils, there exists a number of different configurations and additional devices that are shown to improve the wing's performance [2].

Currently, results in sport series such as F1 and WEC are heavily determined by the success of a team's aerodynamic package, where often millions to hundreds of millions are spent to support the team [3]. This is very different from the early days of development, where knowledge in aerodynamics was first used to reduce drag and increase top speed [4]. Afterwards, development slowly lead to improving lap times with the addition of airfoils generating negative lift, allowing for better handling and cornering speed [5]–[7]. In Formula SAE innovations include the selection of high lift coefficient at low Reynolds number airfoils due to their relatively slow speed [8]–[11], including E423, S1223, FX63137, and LNV109A. The

angle of attack (AoA) will also directly affect the airfoils lift and drag, so care must be taken to select this parameter appropriately in order to avoid boundary layer separation and its negative effects [2], [9].

A very popular device to place on the outer edges of the airfoil is known as an endplate. Here, the device aims to reduce the “spillage” of higher pressure flow on one face, onto the low pressure region on the other by physically obstructing the flow, thus improving efficiency [2]. Another device that is often used in known as a gurney flap, which is essentially just a small strip placed perpendicular to the trailing edge of the airfoil. This device allows flow to better stay attached to the low pressure side of the trailing edge, effectively increasing the wings AoA [2], [12]. A similar flap on the trailing edge of the endplate facing outwards, can also be used to improve the efficiency of the endplate, while also directing flow around the turbulent, drag-producing rotating wheels [2]. A “twisted wing” is the idea of varying the airfoils AoA along its span, in order to compensate for the change in flow caused by the vehicles body [13]. Finally, multiple airfoils can be used to achieve a higher AoA than a single larger airfoil since the gaps between the multiple elements allow for higher energy flow over the top of the initial element to energize the boundary layer of the next element, delaying separation and therefore improving efficiency [9].

The development of better, more efficient devices by major race teams is often shrouded in secrecy as teams want to keep new techniques and understanding to maintain a competitive advantage. Formula SAE teams are generally more open with their progress, and a number of teams discuss the design of their wings; however this paper aims to focus on a more detailed analysis of the design of a wing considering the effects of the aforementioned devices. Therefore, the purpose of this paper is to examine the effects and merits of certain aerodynamic devices added to a base single airfoil during the design process for a Formula SAE car's front wing.

II. METHODOLOGY

The aerodynamics of race cars is an important design consideration that greatly affects the performance of the vehicle. An important aspect during a normal optimization process is the

parameterization of the models geometry [14]. In this optimization process the effect of specific geometric parameters on the aerodynamic properties are studied to develop information using CFD systematic experiments [15], [16]. Here, the main tool to design and analyze the wing will be computational fluid dynamics, specifically ANSYS Fluent. The design will be modeled in 3D and placed directly on the car. The main criteria for design analysis will be the downforce and drag produced by the wing, as well as the flow patterns and interactions produced by the wing. In order to keep under computational resources and simplify the analysis, yaw conditions and the mounting of the wing were not considered.

A. Design Process

The first part of the design process was to select the wing profile to be designed for. With an objective to achieve 75-100 N of downforce based on the cars weight distribution and considering previous results from other teams [9]–[11], three profiles were selected to be analysed, FX 63-137, E423, and S1223 due to their high coefficients of lift. The profiles were taken from the UIUC airfoil database [17]. From the literature, it can be seen that of these airfoils, S1223 has the highest coefficient of lift, therefore it was selected as the base profile [10], [18]. Next, the AoA of this airfoil must be selected. For S1223, maximum lift is generated at 16° in a free stream, however the wing also directly stalls after this, so angles 10°, 12°, 14°, 16°, and 18° were tested on the car.

The size of the wing must also be determined. The width, or span on the wing was based off the maximum width of the car, as per the regulations [1], and was 0.707 m. This will utilize the most area possible and is an obvious choice. To estimate a sufficient chord length, the coefficient of lift formula was used to back-calculate the dimension:

$$A = s * c = \frac{F_L}{0.5\rho V^2 C_L} = \frac{75}{0.5 * 1.225 * 13.889^2 * 2.23} = 0.2846$$

$$c = \frac{0.2846}{0.707} = 0.403 \text{ m}$$

Here we make the assumption that the coefficient of lift will remain the same with the new aspect ratio in order to get a dimension to start testing. The lift force (F_L) was set to the base 75 N in the objective, and the velocity was set to 50 km/h (13.889 m/s). The final value of 0.403 m was therefore set for the chord length. Now the position of the wing relative to the car must be selected. The distance along the length of the car was simply set as the far forward as the regulations allowed to avoid as much interaction with the rest of the car as possible, specifically with the nose cone. The height of the wing was set as the height of the suspension travel, as determined by the team, so as to not damage the wing when braking or turning.

Once the initial airfoil is integrated into the design, the other various aerodynamic devices were considered. It was assumed that the devices have negligible effects on each other to avoid significant testing of various combinations of devices to simplify the design and due to computational constraints. For the order of testing, first an endplate and an endplate with a gurney will be tested and compared with the wing by itself. Then, the airfoil

gurneys will be tested and compared to the previous selected configuration. This will be compared to the twisted wing, and finally a multi element wing will be considered against the final previous configuration.

Now the configurations of each device to be tested must be selected. First, the size of the endplate will be set to the maximum size allowed as per the regulations and again at the height of the suspension travel. This size should yield the maximum benefits from the endplate, as the larger it is, the more flow it will impede, although there is certainly diminishing returns. A gurney flap on the endplate will be tested with a value of 10 mm. The gurney flaps on the airfoil will be tested at two heights based on the recommended values given in the literature above, and therefore to have even numbers 1.25% (5 mm) and 2.5% (10 mm) of the cord length will be used. The twisted wing will be tested with the center section of the wing set at two angles, 0° and 5°. The size of the section with the lower angle will be based on the flow around the nose cone and the separation and the airfoil. Finally, the multi element wing will use a total of two elements to reduce complexity, each being the same profile, and will be based on other multi element wings in the literature.

B. CFD Model & Boundary Conditions

To setup the CFD simulation, some things were done to reduce the complexity. First, it was assumed that flow around the car will be horizontally symmetrical, and therefore symmetry conditions were set in the simulation. This is reasonable since the car itself is symmetric and we are only testing zero yaw conditions. The CAD model of the car provided by the UOIT Formula SAE Electric team was simplified to improve the mesh. The model is not fully featured since only the interactions between the front wing, nose cone, tires, and the beginning of the undertray are significant. Therefore, the entire rear of the car was also removed as seen in Fig. 1.

The flow domain (Fig. 2) was set with the rule of thumb that the inlet distance, height, and width should be around the length of the car (3 m). The outlet was set to 3 times the length of the car (9 m). This sizing is to ensure that the flow has enough room to expand around the car and minimally interact with the walls. Two or three bodies of interest (BOI) were set depending on the simulation: one to capture the entire body and initial wake region, one to capture flow around the tire, and one to capture flow around the wing. These BOIs were used to refine the mesh around the important areas.

Further, the inlet velocity was set to 50 km/h (13.889 m/s), along with the ground and the walls. The outlet velocity was set to 0 gauge pressure, the symmetry plane was set, and the front wheel was set to match the speed of the flow (radial velocity = linear velocity/radius). The simulation was set to the Pressure-Based, Steady, SST k-omega model (with curvature correction), using the coupled solver based on the literature [11], [13]. Ideally transient simulations could have been run due to the turbulent nature of the flow produced, but due to processing power available, the steady SST k-omega model can still give good results for overall flow trends.

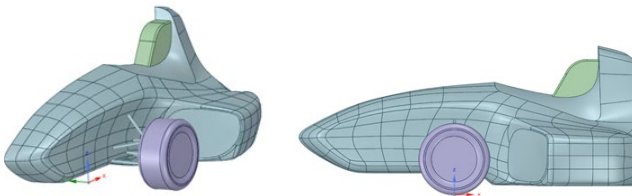


Figure 1. UOIT Formula SAE Electric simplified car model.

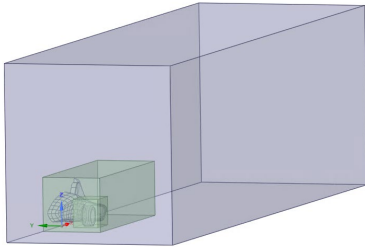


Figure 2. Isometric view of the flow domain, with BOIs.

C. CFD Mesh

The mesh was set to use Poly-Hexcore cell zones with 20 prism layers over the body, wing, tire, and ground in order to capture the boundary layer. Skewness was minimized, and overall element quality were increased via the Fluent diagnostic tools until they were acceptable. The minimum mesh size was 0.5 mm and the maximum was 500 mm, with elements in the BOIs being a maximum of 10 mm, and most elements on the car being 1-5 mm. The mesh averaged approximately 4 million elements depending on which BOIs were included. Initial results with this mesh matched closely to the downforce levels seen in [9], [10].

III. RESULTS AND DISCUSSION

It should be noted that all results are for symmetry conditions unless otherwise noted. Therefore, to get the total lift or drag acting on the car, the values must be doubled. Also, downforce and the coefficient of lift refer to negative lift in all tables and plots.

A. Airfoil Angle of Attack

The first thing to test on the car was the S1223 airfoil at various angles of attack. From Fig. 3 the maximum downforce is created at 12° AoA on the car. This shows that the optimal AoA value from literature [18], for S1223 is likely only possible in the freestream. When mounted to the car, the vehicle body influences the wing, increasing separation and therefore decreasing effectiveness. The downforce on the entire car itself increases to 24 N from an initial value of 1 N with no wing. Drag also increased from 32 N to 34 N.

B. Endplates

The configuration with the 10 mm endplate gurney is shown in Fig. 4 on the right side (the wheel is directly behind). Downforce with just the endplate was found to be 26 N, and with the endplate and gurney, 30 N. Drag increased to 36 N with the endplate and went back to 34 N with the endplate and gurney.

Fig. 5 show that the addition of the endplate gurney seems to redirect flow outwards of the tire behind it, possibly the cause of the slight reduction in drag.

C. Airfoil Gurney

The addition of the gurney can be seen in Fig. 4 as the green piece at the trailing edge of the airfoil. The 10 mm gurney increases downforce to 32 N, while increasing drag to 36 N. The 5 mm gurney further increases downforce to 35 N, while reducing drag to 34 N. This shows that a 10 mm gurney here is too large, producing more drag than desired, while only slightly improving downforce.

D. Twisted Wing

The design for the twisted wing was based on the separation seen in Fig. 5 that occurs near to the nose cone. Note that the separation increases as the wing moves closer to the body. The design can be seen in Fig. 6 below, and the flow particularly to the underbody can be seen improving in the twisted wings versus the non-twisted wing in Fig. 7. The twist of 5° reduces downforce to 21 N, while drag increases slightly to 35 N. The twist of 0° reduces downforce to 27 N while increasing drag to 36 N. This reduction in downforce can be justified based on the desire for cleaner flow into the underbody for a possible diffuser. The twisted section is necessary to combat the separation caused by the interaction between the front nose cone and wing.

E. Multi Element Wing

The multi element wing was tested as shown in Fig. 8. Note that the gurney was removed on the main element since it would interfere with flow from the top of the main element to the bottom of the second element. The addition of the second element increases downforce to 45 N while also increasing drag to 37 N. The L/D efficiency is the highest of all the tested configurations (Fig. 10). Therefore, the multi element wing is the overall best wing tested. The final design can be seen in Fig. 9 and a summary of all the tested wings in Fig. 10 and 11.

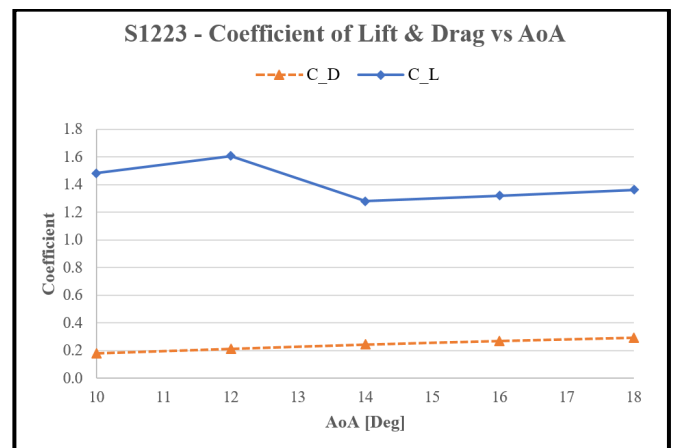


Figure 3. S1223 coefficient of lift & drag vs AoA.

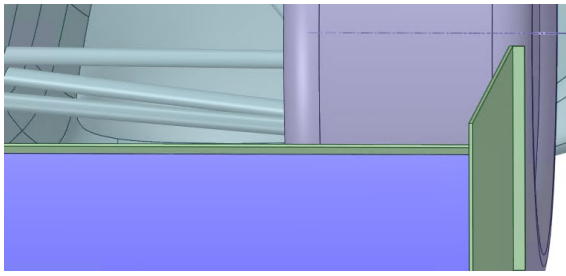


Figure 4. Wing with endplate including a gurney, as well as an airfoil gurney.

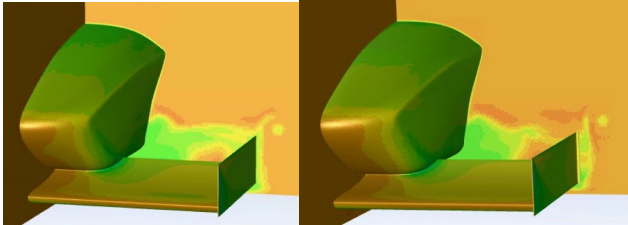


Figure 5. Total pressure with endplate (left). Total Pressure with Endplate & Gurney (right).

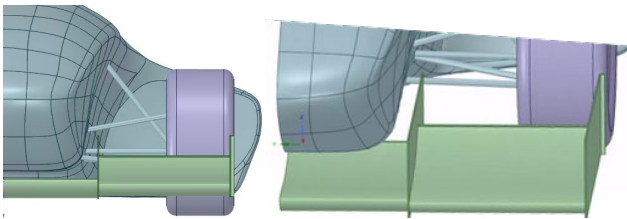


Figure 6. Twisted wing design.

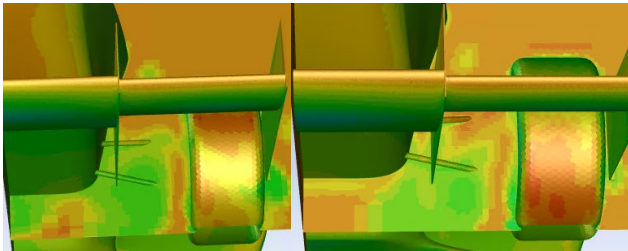


Figure 7. Total Pressure 5° Twist (left). Total Pressure 0° Twist (right).



Figure 8. Multi Element Wing (Second initial element is the twisted section).

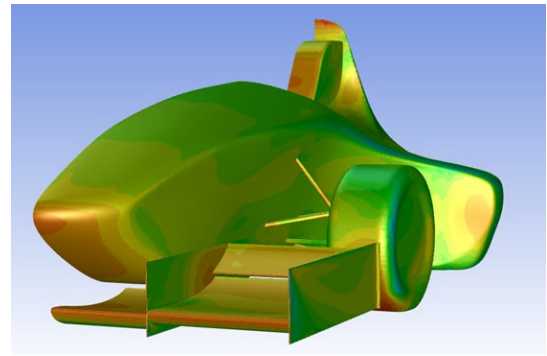


Figure 9. Final wing design on the car.

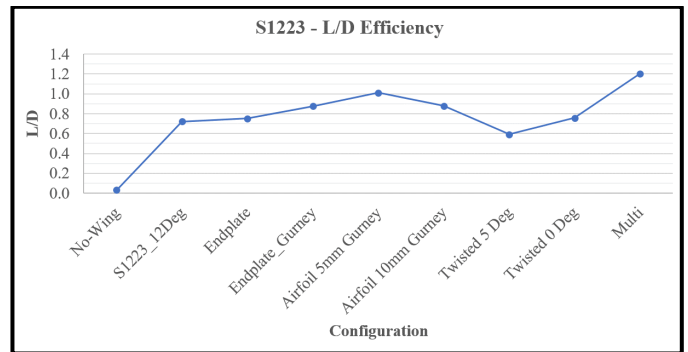


Figure 10. Lift/Drag value for all tested configurations

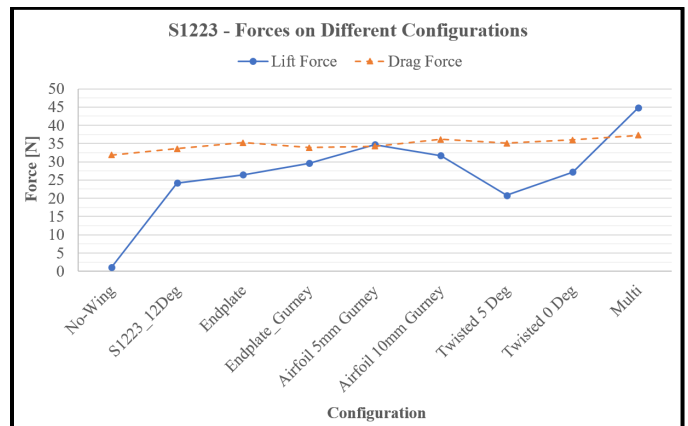


Figure 11. Lift and drag force for all tested configurations.

IV. EVALUATION

To ensure that the developed wing actually improves the performance of the car in a competition environment, testing must be done. By simulating the speed the car can attain in a straight line as well as during cornering, and including braking parameters, the cars performance over a lap can be estimated. Using the software “OptimumLap”, retrieved from [19], lap times for various courses can be found based on the details of an inputted car. This includes weight, power curves, and most importantly for this test, the coefficient of drag and lift. The achieved lap times for a standard Formula SAE track are summ-

TABLE I. LAP RESULTS FOR FORMULA SAE TEST TRACK

	Lap Time [seconds]	Relative [seconds]
No Wing	79.25	+0.75
One Element Wing with 5 mm Gurney	78.66	+0.16
Multi Element Wing	78.50	0

arized in Table 1, and it is clear that the final multi wing configuration is best, with the simpler one element wing still making gains over the car with no wing. An improvement of 0.75 seconds per lap is quite strong in motorsports, and over the course of many laps would result in a strong lead over the car with no aerodynamics.

V. CONCLUSION

This paper set out to design a front wing for a Formula SAE car, focusing on the inclusion of certain aerodynamic devices. Initially the dimensions and placement were chosen to take advantage of the regulations and to produce 75-100 N of downforce, Next, the AoA was chosen to maximize downforce while not stalling the wing. Endplates were added which increased the wings downforce while minimally affecting drag with the addition of an endplate gurney. An airfoil gurney was introduced, which further increased downforce with a negligible change in drag. The twisted wing decreased downforce, but improved flow characteristics into the underbody. Finally, the multi element wing significantly improved downforce with minimal additional drag. All of this resulted in significant lap time reductions tested via the “OptimumLap” software. It is clear that the addition of these devices on a conventional front wing can positively contribute to its production of downforce, as well as the behaviour of flow around the vehicle.

ACKNOWLEDGMENT

Special thanks to the UOIT Motorsports team for their help during the design of this wing.

REFERENCES

- [1] SAE International, “2017-18 Formula SAE Rules.” 2016.
- [2] J. Katz, *Race Car Aerodynamics, Designing for Speed*, 2nd ed. Cambridge: Bentley Publishers, 1995.
- [3] A. Cooper, “Mercedes’ 2017 Formula 1 budget revealed,” *Motorsport Network*, 2018.
- [4] W.-H. Hucho, *Aerodynamics of road vehicles: from fluid mechanics to vehicle engineering*. 1998.
- [5] R. Falconer and D. Nye, *Chaparral: Complete History of Jim Hall’s Chaparral Race Cars 1961--1970*. Motorbooks International, 1992.
- [6] J. Katz, “Aerodynamics of Race Cars,” *Annu. Rev. Fluid Mech.*, vol. 38, no. 1, pp. 27–63, 2006.
- [7] F. Diba, A. Barari, and E. Esmailzadeh, “Handling and safety enhancement of race cars using active aerodynamic systems,” *J. Veh. Syst. Dyn. Int. J. Veh. Mech. Mobil.*, vol. 52, no. 9, pp. 1171–1190, Sep. 2014.
- [8] W. Koos, H. Mohammad, M. Alnouri, and N. Balakrishnan, “Design of a front aerodynamic package,” 2011.
- [9] S. S. Pakkam, “High Downforce Aerodynamics for Motorsports,” North Carolina State University, 2011.
- [10] H. Dahlberg, “Aerodynamic development of Formula Student race car,” KTH Royal Institute of Technology, 2014.
- [11] A. Prasanth, S. Biswal, A. Gupta, and A. Barodawala, “Complete Design and Optimization of the Aerodynamics of a FSAE Car using Solid works ANSYS & XFLR5,” *Proc. World Congr. Eng.*, vol. II, pp. 961–965, 2016.
- [12] J. J. Wang, Y. C. Li, and K. S. Choi, “Gurney flap-Lift enhancement, mechanisms and applications,” *Prog. Aerosp. Sci.*, vol. 44, no. 1, pp. 22–47, 2008.
- [13] M. Arianezhad, “Numerical Study and Optimization of a GT Car Rear-Wing Aerodynamics,” Universitat Politecnica de Catalunya, 2015.
- [14] A. O. Ghani, M. Agelin-Chaab, and A. Barari, “Application Framework for Aero-based Design Optimization of Passenger Cars using NURBS,” *J. Appl. Mech. Eng.*, vol. 04, no. 06, 2015.
- [15] F. Diba, A. Barari, and E. Esmailzadeh, “Dynamic Performance Enhancement of Small Size Racing Car,” in *Canadian Society for Mechanical Engineering International Congress 2012*, 2012.
- [16] A. Barari, F. Diba, and E. Esmailzadeh, “Down Force Control of the Low Velocity Racing Car Using Active Aerodynamic Inverse Wings,” in *ASME International Design Engineering Technical Conferences & Computers and Information in Engineering Conference*, 2011.
- [17] UIUC Applied Aerodynamics Group, “UIUC Airfoil Coordinates Database.” [Online]. Available: http://m-selig.ae.illinois.edu/ads/coord_database.html#N.
- [18] M. S. Selig and J. J. Guglielmo, “High-Lift Low Reynolds Number Airfoil Design,” *J. Aircr.*, vol. 34, no. 1, pp. 72–79, 1997.
- [19] OptimumG, “OptimumLap.” [Online]. Available: <http://www.optimumg.com/software/optimumlap/>.

Computational Studies of the Aerodynamics of a Simplified Miata MX-5

Wing Yi Pao, Remon Pop-Iliev, Ghaus Rizvi, Martin Agelin-Chaab
Faculty of Engineering and Applied Science
UOIT – University of Ontario Institute of Technology
Oshawa, Canada
wingyi.pao@uoit.net

Abstract—Aerodynamics can greatly affect the performance of road vehicles in terms of fuel efficiency and handling characteristics. In high performance vehicles; fuel economy might not be the main priority, however, low drag can allow the vehicle to reach higher top speed. On the other hand, downforce can provide better cornering stability. The top-up and top-down conditions of a convertible racecar were analyzed in this study using Computational Fluid Dynamics (CFD) for the differences in drag, downforce, pressure and turbulence energy distributions. Simplified 2-Dimensional models of the vehicle (Mazda Miata MX-5) were employed to evaluate the effect of the vehicle roof at various driving speeds. The results with the static ground condition were found to agree well with wind tunnel data of the same vehicle model. Additionally, rolling ground boundary conditions were employed to simulate more realistic conditions and to better demonstrate the true ground effect aerodynamics. It was found that top-down (without roof) experienced higher drag forces than the top-up (with roof) condition due to intense turbulence in the cabin area which has caused a large region of pressure drop, and resulted in slow pressure recovery.

Convertible; top-up; top-down; RANS; rolling ground

I. INTRODUCTION

Aerodynamics plays an important role in high performance racing as its impact increases with speed. The balance of the vehicle is rather exceptionally important to navigate around the race course. The convertible Mazda Miata MX-5 is a popular choice of car model being used in endurance races; MX-5 is also a race category by itself. It has been observed that teams have participated in both top-down and top-up configurations. The Miata MX-5 has a relatively short wheelbase compared with other rear wheel drive convertibles, causing the vehicle to be very sensitive to both internal (drive-train, steering) and external (aerodynamics and roads) force inputs [1], and have drawn debates on the most suitable setup for the races.

The top-down condition generally involves complex flow characteristics, resulting in turbulences and large separation bubble due to backward airflow from windshield and A-pillar

into the cabin [2] as seen in Figure 1. The flow within the cabin is often unstable as the cabin contains a number of objects, for example: occupants, seats, and other interior features. Reattachment of flow, the opposite of separation which creates drag, at the rear trunk does not always occur and is highly dependent on the interactions within the cabin [3]. On average, top-down for most convertible vehicle models would have a drag penalty of more than 20% [2].

When comparing between hard-top and soft-top, the surface roughness of soft-top causes more flow separation, thus higher drag, as it decreases surface area for flow attachment. The fabric material of soft-top also induces higher friction drag.

The case of racing is important to maintain balance between drag and downforce. C. Casiraghi et al. [4] have determined that higher downforce helps to increase contact patch to maximize braking forces, thereby reducing braking time needed. This can allow faster entry and exit of a corner, which is essential in racing for higher acceleration during the straight portion of the track. Studies showed aerodynamics of top-down could be improved down to only 10% drag penalty by introducing deflectors, side windows, and roll cage, which promote flow reattachment. [2, 3]

While there are number of factors to consider in race car aerodynamics such as terrain, number of corners, and length of straight roads, there is a passionate debate in the Miata racing community on whether top-up or top-down is more beneficial for racing. Wind tunnel studies were previously conducted on the Miata but this were limited to a few speeds and a static road conditions [5] This study aims to contribute to answer to this debate by providing some insight in determining the choice of vehicle configuration in racing. The main goal of the study is to perform computational analysis on a simplified convertible Miata MX-5, and evaluate the aerodynamics effects caused by the presence of a roof. It will provide visualization of some fundamental aerodynamics attributed to convertibles, as well as insights for high performance vehicle setups for a wider range of conditions than currently available in the literature. .

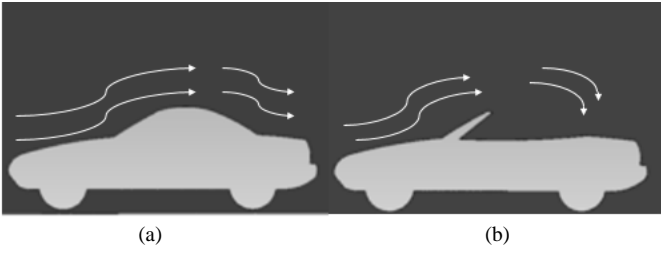


Figure 1. Air-flow characteristics of (a) top-up and (b) top-down.

II. EXPERIMENTAL

Aerodynamic effects were computed using ANSYS Fluent, considering steady state condition. Simplified 2-Dimensional simulations were employed for inexpensive visualization of the effect of the roof on the aerodynamics around a convertible vehicle. Other 3-Dimensional and lateral interactions from pillars and side mirrors were ignored in this study.

All simulations were conducted using a Reynolds-Averaged Navier-Stokes approach, with $k-\omega$ SST turbulence model (two-equation shear stress transport).

A. Computational Fluid Dynamics Model

A 2-Dimensional outline of a full scale model of the 1990 Mazda NA Miata MX-5 was generated. The car body has dimensions of 3.97 m in length and 1.24 m in height. The flow domain has an area of 20×6 m² which allowed approximately 8 m of space in front and behind the vehicle, and 4.75 m above the vehicle, shown in Figure 2 (a).

The meshing of the model consisted of linear elements by the quadrilateral dominant multi-zone method. Figure 2 (b) shows the overall mesh of the full model, a total of 60000 elements and nodes were achieved through the vehicle edge seeding of 0.01 m, air at 0.005 m². Transition ratio was set for 0.272, prism layers of 20 and growth rate of 0.1. A grid independence study was conducted and it confirmed that the results are independent of the grid used. Reference values were computed from the inlet to calculate for lift and drag coefficients.

The $k-\omega$ SST model was chosen for the study as it is suitable for approximating boundary layer without additional inputting functions. The $k-\omega$ SST model is governed by a blending function as shown in Equation (1). It has a solution of 1 within the boundary layer, and 0 within the free stream; the solution affects the turbulence kinetic energy (TKE) dissipation rate in Equation (2). [6]

$$F_1 = \tanh \left\{ \left\{ \min \left[\max \left(\frac{\sqrt{k}}{\beta^* \omega y}, \frac{500\nu}{y^2 \omega} \right), \frac{4\sigma_{\omega 2} k}{C D_{k\omega} y^2} \right] \right\}^4 \right\} \quad (1)$$

$$\frac{\partial \omega}{\partial t} + U_j \frac{\partial \omega}{\partial x_j} = \alpha S^2 - \beta \omega^2 + \frac{\partial}{\partial x_j} \left[(\nu + \sigma_{\omega} \nu_T) \frac{\partial \omega}{\partial x_j} \right] \quad (2)$$

$$+ 2(1 - F_1) \sigma_{\omega 2} \frac{1}{\omega} \frac{\partial k}{\partial x_i} \frac{\partial \omega}{\partial x_i}$$

B. Boundary Conditions

The boundary conditions for the CFD models are as follow: stationary car; no-slip walls; moving sky and ground with the same velocity as inlet; the turbulent intensity of 5.

C. Assumptions

It was assumed that simplified 2-Dimensional models are sufficient for demonstrating differences between top-up and top-down conditions. It represents the symmetry plane of the vehicle. Flows around objects of vehicles such as mirrors, seats, roll-cage, and occupants which result in 3-Dimensional flow interactions were not considered. Wheels were also stationary in this simplified study assuming their effect for both top-up and top-down should be the same.

III. RESULTS AND DISCUSSIONS

A. Validations

Static road conditions was validated through comparison with wind tunnel testing by Auto Bild [5] in 2008 for a Mazda Miata MX-5 at 60km/hr. They studied the differences between top-up with a hard-top and soft-top, as well as top down with an occupant. The wind tunnel had a stationary ground. The same condition was simulated using CFD for top-up and top-down in 2-Dimensions and was compared for drag coefficients as shown in Table 1. The difference between the wind tunnel data and CFD results were within 2.7%.

B. Drag and Lift Coefficients

Drag and lift coefficients were evaluated for different speeds as shown in Figure 3. Results suggested distinct differences between top-up and top-down in terms of pure drag and lift behaviours. Top-down was found to have higher drag (purple) than top-up by a coefficient value of about 0.09. The drag penalty was determined to be 21.5% whereas top-up had less negative lift coefficients (blue) than top-down, implying less downforce.

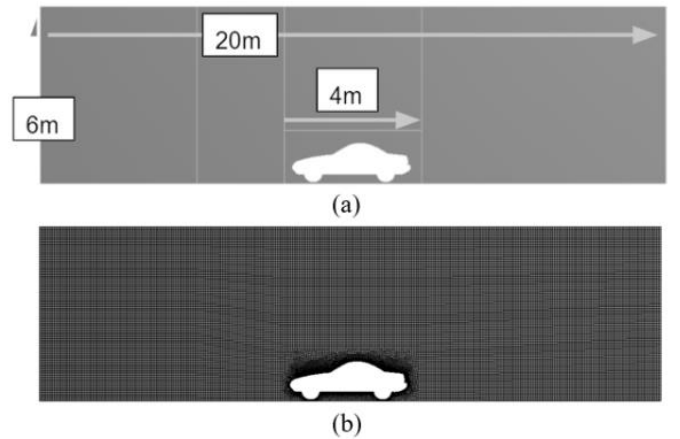


Figure 2. (a) Flow domain dimensions, and (b) Overall mesh.

TABLE I. DRAG COEFFICIENTS

Condition	Wind tunnel	CFD
Top up (hard top)	0.37	0.379
Top up (soft top)	0.39	-
Top down	0.45	0.462

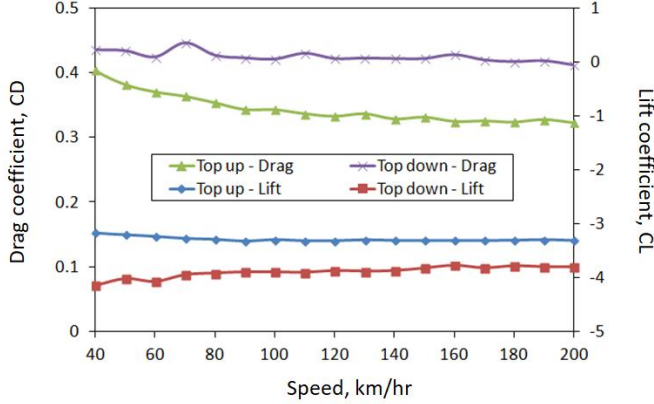
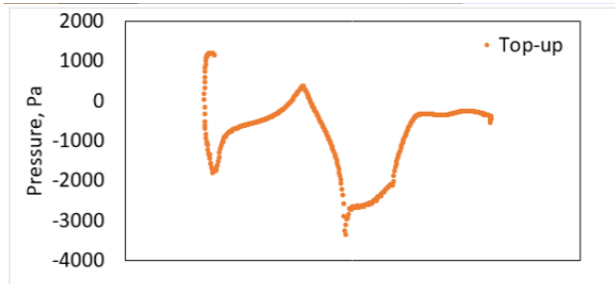


Figure 3. Drag and lift coefficients at various speeds for top-up and top-down conditions.

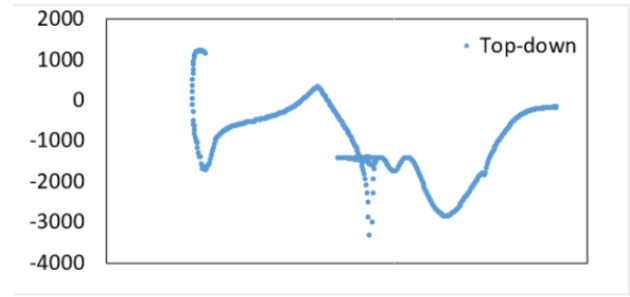
Presence of roof has altered locations of vortices formed from flow separation, which has been delayed towards the rear of the vehicle, instead of being concentrated at the cabin area for the top-down case without a roof. The observed phenomena can be supported by Bernoulli’s Principle, where a faster air stream would lead to lower pressure. Therefore the vehicle would experience lifting force at the top of the roof from the acceleration of flow.

C. Pressure Field

Pressure distributions were evaluated at reasonable racing speed for an MX-5 on the racetrack at 150 km/hr speed. Figure 4 shows the pressure field around the vehicle from front to rear. A stagnation point occurred at the front of the bumper where air strike at maximum pressure, the pressure then dropped quickly for both top-up and top-down conditions as air moved along the hood until it reached the bottom of the windshield to create a secondary peak pressure.



(a)



(b)

Figure 4. Pressure distributions along vehicle length of (a) top-up and (b) top-down condition.

Positive pressure indicates the direction of towards the car body as downforce, while negative pressure pulls away from the body to generate lift. Top-up was seen to have faster pressure recovery from the cabin and before rear trunk region, therefore resulted in the lower pressure difference between front and rear, hence, lower drag.

D. Velocity Vector Field

Figure 5 shows the velocity vector field of top-up and top-down conditions at 150 km/hr. Flow circulations were observed immediately behind the rear region for both top-up and top down conditions. Top-up has formed smaller vortices compared to those seen for top-down configuration. Flow separation can be found at the top of the roof for top-up, which quickly reattached afterward. Flow also reattached for top-down, however, due to the slower recovery, the vortices formed were long and induced large low pressure region.

Flow circulations also occurred in the cabin area for the top-down condition, which was believed to be the cause for higher downforce. The flow in the ambient environment was considerably smooth for the top-up case, while the air on top of the car was disturbed in the top-down case.

E. Turbulence Kinetic Energy Field

Figure 6 shows the evolution of turbulence kinetic energy field using the same scale bars with increasing vehicle speed for both top-up and top-down conditions.

Turbulence resulted from vortices for top-up was found to have a higher intensity than top-down, but the size of bubbles was smaller and not continuous like the ones formed from top-down. There were only two vortices formed for top-up, whereas top-down has formed three with one at the cabin and two behind the car. On the other hand, the turbulences couple between cabin and rear, and intensify to affect the air in the surroundings for the top-down condition.

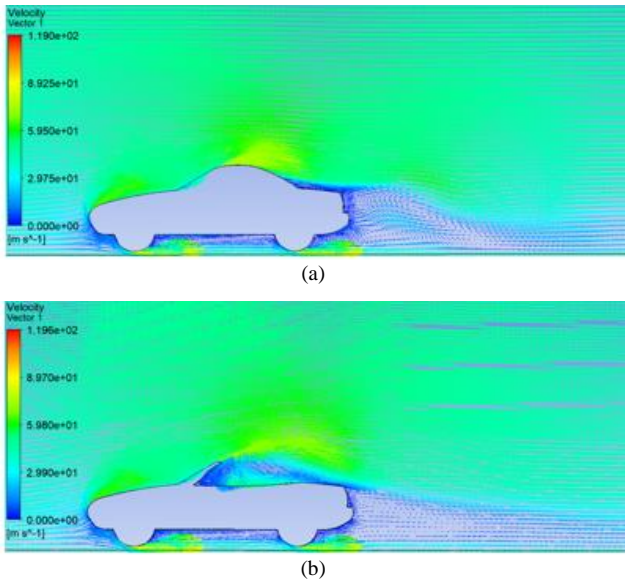


Figure 5. Velocity field at 150 km/hr.

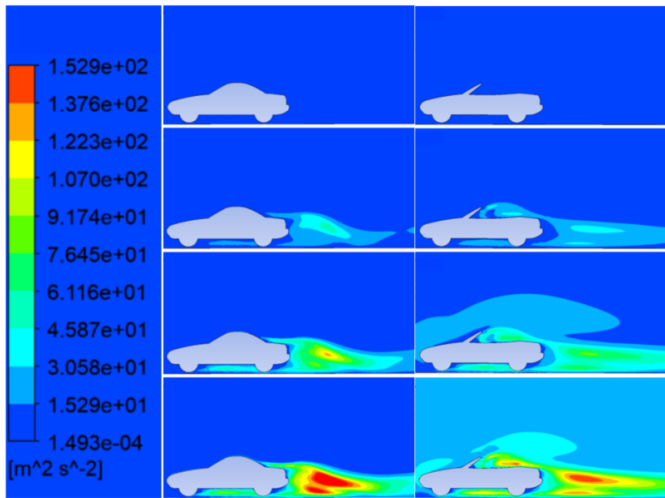


Figure 6. Turbulence kinetic energy field at 50, 100, 150, and 200 km/hr for both top-up and top-down.

F. Stationary and Moving Grounds

The stationary ground where air flow is blocked by car wheels in the model has induced higher drag, the vortex behind the vehicle was found to be larger in general. However, in the case of moving ground, the air was pushed towards the rear, where it interacted with the separation bubble from top of the trunk. From Figure 5 (a), it can be observed that the flow from the bottom of the car has suppressed the circulation bubble from the top, and from Figure 6, a second vortex has formed instead of a huge single vortex.

G. Race Condition Analysis

Vehicle balance is a key requirement when designing for race cars. Aerodynamic benefits are not the only considerations, but also weight and comfort and are discussed below:

- *Drag*: Top-up was found to facilitate more flow reattachment from roof top to rear trunk, therefore resulted in lower drag at higher vehicle speeds; it would allow a higher top speed and acceleration for straight portions of the race track. The top-down option is not entirely eliminated as a drag penalty could be minimized to promote more flow reattachment by installing aerodynamic devices or a roll-cage within the cabin to guide air flow.
- *Downforce*: The lower downforce for top-up could be compensated by a rear wing to improve cornering stability. Whereas higher downforce was found to be an intrinsic property for top-down, which could allow a better grip, and could potentially accommodate a more powerful drive train system.
- *Weight*: Weight reduction is a popular approach to obtain a high power-to-weight ratio, which is directly related to acceleration ability. A hard-top for the top-up condition could be heavy, the effect of weight a penalty and weight distribution can sometimes be more severe than the drag penalty and can offset the vehicle balance.
- *Race duration*: Driving comfort is related to the duration of driving. Comfort is a factor for psychological stability, focus, and judgments. Top-down is likely to have less comfort and more disturbances such as splashing of gravel and rain due to open cabin and turbulence. There could also be a lot of noise which affects communication between driver and team. Large wind force acting on driver's body could also affect the driver's control of the vehicle.

IV. CONCLUSIONS

Computational Fluid Dynamics (CFD) was employed to study the aerodynamic effects of a simplified convertible: Mazda Miata MX-5. The study provided a more comprehensive information on the top than currently exist in the open literature. The differences between top-up and top-down conditions were investigated. Stationary road condition was validated with wind tunnel data where the trend and values agreed well and confirmed that that top-down has more drag than top-up in general. On the other hand, the moving ground was simulated to demonstrate ground effects which are closer to reality. Air was observed to move with the ground, which had the effect of reducing the main flow separation bubble. Hence lower drag coefficients were calculated than the case with the stationary ground.

Additionally, downforce, pressure distribution and turbulence kinetic energy analysis served to provide insight in which configuration (top-up or top-down) is more beneficial in racing. Better fuel economy can be achieved for top-up due to lower drag, where downforce is not a necessity in normal

driving for stability. However for racing, top-down could be more preferred, which can provide higher downforce for faster cornering speed. Since a roll-cage is generally installed in all race cars as a safety measure, running top-down with a roll cage not only being privileged with better performance, it can also save weight by eliminating the roof component. The drag penalty could potentially be reduced to a minimum with other lightweight aero-devices such as deflectors and fender fins.

ACKNOWLEDGMENT

The authors are grateful to NSERC's Discovery Development Grant and NSERC's Chairs in Design Engineering Program for the financial support of this research.

REFERENCES

- [1] A. Soltani, A. Goodarzi, M. H. Shojaiefard, A. Khajepour, "Developing an active variable-wheelbase system for enhancing the vehicle dynamics", Proc IMechE Part D: J Automobile Engineering, vol. 231 no. 12, pp. 1640-1659, 2017.
- [2] R. H. Barnard, "Road Vehicle Aerodynamic Design - An Introduction 3e", MechAero Publishing, Hertfordshire, England, 2009.
- [3] T. Y. Obidi, "Theory and Applications of Aerodynamics for Ground Vehicles", SAE International, Warrendale, PA, USA, 2014.
- [4] C. Casiraghi, "Race Car Aerodynamics", Tatuus Racing, 2010.
- [5] Auto Bild, "The Tops and Flops in the Wind Tunnel" Autobild.de., 2008.
- [6] Autodesk, "SST K-Omega Turbulence Models", Autodesk Knowledge Network, 2018.

Validation of rhoCentralFoam for Numerical Modelling of Underexpanded Free Jets Impinging on Plates

Peter Nielsen, Christopher DeGroot, Anthony Straatman
Mechanical and Materials Engineering Department
Western University
London, Canada

Abstract— This paper looks at assessing the accuracy of an axisymmetric simulation of a moderately under-expanded free jet impinging on a large diameter plate using rhoCentralFoam, a density based solver offered in OpenFOAM. The simulation will be compared to the results of previous experimental and numerical results for a similar simulation. By assessing which aspects of the flow can be accurately resolved using a model that can simulated on standard computing hardware, useful engineering information can be obtain at a lower computational cost.

Keywords: *OpenFOAM, Under-expanded Jet, Impingement, Compressible Flow*

I. INTRODUCTION

Under-expanded free jets are the subject of a lot of study due to their common appearance in many engineering applications including aerospace, manufacturing, and medical devices. Heat transfer, acoustic phenomenon, and forces generated by impingement are all aspects that are important for researchers and industry as they dictate the behavior of the jet for a given application.

Within a supersonic under-expanded free jet there are three key regions, i) the inviscid core ii) the shear layer, and iii) the far field zone. The core of the free jet is can be treated as an inviscid supersonic region until the ambient pressure is reached in the core. This is called the near-field region, and extends until the shear layer reaches the center line of the free jet [1]. Beyond this point, the jet behaves similarly to a subsonic free jet. Inside the near field region, the flow is dominated by compressibility effects and is characterized by a series of Mach diamonds formed by expansion and compression waves. Outside the supersonic core is the shear layer which is characterized by high levels of turbulence.

When looking at Mach diamonds the length and structure vary with several factors, however generally follow certain trends. While empirical relationships are available to approximate the length of the first Mach diamond, a full analytical solution to this problem is challenging to determine due to the influence of the nozzle geometry, fluid properties, and surrounding fluid characteristics [1].

Moderately under-expanded free jets are typically characterized by having a nozzle pressure ratio (NPR) between 2-4, while a highly under-expanded free jet will have a NPR between 4-7. A moderately under-expanded jet will only contain oblique shock waves within the inviscid core, while a highly under-expanded jet will contain a stronger normal shock at the axis of symmetry. A detailed characterization of the different free jets, is provided by Franquent [1].

For an impinging under-expanded jet, a wall is placed in the path of the free jet at a distance shorter than the near field length. When the jet impacts the wall it suddenly decelerates across a normal shock, and then redirected in a radial direction. As large coherent structures impact the solid surface they produce acoustic waves that are propagated back to the jet lip causing instabilities at the nozzle exit far from the coherent structures [2]. These instabilities grow as they move downstream forming the turbulent structures completing the feedback loop. Three main forms of instabilities may be present, Kelvin-Helmholtz (KH) (toroidal), flapping, or Taylor-Goertler (TG) structures. KH and TG instabilities are both formed in the mixing layer of the free jet.

One of the key challenges with this type of flow is the enormous computation resources required to complete the simulation. For many 3-dimensional large eddy simulation (LES) or unsteady Reynolds averaged Navier-Stokes equations (URANS) cases, the number of computer processors required is beyond what is accessible to many industries [3,4]. Furthermore, many flow solvers require a low Courant number (often $Co < 0.5$) to maintain stability, which enforces a very short time step increasing computational cost [4]. A 2-dimensional axisymmetric approach will be the main aspect reviewed, as it provides a means of reducing the computational cost to something accessible to smaller industries. By describing which flow features can be accurately predicted using a less computationally intense setup, then it can be used to provide some relevant engineering information at a far lower cost and complexity. Using an axisymmetric modelling approach will inherently suppress the TG and flapping instability modes, while the KH instabilities could still be captured. The following study was conducted using fairly standard computing hardware with 16 cores. The study uses an unmodified version of

OpenFOAM 5, since there was an available solver that met all needs..

The domain simulated was based on a study conducted by Henderson [5], and a similar LES study conducted by Dauplain [4]. Henderson investigated jet impingement tones of an under-expanded nozzle free jet with an NPR of 4.03, impacting a vertical plate. The nozzle had an exit diameter of 25.4mm (1.0in), and a converging section with an angle of 30°. The lip thickness at the nozzle exit was 1.27mm. While not explicitly stated in the paper, the diagram appears to show a small radius at the nozzle exit which would align the streamlines at the nozzle exit to be parallel. The flow impinged on a large plate of 533mm x 610mm. Flow velocity measurements by Henderson were captured using particle imaging velocimetry (PIV).

The distance between the nozzle exit and plate is the primary variable of interest. Using the same spacing as Henderson, a direct comparison with experimental methods can be made. The plate spacings used were $L/d = [1.65, 2.08, 2.66, 2.80, 3.65, 4.16]$, which occur at various locations within the first, second, and third Mach diamonds.

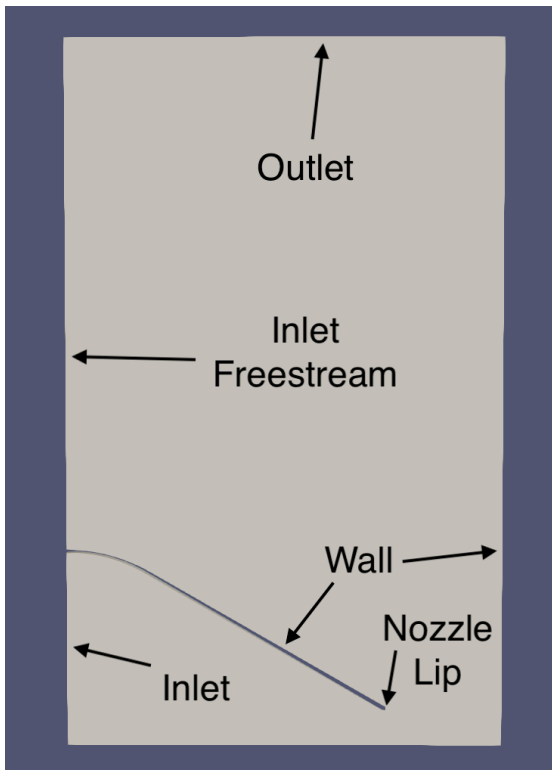


Figure 1: Domain with Boundary Conditions

II. NUMERICAL METHODS

To run the following study, the opensource computational fluid dynamics program OpenFOAM was used and Pointwise was selected for mesh preparation.

Solver

Several compressible flow options are available including sonicFoam, rhoPimpleFoam, and rhoCentralFoam. RhoCentralFoam is the only density based compressible flow solver available in OpenFOAM, and is the best choice for

capturing the shock structures associated with compressible flows.

RhoCentralFoam (rCF) is a density based, transient, compressible solver offered by OpenFOAM, it is based on the high resolution central scheme developed by Kurganov [6]. It is useful for capturing sharp gradients, similar to the type found in under-expanded free jets impinging on walls.

k- ω -SST Turbulence Model

The turbulence model used for the following study was the *k- ω -SST* two-equation model. This model has been used in previous studies of under-expanded free jets [3,7,8,9]. The *k- ω -SST* model uses the *k- ϵ* -model throughout the bulk of the domain, however switches to use the *k- ω* model in the wall region. This is done to overcome the complications with integrating the equations of the *k- ϵ* model through the viscous sublayer [10]. The *k- ω* model has challenges resolving the turbulent viscosity outside of the shear and boundary layer due to its severe sensitivity to inlet conditions, which are often unknown in most engineering cases [10].

Boundary Conditions

Correct specification of boundary conditions is challenging for compressible flows since any acoustic wave must not be allowed to reflect back into the domain. OpenFOAM has a built in “waveTransmissive” boundary condition which is designed to enable waves to easily escape the domain [3,11,12]. However, this boundary condition seemed to have challenges maintaining the far field value used to set the pressure at that face. This resulted in the pressure on faces with outflow to far below their set value, which invalidated the NPR set value and generated a secondary flow based on pressure differences on the outlet faces.

Both the inlet and outlet of the domain use a total pressure boundary condition, given by:

$$P_p = P_0 - \frac{1}{2}|U|^2 \quad (1)$$

The pressure at the inlet and outlet was set so the NPR was 4.0, determined using $NPR = \frac{P_t}{P_{atm}}$. While using total pressure as the boundary condition, a coarse mesh near the outlets can be used to dissipate the waves before they reach the outlet boundary. This enables a total pressure condition to be applied at these boundaries in place of wave transmissive without waves reflecting back into the domain [13] (figure 1).

Temperature set to total temperature at the inlets and zero gradient at the outlets. Temperature values were not specified in the Henderson paper, so an approximate room temperature value of 293 kelvin was applied at any inlets. The complete set of boundary conditions can be viewed in table 1.

TABLE I. OPENFOAM BOUNDARY CONDITIONS

Boundary	Boundary Conditions		
	p	U	T
Inlet	totalPressure	zeroGradient	totalTemperature
Outlet	totalPressure	zeroGradient	totalTemperature

Boundary	Boundary Conditions		
	p	U	T
Inlet Freestream	totalPressure	zeroGradient	totalTemperature

The $k-\omega$ -SST turbulence model was used to characterize the effects of turbulence on the mean flow. The turbulent kinetic energy (k) at the inlet can be calculated using:

$$k = \frac{3}{2} (I |U_{ref}|)^2 \quad (2)$$

The turbulence intensity (I) is provided as a percentage of the mean flow energy. Usually this value is unknown, but approximately in the range of 1% to 5% depending on how intense the turbulence entering the domain is. For the current study, the turbulence intensity was set to 1% since Henderson used methods to reduce the turbulence at the nozzle inlet. U_{ref} is the magnitude of the flow velocity at the inlet boundary face. Since the inlet velocity was not set explicitly by the boundary condition the velocity was guessed using the conservation of mass and subsequently updated with the results from the first test. The turbulent dissipation rate can be calculated using:

$$\omega = \frac{k^{0.5}}{C_\mu L} \quad (3)$$

Where: $C_\mu = 0.09$ in OpenFOAM
 $L = 0.07d_h$

Domain Mesh

The domain was meshed primarily using hexahedral elements in Pointwise. An unstructured mesh was applied to the far field near the outlet boundaries to allow for large size grid elements that ensured no acoustic waves were propagated back into the domain (figure 2). Further levels of refinement were used in the free jet region and shear layer to ensure any potential instabilities and acoustics were properly captured (figure 3).

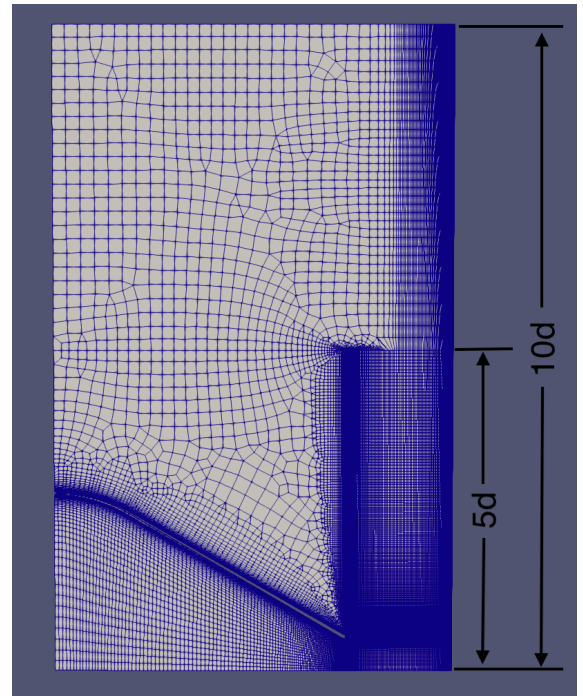


Figure 2: Domain Mesh for $L/d=1.65$

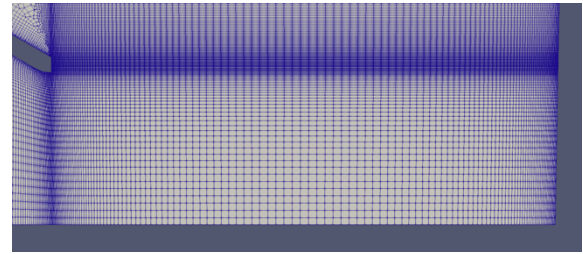


Figure 3: Mesh Quality in Free Jet and Impingement Regions for $L/d=1.65$

Given the total pressure boundary condition applied, the mass flow rate into the domain oscillated during the start-up period. Since the mass flow rate should remain constant, this provided an ideal parameter to ensure the simulation had converged with time. When the oscillations in mass flow rate at the inlet domain were below 1% of the mean mass flow rate, the solution was considered converged with time. To reduce the time required to reach the mass flow rate criteria a very course mesh was used initially, and the results mapped to the refined mesh.

Grid convergence was determined by generating successively more refined meshes, and comparing the position of the first Mach diamond and the behavior of the normal shock leading the impingement region. Each mesh with a higher refinement contained double the elements of the previous mesh level. This meant that the number of divisions on each line in the geometry was 141% of the next level up ($2^{0.5}$). The boundary layer thickness is also reduced by the same percentage as the domain becomes more refined. Each time the field was mapped to a successively more refined mesh, the simulation was given 10^{-2} seconds to stabilize with time. This time was chosen since it represents 20x the time required for the impinging flow to travel $10d$ along the wall. The final mesh used

a grid spacing at the nozzle exit plane of $d/32$. This resulted in a mesh ranging from 48,654 cells for $L/d = 1.65$, to 104,872 cells for $L/d = 4.16$.

III. RESULTS AND DISCUSSION

To validate the accuracy of the study, the results were compared to the studies by Henderson and Dauplain [4,5]. Considered in the studies was the structure of oscillating flow structures and the tones produced by the system in the various cases considered. Dauplain considered four important structures to the flow that were used to compare the accuracy of the simulation [4]:

- 1) Shear Region
- 2) Recirculation Bubble
- 3) Inviscid Core
- 4) Thin Subsonic Region Following Mach Diamond Normal Shocks

1. Shear Region

Using the same characterization for the shear layer as Dauplain, where the shear layer exists in the region where flow velocity is between 50m/s to 300m/s, the size of the shear layer can be visualized (figure 4). Growth of the shear layer appeared to be linear, and grew at an angle of 5.5° . The result was consistent with the growth rate found by Zang for a NPR of 4.0, which slightly overestimated their experimental growth rate of 5.2° [3].

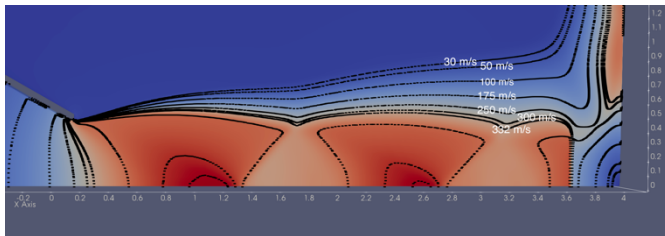


Figure 4; Velocity Profile with Contour Lines to show Shear Region Growth for $L/d=4.16$

2. Recirculation Bubble

No recirculation bubbles were found to be present in the current study. Instead, there was a steady deceleration beyond the impingement shock that continued to the impingement plate. Only in the $L/d = 1.65$ case did some recirculation structures appear. Since a 3-dimensional structure appears to be present within these recirculation bubbles [4], it is expected that using an axisymmetric model suppressed the flow feature (figure 5,6).

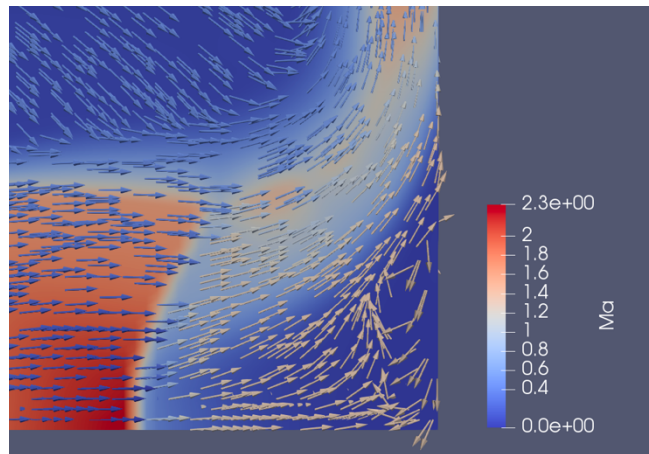


Figure 5: Recirculation Bubble for $L/d=1.65$

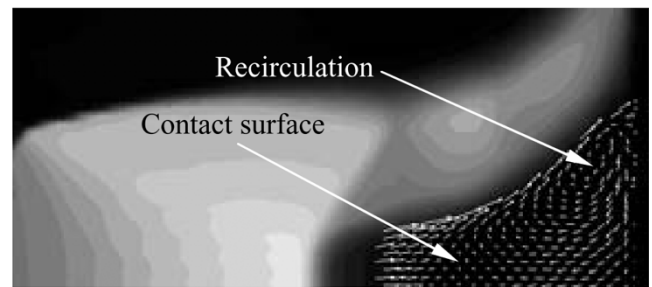


Figure 6: Recirculation Bubble Found by Henderson for $L/d=2.08$ [5]

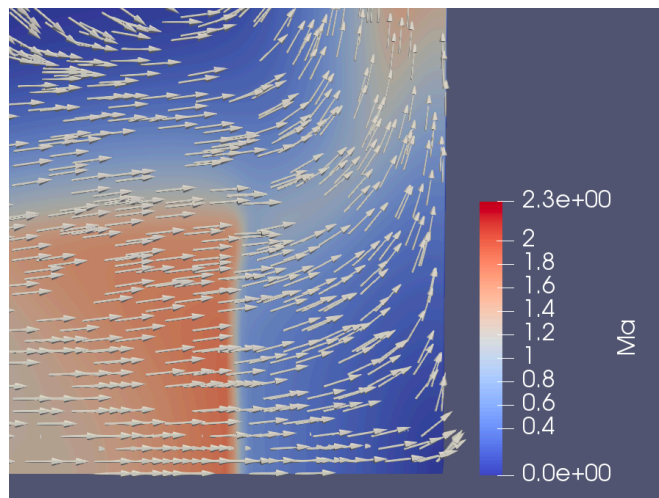


Figure 7: Recirculation Bubble for $L/d=2.66$

3. Inviscid Core

The accuracy of the inviscid core was determined by measuring the length of the first Mach diamond. In Henderson's experiment, the spacing from the jet outlet to the first Mach diamond was $1.6d$. The first Mach diamond was found to have a length of 42mm, which corresponded to a dimensionless distance of $1.65d$ (figure 8). Having a slightly over predicted Mach diamond spacing is consistent with the findings of Zang [3].

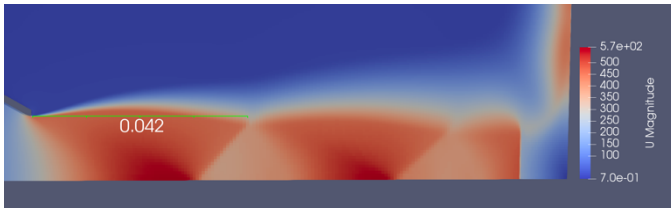


Figure 8: Mach Diamond Spacing (m)

The impingement shock was well predicted only when the impingement plate was located at $L/d=1.65$. For all impingement plates located further downstream the impingement shock was found to be located closer to the plate than in experiment, as shown in (figure 9,10). Since the flow found in the current study was steady in time, many of the features that could have contributed to the position of the normal shock may have been suppressed. Table 2 shows the location of the impingement shock for each case studied.

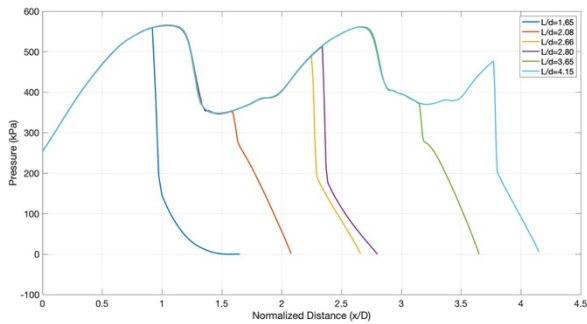


Figure 9: Flow Velocity vs. Normalized Distance (Axisymmetric rCF)

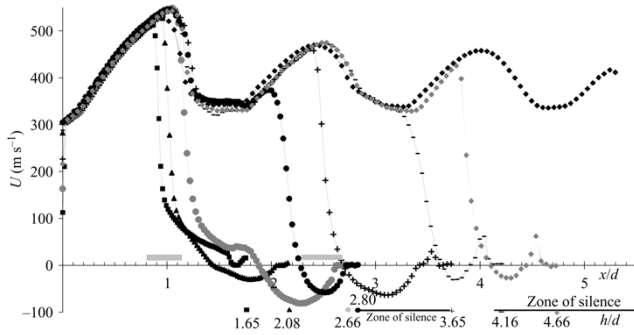


Figure 10: Flow Velocity Vs. Normalized Distance (Experimental) [5]

TABLE II. EXPERIMENTAL SHOCK POSITION VS. PRESENT STUDY SHOCK POSITION, STATED AS NORMALIZED DISTANCE FROM NOZZLE EXIT

Case (L/d)	Boundary Conditions		
	Experimental	Present Study	%Error
1.65	0.85	0.91	7.1%
2.08	0.95	1.59	67.4%
2.66	1.15	2.24	94.8%
2.80	2.00	2.34	17.0%
3.65	2.40	3.15	31.3%
4.16	3.25	3.77	16.0%

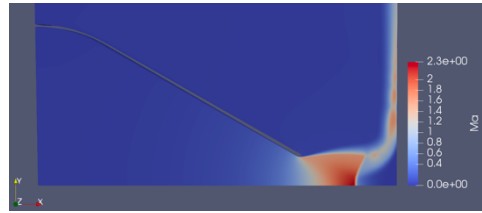


Figure 11: Mach Number Contours for L/d=1.65

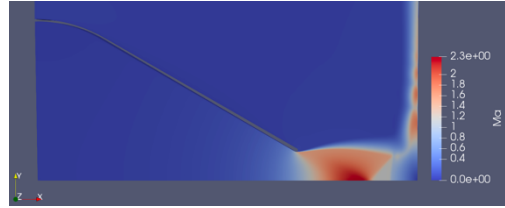


Figure 12: Mach Number Contours for L/d=2.08

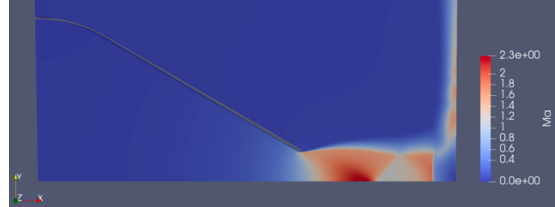


Figure 13: Mach Number Contours for L/d=2.66

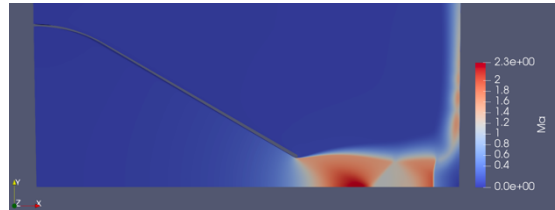


Figure 14: Mach Number Contours for L/d=2.80

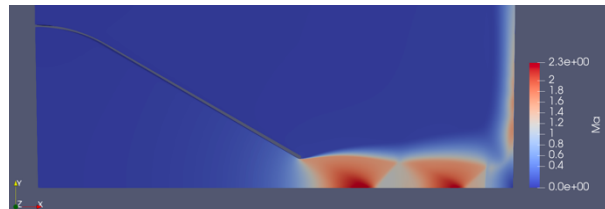


Figure 15: Mach Number Contours for L/d=3.65

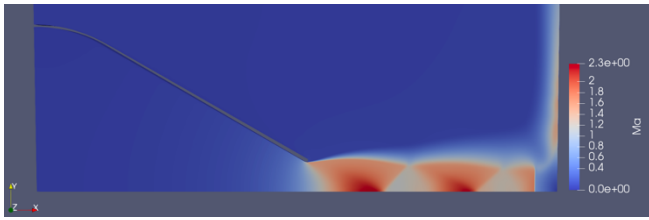


Figure 16: Mach number Contours for $L/d=4.15$

4. Thin Subsonic Region

In the current simulations, no subsonic region or Mach disk is present within the Mach diamond structures, only the normal shock at the impingement region was measured. According to Franquet, a NPR between 2-4 is considered a moderately under-expanded jet which will not contain a Mach disk in the Mach diamonds. Given the current case is looking at the upper limit between moderately under-expanded and highly under-expanded it is challenging to determine if a Mach disk structure would be present [4]. Further, the PIV measurements taken by Henderson are limited when measuring shock features due to the inertia of the particles being unable to match the rapid change in the fluids momentum after the shock.

5. Transient Flow Features

An additional feature to review is the transient features typically found in an impinging jet flow. As mentioned earlier, several types of flow instabilities may be present in this style of flow field. Taylor-Goertler and flapping, require a 3-demsional model to be resolved and thus it was known these modes of instability would be suppressed in current study. The final instability mode, Kelvin-Helmholtz instabilities, appear as vortex rings implying an axisymmetric nature. Without any instabilities in the flow, the fluctuations of the impingement shock were also suppressed, totally removing any acoustic features in the flow.

The current study resulted in a steady time averaged flow with no transient features. While the means that not all information from experiments can be represented in the numerical results, it remains a useful engineering model that allows a significant amount of information to be gained without considering the complex unsteady flow features. Prediction of Mach diamond spacing and shear layer growth were both accurately performed. Furthermore, accurate prediction of the fluid stagnation pressure was found in the impingement region.

Strong toroidal instabilities are present in the simulation when conducted without using a turbulence model (figure 17). This indicates that using a RANS turbulence model may be the aspect of the simulation that is suppressing the Kelvin-Helmholtz instabilities. Further, these instabilities are known to form in the shear layer where velocity gradients are large. If the high turbulent viscosity in the shear layer is enough to suppress these flow features, then the turbulence model used may not be suitable for the given application.

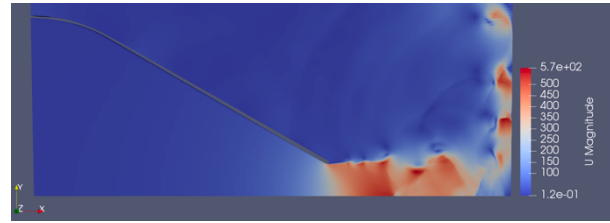


Figure 17: Flow Velocity Without a Turbulence Model for $L/d=2.80$, KH Style Instabilities Found in Flow

IV. CONCLUSION

Using rCF for under-expanded free jets impinging on a large baffle showed close agreement for the Mach diamond spacing and shear region growth, while having poor accuracy for the recirculation bubble and impingement shock location. As expected, TG and flapping flow instabilities were suppressed by the use of an axisymmetric model. However, KH instabilities were unexpectedly suppressed, thus removing all transient phenomenon from the study. It is unknown whether these instabilities were suppressed due to the use of an axisymmetric model or the $k-\omega$ -SST turbulence model. With all instabilities being suppressed, the model was completely stable with respect to time and no acoustics or recirculation bubble was present. Further work is required to determine the impact of the turbulence model transient features of the flow.

REFERENCES

- [1] Erwin Franquet, Vincent Perrier, Stephane Gibout, and Pascal Bruel. Progress in Aerospace Sciences Free underexpanded jets in a quiescent medium : A review. Progress in Aerospace Sciences, 77:25–53, 2015.
- [2] Joel L Weightman, Omid Amili, and Damon Honnery. Nozzle external geometry as a boundary condition for the azimuthal mode selection in an impinging underexpanded jet. Journal of Fluid Mechanics, 862:421–448,2019.6
- [3] B. Zang, Vevak US, H. D. Lim, X. Wei, and T. H. New. An assessment of OpenFOAM solver on RANS simulations of round supersonic free jets. Journal of Computational Science, 28:18–31, 2018.
- [4] A. Dauptain, B. Cuenot, and L. Y. M. Gicquel. Large Eddy Simulation of Stable Supersonic Jet Impinging on Flat Plate. AIAA Journal,48(10):2325–2338, 2010.
- [5] Brenda Henderson, James Bridges, and Mark Wernet. An experimental study of the oscillatory flow structure of tone-producing supersonic impinging jets. Journal of Fluid Mechanics, 542:115–137, 2005
- [6] Alexander Kurganov and Eitan Tadmor. New High-Resolution CentralSchemes for Nonlinear Conservation Laws and Convection Diffusion Equations. Journal of Computational Physics, 160(1):241–282, 2000.
- [7] MMA Alam, T Setoguchi, S Matsuo, and H D Kim. Nozzle geometryvariations on the discharge coefficient. Propulsion and Power Research,5(1):22–33, 2016
- [8] G. Aswin and Debasis Chakraborty. Numerical simulation of transverseside jet interaction with supersonic free stream. Aerospace Science andTechnology, 14(5):295–301, 2010.
- [9] Jie Wu and T. H. New. An investigation on supersonic bevelled nozzle jets. Aerospace Science and Technology, 63:278–293, 2017.
- [10] Florian R. Menter. Review of the shear-stress transport turbulence model experience from an industrial perspective. International Journal of Computational Fluid Dynamics, 23(4):305–316, 2009.

- [11] T. J. Poinso and S. K. Lele. Boundary conditions for direct simulations of compressible viscous flows. *Journal of Computational Physics*, 101(1):104–129, 1992.
- [12] Bin Zang, Vevek U S, and Tze How D. New. OpenFOAM based numerical simulation study of an underexpanded supersonic jet. 55th AIAA Aerospace Sciences Meeting, (January):2017–747,
- [13] Xiaopeng Li, Kun Wu, Wei Yao, and Xuejun Fan. A Comparative Study of Highly Underexpanded Nitrogen and Hydrogen Jets Using Large Eddy Simulation. 20th AIAA International Space Planes and Hypersonic Systems and Technologies Conference, 1, 2015.

Environmental Flows

MIXING IN THE BRAZIL BASIN

Kelly Anne Ogden

Department of Mechanical and Materials Engineering
Western University
London, Canada
kogden3@uwo.ca

Raffaele Ferrari

Department of Earth, Atmospheric, and Planetary
Sciences
Massachusetts Institute of Technology
Cambridge, MA, USA

ABSTRACT

The ocean's meridional overturning circulation has an important influence on Earth's climate. It contributes significantly to the global budget of heat and dissolved gases, including carbon dioxide. The deepest branches of this circulation are associated with abyssal waters rising toward the surface. Recent work has suggested that the rising waters are confined to narrow boundary layers along the ocean ridges and seamounts, where mixing is most intense. However, this is only a theory with limited observational support. To assess this theory, simulations of the Brazil Basin are conducted using the MITgcm, and the results are compared to observational results from the Brazil Basin Tracer Release Experiment (BBTRE).

Agreement between the simulation results and observational data is seen in several qualitative measures. Tracers released during the simulation are tracked and compared to the general paths of observational floats released in the same area (Hogg and Owens, 1999). A simulated tracer patch evolution is also compared to the observational tracer released during the BBTRE. Near bottom velocities in the abyssal canyons are compared to observational data. In each of these measures, the simulation agrees reasonably well with the observations. The simulations are conducted using MITgcm with a specified diffusivity (κ) profile, as a function of height above the bottom, which is based on observations. The simulation results are in good agreement with other observations of the flow, indicating that specifying the diffusivity profile as a function of height above bottom is a reliable approach to modelling vertical diffusivity.

The simulation results show upwelling occurs along the boundaries, whereas the interior waters sink slowly. The magnitude, distribution, and peak volume transport agree with various previously published observations (de Lavergne et al., 2017; St. Laurent et al., 2001; Lumpkin and Speer, 2007). This is also in agreement with the recent theory that the ocean's meridional overturning circulation is closed by upwelling along the boundaries. Furthermore, components of the mass transformation also indicate that the bottom intensified mixing due to the vertical variation of the diffusivity profile is the most significant component of the mass transformation. This work contributes to verifying a reasonable mixing model and confirming the recent theory of deep ocean mixing.

A more reliable estimate for external convective heat transfer coefficient from building surfaces in an urban-setting

Anwar Awol
University of Western Ontario,
UWO
London, ON, Canada
ademsis@uwo.ca

Girma Bitsuamlak
University of Western Ontario,
UWO
London, ON, Canada
gbitsuam@uwo.ca

Fitsum Tariku
British Columbia Institute of
Technology, BCIT
Burnaby, BC, Canada
fitsum_tariku@bcit.ca

ABSTRACT

Available correlations for estimating external convective heat transfer from buildings are reported to produce up to 40% discrepancy in the predicted building's energy demand. These correlations are derived from studies on isolated, low rise, buildings. In addition, there is inconsistency in the aerodynamic exposure conditions considered in different studies. These limits the representativeness of the models in relation to realistic urban surface form and associated local micro-climate surrounding the building. In built neighborhoods, upstream wind and temperature statistics are significantly altered due to the upwind terrain and local built morphology. Some researchers have used local references to address the issue but mostly arrived at considerably diverse results. This is due to inconsistent reference states and specificity of each test configuration. The current study aims to obtain new correlation from Computational fluid dynamics (CFD) for external convective heat transfer coefficient (CHTC); based on a novel urban canopy layer (UCL) flow model derived from analytical/semi-analytical procedure to predict local flow/convective heat transfer characteristics for array of buildings. The study extends the authors' previous research on homogeneous built arrangement by introducing sets of idealized heterogeneity options. Consequently, the present study gives correlations that would serve for different urban morphological settings, besides addressing the issue of consistent local references states. The proper quantification of CHTC greatly contributes towards bridging the performance gap, the discrepancy of building energy use between design stage estimation and the consumption level during operation.

THE ACTUATOR LINE METHOD FOR WIND TURBINE MODELLING APPLIED IN A VARIATIONAL MULTI-SCALE FRAMEWORK

Michael Ravensbergen and Artem Korobenko
Department of Mechanical and Manufacturing Engineering
University of Calgary
Alberta, Canada
michael.ravensbergen@ucalgary.ca

ABSTRACT

High fidelity modelling techniques for wind turbine aerodynamics currently require fine mesh resolution to resolve boundary layer effects near the blades. Such models are referred to as fully resolved and model the entire geometry (blades, hub, and tower) of the turbine. Conversely, the actuator disk method models the entire turbine as a single energy extracting disk. This low fidelity tool lacks the ability to resolve the complex flow patterns around wind turbines. In contrast to the two modelling techniques described above, the actuator line method, introduced by Sorensen and Shen in 2002 allows relatively coarse element resolution while maintaining accurate wake characteristics. As the blades are modelled individually, the framework can resolve the helical vortices that characterize the wake region. The actuator line model is coupled to an unsteady 3D fluid solver, typically using large-eddy simulation (LES). The variational multi-scale concept for LES, introduced in the current form by Bazilevs et. al. 2007, improves on typical LES codes by removing the reliance on an ad-hoc turbulence closure model.

In the present work the *actuator line model* is implemented in a *variational multi-scale* fluid dynamics code to efficiently and accurately model wind turbines. Such a model will enable generation of the, typically complex, flow field present within a wind farm which can then be used to optimize performance (i.e. maximize power production and minimize structural loading) of downstream turbines.

The modelling framework is based on variational multi-scale (VMS) concepts for LES. The main idea is to use variational projections in place of the classical filtered equation approach. Avoidance of filters eliminates the difficulties associated with the use of complex filtered quantities. Furthermore, the VMS method separates the scales *a priori* and models the effect of unresolved scales only in the equations representing the smallest resolved-scales, and not in the equations for the large scales. The domain is discretized into finite elements and the linear finite element method is applied to approximate the solution to the Navier-Stokes equations for incompressible flows. The actuator line concept calculates forces along lines representing wind turbine blades and projects those forces into a computational fluid domain. Each blade is divided into elements, at which the fluid velocity of the background mesh is sampled and the fluid velocity relative to the rotating blade is calculated. Lift and drag forces are then calculated using tabulated aerodynamic data as a function of angle of attack. The aerodynamic force at each blade element is projected back to the mesh using a Gaussian projection, which enters the Navier-Stokes equations through the body force term.

We present results of simulations of the National Renewable Energy Laboratory (NREL) 5 MW reference turbine. Two configurations are tested, a single turbine and two turbines placed one behind the other. The computed power and wake velocity deficit are in good agreement with published numerical data.

The goal of this work is to develop a computationally efficient yet physically accurate unsteady model for a full-scale wind turbine. Potential applications include modelling unsteady flow within a wind turbine array to optimize turbine layout or generate realistic inflow conditions for further simulations on downstream turbines.

FLUTTER INSTABILITY OF A FLAT PLATE DEFORMING WITH LARGE AMPLITUDE TO ALIGN WITH THE FLUID FLOW

Mohammad Tari, Frederick P. Gosselin and Eric Laurendeau

Department of Mechanical Engineering
Polytechnique Montreal
Montreal, Canada
mohammad.tari@polymtl.ca

ABSTRACT

Trees and aquatic plants have evolved to be flexible and *reconfigure* under wind and water flow, i.e., they bend and twist to reduce their drag. However, their flexibility renders them susceptible to flutter and other instabilities under changing configuration. Flutter can give rise to large dynamical loads. There is therefore a trade-off between reconfiguration and stability in flexible structures. Our aim is to find the onset of flutter and to find out whether this reconfiguration strategy is always beneficial. We focus on simplified geometries such as beam and plates to reproduce the complex behaviour of plants under fluid flow. In contrast to their simplicity, these slender structures can exhibit very rich spectra of vibrational characteristics. We consider a two dimensional flat plate initially perpendicular to the fluid flow and held at its center. As the flow speed is increased, in our numerical and experimental approaches, the plate first bends downstream, then as it becomes more and more aligned with the flow, it undergoes high frequency flutter vibrations. In the numerical part, we develop a large displacement structural solver assuming Euler-Bernoulli beam representing the motion of plates in two dimensions. We use an in-house unsteady Reynolds-Averaged Navier–Stokes solver for the simulation of the flow field, and we employ an iterative partitioned technique to couple the structural and fluid solvers and to ensure convergence of the flow and structure variables at the interface level. In addition, we use the Chimera method to handle mesh generation in complex configurations during the simulation. At every iteration, an Arbitrary Lagrangian-Eulerian technique corrects the flow velocity to account for mesh movement. In the experimental part, we perform a series of wind tunnel tests to quantify the stability limit, observe different flutter modes, and validate our numerical method. This combined numerical and experimental approach enables us to study flutter and to provide insights into the drag reduction mechanisms, and post flutter behavior of flexible slender structures.

BIM-CFD INTEGRATED DESIGN PROCESS EXAMPLES FOR NORTHERN ARCHITECTURE

Younis, M.¹, Bitsuamlak. G.T.^{1,2}, Meseret T. Kahsay¹

¹ Department of Civil and Environmental Engineering, and WindEEE Research Institute, UWO

² Boundary Layer Wind Tunnel Laboratory, UWO

London, Canada

myounis4, gbitsuam, mkahsay { @uwo.ca }

ABSTRACT

The infrastructures and houses development in northern Canada have to withstand a harsh environment. The need for innovative building design has become a vital requirement in sustainable and resilient future for the Arctic. This study proposes a framework to integrate building information modeling (BIM) and computational fluid dynamics (CFD) analysis method. The framework is used to assess the wind effect on low-rise buildings with Northern Architecture (e.g. Raised from ground). In this study, a wind performance assessment for low-rise building that is raised from the ground at a height of 0 m, 0.5 m, 1 m, and 2 m and for various wind directions of 0°, 45°, 90° from the north is carried out. For this purpose, BIM modeling procedure in exchangeable format is developed to allow the data transformation between both CFD and 3D modeling tools. High-resolution numerical simulation, through super computers provided by Sharcnet. Reynolds stress model with six equations are used for majority the study cases. LES was also conducted for selected cases for comparison purposes.

Free Surface Flows

Modelling requirements for dynamic multiphase ship simulations

Chunhui Liu

Department of Mechanical and Mechatronics Engineering
University of Waterloo
Waterloo, Ontario, Canada
chunhui.liu@uwaterloo.ca

Kevin McTaggart

Defence Research and Development Canada
Dartmouth, Nova Scotia, Canada
Kevin.McTaggart@drdc-rddc.gc.ca

Xiaohua Wu

Department of Mechanical and Aerospace Engineering
Royal Military College of Canada
Kingston, Ontario, Canada
Xiaohua.Wu@rmc.ca

Jean-Pierre Hickey

Department of Mechanical and Mechatronics Engineering
University of Waterloo
Waterloo, Ontario, Canada
Jean-pierre.hickey@uwaterloo.ca

ABSTRACT

The estimation of ship maneuverability is one of the most important performance indicators for ship navigation. It is also intrinsically tied to ship design and performance characterization. The maneuverability characteristics of a vessel can be estimated through theoretical calculations, experimental/empirical models or numerically with Computational Fluid Dynamics (CFD). The theoretical approach is limited to slender bodies and does not consider the interaction between the hull and the appendages, nor the more complex non-linear effects; this is best suited for order-of-magnitude maneuverability approximations. Empirical modelling informed by experimental tests is the standard approach for the ship maneuverability estimates and relies on the measurement of forces and moments on a subscale ship model undergoing static and dynamic planar motion mechanism (PMM) tests. These experimental tests are expensive and time consuming as special experimental platforms are required and ill-suited for iterative ship optimization. The continually increasing computational power enables the use of CFD to numerically compute static and dynamic stability derivatives on arbitrarily complex ship geometries. Although promising, numerical prediction of these naval flows is highly complex as one must consider the adequate resolution of the gas-liquid interface, complex turbulence effects, and the important wave-hull interactions, among the many other multi-physics interactions.

The inadequate modelling of these complex and coupled phenomena means that CFD simulations of ship maneuverability can easily result in incorrect numerical answers. The standard practice is to assess the validity of the CFD approach by comparing the numerical predictions with well-defined experimental test cases, such as those defined in the context of the SIMMAN Workshop on Verification and Validation of Ship Maneuvering Simulation Method. This essential validation step provides an assessment of the predictive capabilities of the numerical solvers based on the comparison of the measured integral quantities (forces, moments etc.). The validation based on integral quantities, although critical, does not provide any indication on the adequacy of the simulation parameters to model the multi-physics interactions inherent to ship modelling simulations. Given the geometric complexity and multi-scale nature of the problem, the incorrect modelling of the multi-physics interactions may limit the generalizability of these predictive simulations.

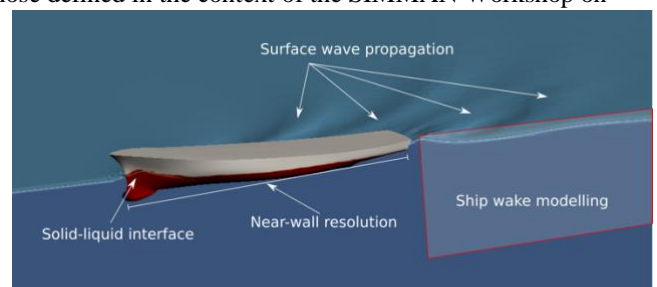


Figure 1 - Multi-physics test cases under consideration.

The present work seeks to assess the modelling requirement for the open-source CFD package OpenFOAM in multiphase ship simulations. To this end, the complexity of a ship simulation is decomposed into well-defined and canonical sub-problems. In the present work, we investigate the numerical simulation requirements for: (1) surface wave propagation at the water-air interface, (2) near wall mesh structure, (3) turbulence modelling in the wake, and (4) wave-hull interaction (see Figure 1). The canonical nature of these flows permits an isolation of the physical complexity, thus enabling quantifiable guidelines for ship modelling. These sub-problems are investigated and compared against experimental data. The findings are then used to simulate full scale ship simulations and the modelling requirements are used to inform the ship modelling community.

NUMERICAL SIMULATIONS OF TWO-BODY INTERACTION IN WAVES

Wei Meng, Heather Peng and Wei Qiu*
Department of Ocean and Naval Architectural Engineering
Memorial University
St. John's, NL, Canada

* Email: qiuw@mun.ca

ABSTRACT

Hydrodynamic interaction between floating bodies in close proximity is one of issues in side-by-side operations, for example, underway replenishment for navy ships and for offloading oil and gas by the offshore industry. In close proximity, large body motions and resonant free surface elevations could occur in gaps, and the hydrodynamic interactions can also affect the mooring line loads. Most of the linear seakeeping programs, based on the potential-flow theory and currently used by the industry, over-predict the free surface elevations between bodies and hence the low-frequency loadings on bodies. A few techniques have been developed to suppress unrealistic large wave elevations in the gap predicted by the potential-flow theory. However, artificial damping coefficients are required as input to these methods. Without providing the experimental data beforehand, the required artificial damping as input cannot be properly determined. Model tests and CFD simulations are needed to understand and determine the free surface damping due to the viscous effect and the artificial damping in a systematic way. Extensive model tests have been carried out at Memorial's towing tank for two-body interaction in waves.

The present paper, focused on CFD simulations, presents numerical methods to solve interaction problems of two bodies in head waves based on OpenFOAM. Solid bodies are modelled by the immersed boundary method. The free surface is captured by employing a volume-of-fluid (VOF) method (Roenby et al, 2016). Waves are generated using the waves2Foam toolbox (Jacobsen et al., 2012). Numerical studies were carried out to examine the effect of domain size and grid distribution/resolution on the solutions. Numerical results were compared with experimental data (Qiu et al, 2019). The potential side-wall effect in the model tests at the towing tank was also investigated.

Time series for the heave motion of Body 1 and the pitch motion of Body 2 for incident waves ($\lambda/L = 1.69$), along with their comparisons with experimental results, are presented in Fig. 1.

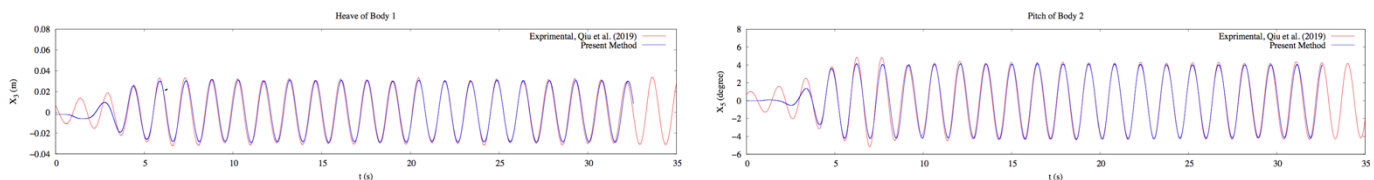


Figure 1: Ship Motions for Incident Waves, $\lambda/L = 1.69$

REFERENCES

- Jacobsen, N. G., Fuhrman, D. R. and Fredsøe, J., 2012, A Wave Generation Toolbox for the Open-Source CFD Library: OpenFoam, *International Journal for Numerical Methods in Fluids*, Vol. 70, No. 9, pp. 1073-1088.
- Qiu, W., Meng, W., Peng, H., Li, J., Rousset, J. M., Rodríguez, C. A., 2019, Benchmark Data and Comprehensive Uncertainty Analysis of Two-body Interaction Model Tests in a Towing Tank, *Ocean Engineering*, Vol. 171, pp.663-676.
- Roenby, J., Bredmose, H. and Jasak, H., 2016, A Computational Method for Sharp Interface Advection, *Royal Society Open Science*, Vol. 3, No. 1.

PERFORMANCE ANALYSIS OF A VERTICAL AXIS HYDROKINETIC TURBINES ARRAY

A. Bayram Mohamed & A. Korobenko
Department of Mechanical and Manufacturing Engineering
University of Calgary
Calgary, AB, T2N 1N4

ABSTRACT

Hydrokinetic energy has been receiving recognition lately as a promising source of clean renewable energy and many investigations have been made to the advancement of hydrokinetic technologies. The two main classifications for hydrokinetic turbines are the horizontal axis and the vertical axis turbines.

Performance prediction of vertical axis hydrokinetic turbines is a challenging research area. This is due to the complexity of the flow field which mainly arise due to the large variations in the angle of attack of the blades, the struts effect and the vortex interactions between blades.

In this paper, the authors present a full-scale, 3D numerical study of an array of two vertical axis hydrokinetic turbines (VAHT). The time-dependent, 3D, incompressible Navier—Stokes equations are discretized using the Arbitrary Lagrangian-Eulerian Variational Multi-scale (ALE-VMS) formulation with sliding interfaces to handle the rotor-stator interactions. The VMS formulation based on scale separation avoids the concept of filtering in LES and provides a theoretical representation of the fine scales in terms of the coarse scales which is also an alternative to RANS models that are carefully tuned for different flow conditions and geometrical settings. Weak enforcement of essential boundary conditions is used for the solid structure surfaces which enhances the formulation by relaxing the requirement of boundary layers resolution.

First, a single turbine is simulated and the computed torque is validated against experimental measurements. Next the computation of an array of two turbines is performed to compute the power deficit of the turbine placed in the wake of the upstream turbine. The results assure the robustness of the ALE-VMS formulation and how it can be used to simulate multiple turbines.

STUDY OF INERTIAL COALESCENCE OF DROPLETS ON A SOLID SUBSTRATE USING LATTICE BOLTZMANN MODELLING

Nilesh D. Pawar, Supreet Singh Bahga, Sunil R. Kale

Department of Mechanical Engineering
Indian Institute of Technology Delhi
Hauz Khas, New Delhi 110016, India
ndpr03@gmail.com

Sasidhar Kondaraju

School of Mechanical Sciences
Indian Institute of Technology Bhubaneswar
Argul, Odisha 752050, India
sasidhar@iitbbs.ac.in

Abstract

Whenever two liquid drops contact, they coalesce to form a single droplet to minimize the surface energy. This process is known as coalescence. It is a fundamental process and has a wide range of applications in droplet condensation, microfluidic devices, inkjet printing, and powder metallurgy.

Coalescence of two liquid drops is described into two stages as shown in Fig.1. In the initial stage, the coalescence starts via formation of the microscopic liquid bridge of infinite curvature. This induces very large capillary pressure which drives liquid into the bridge and as a result bridge grows with time. In the late stage, the combined droplets of elliptical shape relax to a spherical shape. The later stage has been extensively studied in the past. However, the initial stage of coalescence is a topic of significant interest.

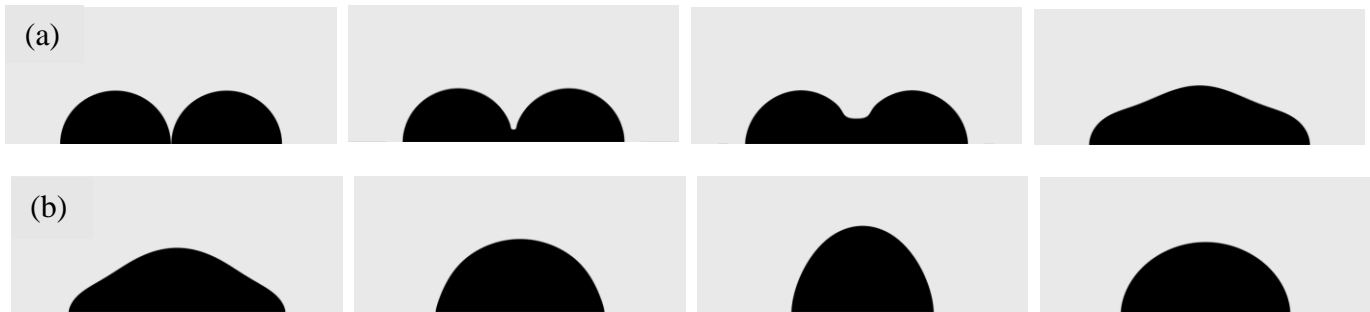


Figure 1: Stages of the coalescence process of two liquid drops. (a) The initial stage, the liquid bridge grows with time. However, the contact line does not move in this regime. (b) The late stage of coalescence where combined droplet relaxes to a spherical shape.

Earlier studies were focussed on the coalescence of free droplets. However, in many applications, e.g., dropwise condensation, coalescing drops are in contact with a solid surface. Besides, the coalescence dynamics of sessile drops on a surface deviates significantly from that of free drops. This is because the presence of solid surface complicates the dynamics of the contact line and slows down the transport of liquid towards the bridge. In this work, we present detailed numerical simulations of the early-stage coalescence of drops on a solid substrate in the inertial regime. In particular, we show the effect of surface wettability and the droplet size on growth dynamics of liquid bridge. Our analysis is based on a two-dimensional pseudo-potential lattice Boltzmann method to simulate coalescence of equal size droplets (symmetric coalescence) and the coalescence of unequal size droplets (asymmetric coalescence). We use Shan and Chen single component multiphase model with the Peng-Robinson equation of state. Our simulation results show that for equal size drop coalescence, bridge height grows with time and follows the scaling law $h \sim t^\mu$. The power law exponent is $1/2$ for $\theta = 90^\circ$ and $2/3$ for $\theta < 90^\circ$. In addition to scaling law, rescaled bridge profile at different times collapses into a single curve showing self-similar behavior in an early stage of coalescence. We then explain the mechanism of coalescence of two unequal sized drops. We also show that the same scaling law of coalescence of equal sized drops is valid for the coalescence of two unequal sized drops.

COMPUTING WAVES UNDER ICE

Olga Trichtchenko
The Department of Physics and Astronomy
The University of Western Ontario
London, ON
otrichtc@uwo.ca

Emilian I. Parau
School of Mathematics
University of East Anglia
Norwich, UK
e.parau@uea.ac.uk

ABSTRACT

In this work, we present a method for computing solutions to different models of three-dimensional, nonlinear, hydroelastic waves, propagating at the interface between a fluid and a sheet of ice. The fluid is assumed to be inviscid and incompressible, and the flow irrotational. The resulting system is the Euler equations. We show how to transform this nonlinear set of equations using the potential flow formulation, and restrict our focus on the boundary of the fluid, resulting in a free boundary problem. We then proceed by numerically solving the resulting boundary integral equations and use a continuation method to obtain nonlinear solution branches for both forced and solitary wave solutions that are either elevation or depression waves. For example, a solitary wave of elevation is shown in Figure 1a and a wave of depression given in Figure 1b, in nondimensional units. Solving the boundary integral equations is computationally intensive. To speed up the convergence, we employ a number of methods such as parallelisation, using inexact Jacobians and using iterative methods with preconditioners that take advantage of the continuation process of obtaining nonlinear solutions. We present the results for different models of ice, as well as compare and contrast solutions in different regimes

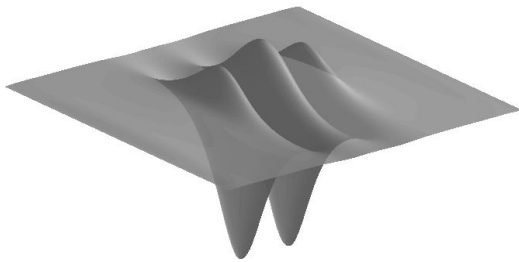


Figure 1a: Hydroelastic wave of elevation.

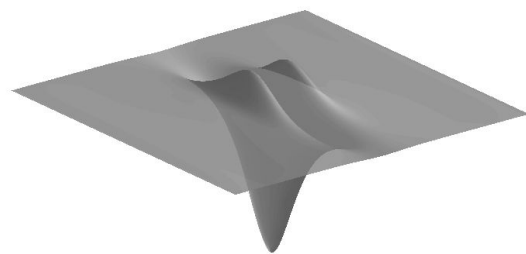


Figure 1b: Hydroelastic wave of depression.

Simulations of Self-Propulsion Model Tests of a Fishing Vessel Using a Body-Force Method Coupled with a RANS Solver

Md Ashim Ali, Heather Peng, and Wei Qiu

*Advanced Marine Hydrodynamics Laboratory
Department of Ocean and Naval Architectural Engineering
Memorial University, St John's, NL, Canada A1B 3X3*

Email: hpeng@mun.ca

Abstract – This paper presents numerical simulations of ship model self-propulsion tests using a simple body-force method coupled with the Reynolds Averaged Navier-Stokes (RANS) solver in the open-source Computational Fluid Dynamics (CFD) package OpenFOAM. The self-propulsion simulations were carried out for a fishing vessel with an optimized bulbous bow and a four-bladed fixed-pitch propeller. The propeller was modeled with an actuator disk method. Unsteady simulations were first performed at the design speed without a propeller to validate the numerical results of resistance, sinkage, and trim against the experimental data. The open-water hydrodynamic characteristics of the propeller were then computed with the body-force method and compared with the experimental data. In the end, the self-propulsion simulations were carried out using the load varying method. The required tow forces and trims are compared with the experimental data for various propeller revolution rates.

Keywords - *Self-propulsion; Fishing Boat; Body-force Method; RANS*

I. INTRODUCTION

Multi-species fishing vessel fleets in Newfoundland and Labrador (NL) have to meet a range of design and operational criteria. Their design speeds are typically between 8 to 12 knots, while the movable fishing gears, for instance, bottom or mid-water trawls, limit the vessel to speeds lower than 4 knots. The vessels energy efficiency at high speeds is usually a challenge.

D. Friis et al. [1] conducted experimental studies on energy efficiency of fishing vessel models with different bows installed. It was found that the wake increased dramatically in the high speed range. In order to minimize the required power and to achieve the optimum propulsion efficiency, it is important to optimize the hull forms and study the hull-propeller interaction in the early design stage.

According to the International Towing Tank Conference (ITTC) procedures [2], three sets of model tests are required for power performance prediction of a full-scale ship, including bare-hull resistance tests, propeller open-water tests, and self-propulsion tests. With the rapid advance in CFD methods and computing power, it becomes feasible to predict the hull-propeller interaction in a reasonable accuracy with CFD methods, and to optimize the design of propeller and hull. Since the hull forms of NL fishing vessels with smaller length-to-beam ratios are much less streamlined than those of merchant ships, such as containerships, CFD modeling settings for large merchant ships may not be applicable to NL fishing vessels. The numerical prediction of bare-hull resistance of a NL fishing vessel has been investigated by M. A. Ali, H. Peng and W. Qiu [3] using OpenFOAM.

It is ideal to simulate propeller-hull interactions using unsteady CFD solvers by considering the free surface effect, the actual geometry of the propeller, and induced ship motions, in which different time scales are required for ship hull and propeller. Since this approach is computationally expensive, less

time-consuming approaches have been developed for use in early design stage.

The most common approach for the prediction of propeller performance is the potential-flow method, which can predict the open-water thrust and torque of the propeller in an acceptable accuracy and with much less computing resources than CFD methods. The potential-flow based methods have been integrated into CFD solvers in various degrees to solve propeller-hull interactions. D. Rijpkema, B. Starke, and J. Bosschers [4] studied the propeller hull interaction by coupling the RANS method and the unsteady Boundary Element Method (BEM) in an iterative way. The effective wake distribution was obtained by using the induced velocities solved by BEM and the nominal wake distribution. S. Gaggero, D. Villa, and S. Brizzolara [5] employed BEM to study the unsteady performance of a propeller in an oblique flow. The comparison of solutions with RANS and BEM was presented for a highly skewed propeller. The RANS method led to greater accuracy.

The propeller can be further simplified as a body force in the simulation of propeller-hull interaction. For example, N. Y. Win, P-C. Wu, Y. Toda, E. Tokgoz, and F. Stern [6] used a simple body-force method, in which the propeller effect was modeled based on a quasi-steady blade element theory and using the total hull-induced velocity computed by CFD. The numerical results based on this coupled method were in a good agreement with the experimental data for a Series 60 hull. The same method was also applied to another ship, KRISO Very Large Crude Carrier (KVLCC2) [7]. B. Windn, S. R. Turnock and D. A. Hudson [8] adopted the blade element momentum theory for the propeller and coupled it with the RANS solver in OpenFOAM to simulate the self-propulsion tests of the KRISO Container Ship (KCS) model. A reasonable agreement between numerical results and experimental data was observed.

The present studies focus on numerical simulations of propeller-hull interactions of a NL fishing vessel. A simple body-force method was adopted to couple with the RANS solver in OpenFOAM. An unsteady solver was employed for the computation of the total resistance, sinkage and trim of the bare hull, and the results were compared with experimental data. The body-force propeller model was first validated using the propeller open-water data. The coupled solver was then applied to the self-propulsion simulations at various revolution rates of the propeller, and the required tow forces and the trims of the vessel were compared with the experimental data.

II. NUMERICAL METHOD

The governing equations for the two-phase incompressible, isothermal, immiscible, and viscous fluid flow are given as follows:

$$\begin{aligned} \frac{\partial(\rho U)}{\partial t} + \nabla \cdot (\rho U U) &= -\nabla p + \nabla \cdot (\mu \nabla U) + \rho g + F + F_b \\ \nabla \cdot U &= 0 \end{aligned} \quad (1)$$

where U is the velocity, p is the pressure, ρ is the density of the fluid, μ is the dynamic viscosity, g is the gravitational acceleration, F is the free surface tension, and F_b is the body force from a propeller model. The free surface tension can be expressed as follows:

$$F = \sigma \kappa(x) n \quad (2)$$

where n is the normal vector, κ is the curvature of the interface, and σ is a constant. The interface curvature κ is given by:

$$\kappa(x) = \nabla \cdot n \quad (3)$$

The interface between air and water is captured using the volume of fluid (VOF) method. The volume fractions of water and air are calculated using the following equation:

$$\frac{\partial \alpha}{\partial t} + \nabla \cdot (\alpha U) = 0 \quad (4)$$

where α is the volume fraction. $\alpha = 1$ represents the cell filled with water, $\alpha = 0$ represents the empty cell, and $0 < \alpha < 1$ represents the interface between air and water. In the numerical simulations, the High Resolution Interface Compression (HRIC) scheme was used to capture the free surface. For turbulence modeling, SST $k - \omega$ and SST $k - \omega$ turbulence models with curvature correction (SSTCC $k - \omega$) were used.

The first-order implicit Euler scheme was applied to discretize the time derivative term in momentum, turbulence, and VOF equations. The convective term in the momentum equations is discretized using Gauss's theorem. Values are interpolated from cell-centers to face-centers using the linear upwind scheme. Van Leer's Total Variation Diminishing (TVD) scheme was used to discretize the convective term in the VOF transport equation. Gauss's theorem with the central-differencing scheme was employed for the diffusion term. The VOF equation is solved using the semi-implicit method with sub-cycling to increase the time step size in numerical simulations. The PISO algorithm was used to couple the pressure and the velocities.

A. Propeller Modeling

In self-propulsion simulations, the effect of propeller was modeled using the proposed load distribution by G. R. Hough and D. E. Ordway [9]. The momentum due to the propeller action is added as the body force in the RANS solver. The body force varies in radial direction and its distribution approximately follows Goldstein's optimum distribution. The resultant total thrust and torque imposed on the fluid should be the same as the prescribed thrust and torque. E. G. Paterson, R. V. Wilson and F. Stern [10] coupled this method with RANS in CFDShip-IOWA. The non-dimensional body forces in the axial and tangential directions are calculated as follows:

$$f_{bx} = A_x r^* \sqrt{1 - r^*} \quad (5)$$

$$f_{b\theta} = A_\theta \frac{r^* \sqrt{1 - r^*}}{r^* (1 - r'_h) + r'_h} \quad (6)$$

where $r^* = \frac{r' - r'_h}{1 - r'_h}$, $r' = \frac{r}{R_P}$, $r'_h = \frac{R_H}{R_P}$, r is the radius of a propeller section, R_H is the radius of hub and R_P is the radius of propeller tip. Since the body forces must result in the prescribed thrust, T , and the torque, Q , the coefficients, A_x and A_θ , can be computed from:

$$A_x = \frac{C_T}{\Delta} \frac{105}{16(4 + 3r'_h)(1 - r'_h)} \quad (7)$$

$$A_\theta = \frac{K_Q}{\Delta J^2} \frac{105}{16(4 + 3r'_h)(1 - r'_h)} \quad (8)$$

$$C_T = \frac{T}{\frac{1}{2} \rho V_a^2 \pi R_P^2} = \frac{8K_T}{\pi J^2} \quad (9)$$

$$J = \frac{V_a}{nD} \quad (10)$$

where K_T is the thrust coefficient, K_Q is the torque coefficient, J is the advance coefficient, V_a is the average incoming velocity to the propeller disk, or the speed of advance, n is the rate of revolution, D is the propeller diameter, and Δ is the mean chord length projected into the xz plane.



Figure 1: Model geometry.

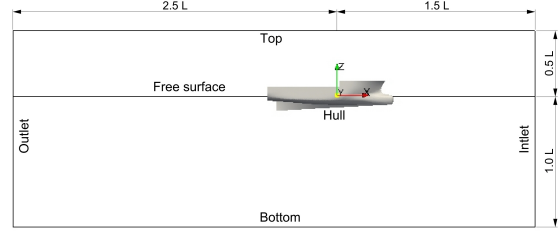


Figure 2: Computational domain.

B. Self-propulsion modeling

The self-propulsion point for a model can be obtained by the load varying method, the constant loading method, or the mixed loading method [11]. In this work, the load varying method was employed to find the model self-propulsion point. In load varying (constant speed) method, the model speed remains constant and the propeller load is changed by adjusting the revolution rate of the propeller. A set of numerical simulations were carried out for different propeller revolutions, and the thrust T , the torque Q , and the tow force F were calculated. The propeller revolution at the model self-propulsion point was then determined by interpolation of the tow force curve versus the propeller revolution. Note that the tow force is referred to the force on the tow post in physical model tests, which is determined from $F = R_T - T$, where R_T is the total resistance of the vessel including the propeller.

In the self-propulsion simulations, the ship model was free to heave and pitch, and other motions were restrained. At each time step, the centre of propeller disk and the axis of propeller rotation were updated based on the predicted position of the model.

III. SHIP GEOMETRY AND GRIDDING

A multi-species fishing vessel model with an optimized bulbous was used in the studies. The hull form of the fishing vessel is shown in Fig. 1. The vessel has a small length-beam ratio of 3.67. A.

TABLE 1. PRINCIPAL PARTICULARS OF THE SHIP MODEL AND THE PROPELLER

Parameters	Model	Units
Length, L	1.833	m
Breadth, B	0.499	m
L/B	3.67	
Draft, T	0.224	m
Wetted Surface Area, S_w	1.110	m^2
Volume of Displacement, ∇	0.072	m^3
LCG	0.878	m
VCG	0.259	m
Propeller Diameter, D	0.1205	m
P/D	1.27	
A_E/A_0	0.906	
Number of Blades, Z	4	

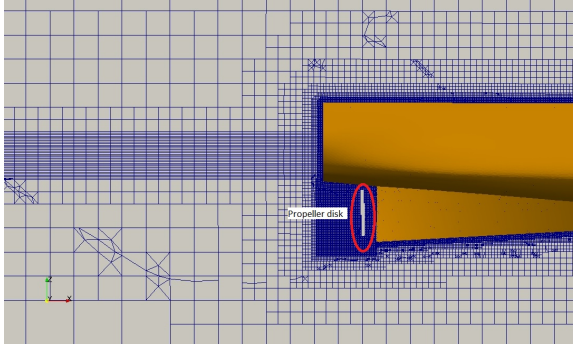


Figure 3: Grid distribution with propeller disk.

Gardner [12] carried out the self-propulsion model tests of the fishing vessel with a 4-bladed fixed pitch propeller using the load varying method. The propeller thrust, torque, and the tow force were measured in each test. The bare-hull resistance tests were carried out with free heave and pitch motions. The wake fraction and trust deduction factor were calculated. The principal particulars of the ship model and the NRC-IOT stock propeller #110R are given in Table 1.

The computational domain for CFD simulation is shown in Fig. 2. The origin, o , of the coordinate system, $oxyz$, was set at the intersection point of the calm water surface, the midship section, and the ship's centreplane. The positive oz points up vertically, and the positive ox points from the stern to the bow. In the computational domain, inlet and outlet boundaries are $1.5L$ and $2.5L$ from the midship section, respectively. The side boundaries are $1.0L$ from the centreplane. The bottom is $1.0L$ below the free surface, and the top boundary was placed $0.5L$ above the free surface. The symmetry boundary condition was imposed on

TABLE 2. COMPUTATIONAL GRIDS FOR SIMULATIONS

	h_i/h_1	$L/\Delta x$	Grid Numbers (million)
GRID-A	1.81	470	0.76
GRID-B	1.41	700	1.60
GRID-C	1.00	940	4.48

the centreplane to reduce the number of grids and computing time for bare-hull resistance simulations.

Grids were generated using blockMesh and navalSnappyHexMesh in OpenFOAM. Using the STL surface of the vessel model, isotropic grids were generated near the ship hull. To reduce the number of grids in the free surface region, anisotropic grids were generated. Fine grids were also generated in the propeller domain so that sufficient number of grids can be distributed inside the actuator disk region. Different grid refinement ratios were employed in the grid generation process because of difficulties in maintaining a constant grid refinement ratio using navalSnappyHexMesh.

For the grid dependency study, three meshes were used with $y^+ \approx 30 \sim 70$. The number of grids for bare-hull resistance computations are summarized in Table 2. In the table, h_i is the cell size which is calculated according to Eq. (11), h_1 is the size for the fine grid, and Δx is the cell size in the x direction. Figures 3 shows the grid distribution near to the stern with the propeller disk for GRID-C.

$$h = \left[\frac{1}{N} \sum_{i=1}^N (\Delta V_i) \right]^{\frac{1}{3}} \quad (11)$$

where ΔV_i is the volume of the i^{th} cell and N is the numbers of cells.

TABLE 3. COMPARISON OF $|E\%D|$ FOR C_T , SINKAGE AND TRIM AT $Fn = 0.34$

GRID	C_T	$ E\%D $	Sinkage (m)	$ E\%D $	Trim (deg)	$ E\%D $
GRID-A	0.0106	12.80	0.0143	6.26	0.5103	6.99
GRID-B	0.0104	10.70	0.0142	5.69	0.5194	5.34
GRID-C	0.0096	1.79	0.0137	1.82	0.5265	4.04
Exp	0.0094	-	0.0135	-	0.5487	-

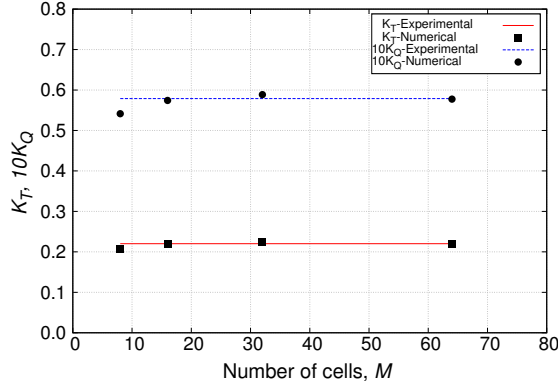


Figure 4: Convergence to the grid numbers along the radial direction of the propeller disk.

IV. VALIDATION STUDIES

A. Open-water simulations

The propeller open-water simulations were validated before the propeller model was coupled with the RANS solver. Grid dependence studies were first carried out to investigate the effect of the number of the grids along the radial direction of the propeller disk, M , on the predicted open-water performance. The predicted K_T and $10K_Q$ at the advance coefficient, $J = 0.30$, are presented and compared with experimental data in Fig. 4. It can be seen that the numerical prediction using $M=32$ leads to a good agreement with the experimental data.

The open-water characteristics of the propeller were then simulated using $M=32$ for $J = 0.10$ to 1.0 , and are compared with experimental data of the NRC-IOT stock propeller #110R in Fig. 5. The predictions with the present propeller model based on the body-force

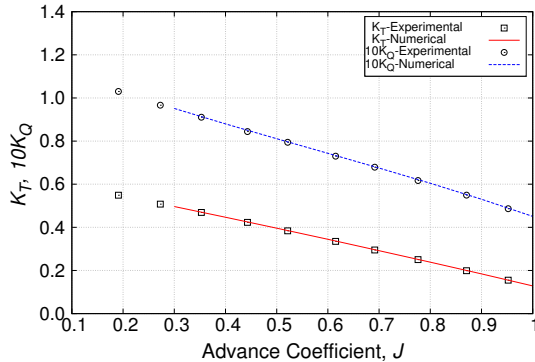


Figure 5: Comparison of open-water characteristics of the propeller.

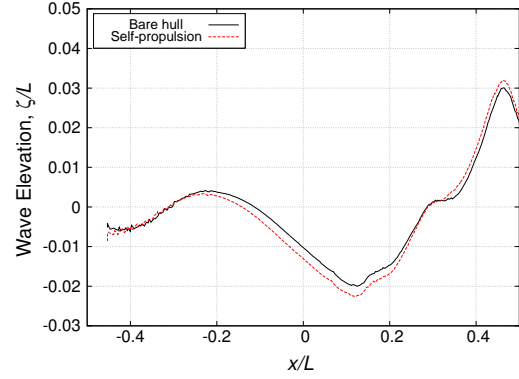


Figure 6: Comparison of wave elevation along the hull.

method are in good agreement with experimental data over a wide range of advance coefficient, J .

B. Bare-hull resistance simulation

The bare-hull resistance, sinkage, and trim were computed using the unsteady solver, *interDyMFoam* in OpenFOAM at the Froude number, $Fn = 0.34$. The predicted total resistance coefficient, sinkage, and trim with the three grids are compared with the experimental data in Table 3.

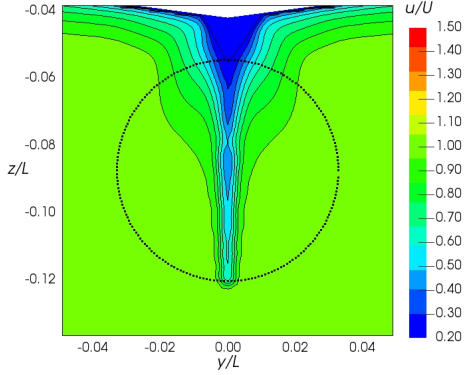
In the table, the relative error is defined as $|E\%D| = |(D - S) \times 100/D|$, where D is the experimental data and S is the numerical result. From the comparison, it can be seen that the relative errors of predicted total resistance, sinkage and trim are less than 5.0 % when GRID-C was used.

C. Wave elevations

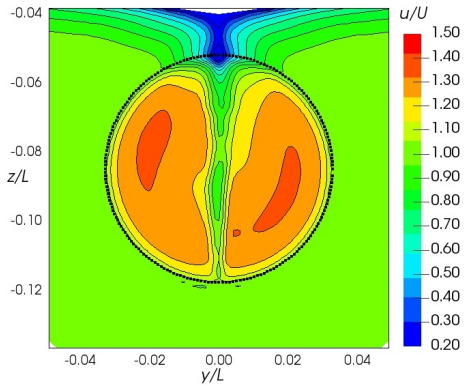
The non-dimensional wave elevations along the hull are compared in Fig. 6 for the bare hull and the self-propulsion case. The predicted wave elevation for the self-propulsion case is higher than that of the bare hull case near the bow and lower near the middle of the model. The difference in the wave elevations is due to different sinkage and trim for the bare hull and the self-propelled hull.

D. Velocities on propeller disk plane

The axial velocities with and without the presence of propeller were computed on the propeller plane using the unsteady solver and compared in Fig. 7 for $Fn = 0.34$. As shown in the figure, strong boundary layer effect due to the skeg is visible. In the case of the axial velocity with the propeller, the average



(a) Axial velocity contours on the propeller plane without propeller.



(b) Axial velocity contours on the propeller plane with propeller at $n = 15.92$ rps and $Fn = 0.34$.

Figure 7: Comparison of axial velocity contour on the propeller plane.

flow is accelerated due to the propeller action. The boundary layer effect due to the skeg is also shown in the distribution of axial velocities on the propeller

plane. The effect of rotational flow on the propeller plane can also be observed. Two strong vortices are seen in the axial velocity contours due to the propeller action.

E. Results of thrust, torque and tow force

In the self-propulsion simulations, the effect of turbulence model on the numerical solution was investigated using two turbulence models, SST $k - \omega$, and SSTCC $k - \omega$ for $Fn = 0.34$. The predicted tow force, F , thrust, T , torque, Q , propeller revolution rate, (n), and trim and sinkage of the model are presented in Table 4. The relative errors, $|E\%D|$, for F and trim, are calculated using the experimental data.

To determine the model self-propulsion point, additional three cases were simulated using different n 's with the SSTCC $k - \omega$ turbulence model. The numerical results are summarized in Table 5. The tow force, F , is plotted against n and compared with experimental data in Fig. 8. Although there is a constant difference between the numerical results and experimental data, the predictions follow a similar trend to that of experimental data. Note that n is 14.55 rps at the self-propulsion point in the experiment while n is 15.22 rps at the numerically obtained self-propulsion point. The relative error is less than 5% error.

F. Pressure distribution

The distribution of dynamic pressure coefficient C_p on the hull is compared in Fig. 9 for the bare hull and the hull with the propeller disk. The pressure at the end of skeg for the self-propulsion case is lower than that for the bare hull case due to the flow acceleration in front

TABLE 4. COMPARISON OF $|E\%D|$ FOR F , SINKAGE AND TRIM AT $Fn = 0.34$

	R_T (N)	T (N)	Q (N-m)	n (rps)	F (N)	$ E\%D $	Sinkage (m)	Trim (deg)	$ E\%D $
$k - \omega$ SST	14.6048	15.9	0.438	15.9218	-1.2952	61.99	-0.0156	0.2810	18.76
$k - \omega$ SSTCC	13.9295	15.9	0.438	15.9218	-1.9705	42.17	-0.0158	0.3324	3.90
Exp.		15.902	0.464	15.8255	-3.4071		-	0.3459	-

TABLE 5. SELF-PROPULSION SIMULATION RESULTS USING THE LOAD VARYING METHOD.

	Numerical			Experimental		
	n (rps)	F (N)	Trim (deg)	n (rps)	F (N)	Trim (deg)
CASE01	13.8751	3.4828	0.4318	13.7760	2.1189	0.4327
CASE02	14.7391	1.7897	0.3635	14.6566	-0.3246	0.4095
CASE03	15.4899	-0.2139	0.3200	15.3975	-2.4043	0.3431
CASE04	15.9218	-1.4624	0.2936	15.8255	-3.4072	0.3459

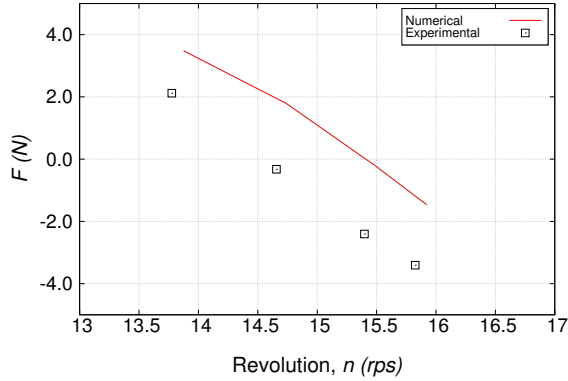


Figure 8: Comparison of tow forces.

of the propeller. However, the pressure distribution on the other part of the hull remains the same in the two cases. The predicted flow streamlines due to the propeller action are presented in Fig. 10.

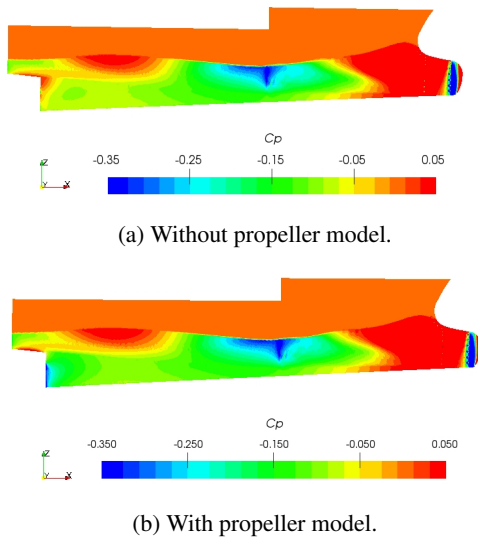


Figure 9: Comparison of pressure distribution on the hull.

V. CONCLUSIONS

The self-propulsion of an optimized fishing vessel model was studied using the unsteady RANS solver with a body-force model in OpenFOAM. The propeller model was validated against experimental data of propeller open-water performance before coupled with the RANS solver.

The total resistance coefficient, sinkage and trim of the vessel model without any appendages were compared

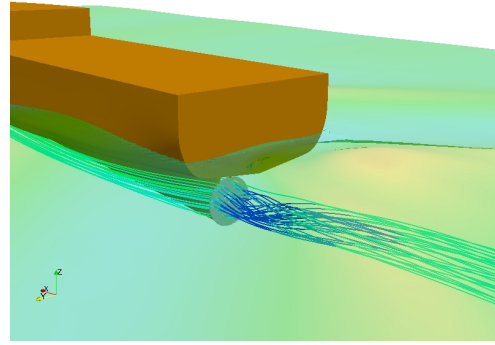


Figure 10: Streamlines around the propeller plane for $Fn = 0.34$.

with the available experimental data. The numerical predictions show less than 5.0% relative error in comparison with the experimental results.

The non-dimensional wave elevations along the ship model were also compared for the bare-hull and the self-propulsion conditions. Greater wave elevations are observed at the bow for the self-propulsion case.

The simulations of self-propulsion tests using the coupled solver led to promising results in terms of the tow force, the trim of the model and the propeller revolution rate at the model self-propulsion point.

ACKNOWLEDGEMENTS

This work was supported by the Natural Sciences and Engineering Research Council of Canada (NSERC).

REFERENCES

- [1] D. Friis, D. Bass, W. Qiu, C. Knapp, R. McGrath, S. Lane, and A. Gardner. "An overview of fishing vessel energy efficiency work in Newfoundland and Labrador, Canada". In International Symposium on Fishing Vessel Energy Efficiency, E-Fishing, 2010.
- [2] ITTC recommended procedures and guidelines, 1978. ITTC performance prediction method, 7.5 0203 01.4, 2017.
- [3] M. A. Ali, H. Peng, and W. Qiu. "Resistance computation of an optimized fishing vessel". In 26th Annual Conference of the Computational Fluid Dynamics Society of Canada, 2018.
- [4] D. Rijpkema, B. Starke, and J. Bosschers. "Numerical simulation of propeller-hull interaction and determination of the effective

wake field using a hybrid RANS-BEM approach". Third International Symposium on Marine Propulsors SMP'13, 2013.

- [5] S. Gaggero, D. Villa, and S. Brizzolara. "RANS and PANEL method for unsteady flow propeller analysis". *Journal of Hydrodynamics*, 22(5, Supplement 1):564 – 569, 2010.
- [6] Y. N. Win, E. Tokgoz, P-C. Wu, F. Stern, and Y. Toda. "Computation of propeller-hull interaction using simple body-force distribution model around series 60 $C_B = 0.6$ ". *Journal of the Japan Society of Naval Architects and Ocean Engineers*, 18:17–27, 2013.
- [7] Y. N. Win, P-C. Wu, K. Akamatsu, H. Okawa, F. Stern, and Y. Toda. "RANS simulation of KVLCC2 using simple body-force propeller model with rudder and without rudder". *Journal of the Japan Society of Naval Architects and Ocean Engineers*, 23:1–11, 2016.
- [8] B. Windén, S. R. Turnock, and D. A. Hudson. "Self propulsion modelling of the KCS container ship using an open source framework". In *17th Numerical towing tank symposium*, 2014.
- [9] G. R. Hough and D. E. Ordway. "The generalized actuator disk". Technical report, Therm Advanced Research, Inc, 1964.
- [10] E. G. Paterson, R. V. Wilson, and F. Stern. "General-purpose parallel unsteady RANS ship hydrodynamics code: CFDSHIP-Iowa". AD-A458092. Iowa Institute of Hydraulic Research, Iowa city, 2003.
- [11] ITTC recommended procedures and guidelines, 2008. ITTC testing and extrapolation methods propulsion, performance propulsion test, 7.5-02-03-01.1, 2008.
- [12] A. Gardner. "Evaluation of bulbous bows on an inshore fishing vessel". Master's thesis, Memorial University of Newfoundland, 2011.

Heat and Mass Transfer

NUMERICAL MODELING OF n-HEPTANE INJECTION AND COMBUSTION IN THE IGNITION QUALITY TESTER WITH ANSYS Forte

Osama Hmood

Department of Mechanical and Aerospace Engineering
Carleton University
Ottawa-Ontario, Canada
e-mail: osama.hmood@carleton.ca

Edgar Matida

Department of Mechanical and Aerospace Engineering
Carleton University
Ottawa-Ontario, Canada
e-mail: Edgar.Matida@carleton.ca

ABSTRACT

Three dimensional numerical modeling of n-heptane injection and combustion are conducted in a constant volume combustion chamber of the ignition quality tester (IQTTM), under different conditions of pressure (10, 15, and 21 bar) and temperature (530-590 °C). The IQTTM is normally used to measure diesel-fuel ratings (i.e., the derived Cetane number), through measurements of the time delay between the start of the fuel injection and auto-ignition. The computational fluid dynamics (CFD) code ANSYS Forte 18.2 is used to model the spray and manipulate the ignition of n-heptane. The features of the advanced adaptive time-step and mesh size for the ANSYS Forte allows for the most efficient solution. The temperature gradient is used to adapt mesh size in the solution field. The Reynolds-averaged Navier–Stokes equations (RANS) approach with the Renormalization group theory (RNG) k-ε model are used for momentum and turbulence in the field of solution. The linearized instability sheet atomization (LISA) model is used to express the fuel transition from injector flow to a fully atomization hollow-cone spray. The measured characteristics of fuel spray (e.g., injection pressure, spray cone-angle, profile of injected mass, and injection duration) are fed into the CFD model. Three reduced-skeletal mechanisms (29 species and 52 reactions, 35 species and 72 reactions, and 159 species and 770 reactions) are used to represent n-heptane chemistry (combustion). The predicted ignition delay (ID) from the three mechanisms are compared with the experimental data showing relatively good agreement.

A New Framework for the Prediction of Radiative Phenomena

William Morin and James McDonald
Department of Mechanical Engineering, U. of Ottawa,
161 Louis Pasteur, Ottawa, Ontario, Canada, K1N 6N5
wmori104@uottawa.ca

Radiation plays an important role in many engineering systems. It is an especially important mode of heat transfer in situations involving combustion. Accurate numerical modelling of combustion remains very challenging for practical applications. Accurate modelling of radiative transfer is also important in many practical applications, such as medical imaging, cancer treatment, nuclear-power generation. Unfortunately, accurate and affordable models for such problems remain elusive [1]. Methods based on the direct tracking of particles are accurate, however, they are prohibitively expensive for many practical problems. More affordable field-based methods exist, but they all suffer from modelling artifacts that can be considered serious. The discrete-ordinates method simplifies the situation by only allowing particles to travel in pre-defined directions. This introduces an artificial asymmetry to the model. Other methods, based on moment closures of the radiative-transfer equation, offer field equations for statistical properties of a distribution function that describes particle velocities. Unfortunately, the most popular form of these closures, based on spherical harmonics, does not guarantee positivity of the solution. It predicts negative numbers of particles and negative energies in some locations. The goal of this project is to further develop and evaluate a new modelling technique that combines the strengths of both the discrete-ordinates and moment-closure methods, without the weaknesses of either.

We have proposed a new Eulerian model for radiative transfer prediction [2]. This model produces field equations, like a moment-based approach. The solutions are therefore far easier to compute, as compared to particle-based methods. The idea is based on a special averaging procedure that we have developed, which is applied to a discrete-ordinates method. The results are an efficient modelling technique that connects the classical spherical harmonics and discrete ordinates models. For isotropic radiation, the spherical harmonics model is recovered exactly. The model then transitions smoothly to cases of pure photon beams, where it recovers a discrete ordinates model. The resulting model maintains positivity of solutions, like the discrete ordinates model, as well as rotational symmetry, like the moment models. Thus, this new model has the strengths of both classical models without the weaknesses.

This presentation builds on the the previous simple computational model and extends it to higher-order statistics of photon motion. A family of models is shown, each being appropriate for varying levels of radiative non-equilibrium. The hyperbolic nature of the models is investigated and the criteria for the preservation of positive densities is demonstrated. An efficient strategy for the implementation of the new velocity-space averaging procedure is shown. The models are implemented within an existing Godunov-type numerical framework for the solution of hyperbolic balance laws. Model refinement is used to locally select the appropriate member of the model hierarchy based on the local state, thus improving the solution accuracy and efficiency. Results are demonstrated for several classical problems in radiative transfer with comparisons to other classical models.

[1] K. Garrett and C. D. Hauck. A Comparison of Moment Closures for Linear Kinetic Transport Equations: The Line Source Benchmark Transport Theory and Statistical Physics, pages 203–235, 2013.

[2] W. Morin and C. J. McDonald. A New Moment Model for Radiative Transport Prediction 25th, Annual Conference of the CFD Society of Canada, 2017.

SURROGATE MODEL FOR PREDICTING REAL-TIME AIRFLOW AND TEMPERATURE DISTRIBUTIONS IN DATA CENTERS

Sahar Asgari, Peiying J. Tsai, Ishwar K. Puri
Dept. of Mechanical Engineering
McMaster University
Hamilton, Ontario, Canada

Rong Zheng
Dept. of Computing and Software
McMaster University
Hamilton, Ontario, Canada

ABSTRACT

Thermal management is an important process during data center (DC) operation. A large modern DC may host thousands of servers that produce significant heat, which must be removed adequately so that DC electronic components function properly.

A major challenge is to effectively manage cooling units to ensure that all servers have acceptable inlet air temperatures while minimizing energy usage and cost. Cooling units are usually controlled by measuring air temperatures using sparsely placed sensors in the DC space. To avoid potential hot spots that are not detected by these sensors, cooling units operate with a safety margin and consequently incur energy costs. Although thermal mapping enables accurate detection of hot spots that can be predicted by Computation Fluid Dynamics (CFD) simulations, accurate simulations are very challenging when conducted in real-time due to the scale and complexity of DCs and the airflows in them.

Here, a thermal model based on a three-dimensional grey box zonal model approach is proposed to reproduce airflow behavior and temperature distribution by dividing the space into several zones in which the mass, energy, and state equations are solved.

We perform CFD simulations for four configurations, namely for in-row, in-rack, raised-floor and top-heat exchanger DCs. To validate these simulation results, experiments are performed in a raised-floor and an in-row cooling unit DC. The simulation results are used thereafter to train the thermal model with machine learning, which reveals various relevant parameters that must be used to extend the applicability of the model for a variety of conditions. The model reproduces the airflow and temperature distributions for the configurations mentioned above, enabling accurate and fast predictions of server inlet and outlet temperatures.

CFD MODELLING OF FLOW AND HEAT TRANSFER IN A THERMOSYPHON

Dwaipayan Sarkar
Dept. of Mechanical & Materials
Engineering
Western University,
London, Canada

Christopher DeGroot
Dept. of Mechanical & Materials
Engineering
Western University
London, Canada

Eric Savory
Dept. of Mechanical & Materials
Engineering
Western University
London, Canada

ABSTRACT

The present work attempts to simulate the evaporation and condensation phenomenon in a two-phase closed thermosyphon and analyze its thermal performance. The volume of fluid (VOF) method in ANSYS FLUENT (Release 18.2) was adopted with two different modelling strategies to model the interaction between the interface responsible for the heat transport mechanism. Whilst the user-defined functions (UDF) have been a more popular choice among the computational fluid dynamics (CFD) practitioners to simulate the phase change process inside a thermosyphon [1,2], incorporation of the Lee model in newer FLUENT versions made it possible to model the mass and energy transfers without any use of external code. Although, UDF functions have shown to predict the heat and mass transfers quite reliably, large relative error exists between the reported experimental and CFD temperature profiles of the heat pipe [2]. As such, the Lee model has not been tested extensively [3] in similar computational scenarios to establish its appropriateness over the UDF functions. The present study aims at comparing the two different evaporation-condensation model in terms of its flow field and temperature profiles and suggest the most optimised model among those. Relative comparisons with the existing experimental results will be made in order to validate the proposed model.

A 2D planar numerical model is being used in the current study to simulate mass and energy transfer within a thermosyphon. The thermosyphon walls are modelled as copper with its length being 0.5m. The evaporator, condenser section is 0.2m in length, while the adiabatic section has a length of 0.1m. The diameter of the thermosyphon is 0.0202m. The geometrical anatomy of the thermosyphon is consistent with the works of Fadhl et al. [2] to draw direct comparisons. Quadrilateral structured grid cells were used to mesh the entire domain with slightly finer mesh at the evaporator and the condenser boundaries. The thermal boundary conditions include constant heat flux at the evaporator boundary and convective heat transfer coefficient at the condenser boundary. All other boundaries are defined as adiabatic walls with zero heat flux. The momentum boundary condition involves no slip walls. A schematic figure of a working thermosyphon with the appropriate boundary conditions is shown in figure 1 for better understanding. Result will be presented to visualize the flow and thermal fields within the thermosyphon for different operating conditions, and comparisons will be made between the different evaporation and condensation models.

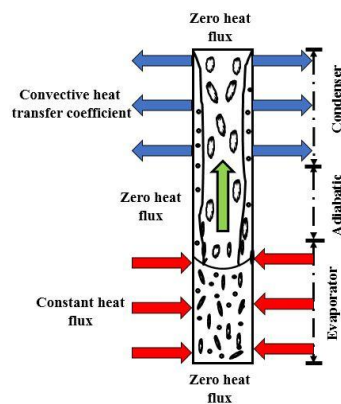


Fig. 1 Schematic of the thermosyphon along with the boundary conditions

REFERENCES

- [1] Lin, Z., Wang, S., Shirakashi, R. and Zhang, L.W., 2013. Simulation of a miniature oscillating heat pipe in bottom heating mode using CFD with unsteady modeling. *International Journal of Heat and Mass Transfer*, 57(2), pp.642-656.
- [2] Fadhl, B., Wrobel, L.C. and Jouhara, H., 2013. Numerical modelling of the temperature distribution in a two-phase closed thermosyphon. *Applied Thermal Engineering*, 60(1-2), pp.122-131.
- [3] Bouhal, T., Agrouaz, Y., Kousksou, T., El Rhafiki, T. and Zeraouli, Y., 2018. Performance optimization of a two-phase closed thermosyphon through cfd numerical simulations. *Applied Thermal Engineering*, 128, pp.551-563.

A NUMERICAL EVALUATION OF NANOFUID MULTIPHASE FLOWS FOR DIFFERENT MICRO-HEAT EXCHANGER GEOMETRIES

Daniel Bahamon
Engineering School
Universidad Pontificia Bolivariana
Medellín, Colombia

César Nieto-Londoño
Engineering School
Universidad Pontificia Bolivariana
Medellín, Colombia

Abstract— This work presents a numerical study of laminar flows through different microheat exchanger's geometries. The investigation concerns the evaluation of thermal effects and hydrodynamics characteristics by varying the Reynolds number and the particle concentration of the $\text{Al}_2\text{O}_3/\text{H}_2\text{O}$ nanofluid. The conservation equations of mass, momentum, energy, and particles concentration were solved using the commercial software ANSYS FLUENT. The performance includes the evaluation of the suggested geometries in terms of pressure drop, temperature profiles, flow rate, and heat transfer coefficient. The geometry resulting from this study reduces the pressure drop and enhances the heat transferred for the given conditions respect to the other geometries used in similar applications. Furthermore, the geometry introduced presents some additional advantage regarding its application to different areas, such as microelectronic cooling, micromixing, and reactions at microscale, among others.

Micro-channel Heat Exchanger; Nanofluid Flow; Heat Transfer Enhancement

I. INTRODUCTION

Continues search of methods and technological advances that mitigate the environmental impact and global warming has been a concern for both industrials and researchers. Nowadays, though a variety of alternatives are known for reducing the carbon footprint, the growing global energy consumption and the following inefficient heat exchanger systems -used primarily in the industry-, continues increasing their contribution to the greenhouse gas emission [1-2]. That is why any improvement achieved in the performance of these systems allows a reduction in energy consumption and therefore, a decrease of the emissions associated with is operation.

Heat exchangers play a fundamental role in the conservation, conversion, and recuperation of energy. The advances in the miniaturization of technology and the need for increasing efficiency of micro-scale devices such as microchannel heat exchangers, micro-reactors, among others, have proven to be beneficial and advantageous over conventional equipment size [3]. Micro-channel heat exchangers, also known as micro-heat exchangers (μHEX), have found application in highly specialized areas such as microelectronics cooling, in the

aerospace, biomedical processes, metrology, robotics, telecommunications, and automotive industries, among others [4-5]. As microheat exchangers have become more advanced and sophisticated, two significant limitations have been identified: (1) a high-pressure drop accompanies the reduction in the dimensions of the channels; and, (2) the fluid properties limit the amount of heat transferred.

Firstly, the heat transfer rate depends on the fluid-solid interaction at the channel's surface. As the channel reduce its size, the heat transfer coefficient tends to grow. Secondly, nanofluids improves heat transfer by modifying thermal transport properties. A nanofluid is a base or carrier fluid (usually water, oil and ethylene glycol) containing nanoparticles in suspension with an average diameter below 100 nm [6]. The main advantage of nanofluids refers to the modification of the thermophysical properties respect to the base fluid due to the addition of metal or metal-oxide particles that usually increase the coefficients of thermal conduction and convection [7-8]. The main characteristic of nanofluids is its ability to enhance heat transfer without altering the fluid's Newtonian behavior due to the addition of small concentrations of solid particles [9-10]. In fact, for a level of CuO nanoparticle up to 2% mass fraction it was found that the heat transfer coefficient obtains its maximum value and for values above 5%, the heat transfer coefficient decreased 7.94% concerning baseline [11]

The use of nanofluids to improving the properties of a base fluid is not a new idea: Maxwell, back in 1873, had proposed to use metal particles for increasing the thermal conductivity of the fluids; however, numerous trails with micrometric sized particles in liquids showed several problems such as sedimentation, accumulation, and obstruction of ducts, and high pressure drops [12]. The development of nanotechnology has opened the opportunity to use nano-sized particles that lack or delay the appearance of most of these problems. Moreover, since Jang and Choi [13] reported that adding small amounts of nanoparticles to traditional heat transfer liquids (in concentrations below 1% in volume) increase more than 50% the thermal conductivity of the fluid [14-15].

The application of μHEX is significant, but the number of studies reported in the literature related to these devices using this specific technology is limited, and even more for numerical simulations whose primary goal is to evaluate the interactions

between fluid and particles [16-17], which in part motivates this work. A summary of critical findings concerning these new applications and technologies can be found in review works like those prepared by [18], and [19], where it can be observed great inconsistency in the reported results in the literature. The following are the main conclusions of those studies: In [18], they reviewed the characteristics of fluid flow in microfluidics systems and concluded that most of the experimental results reported in the literature for pressure drops and friction factors are inconsistent and contradictory. They inferred from the review that the primary reasons for inconsistencies may be: (1) experimental uncertainty in measuring the dimensions of the channel and flows, (2) the difference in surface roughness, and, (3) effects and phenomena not considered (i.e., the Joule effect heating, viscous dissipation, among others). On the other hand, in [19] is a review of the work done on the flow characteristics and heat transfer in microheat exchangers using conventional fluids and nanofluids. They generally found that the amount of research on this regard is relatively new and limited, most of the studies report improvements in heat transfer capabilities, despite that some results challenge the traditional macro-scale theories and limitations on devices and fluids.

This work focuses on a numerical study conducted for single and two-phase flows in microchannel heat exchangers (used as a heat sink) of rectangular cross-section area, where the fluid dynamic characteristics and heat transfer effects were considered, by varying the Reynolds number and the concentration of nanoparticles in the fluid. Pressure drop and temperature profiles, rate, and heat transfer coefficient are used to assess the performance of the devices and realize a comparative analysis between the different geometries evaluated.

This paper is organized as follows. Firstly, is presented the governing equations used to predict the flow and heat transfer of nanofluids in microchannels. The next section depicts the simulation conditions as well the geometries evaluated, boundary conditions applied and numerical approach. Then, is discussed the obtained results considering that the geometries assessed under different operational conditions. The last section details some conclusions.

II. MATHEMATICAL MODELS

The mathematical model describing the physical phenomena taking place in a microheat exchanger includes the conservation equations of mass (continuity), momentum (Navier-Stokes) and energy. For incompressible 3-D steady-state viscous flow, the continuity equation can be expressed as:

$$\nabla \cdot (\rho \vec{u}) = 0. \quad (1)$$

Meanwhile, the momentum equation is given as:

$$\nabla \cdot (\rho \vec{u} \vec{u}) = -\nabla p + \rho \vec{g} + \nabla \cdot \bar{\tau} + \vec{F}, \quad (2)$$

where ρ is the fluid density, \vec{u} the velocity vector, p is the pressure, $\rho \vec{g}$ the gravitational force and \vec{F} includes other external forces that act over the system. The Reynolds stress tensor, $\bar{\tau}$ is given as:

$$\bar{\tau} = \mu[\nabla \vec{u} + \nabla \vec{u}^T] - \frac{2}{3} \nabla \cdot \vec{u} I, \quad (3)$$

being μ the viscosity, and the second term on the right side representing the volume dilatation effect.

The energy equation can be expressed as:

$$\begin{aligned} & \nabla \cdot (\vec{u}(\rho E + p)) \\ &= \nabla \cdot \left(k_{eff} \nabla T - \sum_j h_j \vec{J}_j + (\tau_{eff} \cdot \vec{u}) \right). \end{aligned} \quad (4)$$

where k_{eff} is the effective conductivity, h the enthalpy and \vec{J}_j is the diffusive flux of the specie j . The three terms on the right side correspond to the energy transferred by conduction, species diffusion and viscous dissipation, respectively. E , that is the total energy, is defined as:

$$E = h - \frac{p}{\rho} + \frac{u^2}{2}. \quad (5)$$

These governing equations, together with the boundary conditions given below, were solved using the commercial CFD software ANSYS FLUENT, that employs the finite volume method to achieve its solution.

III. SIMULATION CONDITIONS

The flow was laminar, and the conditions defined to guarantee no phase change of the fluid inside the μ HEX. The channel walls were assumed adiabatic, except the bottom wall, where the device will absorb the heat that is required to dissipate to the environment (a constant heat flux was defined at the bottom wall). Two different approaches (i.e., homogeneous and coupled flow), were considered to study the presences of the nanoparticles in the flow. In the following subsection, the property models, boundary conditions, geometry, and numerical approach are presented in detail.

A. Property models

The nanofluids flow simulations were developed considering the following aspects: (1) regarding homogeneous flow (no-coupled) and (2) coupled flow between the fluid and the particles. For the first one -that ignores effects of the poor distribution of particles in the fluid, accumulation, sedimentation, etc.-, the thermophysical properties of the nanofluids were evaluated by the following equations [20-21].

- Density:

$$\rho_{nf} = (1 - \varphi) \cdot \rho_{bf} + \varphi \cdot \rho_p. \quad (6)$$

- Heat capacity:

$$(\rho \cdot C_p)_{nf} = (1 - \varphi) \cdot (\rho \cdot C_p)_{bf} + \varphi \cdot (\rho \cdot C_p)_p. \quad (7)$$

- Thermal conductivity:

$$k_{nf} = \frac{(k_p + 2 \cdot k_{bf} + 2 \cdot (k_p - k_{bf}) \cdot \varphi)}{(k_p + 2 \cdot k_{bf} - (k_p - k_{bf}) \cdot \varphi)} \cdot k_{bf}. \quad (8)$$

- Viscosity:

$$\mu_{nf} = \mu_{bf}(1 + 2.5\varphi), \quad (9)$$

TABLE I. COEFFICIENTS OF THE THERMOPHYSICAL PROPERTIES OF THE BASE FLUID (LIQUID WATER)

Property	Thermodynamic properties parameters		
	A_i	B_i	C_i
ρ (kg/m ³)	786.83	1.6862	-3.2903E-3
C_p (kJ/kg.K)	4033.033	0.508	---
k (w/m.K)	-0.3838	0.005254	-6.369E-6
μ (Kg/m.s)	0.01574	-8.307E-5	1.118E-7

a. Property = $A_i + B_i.T + C_i.T^2$

In equations (6)-(9), φ is the particle concentration in the solution (or volume fraction) and the sub-indexes nf , bf and p are referred to nanofluid, base fluid and particles, respectively. The initial properties of the base fluid (pure water) were determined by polynomial correlations of temperature, whose coefficients are presented in Table I.

For the coupled simulation in two-phases, the particles were simulated using the Lagrangian approach (discrete phase model in FLUENT), this study concerns only dilute flow. That means that the model considers the interaction between particles and the base fluid, but the interaction between particles was neglected. The momentum equation of a particle within the Lagrangian approach is given as:

$$\frac{d\vec{u}_p}{dt} = F_D(\vec{u}_{bf} - \vec{u}_p) + \frac{g \cdot (\rho_p - \rho_{bf})}{\rho_p}, \quad (10)$$

and the drag force of the particles, F_D , for the laminar flow, is obtained by:

$$F_D = \frac{18 \cdot \mu \cdot C_D}{\rho_p \cdot d_p^2} \cdot \frac{Re_p}{24}, \quad (11)$$

Re_p is the particle Reynolds number, given as,

$$Re_p = \frac{\rho \cdot d_p \cdot |u_p - u|}{\mu}. \quad (12)$$

The drag coefficient, C_D in equation (11), is a function of the relative Reynolds number and can be obtained from:

$$C_D = \alpha_1 + \frac{\alpha_2}{Re_p} + \frac{\alpha_3}{Re_p^2}, \quad (13)$$

where α_1 , α_2 and α_3 are constants defined for smooth spherical particles over several ranges of Re_p .

B. Geometries

Figure 1 shows the micro-heat exchanger's designs evaluated. The starting aim of this study was to find a geometry which allows reducing considerably the pressure drop in the device (used in this case as a heat sink) but maintaining the same dimensions on the structure. After an exhaustive review of different geometries used in the literature, a design proposed as a microchannel reactor for gas-phase partial oxidation of toluene [22] was considered (Figure 1 (a)) as the starting point aiming to the improvement in the residence time of the fluid inside the

device. The dimensions of the plate for each of the designs evaluated were 70x70 mm, with square channels of 1 mm width.

This first geometry variation G2-RECT (see Figure 1 (b)), and from this, several modifications were performed to reduce the pressure drop in the device, obtaining geometries G3-TRIANG (Figure 1 (c)) and G4-HEX (Figure 1 (d)). Meanwhile, the designs G1-INI (Figure 1 (a)) and G5-GROOVES (Figure 1 (e)) were evaluated to compare the new geometries with the most common shapes employed in the literature [23]

C. Boundary conditions

Several flow conditions were defined for the velocity and temperature at the inlet section of each geometry as follows: Reynolds ranges from 2 to 250 and temperatures from 300 to 350 K. The boundary conditions defined for the temperature and the velocity of the fluid (according to the Reynolds numbers) at the entrance of the device, the ambient pressure at the outlet and no-slip condition along the solid-fluid interfaces of the μ HEX. Also, a constant wall heat flux at the bottom wall was established to be 1000 W/m².

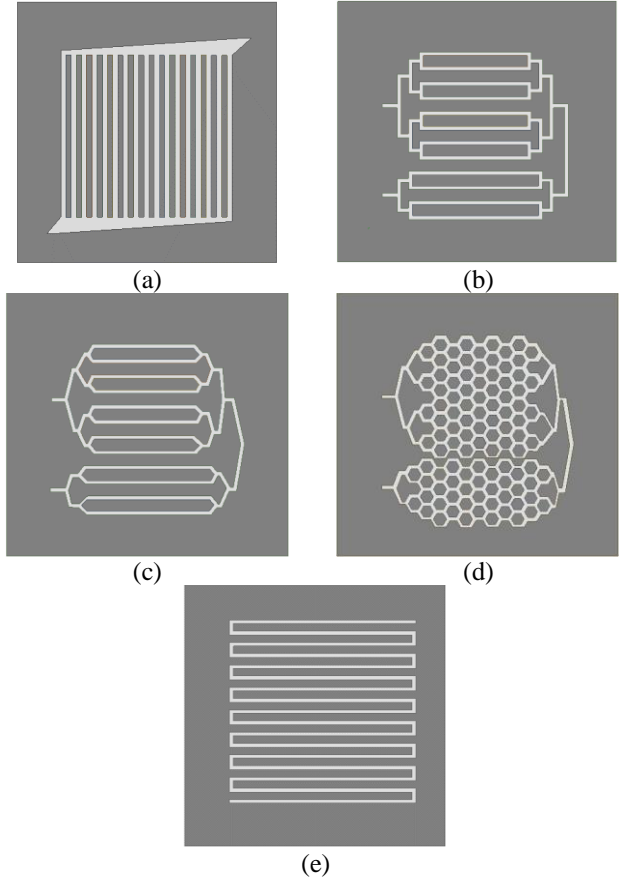


Figure 1. Geometries evaluated in the present study: (a) G1-INI, (b) G2-RECT, (c) G3-TRIANG, (d) G4-HEX, (e) G5-GROOVES. Square channels width: 1mm. Plate dimensions: 70x70 mm.

For the two-phase modeling, Al₂O₃ nanoparticles were used as the solid phase, with water as a base fluid. Particles concentration of 0%, 1%, 2%, and 5% were considered during simulations, and the μ HEX geometries assessment is evaluated in terms of Reynolds number variation. The two phases, solids,

and fluid entered the channel at the inlet boundary with the same uniform axial velocity that was specified according to the Reynolds number.

D. Numerical approach

The equations were numerically solved using the commercial CFD code ANSYS FLUENT. The SIMPLE (Semi-Implicit Method for Pressure-Linked Equations) algorithm links the pressure-velocity equations. It was also set a convergence criterion of 10^{-5} in the Euclidean norm for each simulation, and a first-order scheme was used to interpolate the variables along the control volume surface. By a preliminary evaluation of the effect of mesh refinement, a node grid within 150,000 to 160,000 hexahedral elements was selected for each geometry to ensure a reasonable prediction of the pressure, velocity and temperature profiles inside the devices.

IV. RESULTS AND DISCUSSION

The results for the simulations, both single and two-phase flows, are shown in the following sections. The numerical scheme was assessed by comparing results for the average Nusselt number for pure water flow to corresponding available data in the literature, allowing us to check the accuracy of the results. Then, results for the different approaches, configurations and operational condition are presented to establish the effect of them in the μ HEX performance.

A. Nusselt validation

The average Nusselt number, Nu , was determined for a square channel and compared to the analytical value reported in the literature. For laminar flow into a rectangular cross-sectional area, the Nusselt number is constant and its value depends on whether the heat transferred or the temperature at the wall are constants. In this case, the study evaluates the heat transfer for one wall under constant heat flux, where the Nusselt number has a value of 3.61 [24].

The calculated Nusselt was defined based on the temperature difference between the microchannel wall and the nanofluid mean temperature [25], as:

$$Nu = \frac{h \cdot D_h}{k} = \frac{\dot{q}'' \cdot D_h}{k \cdot (T_{wall} - T_{mean})} \quad (14)$$

where T_{mean} can take the following three values:

- $T_{ref} = 283$ K.
- T_c : is the temperature in the middle (centerline) of the channel.
- T_b : is the bulk temperature, defined as:

$$T_b = \frac{\sum_i u_i \cdot T_i \cdot b_i}{u_{AV} \cdot B}, \quad (15)$$

being u_i the velocity in the center of the control volume (CV), b_i the height of the CV, T_i the temperature in the CV, u_{AV} the average velocity and B the height of the channel.

Figure 2 shows the behavior of the Nusselt number along with the square channel (dimensions: 1 mm wide and 200 mm long). The best approach occurs when the mean temperature is equal to

T_b . From this, the results for Nu in the following sections will consider that $T_{mean} = T_b$. For a more detailed discussion upon the implications that brings either temperature used, or the error incurred refer to [25].

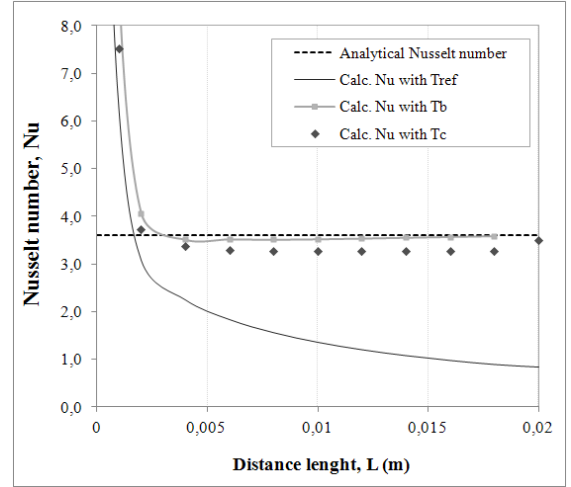


Figure 2. Nusselt number validation using different approaches for the mean temperature of the fluid.

B. Single phase flow

Figure 3 shows the pressure drop through the different geometries evaluated, at different Reynolds numbers at the entrance of the device (maintaining a laminar regime). As can see in Figure 3, the highest values of pressure drop correspond the Geometry G5 (geometry widely found in literature, especially for reactions at micro-scale); this was an expected result due to the number of bends and fluid flow change direction within the device. For the geometry used, the fluid's volume remains constant in a single channel generating higher frictional losses.

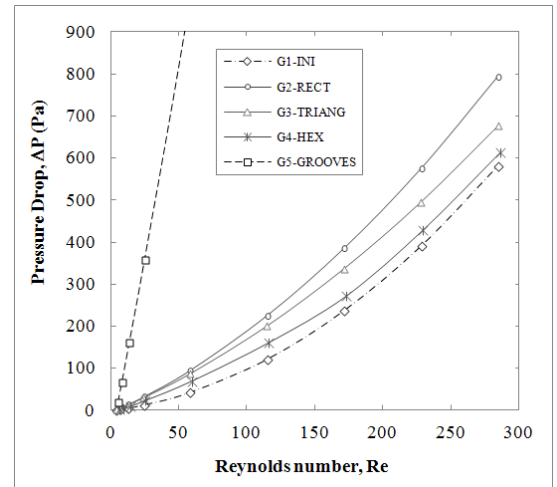


Figure 3. Evolution of pressure drop (ΔP) with the inlet Reynolds number, in the different geometries evaluated (pure water as the base fluid, $\dot{q}'' = 1000$ W/m², $T_{inlet} = 300$ K).

Results for the other geometries show similar pressure drops ranges, being lower the values found for the G1-INI. Something to highlight is the behavior of the proposed geometry, G4-HEX,

which presents a slight increase in the pressure drop concerning G1-INI, a difference that tends to reduce as the Reynolds number increases.

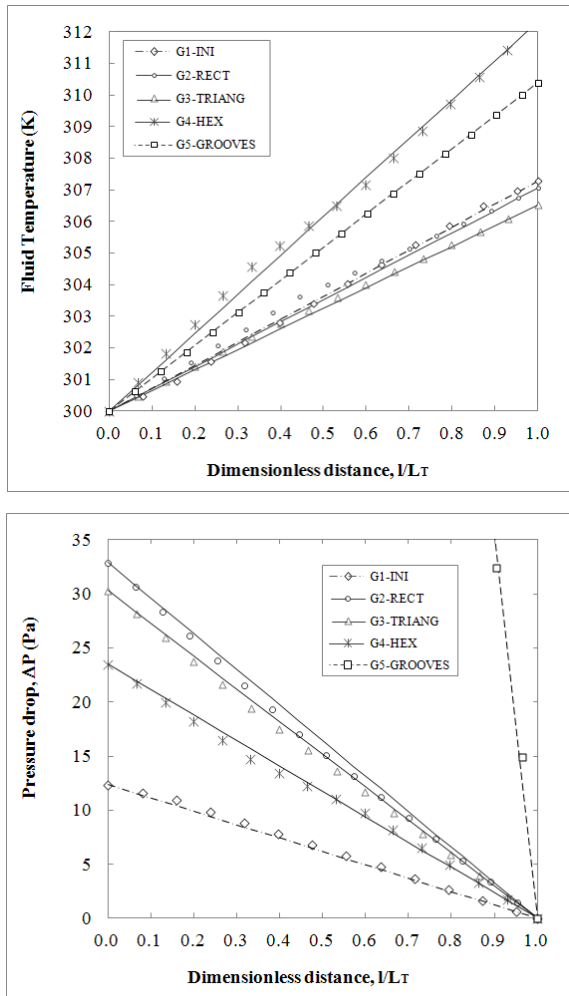


Figure 4. Temperature (above) and pressure (below) profiles along the different geometries, (pure water as the base fluid, $\dot{q}'' = 1000 \text{ W/m}^2$, $T_{inlet} = 300 \text{ K}$, $Re = 25$).

Figure 4 shows the pressure and temperature profiles along the mean distance traveled by the fluid inside the micro-device, where can be observed that the fluid in geometry G1-INI do not have enough residence time to achieve a proper heat transfer. Besides, it does not contain different zones in the device which allows performing several processes within, i.e., a reaction zone.

On the other hand, Figure 5 shows the performance in terms of the heat transferred per unit area against the pressure drop per unit length for the different μHEX considered in the present study. It can be concluded from the results, that geometry G4-HEX presents an enhancement of the heat transferred, mainly due to the extended use of the heat transfer. This geometry shows some other advantages, but in construction and operation terms, as the hexagon forms present a strong resilience to deformation -in nature these geometries are widely used for structures formation: i.e., honeycomb, carbon nanotubes and even in graphene structures [26]-.

C. Two-phase flows

In this section, only results for geometries G2-RECT and G4-HEX are presented, mainly due to the latter showed the most likely behavior during the single-phase analysis. The G2-RECT was used as reference geometry in order to report improvements in the G4-HEX design.

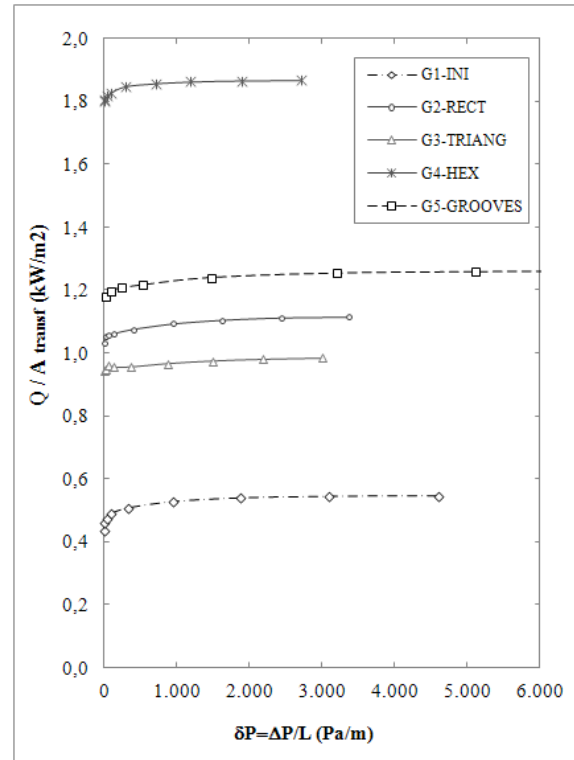


Figure 5. Comparative evaluation of the heat transferred per unit area against the pressure drop per unit length, for the different geometries evaluated.

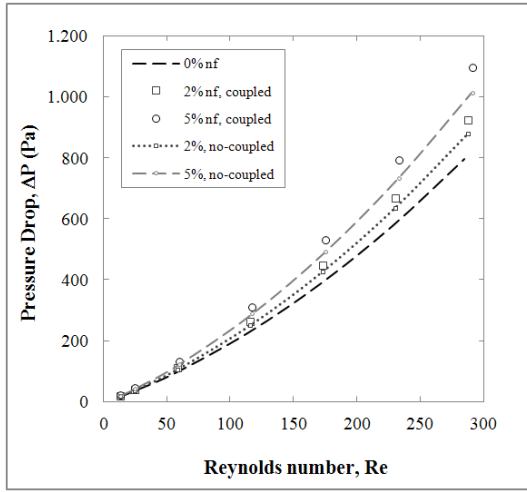
Regarding the behavior of the nanofluids in the selected geometries, Figure 6 shows the pressure drop variation with the inlet Reynolds number under different nanoparticles concentrations, for both geometries selected. In Figure 6, dotted lines correspond to values calculated with the homogeneous model, while continuous lines are for results using the coupled model. Meanwhile, Figure 7 shows a comparative study of the performance within these two devices (like those presented in Figure 5), but in this case including the enhancement achieved by the inclusion of nanoparticles. In general, for both designs, it is observed that for the same velocity flow, the heat transferred with a $\text{Al}_2\text{O}_3/\text{H}_2\text{O}$ nanofluid with a particle concentration of $\phi = 5\%$ inside the G4-HEX geometry, is up to 1.85 times higher of those achieved with the G2-RECT geometry using pure water. Furthermore, the pressure drop is only 1.10 times higher in the G2-RECT design. Additionally, the heat transfer enhancement due only to the change in geometry is up to 1.7 times with even a slight decrease in pressure drop, indicating that the contributions of the nanoparticles are about 10% in the dissipated energy and 35% in the pressure). Also, that enhancement increases non-linearly with the increase in nanoparticles volume showing the main pressures drop differences compared to the pure water when higher concentrations of nanofluids are considered. It is important to

observe that the coupled modeling approach shows higher heat transfer enhancement in comparison with homogeneous results, but also greater pressure drops, which is consistent with the previous studies reported in the literature [16,27].

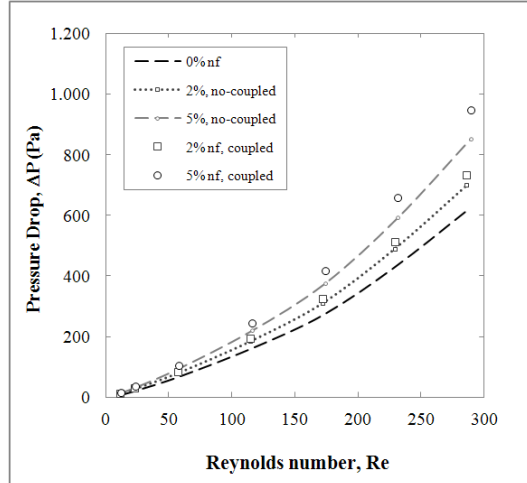
D. Nusselt correlation

Finally, using the results obtained with the coupled two-phase model, and having checked the calculation and behavior of the Reynolds number, two correlations were determined for the heat transfer phenomenon inside the devices -one for each geometry- considering the volume fraction of particles in the fluid. The form of the equation was adopted by the work presented in [28], which showed the best adjustment to experimental studies of Al_2O_3/H_2O nanofluid flows in laminar regime inside microchannels heat sinks, under constant heat flux at the bottom wall; the equation employed is:

$$Nu = \beta_1(1 + \beta_2\phi^{\beta_3})Re^{\beta_4}Pr^{\beta_5}. \quad (16)$$



(a)



(b)

Figure 6. Re vs ΔP for different concentrations of nanoparticles in the nanofluid flow: (a) G2-RECT, (b) G4-HEX.

Table II list the results of the correlation for Nusselt in G2-RECT and G4-HEX, and Figure 8 shows the fitted correlation

obtained for the Nusselt number over the rectangular and hexagonal geometries. The fitted lines present in Figure 8, show a good agreement of the data with a correlation coefficient, r^2 , greater than 0.98 in each case.

TABLE II. NUSSOLT EQUATION'S COEFFICIENT FOR GEOMETRIES EVALUATED.

Geometry	Nusselt number correlation's parameters				
	β_1	β_2	β_3	β_4	β_5
G2-RECT	50.9606	3.3689	0.8106	0.1245	0.6411
G4-HEX	16.6958	16.6581	0.1473	0.1216	0.7951

From the results in Figure 8, is also possible to conclude, the use of a 5% volume concentration of Al_2O_3 represent an enhancement of 14% and 19% in the Nusselt number for geometries G2-RECT and G4-HEX, respectively. It is worth to mention that these correlations are only valid for laminar flows ($5 < Re < 300$) and nanofluid concentrations below 5%.

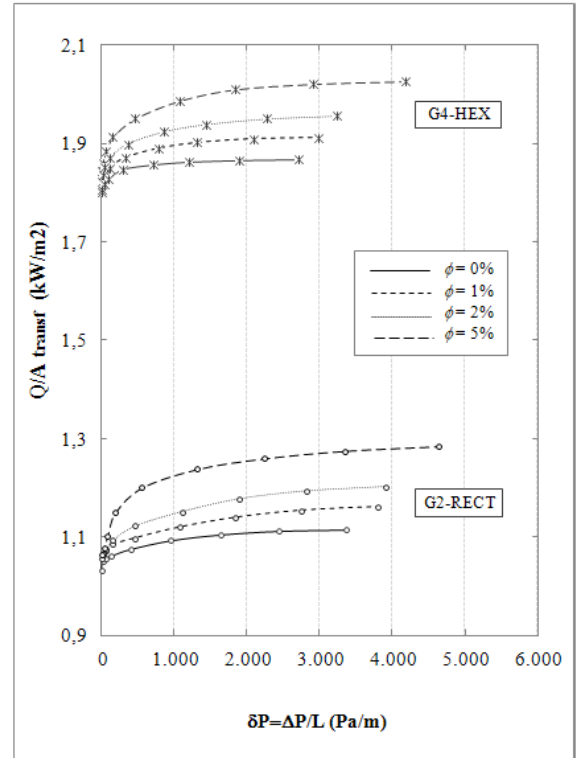


Figure 7. Comparative evaluation of the enhancement in heat transferred per unit area against the pressure drop per unit length, using nanofluids inside the geometries G2-RECT and G4-HEX.

V. CONCLUSIONS

A numerical study was performed with single and two-phase flows (in the laminar regime) for different geometries of micro-heat exchangers, where the heat transfer characteristics and the hydrodynamic parameters were evaluated and reported. The effects of using nanofluids with different volume fractions were evaluated in order to enhance the heat transferred.

A novelty geometry was obtained which allows reducing the pressure drop in the microdevice, while enhancing the heat transfer rate and the residence time respect to the original geometry and the usual devices found in the literature. Furthermore, it can be concluded that the design of the geometries for these types of applications still play a more important role than the fluid to be used, as improvements in operating conditions are not so evident in the second condition.

In addition, a Nusselt number correlations were defined for the most promising geometry (G4-HEX) and the initial design (G2-RECT). It should be noted that this equation is not the most accurate available and does not have a wide range of applicability yet.

However, it is an essential approximation in order to simplify the required calculations for these devices: is easy to use, and provide interesting results for the geometries evaluated. Several studies in this regard are necessary, as the extrapolation to turbulent flows, and the addition of different particle diameters in the nanofluid.

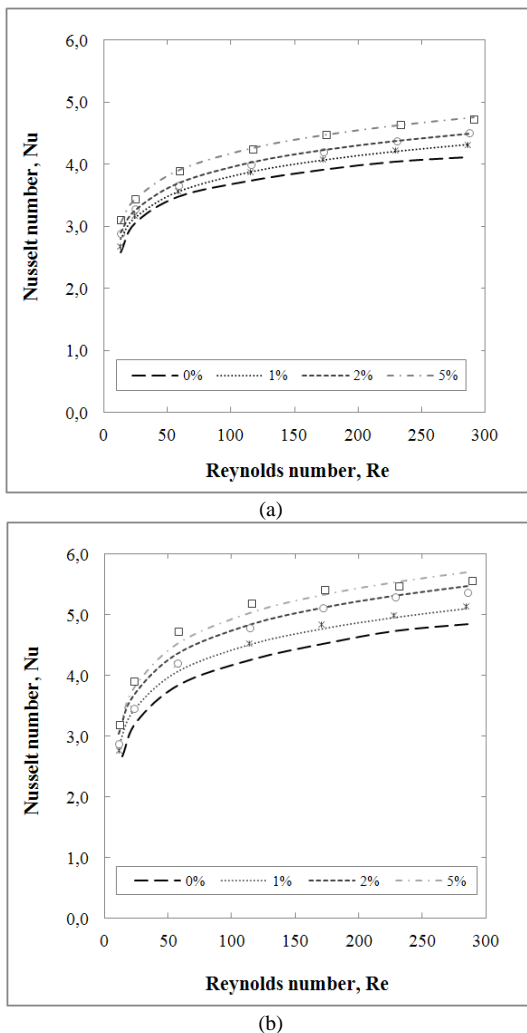


Figure 8. Nusselt correlation adjustment for (a) G2-RECT geometry, (b) G4-HEX geometry (dotted lines: fitted curves using the correlations).

Future work based on this study includes experimental evaluations in order to validate the obtained results and the

correlations proposed, and also take advantage of this new geometry in other applications such as micro-mixers, micro-reactors (using packed bed catalyst).

ACKNOWLEDGMENT

The authors want to express their gratitude to the Energy and Thermodynamic Research Group of the Universidad Pontificia Bolivariana in Colombia, for supporting the accomplishment of this research.

REFERENCES

- [1] Godson, L., Raja, B., Lal, D. M. and Wongwises, S. (2010). Enhancement of heat transfer using nanofluids - An overview. *Renew. Sust. Energ. Rev.*, 14, 629 – 641.
- [2] Hetsroni, G., Mosyak, A., Pogrebnyak, E. and Yarin, L. (2005). Fluid flow in microchannels. *Int. J. Heat Mass Transfer*, 48, 1982 – 1998.
- [3] Tuckerman, D. and Pease, R. (1981). High-Performance heat sinking for VLSI. *IEEE Electron Dev. Lett. EDL-2*, 5, 126–129.
- [4] Eastman, J. A., Phillpot, S. R., Choi, S. U. S. and Keblinski, P. (2004). Thermal transport in nanofluids. *Annu. Rev. Mater. Res.*, 34, 219-246.
- [5] Kakaç, S. and Pramuanjaroenkij, A. (2009). Review of Convective Heat Transfer Enhancement with Nanofluids. *Int. J. Heat Mass Transfer*, 52(13-14), 3187-3196.
- [6] Choi, S. U. S. (1995). Enhancing thermal conductivity of fluids with nanoparticle. *ASME Congress and Exposition*. November 12-17, San Francisco, CA.
- [7] Saidur, R., Leong, K. and Mohammad, H., A review on applications and challenges of nanofluids, *Renewable and Sustainable Energy Reviews*, 15, pp. 1646-1668, 2011. DOI: 10.1016/j.rser.2010.11.035.
- [8] Wong, K.V. and De León, O., Applications of nanofluids: current and future. *Advances in Mechanical Engineering*, 2010. DOI: 10.1155/2010/519659.
- [9] Kamyar, A., Saidur, R. and Hasanuzzaman, M. Application of Computational Fluid Dynamics (CFD) for nanofluids, *International Journal of Heat and Mass Transfer*, 55, pp. 4104-4115, 2012. DOI: 10.1016/j.ijheatmasstransfer.2012.03.052.
- [10] Hernández, D., Nieto-Londoño, C. and Zapata-Benabithé, Z. Analysis of working nanofluids for a refrigeration system, *DYNA* 83 (196), 2015, pp. 176-183. DOI: <http://dx.doi.org/10.15446/dyna.v83n196.50897>
- [11] Baqeri, S., Akhavan-Behabadi, M.A. and Ghadimi, B., Experimental investigation of the forced convective boiling heat transfer of R-600a/oil/nanoparticle, *International Communications in Heat and Mass Transfer*, 55, 2014, pp. 71–76.
- [12] Li, J. and Kleinstreuer, C. (2008). Thermal performance of nanofluid flow in microchannels. *Int. J. Heat Fluid Flow*, 29, 1221 – 1232.
- [13] Jang, S. P. and Choi, S. U. S. (2006). Cooling performance of a microchannel heat sink with nanofluids. *Appl. Therm. Eng.*, 26, 2457 – 2463.
- [14] Saidur, R.; Leong, K. and Mohammad, H. (2011). A review on applications and challenges of nanofluids. *Renew. Sust. Energ. Rev.*, 15, 1646 – 1668.
- [15] Singh, P. K., Harikrishna, P. V., Sundararajan, T. and Das, S. K. (2012). Experimental and numerical investigation into the hydrodynamics of nanofluids in microchannels. *Exp. Therm. Fluid Sci.* (article in press).
- [16] Kalteh, M., Abbassi, A., Saffar-Avval, M. and Harting, J. (2011). Eulerian-Eulerian two-phase numerical simulation of nanofluid laminar forced convection in a microchannel. *Int. J. Heat Fluid Flow*, 32, 107 – 116.
- [17] Wang, X. and Mujumdar, A. (2008). A review on nanofluids-part 1: theoretical and numerical investigations. *Braz. J. Chem. Eng.* 25(4), 613–630.
- [18] Bayraktar, T. and Pidugu, S. (2006). Review: characterization of liquid flows in microfluidic systems. *Int. J. Heat Mass Transfer*, 49, 815–824.

- [19] Mohammed, H., Gunnasegaran, P. and Shuaib, N. (2010). Heat transfer in rectangular microchannels heat sink using nanofluids. *Int. Commun. Heat Mass*, 37, 1496 – 1503.
- [20] Pantzali, M., Mouza, A. and Paras, S. (2009). Investigating the efficacy of nanofluids as coolants in plate exchangers (PHE). *Chem. Eng. Sci.*, 64, 3290 – 3300.
- [21] Leong, K. Y., Saidur, R., Khairulmaini, M., Michael, Z. and Kamyar, A. (2012). Heat transfer and entropy analysis of three different types of heat exchangers operated with nanofluids. *Int. Commun. Heat Mass*, 39, 838 – 843.
- [22] Tu, S., Yu, X., Luan, W. and Lowe, H. (2010). Development of micro chemical, biological and thermal systems in China: a review. *Chem. Eng. J.*, 163, 165-179
- [23] Mohammed, H., Bhaskaran, G., Shuaib, N. and Abu-Mulaweh, H., R (2011). Influence of nanofluids on parallel flow square microchannel heat exchanger performance. *Int. Commun. Heat Mass*, 38, 1 – 9.
- [24] Ebdian, M. A. and Dong, Z. F. (2006). Forced convection, internal flow in ducts (chapter 5). *Handbook of Heat Transfer*. Ed. Rohsenow W. M., Harnett J. P., Cho Y. I., McGraw Hill
- [25] Neale, A., Derome, D., Blocken, B. and Carmeliet, J. (2007). Determination of surface convective heat transfer coefficients by CFD. 11th Canadian Conference on Building Science and Technology. Banff, Alberta.
- [26] Terrones, M., Botello-Méndez, A. R., Campos-Delgado, J., López-Urías, F., Vega-Cantú, Y. I., Rodríguez-Macías, F. J., Elías, A. L., Muñoz-Sandoval, E., Cano-Márquez, A. G., Charlier, J. and Terrones, H. (2010). Graphene and graphite nanoribbons: morphology, properties, synthesis, defects and applications. *Nano Today*, 5, 351-372.
- [27] Kamyar, A., Saidur, R. and Hasanuzzaman, M. (2012). Application of Computational Fluid Dynamics (CFD) for nanofluids. *Int. J. Heat Mass Transfer*, 55, 4104 – 4115.
- [28] Valencia, G., Ramos, M. and Bula, A. (2007). Experimental evaluation of the convective heat transfer coefficients in a nanofluid-cooled milli channels heat sink. *Proceedings of IMECE2007. ASME International Mechanical Engineering Congress and Exposition. Nov 11-15 (Seattle, Washington, USA).*

OPTIMAL CONFIGURATION OF ANGLED RIB TURBULATORS FOR CONJUGATE HEAT TRANSFER SIMULATION

Ramin Jalali, Masoud Darbandi and
Ashkan Bagherzadeh
Department of Aerospace Engineering
Sharif University of Technology

Gerry E. Schneider
Department of Mechanical Engineering
University of Waterloo
Waterloo, Canada

Abstract—Increasing the turbine inlet temperature plays an important role to increase the efficiency of the gas turbine engine. Using the SAS flow causes a reduction in turbine efficiency, thus optimal design of the internal cooling system of the turbine blade could help to increase this efficiency. Computational Fluid Dynamics has become the main tool for the flow and heat transfer phenomena in gas turbine design. In order to couple the hot gas path and coolant flow inside the blade, Conjugate Heat Transfer analysis has become a key part of CFD. The validation of the simulation is done by comparing the results with the experimental data of Hylton on NASA C3X vane. Calculated results agree well with analytical and experimental data. Moreover, In the present study, an optimal design for enhancement of heat transfer and thermal performance for the cooling channels of NASA C3X with square section rib turbulators is investigated to find the most suitable rib geometry. Among various design parameters, two design variables, rib angle ($30 \leq \alpha \leq 90$) and the rib pitch to-height ratio ($6 \leq p/e \leq 18$), were chosen. Approximations for design of the best rib turbulators were obtained using the advanced Response Surface Method (RSM) with functional variables. The second-order response surfaces (or correlations) within the ranges of two design variables were completed by this method. The optimum design point with the highest Nusselt number ratio appears at $\alpha = 59.38$ and $p/e = 6.1$ and the highest thermal performance is at $\alpha = 59.38$ and $p/e = 6.24$. Also the effect of rib turbulators on the NASA C3X vane surface temperature is investigated. The results show that, the average effects of temperature reduction in leading edge, mid chord and trailing edge are 7.1%, 4.3% and 6.8% respectively.

Keywords—CFD; Conjugate Heat Transfer; Cooling Channel; Rib Turbulators; NASA C3x; RSM, ANOVA, DOE

I. INTRODUCTION

The main goal of gas turbine development is to increase its thermodynamics efficiency, where the most significant factor is turbine inlet temperature. Therefore, effective turbine blade and vane cooling strategies are needed. There are some efforts on using high temperature metal alloys, thermal barrier coatings and secondary air system (SAS) cooling flow. Using the SAS flow causes a reduction in turbine efficiency, thus

optimal design of the internal cooling system of the turbine blade could help to increase this efficiency. In the preliminary stage of turbine design, the simulation of this system is very important at various design and off-design points. Computational Fluid Dynamics has become the main tool for the flow and heat transfer phenomena in gas turbine design. In order to couple the hot gas path and coolant flow inside the blade, Conjugate Heat Transfer analysis has become a key part of CFD. but the complex internal cooling system and the complex 3D flow physics make the simulations time consuming.

There have been research efforts in applying the conjugate heat transfer methodology to simulate gas turbine blade heat transfer. Most of the researches on the conjugate heat transfer methodology are on the modelling C3X and MarkII vanes because there are existing experimental data for validation [1-4]. Although 3D numerical simulations of vanes or blades with more complex cooling passages are time consuming, there are some studies [5, 6] that used 3D solver and CHT method to calculate the temperature distribution of vanes and blades with more complex internal cooling passages.

Various cooling schemes, e.g. internal cooling passage, film cooling and impingement cooling have been employed to protect blade from exceeding the maximum allowable temperature. Among these cooling methods, the internal cooling passages play an important role because of the minimal loss in the cooling flow. Generally, these passages are roughened by rib turbulators which increase turbulent intensity, induce reattachment flow, create swirling flow and break boundary layer. These conditions cause a significant increase in cooling passages heat transfer. Moreover, using angled rib turbulators make an impingement effect of the induced swirling flow which enhance the heat transfer in cooling passages.

Numerous researches have been done on the angled rib turbulators in stationary cooling channels. Cho [7] presented that the high heat transfer and thermal performance take place at 60° and 45° of angle of attack respectively. Moreover, Rau [9] and Cho [7] investigated various geometrical factors such as rib height (e), rib angle of attack (α), rib shape and rib arrangement to find the effects of swirling flow on heat transfer and pressure drop characteristics in a stationary duct. In the other works, Kim [9, 10] investigated the channel rotation with

angled rib turbulators. Most of the previous studies have dealt with heat transfer characteristics in angled ribbed channels with a ratio of rib-to-rib pitch to rib height (p/e) ratio higher than 8.0, Liu [11] showed that the heat transfer is high at short p/e . However, at some short rib-to-rib pitch, heat transfer could become lower than that at long rib-to-rib pitch. Therefore, finding out the rib-to-rib pitches with the highest heat transfer and thermal performance is important for optimal rib design. Furthermore, since the rib angle of attack affects the actual rib-to-rib pitch, the combined effects of the rib angle of attack and rib-to-rib pitch should be studied. Kim [12, 13] used the general response surface method for optimizing the shape of the ribbed channels. They found that this method was suitable to choose the best rib geometry for heat transfer enhancement. However, they obtained an optimal shape at rib-to-rib pitches longer than 10.0 using the general method, which has limitations such as the narrow design variable ranges and low physical response. Due to these limitations, the obtained optimum results had discrepancy from the previous experimental results reported by many researchers.

Therefore, the objective of this study is to determine the rib-to-rib pitch and angle of attack that cause a maximum heat transfer and thermal performance using an advanced response method based on the functional design variables with wide design variable ranges compared to the general response surface method. For analysis of heat transfer and friction loss, we conducted numerical conjugate heat transfer simulation (CFD). From the output results, we obtained the second-order correlations with functional design variables and so rib configuration with maximum heat transfer and maximum thermal performance.

II. ADVANCE RESPONSE SURFACE METHOD

In statistics, response surface methodology (RSM) explores the relationships between several explanatory variables and one or more response variables. The response surface of two variables is expressed as in (1):

$$y = C_1x_1^2 + C_2x_2^2 + C_3x_1x_2 + C_4x_1 + C_5x_2 + C_6 \quad (1)$$

In general, the equations are used for the response surface based on approximation. These equations search for the local optimum within the region of interest as reported by Myers [14]. However, the general response surface method is weak in complex functions and has low physical response and selection of design variable ranges. In the other hands, the line resulted from the thermal characteristic of each variable is not to be expressed as a second-order parabola. Giunta [15] and Kim [16] proposed an advanced method which is based on functional variables with physical and thermal characteristics of the design variables to solve these problems. The advanced procedure of the response surface method includes thermal characteristics of the design variables followed by changing each variable, x_i , in (1) into especially functional design variable, $f(x_i)$, as in (2):

$$y = C_1f(x_1)^2 + C_2f(x_2)^2 + C_3f(x_1)f(x_2) + C_4f(x_1) + C_5f(x_2) + C_6 \quad (2)$$

Where $f(x_i)$ subjects to e.g. $\sin(x_i)$, $\log(x_i)$, $\exp(x_i)$, etc. Also, $f(x_i)$ is determined through processes of understanding

thermal characteristics. In the present study, the advanced RSM was used to obtain an optimal configuration of angled ribbed channel. Unknown coefficients (C_i) of a second-order response surface polynomial have been determined by the least squares method. The set of design points was selected by the D-optimal method as suggested by Mitchell [17]. When the observed response values are predicted accurately by the response surface model from the results of ANOVA, Myers [14] and Giunta [15] suggested that the typical values of R^2_{adj} are in the range from 0.9 to 1.0. R^2_{adj} is an adjusted R^2 value in order to account for the degrees of freedom. The multiple determination coefficient (R^2) calculates the proportion of the variation in the response surface around the mean.

A. Design variables and objective functions

In a angled channel with parallel rib arrangement, there are five parameters which are channel diameter (D), rib height (e), rib width (w), rib-to-rib pitch (p) and rib angle of attack (α). Among these parameters, the angled rib-induced the swirling flow and the rib induced reattachment flow greatly affect the heat transfer enhancement. Therefore, we selected two design variables, rib angle of attack (α) and rib-to-rib pitch (p). The pitch is converted to a dimensionless variable, a ratio of rib-to-rib pitch-to-rib height (p/e). The design ranges are presented in Table 1. Also D is according to the Table 2 of NASA C3X [20] cooling channels. Also e/D is 0.048.

TABLE I. DESIGN VARIABLES AND RANGES

Design Variables	Lower bound	Upper bound
α ($^\circ$)	30	90
p/e	6	18

The geometry of the circular channel with rib turbulators of $\alpha = 60^\circ$ and $p/e=6$ is shown in Fig (1.a-1.c).

(a)

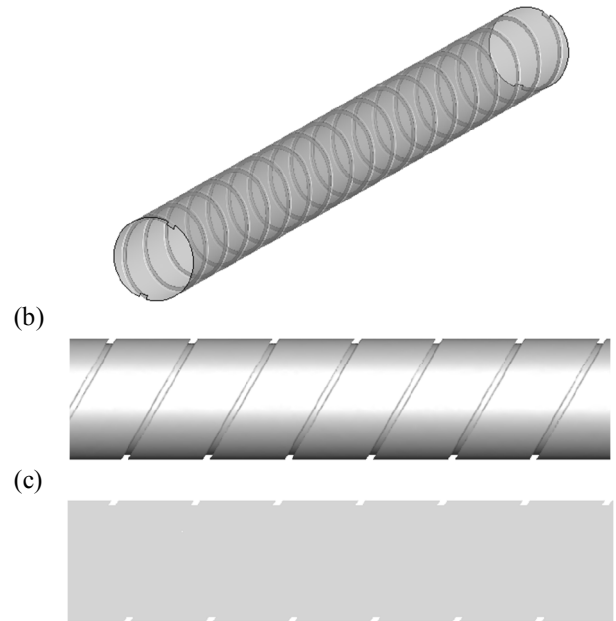


Figure 1. The geometry of the circular channel with rib turbulators of $\alpha = 60^\circ$ and $p/e=6$

The objective function of heat transfer and thermal performance is defined as maximization of the following objective functions:

$$OF_{Nusselt} = \frac{\overline{Nu}}{Nu_0} \quad (3)$$

$$OF_{TP} = \frac{\overline{Nu}/Nu_0}{(f/f_0)^{1/3}} \quad (4)$$

where \overline{Nu} is the averaged Nusselt number; and $Nu=0.023Re^{0.8}Pr^{0.4}$ obtained by Dittus and Boelter [18]. The friction factor, f is calculated with the average pressure drop and f_0 represents the friction factor from the Ka'arma'n-Nikuradse equation proposed by Petukhov [19] is employed as $f_0 = 2(2.236 \ln Re - 4.639)^{-2}$.

III. CFD VALIDATION

In order to validate the CFD results, experimental study of Hylton [20] on NASA C3X vane is chosen as the test case. Cooling channels numbers, diameters and mass flow rates are as Table 2 and Fig 2. The flow conditions were assumed from run 158 of Hylton [20]. The pressure inlet and pressure outlet boundary conditions were assumed for the inlet and outlet of hot gas flow field by specifying the total pressure and temperature at inlet and static pressure at outlet. All the boundary conditions are shown in Fig 3.

TABLE II. COOLING CHANNELS DIAMETER AND MASS FLOW RATE

Channel Number	Channel Diameter (cm)	Mass Flow Rate (g/s)
1	0.630	16.7
2	0.630	17.4
3	0.630	14.8
4	0.630	16.5
5	0.630	17.5
6	0.630	16.5
7	0.630	16.1
8	0.310	5.5
9	0.310	3.49
10	0.198	1.71

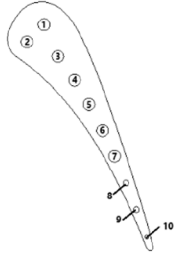


Figure 2. Cooling channels numbering

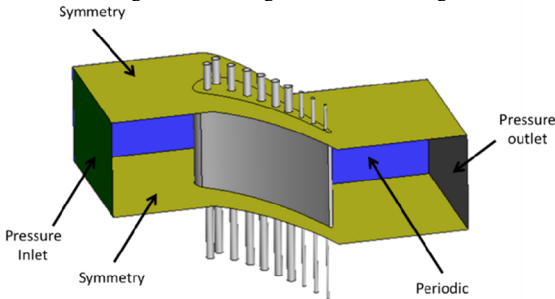


Figure 3. Boundary condition of the hot gas flow field

Fig 4. Shows the comparison of static pressure distribution between current CFD results and experiments (run #158 of Hylton [20]). As it can be seen in this figure, there is a good agreement on the pressure side. On the suction side little difference is visible where a small supersonic region occurs.

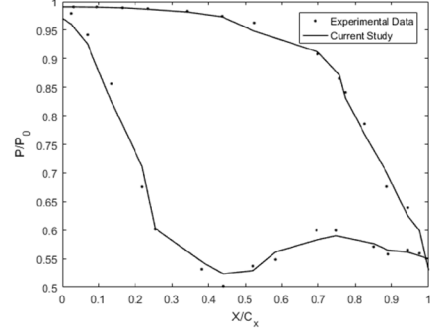


Figure 4. Static pressure distribution on the blade

IV. RESULTS AND DISCUSSION

A. Results of Advance Response Surface Method

In the optimization, the result functions are of a second-order response surface which has six unknown coefficients at two design variables as presented in (1). The thermal characteristics of two design variables show distributions of logarithmic function. To estimate the unknown polynomial coefficients, D-optimal method [17] and a design of experiments, 20 data points are selected. Also, the polynomial coefficients (C_i) are estimated by a least squares method. Therefore, the Nusselt ratios, friction ratios and the thermal performance are induced as (5), (6) and (7) respectively.

$$\begin{aligned} \overline{Nu}/Nu_0 = & 22.6 - 10.7 \log(\alpha) - 14.4 \log(p/e) \\ & + 8.67 \log(\alpha) \log(p/e) - 4.7 [\log(\alpha)]^2 \\ & - 7.32 [\log(p/e)]^2 \end{aligned} \quad (5)$$

$$R^2 = 97.9\% \quad R^2_{adj} = 96.1\%$$

$$\begin{aligned} f/f_0 = & 64.1 - 26.7 \log(\alpha) - 29.9 \log(p/e) \\ & + 15.4 \log(\alpha) \log(p/e) + 4.8 [\log(\alpha)]^2 \\ & - 5.2 [\log(p/e)]^2 \end{aligned} \quad (6)$$

$$R^2 = 97.3\% \quad R^2_{adj} = 95.8\%$$

$$\begin{aligned} \text{Thermal Performance} = & 17.4 - 13.1 \log(\alpha) \\ & - 6.16 \log(p/e) + 3.4 \log(\alpha) \log(p/e) + 2.25 [\log(\alpha)]^2 \\ & - 2.12 [\log(p/e)]^2 \end{aligned} \quad (7)$$

$$R^2 = 98.1\% \quad R^2_{adj} = 96.6\%$$

Fig. 5, 6 and 7 depict the contour maps of averaged Nusselt number ratios, friction factor ratios and thermal performance for rib angle of attack and rib-to-rib pitch in respectively. The contour plot of the response surface was easily able to show the combined effects of two design variables in an angled ribbed channel. Nu ratios higher than 2.4 appear in ranges of $57 \leq \alpha \leq 62$ and $6 \leq p/e \leq 7.2$. The optimum design point with the highest Nusselt number ratio appears at $\alpha = 59.38$ and $p/e = 6.1$ and the highest thermal performance is at $\alpha = 59.38$ and $p/e = 6.24$.

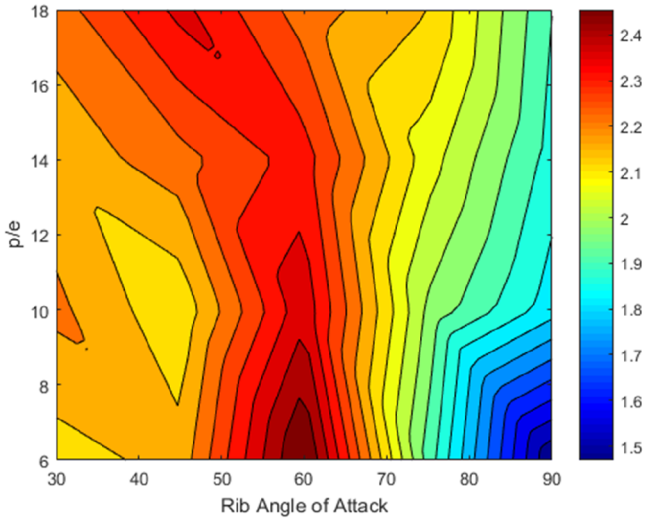


Figure 5. Result map of averaged Nusselt number ratio

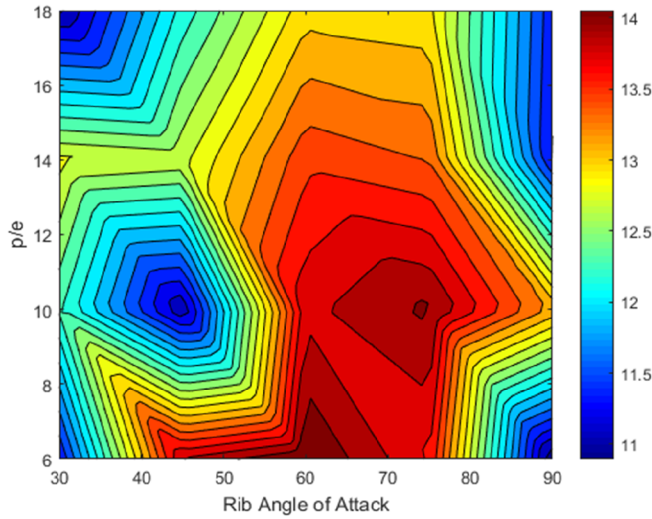


Figure 6. Result map of friction factor ratio

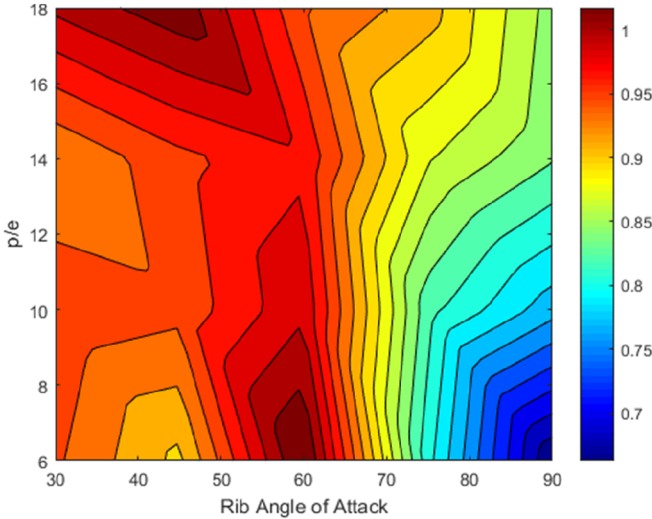


Figure 7. Result map of Thermal Performance

B. Results of 3D Conjugate Heat Transfer Simulation

Using the calculations performed in the previous section, the correlation of the heat transfer coefficient and friction factor were extracted. In this section, using these relations and the 3D numerical conjugate heat transfer simulation, the effect of rib turbulators on the thermal performance of the internal cooling system of NASA C3X has been investigated.

Fig. 8 shows the effect of rib turbulators on the surface temperature of the vane. As it can be seen, using the optimal configuration of rib turbulators causes an impressive effect on vane surface temperature reduction. The results show that, the average effects of temperature reduction in leading edge, mid chord and trailing edge are 7.1%, 4.3% and 6.8% respectively. Therefore, it could be concluded that using rib turbulators on surface temperature reduction is more effective in the leading and trailing edge area.

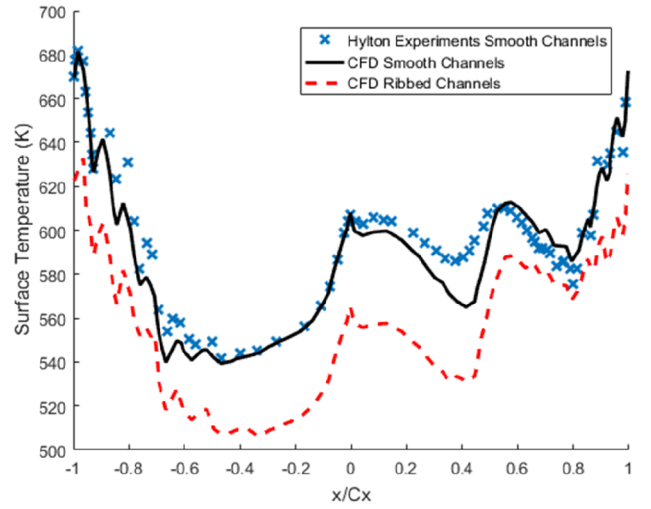


Figure 8. Effect of rib Turbulators on NASA C3X vane surface temperature

V. CONCLUSION

In this work the effect of rectangular rib turbulators angle of attack on the vane surface temperature is investigated. The advance response surface method with logarithmic functional variables using numerical conjugate heat transfer analysis of fluid flow are used to conduct the results. The conclusions are summarized below:

- 1- Numerical conjugate heat transfer simulation results showed reasonable agreement with the experiments.
- 2- Among various design parameters, two design variables, rib angle ($30 \leq \alpha \leq 90$) and the rib pitch to-height ratio ($6 \leq p/e \leq 18$) are selected. The optimum design point with the highest Nusselt number ratio appears at $\alpha = 59.38$ and $p/e = 6.1$ and the highest thermal performance is at $\alpha = 59.38$ and $p/e = 6.24$.
- 3- The effect of rib turbulators on the NASA C3X vane surface temperature is investigated. The results show that, the average effects of temperature reduction in leading edge, mid chord and trailing edge are 7.1%, 4.3% and 6.8% respectively.

ACKNOWLEDGMENT

The authors would like to thank the financial support received from the Deputy of Research and Technology in Sharif University of Technology. Their financial support and help are greatly acknowledged.

REFERENCES

- [1] Ledezma, G. A., Laskowsky, G. M., and Tolpadi, A. K., 2008, Turbulence Model Assessment for Conjugate Heat Transfer in a High Pressure Turbine Vane Model, ASME Paper No. GT2008-50498.
- [2] Wang, Z., Yan, P., Guo, Z., and Han, W., 2008, BEM/FDM Conjugate Heat Transfer Analysis of a Two-Dimensional Air-Cooled Turbine Blade Boundary Layer, *J. Thermal Sci.*, 17(3), pp. 199–206.
- [3] Qiang, W., Zhaoyuan, G., Chi, Z., Guotai, F., and Zhongqi, W., 2009, Coupled Heat Transfer Simulation of a High-Pressure Turbine Nozzle Guide Vane, *Chin. J. Aeronaut.*, 22, pp. 230–236.
- [4] Wang, Z., Yan, P., Huang, H., and Han, W., 2009, Coupled BEM and FDM Conjugate Analysis of a Three-Dimensional Air-Cooled Turbine Vane, ASME Paper No. GT2009-59030.
- [5] Mangani, L., Cerutti, M., Maritano, M., and Spel, M., 2010, Conjugate Heat Transfer Analysis of NASA C3X Film Cooled Vane With an Object-Oriented CFD Code, ASME Paper No. GT2010-23458.
- [6] Ni, R. H., Humber, W., Fan, G., Johnson, P. D., Downs, J., Clark, J. P., and Koch, P. J., 2011, Conjugate Heat Transfer Analysis of a Film-Cooled Turbine Vane, ASME Paper No. GT2011-45920.
- [7] Cho HH, Wu SJ, Kwon HJ, 2000, Local heat/mass transfer measurements in a rectangular duct with discrete ribs. *ASME J Turbomach* 122:579–586
- [8] Rau G, Cakan M, Moeller D, Arts T, 1998, The effect of periodic ribs on the local aerodynamic and heat transfer performance of a straight cooling channel. *ASME J Turbomach* 120:368–375
- [9] Kim KM, Kim YY, Lee DH, Rhee DH, Cho HH, 2007 Influence of duct aspect ratio on heat/mass transfer in coolant passages with rotation. *Int J Heat Fluid Flow* 28:357–373
- [10] Kim KM, Park SH, Jeon YH, Lee DH, Cho HH, 2008 Heat/mass transfer characteristics in angled ribbed channels with various bleed ratios and rotation numbers. *ASME J Turbomach* 130:031021
- [11] Liu Y-H, 2005 Effect of rib spacing on heat transfer and friction in a rotating two-pass rectangular (AR = 1:2) channel. M.S. thesis, Texas A&M University, USA
- [12] Kim HM, Kim KY, 2004 Design optimization of rib-roughened channel to enhance turbulent heat transfer. *Int J Heat Mass Transf* 47:5159–5168
- [13] Kim HM, Kim KY, 2006 Shape optimization of three-dimensional channel roughened by angled ribs with RANS analysis of turbulent heat transfer. *Int J Heat Mass Transf* 49:4013–4022
- [14] Myers RH, Montgomery DC, 2002, Response surface methodology: progress and product optimization using designed experiments. Wiley, New York
- [15] Guinta AA, 1997, Aircraft multidisciplinary design optimization using design of experimental theory and response surface modeling methods. Ph.D. thesis, Department of Aerospace Engineering, Virginia Polytechnic Institute and State University, USA
- [16] Kim KM, 2008, Optimal design of heat transfer systems for enhancing thermal performance and preventing thermal damage. Ph. D. thesis, Yonsei University, Korea
- [17] Mitchell TJ, 1974, An algorithm for the construction of D-optimal designs. *Technometrics* 20:203–210
- [18] Dittus FW, Boelter LMK, 1930, Heat transfer in automobile radiations of tubular type. University of California, Berkeley, Publications in Engineering 2:443–461; 1985 reprinted in *Int Commun Heat Mass Transf* 12:3–22
- [19] Prabhu SV, 1970, Advances in heat transfer 6. Academic Press, New York, pp 503–564
- [20] Hylton, L. D., Mihelc, M. S., Turner, E. R., Nealy, D. A., and York, R. E., 1983, Analytical and Experimental Evaluation of the Heat Transfer Distribution Over the Surfaces of Turbine Vanes, NASA Report No. CR-168015.

NATURAL CONVECTIVE HEAT TRANSFER FROM TWO PARALLEL THIN CIRCULAR VERTICALLY SPACED AXIALLY ALIGNED HORIZONTAL ISOTHERMAL PLATES OF DIFFERENT DIAMETER

Patrick H Oosthuizen
 Department of Mechanical and Materials Engineering
 Queen's University
 Kingston, ON Canada
 patrick.oosthuizen@queensu.ca

Abstract—A numerical study of natural convective heat transfer from two isothermal vertically aligned thin circular horizontal plates having different diameters has been undertaken. The situation where the vertical distance between the two plates is relatively small has been considered and there is consequently an interaction of the flows over the plates which affects the heat transfer rates from the plates. In the present study the diameter of the upper horizontal plate is larger than the diameter of the lower horizontal plate. The effect of the dimensionless vertical spacing between the plates and of the ratio of the diameter of the lower plate to that of the upper plate on the mean heat transfer rates from the entire surface of each plate has been investigated. The results were obtained using the commercial CFD code ANSYS FLUENT[®]. The mean flow has been assumed to be steady and symmetrical about the vertical plate axes. Attention has been limited to the situation where the flow remains laminar. The heat transfer rates considered, expressed in terms of mean Nusselt numbers, will depend on the Rayleigh number, on the relative diameters of the two plates, on the dimensionless spacing between the plates, and on the Prandtl number. Results have only been obtained for a Prandtl number of 0.74. Extensive investigations of the effect of the relative plate diameters and of the dimensionless spacing between the plates on the variation of the Nusselt numbers with Rayleigh number have been undertaken.

Keywords—convective heat transfer; natural convection; horizontal surfaces; numerical

I. INTRODUCTION

Natural convective heat transfer from two thin isothermal vertically aligned horizontal circular plates having different diameters has been numerically investigated here. Cases where the diameter of the bottom plate has a smaller or at most the same diameter as the top plate have been considered.

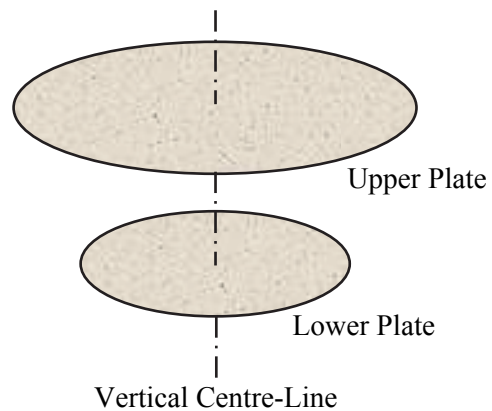


Figure 1. Flow situation considered in present study.

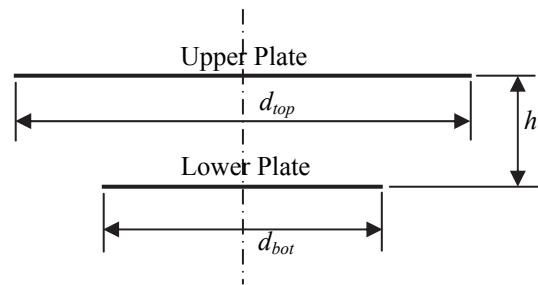


Figure 2. Variables used in defining the flow situation being considered.

The flow situation considered is shown in Fig. 1 and the dimensions used in defining the geometry are shown in Fig. 2. The plate surfaces are assumed to be all at the same temperature, this temperature being higher than that of the surrounding fluid. There is thus heat transfer from both the upper (top) and lower (bottom) surfaces of both plates. In the present study attention has been given to the case where the vertical distance between the plates, h , (see Fig. 2) is relatively small compared to the diameters of the plates with the result that there is an interaction between the flows over the two

plates, this flow interaction affecting the heat transfer rates from the plates.

Attention has here been given to the values of the mean heat transfer rates over the entire surface of the upper plate and over the entire surface of the lower plate.

The situation considered in this study does not directly represent one that occurs in practice but situations in which there are vertically spaced horizontal heated devices having different sizes do arise in practice and the results obtained in the present study should give an indication of what factors have a significant effect on the heat transfer rates in such practical situations.

While there have been a number of studies of natural convective heat transfer from single horizontal two-sided plates, e.g. see [1-7] relatively little attention has been given to natural convective heat transfer when there are two or more vertically aligned relatively closely positioned horizontal plates. Reference [8] describes an experimental study of a case where there is a stack of horizontal plates while a study of heat transfer from a pair of quite widely spaced plates is described in [9]. A numerical investigation of heat transfer from two vertically aligned horizontal circular plates is described in [10] while a numerical investigation of heat transfer from two vertically aligned horizontal two-dimensional plates is described in [11]. There does not appear to be much other available information on the heat transfer rates that arise in situations in which there are two vertically separated heated horizontal plates and the available studies all deal with cases where the two horizontal plates have the same size.

The present study is part of a series of studies of natural convective heat transfer from horizontal and near horizontal surfaces, e.g., see [12-18].

II. SOLUTION PROCEDURE

The two plates have been assumed to be thin and therefore there is no heat transfer from the outer edges of the plates (see Fig. 2). The flow has been assumed to be steady and symmetric about the vertical centre-line through the plates. The Boussinesq approach has been adopted in dealing with the buoyancy forces and with the temperature change induced fluid property changes. The numerical solution has been obtained using the commercial CFD solver ANSYS FLUENT[®]. Extensive grid-independence and convergence criteria testing has been undertaken and the heat transfer results presented in this paper are to within approximately 1% independent of the mesh size and of the convergence criterion used.

III. RESULTS

The mean heat transfer rates from the heated horizontal plates have been expressed in terms of Nusselt numbers based on the diameter of the upper plate and on the difference between the temperature of the surfaces of the heated plates and the fluid temperature in the undisturbed fluid far from the plates. As already mentioned, attention has been given to the values of the mean heat transfer rates over the entire surface of the upper plate and over the entire surface of the lower plate.

These mean heat transfer rates have been expressed in terms of mean Nusselt numbers. These mean Nusselt numbers are dependent on: (1) the Rayleigh number, (2) the dimensionless vertical distance that the two plates are apart, $H = h / d_{top}$, (3) the ratio of the diameter of the lower, generally smaller diameter plate to the diameter of the upper plate, $D_{bot} = d_{bot} / d_{top}$ (4) the Prandtl number, Pr . Results have only been obtained for a Prandtl number of 0.74, i.e., effectively the value for air at ambient conditions. The Nusselt numbers will therefore depend on the Rayleigh number, on the ratio of the diameter of the lower plate to the diameter of the upper plate, and on dimensionless distance between the plates, i.e.:

$$Nu = \text{function}(Ra, D_{bot}, H) \quad (1)$$

Typical variations of the mean Nusselt numbers based on the heat transfer rate averaged over the total surface area of the upper plate, Nu_{top} , with Rayleigh number for various values of the dimensionless vertical distance between the plates, H , and various values of the dimensionless diameter of the lower plate are shown in Figs. 3, 4, 5, and 6.

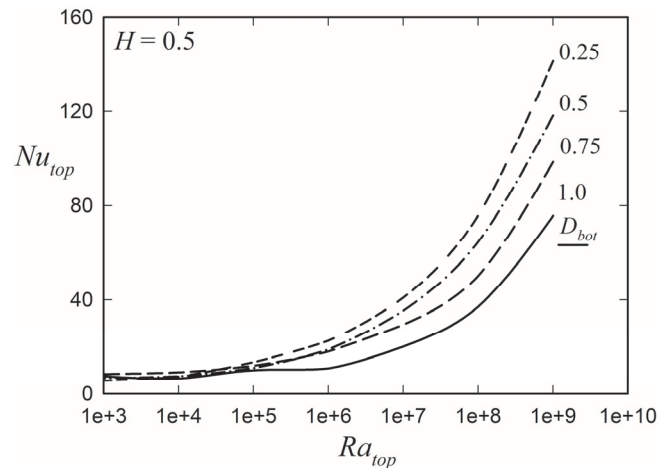


Figure 3. Variations of the mean Nusselt number for the entire upper plate with Rayleigh number for a dimensionless plate spacing, H , of 0.5.

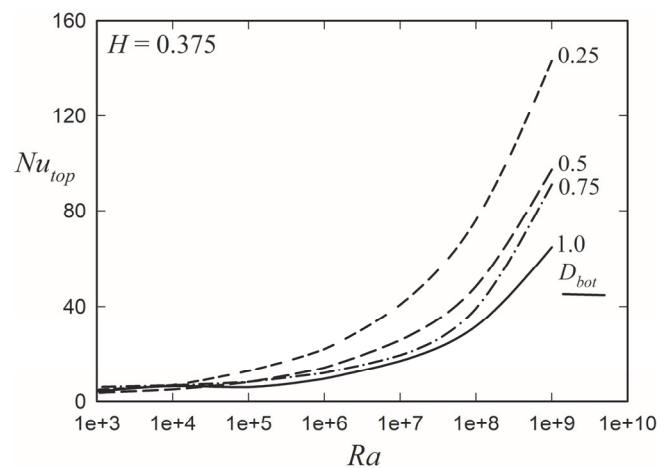


Figure 4. Variations of the mean Nusselt number for the entire upper plate with Rayleigh number for a dimensionless plate spacing, H , of 0.375.

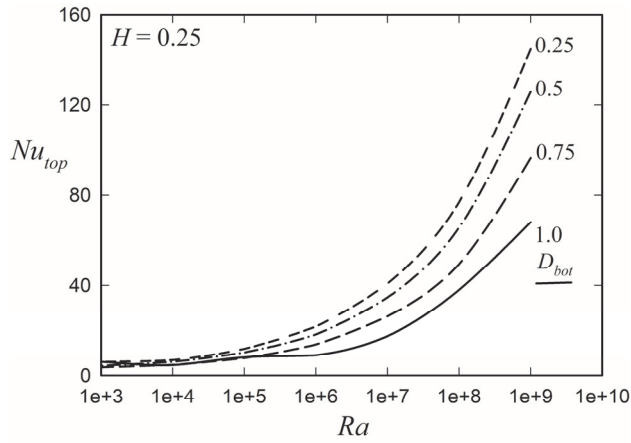


Figure 5. Variations of the mean Nusselt number for the entire upper plate with Rayleigh number for a dimensionless plate spacing, H , of 0.25.

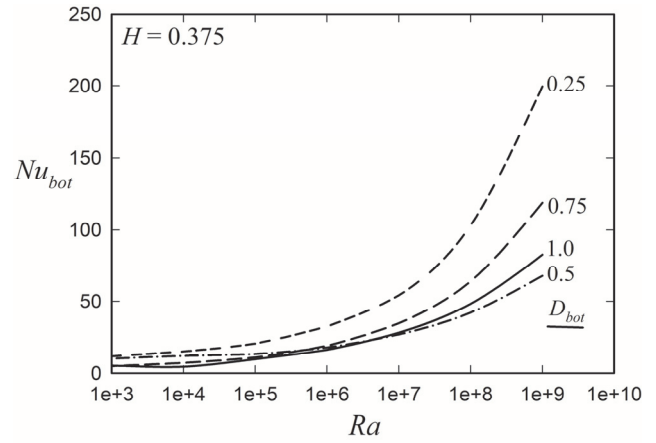


Figure 8. Variations of the mean Nusselt number for the entire lower plate with Rayleigh number for a dimensionless plate spacing, H , of 0.375.

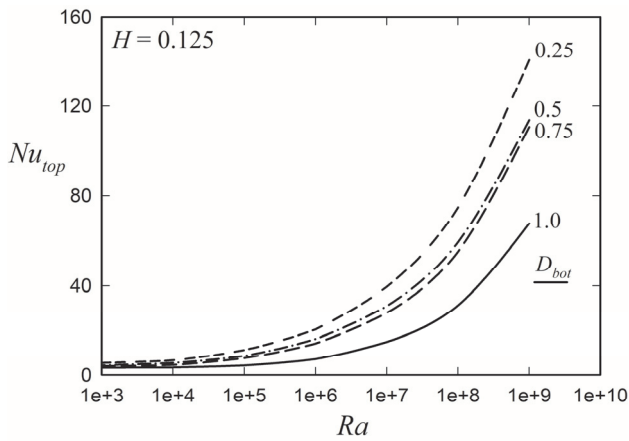


Figure 6. Variations of the mean Nusselt number for the entire upper plate with Rayleigh number for a dimensionless plate spacing, H , of 0.125.

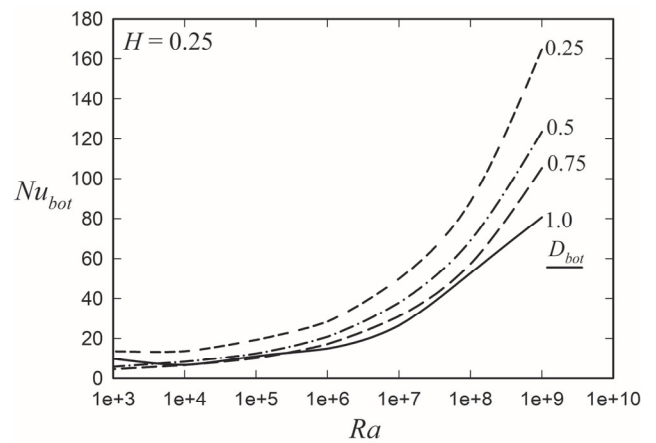


Figure 9. Variations of the mean Nusselt number for the entire lower plate with Rayleigh number for a dimensionless plate spacing, H , of 0.25.

Typical variations of the mean Nusselt number based on the heat transfer rate averaged over the total surface area of the lower plate, Nu_{bot} , with Rayleigh number for various values of the dimensionless vertical distance between the plates, H , are shown in Figs. 7, 8, 9, and 10, these figures each giving results for a different value of H .

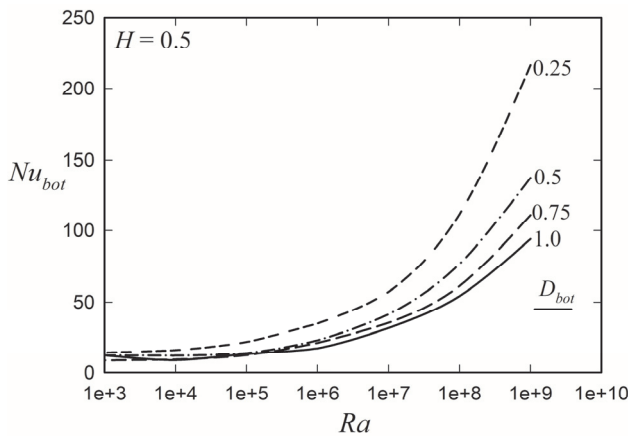


Figure 7. Variations of the mean Nusselt number for the entire lower plate with Rayleigh number for a dimensionless plate spacing, H , of 0.5.

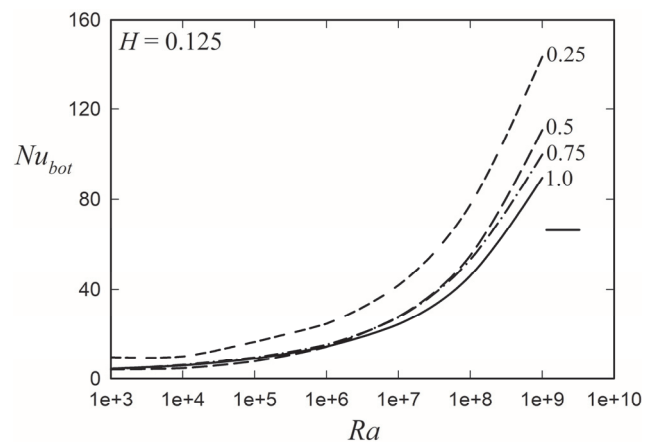


Figure 10. Variations of the mean Nusselt number for the entire lower plate with Rayleigh number for a dimensionless plate spacing, H , of 0.125.

It will be seen from the results given in these figures that both Nu_{top} and Nu_{bot} increase very significantly in value with decreasing D_{bot} at all but at the smallest values of Ra considered. It will also be seen that for the range of values considered, the effect of H on the Nusselt numbers is much smaller than the effect of D_{bot} . The effect of D_{bot} on Nu_{top} and Nu_{bot} is more clearly illustrated by the results shown in Figs. 11 to 14. It will be seen from these figures that the decrease in Nu_{top} and Nu_{bot} with the decrease in D_{bot} over the range of D_{bot} values considered is approximately 50% at all but the lower values of Ra considered.

It will also be seen from the results given in the figures discussed above that under almost all conditions considered the values of the mean Nusselt number for the lower plate is higher than the values of the mean Nusselt number for the upper plate. However it should be noted that these Nusselt numbers for both plates both use the diameter of the upper plate as the reference length.

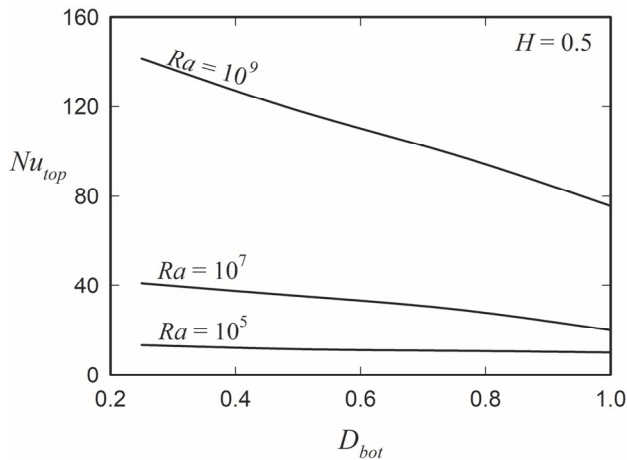


Figure 11. Variations of the mean Nusselt number for the entire upper plate with the dimensionless bottom plate diameter for three different Rayleigh numbers for a dimensionless plate spacing, H , of 0.5

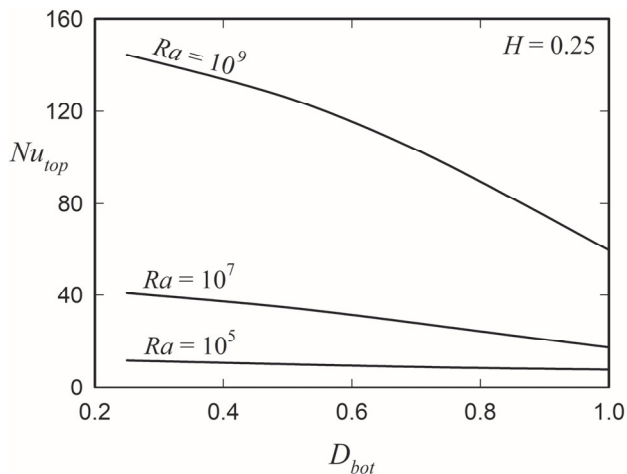


Figure 12. Variations of the mean Nusselt number for the entire upper plate with the dimensionless bottom plate diameter for three different Rayleigh numbers for a dimensionless plate spacing, H , of 0.25.

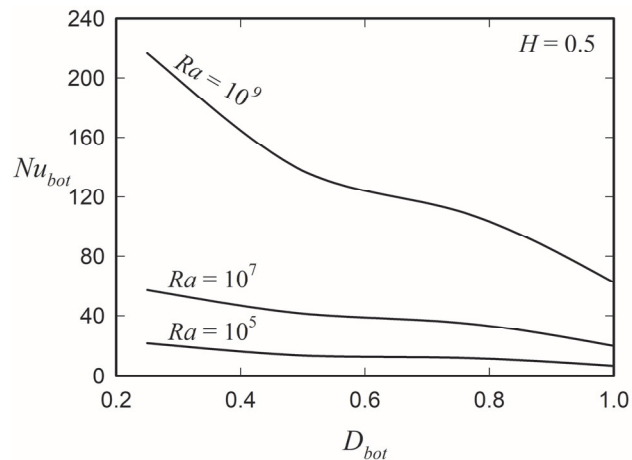


Figure 13. Variations of the mean Nusselt number for the entire lower plate with the dimensionless bottom plate diameter for three different Rayleigh numbers for a dimensionless plate spacing, H , of 0.5.

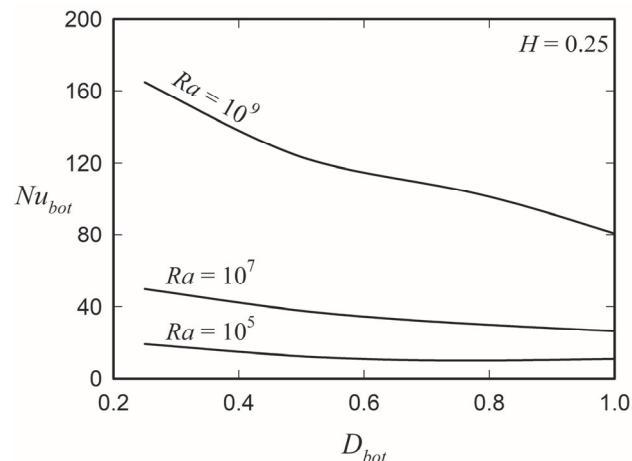


Figure 14. Variations of the mean Nusselt number for the entire lower plate with the dimensionless bottom plate diameter for three different Rayleigh numbers for a dimensionless plate spacing, H , of 0.25

IV. CONCLUSIONS

The results obtained in the present study clearly illustrate the effect of the relative size of the lower plate on the heat transfer rates from the upper and lower plates. In all cases the heat transfer rate from the upper plate, as is to be expected, increases as the relative size of the lower plate decreases. The decrease in the heat transfer rate from the upper plate with the decrease in the relative size of the lower plate over the range of values of the relative size of the lower plate considered is approximately 50% at all but the lower values of the Rayleigh number considered. For the range of Rayleigh number values considered the results also indicate that the effect of dimensionless distance between the plates on the heat transfer rate from the upper plate is much smaller than the effect of the relative size of the lower plate on the heat transfer rate from the upper plate.

ACKNOWLEDGMENT

This work was supported by the Natural Sciences and Engineering Research Council of Canada (NSERC) through its Discovery Grant Program (Grant RGPIN-2015-06444).

NOMENCLATURE

d_{top}	Diameter of upper surface
d_{bot}	Diameter of lower surface
D_{bot}	d_{bot} / d_{top}
h	Vertical distance between plates
H	h / d_{top}
Nu_{top}	Mean Nusselt number based on d_{top} for upper surface
Nu_{bot}	Mean Nusselt number based on d_{top} for lower surface
Pr	Prandtl number
Ra	Rayleigh number based on d_{top}

REFERENCES

- [1] F. Suriano, and K.T. Yang, "Laminar free convection about vertical and horizontal plates at small and moderate Grashof numbers," J. Heat Mass Transfer, vol. 11, no. 3, pp.: 473-490, 1968.
- [2] B. Chambers, and T. Lee, "A numerical study of local and average natural convection Nusselt numbers for simultaneous convection above and below a uniformly heated horizontal thin plate," J. Heat Transfer, vol. 119, no. 1, pp.:102-108, 1997.
- [3] J.J. Wei, B. Yu, H.S. Wang, and W.Q. Tao, "Numerical study of simultaneous natural convection heat transfer from both surfaces of a uniformly heated thin plate with arbitrary inclination," Int. J. Heat Mass Transfer, vol. 38, nos. 4-5, pp.:309-317, 2002.
- [4] J.J. Wei, B. Yu, and Y. Kawaguchi, "Simultaneous natural convection heat transfer above and below an isothermal horizontal thin plate," Num. Heat Transf.: Part A: Applications, vol. 44, no. 1, pp.:39-58, 2003.
- [5] M. Corcione, E. Habib, and A. Campo, "Natural convection from inclined plates to gases and liquids when both sides are uniformly heated at the same temperature," Int. J. Thermal Sciences, vol. 50, no. 8, pp.:1405-1416, 2011.
- [6] L. Fontana. Free convection heat transfer from an isothermal horizontal thin strip: the influence of the Prandtl number. J. Therm. Sci., 23(6):586-592, 2014.
- [7] P.H. Oosthuizen, and A.Y. Kalendar, "A numerical study of the simultaneous natural convective heat transfer from the upper and lower surfaces of a thin isothermal horizontal circular plate," Proc. 2016 ASME International Mechanical Engineering Congress and Exposition (IMECE2016), vol. 8: Heat Transfer and Thermal Engineering, Phoenix, Arizona, November, 2016. doi:10.1115/IMECE2016-65540.
- [8] B.P. Dooher, and A.F. Mills, "Natural-convection thermosyphon heat transfer from a stack of horizontal plates," Experimental Heat Transfer, vol. 13, no. 2, pp:125-136, 2000.
- [9] Wu-Shung Fu, Wei-Hsiang Wang, Chung-Gang Li, Makoto Tsubokura. An investigation of the unstable phenomena of natural convection in parallel square plates by multi-GPU implementation, Num. Heat Transfer, Part B: Fundamentals, 71(1) 66-83, 2017.
- [10] P.H. Oosthuizen, "Natural convective heat transfer from two thin vertically spaced axially aligned horizontal isothermal circular plates," Proc. 2nd Thermal and Fluid Engg. Conf. (TFEC2017). Paper TFEC-IWHT2017-17451, Las Vegas, April, 2017.
- [11] P.H. Oosthuizen, "Natural convective heat transfer from two parallel thin vertically spaced horizontal two-dimensional isothermal plates," Proc. CFD Society of Canada Conference. Paper MS-245, Winnipeg, June 10-12, 2018.
- [12] P.H. Oosthuizen, and A.Y. Kalendar, "Natural convective heat transfer from horizontal and near horizontal surfaces," Springer Briefs in Applied Sciences and Technology. Thermal Engineering and Applied Science, Springer International Publishing, 2018.
- [13] P.H. Oosthuizen, "A numerical study of the effect of adiabatic side sections on natural convective heat transfer from a downward facing heated horizontal isothermal surface," Proc. CFD Society of Canada Conference. Paper MS-223, Winnipeg, June 10-12, 2018..
- [14] P.H. Oosthuizen, and A.Y. Kalendar, "Natural convective heat transfer from upward facing recessed and protruding heated horizontal isothermal circular elements with isothermal vertical side surfaces, Proc. 13th International Conference on Heat Transfer, Fluid Mechanics and Thermodynamics, Slovenia, 17-19 July 2017.
- [15] P.H. Oosthuizen, "Natural convective heat transfer from a horizontal isothermal circular element imbedded in a flat adiabatic surface with a parallel adiabatic covering surface," Proc. 11th AIAA/ASME Joint Thermophysics and Heat Transfer Conference Atlanta, GA. Paper AIAA 2014-3357. <https://doi.org/10.2514/6.2014-3357>
- [16] P.H. Oosthuizen, and A.Y. Kalendar, "Laminar and turbulent natural convective heat transfer from a horizontal isothermal circular element with an unheated inner circular section," Proceedings of the CFD Society of Canada 23rd Annual Conference, June 7-10, 2015, Waterloo.
- [17] P.H. Oosthuizen, "A numerical study of natural convective heat transfer from upward facing recessed and protruding heated horizontal isothermal circular surface," 12th International Conference on Heat Transfer, Fluid Mechanics and Thermodynamics, Spain 11-13 July 2016.
- [18] Patrick H Oosthuizen, "A numerical study of the effect of a plane horizontal covering surface on natural convective heat transfer from a circular horizontal isothermal element that has an inner adiabatic circular section," Proceedings 24th Annual Conference of the CFD Society of Canada, Kelowna, BC, June 26-29, 2016.

A NUMERICAL STUDY OF THE EFFECT OF THIN HORIZONTAL AND VERTICAL ADIABATIC SIDE EXTENSIONS ON NATURAL CONVECTIVE HEAT TRANSFER FROM A DOWNWARD FACING HEATED HORIZONTAL ISOTHERMAL SURFACE

Patrick H Oosthuizen and Jane T Paul
 Department of Mechanical and Materials Engineering
 Queen's University
 Kingston, ON Canada
 patrick.oosthuizen@queensu.ca

Abstract—A numerical study of natural convective heat transfer from a horizontal downward facing two-dimensional isothermal heated surface that has horizontal or vertical thin adiabatic sections extending on each side of the heated surface has been undertaken. The aim of the study was to determine the effect of the relative size of the thin horizontal or vertical side adiabatic sections on the heat transfer rate from the heated surface. The mean flow has been assumed to be steady and symmetrical about the vertical axis through the heated surface. Attention has been limited to conditions under which the flow remains laminar. The numerical results have been obtained using the commercial CFD solver ANSYS FLUENT[®]. The heat transfer rate from the heated surface has been expressed in terms of a mean Nusselt number based on the heated surface width, this Nusselt number depending on the Rayleigh number, on the dimensionless size of the adiabatic side sections, on the orientation of the adiabatic side sections, and on the Prandtl number. Results have been obtained for a Prandtl number of 0.74. Studies of the effect of the dimensionless size and orientation of the adiabatic side sections on the variation of the Nusselt numbers with Rayleigh number have been undertaken.

Keywords—*natural convection; horizontal surface; numerical; side surfaces; two-dimensional*

I. INTRODUCTION

Natural convective heat transfer from a horizontal downward facing two-dimensional isothermal heated surface has been numerically studied. Thin adiabatic horizontal or vertical sections extend from each side of the heated surface as shown in Fig. 1. The heated surface is at a higher temperature than that of the surrounding fluid. The effect of the relative size of the side adiabatic surfaces, $H=s/w$, where w is the width of the heated surface and s is the length of the adiabatic side surface (see Fig. 1) on the heat transfer rate from the heated horizontal surface has studied.

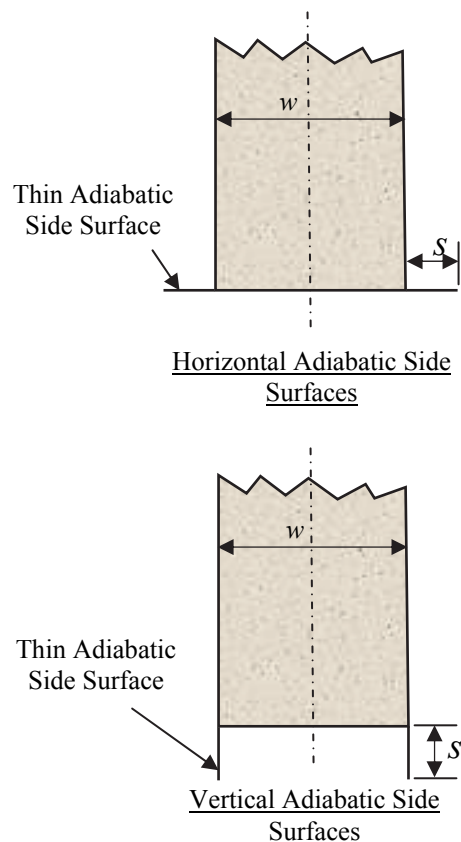


Figure 1. Flow situations considered.

A number of experimental and analytical studies of natural convective heat transfer from downward facing heated horizontal surfaces have been undertaken, e.g., see [1–16], the analytical studies being mainly based on the use of the

boundary layer type equations. Some of these studies have also considered the effect of side adiabatic sections. However, these earlier studies mostly covered a very limited range of the governing parameters or used analytical approaches that are known to give results of limited accuracy for the type of problem here being considered. There have also been some studies of edge conditions on natural convective heat transfer from downward facing heated horizontal surfaces, e.g., see [17–20]. However, the geometries dealt with in these studies differed from those considered in the present study. A consideration of past work in the general area considered in the present study indicated the need for a more detailed numerical study in this area. The present study is part of a larger overall investigation of natural convective heat transfer from horizontal and near horizontal heated surfaces, some of this work being reviewed in [21].

II. SOLUTION PROCEDURE

The flow has been assumed to be steady and it has been assumed that the fluid properties are constant except for the density change with temperature which gives rise to the buoyancy forces, the Boussinesq approximation being used in dealing with this. The flow has been assumed to be two-dimensional and radiant heat transfer effects have been neglected. The flow has been assumed to be symmetric about the vertical center-line shown in Fig.1. Attention has been limited to the case where the flow is laminar. The governing equations subject to the use of the assumptions discussed above and subject to the boundary conditions have been numerically solved using the commercial CFD solver ANSYS FLUENT[®].

Extensive grid and convergence-criteria independence testing was undertaken. The results of this testing indicated that with the meshes used in obtaining the results presented here the heat transfer results, i.e., the Nusselt number values, are grid- and convergence criteria independent to within approximately one per cent.

III. RESULTS

The solution has the following governing parameters:

- The Rayleigh number, Ra , based on the width, w , of the heated surface (see Fig. 1) and on the difference between the temperature of the of the heated surface, T_w , and the temperature of the undisturbed fluid well away from the system, T_f , i.e.:

$$Ra = \frac{\beta g w^3 (T_w - T_f)}{\nu \alpha} \quad (1)$$

- Whether the thin side adiabatic sections are in the horizontal or in the vertical direction
- The dimensionless size of the adiabatic horizontal or vertical side surfaces, i.e.:

$$H = \frac{s}{w} \quad (2)$$

- The Prandtl number, Pr .

As a consequence of the applications that motivated the present study, results have only been obtained for a Prandtl number of 0.74 which is effectively for the value of Pr for air under ambient conditions. Rayleigh numbers of between approximately 10^3 and 10^9 and dimensionless adiabatic horizontal side surface sizes of from 0 to 1 have been considered. The total heat transfer rate from the heated two-dimensional surface, Q' , has been expressed in terms of a mean Nusselt number based on the width, w , of the heated surface and on the difference between the temperature of the heated surface and the temperature of the undisturbed fluid well away from the system, i.e.:

$$Nu = \frac{Q'}{k(T_w - T_f)} \quad (3)$$

In arriving at this equation it has been noted that the heat transfer rate per unit length of the heated surface has been considered with the result that the heated surface area considered is $w \times 1$.

Because a fixed value of Pr is being considered, Nu is a function of Ra , of the dimensionless size of the adiabatic side surfaces, H , and of the direction of the adiabatic sections, i.e., horizontal or vertical.

Typical variations of the mean Nusselt number with Rayleigh number for various values of the dimensionless adiabatic side surface size, H , are shown in Figs. 2 to 6. In all of these figures the variation of the mean Nusselt number with Rayleigh number for the case where the adiabatic side surfaces are horizontal and for the case where the adiabatic side surfaces are vertical are shown. Also shown, for comparison, is the variation for the case where there is no adiabatic side surface, i.e., the case where $H = 0$.

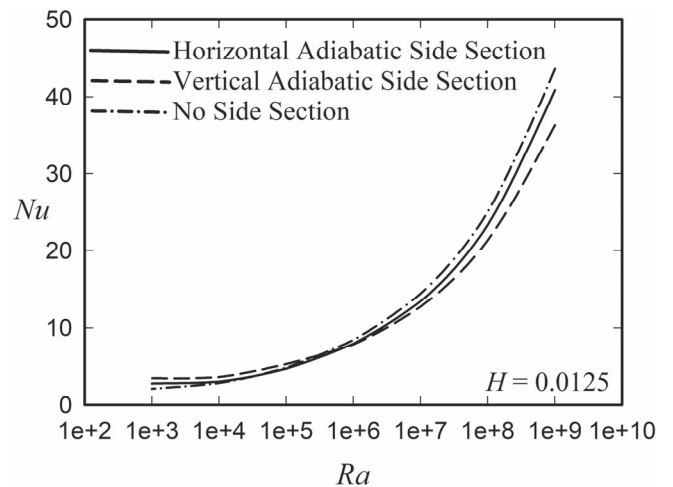


Figure 2. Variations of mean Nusselt number with Rayleigh number for the case where there are horizontal adiabatic side surfaces and for the case where there are vertical adiabatic side surfaces, in both cases H being 0.0125. Also shown is the variation of the mean Nusselt number with Rayleigh number for the case where there are no side surfaces, i.e., for the case where H is zero.

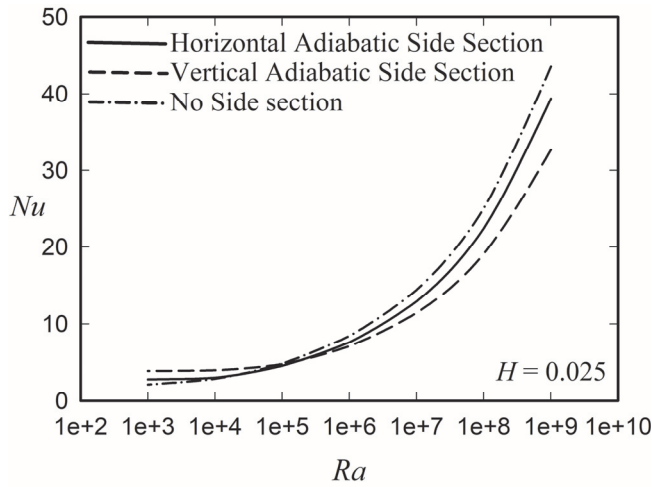


Figure 3. Variations of mean Nusselt number with Rayleigh number for the case where there are horizontal adiabatic side surfaces and for the case where there are vertical adiabatic side surfaces, in both cases H being 0.025. Also shown is the variation of the mean Nusselt number with Rayleigh number for the case where there are no side surfaces, i.e., for the case where H is zero.

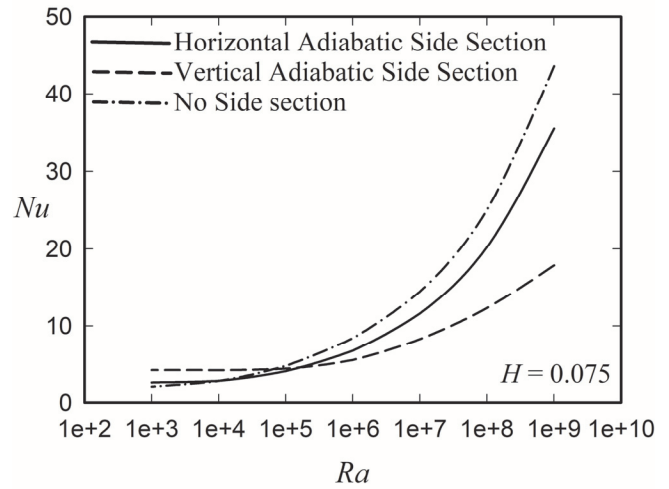


Figure 5. Variations of mean Nusselt number with Rayleigh number for the case where there are horizontal adiabatic side surfaces and for the case where there are vertical adiabatic side surfaces, in both cases H being 0.075. Also shown is the variation of the mean Nusselt number with Rayleigh number for the case where there are no side surfaces, i.e., for the case where H is zero.

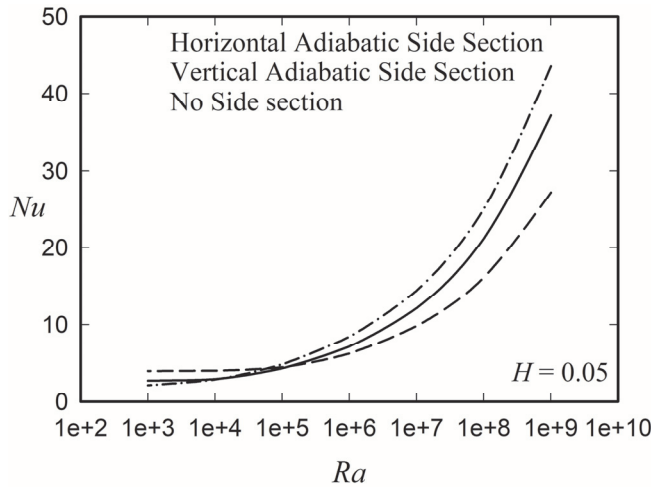


Figure 4. Variations of mean Nusselt number with Rayleigh number for the case where there are horizontal adiabatic side surfaces and for the case where there are vertical adiabatic side surfaces, in both cases H being 0.05. Also shown is the variation of the mean Nusselt number with Rayleigh number for the case where there are no side surfaces, i.e., for the case where H is zero.

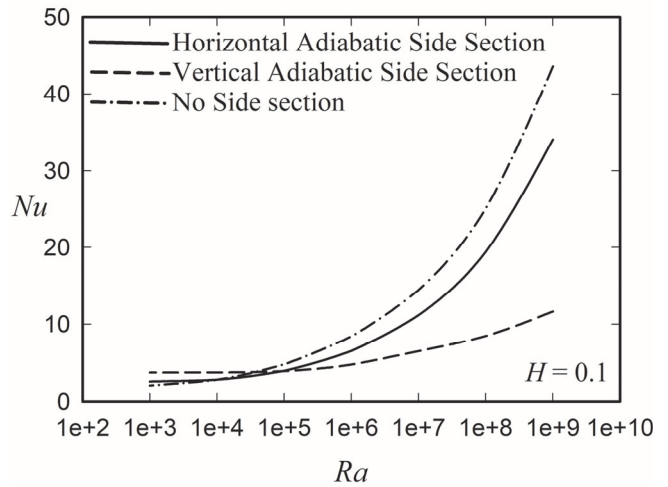


Figure 6. Variations of mean Nusselt number with Rayleigh number for the case where there are horizontal adiabatic side surfaces and for the case where there are vertical adiabatic side surfaces, in both cases H being 0.1. Also shown is the variation of the mean Nusselt number with Rayleigh number for the case where there are no side surfaces, i.e., for the case where H is zero.

From the results given in Figs. 2 to 6 it will be seen that at the larger values of the Rayleigh number the mean Nusselt number is decreased relative to that existing at the same Rayleigh number when there are no side adiabatic sections for both the case of horizontal adiabatic side surfaces and the case of vertical adiabatic side surfaces. In all cases, however, this Nusselt number decrease is greater when the adiabatic side surfaces are vertical than it is when they are horizontal. At the lower Rayleigh numbers considered the Nusselt number changes produced by the presence of the adiabatic side surfaces are relatively small, this being particularly true in the horizontal adiabatic side surfaces case. In the vertical adiabatic side surfaces case in particular at low Rayleigh numbers the presence of adiabatic side surfaces produces an increase in the Nusselt number relative to that existing at the same Rayleigh number when there are no side adiabatic sections.

The effect of the size of the adiabatic side surfaces on the Nusselt number is further illustrated by the results by the results given in Figs. 7 to 10. These figures show the variations of the Nusselt number with the dimensionless adiabatic side surface size, H , for various values of the Rayleigh number. Figures 7 and 8 show results for the horizontal adiabatic side surface case, Fig. 7 giving results for some of the higher Rayleigh numbers considered and Fig. 8 giving results for some of the lower Rayleigh numbers considered. Figures 9 and 10 show results for the vertical adiabatic side surface case, Fig. 9 giving results for some of the higher Rayleigh numbers considered and Fig. 10 giving results for some of the lower Rayleigh numbers considered. These results show clearly how the magnitude of the effect of the adiabatic side surfaces increases in all cases as the dimensionless size of the adiabatic side surfaces increases.

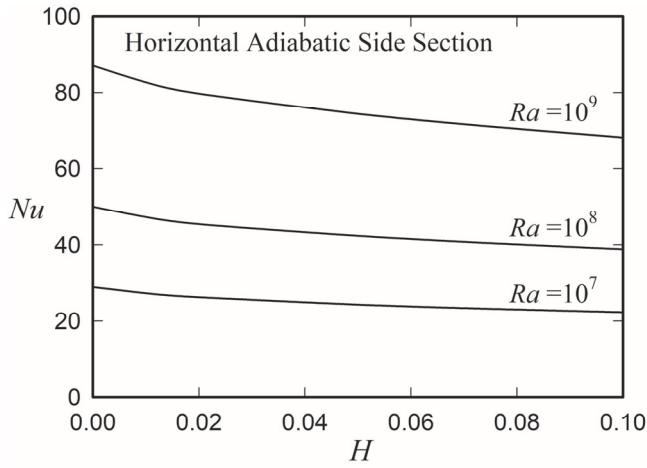


Figure 7. Variations of the mean Nusselt number with H for various higher values of the Rayleigh number for the case where there are horizontal adiabatic side surfaces. The results shown are for some of the higher Rayleigh number values for which results were obtained.

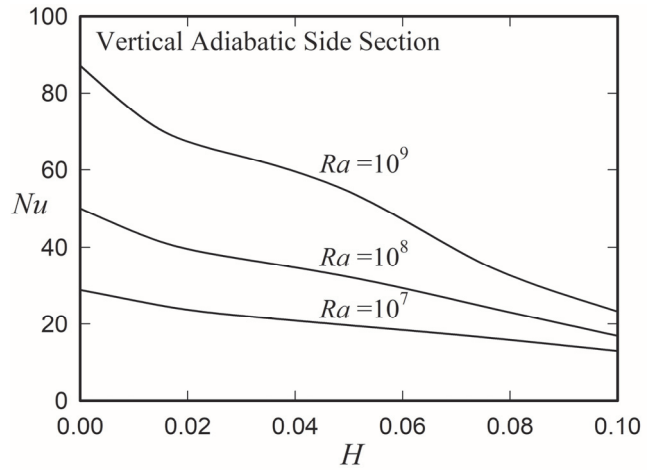


Figure 9. Variations of the mean Nusselt number with H for various higher values of the Rayleigh number for the case where there are vertical adiabatic side surfaces. The results shown are for some of the higher Rayleigh number values for which results were obtained.

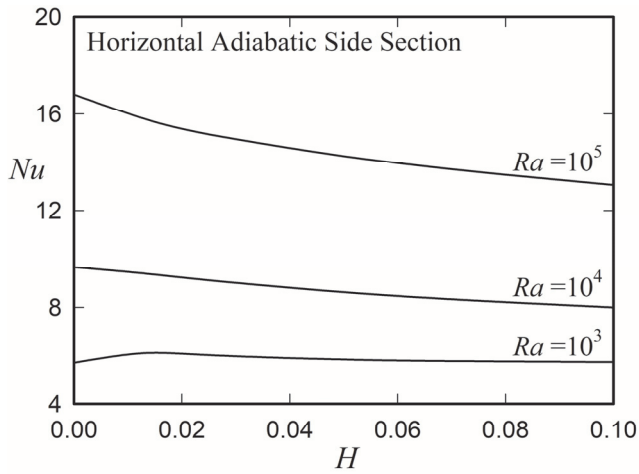


Figure 8. Variations of the mean Nusselt number with H for various lower values of the Rayleigh number for the case where there are horizontal adiabatic side surfaces. The results shown are for some of the lower Rayleigh number values for which results were obtained.

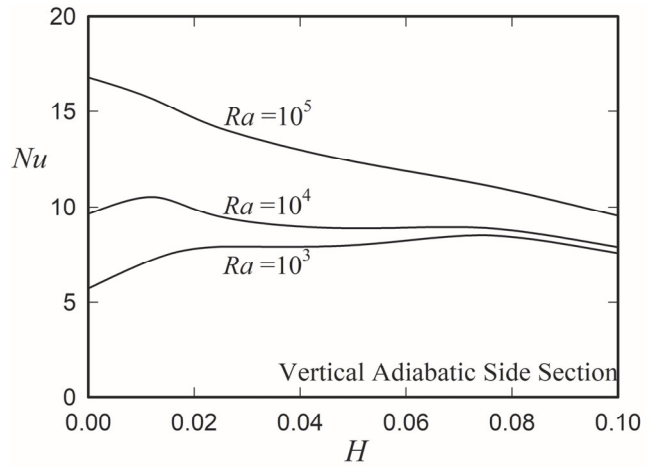


Figure 10. Variations of the mean Nusselt number with H for various lower values of the Rayleigh number for the case where there are vertical adiabatic side surfaces. The results shown are for some of the lower Rayleigh number values for which results were obtained.

The results given in Figs. 7 to 10 also further confirm the conclusions drawn from the results given in Figs. 2 to 6.

An idea of the magnitude of the changes in the Nusselt number caused by the adding of the adiabatic side surfaces can be gained from the results shown in Fig. 11. This figure shows how the ratio of Nusselt number that exists when there are side surfaces having a dimensionless size, H , of 0.1, Nu_{01} , to the Nusselt number that exists under the same conditions when there are no side surfaces, Nu_0 , varies with Rayleigh number. Results are given in this figure both for the case where the adiabatic surfaces are horizontal and for the case where these surfaces are vertical. It will be seen from the results given in Fig. 11 that at the larger Rayleigh numbers considered ($Ra > 10^5$) the presence of both horizontal and of vertical adiabatic side surfaces produces a decrease in the Nusselt number ratio.

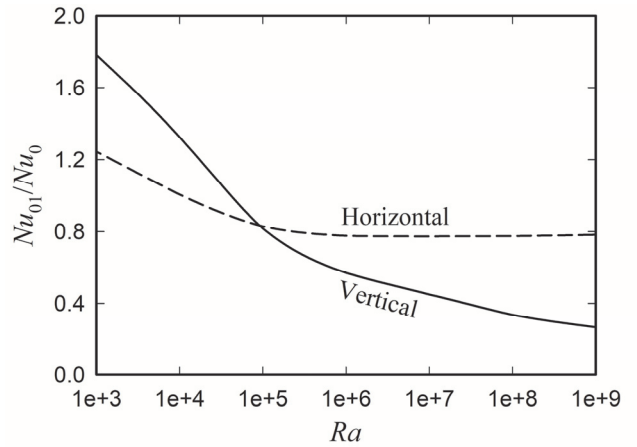


Figure 11. Variations of the ratio of the Nusselt number for the case where $H = 0.1$ to the Nusselt number for the same Rayleigh number for the case where $H = 0$ (Nu_{01} / Nu_0) for the case where the adiabatic side surfaces are horizontal and for the case where they are vertical.

The results also show that the decrease in the Nusselt number ratio is significantly greater when there are vertical side surfaces than what it is under the same conditions when there are horizontal side surfaces. At the lower Rayleigh numbers considered ($Ra < 10^5$) the presence of the side surfaces can produce an increase in the Nusselt number ratio, this increase being much greater when vertical side surfaces are involved than it is when horizontal side surfaces are involved.

IV. CONCLUSION

The results obtained in the present study show that, under all conditions considered, the presence of adiabatic side surfaces whether they be horizontal or vertical causes a significant change in the heat transfer rate compared to that which would exist under the same conditions if there were no side surfaces. Under all circumstances considered the presence of vertical side surfaces produces a greater change in the heat transfer rate under a given set of conditions than that produced by the presence of horizontal side surfaces. At the larger Rayleigh numbers considered ($Ra > 10^5$) the presence of horizontal adiabatic side surfaces or the presence of vertical adiabatic side surfaces produces a decrease in the heat transfer rate. However, the decrease at a given set of conditions is significantly greater with vertical adiabatic side surfaces than it is with horizontal adiabatic side surfaces. At the lower Rayleigh numbers considered ($Ra < 10^5$) the presence of the side adiabatic surfaces can produce an increase in the heat transfer rate, this increase again being greater under a given set of conditions with vertical adiabatic side surfaces than it is with horizontal adiabatic side surfaces.

ACKNOWLEDGMENT

This work was supported by the Natural Sciences and Engineering Research Council of Canada (NSERC) through its Discovery Grant Program (Grant RGPIN-2015-06444).

NOMENCLATURE

g	[m/s ²]	Gravitational acceleration
H	[-]	Dimensionless size of adiabatic side surfaces, s/w
k	[W/mK]	Thermal conductivity
Nu	[-]	Mean Nusselt number based on w
Nu_0	[-]	Mean Nusselt number based on w for the case where there are no adiabatic side surfaces
Nu_{01}	[-]	Mean Nusselt number based on w for the case where there are either horizontal or vertical adiabatic side surfaces with a dimensionless size of 0.1.
Pr	[-]	Prandtl number
Q'	[W]	Heat transfer rate per unit depth from the heated surface
Ra	[-]	Rayleigh number
s	[m]	Size of adiabatic side surfaces
T_f	[K]	Undisturbed fluid temperature
T_w	[K]	Heated surface temperature
w	[m]	Width of heated surface

Greek Symbols

α	[m ² /s]	Thermal diffusivity
β	[1/K]	Bulk coefficient of thermal expansion
ν	[m ² /s]	Kinematic viscosity

REFERENCES

- [1] F.J. Higuera, "Natural convection below heated horizontal rectangular plates," *Int. J. Heat Mass Transf.*, vol. 36, no. 14, pp. 3565-3571, 1993.
- [2] S.N. Singh, and R.C. Birkebak, "Laminar free convection from a horizontal infinite strip facing downwards," *J. Applied Mathematics Physics (ZAMP)*, vol. 20, no. 4, pp. 454-461, 1969.
- [3] T. Aihara, Y. Yamada, and S. Endo, "Free convection along the downward-facing surface of a heated horizontal plate," *Int. J. Heat Mass Transfer*, vol. 15, no. 12, pp. 2535-2549, 1972.
- [4] G.C. Vliet, and D.C. Ross, "Turbulent Natural convection on upward and downward facing inclined constant heat flux surfaces," *ASME. J. Heat Transfer*, vol. 97, no. 4, pp. 549-554, 1975.
- [5] B. Kozanoglu, and F. Rubio, "The characteristic length on natural convection from a horizontal heated plate facing downwards," *Thermal Science*, vol. 18, no. 2, pp. 555-561, 2014.
- [6] T. Schulenberg, "Natural convection heat transfer below downward facing horizontal surfaces," *Int. J. Heat Mass Transfer*, vol. 28, no. 2, pp. 467-477, 1985.
- [7] J. Gryzagoridis, "Natural convection from an isothermal downward facing horizontal plate," *Int. Comm. Heat Mass Transfer*, vol. 11, no. 2, pp. 183-190, 1984.
- [8] R. E. Faw, and T. A. Dullforce, "Holographic interferometry measurement of convective heat transport beneath a heated horizontal circular plate in air," *Int. J. Heat Mass Transfer*, vol. 25, no. 8, pp. 1157-1166, 1982.
- [9] R. E. Faw, and T. A. Dullforce, "Holographic interferometry measurement of convective heat transport beneath a heated horizontal plate in air," *Int. J. Heat Mass Transfer*, vol. 24, no. 5, pp. :859-869, 1981. [https://doi.org/10.1016/S0017-9310\(81\)80009-9](https://doi.org/10.1016/S0017-9310(81)80009-9).
- [10] F. Tetsu, H. Hiroshi, and M. Itsuki, "A theoretical study of natural convection heat transfer from downward-facing horizontal surfaces with uniform heat flux," *Int. J. Heat Mass Transfer*, vol. 16, no. 3, pp. 11-627, 1973.
- [11] G.H. Su, T.W. Wu, and K. Sugiyama, "Natural convection heat transfer of water in a horizontal gap with downward-facing circular heated surface," *Appl. Thermal Engg.*, vol. 28, nos. 11-12, pp. 1405-1416, 2008.
- [12] G.H. Su, and K. Sugiyama, "Natural convection heat transfer of water on a horizontal downward facing stainless steel disk in a gap under atmospheric pressure conditions," *Annals Nuclear Energy*, vol. 34, nos. 1-2, pp. 93-102, 2007.
- [13] M.K. Friedrich, and D. Angirasa, "The interaction between stable thermal stratification and convection under a heated horizontal surface facing downward," *Int. J. Non-Linear Mechanics*, vol. 36, no. 5, pp. 719-729, 2001.
- [14] D.K. Edwards, and J.C. Haiad, "Average Nusselt number on the downward-facing heated plate," *Int. J. Heat Mass Transfer*, vol. 29, no. 10, pp. 1607-1609, 1986.
- [15] E. Radziemska, and W.M. Lewandowski, "Heat transfer by natural convection from an isothermal downward-facing round plate in unlimited space," *Appl. Energy*, vol. 68, no. 4, pp. 347-366, 2001.
- [16] C.E. Kwak, and T.H. Song, "Natural convection around horizontal downward-facing plate with rectangular grooves: experiments and numerical simulations," *Int. J. Heat Mass Transfer*, vol. 43, no. 5, pp. 825-838, 2000. [https://doi.org/10.1016/S0017-9310\(99\)00164-7](https://doi.org/10.1016/S0017-9310(99)00164-7).
- [17] D.W. Hatfield, and D.K. Edwards, "Edge and aspect ratio effects on natural convection from the horizontal heated plate facing downwards," *Int. J. Heat Mass Transfer*, vol. 24, no. 6, pp. 1019-1024, 1981.

- [18] Francisco Restrepo, and Leon R. Glicksman, "The effect of edge conditions on natural convection from a horizontal plate," *Int. J. Heat Mass Transfer*, vol. 7, no. 1, pp. 135-142, 1974.
- [19] R. Goldstein, and K. Lau, "Laminar natural convection from a horizontal plate and the influence of plate-edge extensions," *J. Fluid Mechanics*, vol. 129, pp. 55-75, 1983.
- [20] P.H. Oosthuizen, "A numerical study of the effect of adiabatic side sections on natural convective heat transfer from a downward facing heated horizontal isothermal surface," *Proceedings of the 26th Annual Conference of the Computational Fluid Dynamics Society of Canada*, June 10-12, 2018, Winnipeg, MN, Paper MS-223.
- [21] P.H. Oosthuizen, and A.Y. Kalendar, "Natural convective heat transfer from horizontal and near horizontal surfaces," *Springer Briefs in Applied Sciences and Technology. Thermal Engineering and Applied Science*, Springer International Publishing, 2018.

A NUMERICAL STUDY OF NATURAL CONVECTIVE HEAT TRANSFER FROM A TWO-SIDED CIRCULAR HORIZONTAL ISOTHERMAL ELEMENT HAVING A LINEARLY-INCLINED NONFLAT SURFACE

Rafiq Manna and Patrick H. Oosthuizen
Department of Mechanical and Materials Engineering
Queen's University
Kingston, ON, K7L 3N6, Canada
Email: 15rmm1@queensu.ca

Abstract—Natural convective heat transfer from the top and bottom surfaces of a two-sided circular horizontal isothermal element with a linearly-inclined nonflat surface of different heights and locations has been numerically investigated. The case where the height of the element surface increases linearly from the outer edge to a maximum at the center of the upper surface, lower surface and both upper and lower surfaces of the element has been considered. The use of the nonflat surface was to determine if heat transfer rate can be increased compared to that of the plane surface. The top and bottom surfaces of the element are assumed to be isothermal and at the same temperature which is higher than that of the surrounding fluid. The range of conditions considered is such that laminar, transitional, and turbulent flow occurs over the element. The flow was assumed to be steady and axisymmetric about the vertical center line of the circular element. The fluid properties have been assumed constant except for the density change with temperature which gives the rise to the buoyancy forces (i.e. the Boussinesq approach has been adopted). Radiation heat transfer has been neglected. The standard k -epsilon turbulence model with full account being taken of buoyancy force effects has been used and the solution has been obtained using the commercial CFD solver ANSYS FLUENT[®]. For each of the three cases considered the mean heat transfer rate from the element was expressed in terms of Nusselt number based on the diameter of the element. The Nusselt number is dependent on the Rayleigh number, on the dimensionless height of the nonflat surface and on the Prandtl number. Results have only been obtained for a Prandtl number of 0.74, which is effectively the value for air. Dimensionless heights of 0.1, 0.2 and 0.3 and Rayleigh numbers of approximately between 10^4 and 10^{14} have been considered. The results show that the use of a nonflat surface of situations considered can produce a heat transfer rate enhancement under many conditions, but this enhancement is relatively small.

Keywords-Natural Convective; Numerical; Linearly-Inclined Nonflat Surface; Two-Sided; Circular; Horizontal; Dimensionless Height; Heat Transfer Enhancement

I. INTRODUCTION

The use of the linearly-inclined nonflat surface to increase the natural convective heat transfer rate from an isothermal circular horizontal element has been numerically undertaken. The main aim of the present study is to determine whether the heat transfer rate can be increased using this approach. The increase in the heat transfer rate by the use of such surface is associated with the increase in the effective area and with the flow changes over the surface. Fig. 1 shows a section view of the element which represents the situation considered here.

Natural convective heat transfer from horizontal two-sided elements has been barely studied in the past, e.g., see [1-10]. The use of a wavy surface to increase the heat transfer rate from horizontal elements under various situations has been widely considered, see [11-17]. Few studies, however focused on the two-sided element, e.g. see [18]. It has been indicated from these studies that there is no significant enhancement in the heat transfer rate in many situations when the wavy surface is being used. The use of a nonflat surface to increase the convective heat transfer from a horizontal circular element has been discussed in a very limited studies in the literature, e.g., see [19] which in most gave attention to the situation when the element is single-sided (i.e. one surface of the element is heated). Therefore, the use of a linearly-inclined nonflat surface to increase the heat transfer rate from a two-sided circular horizontal isothermal element has been numerically conducted in the present study.

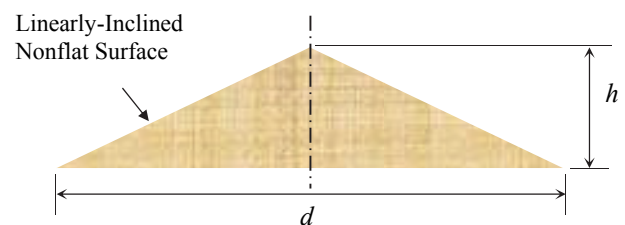


Figure 1. Flow situation considered.

II. SOLUTION PROCEDURE

The flow has been assumed to be steady, two-dimensional and axisymmetric about the vertical center line of the circular heated element, see Fig. 1. The Boussinesq approximation has been used which states that the fluid properties have been assumed to be constant except for the density change with temperature which generates the buoyancy forces. The standard k -epsilon turbulence model with full account being taken of buoyancy force effects has been applied in all situations considered and hence it could be determined when transition to turbulence occurs. This approach has been widely used in the previous studies, see [20-27] and it has been indicated from these studies that for the type of flow situation considered in the present study, the prediction of when transition occurs is of acceptable accuracy. The governing equations subject to the boundary conditions have been solved numerically using the commercial CFD solver ANSYS FLUENT[®]. To ensure that the results obtained are grid independent, a grid-independence using a wide range of grid points and a convergence-criteria independence testing was done and the results presented here are grid-independent to better than one per cent.

III. RESULTS

The solution has the following parameters:

1. The Rayleigh number, Ra , based on the diameter, d , of the circular element (m) and the difference between the element surface temperature, T_w (K), and the temperature of the fluid far from the element, T_f (K), i.e.:

$$Ra = \frac{g \beta \alpha^3 (T_w - T_f)}{\nu \alpha} \quad (1)$$

where, g , is the gravitational acceleration (m/s^2), β , is the bulk coefficient of expansion (K^{-1}), ν , is the kinematic viscosity (m^2/s) and α , is the thermal diffusivity (m^2/s).

2. The dimensionless height of the nonflat surface, H , which is defined as:

$$H = \frac{h}{a} \quad (2)$$

where, h , is the height of the nonflat surface of the circular element (m), see Fig. 1.

3. The Prandtl number, Pr .

Results have been obtained only for a Prandtl number of 0.74, which is the value for air. Nonflat surface dimensionless heights of 0.1, 0.2 and 0.3 located on top side, bottom side and both top and bottom sides of the circular element and Rayleigh numbers of approximately between 10^4 and 10^{14} have been considered.

The mean heat transfer rate from the heated surface, \bar{Q}' (W) has been expressed in terms of a mean Nusselt number based on the diameter, d , of the circular element and the difference between the element surface temperature, T_w , and the temperature of the fluid far from the element, T_f . The mean Nusselt numbers for the top surface, Nu_{top} , the bottom surface, Nu_{bottom} , and for the entire surface of the element,

Nu_{total} , have been considered. The following Nusselt numbers have therefore been introduced:

$$Nu_{top} = \frac{\bar{Q}'_{top} d}{k A_b (T_w - T_f)} \quad (3)$$

$$Nu_{bottom} = \frac{\bar{Q}'_{bottom} d}{k A_b (T_w - T_f)} \quad (4)$$

$$Nu_{total} = \frac{\bar{Q}'_{total} d}{k A_{total} (T_w - T_f)} \quad (5)$$

where \bar{Q}'_{top} , \bar{Q}'_{bottom} , and \bar{Q}'_{total} are the mean heat transfer rate from the top, bottom, and the entire surface of the heated element, respectively (W), k is the thermal conductivity (W/mK) and where, A_b and A_{total} , are the base area of the upper and the lower surfaces of the element (i.e. the area of the plane flat surface), and the total area of the heated surfaces of the element (m^2), respectively. Therefore:

$$\bar{Q}'_{total} = \bar{Q}'_{top} + \bar{Q}'_{bottom} \quad (6)$$

$$A_b = \frac{\pi}{4} d^2 \quad (7)$$

$$A_{total} = 2A_b \quad (8)$$

The Nusselt number given in (3) to (5) is based on the base area of the surface of the circular element, A_b , because the interest here is in the heat transfer from the circular element with nonflat surface relative to that which would exist with the circular element with plane flat surface.

Variations of the mean Nusselt number with Rayleigh number for the top and bottom surfaces of the circular element for various values of dimensionless height and when the nonflat surface is located on the top side, bottom side, both top and bottom sides of the heated element are shown in Fig. 2, Fig. 3 and Fig. 4, respectively. Attention will first be given to the results when the nonflat surface is on the top side of the circular element shown in Fig. 2. It can be seen from this figure that for the top surface of the heated element (Fig. 2a) there is a small amount of heat transfer rate enhancement for the range of Rayleigh number values considered and it is more significant at the lower values of Rayleigh number (i.e. laminar flow region) where the amount of heat transfer rate increases as the dimensionless height of the nonflat surface increases while for the bottom surface of the heated element (Fig. 2b) there is a slight enhancement in the heat transfer rate for the range of Rayleigh number values considered especially at the higher values of Rayleigh number (i.e. turbulent flow region) where it is more significant and there is no considerable effect of the variation of the dimensionless height on the heat transfer rate. Attention will next be turned to the results when the nonflat surface is on the bottom side of the circular element given in Fig. 3. This figure indicates that for the top surface of the heated element (Fig. 3a) the effect of the nonflat surface existence on the heat transfer rate is almost negligible for the range of dimensionless height and Rayleigh number values considered while for the bottom surface (Fig. 3b) there is an enhancement in the heat transfer rate with the increase of the dimensionless height for all values of Rayleigh number considered except when the dimensionless height is equal to

0.1, it will be found the heat transfer rate decreases at higher values of Rayleigh number. Lastly, the results when the nonflat surface is located on both the top and bottom sides of the circular element shown in Fig. 4 will be considered. It will be seen from this figure that for the top surface of the heated element (Fig. 4a) there is a small amount of heat transfer rate enhancement at the lower and intermediate values of Rayleigh number and the heat transfer rate increases as the dimensionless height increases except for the dimensionless height of 0.1 where the heat transfer rate associated with this value is higher than that associated with the other values of dimensionless height at the intermediate values of Rayleigh number. For the bottom surface (Fig. 4b), it can be noted that the heat transfer behavior is similar to that for the bottom surface when the nonflat surface is located on the bottom side of the circular element.

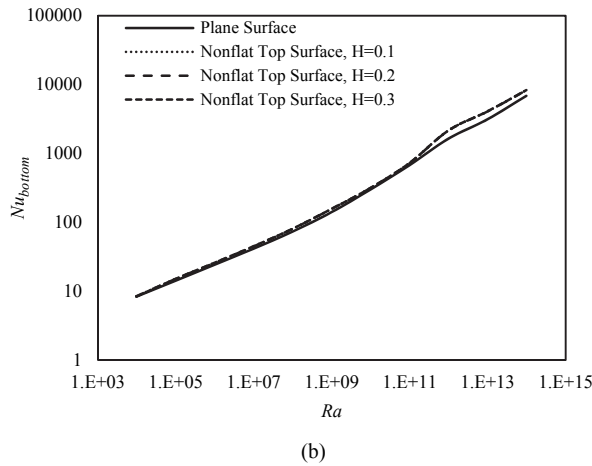
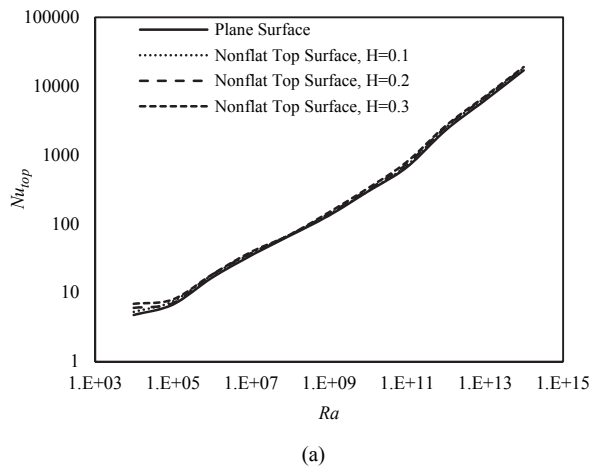


Figure 2. Variations of the mean Nusselt number with Rayleigh number for the circular element when the nonflat surface is on the top surface for various values of dimensionless height, H , (a) top surface and (b) bottom surface.

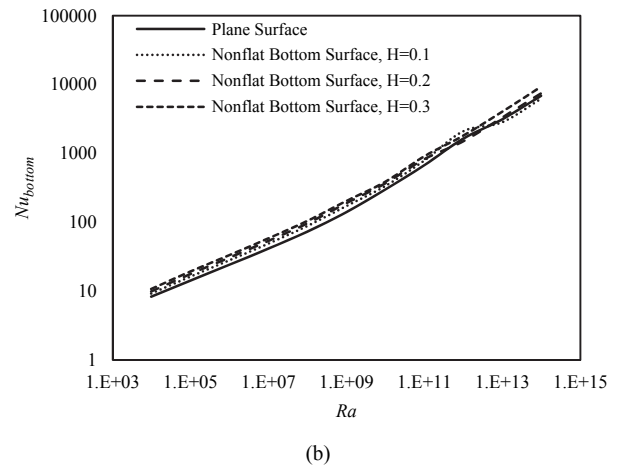
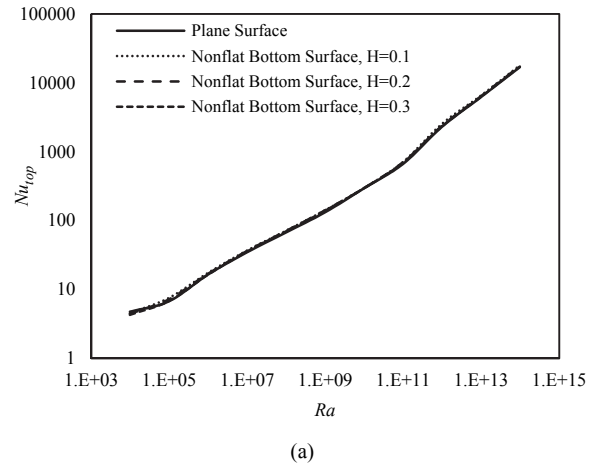
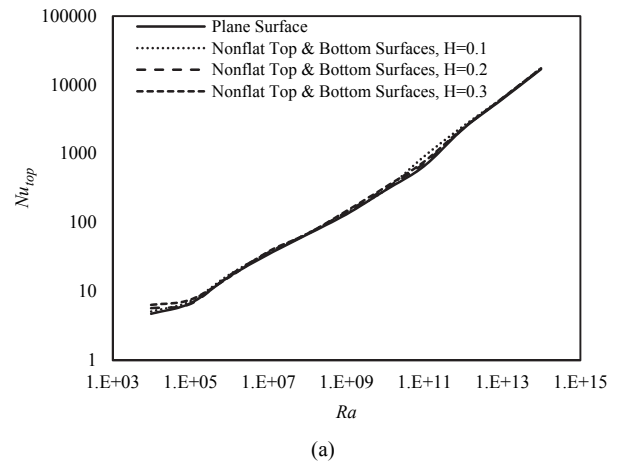


Figure 3. Variations of the mean Nusselt number with Rayleigh number for the circular element when the nonflat surface is on the bottom surface for various values of the dimensionless height, H , (a) top surface and (b) bottom surface.



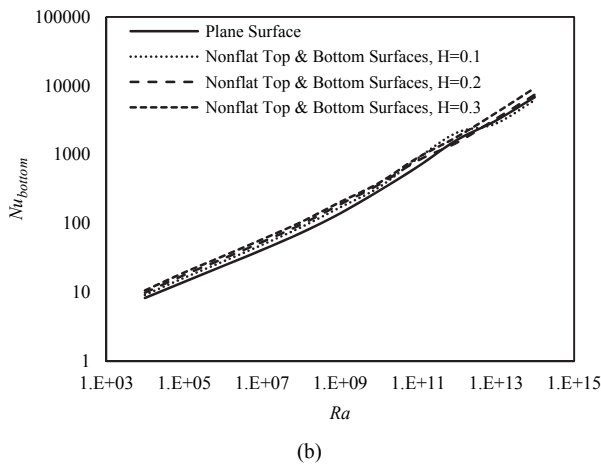
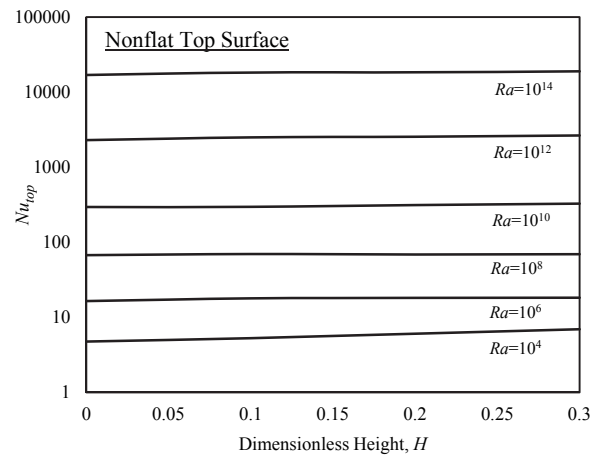


Figure 4. Variations of the mean Nusselt number with Rayleigh number for the circular element when the nonflat surface is on the top and bottom surfaces for various values of dimensionless height, H , (a) top surface and (b) bottom surface.

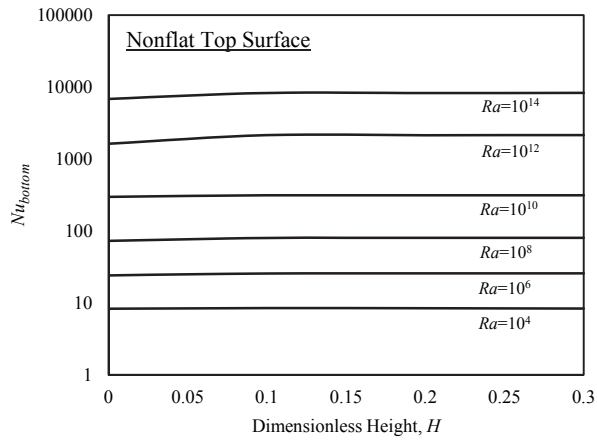
To further illustrate the effect of the dimensionless height of the nonflat surface on the heat transfer rate, variations of the mean Nusselt number with the dimensionless height for the top and bottom surfaces of the circular element for the range of Rayleigh number values considered and when the nonflat surface is located on the top side, bottom side, both top and bottom sides of the circular element are shown in Fig. 5, Fig. 6 and Fig. 7, respectively. Firstly, it can be indicated from the results when the nonflat surface is being on the top side of the circular element given in Fig. 5 that for the top surface of the heated element (Fig. 5a), the dimensionless height variation has an almost negligible effect on the Nusselt numbers except at the lower values of Rayleigh number (approximately less than 10^6). For the bottom surface of the heated element (Fig. 5b), it can be seen that the variation of the dimensionless height has a negligible effect on the Nusselt number except at the higher values of Rayleigh number (approximately higher than 10^{11}), this effect being significant at lower values of dimensionless height (approximately less than 0.1). Attention will secondly be given to the results when the nonflat surface is on the bottom side of the circular element shown in Fig. 6. This figure shows that for the top surface of the heated element (Fig. 6a) the variation of the dimensionless height has no significant effect on the Nusselt numbers unlike the case for the bottom surface (Fig. 6b) where this effect is significant, and the nature of this effect is dependent on the value of Rayleigh number. Lastly, the results when the nonflat surface is being located on both the top and bottom surfaces of the circular element given in Fig. 7 will be considered. It will be seen from this figure that the effect of the dimensionless height variation has an almost negligible effect on the Nusselt numbers for the top surface of the heated element (Fig. 7a) except at the lower values of Rayleigh number (approximately less than 10^6) while this effect is significant for the bottom surface of the heated element (Fig. 7b).

Lastly, an illustration of the effect of the location of the nonflat surface on the circular element on the heat transfer rate will be given. Variations of the mean Nusselt number with

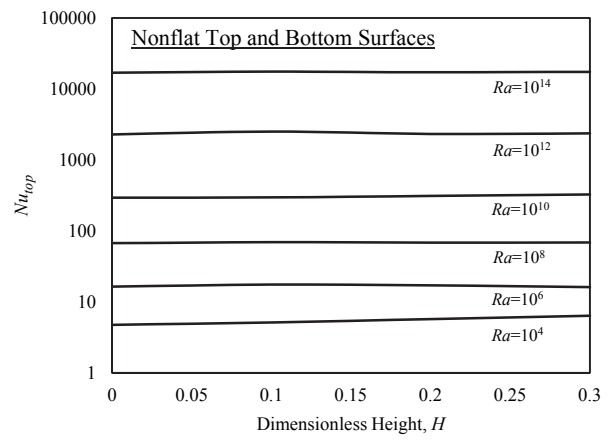
Rayleigh number for the top and bottom surfaces of the circular element at the considered nonflat surface locations on the element for dimensionless height values of 0.1 and 0.3 are given in Figs. 8 and 9, respectively. It will be noted from these figures that the Nusselt number values and hence the heat transfer rates are almost the same when the nonflat surface is either located on the bottom side or on both the top and bottom sides of the heated element in all cases considered except at the intermediate values of Rayleigh number for the dimensionless height value of 0.1 and at the lower values of Rayleigh number for the dimensionless height value of 0.3. Figure 8 shows that for a dimensionless height value of 0.1, the location of the nonflat surface on the heated element does not play a big role in the heat transfer rate change for the top surface of the heated element (Fig. 8a) while the case is different for the bottom surface as can be seen from Fig. 8b such that the heat transfer rate obtained when the nonflat surface is either located on the bottom side or on both the top and bottom sides of the heated element is a little bit higher than that obtained when the nonflat surface is located on the top side at lower and intermediate values of Rayleigh number. At higher values of Rayleigh number, the heat transfer rate is relatively higher when the nonflat surface is located on the top side of the heated element than that when the nonflat surface is either located on the bottom side or on both the top and bottom sides. For the results obtained for the other dimensionless height value of 0.3 given in Fig. 9, it can be indicated that for the top surface of the heated element (Fig. 9a) the heat transfer rate is a little bit higher when the nonflat surface is located on the top side of the heated element, this effect being relatively significant at lower values of Rayleigh number. It can be also seen from this figure that the heat transfer rate when the nonflat surface is on both the top and bottom sides of the heated element is higher than that when the nonflat surface is on the bottom side at the lower values of Rayleigh number. For the results of the bottom surface of the heated element given in Fig. 9b, it will be seen that when the nonflat surface is either on the bottom side or on both the top and bottom sides of the heated element the heat transfer rate is higher than that existing when the nonflat surface is on the top side for the Rayleigh number values of up to nearly 10^{11} after which this behavior is reversed until at Rayleigh number value of approximately 10^{13} , the effect of the nonflat surface location after which being almost negligible.



(a)

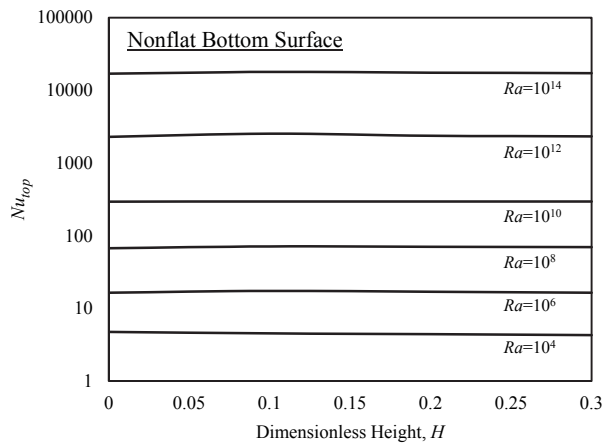


(b)

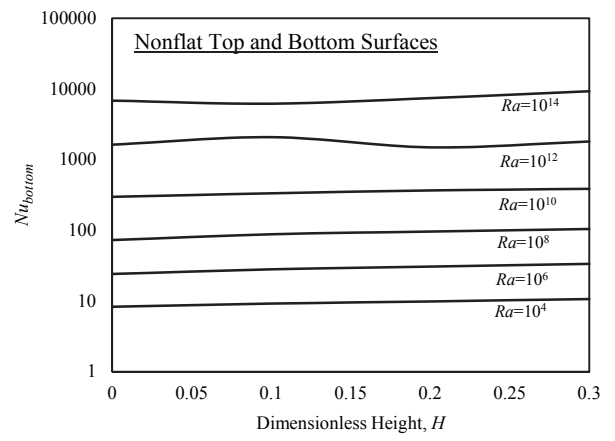


(a)

Figure 5. Variations of the mean Nusselt number for the circular element that has a nonflat top surface with the dimensionless height, H , for various values of Rayleigh number, (a) top surface and (b) bottom surface.

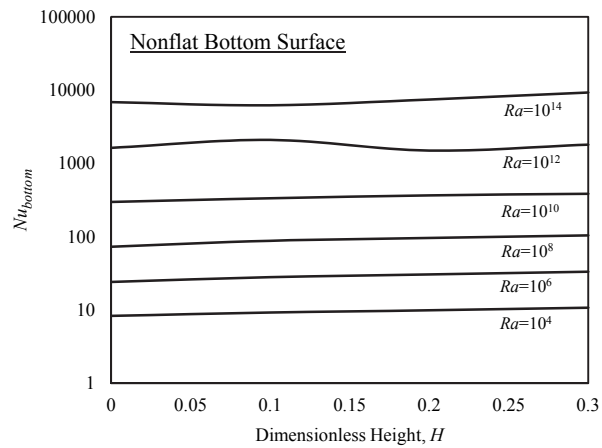


(a)

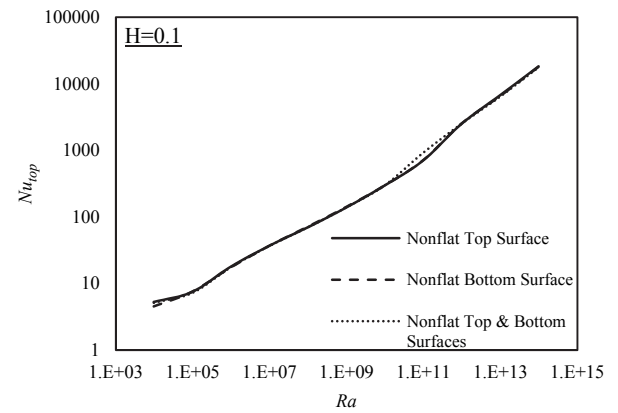


(b)

Figure 7. Variations of the mean Nusselt number for the circular element that has nonflat top and bottom surfaces with the dimensionless height, H , for various values of Rayleigh number, (a) top surface and (b) bottom surface.

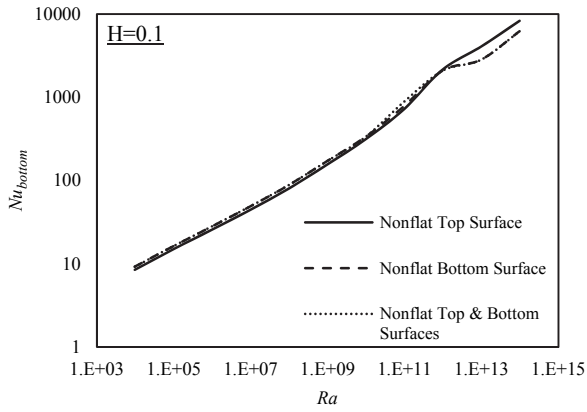


(b)



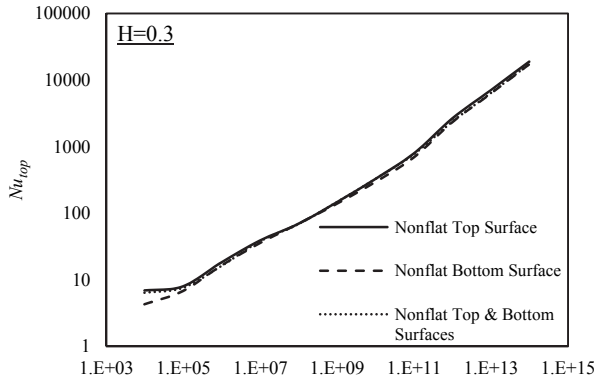
(a)

Figure 6. Variations of the mean Nusselt number for the circular element that has a nonflat bottom surface with the dimensionless height, H , for various values of Rayleigh number, (a) top surface and (b) bottom surface.

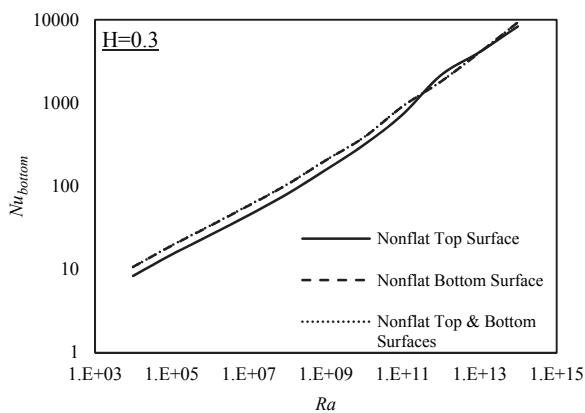


(b)

Figure 8. Variations of the mean Nusselt number with Rayleigh number for the circular element with various nonflat surface locations where the dimensionless height, H , is 0.1, (a) top surface and (b) bottom surface.



(a)



(b)

Figure 9. Variations of the mean Nusselt number with Rayleigh number for the circular element with various nonflat surface locations where the dimensionless height, H , is 0.3, (a) top surface and (b) bottom surface.

IV. CONCLUSION

Simultaneous natural convective heat transfer from the top and bottom surfaces of the circular horizontal isothermal heated element having a linearly-increased nonflat surface located on the top side, bottom side and both the top and bottom sides of the heated element has been discussed in the present paper. Various values of nonflat surface dimensionless heights and a wide range of Rayleigh number have been considered. The results of the present study show that:

1. In most cases, the existence of the nonflat surface on the heated element with various heights considered can produce heat transfer rate enhancement but this enhancement is relatively small.
2. The Nusselt numbers for the top surface are lower than those for the bottom surface at the lower Rayleigh number values but are higher than those for the bottom surface at the higher Rayleigh number values in all of the cases considered.
3. The variation of the dimensionless height of the nonflat surface has a much greater effect on the heat transfer rate from the bottom surface than on the heat transfer rate from the top surface of the heated element, the nature of this effect being dependent on the Rayleigh number value, the only significant effect on the heat transfer rate from the top surface being at the lower values of Rayleigh number.
4. The form of the variation of Nusselt number with the dimensionless height for the top and bottom surfaces of the heated element is similar for the range of Rayleigh number values considered except for the higher values of Rayleigh number.
5. The location of the nonflat surface on the heated element affects the heat transfer rate, the nature of this effect being dependent on the dimensionless height of the nonflat surface and the value of Rayleigh number.

ACKNOWLEDGMENT

This work was supported by the Natural Sciences and Engineering Research Council of Canada (NSERC) through its Discovery Grant Program (Grant RGPIN-2015-06444).

REFERENCES

- [1] B. Chambers, and T. Lee, "A numerical study of local and average natural convection Nusselt numbers for simultaneous convection above and below a uniformly heated horizontal thin plate," *J. Heat Transfer*, vol. 119, no. 1, pp. 102-108, 1997.
- [2] C.J. Kobus, and G.L. Wedekind, "An experimental investigation into forced natural and combined convective heat transfer from stationary isothermal circular disks," *Int. J. Heat Mass Transfer*, vol. 38, no. 18, pp. 3329-3339, 1995.
- [3] C.J. Kobus, and G.L. Wedekind, "An experimental investigation into natural convection heat transfer from horizontal isothermal circular disks," *Int. J. Heat Mass Transfer*, vol. 44, no. 17, pp. 3381-3384, 2001.
- [4] C.J. Kobus, and G.L. Wedekind, "An empirical correlation for natural convection heat transfer from thin isothermal circular disks at arbitrary angles of inclination," *Int. J. Heat Mass Transfer*, vol. 45, no. 5, pp. 1159-1163, 2002.

- [5] J.J. Wei, B. Yu, H.S. Wang, and W.Q. Tao, "Numerical study of simultaneous natural convection heat transfer from both surfaces of a uniformly heated thin plate with arbitrary inclination," *Int. J. Heat Mass Transfer*, vol. 38, nos. 4-5, pp. 309-317, 2002.
- [6] J.J. Wei, B. Yu, and Y. Kawaguchi, "Simultaneous natural-convection heat transfer above and below an isothermal horizontal thin plate," *Numer. Heat Transfer; Part A: Applications*, vol. 44, no. 1, pp. 39-58, 2003.
- [7] L. Fontana., "Free convection heat transfer from an isothermal horizontal thin strip: the influence of the Prandtl number," *J. Thermal Science*, vol. 23, no. 6, pp. 586-592, 2014.
- [8] M. Corcione, E. Habib, and A. Campo, "Natural convection from inclined plates to gases and liquids when both sides are uniformly heated at the same temperature," *Int. J. Thermal Sciences*, vol. 50, no. 8, pp. 1405-1416, 2011.
- [9] P.H. Oosthuizen, and A. Kalendar, "A Numerical study of the simultaneous natural convective heat transfer from the upper and lower surfaces of a thin isothermal horizontal circular plate," *Proc. ASME Int. Mechanical Engg. Congress and Exposition, Paper IMECE2016-65540*, 2016.
- [10] R. Manna, and P.H. Oosthuizen, "A numerical study of natural convective heat transfer from two-sided circular and square heated horizontal isothermal plates having a finite thickness," *Proc. 3rd Thermal & Fluids Engg. Conf. (TFEC)*, Paper TFEC-21540, 2018.
- [11] P.H. Oosthuizen, "A numerical study of natural convective heat transfer from a horizontal isothermal surface with rectangular surface roughness elements," *Proc. 1st Pacific Rim Thermal Engg. Conf. (PRTEC 2016)*, Paper PRTEC-14630, 2016.
- [12] P.H. Oosthuizen, "A numerical study of the effect of triangular waves on natural convective heat transfer from an upward facing heated horizontal isothermal surface," *Proc. ASME 2016 Int. Mech. Engg. Congress and Exposition, Paper IMECE2016-65716*, 2016.
- [13] P.H. Oosthuizen, "A study of the effect of triangular and rectangular surface waves on the natural convective heat transfer from a circular upward facing heated horizontal isothermal surface," *Proc. 13th International Conf. on Heat Transfer, Fluid Mechanics and Thermodynamics*, Paper 1570340040, 2017.
- [14] S. Prétot, B. Zeghmati, and Ph. Caminat, "Influence of surface roughness on natural convection above a horizontal plate," *Advances in Engineering Software*, vol. 31, no. 10, pp. 793-801, 2000.
- [15] S. Prétot, J. Miriela, Y. Bailly, and B. Zeghmati, "Visualization and simulation of the natural-convection flow above horizontal wavy plates," *Numer. Heat Transfer, Part A: Applications*: vol. 43, no. 3, pp. 307-325, 2003.
- [16] S. Siddiqa, and M.D. Anwar Hossain, "Natural convection flow over wavy horizontal surface," *Advances in Mechanical Engineering*, vol. 5, Article ID 743034, 2013.
- [17] S. Siddiqa, M.D. Anwar Hossain, and R.S.R. Gorla, "Natural convection flow of viscous fluid over triangular wavy horizontal surface," *Computers & Fluids*, vol. 106, pp. 130-134, 2015.
- [18] S.D.R. Oliveira, and P.H. Oosthuizen, "A numerical study of the simultaneous natural convective heat transfer from the top and bottom surfaces of a thin horizontal plate having a wavy surface," *Proc. 26th Annual Conf. of the Computational Fluid Dynamics Society of Canada*, Paper CFD2018-MS-224, 2018.
- [19] P.H. Oosthuizen, "A numerical study of natural convective heat transfer from an upward facing circular heated horizontal isothermal element with a non-flat surface," *Proc. 3rd Thermal & Fluids Engg. Conf. (TFEC 2018)*, Paper TFEC-21539, 2018.
- [20] A. Kalendar, A.Y. Kalendar, and Y. Alhendal, "Evaluation of turbulence models for natural and forced convection from flat plates," *Computational Thermal Sciences: An International Journal*, vol.8, no. 6, pp. 567-582, 2016.
- [21] A.M. Savill, "Evaluating turbulence model predictions of transition. An ERCOFTAC special interest group project," *Applied Scientific Research*, vol. 51, nos. 1-2, pp. 555-562, 1993.
- [22] J. Xamán, G. Álvarez, L. Lira, and C. Estrada, "Numerical study of heat transfer by laminar and turbulent natural convection in tall cavities of façade elements", *Energy and Buildings*, vol. 37, no 7, pp. 787-794, 2005.
- [23] O.A. Plumb, and L.A. Kennedy, "Application of a k-ε turbulence model to natural convection from a vertical isothermal surface," *J. Heat Transfer*, vol. 99, no. 1, pp. 79-85, 1977.
- [24] P.H. Oosthuizen, and D. Naylor, "A numerical study of laminar-to-turbulent transition in the flow over a simple recessed window-plane blind system," *Proc. 4th Canadian Solar Buildings Conf.*, 2009.
- [25] R.C. Schmidt, and S.V. Patankar, "Simulating boundary layer transition with low-Reynolds-number k-ε turbulence models: Part 1-An evaluation of prediction characteristics," *J. Turbomachinery*, vol. 113, no. 1, pp. 10-17, 1991.
- [26] X. Albets-Chico, A. Oliva, and C.D. Perez-Segarra, "Numerical experiments in turbulent natural convection using two-equation eddy-viscosity models," *J. Heat Transfer*, vol. 130, no. 7, pp. 072501-1-072501-11, 2008.
- [27] X. Zheng, C. Liu, F. Liu, and C.-I. Yang, "Turbulent transition simulation using the k- ω model," *Int. J. Numer. Methods Eng.*, vol. 42, pp. 907-926, 1998.

A NUMERICAL STUDY OF THE FORCED CONVECTION BOILING OF NANOFLUID REFRIGERANT

Diana C. Hernández

Grupo de Energía y Termodinámica
Universidad Pontificia Bolivariana
Medellín, Colombia
dianacarolina.hernandez@upb.edu.co

Mateo Arango

Grupo de Energía y Termodinámica
Universidad Pontificia Bolivariana
Medellín, Colombia
mateo.arango@upb.edu.co

Zulamita Zapata-Benabithé

Grupo de Energía y Termodinámica
Universidad Pontificia Bolivariana
Medellín, Colombia
zulamita.zapata@upb.edu.co

César Nieto-Londoño

Grupo de Investigación en Ingeniería Aeroespacial
Universidad Pontificia Bolivariana
Medellín, Colombia
cesar.nieto@upb.edu.co

Fernando Toapanta-Ramos

Facultad de Ingeniería Mecánica
Universidad Politécnica Salesiana
Quito, Ecuador
ltoapanta@ups.edu.ec

Abstract—This work comprises the theoretically and computationally study of boiling forced convection of nano-refrigerant R134a/Al₂O₃ through a horizontal tube under 25000 W/m² constant heat flux on the external tube surface. The finite volume method is applied to solve the equations for the multiphase flow together with the turbulence model $\kappa - \epsilon$ and the boiling model to quantify the phase change during the boiling of the nanorefrigerant along the tube. Initially, the numerical results obtained for the boiling of the refrigerant with and without nanoparticles are analyzed; it is possible to identify the phase change processes that take place along the pipeline. From the results obtained, it is possible to conclude that the addition of nanoparticles improves the thermal properties of the refrigerant. However, boiling is a complex phenomenon and the correlations used do not fully predict its behavior.

Forced convective boiling; refrigerant-based nanofluid; phase change; multiphase flow

I. INTRODUCTION (HEADING 1)

Nanofluids are a suspension of particles from 0 to 100 nm in a base fluid presenting thermophysical properties different from those of the base fluid due to the addition of metal particles or metal oxides to increase the thermal conductivity and convective heat transfer coefficient [1]. The main characteristic of nanofluids is the ability to improve heat transfer without altering

the Newtonian behavior of the base fluid with the addition of small concentrations of solid particles [2].

Nanoparticles are used to improve the thermophysical properties of heat transfer fluids (like refrigerants) in order to obtain a higher efficiency of refrigeration and air conditioning systems. Rheological and heat transfer mechanisms studies have been reported for different nanoparticles concentrations of CuO, Al₂O₃, SiO₂, diamond, CNT (carbon nanotubes), TiO₂, considering refrigerants such as R11, R113, R123, R134a and R141b [3].

The heat transfer rate during the phase change, at both the evaporator and condenser heat exchangers, is one of the main factors that affect the efficiency of refrigeration systems [4]. The heat transfer during convective force boiling with refrigerant-based nanofluid was studied by Peng et al. [4], using a mixture of R113 and CuO particles. The experimental tests show an increase of 29.7% in the heat transfer coefficient due to the addition of CuO nanoparticles. The same authors also proposed a correlation for the heat transfer in nano refrigerants, with a deviation of $\pm 20\%$ respect to the experimental results.

The studies reported in the literature focus mainly on the analysis of heat transfer in single-phase nanofluids (i.e., no phase change at the base fluid). However, the study of forced convective boiling of nanofluids in pipes is minimal, a common condition in refrigeration processes, heat exchanger and air conditioning systems. The boiling and the flow regime of

nanofluids in multiphase base fluids are dominated by on properties such as specific heat, density, surface tension, enthalpy of evaporation, among others [5]. In general, there is a need to develop studies that allow understanding of how multiphase fluid properties vary through the boiling process and its effects over all the refrigeration cycle performance.

Mahbulul et al. [6] showed the evaluation of thermophysical properties, pressure drop and heat transfer for Al_2O_3 spherical nanoparticles with 30 nm diameter, suspended in R-134a refrigerant, for nanoparticles concentration between 1 and 5% by volume within a circular cross-section tube. The tube diameter was 8.12 mm with a length of 1500 mm. The inlet pressure and temperature were 706 kPa and 300 K, respectively; with a uniform mass flux of $100 \text{ kg/m}^2\text{s}$, that corresponds to a 5 m/s uniform velocity at the entrance. The thermal boundary condition at the tube's wall was a constant heat flux of 5000 W/m^2 . The authors reported an increase in both heat transfer and pressure drop values as nanoparticles volume concentration raise. This trend would imply an improvement in the performance of the refrigeration systems as both energy efficiency and cooling capacity get better. Additionally, they established that the thermal conductivity, the viscosity, the convective heat transfer and the heat transfer coefficient for the forced convective boiling of the nano-refrigerant ($\text{Al}_2\text{O}_3/\text{R-134a}$) increase with the augment of the volume fraction of the nanoparticles and the temperature, while the thermal conductivity tends to decrease as the particle size gets bigger.

In this work, the forced convection of the refrigerant-based nanofluid $\text{R134a}/\text{Al}_2\text{O}_3$ is analyzed theoretically and computationally through a horizontal circular tube with a constant heat flux at the tube's wall. The equations for the multiphase flow together with the turbulence model $\kappa - \epsilon$ and the boiling model are coupled solved by using the finite volume method implemented in ANSYS FLUENT, to quantify the phase change during the boiling of the nanorefrigerant along the tube. In the following sections, the models used for the development of flow pattern maps are presented, for both biphasic substances (liquid-vapor) and multiphase fluids (liquid-vapor-particles). Additionally, the flow pattern maps created to compare theoretical and computational cases are presented, and then a list is made of the methods and models used for the numerical study. Finally, the results and conclusions of the investigation are presented.

II. MODELS FOR FORCED CONVECTION BOILING

The boiling of fluid occurs when the temperature of the surface exceeds the saturation temperature corresponding to the liquid's pressure. During this process, a heat transfer from the solid surface to the liquid occurs causing a phase change from liquid to vapor. One of the main characteristics of the boiling process is the formation of vapor bubbles, which grow and detach from the surface generating a change in the movement of the fluid near the surface. The convective heat transfer coefficient increases as the phase change occurred due to the combination of the effects of latent heat and buoyancy-driven flow effects [7].

It is called pool boiling when the liquid is at rest and force convective boiling when the movement of the fluid is induced

by external means. In the latter, two phenomena are presented: (1) the nucleated boiling, and (2) the convective boiling. For the study of heat transfer, nucleated boiling is usually calculated from correlations for pool boiling, while for convective boiling, single phase correlations are used, which are modified by a correction factor. This factor usually increases the convective heat transfer coefficient due to the turbulence associated with the density variation of the vapor and liquid phases present in the streams [8].

Different correlations have been proposed to determine the heat transfer coefficient during the phase change in the boiling process. These include correlations of superposition [9], separate effects [10] and asymptotic type [11]. Next, a description of each of them is presented.

A. *Chen's forced convective boiling correlation (1963)*

Chen [9] proposed a correlation for forced convective boiling in vertical tubes. This correlation supposed a superposition of convective and nucleate boiling during the heat transfer process. The pool boiling is evaluated with Forster & Zuber heat transfer coefficient [12]. The coefficient of convective heat transfer for the liquid phase is found using the Dittus-Boelter correlation [13].

B. *Shah's nucleation based correlation (1982)*

Shah [10] developed a correlation for both vertical and horizontal flows, depending on the value of dimensionless numbers. Boiling number Bo , which represents the relationship between the actual heat flow and the maximum heat flow to complete the liquid's evaporation, characterizes the nucleate heat flow boiling. The heat transfer coefficient for the two phases is determined by taking the highest value between the convective heat transfer coefficient and the nucleate boiling heat transfer.

C. *Asymptotic model by Steiner-Taborek (1992):*

Steiner-Taborek [11] developed an asymptotic model for the local heat transfer coefficient in vertical flows. It consists of the evaluation of correlations for both nucleated boiling and forced convective heat transfer. A correction factor is applied to relate the increase in convection in the presence of two phases with the coefficient for a single phase flow at high velocities.

D. *Model of the local evaporative flow pattern of Kattan-Thome-Favrat (1998a, 1998b, 1998c)*

The model presented by Kattan-Thome-Favrat [14], [15], [16] is based on the flow-pattern biphasic maps for the boiling in horizontal tubes developed by themselves. This method covers fully stratified flows, stratified-undulating, intermittent, annular and annular flows with partial drying.

III. FLOW PATTERN MAPS

Flow patterns for the boiling process can be represented into a flow map, that present most flow characteristics obtained from observations of these patterns. In this work, is presented the development of the flow pattern maps for the boiling of refrigerant R134a and nano-refrigerant $\text{Al}_2\text{O}_3/\text{R-134a}$

considering the impact factor of the nanoparticles. Results from both flow pattern maps are compared with the results obtained through the computational analysis with ANSYS FLUENT.

In this analysis, refrigerant flow through a 6 mm diameter circular cross-section tube is considered; at the tube's inlet is defined a velocity of 0.083 m/s, equivalent to a mass velocity of 100 kg/m²s; an average heat flux of 25000 W/m² is applied to the tube's wall.

A. Flow pattern map for refrigerant R134a

The heat transfer coefficient for local boiling (α_{tp}) is evaluated as a function of the dry tube perimeter angle (θ_{dry}), the heat transfer coefficient in the dry zone (α_{vap}), and the heat transfer coefficient in the wet zone (α_{wet}); these parameters are evaluated with an asymptotic model that takes into account the coefficients associated to the nucleated boiling (α_{nb}) and the convective boiling (α_{cb}). Cooper's expression is used to determine the contribution of nucleation [17]:

$$\alpha_{tp} = \frac{d_i \theta_{dry} \alpha_{vap} + d_i (2\pi - \theta_{dry}) \alpha_{wet}}{2\pi d_i}, \quad (1)$$

where d_i is the tube's internal diameter. The heat transfer coefficient in the wet zone is expressed as follows,

$$\alpha_{wet} = (\alpha_{nb}^3 + \alpha_{cb}^3)^{1/3}, \quad (2)$$

where the nucleate boiling heat transfer is evaluated as,

$$\alpha_{nb} = 55 Pr^{0.12} (-\log_{10} Pr)^{-0.55} M^{-0.5} \dot{q}^{0.67} \quad (3)$$

being Pr , the Prandtl number, M the molecular weight and \dot{q} is the heat flow. The convective boiling coefficient is evaluated as,

$$\alpha_{cb} = 0.0133 \left[\frac{4 \dot{m} (1-x) \delta}{(1-\varepsilon) \mu_l} \right]^{0.69} \left[\frac{C_{pl} \mu_l}{k_l} \right]^{0.4} \frac{k_l}{\delta}, \quad (4)$$

where \dot{m} is the mass flow, x the vapor quality, δ is the liquid film thickness in the annular phase, ε the void vapor fraction, and μ_l , C_{pl} and k_l are the dynamic viscosity, the specific heat and the thermal conductivity of the liquid phase.

The heat transfer coefficient of the vapor phase is obtained from the Dittus-Boelter correlation [13], which is defined for turbulent flow as,

$$\alpha_{vap} = 0.023 \left[\frac{\dot{m} x d_i}{\varepsilon \mu_G} \right]^{0.8} \left[\frac{C_{p,G} \mu_G}{k_G} \right]^{0.4} \frac{k_G}{d_i}, \quad (5)$$

where μ_G , $C_{p,G}$ and k_G are the dynamic viscosity, the specific heat and the thermal conductivity of the vapor phase

The void vapor fraction is predicted with the Rouhani-Axelsson model [18] modified by Steiner [19] for horizontal flows, as

$$\varepsilon = \frac{x}{\rho_G} \left\{ [1 + 0.12(1-x)] \left(\frac{x}{\rho_G} + \frac{1-x}{\rho_L} \right)^{-1} + \frac{1.18}{\dot{m}} \left[\frac{g \sigma (\rho_L - \rho_G)}{\rho_L^2} \right]^{1/4} (1-x) \right\}, \quad (6)$$

where g represents the gravity, σ is the surface tension, ρ_L is the liquid density and ρ_G is the vapor density.

The cross-sectional area occupied by the liquid phase (A_L) is given by the following expression, where A is the cross-sectional area of the tube.

$$A_L = A(1 - \varepsilon) \quad (7)$$

For fully stratified flow, the angle of the liquid layer at the bottom of the tube (θ_{strat}), is calculated iteratively using the expression:

$$A_L = 0.5 r_i^2 [(2\pi - \theta_{strat}) - (\sin(2\pi - \theta_{strat}))], \quad (8)$$

where dry angle (θ_{dry}) is

$$\theta_{dry} = \theta_{strat} \frac{(\dot{m}_{high} - \dot{m})}{(\dot{m}_{high} - \dot{m}_{low})}, \quad (9)$$

being \dot{m}_{high} the mass flow in the wavy condition, and \dot{m}_{low} corresponds to the mass flow for the stratified regime. For the conditions when the liquid occupies less than half the cross-sectional area of the tube with low quality ($\delta < d_i/2$), the thickness of the liquid film is determined by:

$$\delta = \frac{d_i}{2} - \left[\left(\frac{d_i}{2} \right)^2 - \frac{2A_L}{2\pi - \theta_{dry}} \right]^{1/2}. \quad (10)$$

For the cases when $\delta > d_i/2$, which is an unreal situation, the expression used is $\delta = d_i/2$.

Kattan-Thome-Favrat [14]-[16] defined the transition boundaries in terms of the mass velocity G for the construction of the flow pattern map, which vary with the quality of the vapor phase. The first boundary G_{strat} , delimits the transition between the stratified regime and the stratified-wavy regime, as follows

$$G_{strat} = \left[\frac{226.3^2 A_{LD} A_{VD}^2 \rho_V (\rho_L - \rho_V) \mu_L g}{x^2 (1-x) \pi^3} \right]^{1/3}, \quad (11)$$

where A_{LD} and A_{VD} are geometric parameters [14], [15].

The next boundary transition, G_{wavy} , is between the stratified-wavy regime and the intermittent-annular regime, and is expressed by

$$G_{wavy} = \left[\frac{16A_{VD}^3 g d_i \rho_L \rho_V}{x^2 \pi^2 (1 - (2h_{LD} - 1)^2)^{0.5}} \right]^{0.5} + 50, \quad (12)$$

where We and Fr are the Weber and Froude numbers, respectively. F_1 and F_2 are parameters defined in (13) and (14), where \dot{q}_{crit} represents the critical heat flow.

$$F_1 = -48.24 \left(\frac{\dot{q}}{\dot{q}_{crit}} \right) \quad (13)$$

$$F_2 = 9.65 \left(\frac{\dot{q}}{\dot{q}_{crit}} \right) + 1.053 \quad (14)$$

The boundary between the intermittent and annular regimes x_{IA} is defined by:

$$x_{IA} = \left[\left(0.34^{1/0.875} \left(\frac{\rho_V}{\rho_L} \right)^{-1/1.75} \left(\frac{\mu_V}{\mu_L} \right)^{-1/7} \right) + 1 \right]^{-1} \quad (15)$$

The transition between the annular and dry flow, G_{dryout} , and the transition between the dry flow and the mist flow, G_{mist} , are defined as:

$$G_{dryout} = \left[\frac{1}{0.235 \left(\ln \left(\frac{0.58}{x} \right) + 0.52 \right) \left(\frac{d_i}{\rho_V \sigma} \right)^{-0.17}} \right]^{0.926} \left(\frac{1}{\rho_V (\rho_L - \rho_V) g d_i} \right)^{-0.37} \left(\frac{\rho_V}{\rho_L} \right)^{-0.25} \left(\frac{\dot{q}}{\dot{q}_{crit}} \right)^{-0.7} \quad (16)$$

$$G_{mist} = \left[\frac{1}{0.0058 \left(\ln \left(\frac{0.61}{x} \right) + 0.57 \right) \left(\frac{d_i}{\rho_V \sigma} \right)^{-0.38}} \right]^{0.943} \left(\frac{1}{\rho_V (\rho_L - \rho_V) g d_i} \right)^{-0.15} \left(\frac{\rho_V}{\rho_L} \right)^{0.09} \left(\frac{\dot{q}}{\dot{q}_{crit}} \right)^{-0.27} \quad (17)$$

A modification of this model was implemented for the wavy stratified flow area, in order to calculate the angle of the dry perimeter of the tube [16]. The following considerations were taken:

- At the slug Zone: $\theta_{dry} = 0$.
- At the stratified-wavy zone:

$$\theta_{dry} = \theta_{strat} \left[\frac{G_{wavy} - G}{G_{wavy} - G_{strat}} \right]^{0.61}$$

- At the slug stratified-wavy zone:

$$\theta_{dry} = \theta_{strat} \left(\frac{x}{x_{IA}} \right) \left[\frac{G_{wavy} - G}{G_{wavy} - G_{strat}} \right]^{0.61}$$

Figure 1 shows the flow pattern map for forced convection boiling of refrigerant R134a at 100 kg/m²s. The dotted lines represent the transition borders between each of the phase

patterns. In this case, the flow is in a stratified phase from quality 0 (in the figure it is represented with a dashed line), up to quality 0.05; then it goes through a stratified-wavy phase until the fluid reaches quality 0.85. Later it is in a dry phase until quality 0.97, and in fog phase until reaching a quality 1.

The heat transfer coefficient in Figure 1 is represented by a continuous red line, that varies considerably as the steam quality increases. Initially, it has a rapid increase up to 3400 W/m²K to the quality of 0.35, at this moment the heat transfer coefficient decreases to 1100 W/m²K for the quality of 0.45 and begins to decrease gradually until full boiling is achieved.

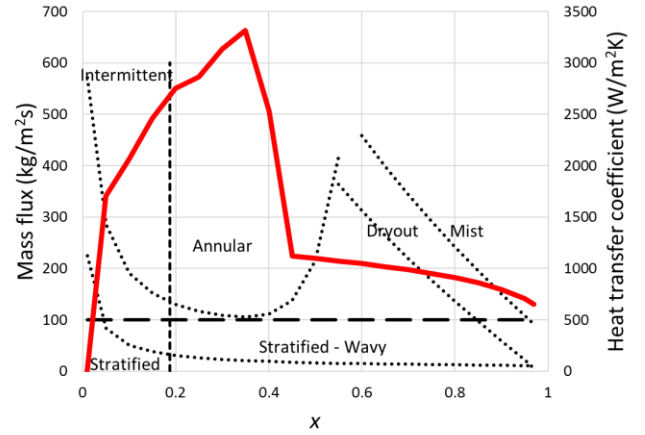


Figure 1. Flow Pattern map for forced convective boiling of refrigerant R134a at 100 kg/m²s.

B. Flow pattern map for nano-refrigerant Al₂O₃/R-134a

To predict the heat transfer coefficient for the forced convective boiling of the nano-refrigerant, (α_{ntp}), Peng correlation was used [4]. In that correlation, an impact factor (F_{HT}) is used to consider the present of nanoparticles in the flow. This impact factor affects the convective heat transfer coefficient of the refrigerant (α_{tp}) and is a function of the volume fraction of the particles (ϕ), the thermophysical properties of both the nanoparticles and the refrigerant, the vapor quality and the mass flow, as follos

$$\alpha_{r,n} = F_{HT} \alpha_{tp}, \quad (18)$$

$$F_{HT} = \exp \left\{ \phi \left[\begin{array}{l} 0.8 \frac{k_p}{k_r} - 39.94 \frac{(\rho c_p)_p}{(\rho c_p)_{r,l}} \\ -0.028G - 733.26x(1-x) \end{array} \right] \right\}, \quad (19)$$

where the subscripts p and r, l represent the properties of the nanoparticles and the liquid refrigerant, respectively.

Figure 2 shows the flow pattern map for the R134a refrigerant with 1 v/v % of Al₂O₃ nanoparticles with 30 nm diameter. The nanoparticles added to the refrigerant modifies the behavior of the heat transfer coefficient (solid blue line in the figure). As can be observed, the heat transfer coefficient decreases from 50000 to 5000 W/m²K when the steam quality attains a value of 0.45, and then gradually increase to 15000 W/m²K as the fluid becomes saturated vapor. Despite the

decrease in the heat transfer coefficient during changing phase, a significant impact of the nanoparticles is observed in the magnitude of its value due to the thermal conductivity of the nanoparticles and the specific heat thereof.

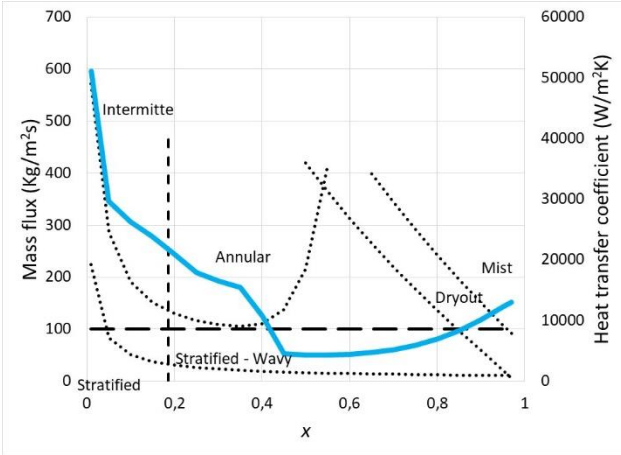


Figure 2. Flow Pattern map for forced convective boiling of nano-refrigerant $\text{Al}_2\text{O}_3/\text{R}-134\text{a}$ at $100 \text{ kg/m}^2\text{s}$.

IV. NUMERICAL SIMULATION OF FORCED CONVECTIVE HEAT TRANSFER

The Eulerian multi-phase model and the Boiling model are used to simulate the forced convection boiling in ANSYS FLUENT inside a horizontal tube of 0.006 m diameter. The constant heat flux boundary condition at the tube's wall causes the boiling of the refrigerant R134a. The general conservation equations of the Eulerian multiphase model are presented below.

A. Continuity equation for a phase

The continuity equation for each phase, q , is expressed as,

$$\frac{\partial}{\partial t} (\alpha_q \rho_q) + \nabla \cdot (\alpha_q \rho_q \vec{v}_q) = \sum_{p=1}^n (\dot{m}_{pq} - \dot{m}_{qp}) + S_q, \quad (20)$$

where α_q and ρ_q represent the volumetric fraction and the density of the phase q , respectively. \vec{v}_q is the fluid's velocity, \dot{m}_{pq} and \dot{m}_{qp} are the mass flows transfer from phase p to phase q and vice versa, respectively. The generation term S_q is zero by default, since there are no volumetric reactions in the flow.

B. Momentum balance for a phase

The momentum balance for each phase is expressed by:

$$\frac{\partial}{\partial t} (\alpha_q \rho_q \vec{v}_q) + \nabla \cdot (\alpha_q \rho_q \vec{v}_q \vec{v}_q) = -\alpha_q \nabla p + \nabla \cdot \bar{\tau}_q + \alpha_q \rho_q \vec{g} + \sum_{p=1}^n (\vec{R}_{pq} + \dot{m}_{pq} \vec{v}_{pq} - \dot{m}_{qp} \vec{v}_{qp}) + (\vec{F}_q + \vec{F}_{lift,q} + \vec{F}_{wl,q} + \vec{F}_{vm,q} + \vec{F}_{td,q}), \quad (21)$$

being $\bar{\tau}_q$ the stress-strain tensor, \vec{F}_q the body external forces, $\vec{F}_{lift,q}$ the lift force, $\vec{F}_{vm,q}$ the viscous force at the wall, $\vec{F}_{vm,q}$ the force of virtual masses, $\vec{F}_{td,q}$ the turbulent dispersion force, \vec{R}_{pq} the interaction force between the phases of the system and p is the pressure for all the phases.

C. Energy conservation

The energy balance for each phase is presented as:

$$\frac{\partial}{\partial t} (\alpha_q \rho_q h_p) + \nabla \cdot (\alpha_q \rho_q \vec{u}_q h_q) = \alpha_q \frac{\partial p_q}{\partial t} + \bar{\tau}_q : \nabla \vec{u}_q - \nabla \cdot \vec{q}_q + S_q + \sum_{p=1}^n (Q_{pq} + \dot{m}_{pq} h_{pq} - \dot{m}_{qp} h_{qp}). \quad (22)$$

Using the RPI model (Rensselaer Polytechnic Institute), the total heat flow from the wall to the liquid is calculated as the sum of the convective heat flux \dot{q}_C , the cooling heat flux \dot{q}_Q , and the evaporative heat flux \dot{q}_E , as

$$\dot{q}_W = \dot{q}_C + \dot{q}_Q + \dot{q}_E. \quad (23)$$

The convection heat flow (\dot{q}_C) is calculated considering the portion of the area covered by the fluid ($1 - A_b$), by subtracting the area covered for the nucleation bubbles (A_b), and is expressed as

$$\dot{q}_C = h_C (T_w - T_l) (1 - A_b), \quad (24)$$

where h_C is the heat transfer coefficient for the single phase, and T_w and T_l are the temperatures of the wall and the liquid, respectively. The cooling heat flow is given by:

$$\dot{q}_Q = \frac{2k_l}{\sqrt{\pi \lambda_l T}} (T_w - T_l), \quad (25)$$

where the liquid conductivity is represented by k_l , T is the periodic time, and λ_l is the thermal diffusivity ($\lambda_l = k_l / \rho_l C_{pl}$). The evaporative heat flow (\dot{q}_E) is given by

$$\dot{q}_E = V_d N_w \rho_v h_{fv}, \quad (26)$$

being V_d the volume of bubbles based on its exit diameter, N_w the active density of nucleation, ρ_v the vapor density, and h_{fv} the latent heat of vaporization. The influence area A_b is based on the exit diameter of the bubble (D_w) and the nucleation density,

$$A_b = K \frac{N_w \pi D_w^2}{4}, \quad (27)$$

where K is an empirical constant that is usually 4. The output frequency of bubbles f in the RPI model is:

$$f = \frac{1}{T} = \sqrt{\frac{4g(\rho_l - \rho_v)}{3\rho_l D_w}}. \quad (28)$$

The expression for the nucleate density is given as,

$$N_w = C^n (T_w - T_{sat})^n, \quad (29)$$

where the experimental parameters C and n were established at 210 and 1805, respectively [13]. Finally, the exit diameter of the bubble is calculated based on the empirical correlation [17]:

$$D_w = \min(0.0014, 0.0006e^{\frac{\Delta T_w}{45.0}}) \quad (30)$$

D. The standard k - ε turbulence model

The standard k - ε model with standard wall functions was adopted as the turbulence model in the boiling flow. The mixed turbulence model of the equations k - ε are:

$$\frac{\partial}{\partial t}(\rho_m k) + \nabla \cdot (\rho_m \vec{v}_m k) = \nabla \cdot \left(\left(\mu_m + \frac{\mu_{t,m}}{\sigma_k} \right) \nabla k \right) + G_{k,m} - \rho_m \varepsilon + \Pi_{k,m} \quad (31)$$

$$\frac{\partial}{\partial t}(\rho_m \varepsilon) + \nabla \cdot (\rho_m \vec{v}_m \varepsilon) = \nabla \cdot \left(\left(\mu_m + \frac{\mu_{t,m}}{\sigma_\varepsilon} \right) \nabla \varepsilon \right) + \frac{\varepsilon}{k} (C_{1\varepsilon} G_{k,m} - C_{2\varepsilon} \rho_m \varepsilon) + \Pi_{\varepsilon,m} \quad (32)$$

where $\sigma_k = 1.0$ and $\sigma_\varepsilon = 1.3$, are the Prandtl numbers for k and ε . $C_{1\varepsilon}$ and $C_{2\varepsilon}$ are constants defined as 1.44 and 1.92, respectively. The generation terms $\Pi_{k,m}$ and $\Pi_{\varepsilon,m}$ are included to model the turbulent interaction between the continuous phase and the dispersed phase.

The mixed density, ρ_m , is evaluated as

$$\rho_m = \sum_{i=1}^N a_i \rho_i \quad (33)$$

whereas the molecular viscosity, μ_m , is given as

$$\mu_m = \sum_{i=1}^n a_i \mu_i \quad (34)$$

and the velocity is evaluated as

$$\vec{v}_m = \frac{\sum_{i=1}^N a_i \rho_i \vec{v}_i}{\sum_{i=1}^N a_i \rho_i} \quad (35)$$

The turbulent viscosity for the mixture, $\mu_{t,m}$, and the turbulence kinetic energy production $G_{k,m}$ are calculated respectively, as,

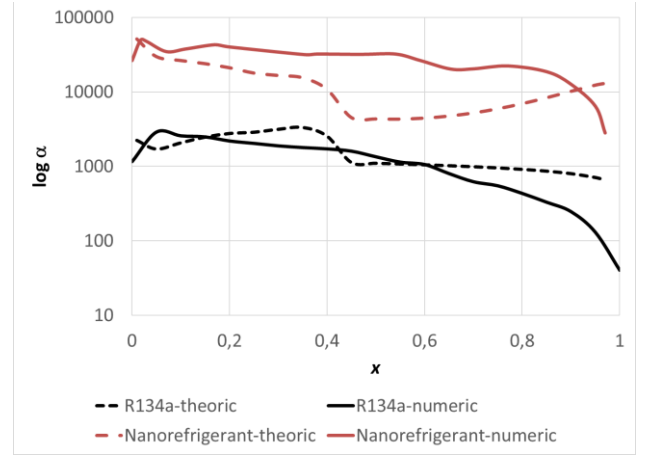
$$\mu_{t,m} = \rho_m C_\mu \frac{k^2}{\varepsilon} \quad (36)$$

$$G_{k,m} = \mu_{t,m} (\nabla \vec{v}_m + (\nabla \vec{v}_m)^T) : \nabla \vec{v}_m \quad (37)$$

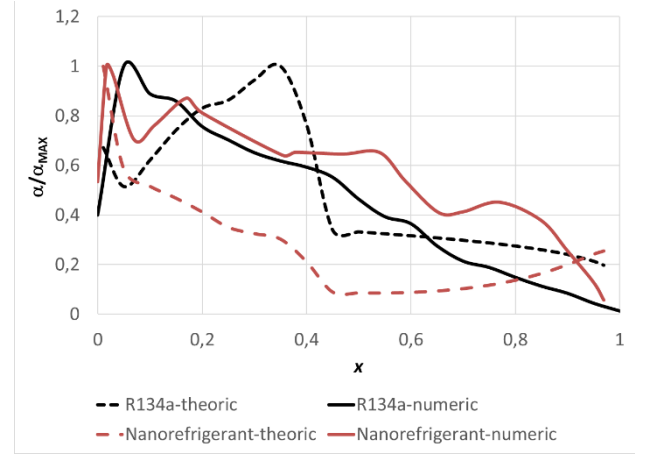
E. Results and Discussion

To predict the phase interaction in ANSYS FLUENT the following models are included: the *Ishii* option is selected for the drag and the *Tomiyaama* option for the lift. *Antal-et-al* model is chosen for the lubrication of the walls, and the *Ranz-Marshall* option for heat interaction. The interfacial area is selected as an *Ia-Symmetric* option. The pressure and velocity field variables are coupled using the *Phase Coupled SIMPLE* scheme, with first order schemes for the discretization of the governing equations.

Figure 3 shows the variation of the heat transfer coefficient with the increase of the vapor quality of refrigerant R134a. A comparison between the results obtained with the Kattan-Thome-Favrat model (1998a, 1998b, 1998c) (broken black line) and the results obtained with the computational simulation (continuous black line) of the forced convective boiling for the refrigerant R134a. Because of the significant differences between the coefficient for refrigerant and nano-refrigerant, results for the logarithm of that coefficient are given in Figure 3a. On the other hand, in Figure 3b, the dimensionless ratio to the maximum value of the same coefficient can be observed.



(a)



(b)

Figure 3. Heat transfer coefficient (Kattan-Thome-Favrat [14], [15], [16] and numerical) for forced convection boiling of refrigerant R134a and refrigerant-base nanofluid R134a/Al₂O₃

The computational results show a rapid increase in the heat transfer coefficient from quality 0 to quality 0.05, an area where the flow is in a stratified phase according to Figure 1. This rapid increase occurs due to the appearance of bubbles inside the flow and the clustering of them. The maximum value obtained is of 3000 W/m²K to 0.05 of quality, while with the theoretical model the maximum value of 3300 W/m²K was obtained at quality of 0.35. The computational results showed a decrease in the heat transfer coefficient from the 0.05 quality that is due to the

transition regime experienced by the refrigerant in the phase change.

Figure 3 also shows the variation of the heat transfer coefficient as function of the steam quality of the nanometer R134a/Al₂O₃ (broken red line, for the theoretical model presented above; and continuous red line, for the numerical results from ANSYS FLUENT). A considerable increase in the magnitude of the heat transfer coefficient is observed when the nanoparticles are added to the refrigerant (see Figure 3a). However, there the numerical prediction is inaccurate respect to the heat transfer coefficient proposed by Kattan-Thome-Favrat model [14-16] when the particle impact factor proposed by Peng [4] is considered.

V. CONCLUSIONS

The addition of Al₂O₃ nanoparticles to the refrigerant R134a generates an increase in the heat transfer coefficient, which would have an impact on the thermal efficiency of refrigeration systems. This increase is due to the thermal conductivity of the solid particles. During the boiling phenomenon, the flow stages that depend on the mass flux and heat flux at the wall. These stages are related to the behavior of the heat transfer coefficient for the phase change of the fluid. The migration of the nanoparticles from the liquid state to the vapor state is a complex phenomenon, and it is necessary to carry out a more detailed study to influence the thermal efficiency of the nano-refrigerant.

The instability and transient behavior of the phenomena inherent of the force convective heat boiling with the migration of the nanoparticles during the fluid's phase change are some of the reasons that affect the numerical predictions. It should also be taken into account that in order to obtain the heat transfer coefficient from the simulations, the results are averaged for the different quality values, given that computationally data is obtained at different points of the wall of the pipeline in which heat transfer. The maximum value of the coefficient of heat transfer obtained for both the theoretical and the computational model coincides for quality of 0.025 and is approximately 5000 W/m²K. Subsequently, a gradual decline is observed until reaching a value of 2800 W/m²K at the end of the boiling of the nano-refrigerant. Nevertheless, future work must be focused on improving numeric prediction of forced convective boiling coefficients considering the transient behavior with the effect of include nanoparticles and other fluids for the nanorefrigerant operation (i.e., refrigerant dilution with oil).

ACKNOWLEDGMENT

This work was granted by Young Researchers program of Colciencias.

REFERENCES

[1] R. Saidur, K. Leong and H. Mohammad, "A review on applications and challenges of nanofluids," ELSEVIER. Renewable and Sustainable Energy Reviews 15, pp. 1646-1668, 2011.

[2] A. Kamyar, R. Saidur and M. Hasanuzzaman, "Application of Computational Fluid Dynamics (CFD) for nanofluids," ELSEVIER. International Journal of Heat and Mass Transfer 55, pp. 4104-4115, 2012.

[3] R. Saidur, S. Kazi, M. Hossain, M. Rahman y H. Mohammed, «A review on the performance of nanoparticles suspended with refrigerants and lubricating oils in refrigeration systems,» ELSEVIER. Renewable and Sustainable Energy Reviews 15, pp. 310-323, 2011.

[4] H. Peng, G. Ding, W. Jiang, H. Hu y Y. Gao, «Heat transfer characteristics of refrigerant-based nanofluid flow boiling inside a horizontal smooth tube,» ELSEVIER. International Journal of Refrigerant 32, pp. 1259-1270, 2009.

[5] Cheng y L. Liu, «Boiling and two-phase phenomena of refrigerant-based nanofluids: Fundamentals, applications and challenges,» ELSEVIER. International Journal of Refrigeration 36, pp. 421-446, 2013.

[6] Mahbulul, S. Fadhilah, R. Saidur, K. Leong y M. Amalina, «Thermophysical properties and heat transfer performance of Al₂O₃/R-134a nanorefrigerants,» International Journal of Heat and Mass Transfer 57, pp. 100-108, 2013.

[7] F. P. Incropera y D. P. De Witt, Fundamentals of heat transfer. 4th edition., New York: Prentice Hall, 1999.

[8] F. Táboas, Estudio del proceso de ebullición forzada de la mezcla amoníaco/agua en intercambiadores de placas para equipos de refrigeración por absorción, Universidad Rovira I Virgili, 2006.

[9] J. Chen, «A correlation for boiling heat transfer to saturated fluids in convective flow,» ASME preprint 63-HT-34 , 1963.

[10] M. M. Shah, «A new correlation for heat transfer during boiling flow through pipes,» ASHRAE Trans. 82(2), pp. 66-86, 1976.

[11] D. Steiner y J. Taborek, «Flow boiling heat transfer in vertical tubes correlated by an asymptotic model,» Heat Transfer Engng 13(2), pp. 43-69, 1992.

[12] H. Forster y . N. Zuber , «Dynamics of vapour bubbles and boiling heat transfer,» AIChE. Journal, vol. 1, n° 4, pp. 531-535, 1955.

[13] F. Dittus y L. Boelter, «Heat transfer in automobile radiators of the tubular type,» Univ. Calif. Publ. Eng. 2 (13), pp. 443-461, 1930.

[14] N. Kattan, J. Thome y D. Favrat, «Flow boiling in horizontal Tubes: Part 1-Development of a diabatic two-phase flow pattern map,» Journal of heat transfer, pp. 140-147, 1998a.

[15] N. Kattan, J. Thome y D. Favrat, «Flow boiling in horizontal tube: Part 2- New heat transfer data for five refrigerants,» Journal of heat transfer, pp. 148-155, 1998b..

[16] N. Kattan, J. Thome y D. Favrat, «Flow boiling in horizontal tubes: Part 3- Development of a new heat transfer model based on flow pattern,» Journal of heat transfer, pp. 156-165, 1998c.

[17] M. G. Cooper, «Saturation Nucleate Pool Boiling - a Simple Correlation,» Institution of Chemical Engineers Symposium Series, vol. 86, pp. 785-793, 1984.

[18] S. Rouhani y E. Axelsson, «Calculation of void volume fraction in the subcooled and quality boiling regions,» International Journal of Heat and Mass Transfer, vol. 13, n° 2, pp. 383-393, 1970.

[19] D. Steiner, «Heat transfer to boiling saturated liquids,» de VDI-Wärmeatlas (VDI Heat Atlas), Du sseldorf, Verein Deutscher Ingenieure, VDI-Gesellschaft Verfahrenstechnik und Chemieingenieurwesen (GCV), 1993, p. Chapter.

[20] L. Wojtan, T. Ursenbacher y J. Thome, «Investigation of flow boiling in horizontal tubes: Part II - Development of a new heat transfer model for stratified-wavy, dryout and mist flow regimes,» International Journal of heat and mass transfer 48, pp. 2970-2985, 2005.

[21] J. R. Thome, «Chapter 10. Boiling heat transfer inside plain tubes,» de Engineering Data Book III, Lausanne, Switzerland, Wolverine Tube, Inc, 2007, pp. 10.1-10.29.

Soot Formation in a Steam-Introduced Kerosene Combustor

Masoud Darbandi and Majid Ghafourizadeh
 Institute for Nanoscience and Nano-Technology,
 Center of Excellence in Aerospace Systems,
 Department of Aerospace Engineering,
 Sharif University of Technology,
 P.O. Box 11365-11155, Postcode 14588-89694,
 Tehran, Iran
 darbandi@sharif.edu

Gerry E. Schneider
 Department of Mechanical and Mechatronics Engineering,
 University of Waterloo,
 Waterloo, Ontario, N2L 3G1, Canada
 gerry.schneider@uwaterloo.ca

Abstract— In this study, we would like to determine how soot formation in a combustor would be changed when different scenarios of steam (water vapor) introduction are applied. Surveying the literature, it can be understood that there is a lack of data and resources in this area. So, it should be studied from different perspectives and it is necessary to researchers be more concentrated and focused on this phenomenon. We consider a combustor burning kerosene to carry out this study numerically. It is a common tradition in each numerical analysis to make sure the numerical tool is fine and appropriate for study providing a reliable solution and valid results. In this regard, we consider a test case (a benchmark combustor) for our simulations. The combustor is fed with kerosene as its fuel. This test case was studied experimentally before and the data of experiment were reported in the published paper available in the literature. We adopt their test case here and simulate it by our numerical tool. We compare our obtained numerical results to the data measured in the experiment. The comparison demonstrates that our numerics can give us a reliable solution predicting the flame structure (the temperature and species concentrations) correctly. Validating our obtained numerical results, we put a step forward to extend the scope of our study further considering different scenarios of steam introduction. We consider two scenarios in our study for the steam injected into the combustor. The first scenario is steam introduction into incoming fuel stream. The second scenario is steam injection into the incoming oxidizer stream. Considering these two scenarios, we change the water vapor contents of fuel or oxidizer streams and simulate the two new test cases again. We compare the results obtained for each of these test cases to those of obtained before for the benchmark test case. Such contrasts are very helpful presenting the clear differences in quantities made due to steam introduction. We are mainly focused on the thermal and soot pollution quantities inside the combustors. Our investigations show that the soot concentration and soot particles diameters reduce using the steam introduction. However, this strategy is more effective in the case of steam injector into the incoming oxidizer stream. Our investigations also show that water introduction would reduce the flame height and the exhaust gases temperature.

However, such reductions are more severe in the case of steam injection into the fuel stream. This paper is very helpful for researchers who seek pollution reduction in combustors.

Keywords-component; Soot pollution, Water vapor introduction, Kerosene, Turbulent flame

NOMENCLATURE

f	=mixture fraction
f'^2	=mixture fraction variance
h	=total enthalpy
m^*	=soot mass fraction
n	=total number of species
n^*	=soot number density
p	=pressure
r	=radial component in cylindrical coordinates
u	=radial velocity component
v	=axial velocity component
z	=axial component in cylindrical coordinates
R	=gas constant
T	=temperature
\mathbf{V}	=velocity vector
W	=molecular weight
Y	=mass fraction
ε	=turbulence dissipation rate
k	=turbulence kinetic energy
μ	=molecular viscosity coefficient
ρ	=mixture density
A	<i>Subscripts, Superscripts, and Accents</i>
e	=effective magnitude
m	=chemical species index counter

II. INTRODUCTION

Soot pollution has always been a main concern in industries burning conventional hydrocarbon fuels. One reason is the dangerous consequences of soot pollutant on the environment and human health in long term periods. Another reason is the deposition of soot particles on the internal surfaces of combustion and other thermal devices. Soot deposition alters

the thermal characteristics of combustion devices and they need to be cleaned periodically to improve their performance.

Soot pollutant reduction has been the subject of many studies in last decades. Different approaches and strategies have been introduced and investigated to reduce the emission of this pollutant from combustion devices. Literature shows that the steam introduction in combustion devices has not been studied yet regarding its effects on soot pollution. Therefore, it is necessary to enrich the gap existed in the literature by conducting various studies and investigating those effects from different viewpoints.

One robust approach for studying different plans (designs) is the numerical simulation of these new cases. It provides us a better perspective about the pros and cons of such designs. The researchers accomplish their studies using numerical simulation to ascertain that their plans would work and achieve their required objectives.

In this paper, we simulate combustor consuming pre-evaporated kerosene considering different scenarios of water vapor introduction. Typically, we need to know more about the precision of our numerical tool for the correct prediction of thermal and soot characteristics of the flame (flame structure). In this regard, we simulate the case introduced and tested experimentally by young et al. [1]. We simulate the test case numerically and compare the obtained results to the data measured in the experiment and published in the literature. Afterward, we consider two different scenarios for steam introduction. We change the mass fraction of H_2O in either incoming fuel or oxidizer steam and simulate these two new test cases. We compare the results obtained for each of these new two cases to those of the benchmark test case without any water introduction. The findings are then discussed elaborately.

III. THE GOVERNING EQUATIONS

Considering the different phenomena happening in the sooting turbulent reacting flow, the governing equations include the equations of fluid flow, turbulence, combustion, energy transfer, and aerosol. They are briefly discussed in this section.

A. The Fluid Flow Equations

The fluid flow equations concern the conservation of mass and momentums. They are as below

$$\nabla \cdot (\rho \mathbf{V}) + \rho \frac{u}{r} = 0 \quad (1)$$

$$\nabla \cdot (\rho \mathbf{V}u) = -\frac{\partial p}{\partial r} + \nabla \cdot (\mu_e \nabla u) + \frac{\mu_e}{r} \frac{\partial u}{\partial r} - \mu_e \frac{u}{r^2} \quad (2)$$

$$\nabla \cdot (\rho \mathbf{V}v) = -\frac{\partial p}{\partial z} + \nabla \cdot (\mu_e \nabla v) + \frac{\mu_e}{r} \frac{\partial v}{\partial r} - \rho \mathbf{g} \quad (3)$$

B. The Turbulence Equations

The turbulent phenomenon is regarded via the modified two-equation $k-\varepsilon$ turbulence model [2]. The transport equations for turbulence kinetic energy and its dissipation rate are as below

$$\nabla \cdot (\rho \mathbf{V}k) = \nabla \cdot \left(\frac{\mu_e}{\sigma_k} \nabla k \right) + \frac{\mu_e}{\sigma_k r} \frac{\partial k}{\partial r} + G_k - \rho \varepsilon \quad (4)$$

$$\nabla \cdot (\rho \mathbf{V}\varepsilon) = \nabla \cdot \left(\frac{\mu_e}{\sigma_\varepsilon} \nabla \varepsilon \right) + \frac{\mu_e}{\sigma_\varepsilon r} \frac{\partial \varepsilon}{\partial r} + \frac{\varepsilon}{k} (c_1 G_k - c_2 \rho \varepsilon) \quad (5)$$

C. The Combustion Equations

The combustion phenomenon is regarded using the flamelet model [3]. We use a detailed chemical kinetics consisting of 121 chemical species and 2613 chemical reactions [4]. The transport equations for mixture fraction and its variance are as follows

$$\nabla \cdot (\rho \mathbf{V}f) = \nabla \cdot \left(\frac{\mu_e}{\sigma_f} \nabla f \right) + \frac{\mu_e}{\sigma_f r} \frac{\partial f}{\partial r} \quad (6)$$

$$\nabla \cdot (\rho \mathbf{V}f''^2) = \nabla \cdot \left(\frac{\mu_e}{\sigma_f} \nabla f''^2 \right) + \frac{\mu_e}{\sigma_f r} \frac{\partial f''^2}{\partial r} + c_g \mu_e (\nabla f)^2 - \rho c_\chi \frac{\varepsilon}{k} f''^2 \quad (7)$$

D. The Energy Equations

The energy equations concern the conservations of total enthalpy thorough the domain. The equation is given by

$$\nabla \cdot (\rho \mathbf{V}h) = \nabla \cdot \left(\frac{\mu_e}{\sigma_h} \nabla h \right) + \frac{\mu_e}{\sigma_h r} \frac{\partial h}{\partial r} + q_{rad} \quad (8)$$

E. The Aerosol Equations

The soot nano-aerosol chemistry and dynamics are regarded via the two-equation soot model [5, 6]. The transport equations for soot mass fraction and its number density are given below

$$\begin{aligned} \nabla \cdot (\rho \mathbf{V}m^*) &= \nabla \cdot \left(\frac{\mu_e}{\sigma_{soot}} \nabla m^* \right) + \frac{\mu_e}{\sigma_{soot} r} \frac{\partial m^*}{\partial r} \\ &+ C_1 \rho^2 \left(\frac{Y_{c_2H_2}}{W_{c_2H_2}} \right)^2 \frac{Y_{c_6H_5}}{W_{c_6H_5}} \frac{W_{H_2}}{Y_{H_2}} e^{-4378/T} \\ &+ C_2 \rho^2 \frac{Y_{c_2H_2}}{W_{c_2H_2}} \frac{Y_{c_6H_6}}{W_{c_6H_6}} \frac{Y_{c_6H_5}}{W_{c_6H_5}} \frac{W_{H_2}}{Y_{H_2}} e^{-6390/T} \end{aligned} \quad (9)$$

$$\begin{aligned} &+ C_3 \rho \frac{Y_{c_2H_2}}{W_{c_2H_2}} e^{-12100/T} (\pi \rho N_A n^*)^{1/3} \left(\frac{6\rho m^*}{\rho_{soot}} \right)^{2/3} \\ &- C_4 \rho \frac{Y_{OH}}{W_{OH}} \sqrt{T} (\pi \rho N_A n^*)^{1/3} \left(\frac{6\rho m^*}{\rho_{soot}} \right)^{2/3} \end{aligned}$$

$$\begin{aligned} \nabla \cdot (\rho \mathbf{V}n^*) &= \nabla \cdot \left(\frac{\mu_e}{\sigma_{nuc}} \nabla n^* \right) + \frac{\mu_e}{\sigma_{nuc} r} \frac{\partial n^*}{\partial r} \\ &+ \frac{C_1}{M_P} \rho^2 \left(\frac{Y_{c_2H_2}}{W_{c_2H_2}} \right)^2 \frac{Y_{c_6H_5}}{W_{c_6H_5}} \frac{W_{H_2}}{Y_{H_2}} e^{-4378/T} \\ &+ \frac{C_2}{M_P} \rho^2 \frac{Y_{c_2H_2}}{W_{c_2H_2}} \frac{Y_{c_6H_6}}{W_{c_6H_6}} \frac{Y_{c_6H_5}}{W_{c_6H_5}} \frac{W_{H_2}}{Y_{H_2}} e^{-6390/T} \\ &- \frac{1}{N_A} \sqrt{\frac{24RT}{\rho_{soot} N_A}} \left(\frac{6\rho m^*}{\pi \rho_{soot}} \right)^{1/6} (\rho N_A n^*)^{11/6} \end{aligned} \quad (10)$$

At last, the mixture density is calculated via the equation of state $p = \rho RT \sum_{m=1}^n Y_m / W_m$.

IV. THE COMPUTATIONAL METHOD

A copy-righted in-house computational fluid dynamics CFD code has been developed in recent years capable of

solving soot formation in turbulent reacting flows. The current authors have developed the code and employed it in numerical simulations of numerous problems. They benchmark test case have been chosen to verify the results. The literature shows that the numerical tool would provide reliable solutions in the simulations of flow, turbulence, combustion, heat transfer, and soot aerosol.

The literature on the tool shows its outstanding capability in numerical simulations; so, we used it again in this study to perform our numerics. The hybrid finite-volume-element approach is the essence of algorithm combining the features of each finite volume and finite element method. Considering the co-located variables, the physical influence scheme is adopted as the convection scheme for cell-face flux calculations. The diffusion flux is also calculated using the convenient shape functions. The more details can be found in Refs. [7-10].

V. THE TEST CASE

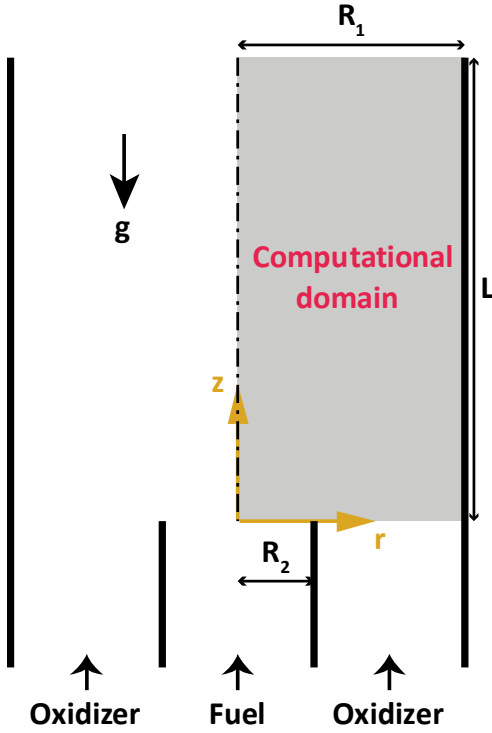


Figure 1. The schematic outline of the burner under study.

In this section, we provide a description regarding the test case under study. We chose the case studied by Young et al. [1] experimentally. The schematic outline of the burner is illustrated in Fig. 1.

As seen in Fig. 1, the burner is axisymmetric. The computational domain is rectangular due to the symmetry of the problem. The combustor is 0.6 and 0.0775 m in length and radius, respectively. The gaseous kerosene is injected at the speed of 22.28 m/s via fuel nozzle and the oxidizer, i.e. dry air, enters as a co-flow stream. The fuel nozzle has a diameter of 1.5 mm. The fuel and oxidizer have the temperature of 598 and 288 K at their intakes.

VI. THE RESULTS AND DISCUSSION

A. Numerical Validation

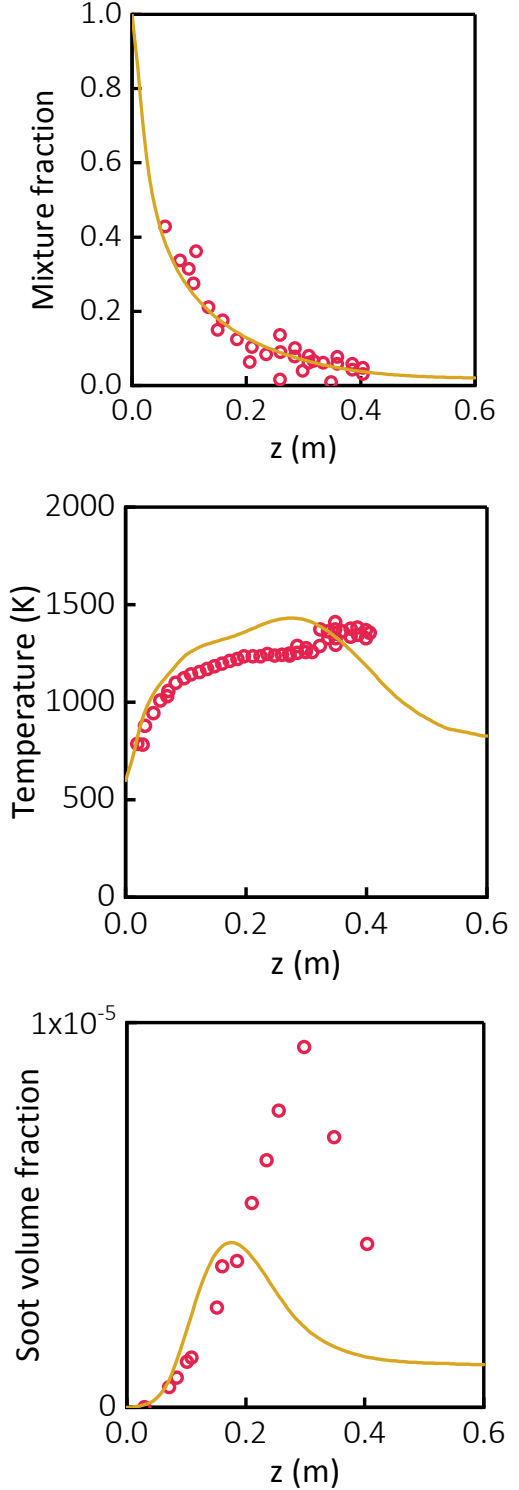


Figure 2. The centerline distributions of mixture fraction, temperature, and soot volume fraction obtained in the current simulation and their comparison against the data of experiment.

The background mentioned above regarding the method would suffice to use the numerical tool in the current study for our simulations; however, to be strict, we assess our tool again in numerical simulation of the flame under study. We use the CFD code to simulate the burner discussed in the previous section and then evaluate the obtained results comparing them to the experiment. We compare the flame structure to that of measured and reported in the literature. We compare the distributions of mixture fraction, temperature, and soot volume fraction inside the flame to those of measurement. Figure 2 shows the results of current solution and their comparison against the experiment. As Fig. 2 shows, the results of current solution can predict the flame structure considering the data of experiment. There is a little difference between the results of current solution and the measured data; however, the differences should be attributed to the models, their underlying simplifications and assumptions. Hence, our numerical equipment would predict the thermal and soot characteristics of the flame.

B. Thermal and soot characteristics of steam-introduced combustor

In this section, we continue our numerical study investigating the changes in thermal and soot characteristics of the combustor when water vapor (steam) is injected in the incoming fuel/oxidizer stream. We consider two different scenarios here; 1) water vapor is introduced in the incoming fuel stream, and 2) water vapor is introduced in the incoming oxidizer stream. In this regard, we change the mass fraction of H_2O of the incoming fuel/oxidizer to another different value and simulate the problem to see how it would affect the behavior of the combustor. To be more specific, we change the mass fraction of H_2O to 0.5. We watch the flame temperature, soot volume fraction, and soot particles dimeters inside the combustor as well as their emission in exhaust gases leaving the combustor. We compare together the results obtained for these considered scenarios to those of obtained before for the benchmark combustor.

Figure 3 shows the results obtained considering the first scenario. As figure shows the mass fraction of H_2O in the incoming fuel stream is changed. Figure 3 also shows the comparison between the results obtained for the combustor considered as scenario 1 to those of obtained for the benchmark combustor discussed in the previous section (without water introduction). As Fig. 3 shows the flame length would reduce and the exhaust gases temperature would decrease when the steam introduction strategy is employed. The Fig. 3 also shows that the concentration and the diameter of the soot particles formed inside would be decrease using the steam introduction strategy. Evidently, the emission of soot pollution to the surrounding atmosphere would also decrease employing the steam introduction approach.

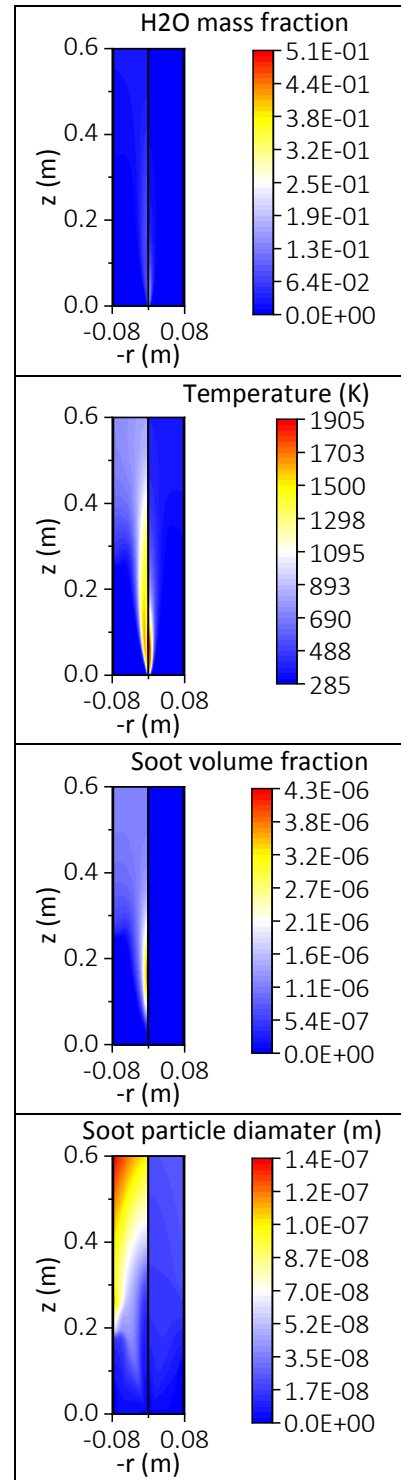


Figure 3. The contours of steam mass fraction, temperature, soot volume fraction, and soot particle diameter inside the combustor when steam is injected in the incoming fuel stream.

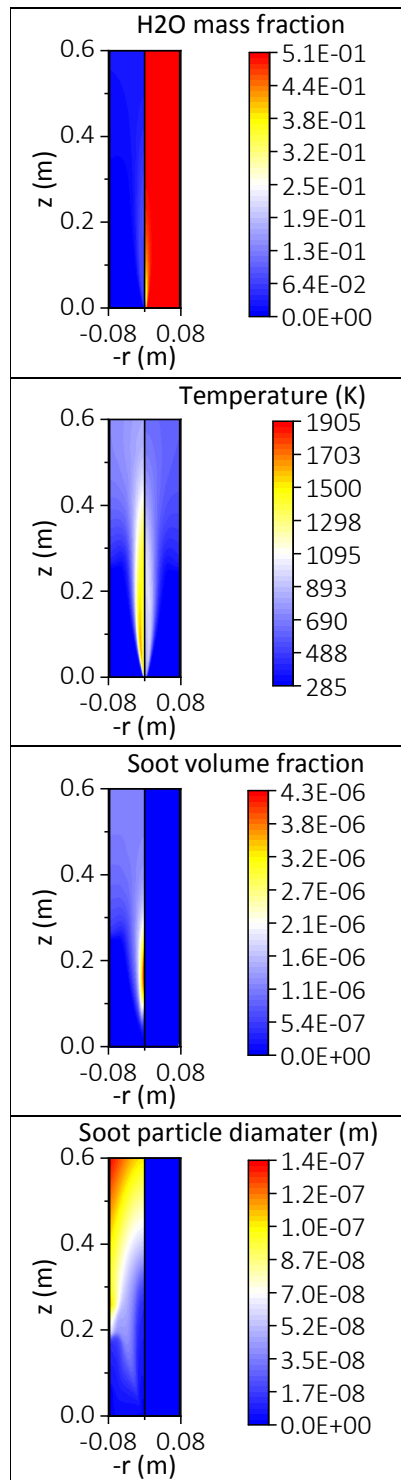


Figure 4. The contours of steam mass fraction, temperature, soot volume fraction, and soot particle diameter inside the combustor when steam is injected in the incoming oxidizer stream.

Figure 4 shows the results obtained considering the second scenario. As figure shows the mass fraction of H_2O in the incoming oxidizer stream is changed. Figure 4 also shows the comparison between the results obtained for the combustor

considered as scenario 2 to those of obtained for the benchmark combustor without water introduction. As Fig. 4 shows the flame length would reduce a little and the exhaust gases temperature would decrease slightly when the steam introduction strategy is employed. In other words, the scenario 1 is more effective than the scenario 2 in reducing the flame length and the exhaust gases temperature. The Fig. 4 also shows that the concentration and the diameter of the soot particles formed inside would be decrease when we introduced steam into the oncoming oxidizer stream. Consequently, the emission of soot pollution to the environment would also decrease introducing steam into the incoming oxidizer stream. Compared to the scenario 1, the soot particles diameters and soot concentration would be reduced more effectively when the scansion 2 is employed.

VII. CONCLUSIONS

A kerosene combustor was simulated numerically employing the steam introduction strategy. First, we needed to know if our numerical tool could give us valid results. In this regard, we considered a benchmark test case with available experimental data published in the literature. We simulated the test case and compared the results to the measured data. The comparison showed the reliability of our numerics in prediction of the flame structure. We continued our investigations considering two scenarios for steam introduction, i.e. water vapor introduction in the incoming fuel/oxidizer stream. We simulated these new test case and compared their results to the results of the benchmark test case. The contrasts showed that both scenarios could reduce the temperature and soot concentration of exhaust gases. Comparing these two scenarios together, they showed that the steam introduction in fuel stream would be more effective in reducing the exhaust gases temperature and the steam introduction in oxidizer stream would be more effective in soot pollutant reduction.

ACKNOWLEDGMENT

The authors, hereby, express their deepest gratitude for the financial support of current work provided by the Deputy of Research and Technology in Sharif University of Technology.

REFERENCES

- [1] [1] K. J. Young, C. D. Stewart, and J. B. Moss, "Soot Formation in Turbulent Nonpremixed Kerosine-Air Flames Burning at Elevated Pressure: Experimental Measurement," *Proceedings of the Combustion Institute*, vol. 25, no. 1, pp. 609–617, 1994.
- [2] [2] J. H. Kent and D. Honnery, "Soot and Mixture Fraction in Turbulent Diffusion Flames," *Combustion Science and Technology*, vol. 54, no. 1–6, pp. 383–397, 1987.
- [3] [3] E. Sozer *et al.*, "Turbulence–Chemistry Interaction and Heat Transfer Modeling of H_2/O_2 Gaseous Injector Flows," in *48th AIAA Aerospace Sciences Meeting Including the New Horizons Forum and Aerospace Exposition*, Orlando, Florida, 2010, pp. AIAA 2010-1525.
- [4] [4] E. Ranzi, A. Frassoldati, A. Stagni, M. Pelucchi, A. Cuoci, and T. Faravelli, "Reduced Kinetic Schemes of Complex Reaction Systems: Fossil and Biomass-Derived Transportation Fuels," *International Journal of Chemical Kinetics*, vol. 46, no. 9, pp. 512–542, 2014.
- [5] [5] M. Darbandi, M. Ghafourizadeh, and M. Ashrafizaadeh, "Effect of Jet Impingement on Nano-Aerosol Soot Formation in a Paraffin-Oil Flame," in *Mathematical and Computational Approaches in Advancing Modern Science and Engineering*, J. Bélair, I. A. Frigaard, H. Kunze, R.

Makarov, R. Melnik, and R. J. Spiteri, Eds. 1 ed. Switzerland: Springer International Publishing, 2016, pp. 89–99.

- [6] [6] M. Darbandi and M. Ghafourizadeh, "Numerical Study of Inlet Turbulators Effect on the Thermal Characteristics of a Jet Propulsion-Fueled Combustor and Its Hazardous Pollutants Emission," *Journal of Heat Transfer*, vol. 139, no. 6, pp. 061201 (1–12), 2017.
- [7] [7] M. Darbandi and M. Ghafourizadeh, "Extending a Hybrid Finite-Volume-Element Method to Solve Laminar Diffusive Flame," (in English), *Numerical Heat Transfer, Part B: Fundamentals*, vol. 66, no. 2, pp. 181–210, 2014.
- [8] [8] M. Darbandi and M. Ghafourizadeh, "Solving Turbulent Diffusion Flame in Cylindrical Frame Applying an Improved Advective Kinetics Scheme," (in English), *Theoretical and Computational Fluid Dynamics* vol. 29, no. 5–6, pp. 413–431, December 2015.
- [9] [9] M. Darbandi and M. Ghafourizadeh, "A New Bi-Implicit Finite Volume Element Method for Coupled Systems of Turbulent Flow and Aerosol-Combustion Dynamics," *Journal of Coupled Systems and Multiscale Dynamics*, vol. 4, no. 1, pp. 43–59, 2016.
- [10] [10] M. Darbandi and M. Ghafourizadeh, "Extending a Low-Order Upwind-Biased Scheme to Solve Turbulent Flames Using Detailed Chemistry Model," (in English), *Numerical Heat Transfer, Part B: Fundamentals*, vol. 73, no. 6, pp. 343–362, 2018.
- [11]

Large Eddy Simulation

LARGE EDDY SIMULATION ON MOVING AND DEFORMING DOMAINS USING THE FLUX RECONSTRUCTION APPROACH

Brian C. Vermeire

Department of Mechanical, Industrial, and Aerospace Engineering
 Concordia University
 Montreal, Canada

brian.vermeire@concordia.ca

ABSTRACT

The ability to perform scale-resolving simulations, such as Large Eddy Simulation (LES) and Direct Numerical Simulation (DNS), on moving and deforming domains has a variety of applications in aerospace engineering including deployment of flaps, slats, spoilers, actuation of control surfaces such as ailerons and elevators, or unsteady phenomena such as dynamic stall. Furthermore, the ability to perform such simulations in the vicinity of complex geometries requires mixed-element unstructured meshes and numerical methods that can achieve high-orders of accuracy for improved accuracy at reduced computational cost. In the current work we discuss implementation of an Arbitrary Lagrangian Eulerian (ALE) framework into the High-Order Unstructured Solver (HORUS) for LES using the Flux Reconstruction (FR) approach. Whereas conventional unstructured CFD solvers typically employ second-order accurate spatial discretizations, the FR approach allows for arbitrarily high-order accuracy via an element-wise polynomial representation of the solution on each element. The FR approach can recover existing high-order unstructured numerical methods, including the Discontinuous Galerkin (DG), Spectral Difference (SD), and Spectral Volume (SV) methods, and can also generate an infinite number of energy-stable schemes via a range of tuning parameters. Previous work has demonstrated that the FR approach can be several orders of magnitude more accurate and, simultaneously, up to an order of magnitude less expensive than industry-standard tools. In the current work we extend the FR approach to moving and deforming domains using the ALE approach.

We will show that this ALE implementation requires solution of a modified set of governing equations

$$\frac{\partial u}{\partial t} + \nabla \cdot F + u \nabla \cdot v_g = 0,$$

where u is the vector of conserved variables, $F = F_e - F_v + F_g$ is the fluxes, v_g is the local mesh velocity, F_e is the inviscid fluxes, F_v is the viscous fluxes, and F_g is the ALE flux induced due to the mesh motion. We note that, unlike conventional ALE formulations, the FR approach also requires computation of an element-wise mesh velocity divergence due to the high-order representation of the mesh. We will discuss important concepts including mesh deformation, free stream preservation, efficient implementation of both explicit and implicit solvers, and relevant concepts for both prescribed motions and Fluid Structure Interaction (FSI) using rigid body dynamics. Verification of the ALE implementation will be demonstrated using advection of an isentropic vortex on a non-linearly deforming mesh, achieving both ideal orders of accuracy and free stream preservation for unsteady compressible flows as shown in Figure 1. The utility of the ALE implementation in HORUS will then be demonstrated for Vortex Induced Vibration (VIV) of circular cylinders in crossflow and, finally, we will demonstrate the suitability of the approach for predicting static/dynamic stall of both low and moderate Reynolds number airfoils using LES, as shown in Figure 2.

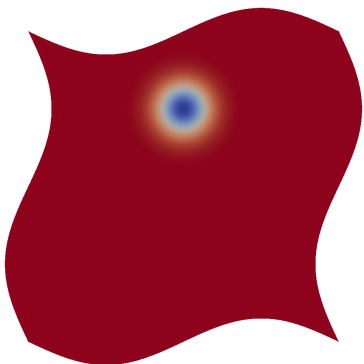


Figure 1: Isentropic vortex verification

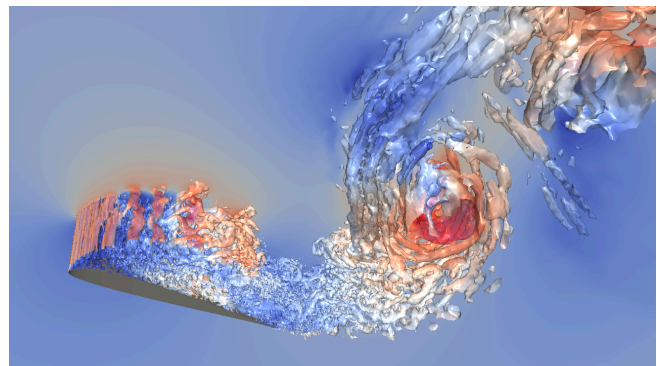


Figure 2: Stalled SD7003 Airfoil

ANALYSIS OF HIGH-ORDER ELEMENT TYPES FOR IMPLICIT LARGE EDDY SIMULATION

Carlos A. Pereira

Department of Mechanical, Industrial and Aerospace
 Engineering
 Concordia University
 Montreal, Canada
 carlos.pereira@concordia.ca

Brian C. Vermeire

Department of Mechanical, Industrial and Aerospace
 Engineering
 Concordia University
 Montreal, Canada
 brian.vermeire@concordia.ca

ABSTRACT

It is expected that the next generation of cleaner and quieter aircraft will rely on the added accuracy of Large Eddy Simulation (LES) and Direct Numerical Simulation (DNS). Hence, the demand to perform scale-resolving simulations, which benefit from the use of high-order spatial discretizations, continues to increase. However, current industry-standard CFD methods are low-order accurate.

Huyhn's high-order Flux Reconstruction approach (FR) is notably accurate for solving complex turbulent flows using DNS and LES. Furthermore, previous research has shown the suitability of high-order FR methods for Implicit Large Eddy Simulation (ILES). For ILES, the error of the spatial discretization is responsible for the modelling of turbulent flows. Hence, analyzing the dissipative and dispersive features of a scheme is necessary for understanding the accuracy and robustness of the results. In this study, we focus on the dissipation and dispersion characteristics of high-order elements within the FR family of schemes using the so-called temporal approach. Specifically, we consider meshes composed of hexahedral, prismatic and tetrahedral volumes, and characterize their suitability for ILES.

A computational domain is split into rectangular cuboids and then sub-split into two prismatic or six tetrahedral elements. Then, we evaluate how well these cuboids can represent wave-like functions for a range of wavenumbers in all directions using Von Neumann Analysis. This is done by prescribing solutions with different wave orientations and magnitudes. Based on the dispersion relations, this prescribed solution is linearly proportional to the frequency of the wave. Deviation from these relations is an indication of waves travelling at different speeds or damping of their amplitude. The results are analyzed based on the dominant mode of the characteristic eigencurves. After a given wavenumber, which is a function of the polynomial degree and direction of the wave vector, the solutions are not accurately represented by the scheme. From the dissipation curves shown below for a given wave direction, it is evident that more than one eigenmode may be considered physical, in particular for the prisms and tetrahedra. However, for this study we focus on the dominant mode at the lowest wavenumbers and its effects on the resolution of turbulent flows.

We support our results by performing a validation study of two well-known turbulent cases: the Taylor-Green vortex, and the turbulent channel flow. We observed that tetrahedral elements allow for more robust schemes at the cost of decreased accuracy and an increase in computational cost, compared to hexahedral discretizations. Finally, we present results from ILES simulations of flow around lifting bodies with mixed-element meshes to qualitatively compare the different element types.

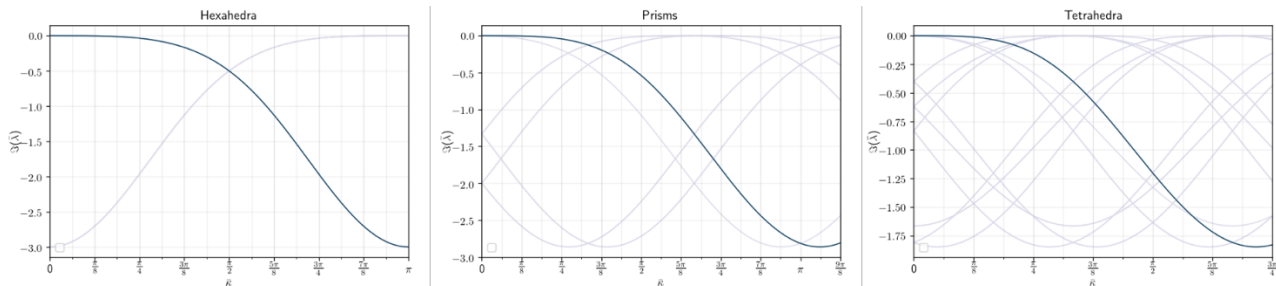


Figure 1. Example dissipation eigencurves for three-dimensional element types.

STABILIZING FILTERS FOR HIGH-ORDER IMPLICIT LARGE EDDY SIMULATION

Mohsen Hamed

Department of Mechanical, Industrial, and Aerospace
Engineering
Concordia University
Montréal, Canada
mohsen.hamed@concordia.ca

Brian Vermeire

Department of Mechanical, Industrial, and Aerospace
Engineering
Concordia University
Montréal, Canada
brian.vermeire@concordia.ca

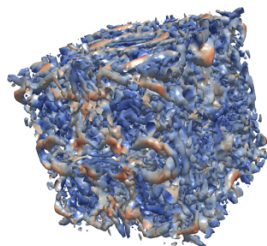
ABSTRACT

High-order Flux Reconstruction (FR) schemes can simulate unsteady turbulent flows using Large Eddy Simulation (LES) and Direct Numerical Simulation (DNS) in the vicinity of complex geometries. The flux reconstruction framework can be used to recover some of the existing schemes, such as the Discontinuous Galerkin (DG) and Spectral Difference (SD) methods, and an infinite number of energy stable schemes. The application of FR schemes can be limited by non-linear instabilities causing nonphysical solutions. FR schemes are more sensitive to numerical instabilities due to their relatively low numerical dissipation. Several stabilization techniques, such as entropy-stable schemes or kinetic energy preserving schemes have been previously identified. However, the capabilities of these approaches to stabilize LES/DNS simulations, without significantly increasing computational cost, on mixed element unstructured grids has remained hitherto intractable. If the solution is represented by modes of higher degree, then the solution will have more oscillatory behavior, giving rise to non-physical solutions and instability.

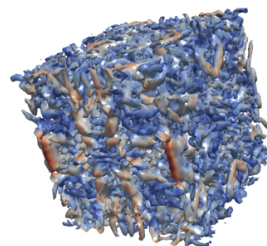
In this paper, filtering, as a stabilization technique, is studied for the hexagonal element type and solution polynomials of degree 3, 4, and 5 at different Mach numbers ranging from 0.1 to 0.5. The filter operator is applied globally to all elements and artificially damps high-frequency oscillations to improve numerical stability. The designed exponential filter function has three parameters. Two of them are fixed at constant values, while the last one is optimized as the minimum value which stabilizes the simulation.

Numerous numerical tests have been performed to investigate the aforementioned parameters in the exponential filter function. The optimum set of these parameters is obtained such that the highest solution polynomial modes are damped while the lower ones remain untouched, in order to preserve accuracy. The filter operator is applied after each time step. Hence, the filter operator is defined here, through the concept of characteristic time, to be independent of the time-step size. Therefore, the solution is filtered with the same filter strength after each characteristic time.

The exponential filter has been implemented and rigorously studied to evaluate its accuracy. To verify the order of accuracy, the advection of an isentropic vortex has been studied both with and without filtering. This case study is commonly used due to its simple implementation and known exact analytical solution at all time. The advection of the vortex with the mean flow is simulated using the Euler equation, where the entropy remains constant everywhere in the domain. To study accuracy for LES, the Taylor-Green vortex test case is studied as a free turbulent flow. The Navier-Stokes equations are solved at a Reynolds number of 1600 with 64^3 total degree of freedom, both with and without filtering and the rate of kinetic energy dissipation and enstrophy are compared. The q-criterion for a sixth order accurate Taylor-Green vortex case is given below, which shows that applying the filter function damped the highest wavenumbers, which are the smallest scales of turbulence. Finally, a wall-bounded turbulent channel flow at Mach number of 0.3, along with an E387 airfoil at a high angle of attack are considered to study the effect of filtering on a previously unstable case. The results show that implementing the filter stabilizes the simulation while preserving accuracy.



(a) without filtering



(b) with filtering

ASSESSMENT OF ERROR ESTIMATORS FOR GRID ADAPTATION FOR LES APPLICATION

Yao Jiang

Department of Mechanical Engineering
McGill University
Montreal, Canada

Siva Nadarajah

Department of Mechanical Engineering
McGill University
Montreal, Canada

Abstract— In the present paper, several error estimators for LES are implemented and compared. An energy spectra analysis of the decaying isotropic turbulence (DIT) test case is carried out and a formula linking the modeled and numerical TKE is verified and tuned for a better estimation of the effective TKE. Based on the proposed formula of numerical TKE, this work makes a comparison study of several practical LES assessment criteria. We apply and compare five different error estimators, including single-grid estimator as well as a two-grid estimator using the periodic hill test case. The error estimation provides a direction on where to refine the grids during the mesh adaptation process and leads to adapted grids based on different estimators. The validation of the periodic hill test case was carried out for the coarse and the fine grids. A new stable pressure forcing term was proposed. Numerical results are validated through a comparison to reference LES and experimental data.

Keywords- large eddy simulation; error estimators

I. INTRODUCTION

The application of Large Eddy Simulation (LES) to high Reynolds number cases usually demands exorbitant computational cost. The mesh adaptation provides an ability to efficiently and strategically use the computational resources. The process is typically based on a quality assessment process or an error estimator. LES intends to resolve the large scales while models the small via a Subgrid-Scale (SGS) model. From an error analysis point of view, both the numerical error, ϵ_n , and the modeling error, ϵ_m , contribute towards the total error [1, 2]. The distinction of the two sources of error is artificial and in practice the two interact and act as a whole and both are affected by the grid size.

The existing error estimators and mesh adaptation procedures for Reynolds-averaged NavierStokes (RANS) solvers could serve as references [3] but cannot be directly applied to LES due to the nature of the turbulence model. On the one hand, in RANS the grid size only affects the numerical error of the solution, such that the RANS error estimators mainly focus on

the discretization error or the residual of the equations, while in LES, apart from some attempts to achieve the grid-independent LES, in most of the LES simulations, the grid size contributes equally to both modeling and numerical errors. On the other hand, different from the RANS equation which incorporates the time averaging process, LES is intrinsically unsteady and chaotic, such that the error estimators should include some averaging processes in space and/or time.

Roache [4] classified the error estimation procedures for RANS, which could also be applied to LES [5]:

1. auxiliary algebraic evaluations on the same grid;
2. additional solutions of the governing equations on other grids;
3. additional solutions of the governing equations on the same grid;
4. auxiliary partial differential equation (PDE) solutions on the same grid.

Estimators belonging to classes 1,3 and 4 are regarded as single grid estimators, while class 2 relies on multiple grids simulations.

Geurts and Frohlich proposed the activity parameter [6]. Celik et al. [7, 5] introduced a family of Index Quality for LES error estimation, based on the effective Kolmogorov scale η_{eff} and the eddy viscosity ν_{eff} which incorporate the contribution from the SGS model and the numerical dissipation. The estimator is extended using the proportion of resolved to total TKE. Instead of using the proportion of resolved TKE, Antepara [8] used the residual velocity magnitude (without scaling) as an error indicator. A similar small energy density indicator depending on the residual velocity magnitude which includes the directional information was developed and employed in [9, 10]. The the wavelet-based adaptative method was applied to LES and leads to a Stochastic Coherent Adaptive Large Eddy Simulation (SCALES) [11, 12, 13] and tested on the decaying isotropic

turbulence case. A SGS model for SCALE was developed in [14]. Another wavelet-based criterion was also developed for LES [15, 16], using wavelet decomposition to detect small scales as a local error indicator.

Some error estimators belonging to the class 2 use more than one grid. Based on the Richardson extrapolation approach [17], Klein assumes that in LES using implicit filtering, the modeling and numerical errors could be combined to a unique function of grid size as an alternative to assess the Index Quality. The modeling and numerical errors, and even the coupling error from the two sources, could also be separated with the help of solving the flow with a systematic grid and model variation [18, 19], which leads to a tremendous increase in the computational cost.

The “error-landscape” method was developed and employed in a series of papers [20, 21, 22, 23], where the error was defined as the distance of LES solution to the DNS solution. The grid size and the model parameter are studied at the same time to form a “landscape” to find their best combination. A global scalar criterion is obtained by comparing the LES result to the reference DNS result. Since the method does not provide local error information and relies on the DNS result, consequently it is not suitable for mesh adaptation.

In the current work the focus is on the error estimation for LES in order to effectively find where to refine the grid to achieve lower error level. The current error estimators are implemented in the post-processing process without modifying the flow solver itself. It should be mentioned that only a posteriori single-error estimators are appropriate for mesh adaptation in practice.

II. IMPLEMENTATION

SYN3D is an in-house code at the Computational Aerodynamics Group at McGill University. SYN3D is a finite-volume based multi-block structured flows solver for compressible flow. The WALE subgrid model is employed for LES simulations.

A. Error Estimators

In this subsection the considered error estimators: activity parameter, index quality, and Richardson extrapolation methods are presented and details of their implementation are provided.

1) *Activity Parameter*: Geurts and Frohlich defined the activity parameter

$$s = \frac{\epsilon_{turb}}{\epsilon_{turb} + \epsilon_{lam}}, \quad (1)$$

where ϵ_{turb} and ϵ_{lam} are the turbulent and viscous dissipation. In order to take into consideration the contribution from the numerical dissipation, a modified version of the activity parameter [7] is used

$$s^* = \frac{\nu_{turb} + \nu_{num}}{\nu_{turb} + \nu_{num} + \nu}, \quad (2)$$

where the numerical viscosity ν_{num} is obtained from the numerical TKE with

$$\nu_{num} = sgn(k_{num})C_\nu\Delta\sqrt{abs(k_{num})}, \quad (3)$$

by referring to the formula in the SGS model proposed by Yoshizawa [24],

$$\nu_{sgs} = C_\nu\Delta\sqrt{k_{sgs}}, \quad (4)$$

with Δ the filter size and C_ν a constant. For LES using implicit filtering, the filter size is approximated by the grid size ($\Delta \approx h$). The relation between the numerical and modeled TKE is estimated by

$$k_{num} = C_n\left(\frac{h}{\Delta}\right)^2k_{sgs}, \quad (5)$$

where C_n is in the magnitude of 1.

2) *Index Quality*: The Index Qualities are defined as,

$$LES_IQ_\eta = \frac{1}{1 + \alpha_\eta\left(\frac{h}{\eta_{eff}}\right)^m}, \quad (6)$$

$$LES_IQ_\nu = \frac{1}{1 + \alpha_\nu\left(\frac{\nu_{eff}}{\nu}\right)^n}, \quad (7)$$

based on the effective Kolmogorov scale η_{eff} and the eddy viscosity ν_{eff} which incorporate the contribution from the SGS model and the numerical dissipation. The determination of the parameters $\alpha_\eta = \alpha_\nu = 0.05$, $m \cong 0.5$ and $n \cong 0.53$ is explained in [7]. The implementation of LES_IQ_ν can be directly fulfilled by using

$$\nu_{eff} = \nu_{num} + \nu_{sgs} \quad (8)$$

and eq. 7 and 3. In the formula of LES_IQ_η in eq. 6, the Kolmogorov length scale is defined by

$$\eta_{eff} = \left(\frac{\nu^3}{\epsilon}\right)^{1/4}, \quad (9)$$

where the dissipation ϵ is estimated from

$$S = \left(\frac{\epsilon}{\nu_{eff}}\right)^{1/2}, \quad (10)$$

where $S = \sqrt{2S_{ij}S_{ij}}$ is the square root of the double inner product of the mean strain rate tensor S_{ij} . The grid cell length scale h is simply

$$h = V^{1/3}, \quad (11)$$

where V is the volume of the cell. The estimator is extended using the proportion of resolved to total turbulent kinetic energy (TKE) based on Pope’s suggestion that a “good” LES approach should resolve at least 80% of the total TKE [25, 26],

$$LES_IQ_k = \frac{k_{res}}{k_{res} + k_{sgs,eff}}, \quad (12)$$

the resolved TKE, k_{res} , is obtained by adding the contribution from the diagonal terms in the Reynolds stress tensor, obtained

by subtracting the instantaneous flow field from the time-averaged solution,

$$k_{res} = \frac{1}{2} \sum_{i=1}^3 u'_i u'_i \quad (13)$$

with

$$u'_i = u_i - U_i, \quad (14)$$

where u_i and U_i are the instantaneous and time-averaged velocities. For a single grid approach, $k_{sgs,eff}$ is the sum of the modeled, k_{sgs} , and numerical TKE k_{num} .

In each of the above formulas, there is one parameter which needs an estimation based on empirical equations.

3) *Richardson Extrapolation* A two-grid Richardson extrapolation is assumed to estimate the effect of modeled and numerical TKE. By modeling the effective TKE by a combined term involving the grid size h , Eq. 12 leads to the expression

$$LES-IQ_k = \frac{k^{res}}{k^{res} + ah^p}. \quad (15)$$

The locally resolved TKE on two simulation on grid h_1 and h_2 ($h_1 > h_2$) for the same test case are noted respectively as k_1^{res} and k_2^{res} , with p the order of accuracy of the scheme and the order of the SGS model and a a constant, which leads to

$$k^{tot} = k_1^{res} + ah_1^p = k_2^{res} + ah_2^p, \quad (16)$$

from which the expression of a for each grid points is obtained

$$a = \frac{k_2^{res} - k_1^{res}}{h_1^p - h_2^p}, \quad (17)$$

and $LES-IQ_k$ is obtained

$$LES-IQ_k = \frac{k^{res}}{k^{res} + \frac{k_2^{res} - k_1^{res}}{h_1^p - h_2^p} h^p}, \quad (18)$$

which could be applied at the same time to the coarse and the fine grid.

4) *Laminar Correction* The above-mentioned estimators are based on the assumption that the flow is turbulent, thus may lead to unreasonable results when applied to laminar or transitional flows. The wrong estimation will also happen when the estimators are applied to the near wall region, where the molecular viscosity is much higher than the eddy viscosity. An empirical laminar flow correction factor was proposed by Celik et al. [5],

$$f_{lam} = 0.5(1 + \tanh(\beta(Re_{tr}^{0.5} - C_{sl}Re_{tr-crt}^{0.5}))), \quad (19)$$

where β and C_{sl} are empirical constant and Re_{tr-crt} is the critical Reynolds number for transitional flow. This scaling function approaches smoothly zero when approaching the wall. The turbulence Reynolds number Re_{tr} is defined as

$$Re_{tr} = \frac{(\frac{2}{3}k_{tot})^{1/2}l}{\nu_{eff}}, \quad (20)$$

where

$$k_{tot} = k_{res} + k_{sgs} + k_{num}, \quad (21)$$

and the integral length scale l is estimated by

$$l = \frac{k_{tot}^{1/2}}{\epsilon}, \quad (22)$$

with the help of eq. 10.

III. RE-EVALUATION OF k_{num}

When using the single grid approach to estimate $LES-IQ_k$, a proper evaluation of the contribution of the numerical dissipation to the effective modeled TKE, or the numerical TKE k_{num} , is necessary. Since the Subgrid-Scale (SGS) model primarily contributes to the modeled TKE in the high wavenumber region while the numerical dissipation contributes to the numerical TKE in a much wider wavenumber range, the relation between the modeled and numerical TKE is not straightforward. A linear relationship between k_{num} and k_{sgs} , as shown in Eq. 5, is assumed in [5]; however, the relation must be verified and the proper ratio investigated. The procedure is proposed based on a spectral analysis for the DIT case [27]. The instantaneous kinetic energy budget equation could be derived from the momentum equation,

$$\frac{\partial E_k}{\partial t} + u_j \frac{\partial E_k}{\partial x_j} = \frac{\partial}{\partial x_i} \left[-\frac{u_i}{\rho} + 2\nu u_j s_{ij} \right] - 2\nu s_{ij} s_{ij}, \quad (23)$$

where $E_k = \frac{1}{2}u_i u_i$ is the kinetic energy. If a time averaging process is applied, the time-averaged kinetic energy could be written as

$$\bar{E}_k = \frac{1}{2}\overline{u_i u_i} = \frac{1}{2}\bar{U}_i \bar{U}_i + \frac{1}{2}\overline{u'_i u'_i}, \quad (24)$$

where $\bar{\cdot}$ means the averaging process, and \cdot' means the fluctuation. $\frac{1}{2}\bar{U}_i \bar{U}_i$ is the kinetic energy of the mean flow while $\frac{1}{2}\overline{u'_i u'_i}$ is the TKE. In LES, the filtered velocity \hat{u}_i is involved in the equation, and the sub-filter part is modeled by a SGS model. For an eddy viscosity model, the change to Eq. 23 is through the replace of ν by ν_{eff} which incorporates the eddy viscosity ν_{sgs} . The conservation equation for kinetic energy of filtered field (KEFF) becomes

$$\frac{\partial E_{filt}}{\partial t} + \hat{u}_j \frac{\partial E_{filt}}{\partial x_j} = \frac{\partial}{\partial x_i} \left[-\frac{\hat{u}_i}{\rho} + 2\nu_{eff} \hat{u}_j \hat{s}_{ij} \right] - 2\nu_{eff} \hat{s}_{ij} \hat{s}_{ij}, \quad (25)$$

where $\hat{\cdot}$ means the filtering process and $E_{filt} = \frac{1}{2}\hat{u}_i \hat{u}_i$ is the KEFF. The time averaging process to E_{filt} leads to the same decomposition as in Eq. 24

$$\bar{E}_{filt} = \frac{1}{2}\overline{\hat{u}_i \hat{u}_i} = \frac{1}{2}\bar{\hat{U}}_i \bar{\hat{U}}_i + \frac{1}{2}\overline{\hat{u}'_i \hat{u}'_i}. \quad (26)$$

LES tries to use the solved KEFF to estimate the filtered kinetic energy (FKE)

$$\hat{E}_k = \frac{1}{2}\widehat{u_i u_i} = \frac{1}{2}\hat{u}_i \hat{u}_i + \frac{1}{2}(\widehat{u_i u_i} - \hat{u}_i \hat{u}_i), \quad (27)$$

TABLE I. DIT Meshes

Mesh	Size
MESH1	64 × 64 × 64
MESH2	128 × 128 × 128
MESH3	256 × 256 × 256

where the last term is modeled by a SGS model. The time averaging process leads the equation to

$$\bar{\hat{E}}_k = \frac{1}{2} \overline{\hat{u}_i \hat{u}_i} = \frac{1}{2} \bar{\hat{U}}_i \bar{\hat{U}}_i + \frac{1}{2} \overline{\hat{u}'_i \hat{u}'_i} + \frac{1}{2} \overline{(\hat{u}_i \hat{u}_i - \hat{u}_i \hat{u}_i)} \quad (28)$$

$$= \frac{1}{2} \bar{\hat{U}}_i \bar{\hat{U}}_i + \text{TKE}_{filt} = \bar{E}_{filt} + k_{sgs}. \quad (29)$$

In the formula, $\frac{1}{2} \bar{\hat{U}}_i \bar{\hat{U}}_i$ is the mean flow kinetic energy of the filtered field, $\frac{1}{2} \overline{\hat{u}'_i \hat{u}'_i}$ is the captured TKE and $\frac{1}{2} \overline{(\hat{u}_i \hat{u}_i - \hat{u}_i \hat{u}_i)}$ is the residual kinetic energy, which is replaced by the modeled TKE using a SGS model k_{sgs} . The last two terms combine to TKE_{filt} , which differs from the real TKE since the application of the filter already takes effect on it. The LES error estimators usually leave out the mean kinetic energy and only consider the proportion of $\frac{1}{2} \overline{\hat{u}'_i \hat{u}'_i}$ to k_{sgs} . When the numerical discretization effect is taken into consideration, the numerical dissipation affects both $\frac{1}{2} \overline{\hat{u}'_i \hat{u}'_i}$ and k_{sgs} , leading to the expression of k_{num} ,

$$k_{num} = \left(\frac{1}{2} \overline{\hat{u}'_i \hat{u}'_i} + k_{sgs} \right) - \left(\frac{1}{2} \overline{\hat{u}'_{i,h} \hat{u}'_{i,h}} + k_{mod,h} \right), \quad (30)$$

such that

$$\text{TKE}_{filt} = \frac{1}{2} \overline{\hat{u}'_{i,h} \hat{u}'_{i,h}} + k_{sgs} + k_{num}, \quad (31)$$

where k_{sgs} and k_{num} could be estimated separately using the Richardson extrapolation or the experimental data. The spectrum plotted for the DIT case is always a *total kinetic energy spectrum* instead of a *turbulent kinetic energy spectrum*, but since the mean velocity is theoretically zero in all three directions, the two spectra should be similar. A safer way is to subtract the mean kinetic energy $\frac{1}{2} \bar{\hat{U}}_{i,h} \bar{\hat{U}}_{i,h}$ from the total kinetic energy to get the turbulent kinetic energy. During the process, attention need to be paid to three points:

1. the LES estimation process omits the impact of spatial discretization to the mean flow, meaning the distance between $\frac{1}{2} \bar{\hat{U}}_i \bar{\hat{U}}_i$ and $\frac{1}{2} \bar{\hat{U}}_{i,h} \bar{\hat{U}}_{i,h}$;
2. in the current DIT case, the fluctuation is decaying in time, such that the time averaging is meaningless. An ensemble averaging instead of the time averaging is used;
3. the role of LES is focused on mimicking the filtered state variables, including the TKE, such that the objective value of obtained TKE using LES is TKE_{filt} instead of the real TKE. The effect of the filter should be properly removed during the evaluation of k_{num} .

The process for the determination of k_{num} based on the DIT case is:

1. generate the box-filtered initial condition for 3 grids: 64^3 , 128^3 and 256^3 ;

2. run simulation with and without a SGS model on 3 grids using the same time step, which is small enough to minimize the effect of temporal discretization;
3. at the same time step, generate the TKE spectra, $E(k)_{SGS}$ and $E(k)_{noSGS}$, based on a spatial averaging of the velocities;
4. rescale $E(k)_{SGS}$ and $E(k)_{noSGS}$ with the initial box-filter energy spectra to remove the effect of filtering process;
5. Eq. 4 gives an estimation of the k_{sgs} , while k_{num} could be estimated through a comparison between the experimental data and $E(k)_{noSGS}$ on 3 levels of grids. The integration of the difference between the spectra without and with the SGS model

$$\int_k (E(k)_{noSGS} - E(k)_{SGS}), \quad (32)$$

measures the loss of captured TKE due to the introduction of the SGS model.

IV. NUMERICAL SET-UP

Two test cases are carried out in the current study. The re-evaluation of k_{num} is through the DIT test case. While the Periodic hill case is employed for the error estimation.

A. Decaying Isotropic Turbulence

The geometry for the DIT case is shown in figure 1. The length of the sides is 2π , while three mesh sizes are tested. A divergence-free velocity field is used as the initial condition and periodic boundary conditions are used in all directions. The case is widely used as a simple case for turbulence model validation. Its isotropicity and periodicity make it an ideal test case for the initial validation and tuning of constants in a turbulence model. The velocity spectra from both measurement data and numerical data are available at non-dimensional time $T = 42, 98$ and 171 .

B. Periodic Hill

The geometry and streamwise velocity contour of the periodic hill case are shown in figure 2. Two mesh size are tested, with periodic boundary conditions in both streamwise and spanwise directions, and no-slip conditions are applied at the upper and lower boundaries. The Reynolds number based

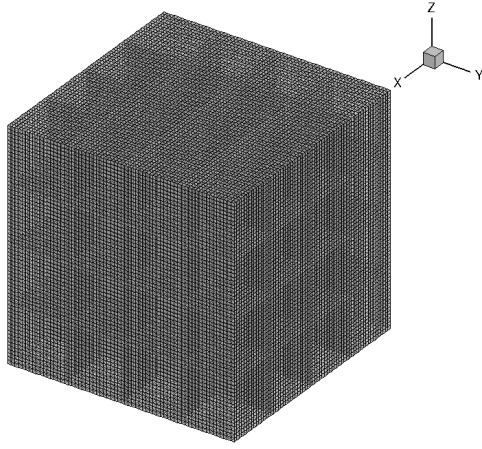


Figure 1. DIT case geometry

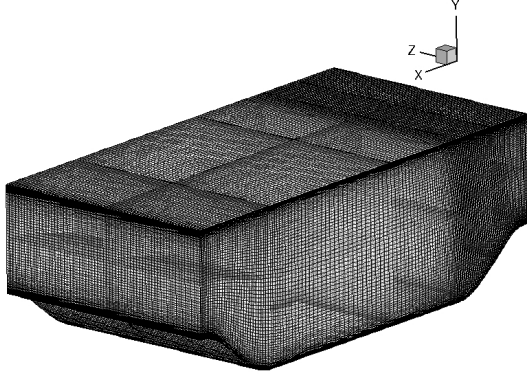


Figure 2. Periodic hill case geometry

on the hill height and mean bulk velocity at the hill crest is $Re = 10600$. The flow is highly unsteady featuring separation from the continuous surface and the separation point oscillates over a large range on the wall. The mean flow is characterized by a separation bubble with an established separation and reattachment point. The form of the bubble depends on two factors: the position of the separation point and the turbulent intensity on the top of the bubble, which determines the level of energy exchange from the mean flow to the bubble region. The experimental data [28], a LES with wall function on fine grid of 4.6M [29] and a very fine wall-resolve LES on 13.1M grid [30] are available as reference data.

Two levels of grids are available for the study. The summary of the grids is shown in Tab. II. MESH2 is refined from MESH1 only in spanwise direction. Both grids are divided into blocks for the multi-block structured solver SYN3D. The first layer cells satisfy $y^+ \approx 1$, which allows the wall-resolved LES on both the

TABLE II. Periodic Hill Meshes

Mesh	Size
MESH1	$160 \times 160 \times 64$
MESH2	$160 \times 160 \times 128$

upper and the lower surfaces. It should be mentioned that the meshes used in the current study are coarser than the LES used in the references, such that the error estimators are expected to give an indication for the adaptation process by show regions to be refined.

1) *Forcing Term* A pressure forcing term is added to the streamwise momentum equation and the energy equation in order to drive the flow to maintain a constant Reynolds number during the simulation. One approach [31] is to adjust the forcing term at every time step depending on the instantaneous mass flux. However, for LES cases, this approach may cause an over correction of the forcing term and may lead to an over estimation of the fluctuation and TKE. A new source term $S = -\frac{dp}{dx} > 0$ is therefore proposed. Considering the friction factor f ,

$$-\frac{dp}{dx} = f \frac{\frac{1}{2}\rho U^2}{D}, \quad (33)$$

where D is the length scale, usually the hydraulic diameter. According to reference

$$f \sim Re^{-0.3} \sim U^{-0.3}, \quad (34)$$

which leads to

$$-\frac{dp}{dx} = CU^{1.7}, \quad (35)$$

such that the averaged mean velocity U is a function of the pressure forcing term S ,

$$U = f(S) = aS^m \quad (36)$$

where $m \approx 1/1.7$ and a a constant. Our targeted inlet mean velocity $U_{targ} = 1$. Using Newton's method to find the zero of $g(S)$,

$$g(S) = f(S) - 1 = aS^m - 1, \quad (37)$$

which leads to

$$S_{n+1} = S_n - \frac{g(S_n)}{g'(S_n)} \quad (38)$$

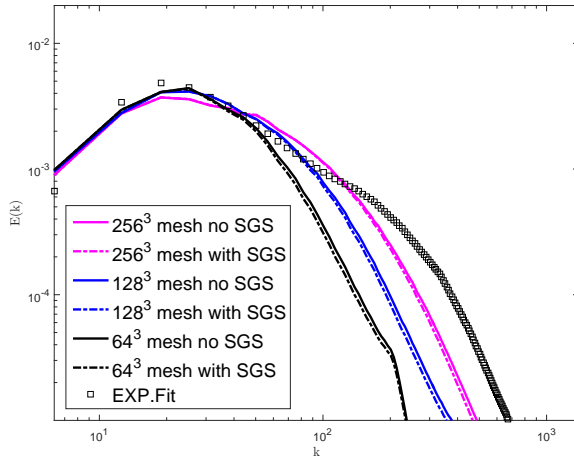
$$= S_n - \frac{U_n - 1}{amS_n^{m-1}} \quad (39)$$

$$= S_n - \frac{S_n(U_n - 1)}{U_n m}, \quad (40)$$

by assuming that $a = U_n/S_n^m$ is constant. The only value to plug in is the order m .

TABLE III. Evaluation of k_{sgs} and k_{num}

	k_{sgs}	k_{num}	k_{num}/k_{sgs}
64	0.008616491	0.0208697	2.42206717
128	0.006267630	0.0198728	3.17070514
256	0.003653684	0.0092877	2.54200063

Figure 3. DIT energy spectra at $T = 98$, for 256^3 , 128^3 and 64^3 grids with and without a SGS model, compared with the experimental data

V. NUMERICAL RESULTS

The current section is divided into three parts. First, the spectral analysis results for the DIT case are presented in order to determine k_{num} . Second, the periodic hill case is validated on two levels of meshes with the current solver and the proposed pressure forcing term. Third, the error estimation for the periodic hill case is presented, with the incorporation of k_{num} .

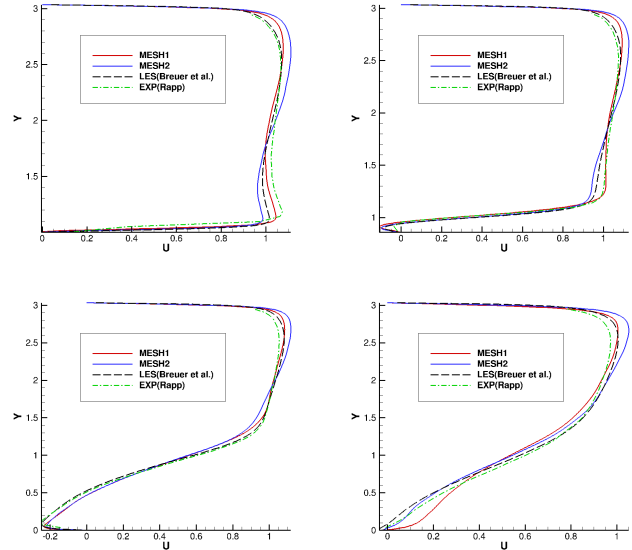
A. Re-evaluation of k_{num}

The energy spectra at $T = 98$ are shown in Fig. 3, which include the simulations with and without a SGS model on three levels of meshes, and compared against the fitted spectrum obtained from [27]. It is shown that even without a SGS model, the loss of captured energy in the high wavenumber region is non-negligible, and primarily due to the filter effect instead of the numerical dissipation.

It is observed that the loss of captured TKE due to the SGS model is only applied to the high wavenumber region, but the amount is relatively small. The evaluation of the numerical TKE k_{num} follows the procedure mentioned in the above sections. After the rescaling with the initial filtered energy spectra, the evaluation of k_{sgs} and k_{num} is presented in Tab. III. It is observed that k_{sgs} and k_{num} do not follow a strictly linear relationship as the grid is refined. Assuming an approximate linear relationship between k_{sgs} and k_{num} , the factor $C_n = k_{num}/k_{sgs}$ is evaluated to be 2.71

B. Periodic Hill Case Validation

The simulation was carried out on two levels of meshes. The results are based on an average over 30 flow through periods in time and in the spanwise direction in space. The mean velocity at four slices at $X = 0.05, 0.5, 2$ and 4 are shown in Fig. 4.

Figure 4. Mean velocity profiles at $X = 0.05, 0.5, 2$ and 4

Both simulations show good agreement with the experimental and reference LES results.

Fig. 5 shows the size of the separation bubble with the contour of the captured TKE. MESH1 shows a small separation bubble due to an over-estimation of the TKE level in the region above the separation bubble, the phenomenon is also reported in [29]. A refinement in the spanwise direction allows for a lower TKE level and a better capture of the bubble length as shown in Tab. IV. MESH1 wrongly predicts the separation point by estimating the separation prior to the top of the hill at a negative X coordinate. Fig. 6 shows the incorrect backflow layer on the top of the hill captured by MESH1 while the error is avoided by the spanwise refinement in MESH2.

Fig. 7 shows the profiles of the Reynolds stress tensor components and the TKE compared with the reference LES and the experimental data at the slice $X = 2$. The studied slices spans across the main flow and the bubble regions, and is characterized by a high TKE value in the mixing layer above the bubble. MESH1 over-estimates all the components and wrongly captures the boundary layer while MESH2 shows great compliance with the reference data.

C. Error Estimation

The error estimators mentioned in the above sections are applied to the periodic hill case on both meshes. The contour of

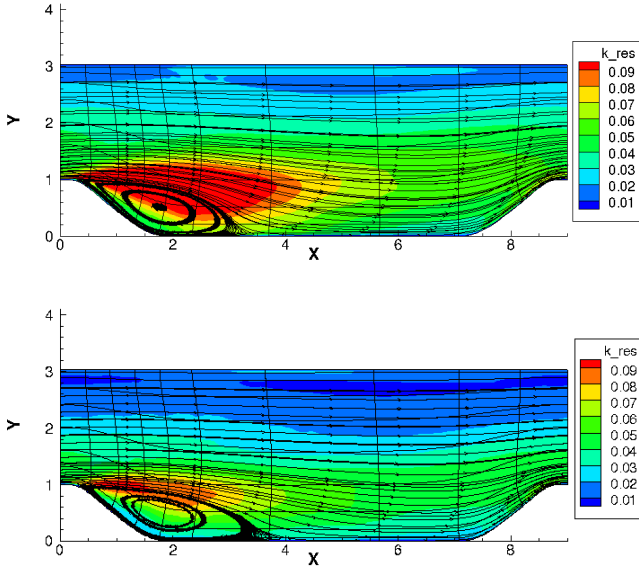


Figure 5. Resolved TKE contour and streamline, top: MESH1; bottom: MESH2

TABLE IV. Separation and Reattachment Points

Mesh	X_{sep}	X_{reat}
MESH1	-0.93	4.06
MESH2	0.22	4.67
LES [29]	0.22	4.72
LES [28]	0.19	4.69

the activity parameter is shown in Fig. 8. The activity parameter is not a practical assessment indicator as mentioned in [7], since in most LES applications it is anticipated that $\nu_t \gg \nu$, such that the activity parameter value is close to 1 except in the near wall region.

Fig. 9 and Fig. 10 show the contours of IQ_ν and IQ_η . Both indicators target a similar region in the center of the computational domain, where the size of grid cells is relatively large. A small region of mixing layer near the separation point is also slightly highlighted. It is also clear that the refinement of MESH2 compared to MESH1 leads to an increase of IQ_ν and IQ_η values in the whole computational domain.

The contour of the single grid IQ_k is shown in Fig. 11. The indicator targets mainly the mixing layer above the separation bubble. Since the correct capture of TKE in the targeted region is essential for the correct prediction of the bubble length, the indicator is expected to give helpful information towards the grid adaptation for LES. It is observed that the IQ_k on MESH2 does not show a clear increase of the value, which is due to the fact that IQ_k measures the percentage of resolved TKE among the total TKE, while MESH1 shows an over-estimation of resolved

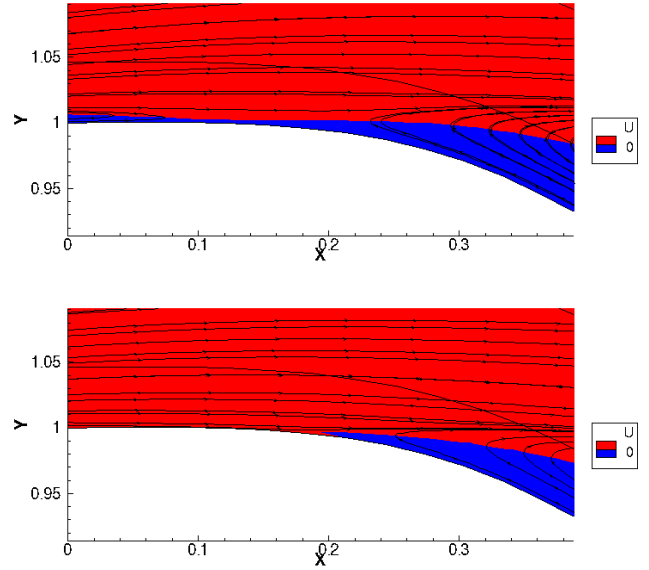


Figure 6. Backflow on the hill top region, top: MESH1; bottom: MESH2

TKE which leads to a slight over-estimation of the IQ_k value.

It should be mentioned that the double grid IQ_k based on the Richardson extrapolation fails to evaluate the current case since the estimator is based on the assumption that the fine grid is able to capture more fluctuations, thus a higher TKE, than the coarse grid. However, in the current case, the coarse grid over-estimates the TKE such that the effective modeled turbulent $k_{sgs,eff}$ is evaluated to be negative, which leads to an incorrect assessment of the error. The fact also shows a limitation of the Richardson extrapolation-based error estimators.

We focus our effort on three estimators, IQ_ν , IQ_η and the single grid IQ_k , which all belong to the family of Index Quality, and demonstrate their profiles at slices $X = 2, 3$ and 4 . Generally, all three indicators show a similar trend. The bubble region is targeted as a low-quality region. MESH2 provides for higher values than MESH1 for all three estimators at slices $X = 3$ and $X = 4$. MESH2 shows a lower IQ_k than MESH1 at $X = 2$ due to the over-estimation of k_{res} on the coarse mesh. Since conceptually IQ_k measures the percentage of the resolved TKE and its value is under 0.8 in most of the region, it is estimated that the modeled and numerical TKE forms a large part of the total TKE. Although IQ_k shows lower values on the whole range compared to IQ_ν and IQ_η , all three indicators show a similar minimum value location in terms of the Y coordinate. For grid adaptation, the essential task of the error estimator is to correctly target the region where the quality is relatively low in the physical space. The study of the periodic hill case on adapted grids is in progress and the updated results will be added for the final submission.

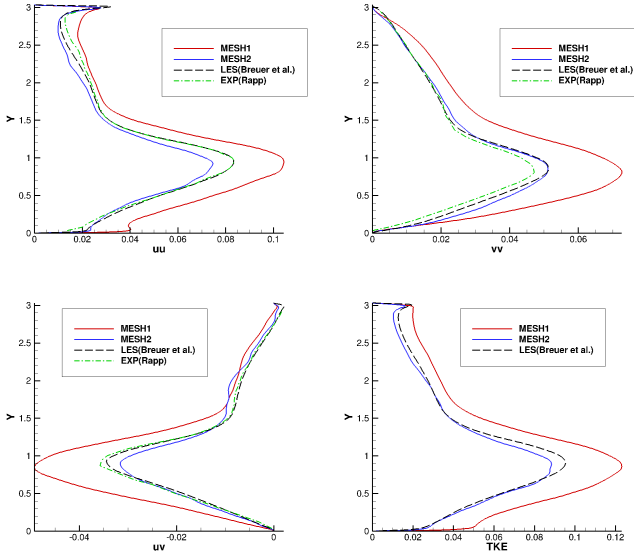


Figure 7. Reynolds stress tensor components profiles at $X = 2$

VI. CONCLUSION

In this work, several quality criteria have been studied and tested. Some of the estimators depend on a proper evaluation of the numerical TKE. A spectral analysis was carried out using the DIT test case in order to draw the relationship linking the modeled and numerical TKE. The periodic hill case was studied and validated with LES on two levels of meshes, which are relatively coarse for a wall-resolved LES simulation. A new stable pressure forcing term was proposed and implemented to avoid the over-estimation of the velocity fluctuations. It is shown that the refinement in only the spanwise direction improves significantly the simulation result by providing excellent agreement of the Reynolds stress tensor and TKE profiles at the slice in the bubble region. The refinement also aids in the capture of the backflow on the hill surface, as well as the length of the separation bubble. Our wall-resolved LES is able to provide for good compliance with the reference LES and experimental data even on a relatively coarse mesh.

Several error estimators for LES have been applied to the periodic hill case in order to analyze their applicabilities and performances. The use of these error estimators is of great importance in the assessment of the quality of LES results and in the grid adaptation for LES, where the grid resolution impacts both the sub-grid model and the numerical dissipation, which leads to the modeled and numerical TKE. Some of the error estimators require only data of a single LES calculation; while, others necessitate two fully resolved LES. The error estimations of different indicators have been investigated on both levels of meshes. Different indicators target different regions for having poor quality. The activity parameter is not shown to be an effective estimator for LES, while IQ_ν and IQ_η provide for similar results by targeting the central region which is characterized by

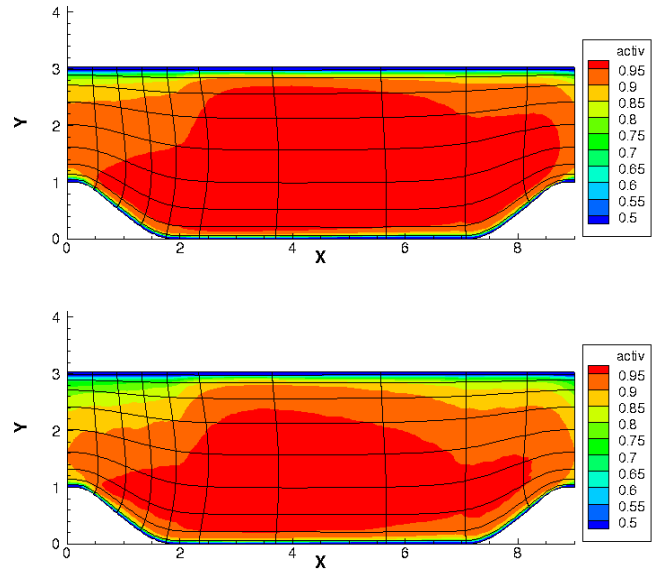


Figure 8. Activity parameter contour, top: MESH1; bottom: MESH2

larger grid cells. As one of the most prominent criteria, IQ_k targets mainly the mixing layer above the separation bubble. All estimators of the Index Quality family highlight more or less the separation point and the mixing layer above the separation bubble.

The error estimators provide for an indication of where to refine the grid for a better LES resolution. The future step of the study is to carry out simulations on adapted grids based on the information provided by different error estimators. For the periodic hill case, it is expected that the error estimators could target regions whose refinement leads to a better resolution of TKE around the separation bubble with the grid refinement approach.

REFERENCES

- [1] B. Vermeire, Adaptive Implicit-explicit Time Integration and High-order Unstructured Methods for Implicit Large Eddy Simulation, Ph.D. thesis, McGill University, Montreal, QC, 2014.
- [2] S. Ghosal, "An analysis of numerical errors in large-eddy simulations of turbulence," *Journal of Computational Physics*, vol. 125 (1), 1996, pp. 187–206.
- [3] A. Hauser and G. Wittum, "Adaptive large eddy simulation," *Computing and Visualization in Science*, vol. 17 (6), 2015, pp. 295–304.
- [4] P. J. Roache, *Verification and validation in computational science and engineering*, Hermosa, 1998.
- [5] I. Celik, M. Klein, and J. Janicka, "Assessment measures for engineering LES applications," *Journal of fluids engineering*, vol. 131 (3), 2009, p. 031102.
- [6] B. J. Geurts and J. Fröhlich, "A framework for predicting accuracy limitations in large-eddy simulation," *Physics of fluids*, vol. 14 (6), 2002, pp. L41–L44.

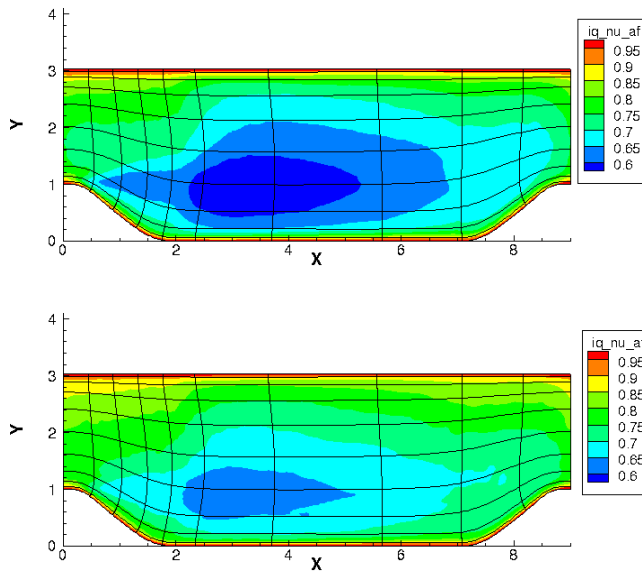


Figure 9. IQ_{ν} contour, top: MESH1; bottom: MESH2

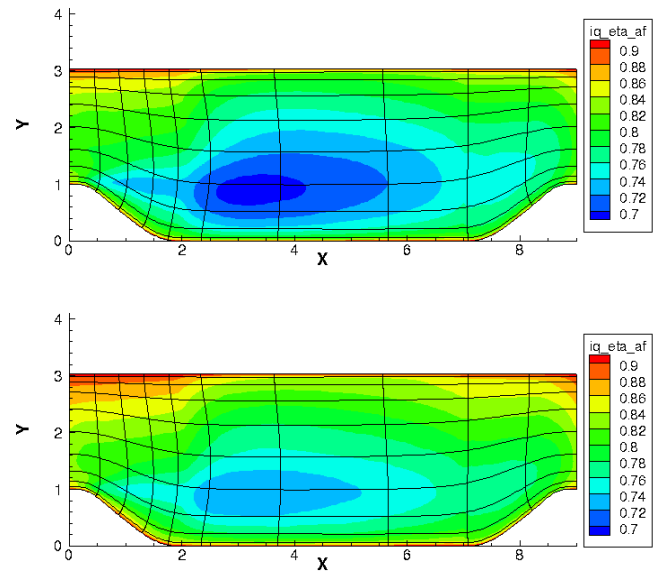


Figure 10. IQ_{η} contour, top: MESH1; bottom: MESH2

- [7] I. Celik, Z. Cehreli, and I. Yavuz, "Index of resolution quality for large eddy simulations," *Journal of fluids engineering*, vol. 127 (5), 2005, pp. 949–958.
- [8] O. Anteparo, O. Lehmkuhl, R. Borrell, J. Chiva, and A. Oliva, "Parallel adaptive mesh refinement for large-eddy simulations of turbulent flows," *Computers & Fluids*, vol. 110, 2015, pp. 48–61.
- [9] S. Toosi and J. Larsson, "Anisotropic grid-adaptation in large eddy simulations," *Computers & Fluids*, vol. 156, 2017, pp. 146–161.
- [10] S. Toosi and J. Larsson, "Grid-adaptation and convergence-verification in large eddy simulation: a robust and systematic approach," in *2018 Fluid Dynamics Conference*, 2018, p. 3406.
- [11] D. E. Goldstein and O. V. Vasilyev, "Stochastic coherent adaptive large eddy simulation method," *Physics of Fluids (1994-present)*, vol. 16 (7), 2004, pp. 2497–2513.
- [12] D. E. Goldstein, O. V. Vasilyev, and N. K.-R. Kevlahan, "CVS and SCALES simulation of 3-d isotropic turbulence," *Journal of Turbulence*, (6), 2005, p. N37.
- [13] K. Schneider and O. V. Vasilyev, "Wavelet methods in computational fluid dynamics," *Annual Review of Fluid Mechanics*, vol. 42, 2010, pp. 473–503.
- [14] O. V. Vasilyev, G. De Stefano, D. E. Goldstein, and N. K.-R. Kevlahan, "Lagrangian dynamic SGS model for stochastic coherent adaptive large eddy simulation," *Journal of Turbulence*, (9), 2008, p. N11.
- [15] B. Sjögren and H. C. Yee, "Multiresolution wavelet based adaptive numerical dissipation control for high order methods," *Journal of Scientific Computing*, vol. 20 (2), 2004, pp. 211–255.
- [16] S. Leonard, M. Terracol, and P. Sagaut, "A wavelet-based adaptive mesh refinement criterion for large-eddy simulation," *Journal of Turbulence*, (7), 2006, p. N64.
- [17] I. Celik and O. Karatekin, "Numerical experiments on application of richardson extrapolation with nonuniform grids," *Journal of fluids engineering*, vol. 119 (3), 1997, pp. 584–590.
- [18] M. Freitag and M. Klein, "An improved method to assess the quality of large eddy simulations in the context of implicit filtering," *Journal of Turbulence*, (7), 2006, p. N40.
- [19] T. Xing, "A general framework for verification and validation of large eddy simulations," *Journal of Hydrodynamics*, vol. 27 (2), 2015, pp. 163–175.
- [20] J. Meyers, B. J. Geurts, and M. Baelmans, "Database analysis of errors in large-eddy simulation," *Physics of Fluids*, vol. 15 (9), 2003, pp. 2740–2755.
- [21] M. Klein, J. Meyers, and B. J. Geurts, "Assessment of LES quality measures using the error landscape approach," in *Quality and Reliability of Large-Eddy Simulations*, Springer, 2008, pp. 131–142.
- [22] J. Meyers, "Error-landscape assessment of large-eddy simulations: a review of the methodology," *Journal of Scientific Computing*, vol. 49 (1), 2011, pp. 65–77.
- [23] F. Ries, K. Nishad, L. Dressler, J. Janicka, and A. Sadiki, "Evaluating large eddy simulation results based on error analysis," *Theoretical and Computational Fluid Dynamics*, 2018, pp. 1–20.
- [24] A. Yoshizawa, "A statistically-derived subgrid model for the large-eddy simulation of turbulence," *The Physics of Fluids*, vol. 25 (9), 1982, pp. 1532–1538.
- [25] P. Benard, G. Balarac, V. Moureau, C. Dobrzynski, G. Lartigue, and Y. D'Angelo, "Mesh adaptation for large-eddy simulations in complex geometries," *International Journal for Numerical Methods in Fluids*, vol. 81 (12), 2016, pp. 719–740.
- [26] J. Gou, X. Su, and X. Yuan, "Adaptive mesh refinement method-based large eddy simulation for the flow over circular cylinder at $Re_D = 3900$," *International Journal of Computational Fluid Dynamics*, 2018, pp. 1–18.
- [27] W. Rozema, H. J. Bae, P. Moin, and R. Verstappen, "Minimum-dissipation models for large-eddy simulation," *Physics of Fluids*, vol. 27 (8), 2015, p. 085107.
- [28] M. Breuer, N. Peller, C. Rapp, and M. Manhart, "Flow over periodic hills—numerical and experimental study in a wide range of Reynolds numbers,"

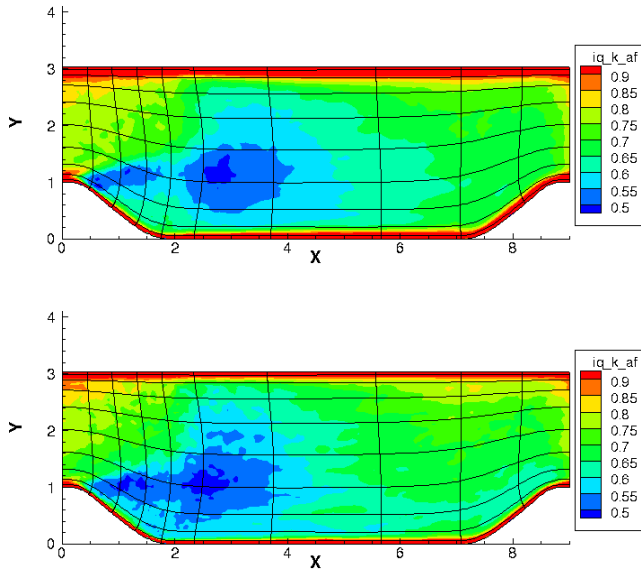


Figure 11. IQ_k contour, top: MESH1; bottom: MESH2

Computers & Fluids, vol. 38 (2), 2009, pp. 433–457.

- [29] L. Temmerman, M. A. Leschziner, C. P. Mellen, and J. Fröhlich, “Investigation of wall-function approximations and subgrid-scale models in large eddy simulation of separated flow in a channel with streamwise periodic constrictions,” *International Journal of Heat and Fluid Flow*, vol. 24 (2), 2003, pp. 157–180.
- [30] C. Rapp and M. Manhart, “Flow over periodic hills: An experimental study,” *Experiments in fluids*, vol. 51 (1), 2011, pp. 247–269.
- [31] C. Benocci and A. Pinelli, “The role of the forcing term in the large eddy simulation of equilibrium channel flow,” *Engineering turbulence modeling and experiments*, vol. 1, 1990, pp. 287–296.

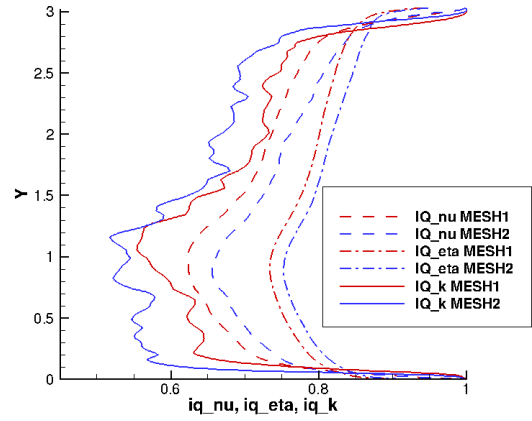


Figure 12. IQ_ν , IQ_η and IQ_k profile at $X = 2$

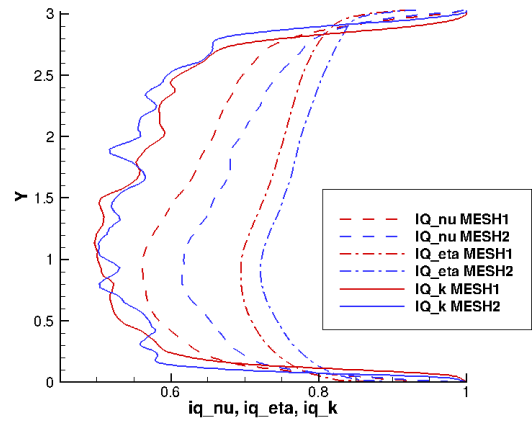


Figure 13. IQ_ν , IQ_η and IQ_k profile at $X = 3$

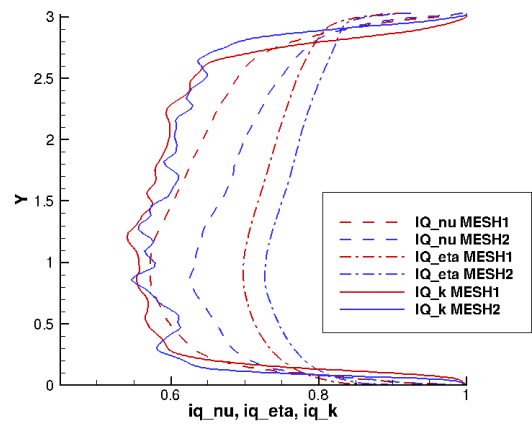


Figure 14. IQ_ν , IQ_η and IQ_k profile at $X = 4$

Influence of rib height in a rib-roughened square duct on turbulent flow using large-eddy simulation

Alex Czehryn
Dept. of Mechanical Engineering
Univ. of Manitoba
Winnipeg, Canada
czehryna@myumanitoba.ca

S. Vahid Mahmoodi J.
Dept. of Mechanical Engineering
Univ. of Manitoba
Winnipeg, Canada
mahmoosv@myumanitoba.ca

Bing-Chen Wang*
Dept. of Mechanical Engineering
Univ. of Manitoba
Winnipeg, Canada
BingChen.Wang@umanitoba.ca

Abstract—In this paper, turbulent flow statistics in a square duct with periodically spaced transverse ribs mounted on one wall are investigated using large eddy simulations (LES). Two different blockage ratios ($Br = H/L_z = 0.1$, and 0.2) at bulk Reynolds number 2800 are methodologically examined with respect to the velocity field, turbulent statistics and turbulent structures. The numerical predictions of turbulence statistics obtained from LES are thoroughly validated against a set of direct numerical simulation (DNS) values. One of the main phenomenon observed was the acceleration of high streamwise momentum convected downstream because of an increase of blockage effect. The blockage effects on turbulent structures are also investigated using two-point spatial autocorrelation.

Keywords—large eddy simulation, ribbed duct flow, turbulence

I. INTRODUCTION

Noticeable disturbances induced by perpendicular ribs within a square duct represent a challenging topic in engineering and perform a crucial role to enhance both turbulence and heat transfer rates in heat exchangers and gas turbine blades. Owing to the interactions between mean streamwise and spanwise velocities, as well as the presence of rib elements, large-scale secondary flows are induced; these secondary flows forcefully interact with the boundary layer of each wall causing variation to the flow structures.

In literature, rib-roughened geometries have been extensively studied using Reynolds-averaged Navier-Stokes equations (RANS), large eddy simulation (LES) and direct numerical simulation (DNS). Due to the technical prevalence of roughness elements, many DNS studies have been conducted to investigate the influence of rough surfaces on turbulent flow structures [1]. Leonardi *et al.* performed direct numerical simulations of channel flow with rib roughness elements at a wide variety of pitch-to-height (P/H) ratios [1]. They observed that

the minimum friction drag and maximum form drag occurred at $P/H = 7$, where the wake reattaches to the bottom rough wall of the channel. Marocco *et al.* conducted simulations for turbulent flow in a ribbed channel, using various low Reynolds number RANS methods, with varying success; they showed that RANS should only be used for qualitative analysis due to deficiencies including incorrect separation and reattachment points [2]–[4]. Tafti investigated the role of subgrid stress modelling in a ribbed duct and concluded that the dynamic model could well predict the major characteristics of the flow, in particular, friction and heat transfer coefficients [5].

From a literature survey, it was found that complex boundary geometries (including surface-mounted ribs) fundamentally alter vortical structures, which are often applicable to heat transfer enhancement. Krogstad *et al.* studied turbulent structures in smooth and rough channels using both hot-wire anemometry and DNS; they discovered that two-dimensional bar roughnesses significantly impacted the turbulent activities (i.e. ejection and sweep events) in the region near the roughness element, while a weaker sensitivity was observed in the outer layer [6]. In a channel flow with cuboidal obstacles, Coceal *et al.* investigated the variation of mean inclination angle of hairpin structures at various wall-normal locations. They analyzed the inclination angle through the ejection-sweep mechanism and the antisymmetric portion of the shear tensor [7].

Other than the aforementioned contributions, the number of methodical studies on highly disturbed turbulent flows in a square duct is minimal. Therefore, a fully encompassing LES study regarding first- and second-order statistics and turbulent coherent flow structures was performed; the flow structures were investigated using two-point correlation. This data is fully validated with the DNS data for a similar geometry. The main objective of this study is to investigate the impact of roughness height on turbulent structures and statistics.

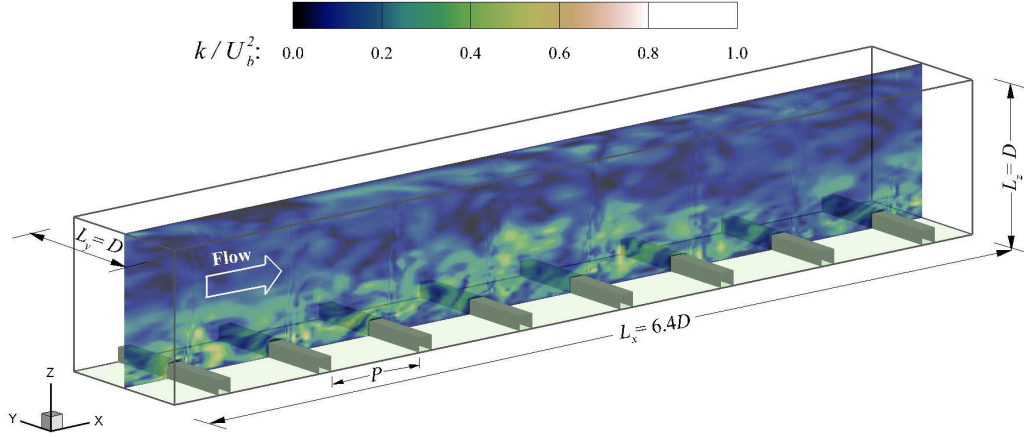


Fig. 1. Computational domain and coordinate system with the contour of the resolved instantaneous velocity fluctuations in the central plane. The origin of the vertical coordinate ($z=0$) is located at the geometrical center of the cross-stream plane in the square duct.

II. METHODOLOGY

The geometry of the domain used for the blockage ratio ($Br = H/L_z$) of 0.1, is shown in Fig. 1. The streamwise, spanwise and wall-normal directions are represented by x , y , and z , respectively. Transverse ribs are periodically repeated along the bottom wall of the closed duct. The origin is located on the downstream side of the first rib, halfway up the duct and halfway through the duct, laterally. The width and height of the duct are equal to the hydraulic diameter, D , with rib heights $0.1D$ and $0.2D$ being studied, resulting in blockage ratios of 0.1 and 0.2, respectively. The width of the ribs is $0.1D$ with a streamwise distance between ribs of $0.8D$, resulting in pitch to height ratios of 8 and 4 for the rib heights of $0.1D$ and $0.2D$, respectively. The domain of the system contains eight ribs, resulting in a streamwise length, L_x , of $6.4D$ and total overall dimensions of $6.4D \times D \times D$ in the x , y and z directions, respectively.

Both numerical simulations are conducted based on $480 \times 96 \times 96$ body-fitted grid points in the x , y and z directions, respectively. The mesh is refined near solid walls to resolve the complex flow physics created by the ribbed areas. The flow is driven by a pressure gradient and is fully developed in the streamwise direction. The nominal Reynolds number is fixed at $Re_b = U_b \delta / \nu = 2800$, where U_b denotes the streamwise bulk mean velocity and δ is half the side length of the square duct. No-slip boundary conditions are applied to all solid walls for the velocity field, and periodic boundary conditions are applied to the inlet and outlet of the duct.

A general curvilinear coordinate system is used, resulting in the following filtered governing equations for continuity and momentum:

$$\frac{1}{J} \frac{\partial (\beta_i^k u_i)}{\partial \xi_k} = 0, \quad (1)$$

$$\begin{aligned} \frac{\partial u_i}{\partial t} + \frac{1}{J} \frac{\partial}{\partial \xi_k} (\beta_j^k u_i u_j) = & -\frac{1}{J\rho} \frac{\partial (\beta_i^k p)}{\partial \xi_k} \\ & -\frac{1}{\rho} \Pi \delta_{1i} + \frac{\nu}{J} \frac{\partial}{\partial \xi_p} \left(\frac{1}{J} \beta_j^p \beta_j^q \frac{\partial u_i}{\partial \xi_q} \right). \end{aligned} \quad (2)$$

These equations are expressed in tensor notation with the streamwise, spanwise and wall-normal directions denoted by x_i for $i=1, 2$, and 3 , respectively. In these equations, J is the Jacobian of the $\partial x_i / \partial \xi_j$ tensor and β_j^i is the cofactor of the same tensor. Further, \bar{u}_i is the resolved velocity, ρ is the density, \bar{p} is the resolved pressure, δ_{1i} is the Kronecker delta and Π is the overall pressure gradient. Due to enhanced resistance caused by the increase of rib height, the value of the external forces necessary to maintain a constant bulk velocity changes. Therefore, an approximate external applied pressure, Π , was initially simulated; after iteratively changing the applied pressure, an appropriate value was found for each case. These values were non-dimensionalized by $\rho U_b^2 / 2\delta$ and were found to be 0.02464 and 0.3818 for $Br=0.1$ and 0.2, respectively.

Due to LES filtering, the sub-grid scale stress tensor, τ_{ij} , needs to be modelled to close the governing equations. The dynamic Smagorinsky model [8] is used to model the sub-grid scale stress tensor, as shown in Eq. (4)

$$\tau_{ij}^* = \tau_{ij} - \frac{\tau_{kk}}{3} \delta_{ij} = -2C_S \bar{\Delta}^2 |\bar{S}_{ij}| \bar{S}_{ij}. \quad (3)$$

Here, $\bar{\Delta}$ is the grid level filter size, \bar{S}_{ij} , represents the filtered strain rate tensor and $|\bar{S}_{ij}|$ denotes the norm of the filtered strain rate. The coefficient for the Smagorinsky model, C_S , is dynamically calculated by the least-squares approach using

$$C_S = -\frac{L_{ij} M_{ij}}{M_{ij} M_{ij}}, \quad (4)$$

where, $L_{ij} = \widetilde{\bar{u}_i \bar{u}_j} - \bar{\tilde{u}_i} \bar{\tilde{u}_j}$, $M_{ij} = \alpha_{ij} - \tilde{\beta}_{ij}$ and $\alpha_{ij} = 2\bar{\Delta}^2 |\bar{S}_{ij}| \bar{S}_{ij}$. The overbar represents filtered quantities at the grid level, whereas a tilde represents filtered quantities at the test-grid level, which are the changing quantities. The Smagorinsky model coefficient is filtered to eliminate illegitimate fluctuations and is clipped to ensure a positive value is achieved, which guarantees stability. To begin the dynamic procedure, a ratio between the filter sizes of the test grid and

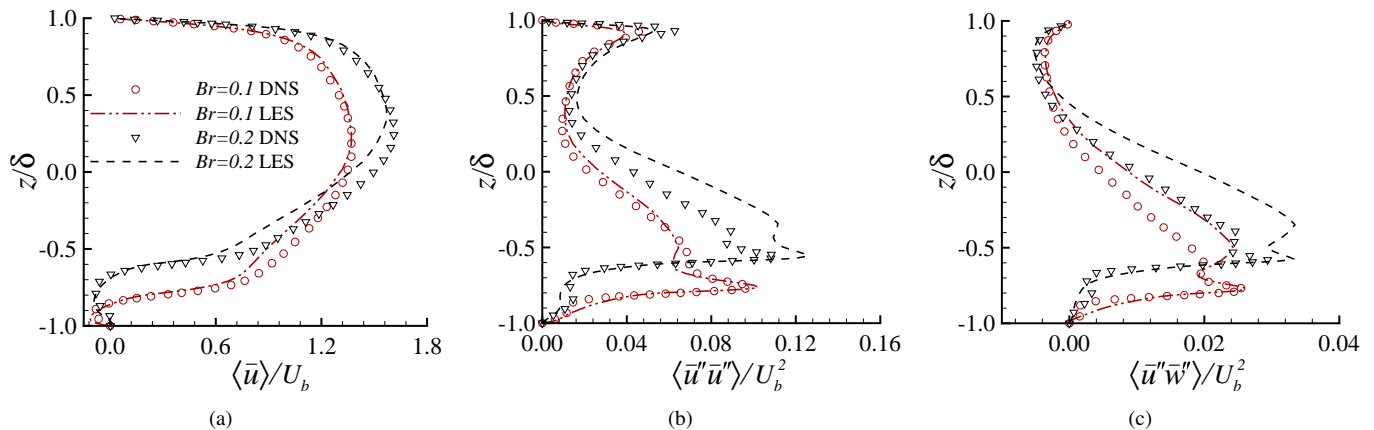


Fig. 2. Comparison of the wall-normal profiles of first- and second-order statistics against DNS data at point $(x/\delta, y/\delta)=(0.4, 0.0)$ for the different blockage ratios. (a) mean streamwise velocity $\langle \bar{u} \rangle$; (b) Reynolds normal stress $\langle \bar{u}'' \bar{u}'' \rangle$; and (c) Reynolds shear stress $\langle \bar{u}'' \bar{w}'' \rangle$.

grid level is set to two ($\tilde{\Delta}/\bar{\Delta} = 2$). Finite volume method (FVM) code developed on FORTRAN 90/95 is used and parallelized to allow for message-passing interface (MPI). A second-order scheme is used for both the spatial and temporal discretization; a central difference scheme is used for the spatial dimensions and the Runge-Kutta method is used for the temporal dimension. The time step was set to $2 \times 10^{-4} \delta / U_b$ and the Courant-Friedrichs-Lewy (CFL) number was set to be 0.2. For this analysis, the resolved instantaneous velocity, \bar{u}_i , is decomposed to the addition of the mean velocity averaged over time and eight rib pitches, $\langle \bar{u}_i \rangle$, and the resolved velocity fluctuations, \bar{u}_i'' . All simulations were complete using 64 central processing unit (CPU) cores on the WestGrid (Western Canada Research Grid) supercomputers. Approximately 185,000 core hours were used for each simulation to solve the velocity field and to collect all statistics.

III. VALIDATION

Extensive validation for wall-normal first- and second-order statistics (i.e. $\langle \bar{u} \rangle$, $\langle \bar{u}'' \bar{u}'' \rangle$ and $-\langle \bar{u}'' \bar{w}'' \rangle$) was completed to validate the results in the central $(x-z)$ plane at $(x/\delta, y/\delta)=(0.4, 0.0)$. The results were compared to a DNS study with identical geometry, and are presented in Fig. 2. Very good agreement was obtained for $\langle \bar{u} \rangle / U_b$, with no major under or overpredictions. In Fig. 2(a), the recirculation zones are distinguishable by the negative streamwise velocity found below the rib crest for both blockage ratios. It is also interesting to note that as the rib height increases, the magnitude of the maximum streamwise velocity becomes larger and the peak location moves towards the smooth top wall. Similar results were obtained by Lee *et al.* who used DNS to study channel flow with three-dimensional cubes on the lower wall [9]. Furthermore, good agreement between the LES predicted and DNS results for the resolved Reynolds stress is observed. The resolved Reynolds stresses are augmented on the bottom half of the duct, with the first peak for the blockage ratio of 0.1 and 0.2 being found in the region immediately above the rib crest, situated at $z/\delta=-0.76$ and -0.56 , respectively. A second maxima for the resolved Reynolds stress is located

near the smooth top wall at approximately $z/\delta=1.0$; which is very similar to a turbulent channel flow [10]. As the rib height increases from the blockage ratio of 0.1 to 0.2, turbulence is promoted and the resolved Reynolds stress values are increased; this increase is demonstrated by the amplified peak near the rough wall for the blockage ratio of 0.2, which is also observed in the DNS results of Nagano *et al.* who studied rough channel flow with varying rib height [11].

IV. RESULTS

In this paper, two different blockage ratios were compared ($Br=0.1$ and 0.2), to understand the blockage effects of ribs on both the mean and turbulent flow fields. In doing so, first- and second-order statistics are investigated by the analysis of friction and form drags, and Reynolds stresses, respectively. Furthermore, turbulent structures are analyzed using streamwise two-point autocorrelation.

A. Mean Flow Field

Figure 3 shows the mean streamwise velocity superimposed with streamlines in the central $(x-z)$ plane for two different rib heights. It is evident from Fig. 3(b) that a large recirculation region (point I), which spans the entire cavity, is apparent immediately behind the rib element. This causes the occurrence of a reattachment point on the upstream vertical wall of rib, generating a high-pressure region; however, for the rib case with $Br=0.1$, the reattachment point (point II) is found approximately at $x/\delta=1.0$, or four times the roughness height from the leeward side of the rib. This observation is consistent with the LES completed by Cui *et al.* for k-type roughnesses [12]. Furthermore, a small recirculation bubble (point III) is formed immediately prior to the downstream rib on the windward face.

In a rib-roughened channel form drag, in addition to skin friction, contributes to the resistance of flow due to the difference of surface-averaged pressure on the windward and leeward sides of the ribs [13]. Figures 4(a) and 4(b) show the contours of the form drag coefficient, $C_p = \langle \bar{p} \rangle / (\rho U_b^2 / 2)$, at the roughness element in the $(x-z)$ central plane for both

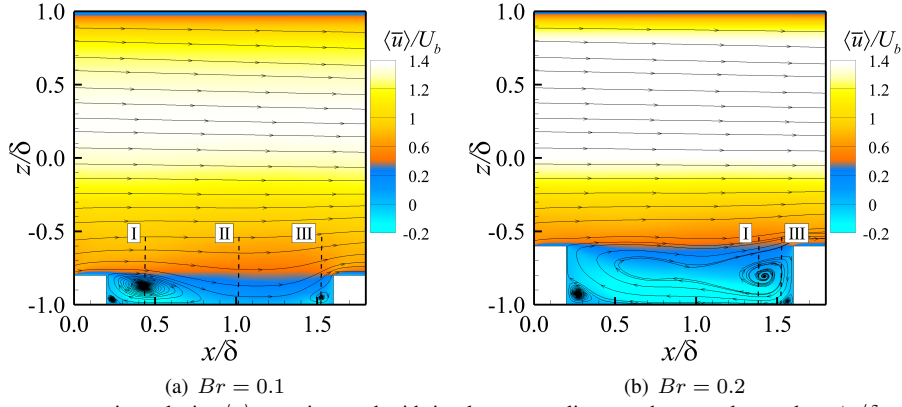


Fig. 3. Contours of the mean streamwise velocity $\langle \bar{u} \rangle$ superimposed with in-plane streamlines on the central $x-z$ plane ($y/\delta = 0$) for (a) $Br=0.1$ and (b) $Br=0.2$.

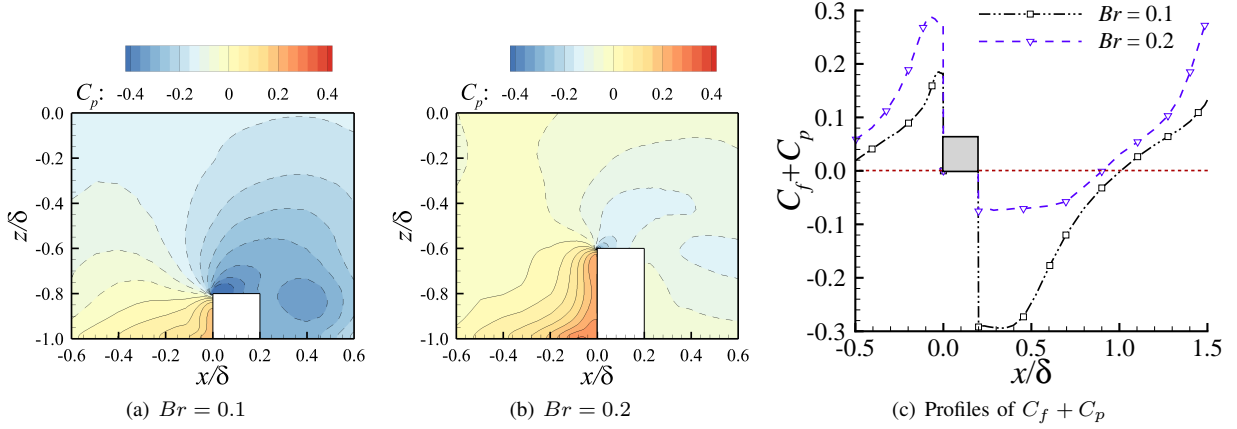


Fig. 4. (a), (b) Contours of the resolved form drag coefficient C_p in the central $x-z$ plane; (c) comparison of the total drag coefficient $C_p + C_f$ for both blockage ratios.

blockage ratios. By comparing Figs. 4(a) and 4(b), it is evident that in the $Br=0.2$, a higher pressure region is apparent near the windward face of the rib, exemplifying the expected results from the larger, more intense recirculation region produced. Oppositely, near the leeward face of the rib, a greater negative value can be observed for the lower blockage ratio. This can be explained by the occurrence of a higher velocity gradient (see Fig. 2(a)) near the leeward face, owing to accelerating flow passing over the rib and a high local total pressure loss induced by the impingement zone. Figure 4(c) compares the streamwise profile of the total drag, $C_f + C_p$, at $(y/\delta, z/\delta)=(0.0, -1.0)$ in the central ($x-z$) plane for both blockage ratios. It is expected that the drag form coefficient retains a negative value further downstream for $Br=0.2$ due to the elongated recirculation region (see Figs. 3(a) and 3(b)); however, from Fig. 4(c), the total drag for $Br = 0.2$ becomes positive before $Br = 0.1$ in the streamwise direction, signifying the fact that the skin friction coefficient, $C_f = \tau_w/(\rho U_b^2/2)$, must be greater for the higher rib case at $x/\delta=1.0$. Here, the skin friction coefficient is based on the local wall friction, τ_w , which is calculated by $\tau_w = \mu[(\partial\langle \bar{u} \rangle/\partial z)^2 + (\partial\langle \bar{w} \rangle/\partial z)^2]_{z=0}^{1/2}$.

B. Second-Order Statistics

The resolved Reynolds stresses are normalized by U_b^2 and are compared at two different location in the streamwise direction, $x/\delta=0.6$ and 1.4 . Comparing the plots for the different blockage ratios, it is clear that the resolved Reynolds stresses are larger for $Br=0.2$ at both streamwise locations due to the promotion of turbulence level caused by the intensified vortex shedding above the rib crest. For the resolved streamwise normal stress, $\langle \bar{u}''\bar{u}'' \rangle$, plots in Figs. 5(a) and 5(d) show a higher level of stress at $x/\delta=0.6$ as compared to $x/\delta=1.4$. This diminishing stress in the streamwise direction can be explained by a dissipation of the shear layer. Another important characteristic of the flow, depicted in Fig. 5(b) and 5(e), is the difference in the peak $\langle \bar{w}''\bar{w}'' \rangle$ magnitude near the rough wall. As the rib height increases, the turbulent energy is redistributed from the streamwise direction to the spanwise and wall-normal directions causing more isotropic flow as compared to the anisotropic flow for the blockage ratio of 0.1. According to a hypothesis created by Townsend [14], the roughness sublayer ends at a wall-normal location of five times the roughness height. Above the roughness sublayer, the turbulent stresses should not express any inhomogeneities along the streamwise direction as the effects of the roughness will not permeate past this point. For $Br=0.1$, which has a roughness sublayer ending

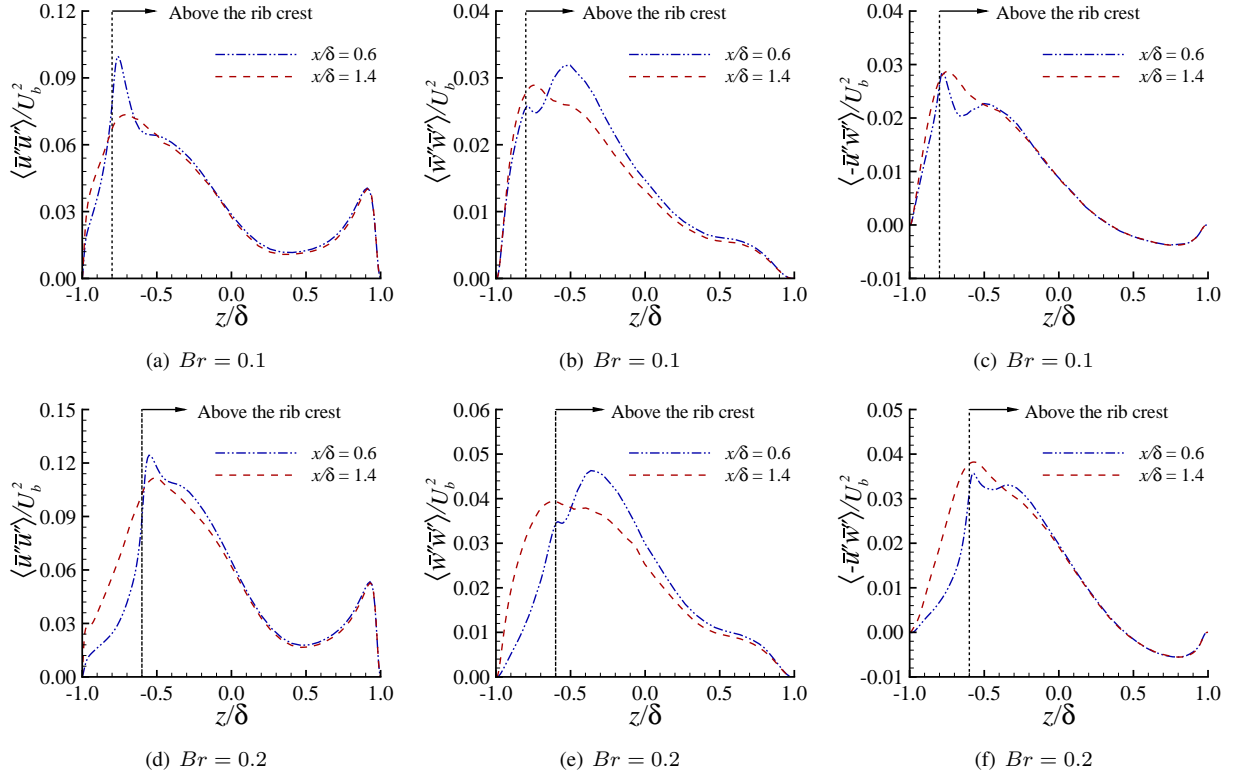


Fig. 5. Wall-normal profiles of (a), (d) Reynolds normal stress $\langle \bar{u}''\bar{u}'' \rangle$; (b), (e) Reynolds normal stress $\langle \bar{w}''\bar{w}'' \rangle$; and (c), (f) Reynolds shear stress $\langle -\bar{u}''\bar{w}'' \rangle$ in the central (x - z) plane at $(x/\delta, y/\delta)=(0.6, 0.0)$ and $(x/\delta, y/\delta)=(1.4, 0.0)$, respectively.

at $z/\delta=0.0$, Figs. 5(a)-(c) show that the resolved Reynolds stresses are essentially converged for the two streamwise locations above the hypothesized roughness sublayer, thereby agreeing with the Townsend Reynolds number similarity on rough walls hypothesis. Further, owing to the existence of the mean recirculation bubble within the cavity, a negative resolved velocity gradient, shown in Fig. 2(a), and a positive resolved Reynolds shear stress, found below the rib crest, are indicative of negative turbulent production.

C. Turbulent Flow Structures

The effects of rib height on turbulent flow structures can further be studied by comparing the values of the spatial two-point autocorrelation of velocity fluctuations and is defined as:

$$R_{ij}^s(x, z) = \frac{\langle \bar{u}_i''(x, z)\bar{u}_j''(x_{ref}, z_{ref}) \rangle}{\sqrt{\langle \bar{u}_i''(x, z)^2 \rangle \langle \bar{u}_j''(x_{ref}, z_{ref})^2 \rangle}}. \quad (5)$$

In this equation, the superscript s stands for spatial correlation and (x_{ref}, z_{ref}) relates to the coordinate of the reference point. The reference points were chosen at $x/\delta=0.6$, with the wall-normal coordinates, $z/\delta=-0.76$ and -0.56 , chosen to coincide with the maximum $\langle \bar{u}''\bar{u}'' \rangle$ and $-\langle \bar{u}''\bar{w}'' \rangle$ values previously observed. The angle of inclination for the two-point autocorrelation should be studied as it has been shown by Christensen *et al.* to be similar in magnitude to the inclination of hairpin vortex packages in instantaneous snapshots [15]. For this study, the angle of inclination was determined by using

a least-squares fit to the point farthest away from the self-correlation peak (where $R_{uu}=1$) in the upstream direction.

Based on the studies of Coceal *et al.* [7] and Adrian *et al.* [16], two main phenomena impact the angle of inclination for the two-point autocorrelation. First of all, the antisymmetric part of the shear tensor (i.e., $\Omega_{ij} = 0.5(d\langle \bar{u}_i \rangle / dx_j - d\langle \bar{u}_j \rangle / dx_i)$) causes the vorticity to be rotated towards the streamwise direction, leading to a decrease in the angle of inclination. Simultaneously, through a process called self-induction, the rotation of the legs of a hairpin structure cause the harpin structure itself to rotate towards the vertical; this causes the angle of inclination to increase. It has been proven by Adrian *et al.* that both of these phenomena decrease as the distance from the bottom wall increases [16]. Therefore, it is expected that the angle of inclination is determined by the equilibrium of these phenomena. From Figs. 6(a) and 6(b), the angle of inclination is shown to decrease above the rib crest for higher blockage ratios reflecting a combination of the antisymmetric part of the shear tensor being sustained and the self-induction decaying at greater rates than in the lower blockage ratio.

V. CONCLUSIONS

A comparative study on the height of rib roughness elements in square duct flow has been conducted using LES. The normalized Reynolds number for both simulations was fixed at 2800 with respect to the bulk velocity. The simulation

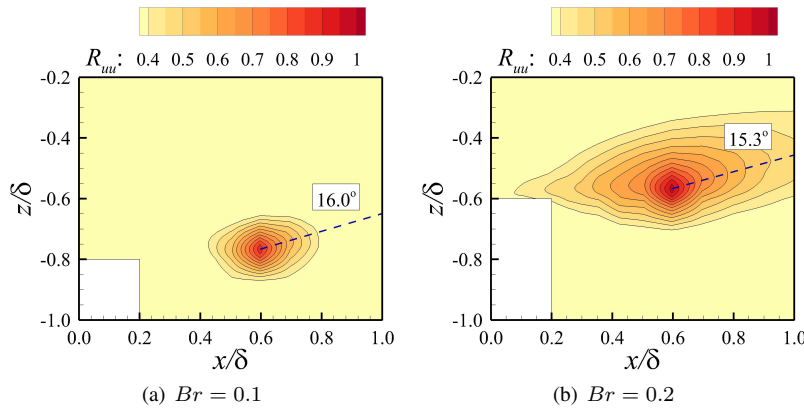


Fig. 6. Contours of the two-point autocorrelation in the central (x - z) plane at (a) $z/\delta = -0.76$ and (b) $z/\delta = -0.56$ for the $Br=0.1$ and 0.2 , respectively.

results are validated by comparing the statistics of the first- and second-order moments of the turbulence field against the obtained results from a DNS study with similar cases. The differences observed in the variation of turbulent behaviour for both blockage ratios were analyzed in terms of the mean flow field, second-order statistics and coherent flow structures. From the mean flow field, it was observed that enhanced blockage effects led to an increased pressure zone on the windward face of the rib, owing to the intensified recirculation region. As a consequence, a higher streamwise momentum convected downstream. With respect to Reynolds stresses, it was observed that the perpendicular ribs induce much higher turbulence level in the bottom half ($z/\delta < 0.0$) of the duct, compared with the smooth top wall. The streamwise two-point autocorrelation was then plotted and the angle of inclination, which can also be related to the angle of hairpin legs, was determined with results showing a greater angle observed for $Br=0.1$. This was attributed to the equilibrium of the frequency of ejection events and the antisymmetric portion of the stress tensor.

ACKNOWLEDGMENT

The computational resources provided by WestGrid (Western Canada Research Grid) are appreciated.

REFERENCES

- [1] S. Leonardi, P. Orlandi, R. J. Smalley, L. Djenidi, and R. A. Antonia, "Direct numerical simulations of turbulent channel flow with transverse square bars on one wall," *J. Fluid Mech.*, vol. 491, pp. 229–238, 2003.
- [2] L. Marocco, D. Fustinoni, P. Gramazio, and A. Niro, "First numerical results on forced-convection heat transfer inside a rectangular channel with straight ribs on lower and upper walls," in *29th UIT Heat Transfer Conferenc.* ETS, 2011, pp. 217–222.
- [3] L. Marocco, P. Gramazio, D. Fustinoni, and A. Niro, "Numerical simulation of forced-convection heat transfer in a ribbed channel with high blockage," in *30th UIT Heat Transfer Conference.* Società Editrice Esculapio, 2012, pp. 259–263.
- [4] L. Marocco and A. Franco, "Direct numerical simulation and rans comparison of forced turbulent convective heat transfer in a staggered ribbed channel with high blockage," *J. Heat Transfer*, vol. 139, no. 2, p. 021701, 2017.
- [5] D. K. Tafti, "Evaluating the role of subgrid stress modeling in a ribbed duct for the internal cooling of turbine blades," *Int. J. Heat Fluid Flow*, vol. 26, no. 1, pp. 92–104, 2005.
- [6] P.-Å. Krogstad, H. I. Andersson, O. M. Bakken, and A. Ashraffian, "An experimental and numerical study of channel flow with rough walls," *J. Fluid Mech.*, vol. 530, pp. 327–352, 2005.
- [7] O. Coceal, A. Dobre, T. G. Thomas, and S. E. Belcher, "Structure of turbulent flow over regular arrays of cubical roughness," *J. Fluid Mech.*, vol. 589, pp. 375–409, 2007.
- [8] D. K. Lilly, "A proposed modification of the germano subgrid-scale closure method," *Physics of Fluids A*, vol. 4, no. 3, pp. 633–635, 1992.
- [9] J. H. Lee, H. J. Sung, and P.-Å. Krogstad, "Direct numerical simulation of the turbulent boundary layer over a cube-roughened wall," *J. of Fluid Mech.*, vol. 669, pp. 397–431, 2011.
- [10] J. Kim, P. Moin, and R. Moser, "Turbulence statistics in fully developed channel flow at low reynolds number," *J. Fluid Mech.*, vol. 177, pp. 133–166, 1987.
- [11] Y. Nagano, H. Hattori, and T. Houra, "Dns of velocity and thermal fields in turbulent channel flow with transverse-rib roughness," *Int. J. Heat Fluid Flow*, vol. 25, no. 3, pp. 393–403, 2004.
- [12] J. Cui, V. C. Patel, and C.-L. Lin, "Large-eddy simulation of turbulent flow in a channel with rib roughness," *Int. J. Heat Fluid Flow*, vol. 24, no. 3, pp. 372–388, 2003.
- [13] A. Ashraffian, H. I. Andersson, and M. Manhart, "Dns of turbulent flow in a rod-roughened channel," *Int. J. Heat Fluid Flow*, vol. 25, no. 3, pp. 373–383, 2004.
- [14] A. A. Townsend, "The structure of turbulent shear flows," 1976.
- [15] K. T. Christensen and Y. Wu, "Characteristics of vortex organization in the outer layer of wall turbulence," in *Turbulence and Shear Flow Phenomena digital library online*, 2005.
- [16] R. J. Adrian, C. D. Meinhart, and C. D. Tomkins, "Vortex organization in the outer region of the turbulent boundary layer," *J. Fluid Mech.*, vol. 422, pp. 1–54, 2000.

Multiphase Flows

Numerical Study of Droplet Behavior using Lattice Boltzmann Method

Zhe (Ashley) Chen
 Department of Mechanical Engineering
 University of Alberta
 Edmonton, AB
 zhe8@ualberta.ca

Alexandra Komrakova
 Department of Mechanical Engineering
 University of Alberta
 Edmonton, AB
 komrakov@ualberta.ca

ABSTRACT

Direct numerical simulations (DNSs) of complex multiphase systems (liquid-liquid and gas-liquid) is a subject of ongoing research since there are numerous numerical issues that need to be addressed in order to produce accurate and physically realistic results. The key challenges of the numerical techniques are related to the ability of the method to handle high density and viscosity ratios, conserve mass of the dispersed phase, and accurately capture the moving contact line when there is an interaction of the dispersed phase with the solid surface.

In this study, the diffuse interface lattice Boltzmann method (LBM) proposed by Fakhari et al. (Fakhari, 2017) is used to perform three-dimensional simulations of liquid-liquid and liquid-liquid-solid systems. The objective of the study is to assess the capabilities of the method when applied to a wide variety of the benchmarks. For instance, the ability of the method to capture the equilibrium contact angle was tested. The numerical results are shown in Figure 1. The maximum relative deviation between the numerical and analytical predictions of the maximum height of the drop when equilibrium is achieved is less than 5% for θ in the range $(60-120)^\circ$.

Then the gravity-driven flow of the drop inside the narrow channel was investigated. The sample results are given in Figure 2 (left). Initially spherical drop is injected at the bottom of the channel. Due to gravity, it travels upward and deforms. Eventually it reaches a terminal velocity shown in Figure 2 (right). The detailed results of these problems will be presented at the conference.

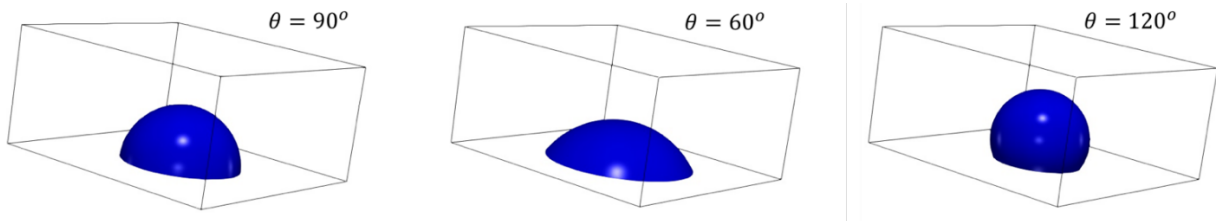


Figure 1. Liquid-liquid-solid equilibrium for different properties of the solid surface (variation in contact angle)

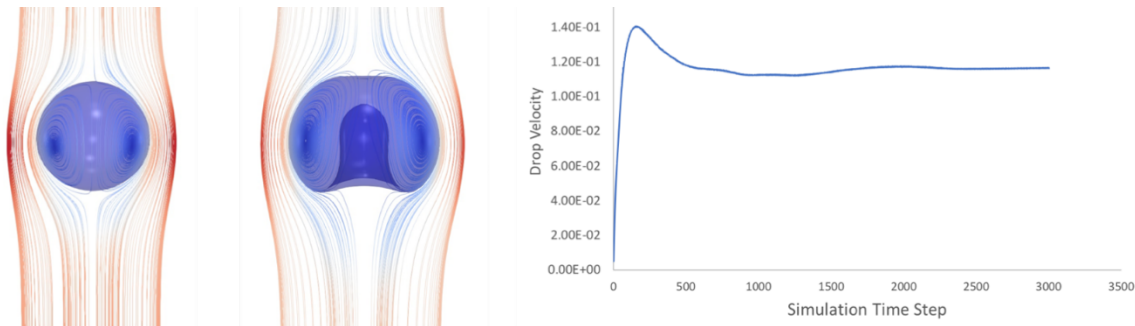


Figure 2. Gravity-driven drop in a narrow channel (drop shape and velocity of the drop as a function of a time step).

REFERENCES

Fakhari, A., & Bolster, D. (2017). Diffuse interface modeling of three-phase contact line dynamics on curved boundaries: A lattice Boltzmann model for large density and viscosity ratios. *Journal of Computational Physics*, 620-638.

Numerical study of atomization mechanisms of laminar liquid jets in high-viscous gaseous crossflows

Mohammad Hashemi¹, Mehdi Jadidi¹, Ali Dolatabadi¹

¹ Department of Mechanical, Industrial and Aerospace Engineering, Concordia University, Montreal, QC, Canada H3G 1M8

Abstract

Atomization of liquid jets in subsonic gaseous crossflows is of great importance in thermal spray coating process. In this process, suspensions and solution precursors are injected into high-viscous plasma crossflows where the gas-flow Reynolds number is around 10. The coatings' quality strongly depends on the breakup of liquid jets in plasma crossflows. In the absence of comprehensive atomization measurements, robust numerical simulations have suggested a detailed picture of atomization process in recent years. Although the numerical simulation is a powerful alternative for understanding the atomization mechanisms, enormous amount of meshes should be generated to capture the finest droplets generated by primary or secondary breakups. Therefore, they are computationally too expensive. In this work, an Eulerian/Lagrangian numerical model is used to handle this issue. The conservation of mass and momentum, and capturing the interface are solved by an Eulerian computational fluid dynamics (CFD) code, known as Basilisk. In the Eulerian solver, the incompressible variable-density Navier–Stokes equations are solved by using finite volume schemes. The interface is tracked by a geometric volume-of-fluid (VOF) approach. In this study, the fine droplets are filtered based on size and shape criteria. Then, their motion is modeled by a Lagrangian point particles (LPP) approach. At first, the detailed simulation results at a rather high density ratio ($\rho_l/\rho_g \sim 845$) are validated with previous researches on surface wavelength, breakup location and column trajectory. Then, a parametric study is performed on the atomization process in a wide range of gas-flow Reynolds numbers ($Re_g = 5.5 - 5500$). The mass flow rate, size and velocity of droplets generated along the jet column are investigated and compared with experimental measurements in the literature. Ultimately, the effect of gas viscosity on jet deformation and breakup physics are analyzed.

Keywords

Atomization; Multiphase flow; Eulerian/Lagrangian solver; Volume-of-fluid; Thermal spray coating; Plasma crossflow

A MULTI-REGION CFD MODEL FOR AIRCRAFT GROUND DEICING BY LIQUID SPRAY

Sami Ernez and François Morency
Department of Mechanical Engineering
École de technologie supérieure
Montréal, Québec, Canada
Email: sami.ernez.1@etsmtl.net

ABSTRACT

Several researches have focused on the development of CFD models for deicing aircraft in flight to help in the design of ice protection system (Al-Khalil & Potapczuk, 1993; Morency, Tezok, & Parashivoiu, 2000; Liu & Hua, 2004). On the ground, aircrafts also undergo icing phenomenon. Several accidents caused by this phenomenon have been recorded off (Moshansky, 1992; National Transportation Safety Board, 1993) as a result of which the aircraft ground deicing was designed and imposed. The aircraft ground deicing process used at most airports is carried out using an impinging spray. The standard for surface decontamination focuses more on the final results than on how to achieve them. Thus, the lack of an optimal deicing scenario causes financial and environmental losses (Transports Canada, 2005). Numerous experimental studies have shown that variation in spray parameters, such as inclination angle and distance, influences the heat transfer between the spray and a wall (Webb & Ma, 1995). This work aims to model the ground deicing process by CFD in order to investigate the effect of the spray parameter on the consumption of deicing fluid.

The CFD test bench of this process must model a turbulent multiphase flow with heat transfer and phase change. The coupling of these physical phenomena is expensive in term of computational resources. A multi-region model is developed on OpenFOAM-v1812. The multi-region approach serves to solve different equations sets on the same computational mesh. Two regions are defined in this study. A first region is defined for the liquid spray, the multiphase flow is treated with a Eulerian-Lagrangian model. The second region is defined for a thin gas layer, a liquid film and ice. The multiphase flow in this region is carried out with a Eulerian-Eulerian model based on (Rusche, 2002) work. Finally, the enthalpy-porosity technique of (Voller, Cross, & Markatos, 1987) is used to model ice melting on the second region. The two regions exchange mass, momentum, energy and species via source terms injected on the interface separating them.

The spray droplets are modeled as Lagrangian particles in order to minimize the droplet size constraint on the mesh. Near the contaminated surface, those particles are converted in a Eulerian field (Volume of fluid) to interact with ice and a liquid film. The liquid film is composed of the deicing fluid and water from the ice melting. Spraying and ice melting are verified separately and then coupled. The coupled model is first verified using a clean flat plate and then a contaminated surface. The time evolution of ice thickness is presented for different spray configurations. The deicing fluid consumption is then determined for each configuration. This model simulates the aircraft ground deicing process. It is important to mention that no similar CFD model is present in the literature.

Moshansky, T. H. V. P. (1992). *Commission of inquiry into the Air Ontario crash at Dryden, Ontario: Final Report: Technical Appendices. Canadian Cataloguing in Publication Data* (Vol. Appendix 4).

National Transportation Safety Board. (1993). *Aircraft Accident Report Washington, D.C. 20594 AIRCRAFT, Takeoff stall in icing Conditions USAIR flight 405 FOKKER F-28, New York March 22, 1992*. Retrieved from <http://www.ntsb.gov/investigations/AccidentReports/Reports/AAR0003.pdf>

Rusche, H. (2002). *Computational Fluid Dynamics of Dispersed Two-Phase Flows at High Phase Fractions*. Retrieved from <http://powerlab.fsb.hr/ped/kturbo/OpenFOAM/docs/HenrikRuschePhD2002.pdf>

Transports Canada. (2005). *Guidelines for Aircraft Ground Icing Operations (Chapter 13)*. Ottawa. Retrieved from <http://www.tc.gc.ca/publications/en/tp14052/pdf/hr/tp14052e.pdf>

Voller, V. R., Cross, M., & Markatos, N. C. (1987). An Enthalpy Method For Convection / Diffusion Phase Change, *24*, 271–284.

Webb, B. W., & Ma, C.-F. (1995). Single-Phase Liquid Jet Impingement Heat Transfer. *Advances in Heat Transfer*, *26*, 105–217. [https://doi.org/10.1016/S0065-2717\(08\)70296-X](https://doi.org/10.1016/S0065-2717(08)70296-X)

Novel Impeller Designs for Bioreactor Applications: CFD Analysis of Shear Stress

Sinthuran Jegatheeswaran (PhD student)

Chemical Engineering Department
Ryerson University
Toronto, Canada
s2jegath@ryerson.ca

Farhad Ein-Mozaffari (Professor)

Chemical Engineering Department
Ryerson University
Toronto, Canada
fmozaffa@ryerson.ca

ABSTRACT

The worldwide mammalian cell culture capacity to produce biopharmaceuticals was estimated to be 1.7 million litres in 2004 [1]. In 2021, the global market is expected to be around \$4.3 billion among which the single-use bioreactor is anticipated to generate the largest revenue [2]. One of the major challenges in bioreactors for the applications of fermentation and wastewater treatment is maintaining a critical level of dissolved oxygen concentration in highly viscous fluids to ensure the survival of microorganisms. The shear created by the impeller is not enough to deform and to break the bubbles away from the impeller region. As a result, inadequate oxygen concentration in the bulk fluid away from the impeller region causes the micro-organisms to die, resulting in an ineffective biochemical process. Even though a high impeller speed may deform the entire fluid and result in a complete gas dispersion, the cell damage associated to shear stress can be predominant. To alleviate the cell damage, a few prototypes of low-shear impeller designs were developed, with the help of valuable CFD insights, for the bioreactor applications. In a 50 L tank vessel, the electrical resistance tomographic (ERT) technique was used to characterize the gas dispersion in non-Newtonian fluids using a coaxial mixer, which is a combination of central impeller and a slowly moving anchor near the wall. The computational fluid dynamics (CFD) multiphase model was validated using experimentally measured power consumption and local gas holdup. The experiments were conducted within the range of generalized Reynolds number ($102.23 < Re_g < 172.15$) and gas flow number ($0.0038 < Fl < 0.0056$).

1. A. Sinclair, (2004), Advances in Large-scale Biopharmaceutical Manufacturing and Scale-up Production (Langer, E. S., ed.), ASM Press and the Institute for Science and Technology Management, Washington, DC
2. S.S. Dewan, Single-use technologies for biopharmaceuticals: Global markets, BCC Research LLC, 2017:
<https://www.bccresearch.com/market-research/biotechnology/single-use-technologies-biopharmaceuticals-report-bio099c.html>

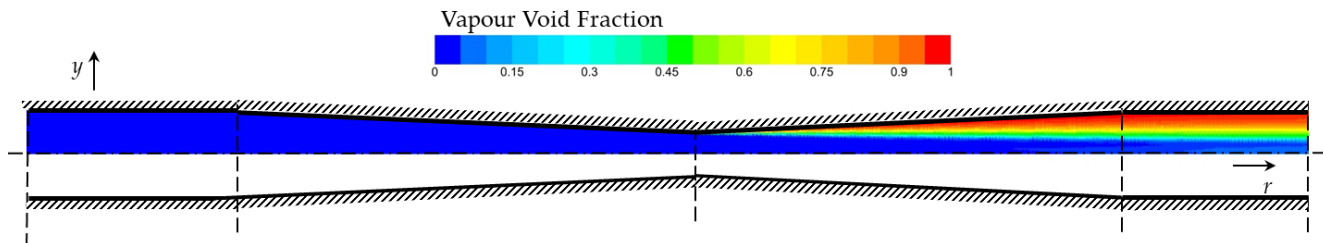
The Effects of Turbulent Models on Multiphase Flashing Flow

Tarek H. Nigim, Lei Li, Carlos F. Lange
Department of Mechanical Engineering
University of Alberta
Edmonton, Canada
carlos.lange@ualberta.ca

ABSTRACT

Flashing is a complex multiphase flow with a phase change process. It occurs due to the reduction of the local pressure of a liquid phase below the local saturation pressure. Flashing flow is a common phenomenon in many industrial applications such as desalination, vacuum freezing, refrigeration, food processing, inflow control devices (ICD) for oil and gas field, and loss-of-coolant accidents (LOCA) of pressurised water in nuclear reactors. Flashing can be intentional, for example, when it is used in the process of desalination. But flashing can also be detrimental, when it occurs in flow control nozzles that were not designed for flashing.

In the present work, we have studied the effects of different turbulent models on a computational field model that is built to predict the multiphase flashing flow inside a converging-diverging nozzle. The commercial computational fluid dynamics (CFD) code Fluent is used for this purpose. The model was applied to predict the multiphase flow field of a well-known converging-diverging nozzle to calculate the inception of flashing and the vapour void fraction inside the nozzle for validation. $k-\epsilon$ Standard, $k-\epsilon$ Realizable, $k-\epsilon$ RNG, $k-\omega$, and Reynolds stress model (RSM) are the turbulent models that are compared in our current study. For each turbulent model case, the vapour void fraction and the gauge pressure along the converging-diverging nozzle is used for comparing the predicted results with high quality experimental data from the literature. The final comparison will also evaluate the cost benefit of using the various turbulence models, depending on their numerical performance, in order to identify the best model to use in the extensive parametric study that will follow.



CFD prediction of vapour void fraction inside the converging-diverging nozzle under flashing condition

Mass-Density-Based Model Using a Gaussian Moment Method for Polydisperse Multiphase Flow

James G. M^cDonald, Jarod Ryan
Mechanical Engineering, University of Ottawa
Ottawa, Canada
JRYAN062@uottawa.ca

Lucian Ivan
Nuclear Engineering & Systems Analysis Division
Canadian Nuclear Laboratories
Chalk River, Ontario, Canada, K0J 1J0
lucian.ivan@cnl.ca

ABSTRACT

Multiphase flow is used to refer to any fluid flow that consists of more than one phase. Multiphase flows are extremely important in engineering applications and there are many different models that are used for these applications. Recently, a new model for the flow of small particles within a background medium that includes a direct treatment for the high-order statistics of the particle movements and “internal” differentiating variables has been proposed [1]. This current model uses statistics that are based on the number density of particles, which means that small particles have as equal importance as compared to larger particles. This may not be desirable as larger particles carry more mass and may be more important in certain applications. This presentation shows the differences in the model when it is rebuilt from the ground up using mass-weighted statistics.

The method of moment closures from the kinetic theory of gas is able to produce partial differential equations that are capable of describing the evolution of arbitrary statistics describing the movement of a large collection of particles. The distribution function from the kinetic equation contains a description of the evolution of a particle through space and time. By taking moments of the distribution function, macroscopic observable properties can be determined. In order to be able to close the system of equations, one must restrict the distribution function to a prescribed form. Moment closure is a technique that is used to close off the infinite series of equations that would be needed to model a particle phase with infinite degrees of freedom. This form must have as many unknown free parameters as there are in the desired model and any moments in the system can then be integrated to be solved.

The flow of interest in this research involves particles that will range in size, however the volume of each individual particle remains constant with time. Therefore, while the particles may have a variety of different diameters, each particle will have a diameter that does not change in time. Using the same mathematical methodology that was used for the previous model, a fifteen-moment polydisperse Gaussian model based on mass-weighted statistics is used to model the particle motion. Using statistics based on the particle motion weighted by the particle mass rather than the number density, a modified set of fifteen partial differential equations is generated.

Results show that the resulting set of fifteen differential equations are, surprisingly, structurally identical to the number based model. However, the variables in the mass density model have an altered meaning. The mass density model is implemented within a two dimensional computational framework in order to run test calculations to compare the difference in solutions. The mass-density-based model is tested and compared against the number-based-density model for cases where an exact solution is known. Therefore, the accuracy of the mass-based model can be determined and compared against the number-based model to determine which model is preferable. More practical test cases are also considered.

References:

- [1] F. Forgues, L. Ivan, A. Trottier, J.G. McDonald, “A Gaussian Method for Polydisperse Multiphase Flow Modelling” Journal of Computational Physics, submitted, 2019

Application of a Piecewise Barotropic Equation of State in a Homogeneous Equilibrium Mixture (HEM) Cavitation Model

S. Rahbarimanesh and J. Brinkerhoff

School of Engineering, University of British Columbia
Kelowna, BC, Canada V1V 1V7
Email: joshua.brinkerhoff@ubc.ca

I.K. Karathanassis and M. Gavaises

School of Mathematics, Computer Science and
Engineering, University of London
Northampton Square, EC1V 0HB London, UK

Abstract—The current paper is intended to address the effects of employing a piecewise two-phase barotropic equation of state in a homogeneous equilibrium phase-change modeling approach. The cavitation model is used for simulating the well-known fundamental test case of diesel cavitation in a throttle geometry, which resembles the flow in industrial applications such as inlet check valves of positive-displacement pumps and nozzle injectors. Comparison of the current results against the available experimental data for the throttle flow shows that the employed equation of state leads to a better match when compared with the commonly-used single-step barotropic equation of state. Such observation highlights the influence of proper capture of state properties of vapor, liquid, and mixture phases on the performance of numerical modeling in cavitation flows.

Keywords-component; cavitation; equation of state; homogeneous equilibrium modeling

I. INTRODUCTION

The process of changing the liquid phase to vapor - termed cavitation - as an important parameter in design of turbomachinery, has been extensively studied through numerical and/or experimental tools within the past decades [1,2]. On the numerical side, these investigations are generally developed using two major approaches: Eulerian-Eulerian and Eulerian-Lagrangian, accompanied by a cavitation model. The former methodology assumes the liquid and vapor as interpenetrating continua and solves the complete set of equations for every phase, whereas the latter approach applies the Eulerian treatment on the continuous phase and the Lagrangian approach for the dispersed phase [3]. In either case, the complexity of the cavitation modeling can vary depending on the assumptions on thermodynamic equilibrium, mechanical and thermal equilibrium, interface capturing and compressibility. For industrial applications including cavitation flows in turbomachinery, which typically involve millions of interacting bubbles, methodologies such as explicit interface tracking with volume of fluid (VOF) are too computationally expensive, and instead mixture approaches i.e. homogeneous [4] or inhomogeneous [5], or the bubble tracking Eulerian-Lagrangian methods [6] have become more popular. More

specifically, in the so-called homogeneous equilibrium mixture (HEM) methodology, both phases are assumed to be completely mixed in cells, in a thermo-mechanical equilibrium condition, with the phase-change being computed by employing, typically, a barotropic equation of state (EOS). Related to this method, Bicer et al. [7] investigated turbulent spray cavitation of water in an injector using the homogeneous equilibrium model coupled with a barotropic equation for the density field. Good agreement between the simulated cavitation region thickness and length with their experimental data was reported. Also, Coutier-Delgosha et al. [8] simulated the shedding behavior of vapor cavities in two venturi-shaped geometries using a homogeneous flow model with variable density and a barotropic equation of state to capture the vaporization and condensation processes. Such formulations are different from the so-called transport equation-based models (TEM) models such as those of Kunz [9], Zwart [10], and Schnerr-Sauer [11] which are developed based on the bubble two-phase flow (BTF) approach [12] and Rayleigh-Plesset equation [13]. These models solve separate transport equations for the liquid and vapor phases with source terms accounting for condensation and vaporization of the two phases. Example of this includes Hidalgo et al. [14] work which used two different cavitation models of Schnerr-Sauer [11] and Zwart [15] to compare unsteady turbulent cavitating behavior of water around a NACA 66 airfoil.

Phase-change modeling through proper calculation of state properties of cavitating fluid has recently been in focus of a limited number of research works. Among them, Goncalves and Patella [16] proposed a convex stiffened gas (the so-called SG) EOS for the pure phases and two formulations for the two-phase mixture: a mixture of stiffened gas and a sinusoidal barotropic EOS, and employed them in a homogenous one-fluid compressible Reynolds-Averaged Navier-Stokes (RANS) solver with a preconditioning scheme. By evaluation of the model for cavitation of a non-isothermal water flow inside a venturi, they reported an overall good agreement with experimental data, especially in the mixture interface regions with large acoustic speed jumps, though noting that the mixture of stiffened gas EOS failed to predict 'quasi-stable' cavity sheets with re-entrant jets. Koukouvinis et al. [17] performed a benchmark numerical modeling of cavitation damage of diesel flow in two distinct injector designs with moving needles, with

the overall goal of correlating pressure peaks due to vapor collapse to erosion development. Using a compressible LES methodology with a TEM-based two-phase homogenous mixture model, they showed that the inclusion of the Tait equation of state for the liquid phase can help capture large negative pressure gradients in cavitating regions. Also using the same Tait EOS for liquid, along with an ideal gas equation for vapor phase, Karathanassis et al. [18], conducted an extensive comparative study to examine the functionality of recently-developed compressible phase-change methodologies, i.e. non-equilibrium models of kinetic theory of gases (Hertz–Knudsen equation) and homogeneous relaxation model (HRM), as well as the equilibrium models of HEM and the bubble-dynamics TEM approach of Zwart-Gerber-Belamri, in a set of benchmark simulations of non-isothermal cavitating water inside a converging-diverging nozzle, a throttle, and a highly-pressurized pipe.

Given the fact that the precision of the cavitation models, even in the most recent studies, is still a challenge [2,16], the current study, as a part of an ongoing industrial project with Westport Fuel Systems©, is focused on improving the accuracy of the HEM methodology through incorporating a piecewise two-phase barotropic EOS which has the capability of capturing physical properties of cavitating flow in liquid, vapor, and vapor-liquid mixture states. As a first step towards this end, the present paper is particularly aimed to assess the efficiency of a HEM-based cavitation solver when used with a piecewise EOS, and compare it with the previously-reported results of the single-step mixture's equilibrium modeling. Successful extension of the current study to other fundamental benchmark 2D-3D validation scenarios can potentially lead the proposed model to be employed for more accurate computation of flow fields in complex cavitating flows, e.g. cryogenic liquefied natural gas (LNG) inside LNG-based fuel systems.

II. NUMERICAL MODEL

A. Governing Equations

The current work employs the currently-available *cavitatingFoam* solver in the open-source CFD package OpenFOAM®. The solver is a fully compressible two-phase flow code which employs homogeneous equilibrium mixture methodology with a single-step barotropic equation of state to describe transient phase-change in isothermal cavitating flows [2,19]. In brief, solution for cavitation of laminar compressible flows in this solver begins with solving the continuity equation for mixture density [19,20]:

$$\frac{\partial \rho_m}{\partial t} + \nabla \cdot (\rho_m \mathbf{u}) = 0 \quad (1)$$

where $\mathbf{u} = (u, v, w)$. The density field from this equation is found from a barotropic closure equation of state correlating ρ_m to mixture pressure p :

$$\frac{D\rho_m}{Dt} = \psi_m \frac{Dp}{Dt} \quad (2)$$

in which,

$$\psi_m = \alpha\psi_v + (1 - \alpha)\psi_l \quad (3)$$

that represents the mixture compressibility model of Waills [21] used in the present work. In this model the volume fraction of vapor α in the mixture is defined by:

$$\alpha = \frac{\rho_m - \rho_{l,sat}}{\rho_{v,sat} - \rho_{l,sat}} \quad (4)$$

where vapor phase density at saturation condition is given by:

$$\rho_{v,sat} = \psi_v p_{sat} \quad (5)$$

Note that subscript ‘ l ’ and ‘ v ’ in above equations describe liquid and vapor phases, respectively. Also, the subscript ‘ sat ’ stands for saturation condition. Mixture density calculations in *cavitatingFoam* are conducted by employing an iterative mixture’s equilibrium equation of state, based on Kärholm et al. [22] theory:

$$\rho_m = (1 - \alpha)\rho_l^0 + (\alpha\psi_v + (1 - \alpha)\psi_l) p_{sat} + \psi_m(p - p_{sat}), \quad (6)$$

where

$$\rho_l^0 = \rho_{l,sat} - \psi_l p_{sat} \quad (7)$$

that predicts density of liquid at the operating temperature. As a result of integrating (2) using (6), a pressure equation for mixture is formulated [19]:

$$\frac{\partial(\psi_m p)}{\partial t} - (\rho_l^0 + (\psi_l - \psi_v) p_{sat}) \frac{\partial\psi_m}{\partial t} - p_{sat} \frac{\partial\psi_m}{\partial t} + \nabla \cdot (\rho_m \mathbf{u}) = 0 \quad (8)$$

in which the velocity field is determined from the momentum equation:

$$\frac{\partial(\rho_m \mathbf{u})}{\partial t} + \nabla \cdot (\rho_m \mathbf{u} \mathbf{u}) + \nabla p = \nabla \cdot [\mu_m (\nabla \mathbf{u} + (\nabla \mathbf{u})^T)] \quad (9)$$

with mixture molecular viscosity μ_m :

$$\mu_m = \alpha\mu_v + (1 - \alpha)\mu_l \quad (10)$$

In *cavitatingFoam*, the PIMPLE algorithm [23] is used to couple the velocity and pressure equations through an iterative multi-step prediction-correction procedure. As a result of this coupling, density, volume fraction, compressibility, and viscosity fields are updated with solution.

B. Piecewise Two-phase Equation of State

Initializing the mixture calculations with the given equations (1)-(10), a piecewise equation of state in the form of equation (11) is implemented into the numerical procedure, as follows [17,24]

$$p(\rho) =$$

$$\left\{ \begin{array}{l} B \left[\left(\frac{\rho}{\rho_l} \right)^n - 1 \right] + p_{sat} \quad \rho \geq \rho_{l,sat} \\ \frac{c_v^2 c_l^2 \rho_v \rho_l (\rho_v - \rho_l)}{c_v^2 \rho_v^2 - c_l^2 \rho_l^2} \ln \left(\frac{\rho}{c_l^2 \rho_l (\rho_l - \rho) + c_v^2 \rho_v (\rho - \rho_l)} \right) + p_{ref} \quad \rho_{v,sat} \leq \rho \leq \rho_{l,sat} \\ \rho R T_{ref} \quad \rho \leq \rho_{v,sat} \end{array} \right. \quad (11)$$

in which B is the bulk modulus of the operating liquid (corresponding to the reference speed of sound), c is the speed of sound, and n is a reference exponent typically set to 7.15 for all weakly compressible materials such as liquids [25]. Also, the subscript ‘*ref*’ stands for reference conditions. Equation of state (11) is a three-step function comprised of a Tait EOS, an ideal gas EOS, and a transitional Wallis-based EOS, respectively used for calculating cavitating flow properties at fully liquid, fully vapor, and mixture states. Such a model resolves the common difficulty with HEM approach through specifying an EOS that covers all possible fluid states [16,17].

III. SIMULATION SETUP

Following the experimental work of Morozov and Iben [26], the modified solver is applied to a cavitating flow of diesel inside a 2D throttle geometry which is made of two high and low-pressure 5×5 mm square-shaped chambers attached via a rectangular throat with the dimension of $295 \times 995 \mu\text{m}$ (Figure 1). The inlet and outlet of the domain are, respectively, located at approximately 17 throttle-widths upstream and 30 throttle-widths downstream, to minimize the boundary influence on the resulting flow. The computational domain is meshed with 1,253,000 non-uniform hexahedral elements, with four levels of refinement for the throat area cells, based on the numerical study of Edelbauer et al. [3]. To sufficiently resolve the grid for high-gradient regions near the walls and shear layer cores, boundary layer mesh generation method was also used consisting of 10 prismatic layers with smallest element thickness of 0.41 mm and wall-normal grading rate of 0.15 [2]. The liquid diesel (initial phase with no vapor) is simulated for an inlet total pressure of 300 bar and a constant pressure of 120 bar in the outlet, at the saturation pressure of 4500 Pa. Liquid diesel operates with the density of 830 kg/m^3 (with the bulk modulus $B = 181 \text{ MPa}$) and the dynamic viscosity of $0.0021 \text{ Pa}\cdot\text{s}$, which correspond to the operating temperature of 320 K.

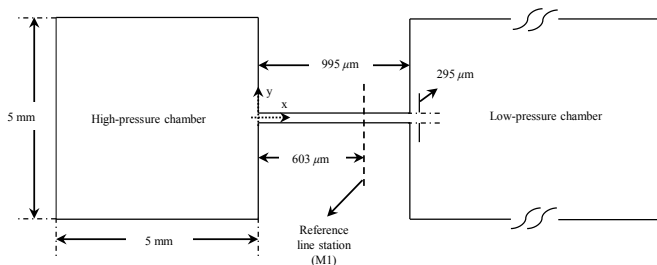


Figure 1: Computational domain for the throttle flow

In order to enhance the accuracy of the numerical solution, high resolution (cubic) total variation diminishing (TVD) scheme with smoother-based solvers is used for resolving spatial terms whereas second-order backward discretization method is employed for temporal terms. The maximum

Courant number was set to 0.4 giving the time step size $\Delta t = 1.48\text{e-}7$ s at statistically-steady state solution. In addition, the maximum acoustic Courant number was set to 1 to stabilize compressible pressure waves, and to reduce artificial diffusion between phases [2].

IV. RESULTS AND DISCUSSION

The current simulations compare the phase-change behavior of the diesel throttle flow for the outlined equations of state. Figure 2(a)-(b) shows the zoomed view of the vapor fraction field, in the throat and around the inlet of the low-pressure chamber, at the time instant $t = 0.0005$ s.

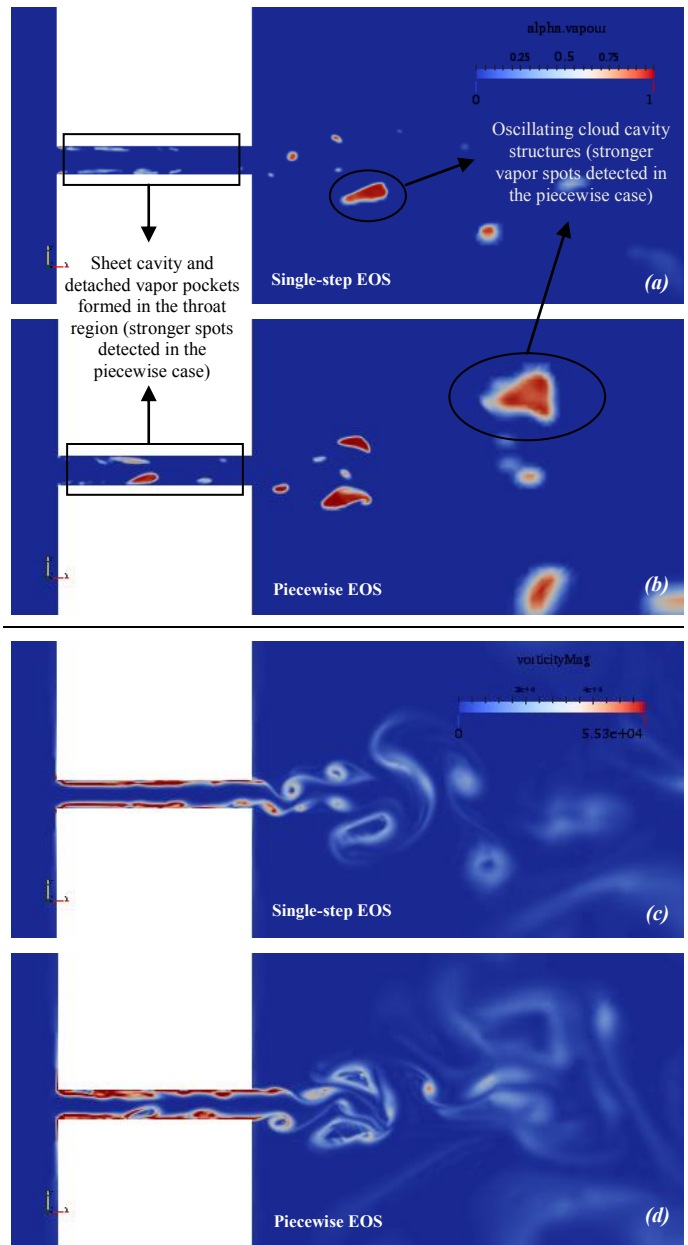


Figure 2: Evolution of the diesel cavitation flow inside the throttle, comparing the single-step and piecewise EOS models: zoomed view of vapor fraction (a-b) and vorticity magnitude (c-d) fields at time instant $t = 0.0005$ s.

As seen, cavitating regions in three major forms of attached sheets, detached cavity pockets, and vortex clouds are predicted by both models. The cavity structures are primarily formed due to separation of the flow in the throat near-wall regions, which leads the local pressure to drop below the saturation pressure (cavity inception), and continues through the formation of attached cavitation sheets. The unstable sheet cavities then separate from the wall due to the presence of re-entrant jets and large adverse pressure gradients, causing the generation of periodic vapor pockets at the rear side of the cavity sheets. Further downstream inside the low-pressure chamber, the transition of sheet cavities with vapor pockets into periodically oscillating cloud cavity structures, together with the significant pressure drop in the inlet of the chamber, cause large levels of unsteadiness particularly in the recirculating vortex centers. This process promotes the formation of strong oscillating cavitation clouds which are heavily reshaped through local shedding mechanisms of the shear layer and vortex-cavity interactions with strong interface density/pressure gradients [2,4,27]. As indicated in the corresponding vorticity contours of Figure 2(c)-(d), the prediction of stronger vortical structures due to stronger velocity gradients in larger recirculating zones in the piecewise EOS case forms stronger vapor spots and thus larger vapor production at the given time instance. This conclusion can be further illustrated in Figure 3, which shows the temporal variation of spatially-averaged vapor fraction field in the domain over approximately 4 flow-through times; the resulting average corresponds to the percentage of the throttle volume filled with vapor. The piecewise EOS model predicts more vapor generation in the domain, as was also qualitatively seen in Figure 2(a)-(b). Such observations are mainly due to the capability of the piecewise EOS model in properly treating the sharp pressure/density gradients in highly-strained shear layers and liquid-vapor interface regions, particularly during condensation-vaporization and vapor collapse processes [16,17].

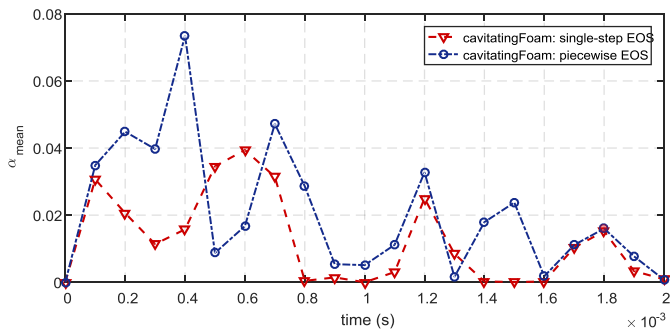


Figure 3: Temporal variation of the spatially-averaged vapor fraction field in the throttle cavitating flow of diesel: comparison of the single-step and piecewise EOS models.

To better examine the accuracy of the discussed EOS models, Figure 4 displays the time-averaged distribution of the velocity magnitude field in the aforementioned tests along a reference line M1 located at $x = 603 \mu\text{m}$ in the throat area (see Figure 1), and compare it against the experimental data of Morozov and Iben [26]. The time-averaging is performed for the extracted instantaneous velocity distributions at 50 consequent time steps over a single flow-through time. As indicated, although the expected top-hat velocity profile is

properly captured by both approaches, the piecewise EOS model shows a better match by giving the maximum velocity of around 189.2 m/s in the contraction zone, in comparison with the smaller maximum velocity of around 173.7 m/s predicted in the single-step case. The improved accuracy in the piecewise EOS model is likely due to the smooth computation of vapor-liquid mixture properties at transition states, which not only enables the solver to more easily handle large and negative ranges of pressures but also prevents the numerical solution from experiencing drastic field variations, thus improving the solution convergence [16]. As shown in Figure 2, the lack of such functionality in the single-step model causes additional numerical diffusion in the shear layers and interface regions of the cavitation flow - in particular in the areas with stronger vapor condensation - which eventually results in under-predicted flow fields.

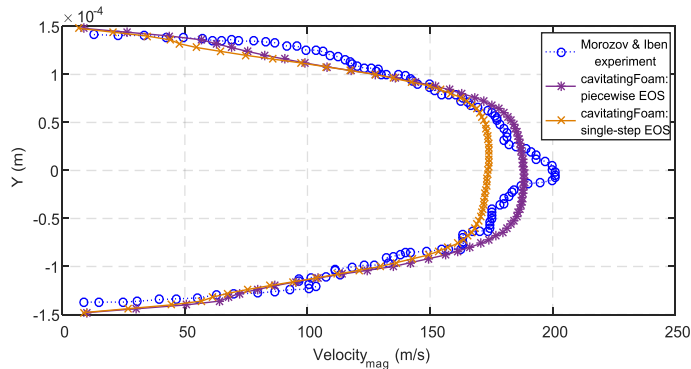


Figure 4: Distribution of the time-averaged velocity magnitude along the reference line M1 in the throttle cavitating flow of diesel: comparison of the single-step and piecewise EOS models, against the Morozov and Iben [26] experiment

V. CONCLUSION

A cavitating flow of diesel in the benchmark throttle geometry is investigated numerically by use of a compressible HEM-based cavitation solver with an incorporated piecewise barotropic equation of state. Validation of the preliminary 2D test results against the experimental data shows that the employed piecewise EOS can more accurately capture the properties of the diesel cavitation flow e.g. mass flow rate, compared with the previously-reported results of a single-step EOS model. This is mainly due to the presence of a well-described continuity in the piecewise EOS formulation, which not only enables the HEM to cover state properties of the cavitation flow in all vapor, liquid, and mixture phases, but improves the functionality of the current cavitation solver in better handling the vapor-liquid transition processes with large pressure and density gradients. It is also indicated that the absence of such a treatment in the single-step EOS approach causes artificial diffusions in the model, as a result of which the computed flow fields are under-predicted. The present work highlights the capability of the piecewise EOS in HEM-based cavitation solvers for accurate calculation of cavitating fields, which could potentially make it a reliable approach for estimating flow parameters in complicated industrial cavitating flows. Follow-on 3D simulations of the present test cases, with and without turbulence modeling, are in progress to extend the validation study, and to explore more details of the vortex-

cavitation instability mechanisms under the given equations of state.

ACKNOWLEDGMENT

The current work is supported by the Natural Sciences and Engineering Research Council of Canada (NSERC), International Institute for Cavitation Research (ICR) at the University of London in the UK, with the cooperation of Westport Fuel Systems©, and ComputeCanada/WestGrid®. Financial and Technical supports are gratefully acknowledged.

REFERENCES

- [1] Z. Jiakai, X. Huangjun, F. Kesong, et al., "Unsteady cavitation characteristics of liquid nitrogen flows through venturi tube," *International Journal of Heat and Mass Transfer*, vol. 112, pp. 544-552, 2017.
- [2] S. Rahbarimanesh, J. Brinkerhoff, J. Huang, "Development and validation of a homogeneous flow model for simulating cavitation in cryogenic fluids, *Applied Mathematical Modeling*," vol. 56, pp. 584-611, 2018.
- [3] W. Edelbauer, J. Strucl, A. Morozov, "Large Eddy Simulation of cavitating throttle flow," in: *Advances in Hydroinformatics*, Springer, pp. 501-517, 2016.
- [4] A. Kubota, H. Kato, H. Yamaguchi, "A new modelling of cavitating flows: a numerical study of unsteady cavitation on a hydrofoil section," *Journal of Fluid Mechanics*, vol. 240, pp. 59-96, 1992.
- [5] M. Pelanti, K. Shyue, "A mixture-energy-consistent six-equation two-phase numerical model for fluids with interfaces, cavitation and evaporation waves," *Journal of Computational Physics*, vol. 259, pp. 331-357, 2014.
- [6] S. Hohmann, U. Renz, "Numerical simulations of fuel spray at high ambient pressure: the influence of real gas effects and gas solubility on droplet vaporization," *Heat and Mass Transfer*, vol. 46, pp. 3017-3028, 2003.
- [7] B. Bicer, A. Tanaka, T. Fukuda, et al., "Numerical simulation of cavitation phenomena in Diesel injector nozzles," in: *16th Annual Conference ILASS-ASIA*, Nagasaki, Japan, pp. 58-65, 2013.
- [8] O. Coutier-Delgosha, J. Reboud, Y. Delannoy, "Numerical simulation of the unsteady behavior of cavitating flows," *International Journal for Numerical Methods in Fluids*, vol. 42, pp. 527-548, 2003.
- [9] R. Kunz, D. Boger, D. Stinebring, et al., "A preconditioned Navier-Stokes method for two-phase flows with application to cavitation prediction," *Computers & Fluids*, vol. 29, pp. 849-875, 2000.
- [10] P. Zwart, A. Gerber, T. Belamri, "A two-phase flow model for predicting cavitation dynamics," in: *5th International Conference on Multiphase Flow*, Yokohama, Japan, 2004.
- [11] G. Schnerr, J. Sauer, "Physical and numerical modeling of unsteady cavitation dynamics," in: *Proceedings of the 4th International Conference on Multiphase Flow (ICMF)*, New Orleans, USA, 2001.
- [12] G. Wang, M. Ostoja-Starzewski, "Large Eddy Simulation of a sheet/cloud cavitation on a NACA0015 hydrofoil," *Applied Mathematical Modeling*, vol. 31, pp. 417-447, 2007.
- [13] X. Zhang, L. Qiu, Y. Gao, et al., "Computational Fluid Dynamic study on cavitation in liquid Nitrogen," *Cryogenics*, vol. 48, pp. 432-438, 2008.
- [14] V. Hidalgo, X. Luo, X. Escaler, et al., "Numerical investigation of unsteady cavitation around a NACA66 hydrofoil using OpenFOAM," in: *27th IAHR Symposium on Hydraulic Machinery and Systems (IAHR) & IOP Conference Series: Earth and Environmental Science*, 2014.
- [15] P. Zwart, A. Gerber, T. Belamri, "A two-phase flow model for predicting cavitation dynamics," in: *5th International Conference on Multiphase Flow*, Yokohama, Japan, 2004.
- [16] E. Goncalves, R.F. Patella, "Numerical simulation of cavitating flows with homogeneous models," *Computers & Fluids*, vol. 38, pp. 1682-1696, 2009.
- [17] P. Koukouvinis, M. Gavaises, J. Li, et al., "Large Eddy Simulation of diesel injector including cavitation effects and correlation to erosion damage," *Fuel*, vol. 175, pp. 26-39, 2016.
- [18] I.K. Karathanassis, P. Koukouvinis, M. Gavaises, "Comparative evaluation of phase-change mechanisms for the prediction of flashing flows," *International Journal of Multiphase Flow*, vol. 95, pp. 257-270, 2017.
- [19] OpenCFD, OpenFOAM User's Guide, <https://github.com/OpenFOAM/OpenFOAM-dev/tree/master/applications/solvers/multiphase/cavitatingFoam> and <http://www.opencfd.co.uk/>.
- [20] OpenCFD, OpenFOAM User's Guide, <https://cfd.direct/openfoam/user-guide/>.
- [21] G. Wallis, *One-dimensional Two-phase Flow*, New York: McGraw-Hill, 1969.
- [22] F. Kärrholm, H. Weller, N. Nordin, "Modeling injector flow including cavitation effects for Diesel applications," in: *ASME Fluids Engineering Conference*, pp. 465-474, 2007.
- [23] H. Aguerre, S. Damián, J. Gimenez, et al., "Modeling of compressible fluid problems with OpenFOAM using dynamic mesh technology," *Mecánica Computacional*, vol. 32, pp. 995-1011, 2013.
- [24] C. Brennen, *Cavitation and Bubble Dynamics*, Cambridge University Press, 2013.
- [25] M.J. Ivings, D.M. Causon, E.F. Toro, "On Riemann solvers for compressible liquids," *International Journal for Numerical Methods in Fluids*, vol. 28, pp. 395-418, 1998.
- [26] A. Morozov, U. Iben, "Experimental analysis and simulation of cavitating throttle flow," *6th International Conference on Heat Transfer, Fluid Mechanics and Thermodynamics (HEFAT 2008)*, Pretoria, South Africa, 2008.
- [27] S. Rahbarimanesh, J. Brinkerhoff, "Diffusion angle effects on cavitating flow of Liquefied Natural Gas (LNG) inside a Laval nozzle," *Proceedings of the 26th Canadian Congress of Applied Mechanics (CANCAM 2017)*, Victoria, Canada, 2017.

Advances and challenges in simulation of LNG behavior inside a tank

E. Tahmasebi, A. Stroda, S.P. Pendli & J. Brinkerhoff

Department of Mechanical Engineering
University of British Columbia Okanagan,
Kelowna, BC, Canada
ehsan.tahmasebi@ubc.ca

Abstract— Liquefied natural gas is predicted to continue its growth as an alternative fuel for the heavy-duty automotive and shipping sector. In recent years, rapid advances in computational fluid dynamics capabilities have led to improvements in the rate of development and cost reduction for cutting edge technology. However, in the field of LNG, currently available tools are not capable of reliably predicting many of the behaviors specific to cryogenics and multispecies cryogenics. This review surveys the current state of the solvers and studies in the field. Focus is given to variable LNG composition and the corresponding thermophysical properties, tank motion, and thermally-driven phase change as these are the main factors driving LNG behavior in fuel tanks. It is demonstrated that oversimplification of the LNG composition fails to give full insight into many of the processes taking place. Tank motion is adequately addressed in the current solver state, however the simultaneous consideration of fluid properties, tank motion, and thermally-driven phase change are the next necessary step. While thermally-driven phase change in cryogenic fluids is well researched, implementation and validation of the physical models in general purpose CFD codes is lacking.

Keywords- *Liquid natural gas, two-phase flow, thermal driven phase change, mixture properties, sloshing*

I. INTRODUCTION AND MOTIVATION

Liquefied natural gas (LNG) is projected to continue growing its energy market share by more than 25% over the next decade to over 500 million tons per annum by 2030 [1]. LNG has proven to be a viable alternative to heavy diesel fuels in applications from the marine industry to heavy trucking. As the market continues to expand and diversify, the development of new technology will be required to continue pushing the envelope of efficiency and safety. In the development process, computational tools and models play an integral role. However, the current generation of computation fluid dynamics (CFD) tools fail to accurately replicate many phenomena applicable to cryogenic fluids such as LNG.

The benefits of LNG are accompanied with engineering challenges. LNG is a cryogenic fuel that must be kept below its boiling point to remain liquid. Heat transfer and pressure drop may cause phase change to vapor through cavitation and

boiling. To facilitate the safe adoption of LNG fuels in the trucking and marine industries, design tools are required that can predict its behavior and accurately model the methane emissions associated with LNG spills. In this study, previous works addressing the issues and challenges of simulating LNG behavior are presented.

To address the current lack of suitable CFD tools for the LNG industry, the development of such a tool has begun in *OpenFOAM*; an open source CFD toolbox. A wide array of solvers currently exists in *OpenFOAM*, however none completely met the requirements necessary to simulate LNG at the level it is required. In Figure 1 the roadmap for developing the desired solver is presented.

II. LNG COMPOSITION AND THERMOPHYSICAL PROPERTIES

Fluid transport and thermodynamic properties used in a CFD solver are integral to the validity of the solution, and in cryogenic liquids this becomes even more important as they commonly operate near the saturation temperature and pressure of the fluid. When operating near the saturation state of a fluid, many of the properties become highly influenced by changes in temperature. As well as being a cryogen, LNG is made up of a delicate mixture of hydrocarbons, CO₂, liquid nitrogen (LN) and other trace species. Typical LNG ranges between 85% and 95% methane [2] which can have significant effects on its behavior. The composition of LNG also changes by the process of aging (or weathering) where heat transfer causes phase change and a preferential evaporation of certain species occurs. Only by accurately predicting the variable composition of LNG in both liquid and gas phase the process of boil off venting and roll over can be considered during the storage design process.

A. Literature review

Historically, CFD simulations have been conducted by approximating the properties of LNG as pure methane as is done by Ahammad et al. [3], Chen et al. [4] and Saleem et al. [5]. These cases study scenarios ranging from LNG evaporators, to monitoring of tank pressure, to predicting boil off gas (BOG) generation. However, by ignoring the effects of the multiple different species in the LNG mixture, vital details related to the properties and physical phenomena can be missed.

LNG solver roadmap

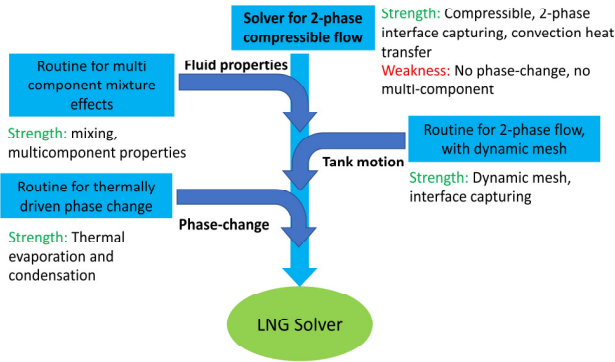


Figure 1. Road map of desired in-tank LNG solver

In the development of an analytical weathering prediction model [6] the full effect of multiple components was considered and the presence of nitrogen had a sizable effect on the quantity and quality of the boil off gas. The effect of nitrogen and other heavier hydrocarbons is completely ignored by the pure fluid assumption and fails to provide any insight into the layering and roll over phenomena that can occur due to phase change at the free surface. Roll over occurs when lighter hydrocarbons (usually the methane) is preferentially evaporated from the free surface causing an increase in density of the liquid near the top. This configuration can become unstable and the heavy liquid may roll under, exposing lighter (i.e. methane rich) liquid to the surface where it quickly and sometimes forcefully evaporates causing high spikes in the pressure of the storage tank. While roll over phenomenon is more relevant to large storage tanks, failing to predict the event in any size tank can be detrimental.

B. Comparison of current CFD solvers

Some of the currently available solvers in OpenFOAM that are potentially relevant to simulation of LNG in tanks are listed below and evaluated to identify their positive and negative attributes. Key features necessary to fully capture the dynamics of LNG from a fluid properties standpoint include: (i) Miscibility of multiple liquid and gas species to capture the composition and varying fluid properties; and (ii) compressibility to provide accurate pressurization of the tank as thermal/density driven convection in both the liquid and gas phases.

compressibleInterFoam

Pro: Basic and clean starting point for the development of a compressible solver.

Con: Does not contain ability to simulate miscible mixing of fluids.

compressibleMultiphaseInterFoam

Pro: Compressible with multiple species.

Con: Species are all immiscible (e.g. oil, water, mercury).

interMixingFoam

Pro: Capable of two miscible species and one immiscible specie (e.g. liquid methane + liquid ethane and vapor).

Con: Incompressible and limited in number of species.

multiphaseEulerFoam

Pro: Can simulate n number of compressible and miscible species.

Con: Mixed of miscible species quickly separate by density, not realistic of LNG.

Based on the basic advantages and disadvantages outlined above a new solver is being developed from the basis of *compressibleInterFoam*. The new solver uses techniques employed by *interMixingFoam* to achieve the compressible miscible mixing capability required for LNG. In Figure 2 the graphical results of α (i.e. methane rich composition) are shown in an induced roll over case using *interMixingFoam*. To illustrate another feature of the solver; the decay of inhomogeneity is visualized in Figure 3 by plotting the difference in maximum and minimum α concentration between the bottom and top of the domain. After 30 seconds the heavy region of simulated methane-ethane mixture has fallen to the bottom and diffusion restores the homogeneity of the system over the next 510 seconds.

III. TANK MOTION

Most of today's LNG is transported either by heavy trucks or large ship tanks. Motion of the tank induced by the carrying vehicle has the potential to cause sloshing. The sloshing dynamics greatly enhances mixing and has the potential to cause faster tank pressurization as a result of the enhancement of phase change triggered by the modified pressure gradients. By analyzing the motion of the tank the proper phase change rates may be calculated as it takes into account the possibility of cavitation.

A. Literature review

There have been various studies conducted experimentally and numerically to understand the sloshing dynamics of various systems. Most of the experimental studies in sloshing have been conducted with water and stable fluids of varying viscosity, rather than a cryogenic fluid such as LNG.

Bass et al. [7] indicated the importance of sloshing pressure data to establish long term operational worst case pressures for design of tank purposes. It is mentioned that the compressible phenomenon involves controls of the pressure, which is a function of time. Brar et al. [8] studied the motion of fluid in an elliptical tank through experimentation as well as simulation in

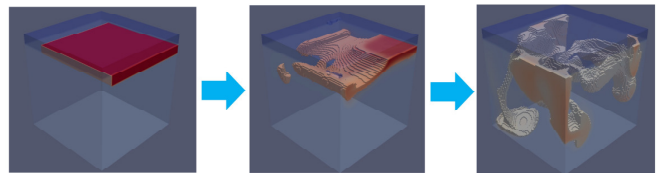


Figure 2. Sample of the results with *interMixingFoam* for mixing miscible fluids: Observable motion of the heavy mixture falling, mixing and diffusing.

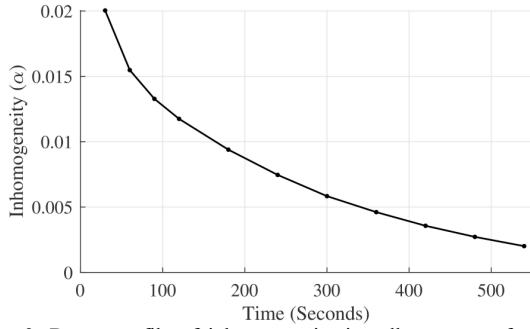


Figure 3. Decay profile of inhomogeneity in roll over case from Figure 2 starting at 30 seconds measured by the difference in maximum and minimum α from bottom to top of the domain. By 30 seconds the heavy (ethane rich) composition has settled to the bottom and begins to diffuse and lightly convect to achieve a homogeneous composition throughout.

COMSOL. It is concluded that various configurations of baffles in the tank effect the average and maximum pressure at the walls. Sanapala et al. [9] studied sloshing sourced from tanks subjected to wind or earthquake excitation. The study uses *interDymFoam*; a multiphase incompressible solver from the *openFoam* library, to study the influence of resonant harmonic excitation on free surface displacement, pressure distribution and slosh forces.

The studies by Lee et al. [10] and Wemmenhove et al. [11] on sloshing were performed using a VOF model. Lee [10] performed a parametric sensitivity study on LNG tank sloshing loads using the VOF model in FLOW3D. The importance of gas compressibility over viscosity and density ratio at peak pressures is shown. This study also shows that the peak pressure is greater in a 25% filled tank than a 50% filled tank. Lee [10] mentions the need for a more sophisticated numerical model that includes gas compressibility, bubbles, and thermodynamic properties to simulate the increase in impact pressure below the critical pressure level. Wemmenhove [11] validated numerical sloshing for different filling ratios and types of motion in a tank using an improved VOF (iVOF) model. The two-phase flow model showed that the filling ratio and the irregular motion strongly effects the two-phase flow effects like air entrapment and entrainment. The two-phase model better agreed with the experimental data when compared to a typical one phase flow solver.

Zhao et al. [12] used a coupled level set and VOF method (CLSVOF) to predict sloshing in his study of 3D sloshing in a partially filled LNG tank in transverse motion. The CLSVOF method used captures the details of the interface breaking into small droplets while maintaining the smooth interface due to the level set phenomenon. This study also shows the variation of location and peak pressures in the tank occurred at low and high filling levels. Chen et al. [13] used the *interDymFoam* solver in the OpenFOAM library to validate numerical sloshing at different filling levels. Peric et al. [14] compared the body force and the moving grid methods to analyze the sloshing problem. Loots et al. [15] used iVOF numerical method and experiments to validate the sloshing dynamics. The importance of small cell sizes and time steps to study numerical sloshing was highlighted.

All the reviewed studies indicate the necessity to accommodate compressibility and tank motion to accurately capture the behavior of LNG stored and transported in a tank.

B. Comparison of current CFD solvers

Most of the studies reviewed revealed that much of the use of numerical sloshing is only seen in incompressible multiphase or single-phase solvers. However, most of the studies reviewed strongly indicate the need of a more specific solver that can simultaneously predict phase change, heat transfer, variable fluid thermophysical properties, and potentially cavitation with sloshing. The following two-phase solvers are considered for the effects of compressibility, and pressure predictability for sloshing dynamics:

compressibleInterFoam

Pro: Considers compressibility effects, heat transfer, two phase solver, better prediction of pressure in the tank.

Con: Uses body force term to generate sloshing as there is no dynamic meshing, immiscible, no phase change, no multi-component

interDymFoam

Pro: Heat Transfer, two-phase solver, ability to dynamic meshing to define motion in the tank thereby generating sloshing.

Con: Does not consider compressibility, immiscible, no phase change, no multi-component

compressibleInterDymFoam

Pro: Considers compressibility, heat transfer, two phase solver, better pressure prediction, Ability to dynamic mesh to generate sloshing, easier implementation to the potential solver that is based on *compressibleInterFoam*.

Con: Immiscible, no phase change, no multi-component.

From the available solvers *compressibleInterDymFoam* is seen as the most eligible candidate to be considered for development of a general-purpose solver for LNG applications due to its ability to accurately predict pressure, phase-fraction, and compressibility along with the dynamic motion that accompanies sloshing phenomenon.

A sample case of a 1 m³ cube with 50-vol% liquid/vapour methane fraction is simulated over a linear translational acceleration of 10⁴ m/s² over a displacement of 1 meter to demonstrate the ability of *compressibleInterDymFoam*. Figure 4 shows a distribution of the phase-fraction (α) of LNG at three dynamic viscosity, 7.17×10^{-5} , 7.17×10^{-3} and 7.17×10^{-1} Pa.s. It is seen that the magnitude of the sloshing wave decreases as the dynamic viscosity is increased. The higher the viscosity also proves to take more time to excite and is more quickly damped. The pressure distribution at various times is also compared with the phase fraction in the volume during sloshing in Figure 5.

IV. THERMALLY-DRIVEN PHASE CHANGE

A. Literature review

In general, LNG inside the tanks is found as a two-phase flow of liquid and vapor at its saturation state. Although

vacuum-jacketed tanks try to minimize the heat transfer from the atmosphere to the LNG, heat flux from the wall is not negligible. This heat transfer will cause a gradual phase change from liquid to vapor and a concomitant increase in the tank pressure. Moreover, the complexity of the evaporation process of a cryogenic petrochemical mixture is complex; appropriate models for phase equilibrium must be employed in order to understand and predict the LNG behavior inside the tank.

controlled with an empirical rate parameter, and was set proportional to the relative temperature difference from the saturated condition:

$$S = r\alpha\rho_L \frac{T - T_{sat}}{T_{sat}} \quad \text{if } T > T_{sat},$$

and

$$S = r(1 - \alpha)\rho_V \frac{T - T_{sat}}{T_{sat}} \quad \text{if } T < T_{sat}. \tag{1}$$

In these equations, r acts as a surrogate for the characteristic thermal time scale of a mesh cell, and should therefore depend on the simulation mesh resolution and fluid properties [17].

Thiele [19] by using similar rate-parameter-based approach for modeling horizontal film condensation, and applying a limiting condition to ensure that the amount of vapor condensed per step did not exceed the amount present in the cells, showed that the rate parameter approach with fixed r did not yield convergent results with increasing mesh resolution. Thiele [19] adapted his model in the *OpenFOAM interFoam* solver. He developed a simplified model to capture the interface during condensation. However, the applicability of this approach to general phase change configurations is unclear.

Based on the reviewed investigations, the most successfully validated phase-change models have relied on geometric interface reconstruction or direct tracking and advection of the interface, which are both computationally expensive and difficult to perform on unstructured meshes. An alternative approach is investigated by [17,20] and later by [21,22] in which cells containing the interface are identified using a relatively simple and fast graph traversal algorithm. Condensations and boiling phase-change source terms are then applied to the interface cells. Interface cells are forced to the equilibrium state instantaneously, similar to rate parameter methods. They validated their model for film condensation problems, and then implement some studies on drop condensation, evaporation, and nucleate boiling. Their customized solver, which is based on *interFoam*, is named *interThermalPhaseChangeFoam*.

In the recent years, in addition to research on pressure-driven phase change in cryogenic flows [23,24], several studies have concentrated on CFD simulation of the thermally-driven phase change in cryogenic fluids, including nucleate boiling [25–27], film and pool boiling [3,28], and boiling in full scale, stationary storage vessels [5,29,30].

B. Comparison of current CFD solvers

Among the current multiphase solvers in standard *OpenFoam* package and also extended solvers, three solvers are selected to evaluate their performance on modeling the thermal driven phase changing inside the cryogenic tanks: *interThermalPhaseChangeFoam* [21,22] *cryoCavitatingFoam* [23,31], and *compressibleInterFoam* [32]. The performance of these solvers in capturing thermally-driven phase change inside the tank and predicting the evaporation rate and tank pressure is summarized below.

compressibleInterFoam

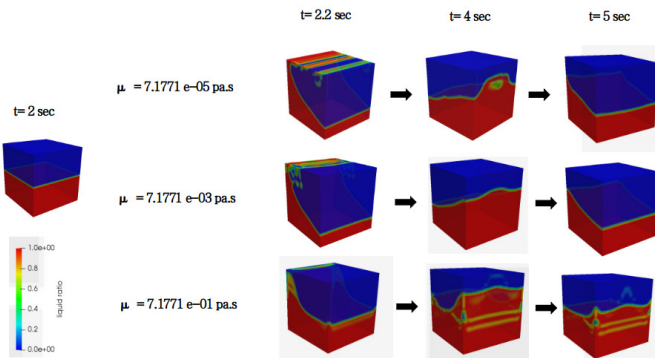


Figure 4. Shloshing in a 1 m³ cube for LNG at three different viscosity in *compressibleInterDymFoam*

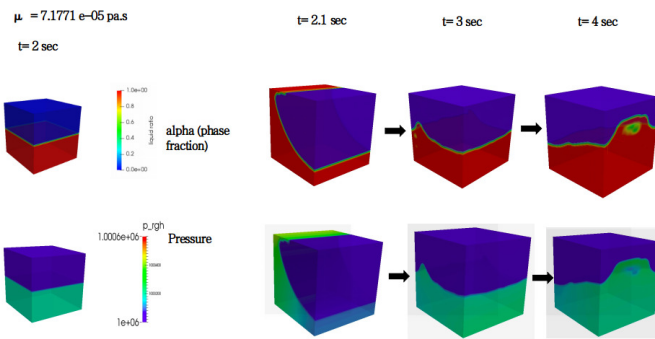


Figure 5. Phase-fraction and pressure distribution in the 1 m³ cube for LNG at 7.17×10^{-5} Pa.s in *compressibleInterDymFoam*

Simulation of two-phase liquid-gas flows without phase change are mature in both commercial and open-source codes. Most of these codes track the fluid phase with a phase-fraction field that varies from zero (for the vapor) to one (for the liquid phase) [17]. In volume of fluid (VOF) models, the local fluid properties are weighted by the phase-fraction and form a single set of governing equations valid for the entire simulation domain. Multiple formulations have been proposed for the phase-change terms in these models including empirical rate parameters, adaptation of experimentally developed heat-transfer correlations, and direct evaluation of inter-facial transport rates.

Yang et al. [18] studied the boiling of the R141b in horizontal tubes. Their simulations used compressible momentum and continuity equations and coupled phase-change source terms added to the phase and thermal energy transport equations. The rate of phase change at the interface was

Pro: Compressible two-phase solver, considering the convection heat transfer, and temperature variant density.

Con: Does not considering phase change
interThermalPhaseChangeFoam

Pro: Modeling condensation, and nucleate boiling. Include selective models for phase changing

Con: Thermal convection and change in the density is not included, Pressure and temperature results are not convincing,

cryoCavitatingFoam

Pro: Modeling cavitation with customized variable thermophysical properties, reliable prediction of the pressure driven phase change

Con: Not suitable for thermal driven phase change, results for the studies with small pressure gradient and large portion of the vapor phase inside the geometry are not reliable.

For illustrate purposes, a simulation of liquid methane boiling inside a 280-litre tank, with a wall heat flux of 5000 W/m² was performed using *interThermalPhaseChangeFoam*; the results are presented in Figure 6. Evolution of the phase fraction that qualitatively resembles nucleate boiling at the wall is captured. However, the lack of compressibility and absence of natural convection results in a physically unrealistic simulation, and motivates further development of more accurate, general-purpose CFD solvers LNG storage vessels.

V. CONCLUSION

As the LNG industry continues to grow into its predicted role as a lower-carbon alternative fuel, simulation-based design tools must follow to meet the demand of advancing technology. However, current CFD tools are ill-suited to the challenges of capturing the phenomena taking place in LNG.

The current generation of CFD solvers and research fails to account for the multispecies nature of LNG and its effect on aging, roll over, and thermophysical properties compared to the pure fluids. This oversimplification to a pure fluid is inadequate in many ways, and even incapable of answering composition-based questions which are at the core of LNG storage design. The same trend is seen in currently available solvers where there is a complete lack of suitable tools to address the problem in full. The development of new tools is seen as necessary and unavoidable. Understanding the behavior of LNG under sloshing is relevant in scales ranging from large ocean transporters to small and medium size commercial trucking under carriage tanks. Due to the close thermodynamic proximity of the operating conditions to the saturation condition of the LNG and the pressure gradients caused by the acceleration and deceleration of the storage tank, the potential for inertially-driven phase change (cavitation) is very real. While these pressure gradients due to the motion of the tank can be simulated, they have not yet been coupled with a phase change mechanism—a necessary next step for CFD solver development for LNG applications.

Under storage conditions, thermally-driven phase change is the dominant source of mass transfer between liquid and vapor in LNG and other cryogenic systems. While thermal phase change

models are well developed for non-cryogenic liquids, there are a lack of suitable models to accurately and physically capture thermally-driven phase change in LNG tanks. Recent experimental studies have shed light on the mechanism and rates expected for the evaporation of LNG and other cryogenics at the free surface. These models need to be implemented into a new suite of bespoke CFD solvers tailored for LNG storage applications. The development of such solvers is currently ongoing within the authors' research group.

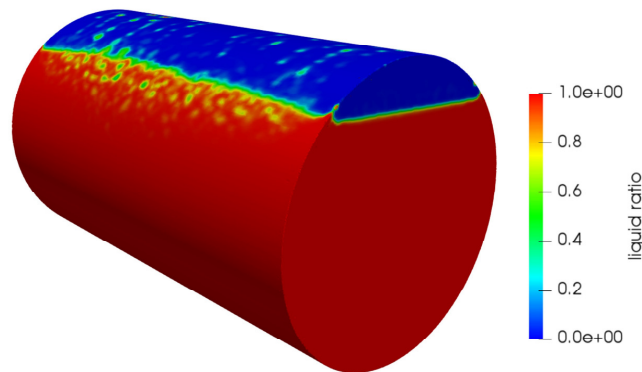


Figure 6. Sample of the results for simulating boiling inside the tank with *InterThermalPhaseChangeFoam*

REFERENCES

- [1] Royal Dutch Shell plc, Shell, Shell LNG Outlook 2018, 2018. www.shell.com. (accessed February 6, 2019).
- [2] GLobal LNG Fundamentals, n.d. <https://energy.gov/ia/downloads/supporting-development-natural-gas-markets-and-> (accessed February 15, 2019).
- [3] M. Ahammad, T. Olewski, L.N. Véchet, S. Mannan, A CFD based model to predict film boiling heat transfer of cryogenic liquids, *J. Loss Prev. Process Ind.* 44 (2016) 247–254. doi:10.1016/j.jlp.2016.09.017.
- [4] C. Fang, M. David, A. Rogacs, K. Goodson, Volume of Fluid Simulation of Boiling Two-Phase Flow in a Vapor-Venting Microchannel, *Front. Heat Mass Transf.* 1 (2010). doi:10.5098/hmt.v1.1.3002.
- [5] A. Saleem, S. Farooq, I.A. Karimi, R. Banerjee, A CFD simulation study of boiling mechanism and BOG generation in a full-scale LNG storage tank, *Comput. Chem. Eng.* 115 (2018) 112–120. doi:10.1016/j.compchemeng.2018.04.003.
- [6] C. Migliore, C. Tubilleja, V. Vesovic, Weathering prediction model for stored liquefied natural gas (LNG), *J. Nat. Gas Sci. Eng.* 26 (2015) 570–580. doi:10.1016/j.jngse.2015.06.056.
- [7] R.L. Bass, J. E. B. Bowles, R.W. et al Trudell, Modeling Criteria for Scaled LNG Sloshing Experiments, *J. Fluids Eng.* 107 (1985) 272–280. doi:10.1115/1.3242473.
- [8] G.S. Brar, S. Singh, An Experimental and CFD Analysis of Sloshing in a Tanker, *Procedia Technol.* 14 (2014) 490–496. doi:10.1016/j.protcy.2014.08.062.
- [9] V.S. Sanapala, K. Velusamy, B.S.V. Patnaik, CFD simulations on the dynamics of liquid sloshing and its control in a storage tank for spent fuel applications, *Ann. Nucl. Energy.* 94 (2016) 494–509. doi:10.1016/j.anucene.2016.04.018.
- [10] D.H. Lee, M.H. Kim, S.H. Kwon, J.W. Kim, Y.B. Lee, A parametric sensitivity study on LNG tank sloshing loads by numerical simulations, *Ocean Eng.* 34 (2007) 3–9. doi:10.1016/j.oceaneng.2006.03.014.

- [11] R.; Wemmenhove, R.; Luppés, A.; Veldman, T. Bunnik, Numerical simulation of sloshing in LNG tanks with a compressible two-phase model, 2007. <http://www.rug.nl/research/portal>. (accessed February 15, 2019).
- [12] Y. Zhao, H.C. Chen, Numerical simulation of 3D sloshing flow in partially filled LNG tank using a coupled level-set and volume-of-fluid method, *Ocean Eng.* 104 (2015) 10–30. doi:10.1016/j.oceaneng.2015.04.083.
- [13] Y. Chen, M.-A. Xue, Numerical Simulation of Liquid Sloshing with Different Filling Levels Using OpenFOAM and Experimental Validation, *Water.* 10 (2018) 1752. doi:10.3390/w10121752.
- [14] M. Peric, T. Zorn, O. el Moctar, T.E. Schellin, Y.-S. Kim, Simulation of Sloshing in LNG-Tanks, *J. Offshore Mech. Arct. Eng.* 131 (2009) 031101. doi:10.1115/1.3058688.
- [15] E. Loots, W. Pastoor, B. Buchner, T. Tveitnes, The numerical simulation of LNG sloshing with an improved volume of fluid method, *Proc. Int. Conf. Offshore Mech. Arct. Eng. - OMAE. 1 A* (2004) 1–9. <http://www.scopus.com/inward/record.url?eid=2-s2.0-11244272780&partnerID=40&md5=1d9810720ec078ab0fd8e2f2dcd51f70>.
- [16] C. Baumgarten, *Mixture formation in internal combustion engines*, Springer, 2006.
- [17] A.S. Rattner, S. Garimella, Simple Mechanistically Consistent Formulation for Volume-of-Fluid Based Computations of Condensing Flows, *J. Heat Transfer.* 136 (2014) 071501. doi:10.1115/1.4026808.
- [18] Z. Yang, X.F. Peng, P. Ye, Numerical and experimental investigation of two phase flow during boiling in a coiled tube, *Int. J. Heat Mass Transf.* 51 (2008) 1003–1016. doi:10.1016/j.ijheatmasstransfer.2007.05.025.
- [19] R. Thiele, *Modeling of Direct Contact Condensation With OpenFOAM*, Master Thesis. (2010) 60.
- [20] A.S. Rattner, *SINGLE-PRESSURE ABSORPTION REFRIGERATION SYSTEMS FOR LOW-SOURCE-TEMPERATURE APPLICATIONS*, Georgia Institute of Technology, 2015.
- [21] M. Nabil, A.S. Rattner, Supplemental Material (interThermalPhaseChangeFoam—A framework for two-phase flow simulations with thermally driven phase change), *SoftwareX.* 2014 (2016) 1–4. doi:10.1037/0021-843X.116.1.16.supp.
- [22] M. Nabil, A.S. Rattner, A Computational Study on the Effects of Surface Tension and Prandtl Number on Laminar-Wavy Falling-Film Condensation, *J. Heat Transfer.* 139 (2017) 121501. doi:10.1115/1.4037062.
- [23] S. Rahbarimanesh, J. Brinkerhoff, J. Huang, Development and validation of a homogeneous flow model for simulating cavitation in cryogenic fluids, *Appl. Math. Model.* 56 (2018) 584–611. doi:10.1016/j.apm.2017.12.004.
- [24] S. Rahbarimanesh, J. Brinkerhoff, A Numerical Study on the Effects of Cavitation Number on Cavitating Mixing Layer of Liquefied Natural Gas (LNG) behind a Flat Plate Splitter, (2018).
- [25] J. Zhu, D. Zhao, L. Xu, X. Zhang, Interactions of vortices, thermal effects and cavitation in liquid hydrogen cavitating flows, *Int. J. Hydrogen Energy.* 41 (2016) 614–631. doi:10.1016/j.ijhydene.2015.10.042.
- [26] Z. Xiaobin, X. Wei, C. Jianye, W. Yuchen, K. Tang, CFD simulations and experimental verification on nucleate pool boiling of liquid nitrogen, *Phys. Procedia.* 67 (2015) 569–575. doi:10.1016/j.phpro.2015.06.077.
- [27] G.H. Yeoh, X. Zhang, Computational fluid dynamics and population balance modelling of nucleate boiling of cryogenic liquids: Theoretical developments, *J. Comput. Multiph. Flows.* 8 (2016) 178–200. doi:10.1177/1757482X16674217.
- [28] Y. Liu, T. Olewski, L.N. Véhot, Modeling of a cryogenic liquid pool boiling by CFD simulation, *J. Loss Prev. Process Ind.* 35 (2015) 125–134. doi:10.1016/j.jlp.2015.04.006.
- [29] M.S. Zakaria, K. Osman, M.N.A. Saadun, M.Z.A. Manaf, M. Hanafi, M. Hafidzal, Computational Simulation of Boil-Off Gas Formation inside Liquefied Natural Gas Tank Using Evaporation Model in ANSYS Fluent, *Appl. Mech. Mater.* 393 (2013) 839–844. doi:10.4028/www.scientific.net/AMM.393.839.
- [30] Z. Zakaria, Rollover Phenomena in Liquefied Natural Gas Storage : Analysis on Heat and Pressure Distribution Through CFD Simulation, 8 (2017) 392–400.
- [31] S. Rahbarimanesh, J. Brinkerhoff, A Numerical Study on the Effects of Cavitation Number on Cavitating Mixing Layer of Liquefied Natural Gas (LNG) behind a Flat Plate Splitter, in: 10th Int. Symp. Cavitation, 2018.
- [32] J. Haider, *Numerical Modelling of Evaporation and Condensation Phenomena*, 2013.

CFD SIMULATION OF BUBBLE COLUMN REACTORS IN THE PRESENCE OF INTERNALS

Glen Cletus DSouza¹, Tuntun Kumar Gaurav², Chao Zhang³, Anand Prakash^{1,*}

¹Department of Chemical and Biochemical Engineering, The University of Western Ontario, London, Ontario N6A 5B9, Canada

²Department of Chemical Engineering and Applied Chemistry, University of Toronto, Toronto, Ontario M5S 3E5, Canada

³Department of Mechanical and Materials Engineering, The University of Western Ontario, London, Ontario N6A 5B9, Canada

Email: aprakas2@uwo.ca

Abstract— Bubble columns are multiphase reactors that have found several industrial applications owing to several attractive features. The most notable of these include excellent thermal management, low maintenance cost due to simple construction and absence of moving parts. In order to attain desired performance for a given application, these reactors are usually equipped with internals such as vertical tube bundles to facilitate heat transfer. The presence of these internals alter the column hydrodynamics and it becomes increasingly necessary to quantify these changes in order to design the reactors. In the current study, 2-D CFD simulations have been carried out for the bubble column reactors in the presence and absence of internals and the results have been compared. The simulations have been carried out using Eulerian-Eulerian model without the Population Balance Model (PBM) and the results have been compared with those using the PBM. The simulations have been used to examine various parameters such as phase holdups, liquid axial velocities and Reynolds stresses. The numerical results for the liquid axial velocities in the hollow bubble column have been compared with the experimental and numerical results from literatures. Based on the comparison of the liquid axial velocity profiles, it could be concluded that the predicted axial velocities exhibit similar trends as the experimental results. It was noticed that the predicted liquid axial velocity in a hollow bubble column without the BM is lower than that when the PBM is used. The vector plots signify the funneling effect induced in the presence of internals when compared to the hollow bubble column. Also, it was noticed that a higher level of turbulence could be seen in the hollow bubble column as the eddy formation was deterred due to the presence of vertical internal rods.

Keywords- *Bubble Column Reactor, Computational Fluid Dynamics (CFD), Simulation, Vertical Internals, Hollow Bubble Column*

I. INTRODUCTION

Bubble columns are a type of multiphase reactors in which reactions between gas and liquid phases (two-phase system) or between gas, liquid and solids (three-phase system) are usually carried out. These are employed in chemical and biochemical industries owing to their excellent thermal management, simple design, absence of moving parts and high mixing effects. The gas can be introduced into the column using a sparger and can be directed either in a co-current or a counter-current fashion with respect to the liquid or slurry [1–6]. Numerous experimental studies have been carried out to study the hydrodynamics of these reactors. Computational Fluid Dynamics (CFD) simulations have emerged as a promising tool to investigate the column hydrodynamics and parameters including gas holdup profiles, liquid velocity profiles, shear stresses and turbulence profiles.

Two-fluid models such as Eulerian-Eulerian (E-E) and Eulerian-Lagrangian (E-L) models have been employed in modelling multiphase flows in the bubble column [7,8]. In the E-E model, the continuous and dispersed phases are treated as interpenetrating continuum. In the E-L method, the discrete bubbles, which form the dispersed phase in the column, are tracked by equations of motion which is accomplished by solving the force balance equations. It has been found that the computational time required for tracking the bubbles in the dispersed phase using the E-L model is very high [9]. On the other hand, E-E model based on the two-fluid theory, which treats both phases as continuum and their mechanics are derived by solving the governing partial differential equations [10]. When the bubbles advance upwards from the gas sparger, it has been observed that they coalesce, break and change sizes and shapes. Bubble coalescence and breakup are important parameters that directly affect the interfacial forces within the column. These forces directly affect the gas holdup profile, circulations and axial velocity patterns in the column. Therefore, it becomes necessary to determine the bubble size distribution.

The bubble size distribution within a bubble column varies under different operating conditions. The Population Balance Model (PBM) is widely used to predict the bubble size distribution in CFD simulations of a bubble column reactor. The PBM, which was developed by Hounslow et al. [11], is employed to model the bubble breakup and coalescence. The governing equation for this model given by Ramakrishna et al. [12] has been frequently used [13]. However, the PBM fails at higher superficial gas velocities [2].

In the current study, simulations have been carried out for a hollow bubble column and bubble columns in the presence of vertical internals. The liquid axial velocity profiles, air velocity contours, water volume fraction contours and turbulence parameters have been analyzed and compared. In addition, a comparison has been carried out for the liquid axial velocities of hollow bubble column between the numerical and experimental results from the literature.

II. NUMERICAL MODELLING

A 2-D hollow bubble column and 2-D bubble column in the presence of 15 vertical internal tubes geometry have been simulated. Ansys Fluent v19.2 was used for the simulations. The height and diameter of the bubble column are 2.5m and 0.15m, respectively. A grid independence test was carried out for all the geometries. The column with internals requires higher grid density to capture the velocity gradients at the walls and near internals. The numerical modelling is carried out using the E-E approach. Simulations have been carried out with and without using the PBM. The pressure-based solver was employed in both simulations since the flow is incompressible.

2.1 Governing Equations

The mass conservation equation for the multiphase flow within a bubble column can be described by the follow equation.

$$\frac{\partial(\delta_k \rho_k)}{\partial t} + \nabla \cdot (\rho_k \delta_k \vec{v}_k) = 0 \quad (1)$$

$$\begin{aligned} \delta_k &= \text{Volume fraction of the } k^{\text{th}} \text{ phase} \\ \rho_k &= \text{Density of the } k^{\text{th}} \text{ phase} \\ \vec{v}_k &= \text{Velocity vector of the } k^{\text{th}} \text{ phase} \end{aligned}$$

In Eq. (1), the subscript 'k' denotes each of the phases present in the multiphase flows, the liquid or gas phase.

The momentum conservation equation for the multiphase flow can be given by the following equation.

$$\frac{\partial(\rho_k \delta_k \vec{v}_k)}{\partial t} + \nabla \cdot (\rho_k \delta_k \vec{v}_k \vec{v}_k) = -\delta_k \nabla p + \nabla \cdot \bar{\bar{\tau}}_k + \rho_k \delta_k \vec{g} + \sum_{p=1, k \neq p}^M (R_{pk} + \dot{m}_{pk} \vec{v}_{pk} - \dot{m}_{kp} \vec{v}_{kp}) + (\vec{F}_{lift} + \vec{F}_{TD}) \quad (2)$$

In Eq. (2), \vec{g} = acceleration due to gravity (m/s²); p = pressure shared by all the phases (pascal); \vec{v}_k = velocity; \vec{F}_{lift} and \vec{F}_{TD} = Non-interfacial lift and drag forces acting between the gas and liquid phases; $\bar{\bar{\tau}}_k$ = Reynolds stress tensor for turbulence

The Reynolds stress tensor for turbulence in Eq. (2) can be determined using the following equation.

$$\bar{\bar{\tau}}_k = \mu_k \delta_k (\nabla \vec{v}_k + \nabla \vec{v}_k') \delta_k (\lambda_k - \frac{2}{3} \mu_k) (\nabla \vec{v}_k \bar{\bar{I}}) \quad (3)$$

where \vec{v}_k' is the fluctuation of the velocity in the x-direction;
 $\bar{\bar{I}}$ = Identity Matrix

R_{pk} is the force of interaction between the gas and liquid phase, which can be described as

$$R_{pk} = K_{pk} (\vec{v}_p - \vec{v}_k) \quad (4)$$

$$\text{where, } K_{pk} = 0.75 \delta_g \delta_l \frac{\rho_l}{d_a} C_d \cdot |(\vec{v}_g - \vec{v}_l)| \quad (5)$$

Here, δ_g and δ_l are the volume fractions of the gas and liquid phases, respectively and C_d is the coefficient of the drag force.

2.2 Turbulence Model

The Reynolds Stress Model was used to model the turbulent nature of the gas and liquid flows in the bubble column.

$$\frac{\partial(\rho_l u_i u_j)}{\partial t} + C_{ij} = -D_{T,ij} + D_{L,ij} - P_{ij} + \varphi_{ij} - \epsilon_{ij} - F_{ij} \quad (6)$$

In the above equation, the various notations represent the following terms:

C_{ij} = Convection term; $D_{T,ij}$ = Turbulent Diffusion term;

$D_{L,ij}$ = Molecular Diffusion term; ϵ_{ij} = Dissipation term

P_{ij} = Stress Production term; φ_{ij} = Pressure Strain term;

Each of the term has been described in the following equations:

$$C_{ij} = \frac{\partial}{\partial x_k} (\rho_l u_k u_i' u_j') \quad (7)$$

$$D_{T,ij} = \frac{\partial}{\partial x_k} (\rho_l u_k' u_i' u_j' + p' (\delta_{kj} u_i' + \delta_{ik} u_j')) \quad (8)$$

$$P_{ij} = \rho_l (\overline{u_k' u_i'} \frac{\partial u_j}{\partial x_k} + \overline{u_k' u_j'} \frac{\partial u_i}{\partial x_k}) \quad (9)$$

$$\varphi_{ij} = p' (\frac{\partial u_i'}{\partial x_j} + \frac{\partial u_j'}{\partial x_i}) \quad (10)$$

$$\epsilon_{ij} = 2 \mu_L \frac{\partial u_i'}{\partial x_j} \quad (11)$$

2.3 Drag Model

The drag model is employed to capture the dynamics of both the phases. To capture the effect of surface tension between the selected phases, an appropriate drag model needs to be used. In the E-E model, the drag force is the most dominant force compared to the other forces within the system. The drag force models that are widely used in the bubble column simulation include the Schiller – Naumann Drag model correlation. The details of this correlation are outlined in Table 1.

Table 1. Drag model parameters

	Schiller and Naumann [10]
Drag Coefficient (Ca):	$C_d = \begin{cases} \frac{24 (1+0.15 N_{Re}^{0.687})}{N_{Re}}, & N_{Re} \leq 1000 \\ 0.24, & N_{Re} > 1000 \end{cases}$ where $N_{Re} = \frac{\rho_{lg} \vec{v}_l - \vec{v}_g d_{lg}}{\mu_{lg}} \text{ and } \mu_{lg} = \delta_l \mu_l + \delta_g \mu_g$

2.4 Lift Force

Lift force is the force that acts between the two phases within a bubble column. The lift force generally comprises of two components – Magnus force and Saffman forces. The former is responsible for the forces involving bubble rotation and the latter is a result of the shear stress around the gas bubbles. The lift force can be numerically described using the following equation:

$$\vec{F}_{lift} = -C_L \epsilon_g \rho_l (\vec{v}_a - \vec{v}_l) X (\nabla \times U_a) \quad (13)$$

Table 2. Lift force parameters

	Tomiyama[10]
Lift Coefficient (Cl):	$C_L = \begin{cases} \min [0.288, \tanh(0.121 N_{Re,g})], f(E'_o), & E'_o \leq 4 \\ f(E'_o), & 4 < E'_o \leq 10 \\ -0.27, & 10 < E'_o \end{cases} \quad (14)$
	where, E'_o is modified Eotvos number to estimate the deformable bubble size $f(E'_o) = 0.00105 E_o'^3 - 0.0159 E_o'^2 - 0.0204 E_o' + 0.474 \quad (15)$

2.5 Population Balance Model

The PBM is an effective tool used in simulating the bubble size distribution. The PBM is employed to model the bubble coalescence and breakup rates for bubbles of different sizes within a bubble column. The interphase forces are calculated using the bubble size distribution and kinetic energy dissipation rate. Homogenous discrete PBM assumes equal velocity for all the bubble size distributions under consideration. This reduces the computation cost and uses a single gas phase momentum equation for the entire bubble size distribution similar to the single bubble size model.

The PBM equation can be written as:

$$\frac{\partial n(s,t)}{\partial t} + \nabla \cdot (U_g n(s,t)) = \int_0^\infty b(s') \beta(s,s') n(s') ds' + \frac{1}{2} \int_0^s c(s-s',s') n(s-s') n(s') ds'' - b(s) n(s) - \int_0^\infty c(s,s') n(s) n(s') ds'' \quad (16)$$

where $n(s,t)$ denotes the number size distribution of bubble of length s .

The terms on the LHS representing the variation and convection terms, respectively, while the terms on the RHS represent the bubble birth due to breakup and coalescence,

and bubble death due to breakup and coalescence respectively.

Table 3. Population Balance Model Parameters

Phenomena	Governing Equation
Bubble birth due to coalescence	$B_c = \frac{1}{2} \int_0^s c(s-s',s') n(s-s') n(s') ds''$
Bubble birth due to breakup	$B_b = \int_0^\infty b(s') \beta(s,s') n(s') ds'$
Bubble death due to coalescence	$D_c = \int_0^\infty c(s,s') n(s) n(s') ds''$
Bubble death due to breakup	$D_b = b(s) n(s)$

Equation (16) is an equation that consists of both derivatives and integrals of bubble size function. This equation has been solved using multiple approaches in the literature. Ramakrishna et al. [12] have discussed the discrete method and this has been widely employed in the literature.

2.6 Solution Methods and Boundary Conditions

Table 4. Inlet Boundary Conditions for the Air Phase

Superficial Gas Velocity	0.147 m/s
Smaller Air Fraction	Diameter = 0.005 m; Volume Fraction = 0.3
Medium Air Fraction	Diameter = 0.007 m; Volume Fraction = 0.6
Larger Air Fraction	Diameter = 0.01m; Volume Fraction=0.1

Table 5. Inlet Boundary Conditions for the Liquid Phase

Velocity Magnitude	0 m/s (Stationary bed)
Turbulence Specification	K and Epsilon
Turbulent Kinetic Energy (m ² /s ²)	0.01
Turbulent Dissipation Rate (m ² /s ³)	0.01

In this work, the Green Gauss Cell based method has been used. The momentum equation was discretized using the QUICK method for accuracy and convergence while the QUICK was also used for the volume fraction. For the rest, the second order upwind scheme is used. A time step of 0.001s was used to run the simulation. The simulation was carried out for about 280s and averaging was carried out after the flow reached a quasi-steady state at about 30s.

The inlet boundary conditions for the gas and liquid phase is given in Table 4 and Table 5. Table 7 gives a summary of all schemes used.

2.7 Computational Domain and Mesh

Table 7. Solution methods

Scheme	Phase Coupled SIMPLE
Spatial Discretization: Gradient	Green-Gauss Cell Based
Spatial Discretization: Momentum	QUICK
Spatial Discretization: Volume	QUICK

Fraction	
Spatial Discretization: Turbulent Kinetic Energy	Second Order Upwind
Spatial Discretization: Turbulent Dissipation Rate	Second Order Upwind
Transient Formulation	Bounded Second Order Implicit

Figures 1 (a) and (b) depict the computational domain and meshes for the hollow bubble column and the bubble column with vertical internals, respectively. For the hollow bubble column, it can be seen that the mesh is very dense near the walls of the bubble column which is necessary to capture the velocity variations and downward water flows in the near wall region. For the bubble column with internal rods, dense meshes are used near the internal rods and the column walls.

III. RESULTS AND DISCUSSIONS

Figure 2 presents the predicted liquid axial velocity profiles for hollow bubble column and the comparison with the numerical results from other researchers. It can be seen that at a superficial gas velocity of 0.147 m/s without using the PBM, a maximum velocity of 0.4 m/s is at the center of the bubble column ($r/R = 0$). This is quite close to the maximum liquid axial velocity obtained by Bhole et al. [7] and Sanyal et al. [8]. It can be seen that the axial velocity decreases along the radial direction from the center to the wall and reaches to zero at $r/R=0.6$, then, the direction of the liquid flow changes from upward (positive) to downward (negative). A similar trend was observed in the simulation for hollow bubble column by Gaurav et al.[2]. In their simulation where the PBM was used, for a superficial gas velocity about 0.12 m/s, the maximum velocity is 0.25 m/s at the center of the bubble column ($r/R=0$). The liquid axial velocity decreases along the radial direction from the center towards to the wall and the direction of the liquid flow reverses from upward to downward at $r/R=0.57$. Compared with the present study, it can be seen that the simulation using the PBM exhibits lower velocities in the core region and higher velocities in the annular region of the bubble column.

Figure 3 illustrates the comparison of the predicted liquid axial velocity profiles for hollow bubble column with the experimental results. Kalaga et al.[6] employed the Radioactive Particle Tracking (RPT) technique to measure the hydrodynamics in a bubble column of 0.12 m diameter. In their study, it can be seen that for a superficial gas velocity $V_g = 0.132$ m/s, the maximum upward axial velocity is 0.24 m/s in the center region of the bubble column. The velocity thereby decreases along the radial direction towards to the wall and the flow direction reverses at $r/R=0.77$. Wu et al. [14]employed the Computer Automated Radioactive Particle Tracking (CARPT) to measure liquid axial velocities in the bubble column reactor. In this case, for $V_g = 0.171$ m/s, the maximum upward liquid axial velocity is 0.642 m/s at the center region of the bubble column reactor and the maximum downward liquid axial velocity is 0.48 m/s near the wall. In the present work, for $V_g = 0.147$ m/s, the maximum upward liquid axial velocity is 0.4 m/s at the center of the bubble column ($r/R = 0$). Therefore, the predicted maximum upward

liquid axial velocity in the present work at $V_g=0.147$ m/s falls between the experimental data for $V_g = 0.171$ m/s and $V_g = 0.132$ m/s. Chen et al. [15] also employed CARPT to measure the liquid axial velocities in the bubble column. However, in this case, for $V_g = 0.10$ m/s, the maximum upward liquid axial velocity is about 0.556 m/s in the center region of the bubble column, which is on the higher side than that at a higher superficial gas velocity ($V_g = 0.132$).

The volume fraction contours of the liquid phase in the hollow bubble column and bubble column with vertical internals are presented in Figures 4 (a) and (b), respectively, which are the average values after 200s. Figure 4 also indicates that the air bubbles displace the stationary liquid water bed in the upward direction towards the top of the bubble column reactor. Therefore, the liquid volume fraction is lower at the bottom of the bed and higher at the top of the bed.

Velocity vectors of the liquid volume fraction at the bottom section of the bubble column between vertical positions of $y=0$ and $y=0.2$ m are displayed in Figure 5. The maximum velocity of the liquid phase in the hollow bubble column is about 1.24 m/s, which is near the wall region. In contrast, the maximum velocity of the liquid phase in the bubble column with vertical internals is about 1.3 m/s, which is close to the inlet and the column wall. There are strong liquid circulations in the hollow bubble column in the bottom section of the bubble column in comparison with those in the bubble column with vertical internals as shown in Figure 5. Also, from the vector profiles, it is evident that the liquid water flows mainly in the upward direction in the center of the bed and in the downward direction near the wall.

Vectors for liquid velocity at the middle section of the bubble column reactor between vertical positions of $y=0.9$ and $y=1.2$ m are displayed in Figure 6. On comparison between the velocity vectors of the hollow bubble column and bubble column with internals, it can be seen that the presence of vertical internals in the bubble column causes a greater degree of turbulence in the center region of the column. Liquid recirculation is noticed in the presence of internals, which leads to a better mixing. In the case of the hollow bubble column, the similar trend in liquid flow is observed in the middle section of the bubble column compared to the bottom section of the bubble column.

Figures 7 (a) and (b) show the liquid velocity vectors at the top section of the hollow bubble column reactor and bubble column reactor with internals between vertical positions of $y=1.5$ and $y=1.9$ m, respectively. It can be seen that the funneling effect is evident in the presence of vertical internals. On the other hand, in the hollow bubble column, the flow is in a regular upward fashion in the center region of the column and the liquid circulation exists. In both the cases, near the wall regions, the liquid flows in the downward direction.

The liquid velocity contours for the hollow bubble column and bubble column with vertical internals are presented in Figures 8 (a) and (b), respectively. It can be seen that the maximum liquid velocity is about 1.07 m/s and 1.12 m/s for the hollow

bubble column and bubble column with internals, respectively. It can be observed that the liquid velocity is higher in the hollow bubble column than that in the bubble column with vertical internals. The liquid velocity increases in the vicinity of internals.

Axial velocity profile for bubble column with vertical internals has been presented in Figure 9. It can be observed that the maximum velocity of 0.6 m/s in the positive Y-direction has been experienced at the core of the bubble column. On moving from the core to the annular region, the velocity decreases and at $r/R=0.25$ (left of the internal wall) there is a reversal of direction in the liquid flow. At the position of the internal ($r/R = 0.4$), the water velocity is zero due to the non-slip boundary conditions at the internal walls. Thereafter, the liquid axial velocity increases in the negative Y-direction because of the flow reversal in the presence of internal rod. The maximum velocity exhibited in the negative Y-direction is about 0.65 m/s.

The comparison of the liquid axial velocity profile for the bubble column with vertical internals with that for the hollow bubble column is given in Figure 10. The axial velocities for both the cases are taken at a vertical distance of 0.7m from the inlet of the bubble column reactor. The maximum upward axial velocities are at the center of the bubble column in both the cases. In both the cases, the axial velocity decreases along the radial direction from the center to the wall. With the internal rods, the liquid flow reverses the flow direction at $r/R=0.4$ from upward to downward. For the hollow bubble column, the direction of liquid flow reverses at $r/R=0.6$. The maximum upward and downward liquid velocities are higher in the bubble column with internals than those without internals.

The air velocity contours for the hollow bubble column are presented in Figure 11 for different air bubble sizes. The maximum velocities for the small, medium and large air bubbles are 1.04, 1.04 and 1.24 m/s, respectively. The highest velocities in all the three cases is at the center region of the bubble column reactor. This means that air bubbles of all sizes tend to rise in the middle region of the bubble column reactor with high velocities. The rise of bubbles in the core region of the bubble column tends to displace the stationary liquid bed in the upward direction. The air velocity contours for bubble column with vertical internal rods are presented in Figure 12. The maximum velocities for the smaller, medium and larger air bubbles are 1.06, 1.07 and 1.24 m/s, respectively.

The variation of Reynolds number for the turbulence regime for hollow bubble column and bubble column with vertical internals are illustrated in Figures 13 (a) and (b), respectively. The Reynolds number is highest at the inlet for both the cases. The maximum values of Reynolds number at the inlet for hollow bubble column is about 3.64×10^4 and for bubble column with vertical internals, it is about 5.29×10^4 . The turbulent Reynolds number is on the higher side in the center of the hollow bubble column due to the presence of eddy like flows. Presence of internals breaks the eddy formation and hence the turbulence Reynolds number is lower in this case.

Figures 14 (a) and (b) illustrate the turbulent viscosity contour plots for hollow bubble column and bubble column with vertical internals, respectively. Reynolds stresses are related to the mean velocity gradients and turbulent viscosity within a system [10]. It is evident from the contour plot that turbulent viscosity of water in the case of hollow bubble column is higher than the one with internals. Since the turbulent viscosity is directly proportional to the number of eddies formed within a system, it can be ascertained that internals break the eddies formed within the system.

The turbulent kinetic energy contour plots for hollow bubble column and bubble column with vertical internals are illustrated in Figures 15 (a) and (b), respectively. It has been reported that turbulent kinetic energy reduces in the presence of internals as the hydraulic diameter of the eddies is lower due to the smaller pitch of the circular tube internals [1]. In the present work, it is evident that the turbulent kinetic energy is reduced in the presence of internals at the core of bubble column reactor. However, near the inlet, it has a higher value for the column with internals.

IV. CONCLUSIONS

The effect of vertical internal rods on the column hydrodynamics in a bubble column reactor were evaluated in the current study and validated using data from literature. Hollow bubble column simulations were carried out and the comparisons have been made with bubble column with vertical internals. Additionally, the effect of PBM on the liquid axial velocities has been discussed. The simulated results were in accordance with the experimental and simulation results from the literature. Based on these results, it can be concluded that 2D Eulerian simulations can be used as a tool to predict the hydrodynamics and turbulence characteristics in a bubble column reactor. Further validation studies need to be carried out to verify the gas holdup values within a bubble column reactor in the absence of PBM. Additional simulations using 3D geometry can be carried out and compared with the 2D geometry.

REFERENCES

- [1] K. J. H. George, A. K. Jhavar, and A. Prakash, "Investigations of flow structure and liquid mixing in bubble column equipped with selected internals," *Chem. Eng. Sci.*, vol. 170, pp. 297–305, 2017.
- [2] T. Gaurav, "Numerical Investigations of Bubble Column Equipped with Vertical Internals in Different Arrangements," *MESc. Thesis, Univ. West. Ontario*, 2018.
- [3] A. K. Jhavar and A. Prakash, "Bubble column with internals: Effects on hydrodynamics and local heat transfer," *Chem. Eng. Res. Des.*, vol. 92, no. 1, pp. 25–33, 2014.
- [4] G. Besagni, F. Inzoli, and T. Ziegenhein, "Two-phase bubble columns: A comprehensive review," *ChemEngineering*, vol. 2, no. 2, p. 13, 2018.
- [5] A. K. Jhavar and A. Prakash, "Influence of bubble column diameter

- on local heat transfer and related hydrodynamics,” *Chem. Eng. Res. Des.*, vol. 89, no. 10, pp. 1996–2002, 2011.
- [6] D. V Kalaga *et al.*, “Comparative analysis of liquid hydrodynamics in a co-current flow-through bubble column with densely packed internals via radiotracing and Radioactive Particle Tracking (RPT),” *Chem. Eng. Sci.*, vol. 170, pp. 332–346, 2017.
- [7] M. R. Bhole, J. B. Joshi, and D. Ramkrishna, “CFD simulation of bubble columns incorporating population balance modeling,” *Chem. Eng. Sci.*, vol. 63, no. 8, pp. 2267–2282, 2008.
- [8] J. Sanyal, S. Vásquez, S. Roy, and M. P. Dudukovic, “Numerical simulation of gas–liquid dynamics in cylindrical bubble column reactors,” *Chem. Eng. Sci.*, vol. 54, no. 21, pp. 5071–5083, 1999.
- [9] A. Weber and H.-J. Bart, “Flow simulation in a 2D bubble column with the Euler-Lagrange and Euler-Euler method,” *arXiv Prepr. arXiv1706.05836*, 2017.
- [10] ANSYS, “Ansys Fluent Theory Guide,” vol. 15317, p. 513, 2013.
- [11] M. J. Hounslow, R. L. Ryall, and V. R. Marshall, “A discretized population balance for nucleation, growth, and aggregation,” *AIChE J.*, vol. 34, no. 11, pp. 1821–1832, 1988.
- [12] S. Kumar and D. Ramkrishna, “On the solution of population balance equations by discretization—I. A fixed pivot technique,” *Chem. Eng. Sci.*, vol. 51, no. 8, pp. 1311–1332, 1996.
- [13] T. Wang, “Simulation of bubble column reactors using CFD coupled with a population balance model,” *Front. Chem. Sci. Eng.*, vol. 5, no. 2, pp. 162–172, 2011.
- [14] Y. Wu, B. C. Ong, and M. H. Al-Dahhan, “Predictions of radial gas holdup profiles in bubble column reactors,” *Chem. Eng. Sci.*, vol. 56, no. 3, pp. 1207–1210, 2001.
- [15] J. Chen, A. Kemoun, M. H. Al-Dahhan, M. P. Duduković, D. J. Lee, and L.-S. Fan, “Comparative hydrodynamics study in a bubble column using computer-automated radioactive particle tracking (CARPT)/computed tomography (CT) and particle image velocimetry (PIV),” *Chem. Eng. Sci.*, vol. 54, no. 13–14, pp. 2199–2207, 1999.

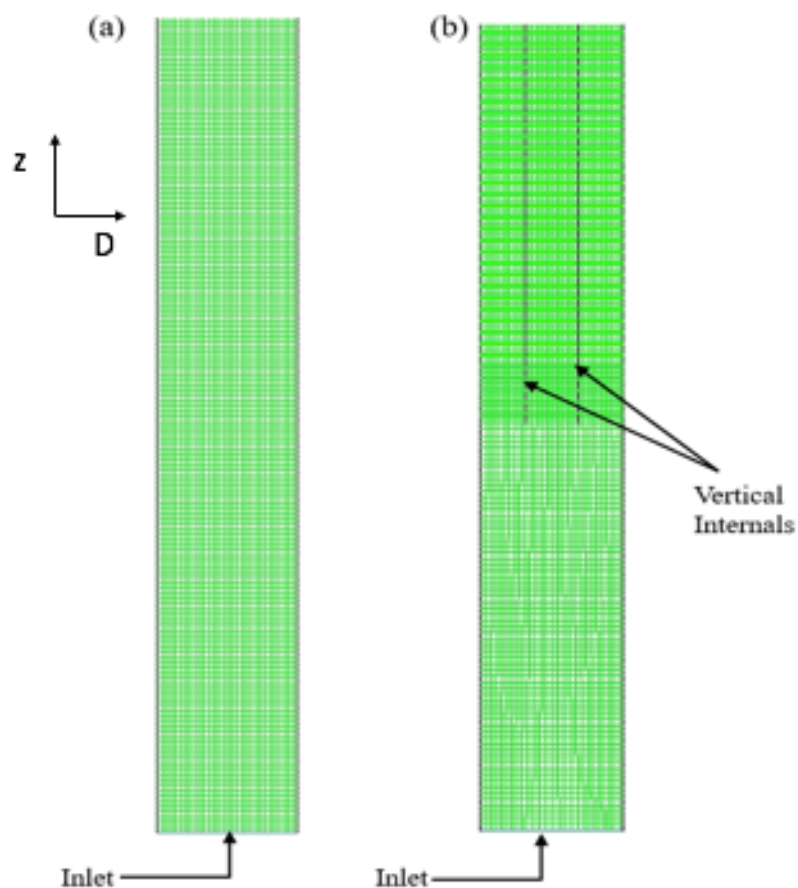


Figure 1. Computational domain and mesh
 (a) Hollow bubble column and (b) Bubble column with vertical internals

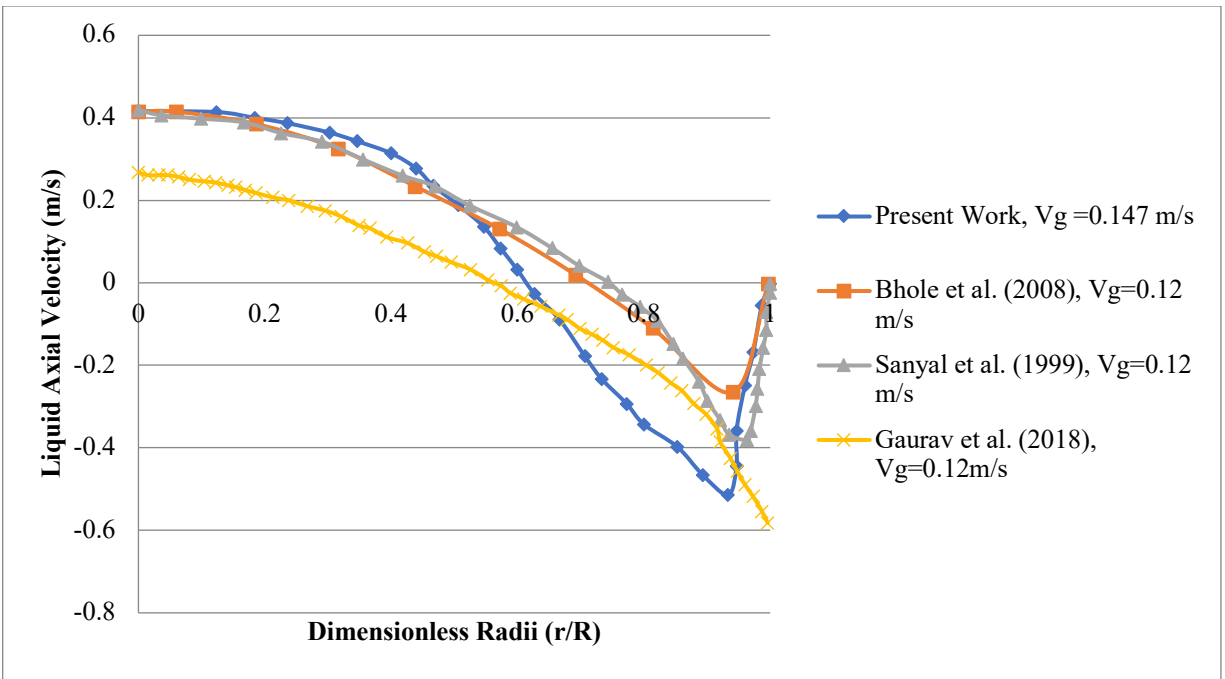


Figure 2. Comparison of the liquid axial velocity profile along the radial direction for the hollow bubble column with other numerical results at $z/D=4.67$

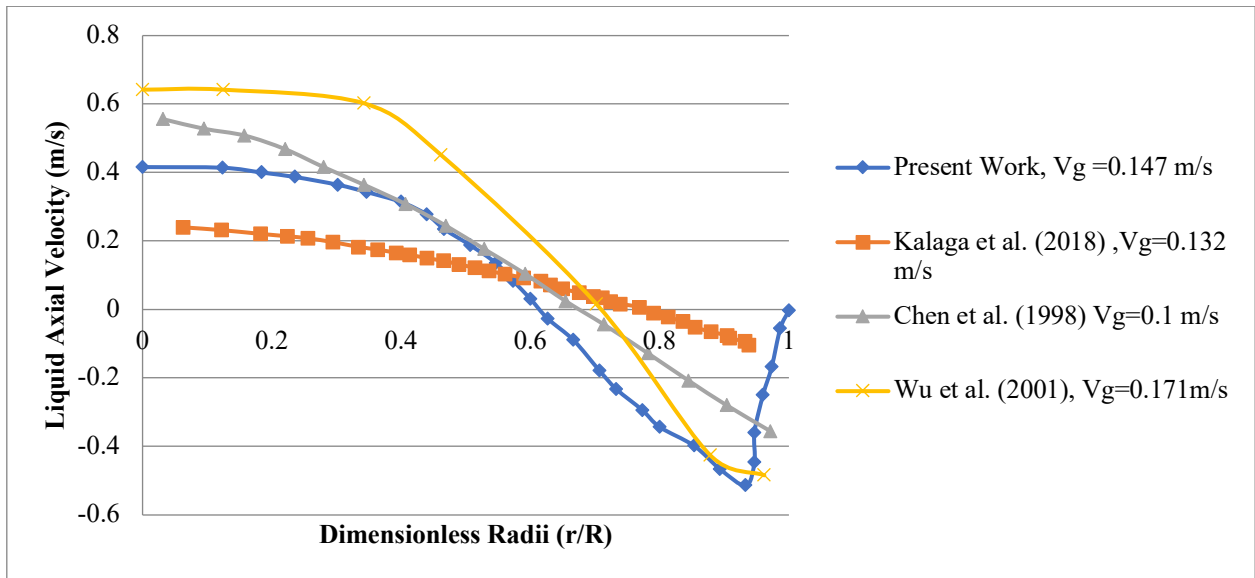


Figure 3. Comparison of the liquid axial velocities for the hollow bubble column with the experimental data

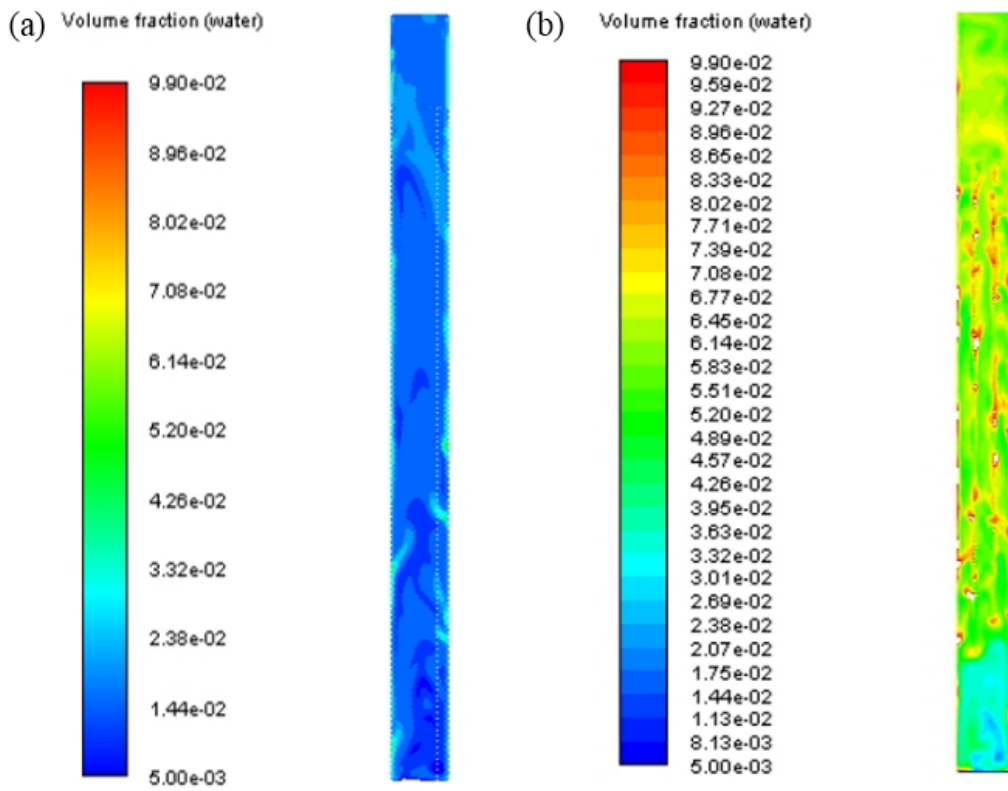


Figure 4. Liquid volume fraction contours
 (a) Hollow bubble column and (b) Bubble column with vertical internals

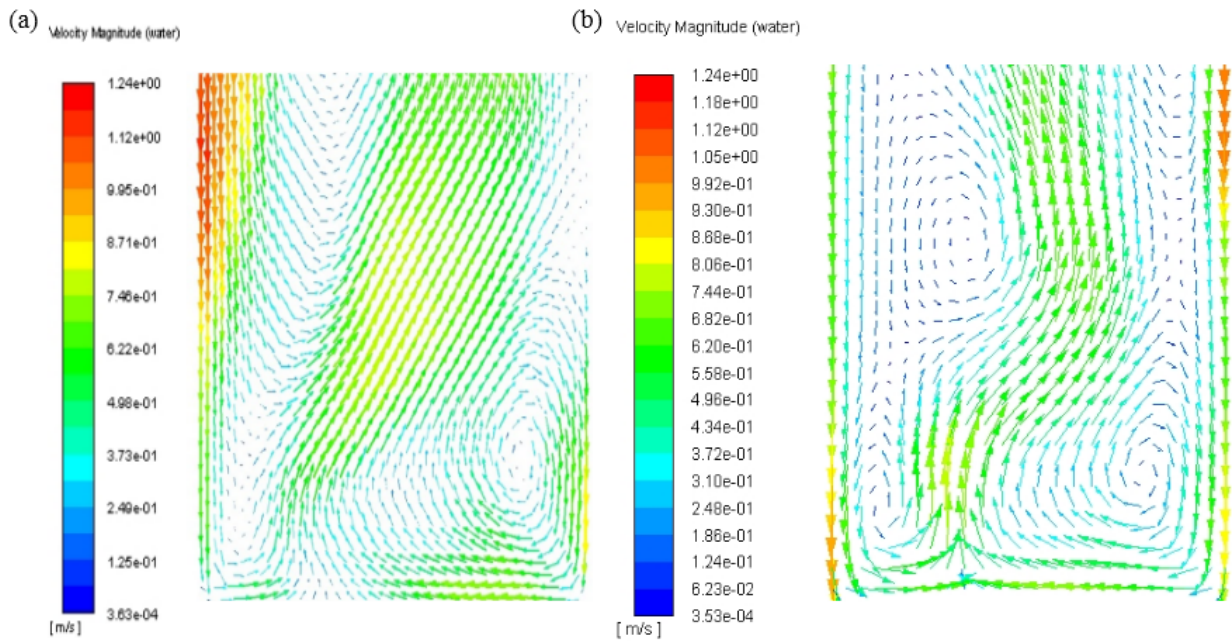


Figure 5. Liquid velocity vectors at the bottom section of the column
 (a) Hollow bubble column and (b) Bubble column with vertical internals

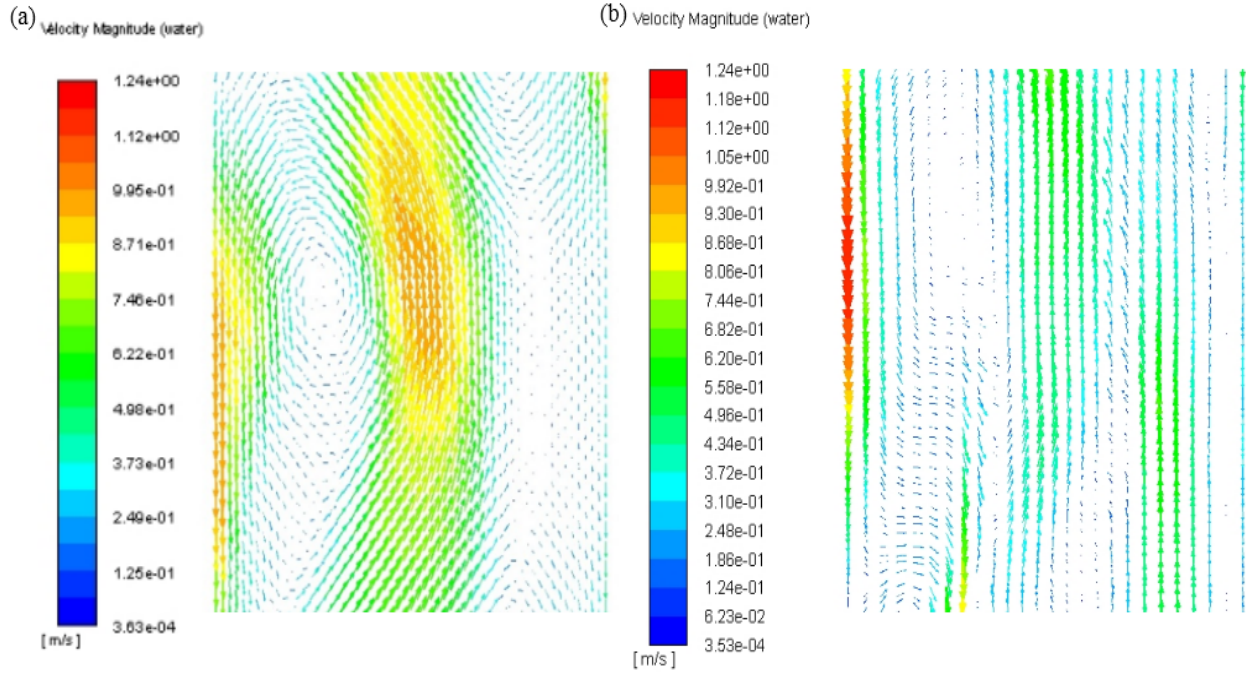


Figure 6. Liquid velocity vectors at the middle section of the column
 (a) Hollow bubble column and (b) Bubble column with vertical internals

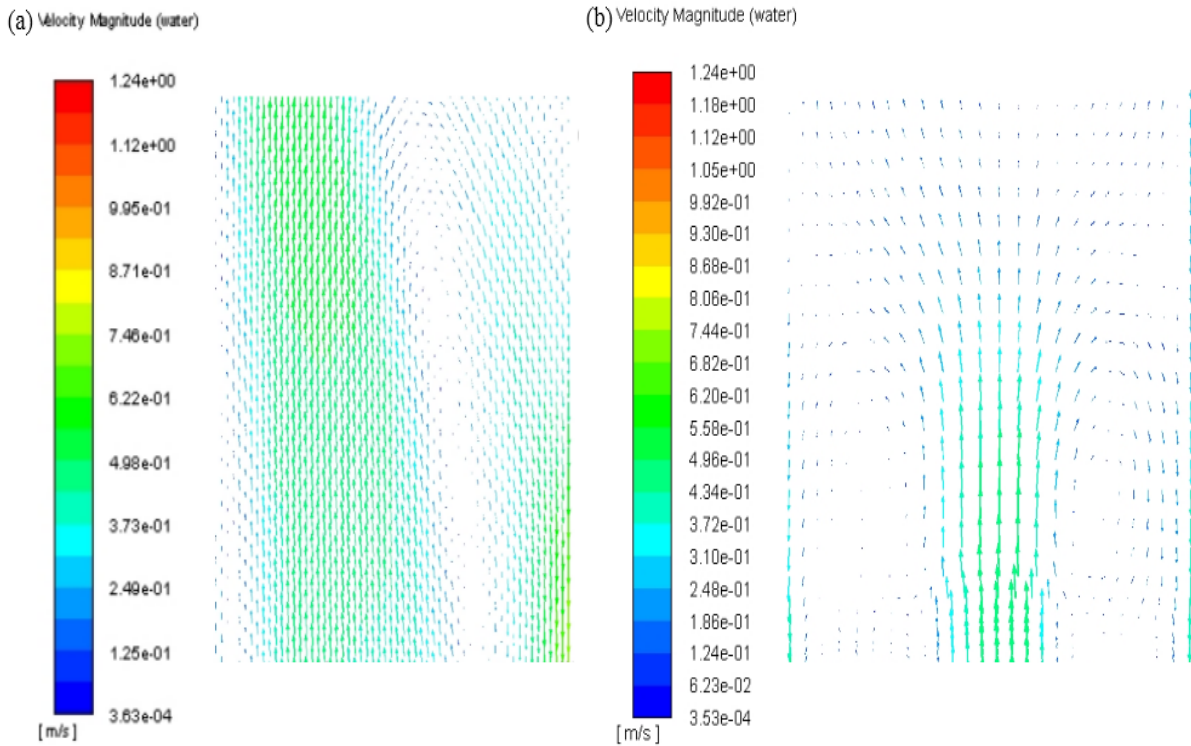


Figure 7. Liquid velocity vectors at the top section of the column
 (a) Hollow bubble column and (b) Bubble column with vertical internals

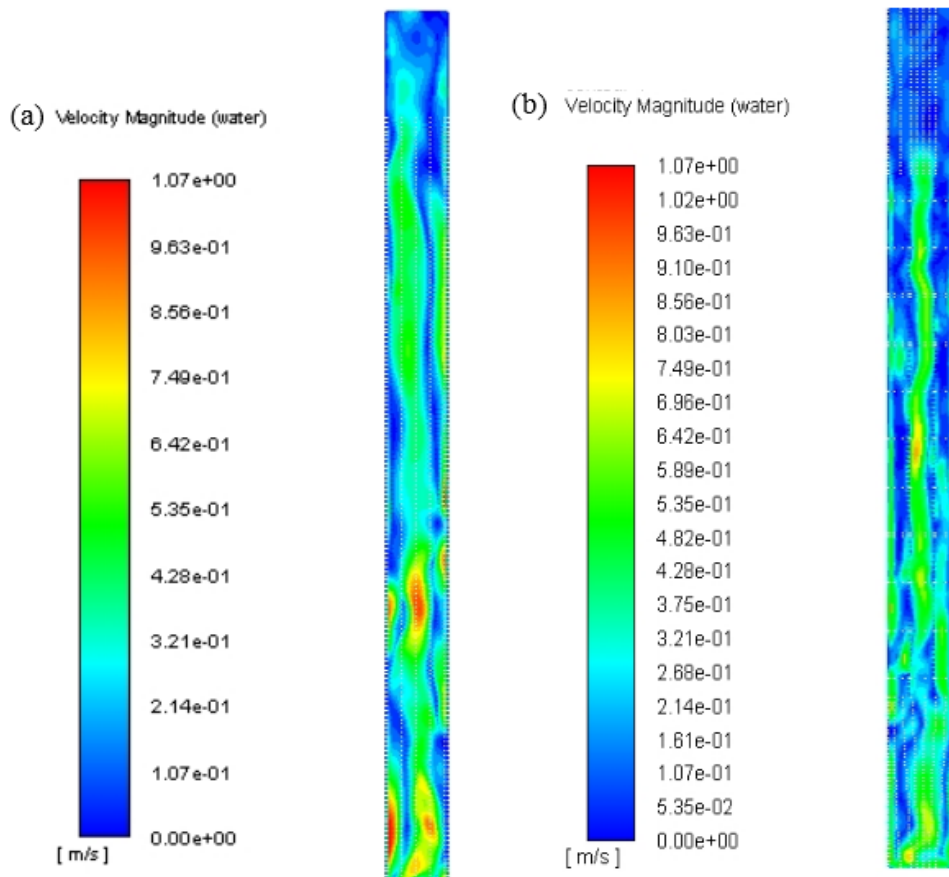


Figure 8. Liquid velocity contours
 (a) Hollow bubble column and (b) Bubble column with vertical internals

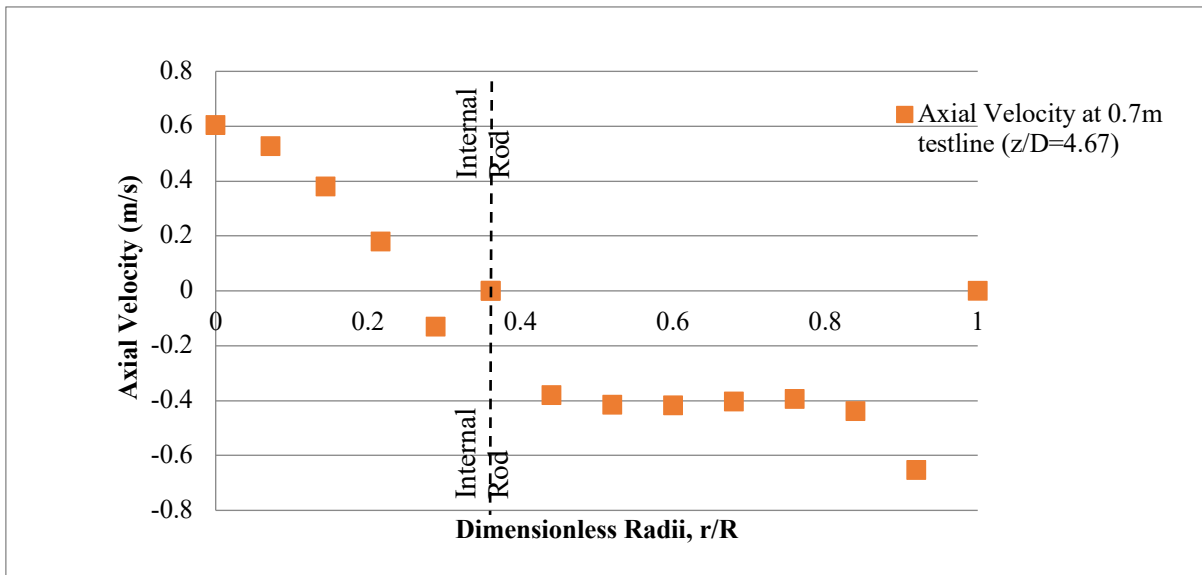


Figure 9. Liquid axial velocity profile for bubble column with vertical internals

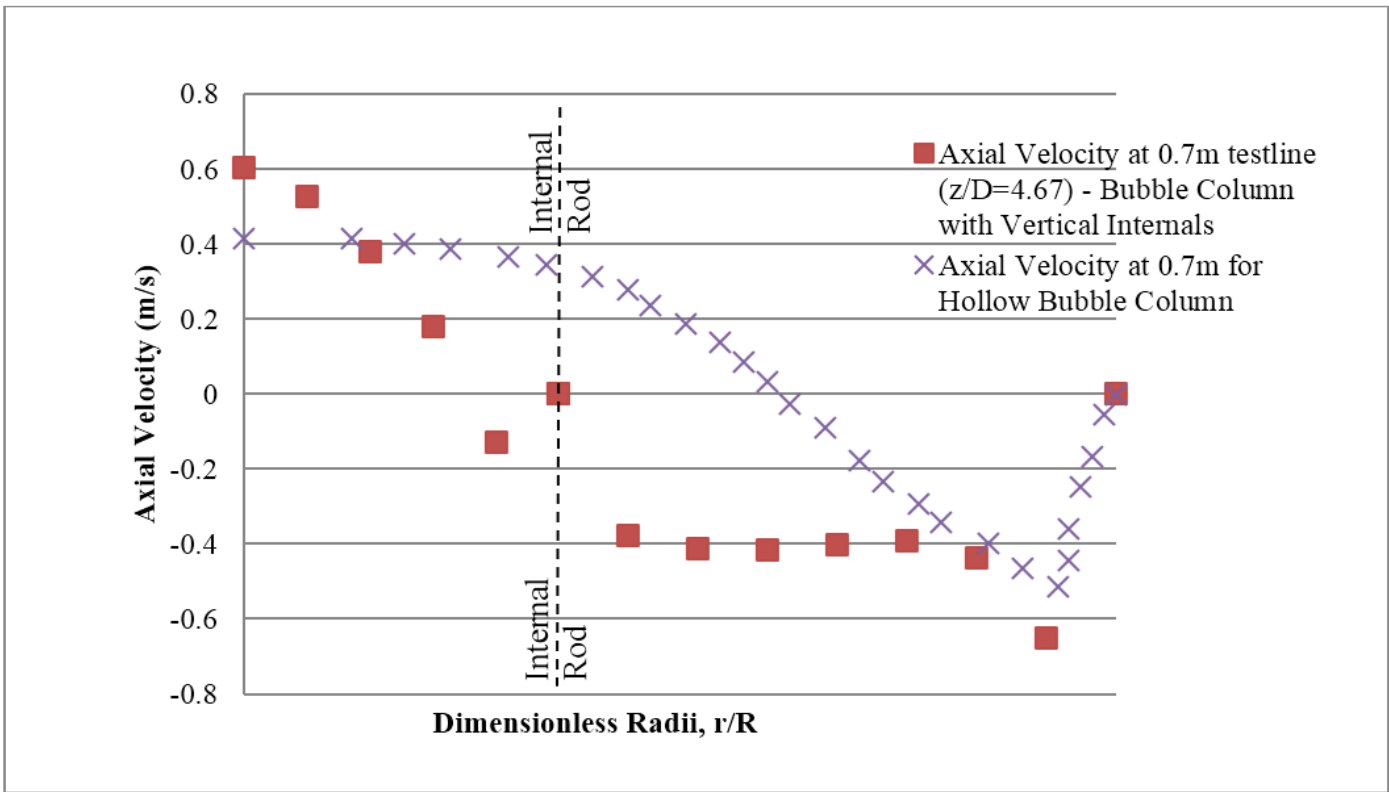


Figure 10. Comparison of the axial velocity profiles for bubble column with vertical internals and hollow bubble column

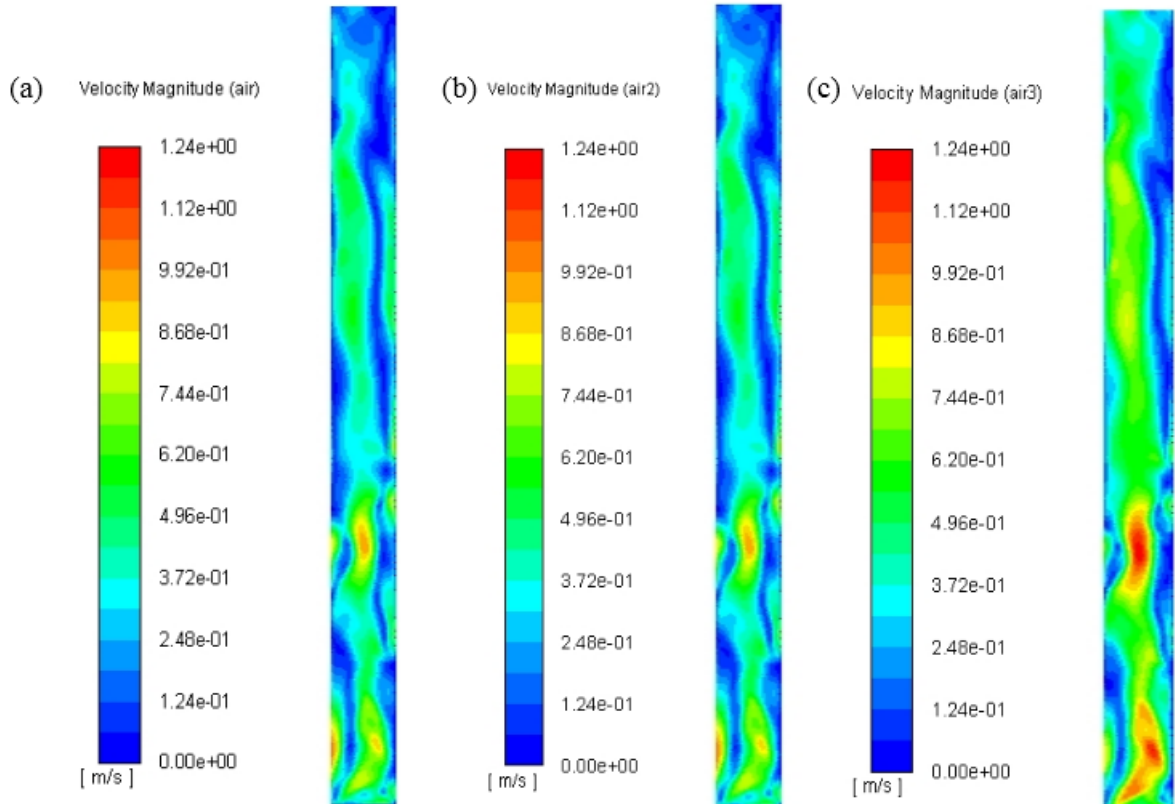


Figure 11. Gas velocity contours for the hollow bubble column (a) Small air bubble, (b) Medium air bubble and (c) Large air bubble

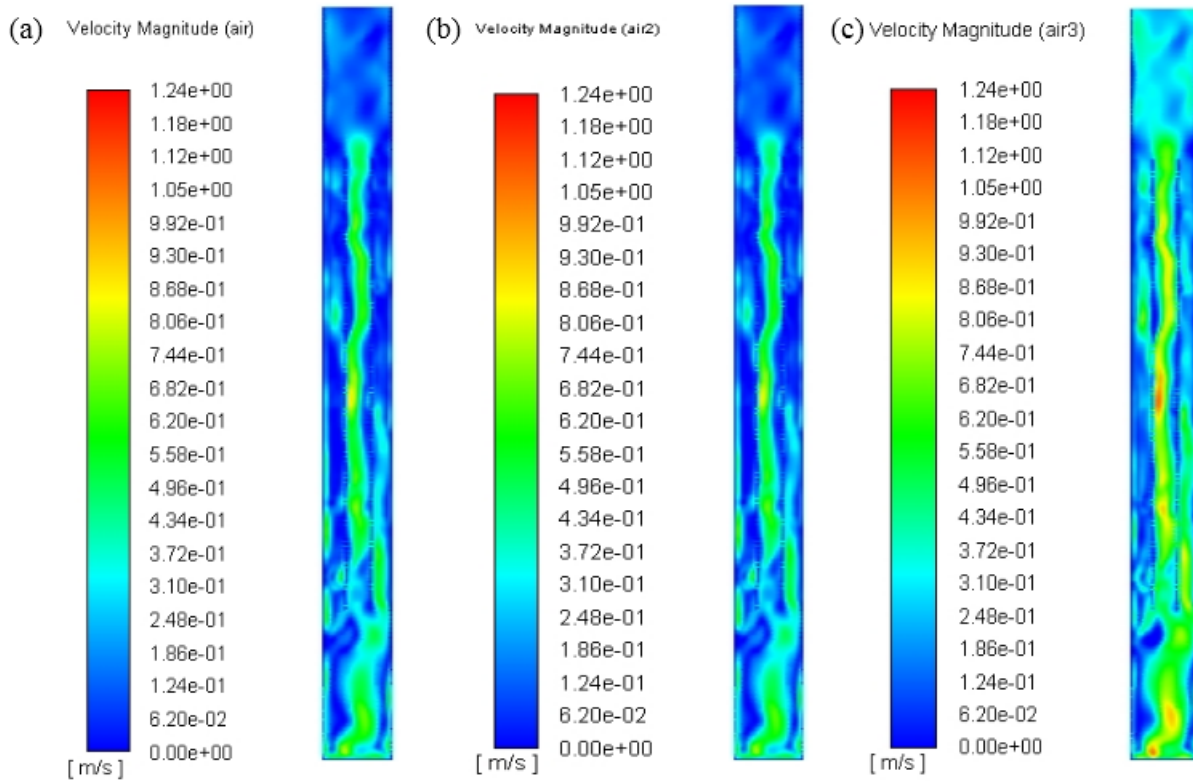


Figure 12. Gas velocity contours for the bubble column with vertical internals
 (a) Small air bubble, (b) Medium air bubble and (c) Large air bubble

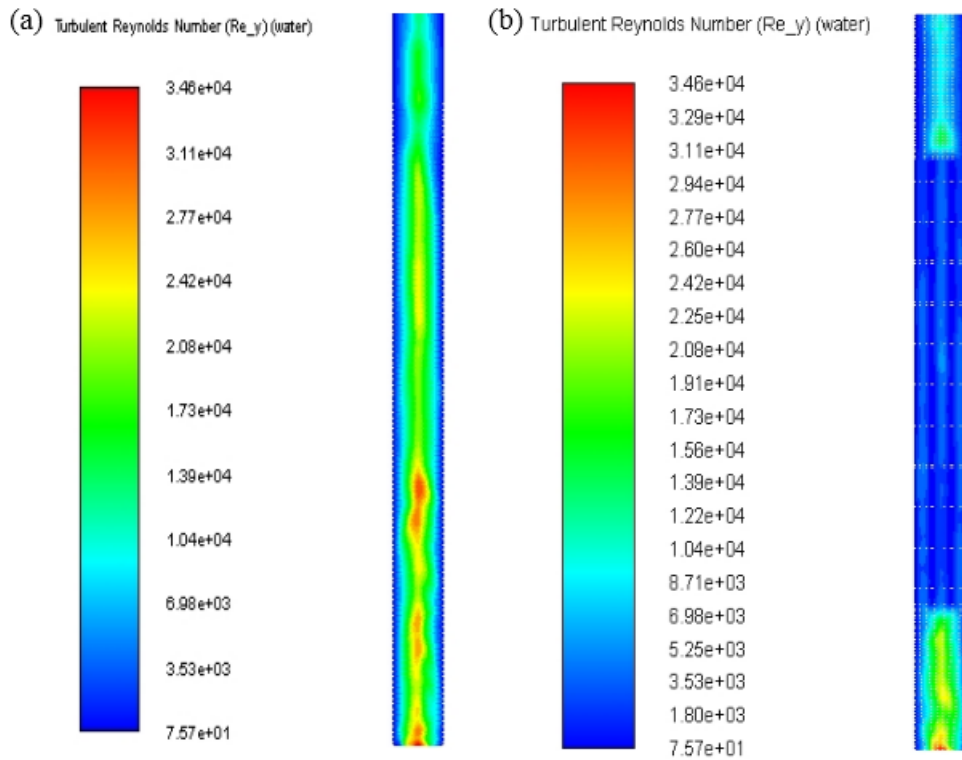


Figure 13. Turbulent Reynolds number contours for the liquid phase
 (a) Hollow bubble column and (b) Bubble column with vertical internals

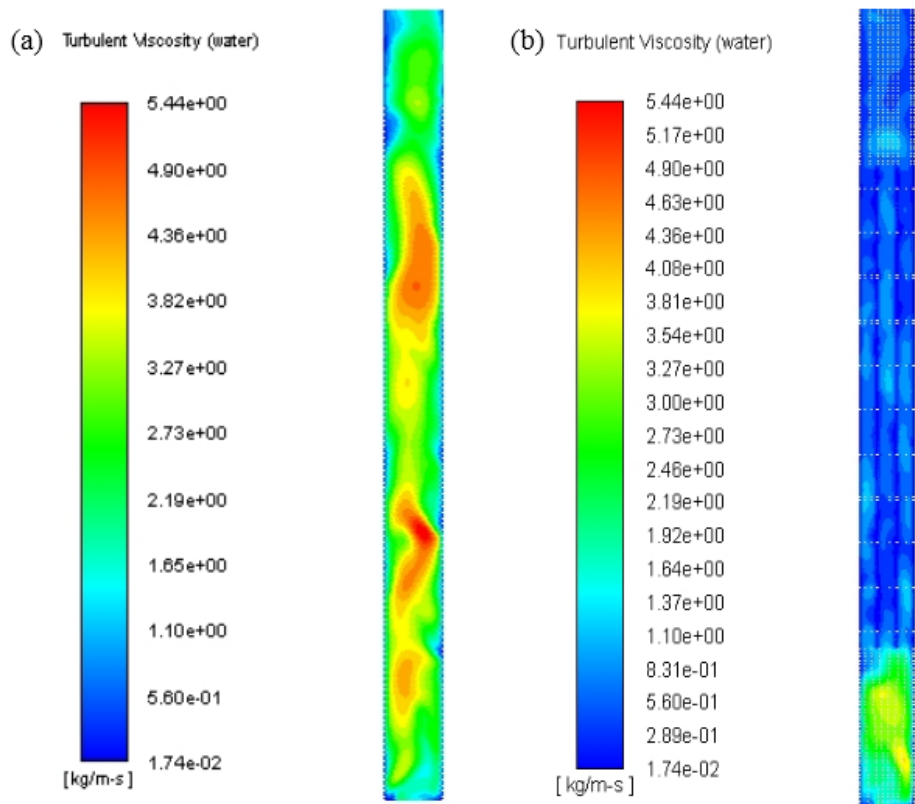


Figure 14. Turbulent viscosity contours for the liquid phase
 (a) Hollow bubble column and (b) Bubble column with vertical internals

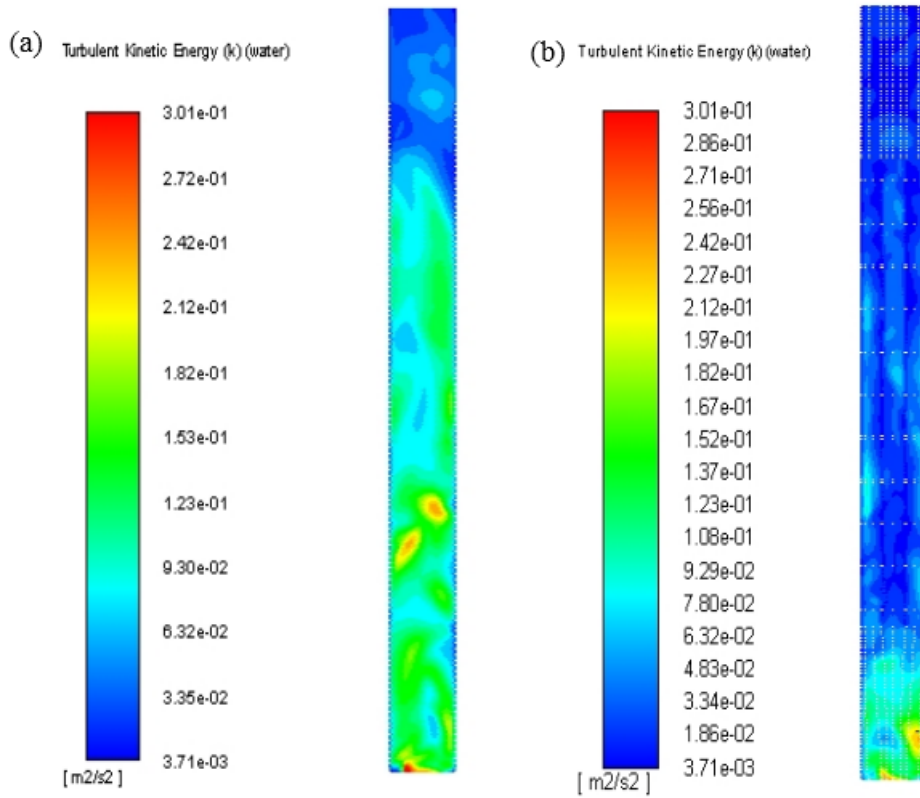


Figure 15. Turbulent kinetic energy contours for the liquid phase
 (a) Hollow bubble column and (b) Bubble column with vertical internals

CFD-PBM study of bubble column reactor integrated with mass transfer calculations

Ahmed Khalil

Department of Mechanical and Materials Engineering

University of Western Ontario

London, Canada

Christopher DeGroot

Department of Mechanical and Materials Engineering

University of Western Ontario

London, Canada

Abstract—In the present study, the sensitivity of the CFD simulation of bubble column reactor with presumed constant bubble size is studied. Then, the incorporation of PBM to CFD is conducted to illustrate the accuracy that PBM can offer. The most common bubble coalescence and PBM solution methods are investigated to optimize the accuracy and computational cost required for this kind of simulation. It is illustrated that it is essential for adopting uniform bubble simulations to determine the bubble size based on the critical diameter of lateral force sign inversion; not the experimental observation. However, using unrealistic bubble size leads to inaccurate calculations of mass transfer rate. Moreover, the anisotropy of the turbulence in bubble columns is investigated and the its effect of the performance of the PBM is studied. Finally, feasibility of using the inhomogeneous discrete method to account for the different rising velocity of different groups of bubbles is reported.

Keywords: *CFD; PBM; bubble column reactor; multiphase flow*

I. INTRODUCTION

Bubble column reactors represent a main component of numerous industrial systems. For instance, bubble columns are included in biochemical, petrochemical, and biological treatment of wastewater applications. The research community has been concerned with studying the hydrodynamics of bubble columns for the last three decades. Many experimental and numerical studies have been conducted to understand and, consequently, improve the performance of bubble columns by maximizing the usage of the limited volume available. The function of a bubble column is to facilitate mixing as well as mass and heat transfer between the different phases that are included in the reactions within the bubble column. This objective is achieved by sparging air from the bottom of the bubble column. Air pushes the liquid phase in the lateral and axial directions thereby improves the mixing. The key to understanding bubble column performance operating in batch mode is to precisely predict the behavior of the gas phase motion and the bubble size evolution along the bubble column. Afterwards, calculation of mass and heat transfer

rates based on the hydrodynamic fields obtained from the simulation is essential to serve the final target of the study.

Experimental studies of bubble column are tedious and accompanied with high uncertainty of the measurements. This uncertainty comes from existence of multiple phases in the system. Although many experiments [1]–[4] and [5] have been conducted producing a huge amount of data and correlations, the design of bubble columns is more based on the experience of the designer, especially, with various spargers type operating over a wide range of operating conditions. The main aspects affecting the performance that have been studied in the literature are: column aspect ratio, sparger type and position, properties of liquid phase and gas flow rate. Computational fluid dynamics (CFD) is a promising numerical approach that can be used as an affordable design tool for improving the performance of bubble columns. CFD has witnessed a huge development in the techniques used for simulating multiphase flows, resulting in significant improvements in the accuracy of solutions. These predictions can be used for scaling up the bubble column and optimizing its performance.

Many workers in the literature have attempted to study the hydrodynamics of bubble columns using various numerical approaches available, namely, the Euler-Lagrange framework [6], [7] and the two-fluid model in the Euler-Euler framework [8]–[10]. Euler-Lagrange treats the continuous phase as a continuum in Eulerian framework. The dispersed phase is tracked by solving Newton's second law on the trajectory of the individual bubbles in the numerical domain. It is very computationally expensive to use this model for high gas flow rates, since it tracks the individual bubbles in the computational domain, which are large in number. Hence, it is only applicable for limited low flow rates of the dispersed phase and a limited number of the particles in the domain. On the other hand, the most common model is the Eulerian or two-liquid model that solves a set of continuity and momentum equations for each phase in Eulerian framework. It assumes that the immiscible phases in the domain are interpenetrating continuum. The momentum and continuity equations are derived by ensemble averaging the single-phase

form of the fundamental conservation equations for each phase [11]. Averaging of the hydrodynamic field leads to loss of the interfacial boundary between the different phases in the system. Therefore, the interactions between these phases need to be modelled. Generally, the complexity of the multiphase flow arises from these interactions between the different phases in the system. Modelling the interactions is a complex process and can result in remarkable error in the numerical simulation. Many closure models for the interfacial forces, turbulence interactions, and bubble size distribution have been developed in the literature. Numerous closures are proposed to model the interfacial forces between the phases. These forces include drag [12]–[15], virtual mass [16], turbulent dispersion [17]–[19], lift and wall forces [12], [20]. Including all known interfacial forces makes the simulation approach the real physics of the problem. However, not all the forces have a considerable influence on the results and only offer additional computational cost and solution instability. As all the forces are modeled due to the loss of the interfacial boundaries between the phases in the Eulerian model, various models were developed either by experimental observation or analytical solution of a simplified problem.

Representation of computational domain as 2D or 3D domain is an active argument in the literature. Many studies in the literature were conducted to compare the 2D and 3D simulations. The simplification of the domain is to 2D to reduce the requirement of the simulation in terms of computational cost and the stability of the solution was discussed. However, it is agreed that the 2D axisymmetric is not appropriate for this kind of simulations as illustrated in the results reported in [21], [22]. It was explained by [21] that using 2D axisymmetric simulation does not capture the lateral movement of the bubble plume in the bubble column thus inaccurate results are obtained. Therefore, authors recommended using 3D simulation for studying the bubble column reactor. On the other hand, using 2D planar approach showed a good performance and a good compromise between the accuracy and computational power required [23]. Thus, in this work, the bubble column of interest is represented as a planar 2D domain. Despite of the significant influence of the bubble size in the system, many researchers in the literature assumed a constant bubble size throughout the whole domain. The uniform bubble size assumption used in these studies is based on the experimental observation [8], [9], [24], [25], empirical correlation developed in the literature [26] or assumed without justification. This assumption is unrealistic and disregards the fact of the interaction between the bubbles and continuous phase leads to coalescence and breakage of the bubbles. Consequently, the bubble size distribution (BSD) is alternating along the domain and is dependent on the hydrodynamics of the continuous phase. The BSD plays an imperative role in computing the value of different interfacial forces and defining the sign of these forces. Many works in

the literature [21], [27]–[29] are concerned with including the evolution of BSD in the domain by including the population balance (PB) equation in the simulation. The population balance (PB) equation is a statistical equation that is used to trace the bubble size of a dispersed phase in multiphase flow, and was formulated by [30]. It is integrated in the CFD as a conventional convection-diffusion transport equation with source terms that represent the coalescence, breakup, and growth of bubbles. The mechanisms of bubble breakup and coalescence are very dependent on the hydrodynamics of the surrounding continuous phase. These mechanisms were well studied, and numerous mechanistic models were proposed in the literature [31]–[33].

In the present work, 2D CFD simulations of a bubble column operating at heterogenous mode are reported. Experimental data from [1] are used for validation and discussion. Uniform and variable bubble size distribution are assumed. Population balance model is included in the CFD simulations with variable bubble size to capture the evolution of the bubble size distribution in the bubble column. Moreover, the anisotropy of the turbulence influence on the results is investigated. Nevertheless, a simple discrete method is compared to the inhomogeneous discrete method to study the feasibility of solving more than one set of governing equations for the gas phase to take into account the difference rising velocity of the classes of small bubbles and the class of large bubbles.

II. MODEL DESCRIPTION

A. Euler-Euler two-phase model

In the present work, the Eulerian model is adopted to simulate multiphase problem in the bubble column. The mass and momentum conservation equations that describe the motion of different phases are given as follows

$$\nabla \cdot (\rho_i \alpha_i U_i) = 0 \quad (1)$$

$$\begin{aligned} \frac{\partial (\rho_i \alpha_i U_i)}{\partial t} + \nabla \cdot (\rho_i \alpha_i U_i U_i) \\ = -\alpha_i \cdot \nabla \cdot p + \nabla (\alpha_i \tau_i) + F_{i,j} + \alpha_i \rho_i g \end{aligned} \quad (2)$$

where the subscript i distinguishes the conservation equations of the i^{th} phase in the model. The subscript l stands for the liquid (primary) phase and g stands for the gas (secondary) phase. The volume fraction is denoted α_i , for each of the primary and secondary phases. At any computational cell in the domain, the summation of the volume fraction of all phases is unity. However, the pressure field is a common field of the all phases in the model. The shear tensor and momentum exchange force are represented by τ_i and $F_{i,j}$, respectively. The exchange force term includes the interfacial forces between the phases, namely, drag, virtual mass, lift

wall forces, in addition to turbulent dispersion force. Drag force is modelled according to

$$F_D = \frac{3}{4} \alpha_g \rho_l \frac{C_D}{d_b} (u_g - u_l) |u_g - u_l| \quad (1)$$

where C_D is the drag force coefficient which is modelled herein using [12] to model as recommended for modelling the churn-turbulent regime [10], [34]. Moreover, virtual mass force is included using the model of [35] with virtual mass coefficient of 0.5. The lateral lift force is modelled by

$$F_T = -C_T \rho_L \frac{\pi d^3}{6} (V_g - V_l) \times \text{rot}(V_l) \quad (4)$$

The lift force coefficient, C_T , is obtained from the work of [36]. Nevertheless, the averaging of the drag force results in a term that is neglected in most of the works in the literature. However, authors of [37] claimed that this force has a significant role in smoothing out the gas holdup distribution in the lateral direction. Therefore, the turbulent dispersion force model of [17], given as

$$F_{td} = C_{TD} k_{gl} \frac{\nu_l}{\sigma_{ql}} \left[\frac{\nabla \alpha_g}{\alpha_g} - \frac{\nabla \alpha_l}{\alpha_l} \right] \quad (5)$$

is adopted since it is the most general model and can be used for broad range of flow conditions and regimes. The coefficient C_{TD} is a constant (default =1), k_{gl} is the interphase exchange coefficient that is defined in the drag force model, ν_l is the liquid kinematic viscosity and σ_{gl} is Schmidt number of default value of 0.9.

B. Turbulence model

Turbulence modelling in the multiphase hydrodynamics of bubble columns is complicated, especially, if the turbulence of the dispersed gas phase is included. Neglecting the turbulence in the gas phase is plausible assumption since modelling turbulence in the gas phase has insignificant effect on the solution and offers more convergence stability. However, the influence of the dispersed phase on the turbulence of the continuous phase can be significant, as observed in the experimental work of [38]. Many models have been developed in the literature to account for the turbulence induced by bubble in the continuous liquid phase [39]–[41]. Sato et al's model [39] includes the effect of bubble-induced turbulence indirectly by including an additional term in the turbulent viscosity. Then, the turbulent kinetic energy and dissipation rate are derived. On the other side, the other two models include an additional source term to the equations of the turbulent kinetic energy and dissipation rate which can be directly solved and incorporated with PBM.

Comparisons between the common turbulence models have been made. The superiority of RNG $k-\varepsilon$ was illustrated in

[42]. However, authors of [38] discussed the invalidity of the assumption of isotropic turbulence in bubble column reactors. The authors proposed that the turbulence in bubble column is highly anisotropic. The work of [43] supported the invalidity of the isotropy assumption for studying the turbulence in bubble columns. Standard $k-\varepsilon$, LES, and RSM models were compared in [43]. The ability of LES model to capture the dynamic structure in the bubble column was demonstrated. Moreover, the predictions of the Reynolds stress (radial and axial) were compared against experimental data and RSM model showed a better agreement than the LES model. In this work, RSM model is used to take account for the anisotropy of the turbulence thereby minimizing the error that may come from the turbulence model.

C. Population balance model

The population balance model (PBM), formulated in [30], is a statistical model that traces a property of a dispersed phase in a multiphase flow. It is a promising approach if it is employed to simulate the evolution of gas phase characteristics in a bubble column by providing an additional coordinate. This coordinate describes the bubble size distribution at each point in the domain and its evolution with time. The application of PBM in CFD is carried out using many methods. Herein, the bubble size coordinate is discretized to 20 classes such that each class is represented by a pivot size. The bubble size is presumed to have a maximum value of 40 mm and minimum of 0.5 mm. The discretization of the bubble size distribution is performed such that the volume geometric ratio between each size to the next larger one is unity. However, all these classes can have the same velocity field, i.e. the simple discrete/class method, or be separated by solving more than one set of continuity and momentum equation for the gas phase, i.e. the inhomogeneous discrete method. In the present work, both of these methods are used and compared to investigate the influence of computing two velocity fields for the gas phase, one for small bubbles and one for large bubbles. A conventional convection-diffusion transport equation is solved for each class. The evolution of the bubble size along the bubble column is simulated by the source terms in the transport equation of each class. These source terms represent the death and birth rates of the bubbles in each class by coalescence with other bubbles and breakup of larger bubble. Mechanistic models of the coalescence and breakup have been developed and proposed in the literature [31], [33], [44], [45]. In the present work, Lehr's and Luo's models are adopted and compared in terms of local gas holdup radial profiles.

D. Computational domain and solution

Experimental data used in the present work are extracted from the work of [1] on a gas-liquid-solid system that can operate at very high pressures. Herein, only results obtained under the

atmospheric conditions are considered for validation and discussion. In the experiments, a liquid recycle pan was placed in the freeboard region for the recycling of the liquid phase and releasing the gas phase. Gas was sparged from the bottom of the bubble column in the plenum chamber via $10\mu\text{m}$ openings of a porous pipe. Then, it flowed through a perforated distributed plate with 23 holes of 3.175mm in diameter. The local gas holdup profiles were measured using an optical probe that was inserted in the system using a port at height of 1045 mm above the distributor plate. It was observed that at high gas flow rates in still liquid, a gas pocket is formed underneath the distributor plate. Therefore, the computational domain includes the space above the distributor only, which has a height of 62 inches and 4 inches in diameter and considering the plate as a gas sparger with air volume fraction equal to the ratio of opening area to the total area. ANSYS FLUENT, Release 18.0 (Ansys Inc., US) is used to solve the governing equations and post-processing the solution. The bottom of the column is defined as a velocity inlet boundary condition (i.e. velocity specified and pressure extrapolated from the interior of the domain) with gas normal velocities corresponding to superficial velocities of 120 mm/s and 75 mm/s . For the constant bubble size simulations, the bubble size at the inlet is the same as in the rest of the domain. However, for simulations that include PBM, a log-normal bubble size distribution is assumed at the inlet. The free surface is specified as pressure outlet because of the foam used in the experiment for degassing the liquid phase at the freeboard. The solution of the governing equations is carried out with very small time-step (0.001 s) because of the solution instability. All the results presented hereafter are averaged over long simulation time after the quasi-steady state solution is reached by monitoring the global gas holdup. The sampling time is long enough such that the result does not change with any further time step solution. The solution is started with first-order advection schemes for better convergence characteristics. Afterwards, higher-order advection schemes are used to eliminate false diffusion of the lower order schemes.

III. Results and discussion

A. Population balance model results

Population balance model (PBM) is integrated in the solution of the hydrodynamic fields by using Sauter diameter at each computational cell in computing the interfacial forces between phases instead of using a uniform constant bubble size. Models of bubble breakage and coalescence rates are used to compute the birth and death rates of each bubbles class. The Lehr's breakage model [33] is used for all the cases, while Lehr's [33] and Luo's [31] models for coalescence rate are used and compared. The dispersed gas phase hydrodynamic fields are computed using one set of governing equations (homogeneous method) as well as two

sets of governing equations (inhomogeneous method) to determine the influence of computing the same velocity field of the gas phase for all the bubble sizes, and separately computing two velocity fields for two groups of bubbles, small and large bubbles. The results are compared in Fig.1 and Fig.2. Fig.1 shows the radial local gas holdup distribution for superficial gas velocity of $U_g = 120\text{ mm/s}$. It is clear that the parabolic shape of the local gas holdup profile is captured by the all models. As depicted, a good quantitative matching with the experimental data is obtained for all the combinations of the solution methods and coalescence rate models except for the simulation employing homogeneous method with Luo model for the coalescence rate calculations. In this simulation, the overprediction of gas holdup level can be explained as the Luo's model predicts lower coalescence rate that leads to similar Sauter diameter to estimated, consequently lower rising velocity and higher gas holdup are obtained. On the other hand, small discrepancies between the experimental and numerical results near the wall is observed for the other models. These discrepancies might be because of using enhanced wall function for the liquid phase only. The models are examined for lower superficial gas velocity, as well. Fig.2 shows the profiles determined by the same models against the experimental work for superficial air velocity $U_g = 75\text{ mm/s}$. With the lower gas velocity, the coalescence is supposed to be predominant. Despite of the gas holdup profile shape is well captured; the level is underestimated along the radial direction. Low predicted level of gas holdup is an indication either the coalescence of bubbles is overestimated, or the drag force models needs to be modified to account for bubbles motion hindering due to the presence of small bubbles. Therefore, herein, further investigation is conducted to isolate the effect of each factors by assuming single bubble size for the gas phase. However, as will be shown in the following sections, the constant bubble size of 6 mm is used and results in better prediction of the gas holdup levels, but it fails to capture the gas holdup profile. We can make a rough conclusion of this is that both the drag force model and the breakage and coalescence models need to be enhanced for more accurate prediction.

B. Constant bubble size results

The effect of uniform bubble size assumption is made to examine the feasibility of using this approach and avoid the burden of using the computationally expensive PBM with the CFD study. The obtained gas holdup profiles are compared against experimental data and the results of the models based on PBM. Three different bubble sizes larger than the critical bubble diameter of the lateral lift force model, as specified in [46], are examined as illustrated in Fig.3 and Fig.4. It is obvious that the selection of the representative bubble size

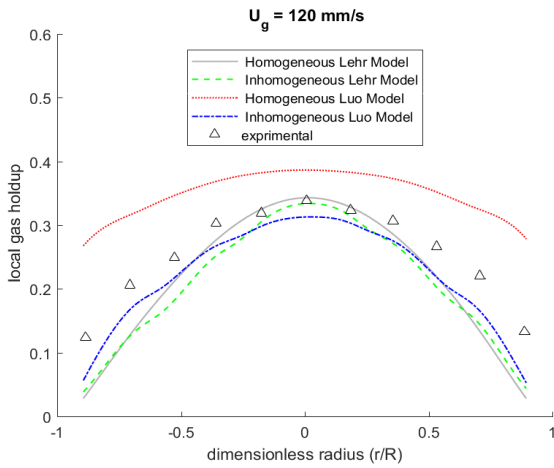


Figure 1: radial gas holdup distribution of $U_g=120$ mm/s

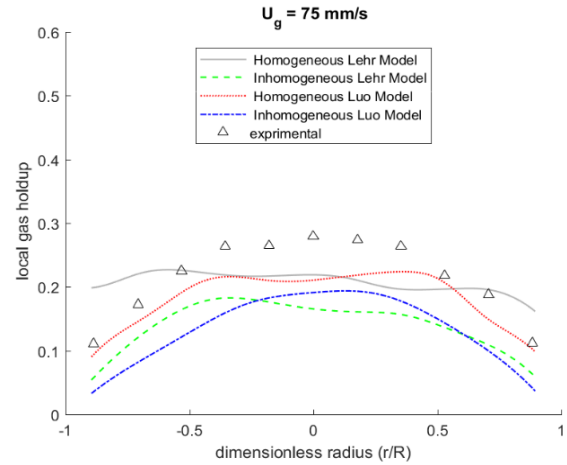


Figure 2: radial gas holdup distribution for $U_g = 75$ mm/s

has a remarkable effect on the gas holdup profile. For the 6mm-diameter simulation, a flatter gas holdup profile is obtained due to the dependency of the lateral lift force on the bubble size. According to Tomiyama's model [46], in the bubble columns with stagnant liquid the lift force sign is inverted at the bubble size of 5.8 mm as demonstrated in [47]. Therefore, two peaks near the wall are observed as the lateral force pushes the bubbles towards the wall. On the other hand, for the 10 mm and 15 mm simulations, the gas holdup profile shape with peak at the center of the column is well captured. However, quantitatively, it slightly mismatches the levels of the gas holdup along the radial direction. The same observation can be stated for the case of 75 mm/s air superficial velocity.

Results obtained using PBM are also plotted on the same figures to illustrate that the constant bubble size simulations of 10 mm and 15 mm give a similarly accurate prediction of radial gas holdup distribution as PBM with much lower computational cost. However, the comparison between PBM and classical model using uniform bubble size cannot be based on the radial gas holdup distribution only as discussed hereafter. The lateral force shows a good performance by accurately capturing the shape of the profile for variable and constant bubble size. Therefore, the other main significant force that has an essential role in determining quantitatively the gas hold profile is the drag force. The model of the drag force should be modified based on the turbulence field and the fractions of the large and small bubbles.

C. Influence of turbulence model

Two turbulence models are used, the Reynolds Stress model (RSM) and RNG $k-\epsilon$ model, to illustrate the effect of turbulence anisotropy on PBM prediction and consequently on Sauter diameter and gas holdup. For all the simulations,

homogeneous discrete method is used with Lehr's model for the evolution of the coalescence and breakage rates. The results show that considering the anisotropy of turbulence by employing the RSM does not have a significant effect on the results. The local gas holdup profiles are compared in Fig. 5 and Fig.6 for the superficial gas velocity of 120 mm/s and 75 mm/s. Gas holdup profiles predicted by both the turbulence models are very close qualitatively and quantitatively. The predicted average Sauter diameter, for the 120 mm/s simulations, is 29.6 mm and 29 mm, and for 75 mm/s, is 4.15 mm and 6 mm, using RNG $k-\epsilon$ and RSM, respectively. The predicted average Sauter diameters indicate the reason of the mismatching with the experimental data for the superficial velocity of 75 mm/s. As shown in the previous section, the simulation adopting constant bubble size of 6 mm could not match the experimental gas holdup profile and produce a flat profile with higher gas holdup. However, it is obvious that the effect of the turbulence on the predicted bubble size and gas holdup is insignificant.

D. Effect of bubble size distribution on gas-liquid mass transfer

Assessment of the constant bubble size assumption in comparison to the PBM model cannot be based solely on the local gas holdup distribution, since this does not give any indication regarding the ability to model the gas-liquid mass transfer rate. This is an important simulation parameter, since main goal of bubble columns is to facilitate the mass and heat transfer in compact volume. Therefore, other models concerned with the mass and heat transfer phenomena are commonly integrated with these studies. These models depend on the gas holdup distribution and interfacial area, consequently the calculation of the mass and heat transfer rate would be affected by the assumption made regarding the

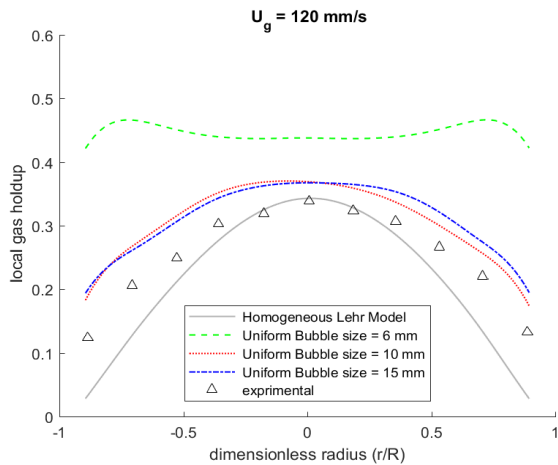


Figure 3: radial gas holdup distribution for $U_g = 120$ mm/s

bubble size in the domain. Therefore, the global gas holdup and oxygen mass transfer coefficient are computed for the sake of comparison between the models. However, for further validation of the models the calculated global gas holdup is compared to the experimental measurement reported in [1] as shown in Fig.7. Assumed bubble sizes in the uniform bubble size cases have significant effects on the global gas holdup. Therefore, many trials are required to specify the appropriate bubble size for each case regardless the experimental observation. On the other hand, capturing the correct gas holdup does not necessarily lead to correct local gas holdup profiles, especially, for the simulation with low coalescence rate where the bubble size is close to the critical bubble size of the lateral force. It is clear that PBM model gives a better matching both cases of superficial velocity of 75 mm/s and 120 mm/s. Furthermore, oxygen volumetric mass transfer is computed based on the presumed bubble size, for the uniform bubble size simulations, and Sauter diameter, for the PBM simulations. No experimental data are available for

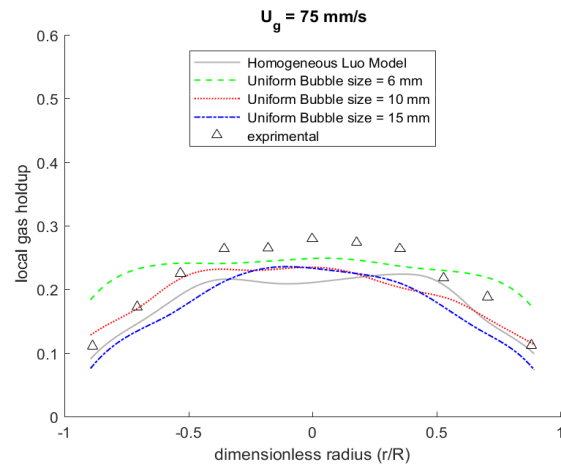


Figure 4: radial gas holdup distribution for $U_g = 75$ mm/s

validation; however, this study is beneficial for the sake of comparison between the models adopted in this study. The volumetric mass transfer coefficient k_L is computed using the well-known Higbie's model [48] as following:

$$k_L = \sqrt{\frac{D_L \cdot U_b}{\pi d_b}} \quad (6)$$

where D_L is the oxygen diffusion coefficient in water at 20 °C ($=1.89 \times 10^{-9} \text{ m}^2 \text{ s}^{-1}$), U_b is the slip velocity of the bubbles (ms^{-1}), d_b is the bubble diameter (m). The superficial area is computed based on the diameter used for k_L calculation for each case. As illustrated in Fig.8, the average global $k_L a$ is very sensitive to the models. For the constant bubble size simulations, the $k_L a$ is higher for the smaller bubble size. This is a result of the fact that the smaller bubble diameter has a higher surface-to-volume ratio. Furthermore, the gas holdup for small bubbles is higher than that of large bubbles. On the

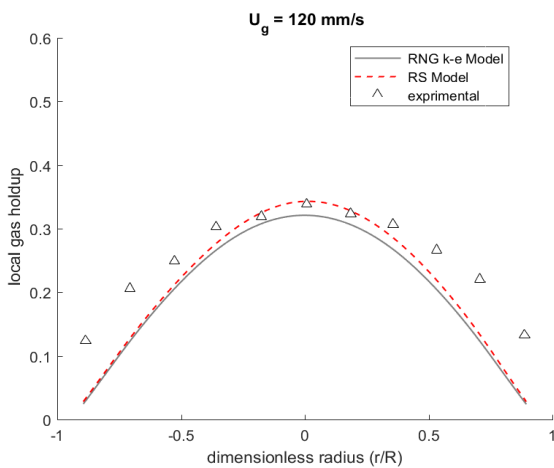


Figure 5: radial gas holdup distribution for $U_g = 120$ mm/s

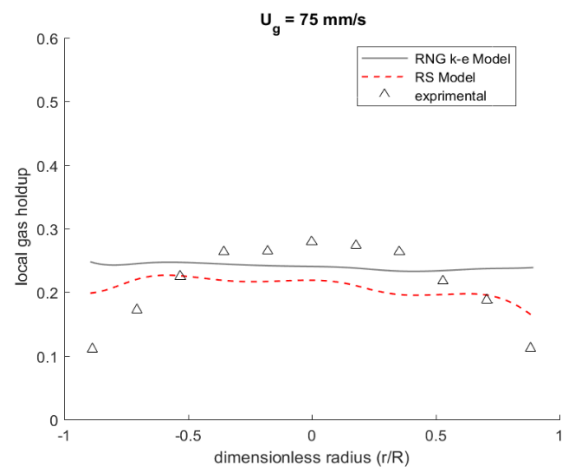


Figure 6: radial gas holdup distribution for $U_g = 75$ mm/s

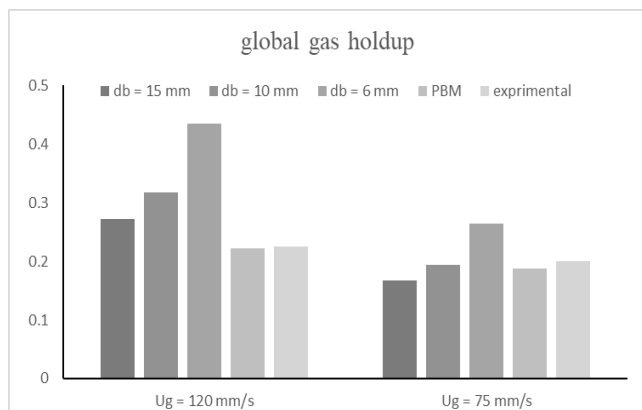


Figure 7: global gas holdup comparison

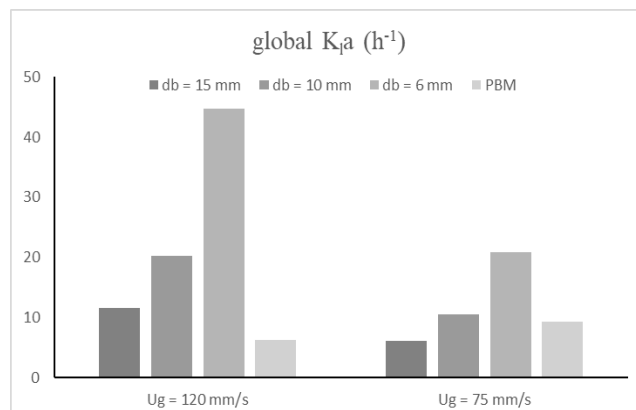


Figure 8: volumetric oxygen mass transfer coefficient in water

other hand, PBM variable Sauter bubble diameter has a significant effect on the calculation of the $k_{L,a}$.

IV. Conclusion

Uniform bubble size simulation is affordable and produces a reasonable prediction of the local gas holdup profile. But, using this assumption gives an inaccurate prediction of the global gas holdup. Moreover, the dependent models of mass and heat transfer are sensitive to the presumed bubble size. PBM is computationally expensive, but it is suitable to use for all operating conditions and evaluates the bubble size distribution based on the hydrodynamic fields of the liquid phase. Therefore, the dependent mass and heat transfer models can be more reliably implemented after isolating the error that would be due to assuming wrong representative bubble size. PBM has great potential for multiphase flow simulations with the development of more accurate coalescence and breakup models along with better drag models. The anisotropy of turbulence does not have a significant effect on the performance of the PBM. However, RSM computational cost is much higher than the RNG $k-\epsilon$ model.

V. References

- [1] D. Pjontek, V. Parisien, and A. Macchi, "Bubble characteristics measured using a monofibre optical probe in a bubble column and freeboard region under high gas holdup conditions," *Chem. Eng. Sci.*, vol. 111, pp. 153–169, 2014.
- [2] D. Darmana, R. L. B. Henket, N. G. Deen, and J. A. M. Kuipers, "Detailed modelling of hydrodynamics, mass transfer and chemical reactions in a bubble column using a discrete bubble model: Chemisorption of CO₂ into NaOH solution, numerical and experimental study," *Chem. Eng. Sci.*, vol. 62, no. 9, pp. 2556–2575, 2007.
- [3] A. Amaral, G. Bellandi, U. Rehman, R. Neves, Y. Amerlinck, and I. Nopens, "Towards improved accuracy in modeling aeration efficiency through understanding bubble size distribution dynamics," *Water Res.*, vol. 131, pp. 346–355, 2018.
- [4] R. Krishna and J. Ellenberger, "Gas Holdup in Bubble Column Reactors Operating in the Churn-Turbulent Flow Regime," *AIChE J.*, vol. 42, no. 9, pp. 2627–2634, 1996.
- [5] R. Rzehak, M. Krauß, P. Kováts, and K. Zähringer, "Fluid dynamics in a bubble column: New experiments and simulations," *Int. J. Multiph. Flow*, vol. 89, pp. 299–312, 2017.
- [6] A. Sokolichin, G. Eigenberger, A. Lapin, and A. Lübbert, "Dynamic numerical simulation of gas-liquid two-phase flows: Euler/Euler versus Euler/Lagrange," *Chem. Eng. Sci.*, vol. 52, no. 4, pp. 611–626, 1997.
- [7] E. Delnoij, F. A. Lammers, J. A. M. Kuipers, and W. P. M. Van Swaaij, "Dynamic simulation of dispersed gas-liquid two-phase flow using a discrete bubble model," *Chem. Eng. Sci.*, vol. 52, no. 9, pp. 1429–1458, 1997.
- [8] D. Zhang, N. G. Deen, and J. A. M. Kuipers, "Numerical simulation of the dynamic flow behavior in a bubble column: A study of closures for turbulence and interface forces," *Chem. Eng. Sci.*, vol. 61, no. 23, pp. 7593–7608, 2006.
- [9] L. Gemello, V. Cappello, F. Augier, D. Marchisio, and C. Plais, "CFD-based scale-up of hydrodynamics and mixing in bubble columns," *Chem. Eng. Res.*

- Des.*, vol. 136, no. 69, pp. 846–858, 2018.
- [10] X. F. Liang, H. Pan, Y. H. Su, and Z. H. Luo, “CFD-PBM approach with modified drag model for the gas-liquid flow in a bubble column,” *Chem. Eng. Res. Des.*, vol. 112, pp. 88–102, 2016.
- [11] M. Ishii, *Thermo-fluid Dynamics Two-phase flow*. 2011.
- [12] A. Tomiyama and I. Kataoka, “Drag Coefficients of Single Bubbles under Normal and Micro Gravity Conditions,” *JSME Int. J.*, vol. 41, no. 2, pp. 472–479, 1998.
- [13] D. Z. Zhang and W. B. VanderHeyden, “The effects of mesoscale structures on the macroscopic momentum equations for two-phase flows,” *Int. J. Multiph. Flow*, vol. 28, no. 5, pp. 805–822, 2002.
- [14] J. R. Grace, “Shapes and velocities of single drops and bubbles moving freely through immiscible liquids,” *Chem. Eng. Res. Des.*, vol. 54, pp. 167–173, 1976.
- [15] A. Naumann and L. Schiller, “A drag coefficient correlation,” *Z. Ver. Dstch. Ing.*, vol. 77, p. 51, 1935.
- [16] M. Rafique, P. Chen, and M. P. Duduković, “Computational modeling of gas-liquid flow in bubble columns,” *Rev. Chem. Eng.*, vol. 20, no. 3–4, pp. 225–375, 2004.
- [17] A. Burns, T. Frank, I. Hamill, and J. Shi, “The Favre averaged drag model for turbulent dispersion in Eulerian multi-phase flows,” *5th Int. Conf. Multiph. Flow*, no. 392, pp. 1–17, 2004.
- [18] M. A. Lopez De Bertodano, “Two fluid model for two-phase turbulent jets,” *Nucl. Eng. Des.*, vol. 179, no. 1, pp. 65–74, 1998.
- [19] A. D. Gosman, C. Lekakou, S. Politis, R. I. Issa, and M. K. Looney, “Multidimensional modeling of turbulent two-phase flows in stirred vessels,” *AIChE J.*, vol. 38, no. 12, pp. 1946–1956, 1992.
- [20] P. G. Saffman, “Corrigendum to ‘The lift force on a small sphere in a slow shear flow.’,” *J. Fluid Mech.*, vol. 22, 1968.
- [21] P. Chen, M. P. Duduković, and J. Sanyal, “Three-dimensional simulation of bubble column flows with bubble coalescence and breakup,” *AIChE J.*, vol. 51, no. 3, pp. 696–712, 2005.
- [22] R. Krishna, J. M. Van Baten, and M. I. Urseau, “Three-phase Eulerian simulations of bubble column reactors operating in the churn-turbulent regime: A scale up strategy,” *Chem. Eng. Sci.*, vol. 55, no. 16, pp. 3275–3286, 2000.
- [23] H. A. Jakobsen, B. H. Sannaes, S. Grevskott, and H. F. Svendsen, “Modeling of Vertical Bubble-Driven Flows,” *Ind. Eng. Chem. Fundam.*, vol. 36, pp. 4052–4074, 1997.
- [24] R. M. A. Masood and A. Delgado, “Numerical investigation of the interphase forces and turbulence closure in 3D square bubble columns,” *Chem. Eng. Sci.*, vol. 108, pp. 154–168, 2014.
- [25] M. Simonnet, C. Gentric, E. Olmos, and N. Midoux, “CFD simulation of the flow field in a bubble column reactor: Importance of the drag force formulation to describe regime transitions,” *Chem. Eng. Process. Process Intensif.*, vol. 47, no. 9–10, pp. 1726–1737, 2008.
- [26] P. Chen, J. Sanyal, and M. P. Duduković, “Numerical simulation of bubble columns flows: Effect of different breakup and coalescence closures,” *Chem. Eng. Sci.*, vol. 60, no. 4, pp. 1085–1101, 2005.
- [27] G. Yang, K. Guo, and T. Wang, “Numerical simulation of the bubble column at elevated pressure with a CFD-PBM coupled model,” *Chem. Eng. Sci.*, vol. 170, pp. 251–262, 2017.
- [28] T. Wang, J. Wang, and Y. Jin, “Population balance model for gas - Liquid flows: Influence of bubble coalescence and breakup models,” *Ind. Eng. Chem. Res.*, vol. 44, no. 19, pp. 7540–7549, 2005.
- [29] C. B. Vik, J. Solsvik, M. Hillestad, and H. A. Jakobsen, “A multifluid-PBE model for simulation of mass transfer limited processes operated in bubble columns,” *Comput. Chem. Eng.*, vol. 110, pp. 115–139, 2018.
- [30] H. M. Hulburt and S. Katz, “Some problems in particle technology,” *Chem. Eng. Sci.*, vol. 19, no. 8, pp. 555–574, 1964.
- [31] H. Luo and H. F. Svendsen, “1996-Theoretical model for drop and bubble breakup in turbulent dispersions.pdf,” vol. 42, no. 5, pp. 1225–1233, 1996.
- [32] T. Wang, J. Wang, and Y. Jin, “A CFD-PBM coupled model for gas-liquid flows,” *AIChE J.*, vol. 52, no. 1, pp. 125–140, 2006.
- [33] F. Lehr, M. Millies, and D. Mewes, “Bubble size distributions and flow fields in bubble columns,” *AIChE J.*, vol. 42, no. 11, pp. 1225–1233, 2002.
- [34] M. Pourtousi, J. N. Sahu, and P. Ganesan, “Effect of

- interfacial forces and turbulence models on predicting flow pattern inside the bubble column,” *Chem. Eng. Process. Process Intensif.*, vol. 75, pp. 38–47, 2014.
- [35] D. A. Drew and R. T. Lahey, “The virtual mass and lift force on a sphere in rotating inviscid flow,” *Int. J. Multiph. Flow*, vol. 13, no. 1, pp. 113–121, 1987.
- [36] A. Tomiyama, H. Tamai, I. Zun, and S. Hosokawa, “Transverse migration of single bubbles in simple shear flows,” *Chem. Eng. Sci.*, vol. 57, no. 11, pp. 1849–1858, 2002.
- [37] D. Lucas, E. Krepper, and H. M. Prasser, “Use of models for lift, wall and turbulent dispersion forces acting on bubbles for poly-disperse flows,” *Chem. Eng. Sci.*, vol. 62, no. 15, pp. 4146–4157, 2007.
- [38] R. F. Mudde, J. S. Groen, and H. E. A. Van Den Akker, “Liquid velocity field in a bubble column: LDA experiments,” *Chem. Eng. Sci.*, vol. 52, no. 21–22, pp. 4217–4224, 1997.
- [39] Y. Sato, M. Sadatomi, and K. Sekoguchi, “Momentum and heat transfer in two-phase bubble flow - II.,” *Int. J. Multiph. Flow*, vol. 7, no. 2, Apr. 1981, pp. 179–190, 1980.
- [40] M. S. Politano, P. M. Carrica, and J. Converti, “A model for turbulent polydisperse two-phase flow in vertical channels,” *Int. J. Multiph. Flow*, vol. 29, no. 7, pp. 1153–1182, 2003.
- [41] A. A. Troshko and Y. A. Hassan, “A two-equation turbulence model of turbulent bubbly flows,” *Int. J. Multiph. Flow*, vol. 27, no. 11, pp. 1965–2000, 2001.
- [42] C. Laborde-Boutet, F. Larachi, N. Dromard, O. Delsart, and D. Schweich, “CFD simulation of bubble column flows: Investigations on turbulence models in RANS approach,” *Chem. Eng. Sci.*, vol. 64, no. 21, pp. 4399–4413, 2009.
- [43] M. V. Tabib, S. A. Roy, and J. B. Joshi, “CFD simulation of bubble column-An analysis of interphase forces and turbulence models,” *Chem. Eng. J.*, vol. 139, no. 3, pp. 589–614, 2008.
- [44] T. Wang, J. Wang, and Y. Jin, “Theoretical prediction of flow regime transition in bubble columns by the population balance model,” *Chem. Eng. Sci.*, vol. 60, no. 22, pp. 6199–6209, 2005.
- [45] M. J. Prince and H. W. Blanch, “Bubble coalescence and break up in air sparged bubble columns,” *AIChE J.*, vol. 36, no. 10, pp. 1485–1499, 1990.
- [46] A. Tomiyama, A. Sou, I. Zun, N. Kanami, and T. Sakaguchi, “Effects of Eotvos Number and Dimensionless Liquid Volumetric Flux on Lateral Motion of a Bubble in a Laminar Duct Flow,” in *Proceedings of the Second International Conference on Multiphase Flow*, 1995, pp. 3–15.
- [47] E. Krepper, D. Lucas, T. Frank, H. M. Prasser, and P. J. Zwart, “The inhomogeneous MUSIG model for the simulation of polydispersed flows,” *Nucl. Eng. Des.*, vol. 238, no. 7, pp. 1690–1702, 2008.
- [48] C. B. Vik, J. Solsvik, M. Hillestad, and H. A. Jakobsen, “Interfacial mass transfer limitations of the Fischer-Tropsch synthesis operated in a slurry bubble column reactor at industrial conditions,” *Chem. Eng. Sci.*, vol. 192, pp. 1138–1156, 2018.

Modification of the CFD Model Based on the Bubble Size for the Three-phase Flow in an Inverse Fluidized Bed

Yunfeng Liu¹, Zeneng Sun², Chao Zhang¹ and Jesse Zhu²

¹Mechanical and Material Engineering
²Chemical and Biochemical Engineering
University of Western Ontario
London, Ontario, Canada
Yliu896@uwo.ca

Abstract— The inverse three-phase fluidized bed has excellent potentials to be used in chemical, biochemical, petrochemical and food industries because of its high contact efficiency among each phase which leads to a good mass and heat transfer. Despite the hydrodynamics of the inverse fluidized bed has been studied experimentally by many researchers, the bubble behaviors in inverse TPFB have not been well understood due to the inadequate experiments data and the limitation of the visualization techniques. In addition, only very few three-phases Eulerian-Eulerian (E-E) CFD models have been developed and for the three-phase fluidization processes, and most of them are assumed to have a constant bubble size even under different superficial inlet gas or liquid velocities. In this study, the proposed CFD model takes the bubble size effects into account and it performs better on estimating the average gas holdup. In addition, a correlation between the bubble size and the superficial gas velocity, gas holdup and physical properties of the liquid and solid phases is proposed based on the numerical results. The predicted bubble size and the gas holdup in the inverse three-phase fluidized beds under a batch mode using the proposed correlation agree well with the experimental data. Therefore, the proposed three-phase E-E CFD model including the effect of the bubble size can be used to predict the performance of the inverse three-phase fluidization system more accurately.

Keywords - *Inverse fluidized bed; three-phase flow; CFD (computational fluidized dynamics); bubble size*

I. INTRODUCTION

Fluidization is a process that converts particles from the solid like state to a fluid like state by injecting liquid or gas flow into the system. With different fluidizing agents, fluidized beds can be categorized as the liquid-solid two-phase fluidization, gas-solid two-phase fluidization and gas-liquid-solid three-phase fluidization. The gas-liquid-solid three-phase fluidized bed (TPFB) has many applications in chemical, biochemical, petrochemical industries because it has a higher

contact efficiency among each phase and good mass and heat transfer features [1]. Fluidized beds can be further divided into the upward fluidized bed and inverse fluidized bed based on the flow direction of the fluidizing agent. In inverse TPFBs, the particle density is usually less than the liquid density, so the fluidization process will start when the drag force and gravity on the particle are balanced with the buoyancy force. The inverse gas-liquid-solid (GLS) fluidized bed can be operated under a continuous mode or batch liquid mode. Under the batch liquid mode, only gas is introduced into the fluidized bed filled with liquid at a certain velocity to include the liquid flow and fluidize solids inside the column. Under the continuous mode, both gas and liquid work as the fluidizing agents to fluidize the packed solids inside the fluidized bed. Compared with the traditional upward TPFB, the inverse TPFB has some advantages such as the lower energy cost.

For the bubble induced TPFB, the gas, which is introduced into the bed through the gas distributor, is usually in the form of small bubbles. It was found that small gas bubbles and the density difference between the solid phase and the liquid-gas mixture would result in the liquid recirculation, which causes the bed to expand in the inverse TPFB under the batch liquid mode [2][3]. In that case, the bubble flow behavior has become an important role in the design and operation of the inverse TPFB under the batch liquid mode since the bubble flow behavior will affect to the mass transfer and mixing in the TPFB. However, only a few literatures reported the relationship between the average bubble size, the inlet superficial gas velocity and the gas holdup, such as a correlation for an upward gas-liquid bubble column under the superficial gas velocities ranging from 0-12 cm/s [4]. Very few research works on the bubble behavior in the inverse TPFB were carried during the past decades.

For the inverse gas-liquid two-phase bubble column, Son et al. [5] studied the bubble behavior and properties in a gas-liquid countercurrent flow bubble column, used for wastewater treatment. Four pipes of 6.35 mm diameter with 28 holes were used as the gas distributor in this experimental study, and the gas distributor is evenly installed at the bottom of the column.

A correlation to calculate the bubble size based on the superficial liquid velocity and gas velocity was developed in their study. It was also found that the gas holdup under the batch liquid mode is smaller than the gas holdup under the continuous mode in a gas-liquid countercurrent bubble column.

Compared to the gas-liquid two-phase flow in a bubble column, less researchers reported studies on the bubble behaviors in inverse TPFB. Cho et al. [6] reported that the bubble size and bubble rising velocity will increase when increasing the gas velocity in an inverse TPFB under the continuous mode. Later, Son et al. [7] studied the bubble behaviors in an inverse TPFB under the continuous mode. The experimental study was conducted at $U_l=10$ mm/s - 50 mm/s, $U_g=0.5$ mm/s - 8 mm/s and $\rho_s=877.3$ kg/m³ - 966.6 kg/m³. A correlation for the bubble size and bubble rising velocity based on the drift flux model was developed. It was also found that the bubble size increases with the increase in the gas velocity, liquid viscosity or liquid velocity, but it will decrease when increasing the particle density. The bubble rising velocity was found to increase with an increase in the gas velocity or liquid viscosity. However, no studies have reported the average bubble size in the inverse TPFB under the batch liquid mode ($U_l=0$) due to the inadequate experiments and the limitation of the visualization techniques. The CFD method allows the model to include the effect of the bubble size, which can be used to further study the relationship between the bubble size and the inlet superficial gas velocity.

The numerical study for predicting hydrodynamics in TPFB has been conducted by a few researchers. Panneerselvam et al. [8] studied the hydrodynamics and flow pattern in an upward TPFB numerically under two different superficial gas velocities, $U_g = 0.2$ m/s and $U_g=0.4$ m/s. The mean bubble sizes used for the gas phase at each inlet superficial gas velocity are 13 mm and 2 mm, respectively, which was determined by comparing the gas holdup from the simulation results with that from the experimental data. Hamidipour et al. [9] conducted the same numerical study as Panneerselvam et al. [8] by using the three-fluid Eulerian-Eulerian model with the KTGP. The same bubble size was used in their study as well. Li and Zhong [10] carried out a numerical study in a TPFB based on the three-fluid Eulerian-Eulerian model. The performances of different drag models between each phase were compared. The range of the inlet superficial gas velocity in the study was from 0.036 m/s to 0.33 m/s, but only one mean bubble size of 0.003 m was used in the simulations at different inlet superficial gas velocities.

It is believed that the bubble size in a TPFB increases with the increase in the superficial gas velocity. [5,11,12]. However, most numerical studies on TPFBs used only one bubble size for the gas phase even under the different inlet superficial gas velocities. Thus, the objective of this study is to modify the CFD model for the simulation of the inverse TPFB under the batch liquid mode by adjusting the bubble size under different superficial gas velocities. Also, since the numerical studies on the bubble behavior in the inverse TPFB were conducted only for a very small operating range in previous studies, investigations in this work will be carried out for the three-

phases flows in an inverse TPFB under a wide range of operating conditions. In addition, a correlation to predict the bubble size under different inlet superficial gas velocities will be developed.

II. EXPERIMENTAL SETUP OF THE INVERSE THREE-PHASE FLUIDIZED BED

The proposed CFD model has been validated based on the experimental data by Sun [13]. The configuration of the inverse TPFB used by Sun [13] is shown in Fig. 1. The column is made of PVC with 0.153 m in diameter and 3 m in height. The ring shape porous quartz gas distributor with an 8.7 cm outer diameter and a 2.7 cm inner diameter, which can generate very small bubbles, is placed at the bottom of the column. The tap water, air and particles ($\rho_s=930$ kg/m³) are used as liquid, gas and solid phases in the experiment. The tap water and particles are injected into the column before the experiment starts, resulting in the floated particles at the top surface of the water because the particle density is lower than the density of water. During the experiment, only the gas is continuously introduced into the column through the gas distributor, and there is no outflow for particles and liquid. The gas phase is injected into the column as small bubbles from the bottom of the column through the gas distributor, and bubbles leaves the column through the top of the column. The superficial gas velocity at the inlet is from 0 mm/s to 60 mm/s. With an increase in the inlet superficial gas velocity, the coalescence of small bubbles can be observed. The experiment is carried out under ambient temperature and pressure.

In this study, the hydrodynamics in the inverse TPFB will be simulated under different inlet superficial gas velocities with its corresponding bubble size. Therefore, different bubble sizes will be used under different inlet superficial gas velocities. The summary of the operating conditions and properties of each phase are shown in Table I.

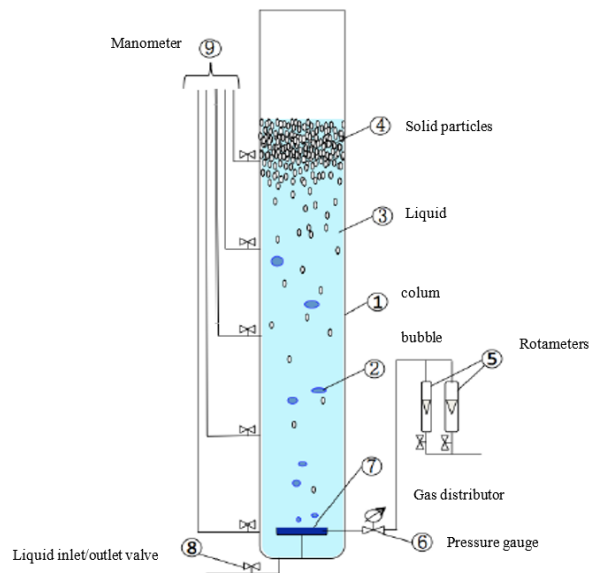


Figure 1. Configuration of the experimental setup of the inverse three-phase fluidized bed [13]

TABLE I. OPERATING CONDITIONS AND PHYSICAL PROPERTIES OF EACH PHASE

Sun [13]	Bubble column (m)	Diameter: 0.153
	U_i (mm/s)	Total height: 3
	U_g (mm/s)	0
	U_s (mm/s)	9,20,30,40,50,60
	Liquid phase density (kg/m ³)	998
	Liquid phase viscosity (kg/m ^s)	0.001003
	Gas phase density (kg/m ³)	1.225
	Gas phase viscosity (kg/m ^s)	1.798×10 ⁻⁵
	Particle diameter (mm)	3.5
	Particle density (kg/m ³)	930
	Solid phase loading	15%
	Pressure	Atmospheric pressure
	Temperature	Ambient temperature

III. GOVERNING EQUATIONS AND NUMERICAL MODELS

The CFD model used in this study to simulate the inverse gas-liquid-solid fluidized bed is based on the three-fluid Eulerian-Eulerian approach. Each phase is treated as interpenetrating continuum which is solved by governing equations. A turbulence model and kinetic theory of granular flow (KTGF) are used to close the governing equation. The liquid phase is set as the primary phase, and the gas and solid phases are the secondary phases in the simulation. The governing equations for each phase are shown as following.

Conservation equation of mass

$$\frac{\partial}{\partial t}(\alpha_p \rho_p) + \nabla(\alpha_p \rho_p \vec{v}_p) = 0 \quad (1)$$

where α , ρ , and \vec{v} are the volume fraction, density and velocity of each phase, the subscript of p can represent liquid, gas and solid phase, respectively. The sum of volume fraction for each phase should be equal to one.

$$\alpha_l + \alpha_g + \alpha_s = 1 \quad (2)$$

Conservation equation of momentum for the liquid phase

$$\frac{\partial}{\partial t}(\alpha_l \rho_l \vec{v}_l) + \nabla(\alpha_l \rho_l \vec{v}_l \vec{v}_l) = -\alpha_l \nabla p + \nabla \bar{\tau}_l + \alpha_l \rho_l \vec{g} + M_l \quad (3)$$

$$\bar{\tau}_l = \alpha_l \mu_l (\nabla \vec{v}_l + \nabla \vec{v}_l^T) - \alpha_l \frac{2}{3} \mu_l (\nabla \vec{v}_l) \bar{I} \quad (4)$$

Conservation equation of momentum for the gas phase

$$\frac{\partial}{\partial t}(\alpha_g \rho_g \vec{v}_g) + \nabla(\alpha_g \rho_g \vec{v}_g \vec{v}_g) = -\alpha_g \nabla p + \nabla \bar{\tau}_g + \alpha_g \rho_g \vec{g} + M_g \quad (5)$$

Conservation equation of momentum for the solid phase

$$\frac{\partial}{\partial t}(\alpha_s \rho_s \vec{v}_s) + \nabla(\alpha_s \rho_s \vec{v}_s \vec{v}_s) = -\alpha_s \nabla p + \nabla p_s + \nabla \bar{\tau}_s + \alpha_s \rho_s \vec{g} + M_s \quad (6)$$

$$\bar{\tau}_s = \alpha_s \mu_s (\nabla \vec{v}_s + \nabla \vec{v}_s^T) + \alpha_s (\lambda_s - \frac{2}{3} \mu_s) \nabla \vec{v}_s \bar{I} \quad (7)$$

where p_s and μ_s are solid phase viscosity and pressure which can be obtained by the KTGF, and $\bar{\tau}$ is the stress of each phase.

The momentum exchange term M_g , M_l and M_s and in governing equations will be closed by considering the interphase interaction forces among each phase including the drag force, lift force, turbulent dispersion force, virtual mass force etc. Only the drag force and virtual mass force will be considered in the present study since the other two forces are negligible. For the drag force between each two phases, the Schiller-Naumann drag model [14] is used.

In present study, the dispersed RNG k- ϵ turbulence model with scalable wall function is used for the liquid phase, since it has a better performance than the standard and realizable k- ϵ models and per-phase RNG k- ϵ model [9]. The turbulence in dispersed phases, which are the gas phase and the solid phase in present study, is derived from the time and length scales instead of transport equations [15]. To describe the solid phase motion, the KTGF is used to in the Eulerian-Eulerian approach to close the solid phase governing equations. The granular temperature is introduced in the KTGF, which is related to the particle random motion, and solid phase stress and pressure can be calculated by using the granular temperature.

Two-dimensional simulations of the three-phase flows are conducted in this study for an inverse TPFB under the batch liquid model. The inverse TPFB shown in Fig. 2 is simplified to a 2D planar computational domain, which is 0.152 m \times 3 m based on the dimensions of the inverse TPFB used in the experiment. A uniform distributed quad grid mesh is used. The grid is 43 \times 850 in the x and H directions. The schematic diagram of the computational domain, mesh, boundary conditions and initial conditions is shown in Fig. 2. The mesh is created by using the commercial software ICM 16.0.

The gas inlet is located at the bottom of the column, and the uniform velocity is used as the inlet boundary condition for the gas phase based on the experimental inlet superficial gas velocity. For the liquid and solid phases, the inlet velocity is zero for a batch liquid mode operation. The outflow is selected as outlet boundary condition for all three phases on the top of the column. The no-slip boundary condition is set for the liquid phase as the wall boundary condition, and the free-slip condition on the wall is used for both the gas bubbles and solid phase, So the specularly coefficient of the solid phase is set to zero which corresponds to the free-slip boundary condition. The particle-particle restitution coefficient is set as 0.95.

The particles have a mean diameter of 3.5 mm. For the gas bubble diameter, since the CFD model proposed in the previous study is modified in this study based on the bubble size, different bubble diameters from 3 mm to 5 mm are used for the gas phase, which depends on the inlet superficial gas velocity.

The initial conditions of the inverse TPFB under the batch liquid operating condition are shown in Fig. 2, which are different from the conventional or circulating fluidized beds. To mimic the experimental condition, the liquid phase is initially patched inside the column, and particles are patched at the top surface of the liquid phase because the density of the particles is less than the density of the liquid phase.

The simulation is conducted using the commercial software Fluent 16.0. The double precision segregated, transient, implicit formulation are used. The phase coupled SIMPLE algorithm is used for the pressure-velocity coupling. The second order upwind scheme is used to discretize the momentum equations while the first order upwind discretization method is used for all other convection terms. The convergence criterion is set as 0.0005 and the time step is set as 0.0001.

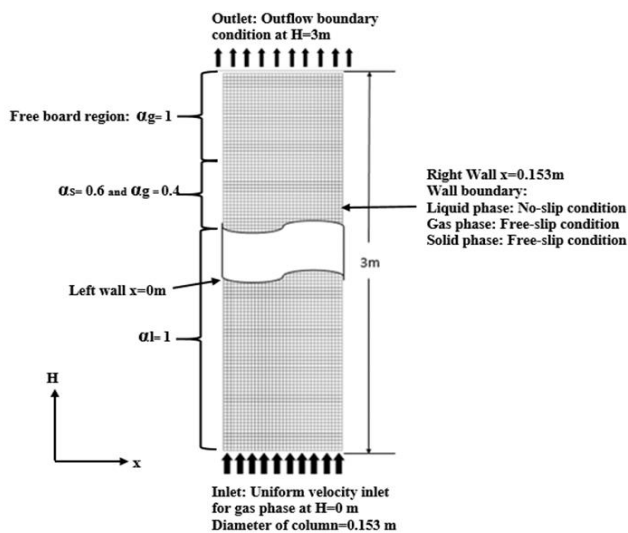


Figure 2. Computational domain of the inverse three-phase fluidized bed under the batch liquid mode

TABLE II. GRID INDEPENDENT TEST

Mesh	Coarse	Medium	Fine
Nodes	22750	37400	286680
Average gas holdup	0.0856	0.0819	0.0816
Difference (%)		4.5%	0.4%

According to the grid independent test, the difference of average gas holdup between the medium mesh and fine mesh is less than 1%. Therefore, the medium size mesh is selected in this study for further simulations.

IV. RESULT AND DISCUSSION

The bubble size is found to have a significant effect on the average gas holdup in the inverse TPFB under the batch liquid mode. Therefore, the three-phase Eulerian-Eulerian CFD model for the inverse TPFB is modified by adjusting the

average bubble size. The effects on the bubble behavior and hydrodynamics in the inverse TPFB are investigated by using the modified CFD model.

A. Bubble size adjustment under different U_g

A fixed mean bubble size of 2 mm was used for the simulations under different inlet superficial gas velocities firstly because the gas bubbles generated from the gas distributor have an average size of 2 mm. According to the experimental study by Sun et al. [13], the gas bubbles inside the inverses TPFB tend to increase from 2 mm to 6 mm with the increase in the inlet superficial gas velocity from 10 mm/s to 60 mm/s. Thus, the constant value (2 mm) of the mean bubble size in the original three-phase CFD model is adjusted with the bubble size obtained from the experiment, which is from 3 mm to 5 mm based on different U_g from 10 mm/s to 60 mm/s. In addition, the mean bubble sizes used in the modified CFD model are given in Table III, which are obtained by a trial-and-error method. Fig. 3 shows the comparison of the predicted average gas holdups under different U_g using the original CFD model and the modified CFD model with the experimental data. It is clear that the gas holdup from the modified CFD model has a better agreement with the experimental data compared to the gas holdup from the original CFD model. Fig. 3 also shows under the same U_g , the average gas holdup predicted by the original CFD model with a constant 2 mm bubble diameter is higher than that from the modified CFD model with bubble size adjustment. The reason could be that the rising velocity of large bubbles is higher than the small bubbles, so the small bubbles will have a longer residence time in the column, which can lead to a higher gas holdup for small bubbles. In addition, it is observed based on the results from the modified CFD model and the experimental data that the increase of the gas holdup with U_g is almost linear when U_g is from 10-30 mm/s, but the increase of the gas holdup is lower when U_g is higher than 40 mm/s. The reason lies in that at a lower inlet superficial gas velocity, the small bubbles have a lower bubble coalescence rate, which lead to the uniform bubble size distribution. Therefore, the gas holdup is increased linearly with the increase in the inlet superficial gas velocity [16]. However, the bubble coalescence rate will increase under a higher inlet superficial gas velocity, so the small bubbles start to coalesce and formulate large bubbles, which leads to a higher rising bubble velocity and less residence time in column. Thus, the increase in the gas holdup with the increase in the inlet superficial gas velocity is lower at a higher inlet superficial gas velocity, which is consistent with the experimental results from Jin et al. [17]. This is also the reason that the difference between the results from the original CFD model and modified CFD model becomes larger when the inlet superficial gas velocity is higher as shown in Fig. 3 since a small mean bubble size is used for all inlet superficial gas velocities in the original CFD model. In addition, the increase in the mean bubble size becomes smaller when U_g is above 40 mm/s when the solids loading is around 15% in the inverse TPFB. The reason is that the intensive interactions between the gas and particles break the large bubbles into small bubbles, so that the increase in the mean bubble size is lower at a higher inlet superficial gas velocity.

TABLE III. BUBBLE SIZES UNDER THE DIFFERENT INLET SUPERFICIAL GAS VELOCITIES

Superficial gas velocity (mm/s)	Mean bubble size used in the modified CFD model (mm)	Mean bubble size used in the original CFD model (mm)
60	5	2
50	4.7	2
40	4.5	2
30	4	2
20	3.5	2
9	3	2

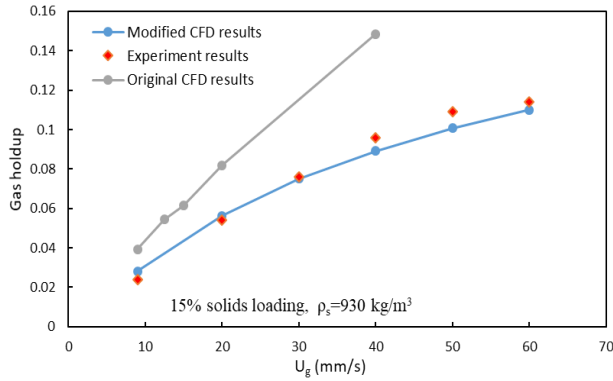


Figure 3. Comparison of the average gas holdup between the numerical results and experimental data under the different inlet superficial gas velocities at 15% solids loading and $\rho_s=930 \text{ kg/m}^3$

Fig. 4(a) shows comparison of axial distributions of the gas holdup from the original CFD model and the modified CFD model under $U_g=20 \text{ mm/s}$. Both the original model and the modified model give a uniform axial distribution of the gas holdup in the inverse TPFB, which is consistent with the experimental data. However, by using the original CFD model with the constant 2 mm bubble size, the axial gas holdup is around 0.08, which is obviously higher than the gas holdup from the experiential data. The axial gas holdup from the modified CFD model with a 3.5 mm bubble size for $U_g = 20 \text{ mm/s}$ shows a better agreement with the experimental data. Similarly, the results from the modified CFD model with the bubble size of 4.5 mm for $U_g=40 \text{ mm/s}$ has a better agreement with the experimental data than the original CFD model as shown in Fig. 4(b).

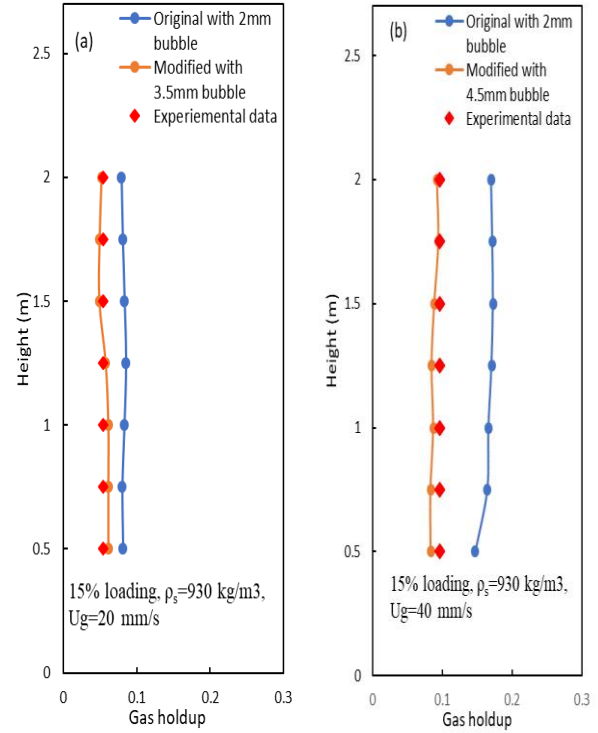


Figure 4. Comparison of the axial gas holdups from the CFD model with 2mm bubble size and modified CFD model with the experiment data at $\rho_s=930 \text{ kg/m}^3$ and 15% solids loading

The time-averaged radial profiles of the gas holdup under three different superficial gas velocities at $H=1.5 \text{ m}$ using the modified CFD model are shown in Fig. 5. The x-axis is the radial position of the column, which is from the left wall ($x=0 \text{ m}$) to the right wall ($x=0.153 \text{ m}$), and the center of the column is at $x=0.0765 \text{ m}$. The radial profiles of the gas holdup are almost flat for $U_g=20 \text{ mm/s}$. When increasing the inlet superficial gas velocity, it is clear that the radial profiles of the gas holdup become less uniform, where the gas holdup is higher at the center region and lower at the near wall region. This non-uniform radial profile is consistent with the most commonly seen experimental results of the gas-liquid two-phase or gas-liquid-solid three-phase bubble column [17–19]. The reason is that the higher inlet superficial gas velocity results in a higher bubble coalescence rates, which lead to the formation of the large bubbles in the column, and large bubbles will stay at the center region of the column. In addition, the small bubbles tend to move toward the wall region due to the wall effect. Thus, large bubbles are dominant at the center region and result in a higher gas holdup at the center region of the column, which leads to a non-uniform profile of the gas holdup in the radial direction.

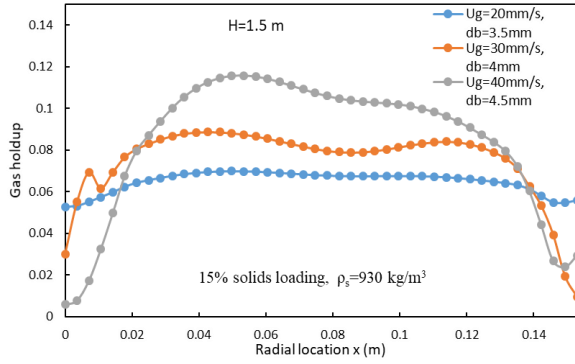


Figure 5. Time-averaged radial gas holdups under different superficial gas velocities from the modified CFD model

B. Mean bubble size correlation

A correlation between the mean bubble size and the average gas holdup under different inlet superficial gas velocities in the inverse TPFB has been proposed in this study. Many factors affect the bubble behavior in the inverse TPFB, such as the inlet superficial gas velocity, the gas holdup, the liquid density, the liquid viscosity and the particle density. As shown in Fig. 3., the mean bubble size is related to the superficial gas velocity and the average gas holdup. The properties of the liquid and the solid phases can also influence the bubble size in an inverse TPFB since they affect the velocity field and the turbulence viscosity. Based on the CFD results and the literature reviews, the bubble size in the inverse TPFB is assumed to be a function of liquid properties, solid density, gas holdup, inlet superficial gas velocity, which is shown as following

$$d_b = f(\rho_l, \rho_s, U_g, \mu_l, \epsilon_g) \quad (8)$$

So the form of the correlation for the mean bubble size can to be written as following

$$d_b = K U_g^a \epsilon_g^b \left(\frac{\rho_l}{\rho_s}\right)^c \quad (9)$$

where $K=0.0112$, $a=0.175$, $b=0.15$ and $c=0.12$ which are determined using Matlab based on CFD results. Therefore,

$$d_b = 0.0112 U_g^{0.175} \epsilon_g^{0.15} \left(\frac{\rho_l}{\rho_s}\right)^{0.12} \quad (10)$$

The experimental studies by Sun et al. [13] were carried out under the inlet superficial gas velocities from 10 to 60 mm/s, the corresponding average gas holdup in the inverse TPFB under the batch liquid mode increases from 0.03 to 0.12 with the increase in the U_g and the bubble size is from 2mm to 6mm. The predicted mean bubble size using the correlation is from 3mm to 5mm for the inlet superficial gas velocity from 10 to 60mm/s. Therefore, the correlation gives a good agreement with the experimental data. Thus, the correlation can be used to approximately estimate the mean bubble size when simulating the flow in the inverse TPFB under the batch liquid mode.

C. Conclusion

In the present study, a modified CFD model for the simulation of an inverse TPFB under the batch mode has been proposed based on the bubble size adjustment. The comparison between the results from the original CFD model with 2mm

bubble size and the modified CFD model indicates that the modified CFD model gives a better agreement with the experimental data than the original CFD model. Large size bubbles will result in a lower gas holdup under the same inlet superficial gas velocity. In addition, with the increase in the mean bubble size and superficial gas velocity, the radial profile of the gas holdup will be less uniform.

A correlation to predict the bubble size is proposed, and it has been validated as a reliable tool to approximately predict the average bubble size or gas holdup in the inverse three-phase fluidized bed under the batch liquid mode. The proposed correlation includes the density ratio of the liquid and the particle, which accounts for the influence of the fluidizing medium on the particle motion, and the parameter K may vary under the different properties of the liquid and the solids phases. Besides, the bubble size is influenced by the type of the gas distributor used at a low inlet superficial gas velocity, which is not taken into account in this study due to inadequate experimental data. Therefore, the correlation and K value can be further modified based on the fluidizing agents and gas distributors. The future work will focus on the modification of the K value, and the proposed correlation can be further modified when more experiments are carried out in the inverse TPFB under the batch liquid mode.

REFERENCES

- [1] K. Muroyama and L. -S Fan, "Fundamentals of gas-liquid-solid fluidization," *AIChE J.*, vol. 31, no. 1, pp. 1–34, 1985.
- [2] T. Renganathan and K. Krishnaiah, "Prediction of Minimum Fluidization Velocity in Two and Three Phase Inverse Fluidized Beds," *Can. J. Chem. Eng.*, vol. 81, no. 3–4, pp. 853–860, May 2008.
- [3] P. Buffière and R. Moletta, "Some hydrodynamic characteristics of inverse three phase fluidized-bed reactors," *Chem. Eng. Sci.*, vol. 54, no. 9, pp. 1233–1242, 1999.
- [4] M. Jamialahmadi and H. Muller-Steinhagen, "Effect of Superficial Gas Velocity on Bubble Size, Terminal Bubble Rise Velocity and Gas Hold-up in Bubble Columns," *Dev. Chem. Eng. Miner. Process.*, vol. 1, no. 1, pp. 16–31, 1993.
- [5] S. M. Son, P. S. Song, C. G. Lee, S. H. Kang, Y. Kang, and K. Kusakabe, "Bubbling behavior in gas-liquid countercurrent bubble column bioreactors," *J. Chem. Eng. Japan*, vol. 37, no. 8 SPEC. ISS., pp. 990–998, 2004.
- [6] Y. J. Cho, H. Y. Park, S. W. Kim, Y. Kang, and S. D. Kim, "Heat transfer and hydrodynamics in two- and three-phase inverse fluidized beds," *Ind. Eng. Chem. Res.*, vol. 41, no. 8, pp. 2058–2063, Apr. 2002.
- [7] K. Il Lee, S. Mo Son, U. Yeong Kim, Y. Kang, S. Hwan Kang, S. Done Kim, J. Keun Lee, Y. Chil Seo, and W. Hyun Kim, "Particle dispersion in viscous three-phase inverse fluidized beds," *Chem. Eng. Sci.*, vol. 62, no. 24, pp. 7060–7067, Dec. 2007.
- [8] R. Panneerselvam, S. Savithri, and G. D. Surender, "CFD simulation of hydrodynamics of gas-liquid-solid fluidised bed reactor," *Chem. Eng. Sci.*, vol. 64, no. 6, pp. 1119–1135, 2009.
- [9] M. Hamidipour, J. Chen, and F. Larachi, "CFD study on hydrodynamics in three-phase fluidized beds — Application of turbulence models and experimental validation," *Chem. Eng. Sci.*, vol. 78, pp. 167–180, 2012.
- [10] W. Li and W. Zhong, "CFD simulation of hydrodynamics of gas-liquid-solid three-phase bubble column," *Powder Technol.*, vol. 286, pp. 766–788, 2015.
- [11] S. M. Son, S. H. Kang, U. Y. Kim, Y. Kang, and S. D. Kim, "Bubble properties in three-phase inverse fluidized beds with viscous liquid medium," *Chem. Eng. Process. Process Intensif.*, vol. 46, no. 8, pp. 736–741, Aug. 2007.

- [12] A. A. Kulkarni and J. B. Joshi, "Bubble formation and bubble rise velocity in gas-liquid systems: A review," *Ind. Eng. Chem. Res.*, vol. 44, no. 16, pp. 5873–5931, Aug. 2005.
- [13] X. Sun, "Bubble induced Inverse Gas-liquid-solid Fluidized bed," University of Western Ontario, 2017.
- [14] L. Schiller and A. Naumann, "A drag coefficient correlation," *Z. Ver. Deutsch. Ing.*, vol. 77, pp. 318–320, 1935.
- [15] Ansys. Inc, "Fluent 16.0 User's Guide." 2014.
- [16] K. Kawagoe, T. Nakado, and T. Otake, "Flow pattern and gas hold up conditions in gas sparged contactors," *Int. Chem. Engng*, vol. 16, no. 1, p. 176, 1976.
- [17] H. Jin, Y. Qin, S. Yang, G. He, and Z. Guo, "Radial profiles of gas bubble behavior in a gas-liquid bubble column reactor under elevated pressures," *Chem. Eng. Technol.*, vol. 36, no. 10, pp. 1721–1728, 2013.
- [18] Y. H. Yu and S. D. Kim, "Bubble characteristics in the radial direction of three-phase fluidized beds," *AIChE J.*, vol. 34, no. 12, pp. 2069–2072, 1988.
- [19] S. Rabha, M. Schubert, and U. Hampel, "Intrinsic flow behavior in a slurry bubble column: A study on the effect of particle size," *Chem. Eng. Sci.*, vol. 93, pp. 401–411, 2013.

Non-Newtonian Flows

STABILITY ANALYSIS OF VISCOPLASTIC FLUIDS WITH WALL SLIP BOUNDARY CONDITIONS

Seyed Mohammad Taghavi
Département de Génie Chimique
Université Laval
Quebec, Canada

Seyed-Mohammad.Taghavi@gch.ulaval.ca

Hossein Rahmani
Département de Génie Chimique
Université Laval
Quebec, Canada

hossein.rahmani.1@ulaval.ca

The effects of wall slip boundary conditions, which frequently occur in non-Newtonian fluid flows, are investigated on the stability of the plane Poiseuille flow of Bingham fluids. To create both symmetric and asymmetric slip cases, different values for the wall slip parameters at the upper and lower walls are considered. To determine the critical Reynolds number as a function of the Bingham number and the wall slip parameters, a two-dimensional linear temporal stability analysis is developed. Neglecting the nonlinear terms in the perturbation quantities, an eigenvalue problem is found, which is subsequently solved via numerical methods. The results are delivered versus a number of dimensionless groups including the Reynolds number, the Bingham number, and the wall slip parameters. Based on the results obtained in this work, increasing the wall slip parameters is found to have a stabilizing effect on the plane Poiseuille flow of Bingham fluids.

NUMERICAL SIMULATION OF THE FORCED OSCILLATIONS OF A WIRE IN NEWTONIAN AND SHEAR-THINNING FLUIDS

Cameron C. Hopkins and John R. de Bruyn
Department of Physics and Astronomy
University of Western Ontario
London, Ontario Canada
Email: debruyne@uwo.ca

ABSTRACT

Forced oscillations of a wire vibrating in Newtonian and shear-thinning fluids described by the Carreau model are studied numerically. Two-dimensional simulations were performed using COMSOL Multiphysics software, a commercial finite-element modelling software package. When subjected to a sinusoidal driving force, the wire exhibits resonant behaviour that depends on the viscosity of the surrounding fluid. The simulations of the wire vibrating in a Newtonian fluid were extremely well described by the theory developed by Retsina et al. [Appl. Sci. Res., **43**, 127-158 (1986); Appl. Sci. Res., **43**, 325-346 (1987)]. Our simulations of a wire vibrating in a Carreau fluid also revealed resonant behaviour, but the shear rate and viscosity in the fluid varied significantly in both space and time. The behaviour of a wire vibrating in a Carreau fluid can be described by the Newtonian theory if the constant viscosity in that theory is set equal to the non-Newtonian fluid viscosity averaged spatially around the circumference of the wire and temporally over one period of oscillation.

Effect of Flow and Elasticity on Nematic Liquid Crystal Lubricants

Arash Nikzad

Department of Mechanical Engineering, University of
British Columbia
Vancouver, Canada
Arash.nikzad@mech.ubc.ca

Dana Grecov

Department of Mechanical Engineering, University of
British Columbia
Vancouver, Canada
Dgrecov@mech.ubc.ca

ABSTRACT

Liquid crystals (LCs) are anisotropic materials with properties of both conventional liquids and solid crystals. The ability of LCs to form ordered boundary layers with good load-carrying capacity, and to lower the friction coefficients, wear rates and contact temperatures of sliding surfaces has been demonstrated [1][2]. The efficiency and durability of journal bearings depend on the lubricant performance. Therefore, a suitable lubricant to reduce the frictional force between the surfaces in mutual contact is necessary. The objective of this study is to analyze the effect of the elasticity and the flow characteristics on the lubricant performance and the microstructure of the LCs using modeling and numerical simulations. The studies have been conducted using a rod-like LC between eccentric cylinders as a preliminary geometry for journal bearings [1]. The flow of LCs involves the interaction of microstructures, which evolve in time and space, with macro-scale flow attributes which makes the flow of LCs much more complex than a simple Newtonian fluid flow. In addition, the flow between eccentric cylinders is very complex as it is a combination of shear, rotational and extensional flows.

A model based on a tensor model (Landau-de Gennes) has been used in this study. In the Landau-de Gennes theory, the flow of LCs is predicted by the evolution of a traceless and symmetric second order parameter tensor (Q) in time, where Q is a function of flow contribution, short-range elasticity, and long-range elasticity [3], [4]. Continuity equation and the evolution equation coupled with modified Navier-Stokes equations for flow of nematic LCs have been solved using a built-in fully coupled solver in COMSOL. Laminar flow module (SPF) and PDE general module (G) in COMSOL Multiphysics for two dimensions have been applied. To solve these set of equations, Multifrontal Massive Parallel sparse direct Solver (MUMPS), which is powerful in solving large sparse matrices, with adaptive relaxation factor, and Backward Differentiation Formula (BDF) for time stepping have been employed. Moreover, the acceptable infinity-norm of error has been set to 10^{-8} as a convergence criterion in this simulation study. Mesh independency and convergence of the final solution study for wall shear stress, first normal difference, and pressure on the inner cylinder, have been considered. The total number of 48000 elements with the average element quality of 0.98 have been employed in this simulation. Regarding the boundary conditions, a constant velocity on the inner cylinder and a fixed outer cylinder along with the boundary condition for the tensor order parameter corresponding to a tangential orientation of molecules with respect to the wall boundaries, have been set in this simulation.

The results have been presented in terms of two dimensionless numbers, the Reynolds (Re) number and the Deborah (De) number. Numerical results have been shown that at constant Re number, the maximum value of pressure distribution increased with the De number. The calculated friction on the inner cylinder has been indicated to be approximately constant for different De numbers. However, the normal force on the inner cylinder increased for higher De number. Furthermore, the effect of liquid crystalline microstructure on the flow properties provides a better understanding of the lubrication performance of LCs as a lubricant. The ordered layer in the vicinity of the inner cylinder surface which may reduce the wear and friction for rubbing surfaces [1], has been observed in this study. To investigate the microstructure of the LC between eccentric cylinders, the ellipsoidal structure has been presented using MATLAB. Groups of defects have been also captured inside the domain.

Reference:

- [1] N. Noroozi and D. Grecov, "Numerical simulation of flow and structure in nematic liquid crystalline materials between eccentric cylinders," *J. Nonnewton. Fluid Mech.*, vol. 208–209, pp. 1–17, Jun. 2014.
- [2] G. Biresaw, "Tribology and the liquid-crystalline state," vol. 441. Washington, DC: American Chemical Society, 1990.
- [3] D. Grecov and A. D. Rey, "Transient rheology of discotic mesophases," *Rheol. Acta*, vol. 42, no. 6, pp. 590–604, Nov. 2003.
- [4] A. Nikzad and D. Grecov, "Numerical Simulations of Nematic Liquid Crystals Flows between Eccentric Cylinders," *Proc. 5th Int. Conf. Fluid Flow, Heat Mass Transf.*, no. 183, pp. 1–5, 2018.

Analyzing the Effect of Rheology of Non-Newtonian fluids in Gas Dispersion with a Coaxial Mixer through Tomography and CFD

Maryam Jamshidzadeh (*Author*)
Dept. of Chemical Engineering
Ryerson University
Toronto, Canada
Maryam.jamshidzadeh@ryerson.ca

Dr. Farhad Ein-Mozaffari (*Author*)
Dept. of Chemical Engineering
Ryerson University
Toronto, Canada
fmozaffa@ryerson.ca

Dr. Ali Lohi (*Author*)
Dept. of Chemical Engineering
Ryerson University
Toronto, Canada
Maryam.jamshidzadeh@ryerson.ca

ABSTRACT

The gas dispersion in non-Newtonian fluids play a significant role in pharmaceutical, wastewater treatment, and biotechnology. In this study, the effect of the rheological behavior of a non-Newtonian fluid on the gas dispersion in a coaxial mixer comprised of two central impellers and a close clearance impeller was investigated. The central impellers were pitched blade turbines and the close clearance impeller was an anchor impeller. The non-Newtonian fluid employed in this study was the CMC solution, which is a shear-thinning fluid. The rheological parameters were measured using a research grade rheometer. The power consumption of the impellers was measured through torque measurements and the gas hold-up was quantified using electrical resistance tomography, which is a non-intrusive flow visualization technique. We also analyzed the effects of the speed ratio of the impellers and the pumping direction of the central impellers on the performance of the coaxial mixer. To determine the interactions between the design parameters and operating conditions, the response surface methodology was utilized. A computational fluid dynamics (CFD) model was also developed for the 3D simulation of the gas dispersion in the non-Newtonian fluid by the coaxial mixer. The sliding mesh technique was used to model the rotation of the impellers. The CFD model was validated using the experimental results of the power consumption and the gas hold-up. The results showed that an increase in the apparent viscosity of the non-Newtonian fluid resulted in a decrease in the gas hold-up. However, by increasing the speed ratio, the gas hold-up was enhanced.

Particulate Flows

Revisting solid-liquid mixing through the development of an open-source CFD-DEM model

Bruno Blais,
Dept. of Chemical Engineering
Polytechnique Montréal
Montréal (QC), Canada

Bruno.Blais@polymtl.ca

Solid-liquid mixing is the unit operation in which particles are suspended in an agitated vessel. Despite its apparent simplicity and its strong industrial relevance, it remains a challenging unit operation for many elements remain unclear. Indeed, for most industrial configurations, it is hard to predict the power consumption and the impeller speed required to suspend the particle to the desired level. Thus, the design of agitated vessel remains very uncertain except for the most basic impeller geometry and particle size distributions.

To shed light on these issues related to solid-liquid mixing, numerical and experimental work is essential. Solid-liquid mixing is complex to model since all types of granular flow regimes (dilute, dense and quasi-static) occur within the stirred-tank. Due to its accurate modeling of the solid phase under all regimes and its relatively low computational cost, unresolved CFD-DEM, which combine traditional computational fluid dynamics for the fluid with the discrete element method (DEM) for the solid, is highly appropriate to investigate mixing operations.

In this work, we discuss the development, verification and validation of an open-source unresolved CFD-DEM based on the CFDEM framework. This models couples CFD-DEM with a semi-implicit immersed boundary technique to simulate rotating turbines in order to study solid-liquid mixing in the laminar and early turbulent regime in classical configurations. We demonstrate throughout extensive experimental validation that unresolved CFD-DEM can predict the degree of suspension and the flow patterns within stirred tanks with a high degree of accuracy. Furthermore, we demonstrate that creative use of the extensive data generated by the particle trajectories allow us to gain insight into the efficiency of the solid-liquid mixing operation. We conclude by discussing some the challenges faced by this type of approach in terms of accuracy, computational costs and modeling hypotheses and some of the future work of our group.

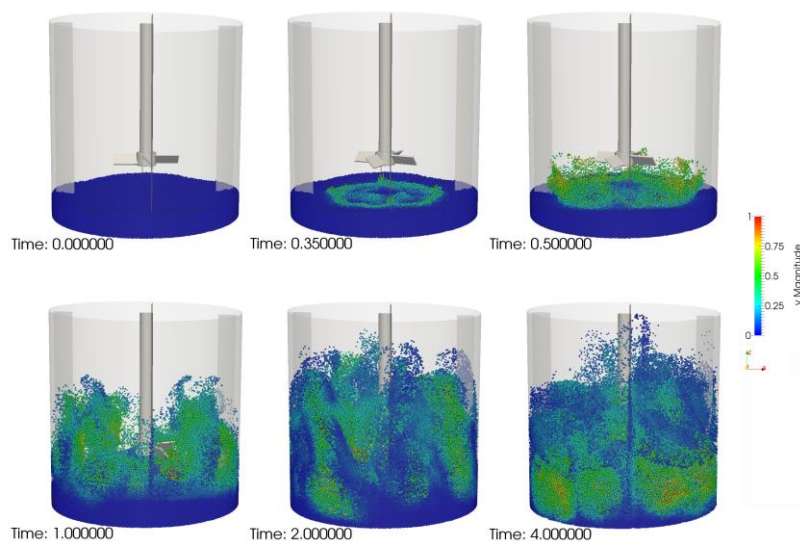


Figure 1: Evolution of the particle distribution in a stirred-tank operated in the early turbulent regime as predicted by CFD-DEM

DEVELOPMENT OF A CFD-DEM MODEL IN NON INERTIAL FRAME FOR SOLID-LIQUID MIXING APPLICATIONS

Bastien Delacroix, Bruno Blais, Louis Fradette and
François Bertrand
Dept. of chemical engineering
Polytechnique Montréal
Montréal (QC), Canada

ABSTRACT

Solid-liquid mixing is a common process in the industry. Indeed, we find such solid-liquid operations in multiple and various sectors such as cosmetics, pharmaceutical or food processing industries. Despite its omnipresence and apparent simplicity, this process is still poorly understood, and the design of these operations still mostly relies on correlations. Important parameters that characterize solid-liquid mixing, like the just-suspended speed (N_{js}) and the homogeneity of the suspension, are difficult to quantitatively predict. Nowadays, industries use complicated setups with new impeller geometries or stirred tank configurations, but it is unclear if these are optimal. Consequently, there is a need for more studies on solid-liquid mixing and, more particularly, for new methods to better understand solid-liquid dynamics.

The goal of this work is to develop a numerical model adapted to solid-liquid applications. The model is based on an unresolved CFD-DEM that combines the Discrete Element Method (DEM) for solid particle dynamics and Computational Fluid Dynamics (CFD) techniques for the fluid phase [1]. One of the problems in CFD-DEM simulation is the modeling of complex rotating geometries. The solution developed in this work relies on the use of a rotating frame linked to the impeller. This idea is really innovative because, to our knowledge, CFD-DEM methods have never been applied in the context of non-inertial frames.

Firstly, we introduce the equations of motion for the liquid and the solid phases in a non-inertial frame. Then, using simple numerical experiments, we validate our DEM model in a rotating frame. This includes investigating the stability of the numerical integration of the DEM underlying equations in a rotating frame, which is not simple because of the addition of a velocity-dependent force related to the Coriolis effect. Once these verifications are done, we describe our coupling strategy for the fluid and the solid phases. The interest of the proposed model is that it is adapted for all types of geometries, regardless of their complexities. Then, the full CFD-DEM model is applied to the study of solid-liquid mixing with a double helical ribbon (DHR), which is a priori well adapted for viscous liquids in the laminar regime. The results from our CFD-DEM model are validated against experimental studies previously carried in our lab [2]. Finally, the model is used to study different factors that influence the quality of mixing in the case of the DHR.

[1] B. Blais, M. Lassaigne, C. Goniva, L. Fradette, and F. Bertrand, "Development of an unresolved CFD-DEM model for the flow of viscous suspensions and its application to solid-liquid mixing," *Journal of Computational Physics*, vol. 318, pp. 201-221, 2016/08/01/ 2016

[2] O. Bertrand, B. Blais, F. Bertrand, and L. Fradette, "Complementary methods for the determination of the just-suspended speed and suspension state in a viscous solid-liquid mixing system," *Chemical Engineering Research and Design*, vol. 136, pp. 32-40, 2018

Variational Data Assimilation Using a Polydisperse Gaussian Model for Short Range Atmospheric Dispersion of Radionuclides

François Forgues, James G. McDonald
Department of Mechanical Engineering
University of Ottawa
Ottawa, Ontario, Canada K1N 6N5
fforg089@uottawa.ca

Volodymyr Korolevych, Luke Lebel, Lucian Ivan
Nuclear Engineering & Systems Analysis Division
Canadian Nuclear Laboratories
Chalk River, Ontario, Canada, K0J 1J0
lucian.ivan@cnl.ca

ABSTRACT

Data assimilation can enhance the prediction accuracy of atmospheric transport and dispersion models used in tracking atmospheric release of radioactive pollution to improve the real-time dose prediction. Data assimilation with traditional atmospheric dispersion models such as Gaussian and puff models have been previously considered. However, there are limitations in providing accurate predictions and reliable estimations in the near range of the release source due to significant modelling errors. Alternatively, the use of traditional, physics-based, Eulerian methods for radioactive-pollution data assimilation would be challenging due to modelling artifacts in describing the transition from granular to dilute particle flow.

Recently, a new Eulerian model has been proposed to treat particle-laden flows and has the potential to model transitional flow regimes at a reduced computational cost relative to Lagrangian particle methods. It takes its roots from the kinetic theory of gases, using a probabilistic treatment for particle behaviour, and it extends the ten-moment Gaussian model for viscous gases to the treatment of a dilute particle phase with an arbitrary number of internal variables. This work considers the application of the model to atmospheric dispersion of particulates, in which the only internal variable chosen for the particle phase is the particle diameter and the particles interact with the background flow, i.e. carrier phase, through aerodynamic forces and are subject to the gravitational field. In this case, the new polydisperse Gaussian model (PGM) comprises 15 equations [1].

The practical application considered to demonstrate the capabilities of the computational framework is the improvement on the prediction accuracy of the particle-laden flow characteristic to a radiological dispersal device (RDD) [2] by assimilating ground measurements collected by deposition witness plates. More specifically, development and testing of the data assimilation methodology for radionuclides in conjunction with PGM is the objective of the current work. The model parameters are computed so as to minimize discrepancies between stationary monitoring observations and model outputs. The PGM parameters are determined with data from certain measurements whereas additional data collected is used to validate the predictions.

This talk will provide details about the devised algorithm to perform variational data assimilation. Additionally, the detection equipment, the process of data acquisition and the collected measurements in the 2012 DRDC Suffield full-scale RDD experiments will be presented. Results to illustrate how the data-enhanced dispersion model performs in the short range will be shown.

References:

- [1] F. Forgues, L. Ivan, A. Trottier, J.G. McDonald, "A Gaussian Method for Polydisperse Multiphase Flow Modelling" *Journal of Computational Physics*, submitted, 2019
- [2] Erhardt, L., Lebel, L., Korpach, E., Berg, R., Inrig, E., Watson, I., Liu, C., Gilhuly, C., Quayle, D., 2016. "Deposition measurements from the full-scale radiological dispersal device field trials", *Health Phys.* 110 (5), 442–457.

COUPLED CFD-DEM MODEL TO SIMULATE TWO-PARTICLE SETTLEMENT IN A NEWTONIAN FLUID: A GRID COMPARISON

Fatemeh Razavi, Alexandra Komrakova, Carlos F. Lange

Mechanical Engineering

University of Alberta

Edmonton, Alberta, Canada

razavi1@ualberta.ca, komrakov@ualberta.ca, carlos.lange@ualberta.ca

ABSTRACT

This research aims to investigate the mesh required to model the particulate-flow accurately and to capture the physics properly. Coupled Computational Fluid Dynamics and Discrete Element Method (CFD-DEM) is used to simulate the particulate-flow. DEM simulations are capable of tracking individual particles' trajectories, considering various forces on the particles caused by interaction with the fluid, with other particles, and with the walls. STAR-CCM+ from Siemens PLM is applied to model the particulate flow. In this study, the problem of settlement of two particles in a Newtonian fluid is used as a benchmark problem to test the CFD-DEM model setup in STAR-CCM+.

Having two particles settling in a fluid, the wake vortexes behind the leading particle causes acceleration of the trailing particle. The wake influences the region between two interacting particles. The acceleration of a particle due to wake attraction is an important classical problem. It reveals the transient nature of the particulate flow, and it explains the tendency of particles to agglomerate in settling flows.

CFD-DEM coupling (data transferring) can be of two types called unresolved and resolved. This division is based on the scale of the particles relative to the mesh size of the fluid domain. If particle sizes are smaller than the computational grid, the particles are assumed not to entirely fill a cell, and unresolved CFD-DEM approach is applicable. If particle sizes are larger than the CFD grid, resolved CFD-DEM is applied. Accordingly, five grid types will be examined, and CFD-DEM model will be tested accordingly:

- 1) Unresolved structured mesh with hexahedral cell type (static mesh)
- 2) Resolved structured mesh with hexahedral cell type (static mesh)
- 3) Unresolved unstructured mesh with polyhedral cell type (static mesh)
- 4) Resolved unstructured mesh with polyhedral cell type (static mesh)
- 5) Chimera grid also called overset mesh (dynamic mesh).

Wake period, time-dependent distance between two particles, the settling velocity of the particles and the drag force on the particles obtained by simulations will be compared to the values available in the literature obtained by experiments or direct numerical simulation. Following having a verified CFD-DEM model and selecting the proper mesh, this model will be applied to study the particulate flow in sand filters applied in oil wells. The focus of this paper is mainly on the grid comparison and benchmarking the created CFD-DEM model. Figure 1 shows the results obtained from the preliminary analysis of unresolved hexahedral mesh. Wake vortexes behind the particles are presented as well as the fluid velocity vectors around the particles.

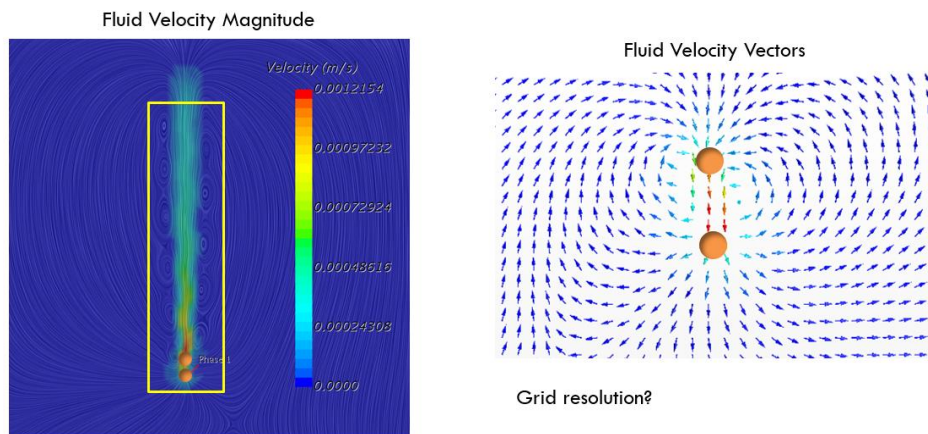


Figure 1: Wake vortexes as the result of fluid-particle interaction (unresolved hexahedral mesh)

Numerical Solution of Multiphase Flow Using New High-Order Moment-Based Eulerian Methods

Andrée-Anne Dion-Dallaire, François Forgues,
 James G. McDonald
 Department of Mechanical Engineering
 University of Ottawa
 Ottawa, Ontario, Canada, K1N 6N5
 adion021@uottawa.ca

Lucian Ivan
 Computational Techniques
 Canadian Nuclear Laboratories
 Chalk River, Ontario, Canada, K0J 1J0

Abstract— Modelling multiphase flow, more specifically particle-laden flow, poses multiple challenges. These difficulties are heightened when the particles are differentiated by a set of “internal” variables, such as size or temperature. Traditional treatments of such flows can be classified in two main categories, *i.e.* Lagrangian particle methods and Eulerian methods. The former are highly accurate but can lead to extremely expensive computations and can be harder to load balance on parallel machines, whereas the latter offer cheaper computations but often introduce modelling artifacts and can become more complicated and expensive when a large number of internal variables are treated. Recently, we have proposed a new model to treat such situations. It takes its roots from the kinetic theory of gases, using a probabilistic treatment for particle behaviour, and it extends the ten-moment Gaussian model for viscous gases to the treatment of a dilute particle phase with an arbitrary number of internal variables. This paper considers the application of the model to atmospheric dispersion of particulates, in which the only internal variable chosen for the particle phase is the particle diameter and the particles interact with the carrier phase through aerodynamic forces and are subject to the gravitational field. In this case, the new polydisperse Gaussian model (PGM) comprises 15 equations, has a closed-form eigensystem and also possesses an entropy. The model is implemented within a new three-dimensional (3D), solution-adaptive, finite-volume parallel computational framework that allows for efficient solutions for problems characterized by a wide range of length scales. The final version of the paper will include a summary of the derivation of the model, its mathematical properties and the description of the 3D solution-adaptive parallel numerical scheme. The computational advantages of the proposed formulation will be demonstrated based on application to several standard test cases and the simulation of multiphase flows typical to those resulting from the detonation of a radiological dispersal device (RDD).

Keywords- *particle-laden flow; Gaussian moment closure; Maximum-entropy modelling;*

I. INTRODUCTION

The current work is concerned with a new Eulerian formulation on how to model particle-laden flows, in which the so-called disperse phase is made up of relatively small, immiscible, solid particles that are suspended in a continuously connected carrier phase. The goal of the work is to provide an alternative Eulerian formulation to Lagrangian particle methods, which are usually confronted with computational inefficiencies as the number of particles becomes large and the flow approaches a local equilibrium, that is able to avoid the modelling artifacts exhibited by traditional, single particle-velocity, Eulerian models.

Recently, we have proposed a new model to treat such situations. It takes its roots from the kinetic theory of gases, using a probabilistic treatment for particle behaviour. This is done with a distribution function, $\mathcal{F}(x_i, v_i, \zeta_0, \zeta_1, \dots, \zeta_N, t)$, that describes the phase-space density of particles at position x_i , with velocity v_i , at time t and with N number of internal variables ζ_i . This distribution function has all the information necessary to fully describe the evolution of particles in space, time and internal variables through the collisionless kinetic equation,

$$\frac{\partial \mathcal{F}}{\partial t} + v_\alpha \frac{\partial \mathcal{F}}{\partial x_\alpha} + \frac{\partial}{\partial v_\alpha} (a_\alpha \mathcal{F}) + \sum_{i=0}^N \frac{\partial}{\partial \zeta_i} (Y_i \mathcal{F}) = 0. \quad (1)$$

Observable properties, such as number density of particles and average velocity, can be obtained by taking moments of \mathcal{F} . For example, the number density of particles is given by

$$n(x_i, t) = \iiint_{\infty} \dots \int \mathcal{F} dv_i d\zeta_i = \langle \mathcal{F} \rangle, \quad (2)$$

where here the angle brackets $\langle \cdot \rangle$ means integrating over all velocity space and the space of each internal variable. The deviations from the local average of a particle's velocity as well as the internal variables can be written as

$$c_i = \begin{bmatrix} v_x - u_x \\ v_y - u_y \\ v_z - u_z \\ \zeta_1 - \bar{\zeta}_1 \\ \zeta_2 - \bar{\zeta}_2 \\ \vdots \\ \zeta_N - \bar{\zeta}_N \end{bmatrix}. \quad (3)$$

The variance-covariance matrix can also be generalized to include the variance of each internal variable, as well as the covariance between the internal variables, along with their covariance with the three components of the particle velocity,

$$n\Psi_{ij} = \langle c_i c_j \mathcal{F} \rangle = \begin{bmatrix} \Theta_{ij} & \Psi_{ij} \\ \Psi_{ij} & \Psi_{ij} \end{bmatrix}. \quad (4)$$

To obtain partial differential equations that describe the evolution of these moments, velocity moments of the kinetic equation are taken, resulting in Maxwell's equation of change. Unfortunately, this technique does not lead to a closed model, since the time evolution of one moment always depends on the space divergence of the moment that is one order higher in velocity. To achieve a closed system, one has to prescribe a specific form for \mathcal{F} . Such techniques are called "moment closures". Models of this type take the form of first-order balance laws and bring many advantages, *e.g.* they are first-order and therefore relatively easy to solve and produce solutions that are relatively insensitive to grid quality.

One prescribed form of the distribution function assumes that it maximizes entropy, while remaining consistent with known moment. This is known to yield systems with global hyperbolicity. The ten-moment Gaussian model [1] is well known in gaskinetic theory to treat viscous gases and is extended here for the treatment of a dilute particle phase with an arbitrary number of internal variables. As an initial case, the model mentioned previously was specialized for the treatment of polydisperse flows subject to aerodynamic drag and gravitational force. For this specific application, the only internal variable chosen is the particle diameter. This new model comprises 15 equations, has a closed-form eigensystem and also possesses an entropy. The dispersal of particles resulting from the detonation of a radiological dispersal device (RDD) [2] is a practical application of this model and a driver for this work. Nevertheless, the model can be applied to a much larger spectrum of problems.

Usually, an RDD comprises an explosive charge and a radioactive source. If such a device detonates, radioactive material would be dispersed through material fragmentation and thermal-gas-dynamics processes. The range of particle size and initial acceleration are determined through the explosive detonation, blast-wave propagation and fireball development, all of which happens on an extremely short time scale. However, following these events, the radioactive particles spread out over large distances on a time scale of minutes to hours, depending on meteorological conditions and terrain topography. The new model is implemented within a new adaptive-mesh-refinement (AMR) framework that allows for efficient solutions across all of these regimes.

The rest of this paper provides a short description of the 15-moment polydisperse Gaussian model (PGM) resulting as a specialization of the general model for a single internal degree of freedom, which in this case it is the particle size. Furthermore, preliminary one-dimensional (1D) results are included to illustrate the capabilities of the new model. The final paper will include additional details regarding the derivation of the model, its mathematical properties and the description of the 3D parallel numerical scheme for its solution coupled to a background gas.

Furthermore, several canonical problems will be included as well as cases typical of RDDs.

II. A 15-MOMENT POLYDISPERSE GAUSSIAN MODEL

The traditional Gaussian model can be extended to an arbitrary number of internal variables through the definition of the column vector

$$V_i = [v_x, v_y, v_z, \zeta_1, \zeta_2, \dots, \zeta_N]^T. \quad (5)$$

This leads to a maximum-entropy distribution of the form

$$\mathcal{F}_G = \frac{n}{(2\pi)^{\frac{3+N}{2}} (\det\Psi_{ij})^{\frac{1}{2}}} \exp\left(-\frac{1}{2}\Psi_{ij}^{-1}c_i c_j\right). \quad (6)$$

In general, particles can interact with the carrier phase through aerodynamic forces. These include lift and drag and can be described by a wide range of models. For the present work, Stokes flow is assumed. The particles are also affected by the gravity and buoyancy forces. The acceleration a single particle experiences is therefore described by

$$a_i = \frac{V_i - v_i}{\tau} + \phi_i, \quad (7)$$

with

$$\tau = \frac{\rho_p D^2}{18\mu_f}, \phi_i = \frac{\rho_p - \rho_f}{\rho_p} g_i. \quad (8)$$

Here, V_i is the background fluid velocity at the position of the particle, μ_f is the background fluid dynamic viscosity, v_i is the particle's velocity, ρ_p is the density of the material making up the particle, ρ_f is the density of the carrier phase, D is the particle diameter and g_i is the gravitational acceleration. The form of the kinetic equation, (1), applied to this specific situation is given by

$$\begin{aligned} \frac{\partial \mathcal{F}}{\partial t} + v_\alpha \frac{\partial \mathcal{F}}{\partial x_\alpha} = & -\frac{\partial}{\partial v_\alpha} \left(\frac{V_\alpha - v_\alpha}{\tau} \mathcal{F} \right) \\ & - \frac{\partial}{\partial v_\alpha} (\phi_\alpha \mathcal{F}). \end{aligned} \quad (9)$$

As the only internal variable used in this work is the logarithm of the diameter, the index for this one internal variable, D , will simply be taken to be d in the rest of the paper. The result of the above theory is a fifteen-moment polydisperse Gaussian model and leads to fifteen first-order hyperbolic PDEs of the form

$$\frac{\partial n}{\partial t} + \frac{\partial}{\partial x_k} (n u_k) = 0 \quad (10)$$

$$\frac{\partial}{\partial t} (n u_i) + \frac{\partial}{\partial x_k} n (u_i u_k + \Theta_{ik}) = S_i^{(2)} \quad (11)$$

$$\begin{aligned} \frac{\partial}{\partial t} n (u_i u_j + \Theta_{ij}) + \frac{\partial}{\partial x_k} n (u_i u_j u_k + u_i \Theta_{jk} \\ + u_j \Theta_{ik} + u_k \Theta_{ij}) = S_{ij}^{(3)} \end{aligned} \quad (12)$$

$$\frac{\partial}{\partial t} (n \mu) + \frac{\partial}{\partial x_k} n (\mu u_k + \Psi_{kd}) = 0 \quad (13)$$

$$\begin{aligned} \frac{\partial}{\partial t} n (\mu u_i + \Psi_{id}) + \frac{\partial}{\partial x_k} n (\mu u_i u_k + u_i \Psi_{kd} \\ + u_k \Psi_{id} + \mu \Theta_{ik}) = S_{id}^{(5)} \end{aligned} \quad (14)$$

$$\begin{aligned} \frac{\partial}{\partial t} n (\mu^2 + \Psi_{dd}) + \frac{\partial}{\partial x_k} n (\mu^2 u_k + 2\mu \Psi_{xd} \\ + u_k \Psi_{dd}) = 0 \end{aligned} \quad (15)$$

where $\mu = \langle \frac{\ln D F}{n} \rangle$ is the local average value of the natural logarithm of the particle diameter. The source terms for Stokes drag, gravity and buoyancy are

$$S_i^{(2)} = \frac{n}{\tau_G} (V_i - (u_i - 2\Psi_{id})) + n\phi_i, \quad (16)$$

$$S_{ij}^{(3)} = \frac{n}{\tau_G} \left(V_i(u_j - 2\Psi_{jd}) + V_j(u_i - 2\Psi_{id}) - 2(u_i u_j - 2u_i \Psi_{jd} - 2u_j \Psi_{id} + 4\Psi_{id} \Psi_{jd} + \Theta_{ij}) \right) + n(u_j \phi_i + u_i \phi_j), \quad (17)$$

and

$$S_{ij}^{(5)} = \frac{n}{\tau_G} (V_i(\mu - 2\Psi_{dd}) - (\mu u_i - 2\mu \Psi_{id} - 2u_i \Psi_{dd} + 4\Psi_{dd} \Psi_{id} + \Psi_{id})) + n\mu \phi_i. \quad (18)$$

where τ_G is the relaxation time for the moments and is given by

$$\tau_G = \frac{\rho p}{18\mu_f} e^{2\mu - 2\Psi_{dd}}. \quad (19)$$

In a 3D Cartesian coordinate system, this leads to a new system of fifteen first-order hyperbolic PDEs of the form of

$$\frac{\partial \mathbf{U}}{\partial t} + \frac{\partial \mathbf{F}_x}{\partial x} + \frac{\partial \mathbf{F}_y}{\partial y} + \frac{\partial \mathbf{F}_z}{\partial z} = \mathbf{S}_1 + \mathbf{S}_2, \quad (20)$$

where the solution vector of conserved variable \mathbf{U} is given by

$$\mathbf{U} = n \begin{bmatrix} 1 \\ u_x \\ u_y \\ u_z \\ (u_x^2 + \Theta_{xx}) \\ (u_x u_y + \Theta_{xy}) \\ (u_x u_z + \Theta_{xz}) \\ (u_y^2 + \Theta_{yy}) \\ (u_y u_z + \Theta_{yz}) \\ (u_z^2 + \Theta_{zz}) \\ \mu \\ (\mu u_x + \Psi_{xd}) \\ (\mu u_y + \Psi_{yd}) \\ (\mu u_z + \Psi_{zd}) \\ (\mu^2 + \Psi_{dd}) \end{bmatrix}, \quad (21)$$

the flux in the x-direction, \mathbf{F}_x is given by

$$\mathbf{F}_x = n \begin{bmatrix} u_x \\ (u_x^2 + \Theta_{xx}) \\ (u_x u_y + \Theta_{xy}) \\ (u_x u_z + \Theta_{xz}) \\ (u_x^3 + 3u_x \Theta_{xx}) \\ (u_x^2 u_y + 2u_x \Theta_{xy} + u_y \Theta_{xx}) \\ (u_x^2 u_z + 2u_x \Theta_{xz} + u_z \Theta_{xx}) \\ (u_x u_y^2 + u_x \Theta_{yy} + 2u_y \Theta_{xy}) \\ (u_x u_y u_z + u_x \Theta_{yz} + u_y \Theta_{xz} + u_z \Theta_{xy}) \\ (u_x u_z^2 + u_x \Theta_{zz} + 2u_z \Theta_{xz}) \\ (\mu u_x + \Psi_{xd}) \\ (\mu u_x^2 + 2u_x \Psi_{xd} + \mu \Theta_{xx}) \\ (\mu u_x u_y + u_x \Psi_{yd} + u_y \Psi_{xd} + \mu \Theta_{xy}) \\ (\mu u_x u_z + u_x \Psi_{zd} + u_z \Psi_{xd} + \mu \Theta_{xz}) \\ (\mu^2 u_x + 2\mu \Psi_{xd} + u_x \Psi_{dd}) \end{bmatrix}. \quad (22)$$

The source vector for Stokes drag, \mathbf{S}_1 , is now

$$\mathbf{S}_1 = \frac{n}{\tau_G} \begin{bmatrix} 0 \\ V_x - (u_x - 2\Psi_{xd}) \\ V_y - (u_y - 2\Psi_{yd}) \\ V_z - (u_z - 2\Psi_{zd}) \\ 2(V_x(u_x - 2\Psi_{xd}) - (u_x^2 - 4u_x \Psi_{xd} + 4\Psi_{xd}^2 + \Theta_{xx})) \\ V_x(u_y - 2\Psi_{yd}) + V_y(u_x - 2\Psi_{xd}) - 2(u_x u_y - 2u_x \Psi_{yd} - 2u_y \Psi_{xd} + 4\Psi_{xd} \Psi_{yd} + \Theta_{xy}) \\ V_x(u_z - 2\Psi_{zd}) + V_z(u_x - 2\Psi_{xd}) - 2(u_x u_z - 2u_x \Psi_{zd} - 2u_z \Psi_{xd} + 4\Psi_{xd} \Psi_{zd} + \Theta_{xz}) \\ 2(V_y(u_y - 2\Psi_{yd}) - (u_y^2 - 4u_y \Psi_{yd} + 4\Psi_{yd}^2 + \Theta_{yy})) \\ V_y(u_z - 2\Psi_{zd}) + V_z(u_y - 2\Psi_{yd}) - 2(u_y u_z - 2u_y \Psi_{zd} - 2u_z \Psi_{yd} + 4\Psi_{yd} \Psi_{zd} + \Theta_{yz}) \\ 2(V_z(u_z - 2\Psi_{zd}) - (u_z^2 - 4u_z \Psi_{zd} + 4\Psi_{zd}^2 + \Theta_{zz})) \\ 0 \\ V_x(\mu - 2\Psi_{dd}) - (\mu u_x - 2\mu \Psi_{xd} - 2u_x \Psi_{dd} + 4\Psi_{dd} \Psi_{xd} + \Psi_{xd}) \\ V_y(\mu - 2\Psi_{dd}) - (\mu u_y - 2\mu \Psi_{yd} - 2u_y \Psi_{dd} + 4\Psi_{dd} \Psi_{yd} + \Psi_{yd}) \\ V_z(\mu - 2\Psi_{dd}) - (\mu u_z - 2\mu \Psi_{zd} - 2u_z \Psi_{dd} + 4\Psi_{dd} \Psi_{zd} + \Psi_{zd}) \\ 0 \end{bmatrix} \quad (24)$$

And the source vector for the gravity, \mathbf{S}_2 , is

$$\mathbf{S}_2 = \begin{bmatrix} 0 \\ n\phi_x \\ n\phi_y \\ n\phi_z \\ 2nu_x \phi_x \\ nu_x \phi_y + nu_y \phi_x \\ nu_x \phi_z + nu_z \phi_x \\ 2nu_y \phi_y \\ nu_y \phi_z + nu_z \phi_y \\ 2nu_z \phi_z \\ 0 \\ n\mu \phi_x \\ n\mu \phi_y \\ n\mu \phi_z \\ 0 \end{bmatrix}. \quad (25)$$

III. FINITE-VOLUME DISCRETIZATION SCHEME

Numerical solutions of the PGM are sought by applying a first-order Godunov-type finite-volume spatial discretization procedure [3] in conjunction with approximate Riemann-solver based flux functions and an operator splitting approach [4]. The latter is required for the treatment of the source term, which can become excessively stiff for very low Stokes numbers. Therefore, the hyperbolic part of the PDEs is treated explicitly whereas the source term related to drag is evaluated analytically. Since accumulation of numerical errors could result in the model leaving the space of realizable states, the use of operator splitting and the treatment of the drag term analytically ensures the distribution function remains positive definite.

The numerical scheme outlined above is illustrated in 1D. The 3D algorithm follows a similar approach. The first step of the explicit scheme can be expressed as where $\tilde{\mathbf{U}}_i^s$ and $\bar{\mathbf{U}}_i^s$ are

$$\tilde{\mathbf{U}}_i^s = \bar{\mathbf{U}}_i^s - \frac{\Delta t}{\Delta x} (\hat{\mathbf{F}}_{i+\frac{1}{2}} - \hat{\mathbf{F}}_{i-\frac{1}{2}}), \quad (23)$$

the average conserved solution vectors in cell i at the beginning of the time step s and the intermediate step, before the contribution of the drag term is applied analytically, respectively. The inter-cellular numerical fluxes in (23), $\hat{\mathbf{F}}_{i+\frac{1}{2}}$, are calculated using the Harten-Lax-van Leer (HLL) flux function [5].

Following the update of the intermediate solution vector $\tilde{\mathbf{U}}_i^s$, the contribution of the source term can be calculated analytically with the corresponding primitive variables. The cell average primitive variables at step $s + 1$ are updated as follows

$$\bar{n}_x^{s+1} = \tilde{n}_x, \quad (26)$$

$$\bar{u}_x^{s+1} = \frac{v_1 + v_2}{2\alpha}, \quad (27)$$

$$\bar{\Theta}_{xx}^{s+1} = (\tilde{\Theta}_{xx} \tilde{\Psi}_{dd} - (\tilde{\Psi}_{xd}^{s+1})^2) \exp\left(-2\frac{\Delta t}{\tau_G}\right), \quad (28)$$

$$\bar{\Theta}_{yy}^{s+1} = \tilde{\Theta}_{yy} \exp\left(-2\frac{\Delta t}{\tau_G}\right), \quad (29)$$

$$\bar{\Theta}_{zz}^{s+1} = \tilde{\Theta}_{zz} \exp\left(-2\frac{\Delta t}{\tau_G}\right), \quad (30)$$

$$\bar{\mu}^{s+1} = \tilde{\mu}, \quad (31)$$

$$\bar{\Psi}_{xd}^{s+1} = \left(v_1 - (\alpha + \tilde{\Psi}_{dd})\right) \bar{u}_x^{s+1}, \quad (32)$$

$$\bar{\Psi}_{dd}^{s+1} = \tilde{\Psi}_{dd}, \quad (33)$$

where

$$\alpha = \sqrt{\Psi_{dd}(\Psi_{dd} + 1)}, \quad (34)$$

$$v_1 = \left((\alpha + \tilde{\Psi}_{dd}) \tilde{u}_x + \tilde{\Psi}_{xd} - \frac{c_1}{\lambda_1} \right) \exp(-\hat{\lambda}_1 t) + \frac{c_1}{\lambda_1}, \quad (35)$$

$$v_2 = \left((\alpha - \tilde{\Psi}_{dd}) \tilde{u}_x - \tilde{\Psi}_{xd} - \frac{c_2}{\lambda_2} \right) \exp(-\hat{\lambda}_2 t) + \frac{c_2}{\lambda_2}, \quad (36)$$

$$\hat{\lambda}_{1,2} = \frac{-1}{\tau_G} (1 + 2\Psi_{dd} \pm 2\alpha), \quad (37)$$

$$c_{1,2} = \frac{-1}{\tau_G} (V_x(\alpha \mp \Psi_{dd}) - \phi_x \tau_G (\Psi_{dd} \pm \alpha)). \quad (38)$$

IV. NUMERICAL RESULTS

To demonstrate the capabilities of the proposed PGM to approximate solutions of the full, high-dimensional kinetic equation, a relevant problem is included herein. The velocity of the background flow is assumed to be zero which allows the exact solution to the full kinetic equation to be constructed. The test case is a Riemann problem, which consists of a single discontinuity in the number density and particle velocity. Although studies have been performed with three different intensities of the source term corresponding to no, medium, and strong drag, only results for the latter are included here.

For this problem, in addition to the exact solution, the numerical solution to a classic single-velocity (or mono-kinetic) model (SVM) is also shown for comparison. This commonly used model consists of two equations and can be seen as a moment closure where the assumed form of the distribution function is a single Dirac delta in velocity space—i.e. all the particles at a given location have the same velocity.

The domain of interest is chosen to be $0 \text{ m} \leq x \leq 20 \text{ m}$. A discontinuity in the particle number density and their velocity is introduced at $x = 10 \text{ m}$. Specifically, the particle number density is set to 100 particles per cubic meter with an average velocity of 5.0 m/s on the left side of the discontinuity and 10 particles per cubic meter with zero velocity for the rest of the

domain. The variance in particle velocity is chosen to be $1.0 \text{ m}^2/\text{s}^2$ in the whole domain. The mean particle diameter is taken initially equal to $28 \text{ }\mu\text{m}$ with a diameter variance of

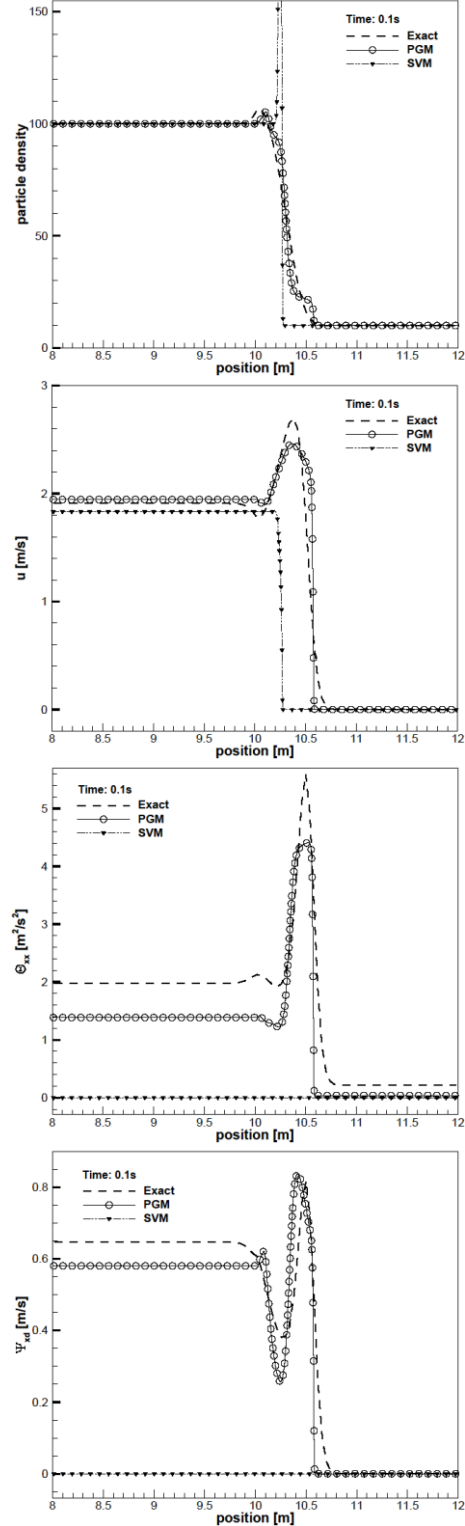


Figure 1. Numerical result for a Riemann problem after 0.1 s with strong drag $\tau = 0.1 \text{ s}$.

$2 \times 10^{-10} \text{ m}^2$. The initial distribution of particle diameters uses the log-normal distribution function. This problem is tested with strong drag, $\tau = 0.1 \text{ s}$.

The results in this section have been obtained using the numerical scheme described in Section III. A 1D grid with 4,000 computational cells has been used to determine the predicted solution and a Courant-Friedrichs-Lewy (CFL) number of 0.5.

The results shown in Fig. (1) demonstrate the PGM prediction for the number density of particles and the average velocity is much closer and follows the same trend as the exact solution compared to SVM. Note that the variance in the x -velocity for the predicted solution relaxes faster compared to the exact solution but is still providing relatively good approximations. The behaviour of the other moment shown here, the covariance between the velocity of particle and the average logarithm of the diameter, are much closer to the exact solution.

V. SCOPE OF FINAL PAPER

The final version of the manuscript will include more details on the computational model and numerical scheme in three dimensions, with an emphasis on the numerical implementation, in conjunction the AMR. The capabilities of the devised framework will be fully illustrated based on standard test problems as well as cases typical of RDDs.

REFERENCES

- [1] C. D. Levermore, "Moment Closure Hierarchies for Kinetic Theories," *Journal of statistical Physics*, vol. 83, pp. 1021-1065, 1996.
- [2] L. Lebel, P. Bourgoin, S. Chouhan, N. Ek, V. Korolevych, A. Malo, D. Bensimon and L. Erhardt, "Radiation Modelling and Finite Cloud Effects for Atmospheric Dispersion Calculations in Near-Field Applications: Modelling of the Full Scale RDD Experiments with Operational models in Canada, Part II," *Health Physics*, vol. 100, no. 5, pp. 518-525, 2016.
- [3] S. K. Godunov, "A difference method for numerical calculation of discontinuous solutions of the equations of hydrodynamics," *Matematicheskii Sbornik*, vol. 89, no. 3, pp. 271-306, 1959.
- [4] R. J. LeVeque, *Finite Volume Methods for Hyperbolic Problems*, Cambridge: Cambridge University Press, 2002.
- [5] A. Harten, P. D. Lax and B. van Leer, "On upstream differencing and Godunov-type schemes for hyperbolic conservation laws," *SIAM Review*, vol. 25, no. 1, pp. 35-61, 1983.

Porous Media

Airflow balancing of a produce drying chamber using a porous media approach

Mahmoud Elhalwagy
Mechanical and Materials Engineering
Western University
London ON, Canada
melhalwa@uwo.ca

Anthony Straatman
Mechanical and Materials Engineering
Western University
London ON, Canada
astraatman@eng.uwo.ca

ABSTRACT

Computational Fluid Dynamics (CFD) is a useful design tool for food processing and storage applications because ventilation, and heat and mass transfer of foods and stored produce can be simulated thereby reducing the reliance on expensive experimental studies. Combined with the use of porous media modelling, CFD may be utilized to model individual fruits or vegetables, stacks of produce and mixed-commodity storage areas. Utilization of porous media concepts for characterizing stacks of produce and food stuffs proves efficient because it is often difficult or unnecessary to characterize each food element separately. The level of resolution depends on whether it is sufficient to characterize the resistance to airflow, heat and mass transfer due to the presence of bodies of foodstuffs, or if it is necessary to consider detailed shape and stacking effects. In other words, it is often sufficient to scale up the flow over individual food elements by averaging over a large volume of the domain. A mathematical averaging of the transport equations is utilized in these cases to volume-average the “porous” domain. The averaging process produces additional terms that characterize the influence of the food elements on the average flow and heat/mass transport. Coefficients in the closure terms are determined either by experiment or by pore-level simulation to facilitate simulation using the volume-averaged approach. By simulation, a small representative domain of foodstuffs (a representative-elemental-volume or REV) must be developed and then simulated from which results can be averaged to obtain the coefficients of closure. Alternatively, the closure coefficients can be obtained from experiments on small stacks of produce.

Herein, simulations were conducted to study the airflow across skids of grapes in a horticultural drying chamber for the purpose of balancing the airflow to produce uniform ventilation across all stacks of produce. The focus of the study was on the approach taken to provide balanced airflow using a computational Fluid Dynamics (CFD) tool combined with experimental data. The process was to first characterize the crate stacks by comparison of CFD simulations of airflow across a single crate stack to experimental data to establish drag parameters in a Darcy-Forchheimer relation. These parameters were then used to simulate a row of stacked skids, connected at their bases, to determine the imbalance of airflow from the first to the last stack. The imbalance was corrected by adding thin, variable-resistance covers to the tops of the stacked skids, where the highest additional resistance was required at the skid directly adjacent to the suction end of the stack row with no additional resistance at the skid farthest from the suction end. The resistance covers were also treated in the simulations as porous media using similar resistance coefficients for a Darcy-Forchheimer-type flow. These covers were then, by a reversed process, converted to perforated plates that could be easily constructed and used in the horticultural chamber to balance the airflow without making any further changes to the system. The corrected model was then used to simulate flow through the entire chamber to confirm that under the conditions of operation, the balance of airflow persists. The study shows that while the unmodified stacks had nearly 20% imbalance from the first to the last stack, the stack with resistance modifiers corrected this imbalance to within 5%, which is considered suitable for operation of the chamber.

Extension of dynamic heat and mass transfer coupling to Turbulent flow at Fluid/Porous interfaces of different permeability

Mahmoud Elhalwagy
Mechanical and Materials Engineering
Western University
London ON, Canada
melhalwa@uwo.ca

Anthony Straatman
Mechanical and Materials Engineering
Western University
London ON, Canada
astraatman@eng.uwo.ca

ABSTRACT

Study of processes involving Porous media and Conjugate Fluid/Porous/Solid domains has attracted significant attention. The applications are numerous including flow, heat and mass transfer processes in packed beds, metal foams, dryers, food processing and storage facilities and different other chemical and catalytic multi-phase applications. Most of the above mentioned applications are turbulent in nature and hence, the challenges of characterizing turbulence and turbulent heat and mass transfer need to be addressed. Due to the fact that all of these applications involve multiple spatial and temporal scales with the presence of turbulence, porous media and macroscopic transport, measurement techniques that characterize these processes locally are either unavailable or limited, leaving only three options for physical model development. The first option is to depend on empiricism as a tool to establish physical thresholds for flow, heat and mass transfer. The second option is to undertake detailed physical modelling for these multiple spatial and time scales. The third option is to compromise between computational time, empiricism and detailed scale modeling in order to have a successful, general and economic modeling process (i.e. a Dynamic Coupling approach).

The present paper describes an extension of the dynamically-coupled heat and mass transfer technique developed by Elhalwagy and Straatman [1] to accommodate simulation of turbulent flow conditions. The extension involves implementation of a volume-averaged turbulence model inside the porous-continuum and, more importantly, a model to properly characterize the transport of turbulence through the macroscopic interfaces that separate the fluid and porous domains. The interface model works for porous regions of high or low permeability and incorporates an expression that permits turbulence decay at the interface to evolve naturally without an ad-hoc switch off that is not accurate for heat and mass transfer predictions. The merits of a dynamic coupling approach are: that it is developed to allow the micro- and macroscopic interfaces to react in a physically correct manner to local and temporal changes that happen during different transport phenomena with minimal case-specificity or empiricism; and it lends itself to numerical solution in a reasonable computational time. The model formulates resistances to heat and mass transfer inside the porous media, at the fluid/porous interface and across the interface so that coupling of each phase within porous media is achieved and physical transfer across the macroscopic interface is also achieved. An enhanced turbulence wall-like treatment is developed for the hydrodynamics and the reflection for it on heat and mass transfer is presented for implicit and explicit CFD interface coupling cases. In other words, the wall-like treatment for turbulent heat and mass transfer is implemented into the dynamic coupling framework that was originally developed for laminar flow [1] allowing the model to numerically treat turbulent hydrodynamics and heat and mass transfer. The wall-like treatment is also capable of allowing turbulence to penetrate the porous interface for high permeability materials or dissipate for low permeability. In this paper, the full mathematics and numerical aspects of the dynamic coupling framework are presented followed by CFD studies for drying of produce slices. An apple slice with a porosity of 0.206 and a potato slice with a porosity of 0.04 are considered.

References

[1] Elhalwagy, M. M., & Straatman, A. G. (2017). Dynamic coupling of phase-heat and mass transfer in porous media and conjugate fluid/porous domains. *International Journal of Heat and Mass Transfer*, 106, 1270-1286.

PREDICTION OF THE OVERALL PERFORMANCE OF CATALYST-COATED PARTICULATE FILTERS USING A LATTICE BOLTZMANN-BASED MODEL

Igor Belot, David Vidal and
François Bertrand*
Dept. of chemical engineering
Polytechnique Montréal
Montréal (QC), Canada

Martin Votsmeier, Barry van Setten
and Robert Greiner
Umicore AG & Co. KG
Hanau, Germany

Robert E. Hayes
Dept. of chemical and materials
engineering
University of Alberta
Edmonton (AB), Canada

ABSTRACT

Because it improves fuel economy, gasoline direct injection (GDI) engine has seen rapid adoption, despite large emissions of nanoparticles and harmful gases. In turn, Gasoline Particulate Filters (GPF) coated with Three-Way Catalyst (TWC) have interested OEMs for their capacity to treat soot aerosols at the same time as NO_x, HC and CO gases while gaining space and reducing costs and complexity. It consists of a honeycomb of parallel channels made in a porous material (cordierite in this work) in which is deposited catalyst coating. However, the impact of a catalyst deposition on the pressure drop (PD) and filter efficiency (FE) of the GPF is still unpredictable. Furthermore, the conversion rates of the catalyst coating depending on its distribution needs more research attention.

In the last decades, the lattice Boltzmann method (LBM) has emerged as a very good numerical method to solve flow into porous media. It has the advantage of being meshfree and largely parallelizable. Here, a four-step numerical model is being developed to shed light on the impact of washcoat deposition on the cordierite porous wall of a clean GPF overall performance. It consists of: (1) the numerical reconstruction of the representative volume of a GPF porous wall from X-ray computed tomography data coated by artificial catalyst deposition algorithms, the computation of both (2) the pressure drop and (3) the catalytic conversion through the coated porous wall by solving through the LBM a coupled Navier-Stokes and advection-diffusion-reaction equations, and (4) the prediction of the GPF filtering efficiency by means of the solution of a Langevin problem.

Using this four-step procedure, a systematic investigation of the performance of different characterized washcoat distributions on a GPF porous wall has been performed and compared to lab and literature experimental data. Counterintuitive results are presented and highlight the complexity of the effects generated by the washcoat deposition into the GPF porous wall. Further numerical analyses allow a better understanding of the physical phenomena involved. Differences up to 30% in filter performance and 50% in conversion performance have been obtained for different washcoat profile uniformities. Once fully developed, the proposed model will provide a complete optimization tool to GPF manufacturers, and thereby help address the issue of air quality in the environment.

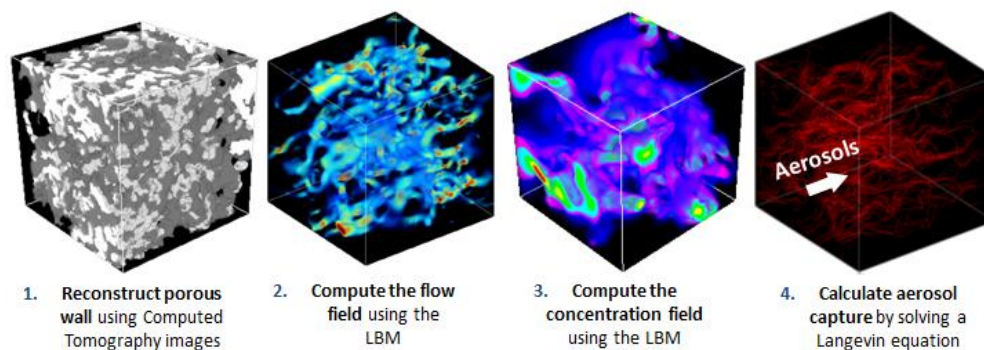


Figure 1: Sketch of the 4-step numerical model used to predict GPF porous wall performance

Modeling of Cathode Oxygen Transport in Polymer Electrolyte Membrane Fuel Cells Based on Measured Permeability and Effective Diffusivity

Jian Zhao, Xianguo Li

20/20 Laboratory for Fuel Cell and Green Energy RD&D, Department of Mechanical and Mechatronics Engineering
University of Waterloo
Waterloo, Canada
xianguo.li@uwaterloo.ca

ABSTRACT

Effective transport of oxygen from cathode channel to reaction sites through the gas diffusion layer (GDL) and catalyst layer (CL) is critical to improving polymer electrolyte membrane (PEM) fuel cell performance at high current density regions. However, how the two oxygen transport mechanisms, i.e., convection and diffusion, in electrodes compete with each other at different operational conditions are still not clear. This is because accurate measurement of the pressure and oxygen concentration gradients across such a thin GDL or CL without damaging their intrinsic structure in an operating PEM fuel cell is almost impractical. In the present study, the two indicators of porous media's capabilities for mass transfer by convection and diffusion, i.e., permeability and effective diffusivity, are experimentally studied by Darcy's and Fick's laws, respectively. Based on the measured *ex-situ* transport properties, a three-dimensional steady-state model is established to study the oxygen transport phenomena in the porous media. The simulation results are validated with the *in-situ* experimental data on the polarization curve. The *ex-situ* experimental results indicate that the permeability of the GDL and CL in the present study is of the order of 10^{-13} and 10^{-15} m^2 , respectively, while the effective diffusivity of GDL and CL is of the order of 10^{-6} and 10^{-7} $\text{m}^2\cdot\text{s}^{-1}$, which are much lower than the values determined by empirical correlations that are widely adopted for PEM fuel cell modeling in literature. The simulation results, using the *ex-situ* experimental results as inputs, show good agreements with the *in-situ* experimental polarization curve. Further analysis of the convective and diffusive oxygen fluxes based on the simulation results demonstrates that the average through-plane diffusive oxygen flux is about 5 times larger than its convective counterpart under small current densities (e.g., $0.10 \text{ A}\cdot\text{cm}^{-2}$), while the diffusive flux can be increased to 7-20 times larger under high current densities (e.g., $1.22 \text{ A}\cdot\text{cm}^{-2}$). It is also observed that the local oxygen transport in the cathode electrode also varies significantly with the locations under different operational conditions, e.g., average current densities. The results suggest that for a given PEM fuel cell, enhancing the convective oxygen transport may be more feasible to improve the cell performance at high current density regions than enhancing the diffusive oxygen transport.

Turbulence

EFFECT OF FREE-STREAM TURBULENCE ON TURBULENT BOUNDARY LAYERS FROM FLAT PLATES

Ivian Magalhaes, Eric Savory
Dept. of Mechanical and Materials Engineering
The University of Western Ontario
London, Canada
ialfaiad@uwo.ca

ABSTRACT

Numerous engineering applications involve incident turbulence on turbulent boundary layers, such as photovoltaic panel systems and turbomachines. The performance of these systems highly depends on how they interact with free-stream flows and investigating this interaction is therefore extremely relevant. The aim of this work is to analyze computationally how the incoming turbulent stream affects the turbulent boundary layer profiles and integral parameters such as skin friction coefficient and shape factor. This work will also enable us to establish a suitable CFD model for this base case that will be used in future work to analyze further cases involving convective heat transfer.

It is known that an increase in the free-stream turbulence intensity (TI) leads to a thicker turbulent boundary layer and higher skin friction coefficient [1,2]. Some studies show that the turbulent boundary layer velocity and thermal profiles can be affected to different extents depending on the free stream turbulence intensity [3,4,5]. On the one hand, the normalized dynamic boundary layer seems to be only affected in the wake region [1,2]. On the other hand, the normalized thermal profiles are more sensitive to changes in the free stream turbulence levels [6]. For TI between 5-7%, experiments show that just the wake region of the boundary layer is influenced [3]. For TI higher than 15%, the wake region as well as the logarithmic region is affected [4,5] and the thermal boundary layer profile is different than those exhibited when the turbulence intensity is negligible, except for the near-wall region.

The works mentioned so far did not investigate how the free stream turbulent characteristics on the plate region affect the observed behaviour. Therefore, in this work a flat plate will be positioned in a nearly uniform region of turbulent kinetic energy (TKE) to assess properly the effect of incoming turbulence on the turbulent profiles. Sarkar [7] demonstrated a numerical tool that can accurately predict the turbulent intensity and integral length scales at the leading edge of the plate if the parameters at the inlet are known and vice-versa. Consequently, it is possible to predict an almost homogeneous region in the domain. Furthermore, it is also possible to position the plate in non-homogeneous regions, where the TKE decays rapidly in the streamwise direction, to verify the influence of this condition on the observed profiles. The full work will contain the simulation results and comparisons with available literature to validate the model and help to shed light upon the noticed inconsistencies [6].

[1] Hancock, P.E. and Bradshaw, P.P. (1983) 'The effect of free-stream turbulence on turbulent boundary layers', ASME. J. Fluids Eng, 105(3), pp. 284-289.

[2] Hancock, P.E. and Bradshaw, P.P. (1989) 'Turbulence structure of a boundary layer beneath a turbulent free stream', Journal of Fluid Mechanics, vol. 205, pp. 45-76.

[3] Simonich, J. C. and Bradshaw, P. (1978) 'Effect of free-stream turbulence on heat transfer through a turbulent boundary layer', 100(4), pp. 671-677.

[4] Maciejewski, P. K. and Moffat, R. J. (1992) 'Heat transfer with very high free-stream turbulence: Part I - Experimental data', Journal of Heat Transfer, 105, pp. 33-40.

[5] Maciejewski, P. K. and Moffat, R. J. (1992) 'Heat transfer with very high free-stream turbulence: Part II - Analysis of the results', Journal of Heat Transfer, 105, pp. 41-47.

[6] Kondjoyan, A., Péneau, F. and Boisson, H. C. (2002) 'Effect of high free stream turbulence on heat transfer between plates and air flows: A review of existing experimental results', International Journal of Thermal Sciences, 41(1), pp. 1-16.

[7] Sarkar, D. (2018) 'A numerical tool for predicting the spatial decay of freestream turbulence', MEng Thesis, Electronic Thesis and Dissertation Repository, The University of Western Ontario. 5331.

Hyperbolic Turbulence Models for Moment-Closure Solvers

Chao Yan , James McDonald
Mechanical Engineering Department
University of Ottawa
Ottawa, Canada
cyan101@uottawa.ca

ABSTRACT

Moment closure methods from the kinetic theory of gases have found recent interest for the modelling of continuum-regime flows. In the past twenty years, the first-order moment transport equations, which are derived from Boltzmann equation, have been developed and used to solve various fluid problems. Compared to the traditional fluid models, moment models have many physical and numerical advantages. These sets of equations are first-order hyperbolic partial differential equations in conservation form, which can be solved accurately and efficiently by many numerical methods. However, the lack of turbulence models has, until now, restricted their application to laminar flows.

As the vast majority of practical engineering-flow problems are turbulent, this severely limits the current practical applicability of moment methods. In order to produce a useful turbulent solver, the technique of Reynolds averaging is applied to the moment equations. This leads to a separation of large scale effects from smaller scales, which must be modelled. This presentation demonstrates Reynolds and Favre averaging of a commonly used ten-moment transport model for incompressible and compressible flows respectively. The result is that the first-order turbulent equations have far fewer un-closed terms than the traditional Reynolds or Favre averaged Navier-Stokes equations, suggesting less modelling is required. Based on the physical property of those un-closed terms, a full Reynolds stress model (SSG-LRR) is proposed and coupled to the moment transport equations. The coupled model provides time varying turbulence information and supplies all closure models, which closes the equation system. This model has been implemented to solve a mixing layer flow problem. Comparing to the Reynolds Averaged Navier-Stokes k-epsilon and k-omega model, the ten-moments SSG-LRR model seems to predict a slightly higher diffusivity and lower turbulence kinetic energy within the shear layer.

Even though the new model is able to predict full turbulent properties, it introduces second order derivatives back into the first order model. Due to the nature of turbulence, being largely diffusive, existing turbulence models are traditionally built with second derivatives. When similar closing techniques are used for the moment equations, all attractive features of purely hyperbolic model are lost. To restore the first order partial differential equations, this presentation proposed a relaxation technique to replace convection-diffusion like partial differential equations in the turbulence model.

The relaxation technique is a method that replaces convection-diffusion equations by multiple first order hyperbolic relaxation equations. As a macroscale mathematical model, convection-diffusion equations, an important class of partial differential equations, has been widely used to describe flow transport phenomena in science and engineering. But, due to various flow conditions and fluid properties, the solution to these equations can present serious numerical difficulties. Comparing to the traditional numerical scheme that is applied to solve convection-diffusion equations, the equivalent relaxation systems has been shown to provide accurate numerical solution with large time steps, which lead to a greatly improved efficiency.

As a first study, this talk proposes using the relaxation method to replace traditional one-equation turbulence models, which are convection-diffusion like equation that predicts time variation of turbulence kinetic energy. In addition, the Boussinesq approximation is used to approximate the components of the Reynolds stress tensor. The production term on the right hand side of model can be replaced by the generalized pressure tensor in ten-moments model, which simplifies the mathematical form. The derived equivalent hyperbolic relaxation equations have an asymptotic form that matches the original one equation turbulence model. The eigenstructure of the new hyperbolic turbulence model is analysed and its dispersive behaviour is explored. Numerical experimentation demonstrating the efficient solution of the new model is demonstrated.

MECHANISM FOR TRANSITION TO TURBULENCE IN A LAMINAR SEPARATION BUBBLE ON AN AIRFOIL

Joshua R. Brinkerhoff
School of Engineering
University of British Columbia – Okanagan campus
Kelowna, BC
joshua.brinkerhoff@ubc.ca

ABSTRACT

The aerodynamics of airfoils at transitional Reynolds numbers has received increased attention recently due to applications in wind turbines and aeroengine turbomachinery. Cruising at altitude or operation of wind turbines at below-rated speeds can produce Reynolds numbers in the transitional range (50,000-250,000) where flow separation from the blade suction surface occurs and the performance becomes very sensitive to the location and progression rate of transition in order to promote turbulent reattachment. Design optimization of turbine blade shapes for these conditions has motivated research of the transition process in order to develop general predictive models of transition. The initial growth of disturbances in the attached and separated regions of the flow has been linked to a convective inviscid instability of the separated shear layer. Exponential growth of this mode leads to roll-up of the shear layer and periodic shedding of coherent vortices from the separated region. More recently, subsequent instability modes have been identified that interact with the initial inviscid mode to promote full breakdown of the flow to turbulence. Spatially-resolved measurements as well as numerical simulations have highlighted the importance of three-dimensional secondary modes in the final stages of transition. However, the nature of such secondary modes, their interaction with the convective inviscid mode, and their combined role in the breakdown to turbulence remains unclear.

The present research investigates mechanisms for transition to turbulence through a very-high-resolution direct numerical simulation (DNS) of a NACA 0018 airfoil at 5° incidence and a Reynolds number of 100,000. The DNS is conducted with special consideration towards resolving the receptivity of the flow to natural disturbances present in the environment and the development of secondary instability modes. The results are very carefully validated against experimental measurements and show good agreement in terms of pressure distribution, integral parameters, separation/transition/reattachment locations, mean and fluctuating velocity profiles, disturbance growth rates, and turbulence spectra.

The DNS results confirm that the initial growth of disturbances in the boundary layer is due to inviscid amplification of natural disturbances that penetrate into the attached boundary. The amplification of disturbances in the boundary layer commences at about 10% chord following the selective inclusion of low-amplitude, low-frequency streamwise velocity fluctuations from the free stream into the boundary layer. Exponential growth of these disturbances occurs upstream of the separation point and continues at a consistent rate in both the attached and separated regions of the flow. The disturbances reach nonlinear amplitudes and saturate with a maximum amplitude equal to approximately 10% of the reference velocity. The location of maximum disturbance amplitude closely corresponds to the chordwise location of maximum shape factor, while in the wall-normal direction the maximum disturbance amplitude coincides with the boundary layer displacement thickness. Saturation of the primary mode occurs as the separated shear layer rolls up into periodically-shed spanwise vortices at a frequency that matches that expected for a Kelvin-Helmholtz instability.

While shed spanwise vortices are initially quite homogeneous in the spanwise direction (i.e. 2D), they develop significant spanwise inhomogeneities within 1-2 shedding periods. The 3D breakdown of the shed vortices is attributed to the growth of secondary instability modes, as seen through the generation of streamwise-oriented vortex filaments between successively-shed spanwise vortices. Growth of the vortex filaments begins at a chordwise location that approximately corresponds to the time-averaged transition onset location and is localized at two locations in the boundary layer: very near the wall due to an absolute mode triggered by the upstream-stretching of the vortex filaments by the reversed flow, and near the displacement thickness height due to a hyperbolic instability of the separated shear layer. The wavenumbers associated with the maximum amplification rate of the secondary mode in the two wall-normal locations are compared with the observed spacing of coherent vortices in the transitional region in order to explain how each secondary mode contributes to the overall transition process. Analysis of budgets for the vorticity and enstrophy transport equations provide a mechanistic explanation of the mutual interaction of mean and fluctuating strain rates, primary vortex roll-up, and amplification of secondary instability modes during transition.

Simulation of Shallow Open-Channel Flow past a Vertical Cylinder using IDDES-VOF Approach

Subhadip Das

Civil & Environmental Engineering
University of Windsor
Windsor, Canada
e-mail: das11b@uwindsor.ca

Vimaldoss Jesudhas

Civil & Environmental Engineering
University of Windsor
Windsor, Canada
e-mail: jesudha@uwindsor.ca

S. Abishek

Civil & Environmental Engineering
University of Windsor
Windsor, Canada
e-mail: Abishek.Sridhar@uwindsor.ca

Ram Balachandar

Civil & Environmental Engineering
University of Windsor
Windsor, Canada
e-mail: rambala@uwindsor.ca

Ronald Barron

Mathematics & Statistics
University of Windsor
Windsor, Canada
e-mail: az3@uwindsor.ca

ABSTRACT

Recently, the use of hybrid RANS – LES turbulence modelling approaches to model complex flow fields have become hugely popular. However, applications of these approaches are not universal, and may cause erroneous results due to issues associated with the switching between the RANS and LES regions. The objective of this study is to establish a best practice guideline for setting up the Improved Delayed Detached Eddy Simulation (IDDES) for shallow open-channel flows. IDDES uses RANS in the near-wall region and LES away from it. It is effective in reducing the solution time without significantly affecting the fidelity of the simulations. IDDES uses a blending function to switch between the RANS or the LES approaches. The blending function depends on the turbulent viscosity, Reynolds stresses and the wall normal distance. The first two parameters are more critical as they are influenced by the turbulence specification and grid size. If the specified turbulent intensity and length scale are high, the turbulent viscosity will also be high, thereby affecting the local Reynolds stresses. Similarly, if a higher specific dissipation caused by a fine mesh can also increase the turbulent viscosity. Hence specifying the correct boundary/initial conditions is critical to achieve the desired LES and RANS regions in the flow. The present paper presents the procedure for establishing the necessary boundary/initial conditions for IDDES by simulating the shallow open-channel flow past a slender cylinder. Another important aspect is the generation of an optimized grid for the IDDES simulation. A very fine grid eliminates the computational cost advantage of IDDES in comparison with LES. On other hand, if mesh is not fine enough, IDDES blending function generates an LES region that is not ideal for resolving the complete anisotropic structures in the flow. A procedure for generating an optimized grid for IDDES simulations is presented with detailed discussions. The present simulations use the volume of fluid (VOF) multiphase model in conjunction with IDDES to capture the free-surface deformations. A major concern in this approach is the artificial deformation of the interface. Suitable inlet conditions must be provided in the air region to eliminate the artificial shear and waves at the air-water interface (free-surface). Additional simulations are necessary to obtain these inlet conditions. Moreover, a sharpening factor is used in the VOF model to avoid the artificial diffusion at the air-water interface. The choice of this sharpening factor is also not trivial. These issues are examined in detail in the present paper.

Key words: IDDES, VOF, free surface fluctuation, turbulent length scale, turbulent viscosity, IDDES blending function.

Simulations of 3D Turbulent Flow around a Circular Pier with a Splitter Plate

Salar Kheshtgar

Dept. of Building, Civil and Environmental Engineering
Concordia University
Montreal, Canada
Salar.kheshtgar@gmail.com

S. Samuel Li

Dept. of Building, Civil and Environmental Engineering
Concordia University
Montreal, Canada
sam.li@concordia.ca

ABSTRACT

The flow of water around a bridge pier is of great interest for hydraulic engineering applications. The water flow becomes detached from the wall surface of the pier, giving rise to turbulent eddies and horseshoe vortices. There have been numerous cases where such turbulent motions result in severe sediment scour at bridge piers, compromise their foundations, and eventually cause bridge structural failures. Unexpected repair of structural damages and re-construction are very expensive. Previously, substantial efforts have been made to suppress flow separation and eddy motions around piers. However, it is still far from being successful in avoiding the resultant erosive action. The purpose of this work is to explore the use of a splitter plate to control flow separation and vortex shedding, which is the key issue. We take the CFD approach, which is much less expensive than laboratory experiments and field investigations.

We perform three-dimensional CFD simulations of turbulent flow around a circular pier, on the basis of Reynolds-averaged Navier-Stokes equations for viscous incompressible flow. The computational model domain is a rectangular channel with zero longitudinal slope. The channel has a length of 16 cm and a width of 8 cm. The depth of flow is 5.5 cm. A circular pier of $D = 10$ mm in diameter is placed at the channel centre, and a splitter plate of different longitudinal length (or tail length ranging from $L = 0.25D$ to $1.5D$) is attached to the leeside wall of the pier. The CFD model domain is covered with structured tetrahedral mesh, with a total of close to 512,000 nodes. The approach flow Reynolds number is 10000. We use the SST $k-\omega$ model for turbulence closure. Although the model geometry is quite simple, the flow around the geometric setup is very complicated. The complication lies in flow separation, vortex shedding, turbulence, and their interaction. We quantify the effects of splitter plates of different configurations on the velocity field, turbulence kinetic energy distribution, vortex patterns, and bed shear stress distribution.

We present the results of the drag coefficient and lift coefficient as a function of the splitter length relative to the pier diameter. These two coefficients decrease with an increase in the relative splitter length. These results help determine the optimal splitter length. Without a splitter plate, vortex shedding occurs at a high frequency at the downstream of the pier. The associated adverse pressure gradient causes unsteady flow separation. The introduction of a splitter plate is shown to reduce vortices to a substantial extent. The plate divides the wake region and prevents the interaction between the two divided sides. In fact, this division works effectively to reduce the formation of vortices from either side of the splitter plate.

Turbulence kinetic energy is one of the most critical factors to control in order to avoid channel-bed erosion. At places of high turbulence kinetic energy, bed erosion is the most significant. We examine contours of the intensity of turbulence kinetic energy near the bed and confirm the beneficial effect of a splitter plate in reducing the intensity. The use of a plate effectively eliminates regions of high turbulence kinetic energy, which is reduced to the level in the far wake. Also, the use of a plate is shown to effectively reduce the magnitude of vertical or down-flow velocity, which is related to the horseshoe vortices.

The results from this research work offer the potential to improve the design of new bridge piers and to modify existing piers. This represents an important contribution in hydraulic engineering applications. The results also have important implications to mechanical engineering and naval engineering applications. Further studies should be carried out systematically to investigate effects of a splitter plate in different conditions of the Reynolds number, pier surface roughness, approach flow turbulence, and channel aspect ratio.

Application of recurrence CFD to study mass transport in turbulent vortex shedding after a cylinder

Sanaz Abbasi, Thomas Lichtenegger
 Department of Particulate Flow Modeling
 Johannes Kepler University
 Linz, Austria

sanaz.abbasi@jku.at, thomas.lichtenegger@jku.at

Sanaz Abbasi, Thomas Lichtenegger
 Linz Institute of Technology
 Johannes Kepler University
 Linz, Austria

Abstract—Even though the application of computational fluid dynamics (CFD) has expanded in many areas recently, resolving a wide range of temporal and spatial scales makes it numerically expensive for complex systems. Recurrence CFD (rCFD) aims to tackle this issue by making use of reappearing patterns in many flows. Here we present that rCFD is capable of showing promising results just by time-extrapolating the recurrent behavior of turbulent vortex shedding based on a database of flow fields acquired from a short-time conventional simulation. It is notable that we achieve a speed-up factor of 100 compared to our large eddy simulation (LES).

Keywords- *large eddy simulation; recurrence statistics; recurrence CFD; time extrapolation;*

I. INTRODUCTION

The growing functionality of computational fluid dynamics (CFD) in a vast range of fields has raised the computational cost of simulations because of high temporal and spatial resolutions. So far different approaches have been introduced to increase the efficiency as well as maintaining the accuracy of CFD; however, it still remains an open question how to best overcome these highly expensive calculations. A recent approach to meet this challenge has been introduced by Lichtenegger and Pirker called recurrence CFD (rCFD) [1]. This method is applied to systems showing reappearing patterns such as vortex shedding after blunt bodies. The main idea of rCFD is to time-extrapolate the recurring structures for arbitrary long durations just based on carrying out recurrence analysis, introduced by Eckmann et al. [2], for a database of flow fields obtained from a short-time detailed simulation. This full simulation can be any of the CFD methods, e.g. Direct Numerical Simulations (DNS), Large Eddy Simulations (LES), etc. Along with the long-time evolution of flow fields we can also study passive transport or weakly coupled flows which is considerably cheaper.

In this work our purpose is to investigate the rCFD performance on turbulent vortex shedding after a circular cylinder at $Re=3900$ with a mass transport study, i.e. how much it is possible to use lower resolutions.

First, a review of set of equations and the rCFD approach is explained in Sec. II. Then Sec. III describes the main parameters and the setup for LES and rCFD. In Sec. IV we present the acquired results, the recurrence statistics of the flow as well as the performance analysis. Finally Sec. V draws the conclusion and an outlook on our future work.

II. THEORETICAL BACKGROUND

Here, we present a brief review of the system of equations from LES perspective, and then we represent the procedure of the rCFD method.

A. Equations of motion

The filtered Navier-Stokes equations for a single-phase incompressible flow are

$$\nabla \cdot \bar{\mathbf{u}} = 0 \quad (1)$$

$$\partial \bar{\mathbf{u}} / \partial t + (\bar{\mathbf{u}} \cdot \nabla) \bar{\mathbf{u}} = -\nabla \bar{p} / \rho + \nabla \cdot \nu \nabla \bar{\mathbf{u}} - \nabla \cdot \boldsymbol{\tau}^r \quad (2)$$

where $\bar{\mathbf{u}}$ and \bar{p} are the filtered velocity and pressure, respectively and ν is viscosity [3]. By selecting the conventional Smagorinsky model [4] which assumes a local equilibrium for turbulent kinetic energy (k), the relationship between the residual stress tensor ($\boldsymbol{\tau}^r$) and the sub-grid scale viscosity (ν_{sgs}) can be written as

$$\boldsymbol{\tau}^r = -2\nu_{sgs} \bar{\mathbf{S}} \quad (3)$$

$$\nu_{sgs} = C_k \sqrt{k} \Delta, \quad (4)$$

where the filtered rate of strain tensor is defined as

$$\bar{\mathbf{S}} \equiv (\nabla \bar{\mathbf{u}} + (\nabla \bar{\mathbf{u}})^T) / 2. \quad (5)$$

The model coefficient is set to $C_k=0.094$ and Δ is the cube root of cell volume. In addition to these equations, we add passive transport of a scalar concentration (\bar{C})

$$\partial \bar{C} / \partial t + (\bar{\mathbf{u}} \cdot \nabla) \bar{C} = \nabla \cdot \mathbf{D} \nabla \bar{C} - \nabla \cdot \boldsymbol{\tau}^c + S \quad (6)$$

to the set of equations where S is the source term and diffusivity is calculated by $\mathbf{D} = \nu / \text{Sc}$ where Sc is the Schmidt number. Also the residual scalar flux is modeled similar to the residual stress tensor as

$$\boldsymbol{\tau}^c = \mathbf{D}_{\text{sgs}} \nabla \bar{C}. \quad (7)$$

B. Recurrence statistics

The purpose of the rCFD method is the fast time extrapolation of a system's behavior. To start with rCFD, we need to store a sufficient amount of data from the full simulation. This database should be recorded with a specified frequency (f_{rec}) within which the flow fields do not have strong changes and it should span several pseudo-periods of the flow. In order to quantify a system's degree of similarity, a distance norm

$$D(t, t') \equiv \left[\int d^3 r (\mathbf{u}(\mathbf{r}, t) - \mathbf{u}(\mathbf{r}, t'))^2 / N \right]^{1/2} \quad (8)$$

normalized by

$$N \equiv \max_{t, t'} \int d^3 r (\mathbf{u}(\mathbf{r}, t) - \mathbf{u}(\mathbf{r}, t'))^2 \quad (9)$$

is defined to compare the flow fields at two times. Calculating the distance norm for all of the times in the database generates a distance matrix ($D_{m,n}$), such that we can identify the most similar state to time t by finding the minimum value in the distance matrix [1].

C. Recurrence CFD

As mentioned before, by knowing the time evolution of the flow, we can study species transport for any arbitrary duration just by solving one scalar transport equation. In this regard, we need to generate a recurrence path starting at a given begin time ($t_i^{(b)}$). During a time interval of random length the flow fields are updated according to the database and the most similar state ($t_{i+1}^{(b)}$) is identified at the end of the interval ($t_i^{(e)} = t_i^{(b)} + \Delta t_i$). Further steps are taken from there on. Again after a random number of steps [$t_{i+1}^{(b)}$, $t_{i+1}^{(e)} + \Delta t_{i+1}$], the most similar state ($t_{i+2}^{(b)}$) is obtained from the recurrence statistics and so on [5]. As a result, the recurrence process can be proceeded to extrapolate the fluid flow for longer times. Therefore, (10)

$$\partial C / \partial t + (\mathbf{u}_{\text{rec}} \cdot \nabla) C = \nabla \cdot \mathbf{D}_{\text{rec}} \nabla C + S \quad (10)$$

can be solved much faster than conventional methods where \mathbf{u}_{rec} is the velocity stored in the database, and the recurrence diffusivity is concluded from $\mathbf{D}_{\text{rec}} = \mathbf{D} + \mathbf{D}_{\text{sgs}}$. \mathbf{D}_{sgs} can be directly saved in the database or modeled as (4)

$$\mathbf{D}_{\text{sgs}} = C_k \sqrt{k_c} \Delta / \text{Sc}_i. \quad (11)$$

In (11), k_c is the mapped turbulent kinetic energy on the coarser grid [6].

III. SIMULATION SETUP

In this section, we describe the setup of our simulations. The selected case to investigate the performance of rCFD is species transport in the wake region of turbulent vortex shedding after a cylinder at $\text{Re} = 3900$.

A. LES

The computational grid built for LES is shown in Fig. 1 and has about 3.85×10^6 cells. The distance between inlet and outlet was $30D$ and the dimensions in the transverse and span-wise direction were $10D$ and πD , respectively. The mesh was resolved near the cylinder to avoid using wall functions, and inlet boundary condition was treated as laminar. Besides a cell set was created at $x/D=2.85$ with a length of $0.3D$ with the aim of adding a constant source of species. The set of equations was solved using PISO algorithm along with the Smagorinsky model as SGS model with the OpenFOAM toolbox. Also, laminar and turbulent Schmidt numbers were 0.9 and 0.7, respectively. Time step was $\Delta t = 10^{-3} D/U_\infty$ which ensured a Courant number of less than 0.3. It is notable that the discretization schemes applied here for transient term was first-order implicit Euler and for gradient and divergence was second-order central difference.

B. rCFD

As explained, in rCFD we just solve one scalar equation. Therefore, there is no requirement of resolving the mesh for solving the continuity (1) and momentum (2) equations, and we could use coarser grids and greater time steps. As a result the computational grid built for rCFD depicted in Fig. 2 has about 4.75×10^5 cells which was more than 8 times less than the LES computational grid, and the time step was 5 times greater than LES ($\Delta t_{\text{rCFD}} = 5 \times \Delta t_{\text{LES}}$).

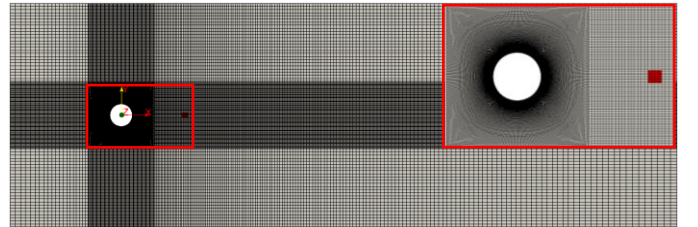


Figure 1. Computational grid built for LES. The fine grid region and the source location are magnified.

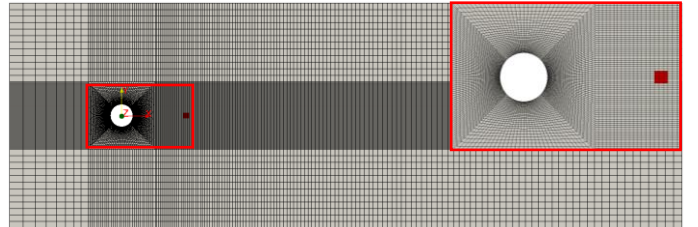


Figure 2. Computational grid built for rCFD. The fine grid region and the source location are magnified.

IV. RESULTS

First, we validate the LES results in this section. Then, the study on species transport followed by performance analysis is explained. The mean values are time-averaged over almost 75 vortex shedding periods.

A. LES results

We define lift (C_L) and drag (C_D) coefficients by $C_L=2F_L/\rho_\infty U_\infty^2 A$ and $C_D=2F_D/\rho_\infty U_\infty^2 A$ [7] where A is the cross section area and F_L and F_D are normal and tangential forces acting on the cylinder surface, respectively. Here, the computed $C_{L,rms}$ was 0.134 and mean drag coefficient was $\langle C_D \rangle = 1.1$. In comparison with other LES data from Lysenko et al. [8] and DAlessandro et al. [9], we can say that lift and drag coefficients are in the optimal ranges of [0.04-0.44] and [0.84-1.18], respectively. The Strouhal number ($St=f_{vs}D/U_\infty$) which can be determined via Fast Fourier transform of lift coefficient. The St obtained by this simulation is 0.224.

The mean velocity profiles at different locations in the wake region of the cylinder are plotted in Fig. 3 and compared with the experimental measurements of Parnaudeau et al. [10] and Ong and Wallace [11]. It is evident that the present results are in a very good agreement with the experimental data. As mentioned before, the aim of performing LES is to validate our model and computational domain to be confident about getting appropriate results in simulation of species transport.

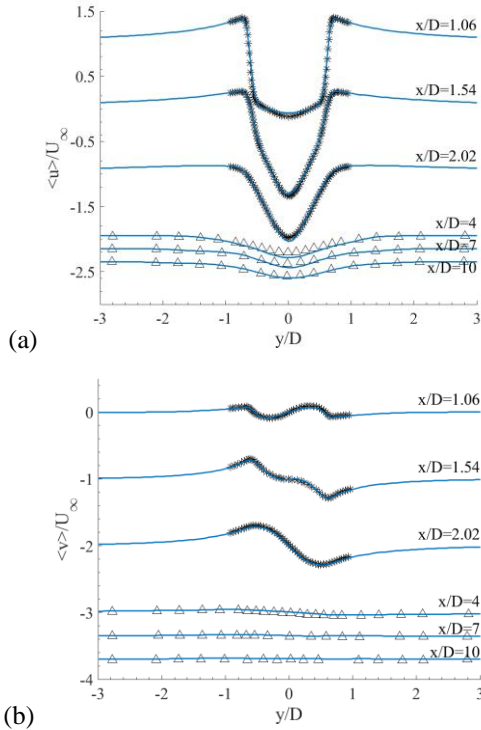


Figure 3. Mean (a) stream-wise (b) transverse velocity profiles at various sections of the wake region of the cylinder over 75 shedding cycles at $Re=3900$. – depicts LES results and experimental data are sketched from *: [10] and Δ [11].

B. Recurrence statistics

To start with the rCFD procedure, an adequate amount of data should be saved in the database. In this process, we recorded a database over 5 shedding cycles with the recurrence frequency 450 times greater than shedding frequency ($f_{rec} = 450 f_{vs}$) and calculated the distance matrix. Fig. 4 displays the concluded distance plot. The periodicity of the flow can be observed in this plot. However, by plotting a line for two times corresponding to $t = 1$ and $t = 2 \tau_{vs}$ in Fig. 5, we can conclude that although parallel to the main diagonal the local minima are located at the multiples of f_{rec} , the flow is not fully periodic. That's the reason why we need to cover several shedding cycles in our database.

C. Species transport

The final step after storing the required data and calculating the distance matrix is to carry on the process only with solving one mass transport equation. As described we studied species transport by adding a source in the wake region. A qualitative comparison of the time-averaged amount of species is demonstrated in Fig. 6. Also to have a quantitative comparison we plotted the time-averaged species profiles at different sections of the wake region in Fig. 7. As we can see rCFD is in a very good agreement with LES, and the error of total amount of species in the domain is less than 1.1%. It can be noted that there is no need for fine mesh to solve a passive scalar equation and it can be done in an extremely short time by using rCFD.

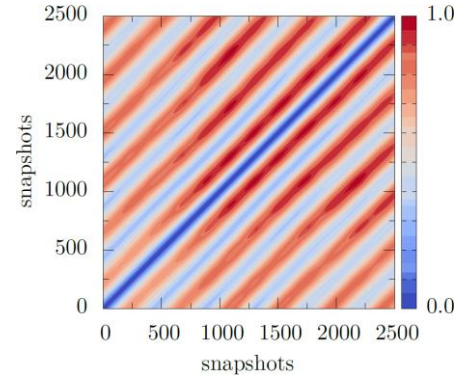


Figure 4. The distance plot calculated for a database comprised of 5 vortex shedding periods. Parallel to the main diagonal, weaker local minima are located which are separated by pronounced maxima.

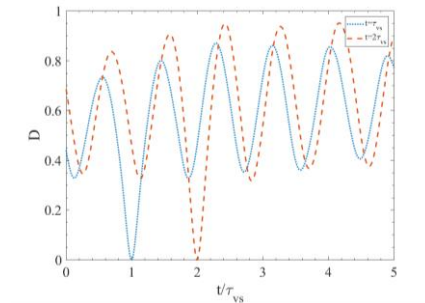


Figure 5. Line plots for distance norms at the times of 1 (–) and 2 (–). Local minima shows the periodicity at multiples of shedding frequency, however the flow is not fully periodic.

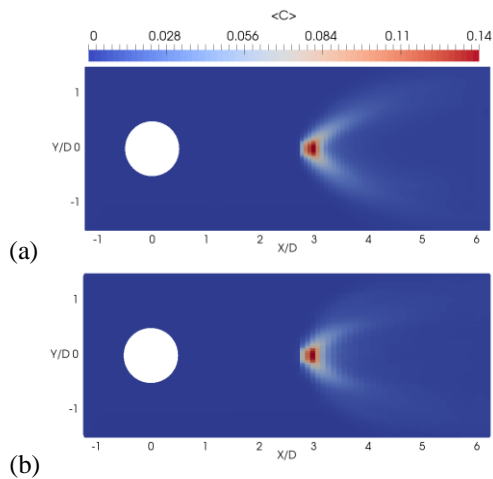


Figure 6. Snapshots of mean species over 75 shedding cycles in the wake region for (a) LES and (b) rCFD. The results are comparable.

D. Performance

Now we talk about the efficiency of rCFD method comparing to LES. We noted that rCFD computational grid was about 8 times coarser than LES. Additionally, rCFD time step was 5 times greater than the LES time step which resulted in the improvement of the performance. The computation time was decreased substantially and the process was approximately 100 times faster than the full simulation. The LES carried out on 40 processors with a total time of 220 hours, on the other hand the simulation time for rCFD in total for this case was about 2 hours only on 4 processors. Although there was a requirement of higher memory (almost 80 GB), we still could reduce the computational cost considerably and run a simulation for whatever longer times that we want in a very short time.

V. CONCLUSION

In this paper, we demonstrated the application of the rCFD method by performing LES and rCFD for the turbulent vortex shedding after a cylinder at Reynolds number 3900 and with the purpose of studying the species transport we added a constant source after the cylinder in the wake region. The good agreement of time averaged species between rCFD and LES represents that short time series of the velocity field contain most of the relevant information required for long-term studies if reappearing patterns prevail and smallest-scale structures are not of interest. The speed-up factor of two orders of magnitude is the outcome of mesh coarsening and reduction of the temporal resolution. In conclusion, we can state that rCFD has been really successful in decreasing the computational cost along with maintaining the accuracy. The future work will be done on examining the method's accuracy and its limit by further mesh coarsening and greater time intervals for our database, and also apply the method to coupled, multi-phase problems.

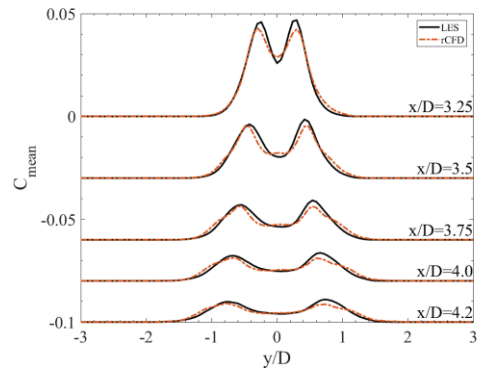


Figure 7. Mean species profiles at different section of the wake region over 75 shedding cycles at $Re=3900$. rCFD shows promising results on a very lower spatial and temporal resolution compared to LES.

ACKNOWLEDGMENT

This work was partly funded by the Linz Institute of Technology (LIT), Johannes Kepler University (project LIT-2016-1-YOU-007). We furthermore acknowledge the support from K1-MET GmbH metallurgical competence center.

REFERENCES

- [1] T. Lichtenegger and S. Pirker, "Recurrence CFD - A novel approach to simulate multiphase flows with strongly separated time scales", *Chem. Eng. Sci.*, Vol. 153, pp. 394-410, 2016.
- [2] J.P. Eckmann, S.O. Kamphorst, and D. Ruelle, "Recurrence plots of dynamical systems", *Europhys. J.*, Vol. 4, pp. 973-977, 1987.
- [3] Pope S.B., *Turbulent Flows*, Cambridge University Press, 2000.
- [4] Smagorinsky, J., General circulation experiments with the primitive equations, *Mon. Weather Rev.*, Vol. 91, pp. 99-164, 1963.
- [5] T. Lichtenegger, E.A.J.F. Peters, J.A.M. Kuipers and S. Pirker, "A recurrence CFD study of heat transfer in a fluidized bed", *Chem. Eng. Sci.*, Vol. 172, pp. 310-322, 2017.
- [6] S. Abbasi, S. Pirker, T. Lichtenegger, "Application of recurrence CFD (rCFD) to species transport in turbulent vortex shedding", unpublished.
- [7] P. Beaudan, and P. Moin, "Numerical experiments on the flow past a circular cylinder at sub-critical Reynolds number", NASA STI/Recon Technical Report, Report No. TF-62, 1994.
- [8] D.A. Lysenko, I.S. Ertesvåg and K.E. Rian, "Large-Eddy Simulation of the Flow Over a Circular Cylinder at Reynolds Number 3900 Using the OpenFOAM Toolbox", *Fl. Turb. Combust.*, Vol. 89, pp. 491-518, 2012.
- [9] V. D'Alessandro, S. Montelpare and R. Ricci, "Detached-eddy simulations of the flow over a cylinder at $Re = 3900$ using OpenFOAM", *Comp. and Fluids*, Vol. 136, pp. 152-169, 2016.
- [10] P. Parnaudeau, J. Carlier, D. Heltz, and E. Lamballais, "Experimental and numerical studies of the flow over a circular cylinder at Reynolds number 3900", *Phys. Fluids*, Vol. 20, pp. 85-101, 2008.
- [11] L. Ong and J. Wallace, "The velocity field of the turbulent very near wake of a circular cylinder", *Exp. in Fluids*, Vol. 20, pp. 441-453, 1996.
- [12] L.M. Lourenco, and C. Shih, "Characteristics of the plane turbulent near wake of a circular cylinder". A particle image velocimetry study, Published in Kravchenko and Moin (2000), 1993.
- [13] A.G. Kravchenko and P. Moin, "Numerical studies of flow over a circular cylinder at $Re_D=3900$ ", *Phys. Fluids*, Vol. 12, pp. 403-417, 2000.

THE ROD-AIRFOIL PROBLEM: CAPABILITIES AND LIMITATIONS OF QUASI-TWO DIMENSIONAL COMPUTATIONS FOR PREDICTION OF NEAR-FIELD VELOCITY FLUCTUATIONS

Hanieh Khalili Param

Department of Mechanical, Automotive, and Material
Engineering
University of Windsor
Windsor, ON N9B 3P4 Canada
e-mail: khalilih@uwindsor.ca

Jeffrey J. Defoe

Department of Mechanical, Automotive, and Material
Engineering
University of Windsor
Windsor, ON N9B 3P4 Canada
e-mail: jdefoe@uwindsor.ca

Abstract— In this paper the classical rod-airfoil problem is treated numerically with a quasi-2D approach. Unsteady Reynolds-averaged Navier-Stokes (URANS) computations, scale adaptive simulations (SAS), and large eddy simulations (LES) are employed. The focus is on near-field velocity data. The free stream Mach number is 0.2 and Reynolds number, based on the rod diameter, is 48,000 with zero airfoil angle of attack. Comparisons with experimental data are carried out for mean and root-mean-squared velocity fields as well as velocity autocorrelation spectra. The key findings are that (1) despite using a quasi-2D computational domain, the time-averaged quantities are in general in good agreement with the experiments, especially for the LES results; and (2) it is possible to correct near-field spectra data from the quasi-2D computations to predict the frequency distributions of the local velocity fluctuations to within reasonable agreement with experiment. More specifically, the URANS and SAS computations overestimate the strength of the rod vortex shedding, yielding over-prediction of the associated tonal velocity fluctuations. On the other hand, the LES computation captures the broadband fluctuations accurately but fails to produce strong tonal fluctuations due to the restrictions on coherent structures size imposed by the quasi-2D domain.

Keywords- *Tonal noise, broadband noise, large eddy simulation, scale-adaptive simulation, velocity spectra, URANS model, rod-airfoil configuration.*

I. INTRODUCTION

The classical rod-airfoil problem is often used as a benchmark for numerical approaches for the prediction of aeroacoustic noise generation and/or propagation [1, 2]. This is due to both the availability of experimental data [3] and the relatively simple problem geometry. This configuration involves an airfoil located in the wake of a cylindrical rod in an external flow. At high Reynolds numbers, the nature of flow is turbulent which produces random perturbations in the rod wake

region that are combined with periodic Strouhal vortex shedding. When the turbulent eddies interact with the downstream airfoil, additional noise sources arise. Many numerical studies have been carried out for this configuration to predict sound spectra radiated by the turbulent flow. Casalino et al., studied this problem applying unsteady URANS simulation on a two dimensional domain. They used a statistical model in a time-domain acoustic analogy to consider three dimensional spanwise effects for far-field noise prediction. As a results, sound prediction accuracy improved about 20% and the broadband part of the noise is well predicted [4]. The Large Eddy Simulation (LES) approach has been widely implemented for this configuration as well. For the first time, Boudet et al. carried out LES simulations (finite volume method) on multi-block structured grids using the Ffowcs Williams & Hawkings (FW-H) acoustic analogy for far field noise prediction, and compared it to the experimental far field spectra [1]. Greschner et al. studied far-field pressure spectra conducting a Detached Eddy Simulation (DES)/FW-H aeroacoustic approach by using the acoustic analogy both with and without volume source terms, that is, by using a permeable surface vs. the airfoil/rod surfaces for integration of the near-field acoustic pressure. It was demonstrated that including the volumetric source terms increases the accuracy of broadband noise prediction for frequencies above 3 kHz [5]. Berland et al. [6] used the direct noise calculation of the sound sources for an airfoil in the wake of a rod by using high order spectral-like compressible LES simulations. An overset grid method was applied due to the complexity of the geometry to deal with turbulent flow developments as well as the radiated sound field around multiple solid bodies. The consistency of turbulence statistics results as well as the sound radiation in the far-field with the measured data, proved that using of high-order discretization tools on overset grid makes it feasible to perform direct noise calculations. Giret et al. employed LES on an unstructured grid for studying the noise generated by the rod wake interaction with the airfoil, introducing an advanced-time formulation of the FW-H acoustic analogy. They assessed the influence of two parameters, the spanwise extent of the

computational domain as well as the sensitivity of the results to the rod/airfoil misalignment. It was demonstrated that larger spanwise extents improves the prediction accuracy for acoustic pressure at lower frequencies. Small changes to the rod-airfoil alignment did not yield significant improvements in agreement with the experimental data despite the fact that a small amount of misalignment was observed in the experimental setup. A non-dimensional uncertainty of ± 0.4 (based on rod diameter) between the axes of the rod and airfoil causes an uncertainty of 0.5-1.0 dB in overall sound pressure level [7].

From the perspective of experimental studies, Jacob et al.'s work [3] has been the most prominent set-up since they provided extensive aerodynamic results as well as aeroacoustic data for both near-field and far-field which facilitated other researchers' numerical work to be benchmarked. The spanwise extent of the test-bed in Jacob's work, was about 30 rod diameters which requires large meshes for aeroacoustic numerical simulations and leads to high computational costs. Therefore, numerical computational domains are typically modified in spanwise extent. Despite accelerating the acoustic calculations, the sound pressure level (SPL) obtained from the numerical results must be modified to be comparable with experiment. Kato [8, 9] proposed corrections, to be applied to the numerical sound pressure level (SPL) in the far-field for computational domains with different spanwise extent than the experimental set-up.

It is inferred from this brief review that, despite several studies of the rod-airfoil configuration, to the best of the authors' knowledge, application of the Scale Adaptive Simulation (SAS) model [10, 11] for the prediction of flow physics and radiated noise has not been done and thus no comparisons of this prediction approach to other Scale Resolving Simulation (SRS) methods exist. Most studies have utilized three dimensional geometry with hybrid acoustic approaches for far-field noise prediction, even though the aerodynamic near-field has been simulated with high fidelity approaches, such as LES. The objective of this paper is to compare the ability of different numerical models to capture the detailed physics of the turbulent near-field flow. To render the problem tractable, a quasi-two dimensional (2D) computational domain is considered. Thus a second objective is to assess the feasibility of implementing such a quasi-2D computational domain by imposing modifications to the velocity fluctuations in the near field, to correct the numerical results. Since far-field noise prediction using acoustic analogy methods such as the FW-H approach relies on accurate generation of the acoustic sources and their propagation to an integration surface, the far-field noise is fundamentally governed by the near-field predictions [5, 12]. Three unsteady CFD approaches are considered: URANS, SAS, and LES.

The key findings are that (1) despite using a quasi-2D computational domain, the time-averaged quantities are in general in good agreement with the experiments, especially for the LES results; and (2) it is possible to correct near-field spectra data from the quasi-2D computations to predict the frequency distributions of the local velocity fluctuations to within reasonable agreement with experiment.

II. METHODOLOGY

A. Computational Domain and Boundary Conditions

Fig. 1 shows schematic view of the computational domain employed in this paper, which is based on Jacob et al.'s [3] work. The configuration consists of a rod as well as a NACA0012 airfoil located one chord downstream of the rod. The rod diameter is one-tenth of the airfoil chord and its center is aligned with the airfoil chord line. The computational domain extends three airfoil chords away from the line of symmetry in the y direction. The inlet boundary is located 5 chords upstream of the airfoil leading edge and the outlet boundary is located 8 chords downstream of the airfoil trailing edge. This computational domain size is known to be sufficient from the literature for near-field fluctuations studies [2, 7].

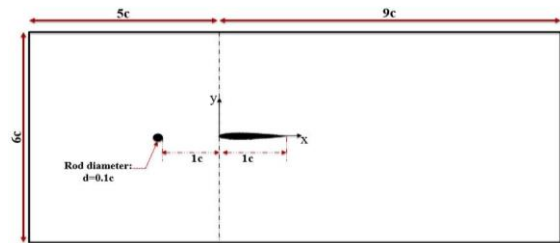


Figure 1. Computational domain used in this paper

The flow condition considered is an angle of attack of zero, Reynolds number based on rod diameter $Re_d=48000$, and free-stream Mach number of approximately 0.2. This condition has been assessed in the literature, so it is expected that the broadband fluctuations are the dominant contributors to the total fluctuating energy in the near field [3, 13]. Recall that, in Jacob et al.'s experimental setup, the spanwise length of the rod and airfoil was three airfoil chords (30 rod diameters). In this paper we consider a quasi-2D approximation of this experimental setup: a single cell in the spanwise direction is used, with spanwise size of $d/30$. Details of the boundary conditions are provided in Table 1. For the SRS models (SAS & LES), the vortex method was employed at the inlet boundary condition to add perturbations in space and time onto the mean velocity as detailed by Mathey et al. [14].

TABLE I. SUMMARY OF BOUNDARY CONDITIONS

Boundary	Boundary Condition Type
Inflow	Uniform velocity inlet
Outflow	Pressure outlet
$z/d=\pm 1/60$	Periodic boundary condition
$y/d=\pm 30$	Symmetry boundary conditions
Rod & Airfoil Walls	No slip wall boundary conditions with standard wall function

B. Governing Equations and Numerical Model

The transient form of the incompressible three-dimensional Navier-Stokes equations are employed. The incompressible approximation is justified by the fact that for the vast majority of the flow field, the Mach number is expected to be below 0.3; only for a very small region around the rod would the Mach number be expected to be much higher (at most 0.4). Further,

in the literature, both incompressible and compressible approaches have been used to solve the rod-airfoil problem [13], with no significant difference observed for the near-field fluctuating quantities. Of course it is not possible to capture acoustic propagation due to the incompressible approach, but local values of fluctuating quantities can still be assessed. For RANS simulations, the realizable $k-\varepsilon$ model [15, 16] is employed. The LES computations employ the dynamic sub-grid scale (SGS) model [17, 18]. The finite volume method [16] is utilized for discretization of the governing equations in the commercial solver ANSYS Fluent 19.0. Pointwise V18.2R1 is utilized to create a fully structured, multi-block hexahedral mesh. The blocking topology (O-grid type as well as a C-grid type) and grid resolution around the rod and airfoil is displayed in Fig. 2 for the finest grid used.

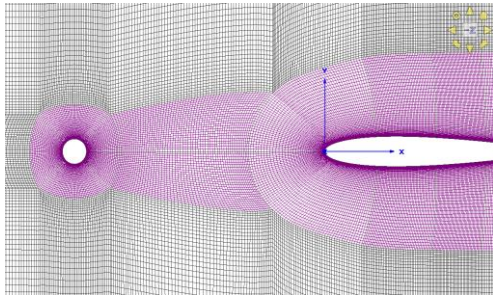


Figure 2. Zoom view in blocking topology and grid resolution around the rod and airfoil

To determine an appropriate boundary layer grid resolution for the LES computation, the wall $\Delta y^+ = y / \left(\nu \sqrt{\rho / \tau_w} \right)$ is kept on the order of unity, but also Δx^+ and Δz^+ are kept below 20 and 40 respectively to resolve wall boundary layers properly [19]. To correctly capture the development of the flow field, a suitable time step size should be selected corresponding to a Courant–Friedrich–Lewy (CFL) number below 0.5 which yields a non-dimensional constant time step size of $\Delta t / (c / U_0) = 7.2 \times 10^{-4}$. The total flow time for the SAS and LES computations is determined by convergence of the statistics. This resulted in a total flow time of almost 14 domain flow-through times. The time averaging process is launched after 7 flow-through times by washing out the initial transient conditions and attaining a semi-steady state operating condition. Thus, data sampling is done over the last 7 flow-through times. Table 2 comprises a summary of the numerical details and discretization schemes.

To find an appropriate overall grid resolution for the SRS computations, three grids with approximately 4×10^4 (coarse), 1×10^5 (medium), and 2×10^5 (fine) cells are assessed with RANS simulations. The relevant metric is the ratio of the integral length scale (L_0) to grid spacing and a target range of 5-10 is required to obtain a proper LES solution [20]. However to make this assessment with RANS computations, the solution also needs to be grid-independent; Table 3 compares the averaged values of mean and root mean squared (RMS) velocities at different streamwise locations (x/c) located at the symmetry plane ($z=0$) for the three grids. The mean flow characteristics are converged to within 8% for the fine grid.

Though this suggests there may be a benefit to further grid refinement, the fundamentally unsteady nature of the flow means that better convergence using RANS is unlikely. L_0 is estimated by $k^{1.5} / \varepsilon$, where k is the turbulence kinetic energy and ε is the turbulent eddy dissipation rate, for the medium and fine grids. Based on this assessment, the fine grid is the only one adequate for use in the LES computation. For consistency, this fine grid is used for the URANS and SAS computations too.

Fig. 3 displays the L_0 / Δ contour in the range between 5 and 20 for the fine grid which verifies the adequate grid resolution for the SRS simulations. Higher values (i.e., $L_0 / \Delta > 20$ areas without contour) imply higher grid points per integral length scale, or higher spatial resolution. Finally, Δy^+ is checked for the fine grid near the rod and airfoil walls. The highest value of Δy^+ is lower than 2.5, which is an acceptable value for SRS models [19].

TABLE II. SUMMARY OF NUMERICAL METHODS

Parameter	Description
Pressure–velocity coupling algorithm	SIMPLE algorithm
Time discretization	Implicit second-order scheme
Convection term	Bounded Central difference scheme
Non-dimensional time step size	7.2×10^{-4}
Sampling time	7 flow-through times ($\approx 120,000$ time steps)

TABLE III. GRID DEPENDENCY STUDY

Parameter	Location (x/c)	Grid Size		
		Coarse	Medium	Fine
$\frac{U_0 - U_{mean}}{U_0}$ (%)	-0.87	10.86	10.92	11.3
	-0.25	4.96	4.3	4.65
	0.25	0.03	-0.14	-0.16
	2	6.58	8.32	8.8
$\frac{U_0 - u_{rms}}{U_0}$ (%)	-0.87	89.75	95.3	95.62
	-0.25	98.5	96.4	98.1
	0.25	81.3	93.2	98.05
	2	89.2	96.51	97.8

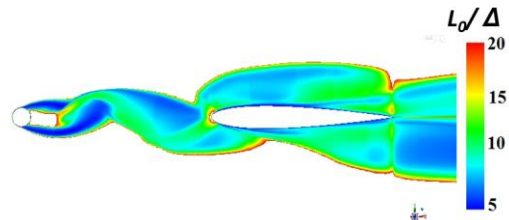


Figure 3. Integral length scale to grid spacing ratio (L_0 / Δ) contour for fine grid

III. DISCUSSION OF RESULTS

A. Verification of Results: Mean and RMS velocity profiles

Fig. 4 illustrates the non-dimensional mean axial velocity contour for the LES computations. The vertical black lines show the locations where the comparison between numerical simulations and experimental data is done. Fig. 4 demonstrates that the averaged velocity field is symmetric which indicates that the unsteady solution is no longer influenced by the initial transients. The mean and RMS velocity profiles for the URANS, SAS as well as LES computations are compared against Jacob et al.'s [4] measurements at four axial locations: (a) incoming flow before the rod at $x/c = -2.21$, (b) wake region between rod and airfoil at $x/c = -0.87$, (c) aside the airfoil at $x/c = 0.25$, and (d) downstream of the airfoil trailing edge at $x/c = 2$. Fig. 5 depicts mean velocities while Fig. 6 shows the RMS velocities. All velocities are nondimensionalized with the free-stream velocity U_0 . The experimental data for $|y|/c > 1$, as a result of being influenced by the jet shear layer effect, are not valid for the assessment of numerical simulations [3, 6, 13, 21]. So the discussion which follows is restricted to $|y|/c \leq 1$.

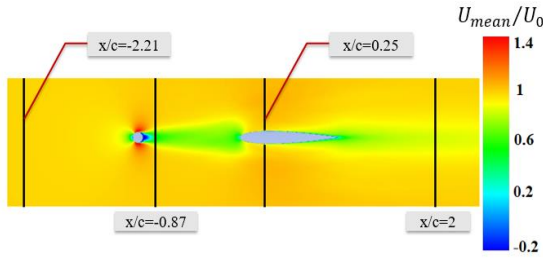


Figure 4. Nondimensional mean axial velocity contour at mid-plane for LES model

The incoming flow at $x/c = -2.21$ is highly uniform for all three numerical approaches, with low turbulence ($u_{rms}/U_0 \approx 0.78\%$). These results are in good agreement with the experimental data for the region of interest, $|y|/c < 1$.

Fig. 5 (b) and 6 (b) show the mean and RMS axial velocity profiles between the rod and airfoil (at $x/c = -0.87$), respectively. At this location, the mean velocity is significantly decreased near the center-line ($|y|/c < 0.25$) due to the presence of the rod wake. The turbulence intensity is markedly increased within the wake (see Fig. 6 (b)). The wake is also narrower in the URANS computation by 50%. The SAS approach correctly resolves the wake width and depth. The wake depth is over-predicted by the LES computation; this is thought to be an artifact of the quasi-2D approach used. Also, the URANS and SAS models could not capture the turbulence intensity variation in the wake region (instead showing low turbulence in the center of the wake), whereas, LES results show the most promising agreement with the experimental data in this area, though over-prediction again occurs, consistent with the mean wake characteristics. The totally different prediction of turbulence intensity variation by URANS in this

location has been shown in literature as well [1]. Beyond $|y|/c = 0.2$ (out of the wake), the LES and SAS models show excellent agreement with the measurements with the error below 2%.

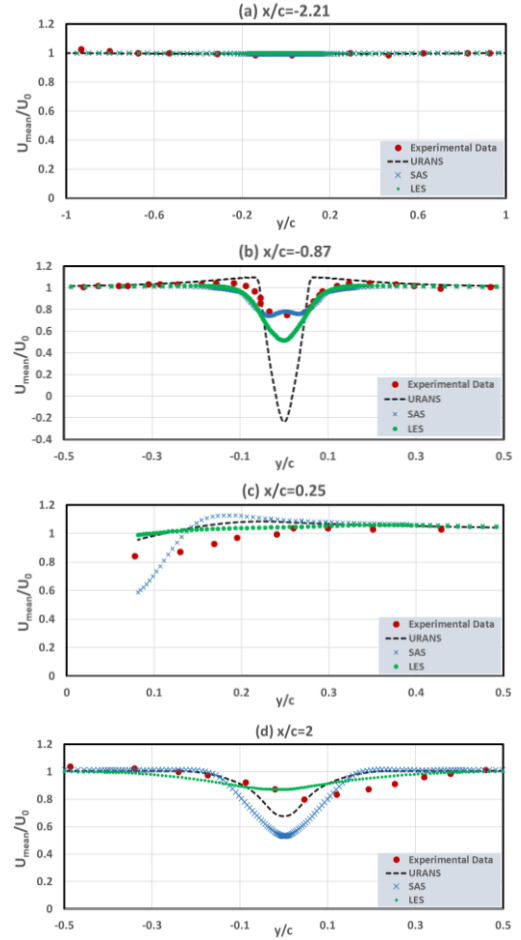


Figure 5. Comparison of mean velocity profiles with experimental data at: (a) $x/c = -2.21$; (b) $x/c = -0.87$; (c) $x/c = 0.25$; (d) $x/c = 2$

Fig. 5 (c) and 6 (c) illustrate the mean and RMS velocity profiles further downstream, aside the airfoil ($x/c = 0.25$). Experimental data for velocity profiles are available only on one side of the airfoil ($y > 0$) at this location; thus the CFD data is only shown for this region. Owing to the symmetric geometry, the CFD data is identical for $y < 0$ for time-averaged profiles. The SAS model predicts a significant velocity decrease close to the airfoil surface. It seems that this velocity deficit results from overestimating the strength of the induced vortex shedding behind the rod. This strong vortex shedding will be affected less by dissipation (vortex break-down) in the SAS computations and will be stretched further downstream over the airfoil leading edge. Tracking the instantaneous vorticity field at several successive time intervals supported this justification. For $y/c > 0.2$, all the numerical approaches predict minimal influence from the rod-airfoil system for the mean velocity (the velocity is essentially the free-stream value). In Fig. 6(c), despite the over-estimation of turbulence

intensity in the LES computation, the trend is well captured. This suggests that the diffusion of turbulent eddies away from the airfoil is being well-captured by the LES computation.

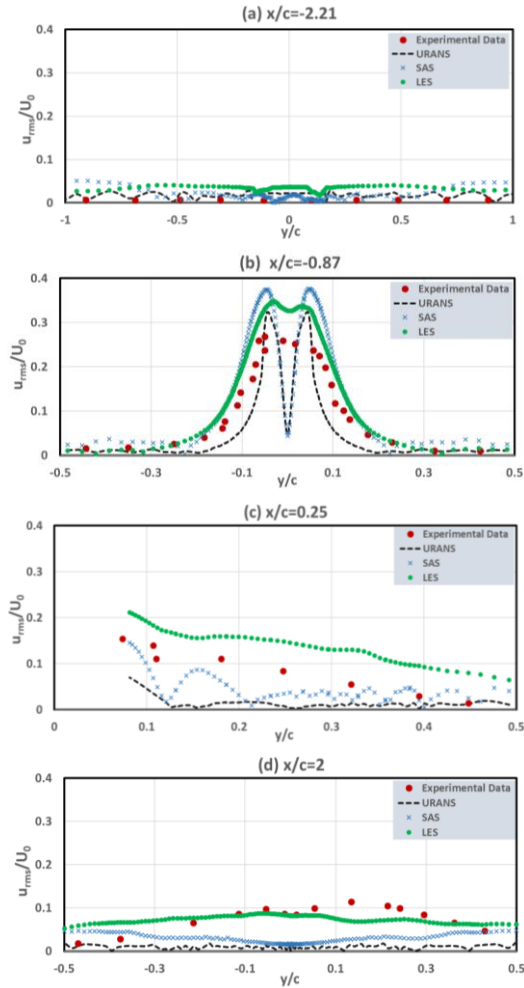


Figure 6. Comparison of RMS velocity profiles with experimental data at: (a) $x/c = -2.21$; (b) $x/c = -0.87$; (c) $x/c = 0.25$; (d) $x/c = 2$

Finally, the mean and RMS axial velocity profiles in the wake of the airfoil are depicted in Fig. 5 (d) and 6 (d). Note that there are two main differences between the experiment and simulations: (1) The airfoil is somewhat offset in the positive y -direction by about 2% of chord in the experiment, and (2) there is a slight angle-of-attack (around 2°) for the airfoil. These make the measured profiles slightly asymmetric, whereas the averaged numerical profiles are nearly symmetric. Due to the slight asymmetric condition in the experimental setup, the peak of the velocity deficit for the hot-wire data is not aligned with the numerical results (See Fig. 5(d)). However, for both mean and RMS but especially the RMS profiles, the LES results fitted better to the measurements. The maximum error of LES prediction for mean velocity is below 10%. The SAS computation overestimates the mean velocity reduction in the airfoil wake, even more so than does the URANS approach. Out of the wake region, the consistency between numerical results and measured data improves significantly for mean velocity.

To illustrate major vortical structures, the z -vorticity field which is made non-dimensional based on the rod diameter and incoming velocity ($\omega d/U_0$), is presented in Fig. 7 for the three models.

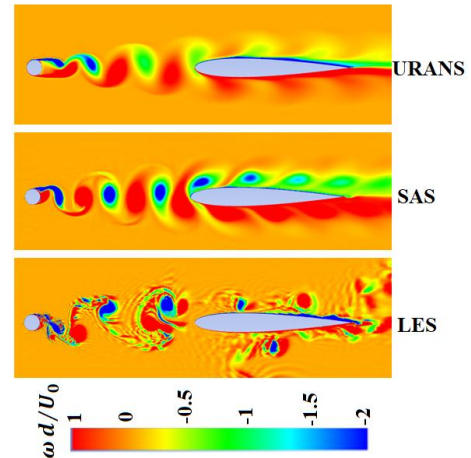


Figure 7. Non-dimensional z -vorticity contours at mid-plane for three different turbulent models; Top: URANS; Middle: SAS; Bottom: LES

The three pictures demonstrate how the vortices shed behind the rod interact with the airfoil. The two sets of vortices shed from each side of the rod are rolling up and impinging on the airfoil leading edge in the URANS and SAS computations. Even aside the airfoil the shed vortices remain clearly defined, while more vortex break-down is visible in the LES computation. The instantaneous snapshot confirms that RANS only predicts the von-Karman vortices that are arranged in a stable deterministic vortex street. SAS compared to URANS seems to show sharper gradients of velocity – there is less eddy dissipation. This introduces extra harmonics to the tonal fluctuations captured by the Strouhal vortex shedding. It will be demonstrated in the next section, where velocity spectra are presented, that the rod vortex shedding is strongly over-predicted by the URANS and SAS computations. In contrast, the contour plot from the LES computation provides a visual depiction of the breakdown of the vortices shed from the rod to a wide range of scales, indicative of broadband fluctuations in the local flow variables. The vortical structures also extend further in the transverse direction owing to the presence of small structures rather than strong von-Karman vortices which can be convected further downstream (along x direction) with less dissipation.

B. Power spectral density (PSD) Results: Velocity Spectra

The mean and RMS velocity distributions are unable to indicate the frequency content of the unsteady fluctuations. For this, we employ the power spectral density (PSD) of the velocity fluctuations. Experimental data are available at a few locations in the near-field rod wake region close to the airfoil. Power spectral density is defined as the magnitude of the Fourier transform of the autocorrelation of a variable (here chosen to be the velocity component in the free-stream direction due to the availability of experimental data). Since there is a huge discrepancy between the spanwise extent of the

test-bed in Jacob's experimental (about 30d) and our quasi-2D computation (d/30); 900 times smaller, thus corrections are required to compare spectral results from the current computations to Jacob's experimental data. As mentioned earlier, Kato [8] proposed corrections, to be applied to the numerically predicted sound pressure level (SPL) in the far-field, as follows:

$$SPL_e = SPL_s + 10 \log \left(\frac{L_e}{L_s} \right); \text{ for } L_c \leq L_s \quad (1)$$

$$SPL_e = SPL_s + 10 \log \left(\frac{L_e}{L_c} \right) + 20 \log \left(\frac{L_c}{L_s} \right); \text{ for } L_s \leq L_c \leq L_e \quad (2)$$

$$SPL_e = SPL_s + 20 \log \left(\frac{L_e}{L_s} \right); \text{ for } L_e \leq L_s \quad (3)$$

Where SPL_e and SPL_s are for the sound pressure level (SPL) of experimental and numerical models, respectively. Also, L_e and L_s represent the span of the experimental and numerical models. L_c is the equivalent coherence length for surface pressure fluctuations in the spanwise direction which is estimated, for the problem currently under consideration, to be 6.5d-7d from Jacob et al.'s experimental work [3]. Since our computational domain's spanwise extent is smaller than the coherence length scale, equation 2 would be applicable if far-field data was the focus. Equation 2 can be rewritten in the following form:

$$SPL_e = SPL_s + 10 \log \left(A \frac{L_c L_e}{L_s^2} \right); \text{ for } L_s \leq L_c \leq L_e \quad (4)$$

where A is a constant which is equal to unity for Kato's approach. This correction has been employed successfully in the literature [5, 13, 22], including for cases where the far-field SPL_s are obtained using acoustic analogy approaches such as the FW-H method [5, 22]. This implies that the correction is actually applied to the near-field fluctuations since the propagation to the far-field is done analytically rather than as part of the solution of the governing equations. Therefore, in this paper we explore the application of Kato's correction to the near-field spectra directly. It can also be shown that a constant correction to an overall SPL is equivalent to the same correction being applied to all frequencies comprising the spectrum from which the overall SPL is computed. This further implies that the actual fluctuating signal can be amplified by the correction factor, allowing the same correction approach to be applied to the spectra of autocorrelations [13]. In this paper, we demonstrate for the first time that even by considering quasi-2D numerical models, the near-field velocity spectra can be corrected in a manner analogous to Kato's approach. The results of all numerical simulations with different models in this paper are examined at various locations and finally the following formula for near-field autocorrelation spectra is proposed, following the form of Equation 4:

$$S_{uu}(\omega)_e = S_{uu}(\omega)_s + 10 \log \left(A \frac{L_e L_c}{L_s^2} \right); \text{ for } L_s \leq L_c \leq L_e \quad (5)$$

A is a constant (depends on neither frequency nor location) which is equal to 2.0×10^{-4} . This value maximizes agreement

between the all numerical simulations and the measured data. The corrected velocity autocorrelation spectra are presented for the three numerical models in Figs. 8 and 9. Fig. 8 depicts nine velocity spectra for three different traverse locations (at $x/c = -0.87$) at the region near rod wake. The spectra (in dB) are plotted against the dimensionless frequency.

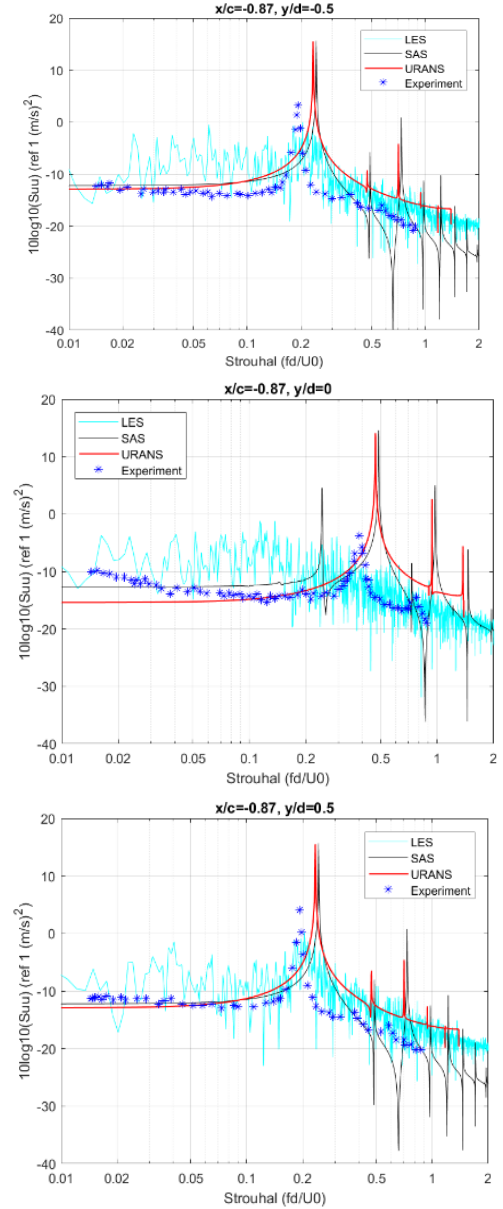


Figure 8. Velocity spectra profiles at three different transverse positions along the same axial location ($x/c = -0.87$)—Comparison of three numerical models, URANS, SAS and LES against measured data

As described in the previous section, the fluctuations in this region are mainly due to the vortices shed from the rod. The shedding Strouhal number is about 0.19 which can be seen in the plots of the upper and lower points (i.e., $y/d = \pm 0.5$) as the location of peak in the experimental data. At these two points the shedding frequency is predicted to be higher (about 20%) by the URANS and SAS models. The velocity fluctuations at

these locations are mainly affected by the vortices which are shed from one side of the rod whereas the vortices from both sides of the rod contribute equally to the velocity fluctuations at points on the x-axis. In both cases the fundamental frequency is supplemented by harmonics. This is visible in the experimental data as well as the URANS and SAS computational results.

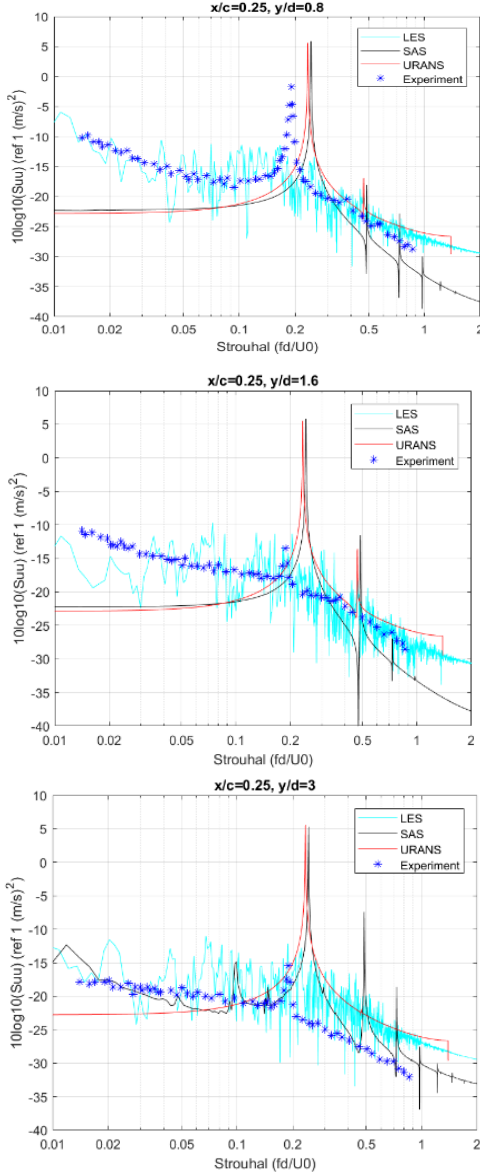


Figure 9. Velocity spectra profiles at three different transverse positions along the same axial location ($x/c = 0.25$)—Comparison of three numerical models, URANS, SAS and LES against measured data

The broadband portion of the spectrum is relatively well-captured by the corrected LES results, though no peaks are predicted. It is nearly the opposite for the URANS and SAS approaches: it is primarily tonal peaks that are predicted. The general roll-off of amplitude with frequencies above the fundamental shedding frequency is captured by all three numerical approaches. The URANS and SAS over-predict the amplitude of the tonal fluctuations as well as the exact value of shedding frequency. The amplitude of the broadband spectrum

is well-captured by the LES computations and at the upper and lower points, the dominant Strouhal number is captured, though it is more of a hump in the broadband spectrum than a strong tone. For the centre point, the shedding frequency cannot be observed in the LES data. To the best of the authors' knowledge, the relative reduction in the tonal components of the spectra for the LES computation is attributable to the quasi-2D computational domain: this constrains the size of coherent structures that can form. The main difference between URANS and SAS spectra is that the SAS data predicts additional tonal peaks due to reduced eddy dissipation. Fig. 9 shows the velocity autocorrelation spectra for three points with different vertical distances along the airfoil (i.e., $x/c = 0.25$). Getting far from the x-axis, the experimental results exhibit a decay in tonal fluctuation amplitude. The unsteadiness is still dominated by shed vortices from the rod though the vortex strength has been dissipated due to the distance from rod. Hence, other than the fundamental frequency (i.e., $St=0.19$), other harmonics are hardly visible in the experimental data. Unlike URANS and SAS with sharp peaks, LES shows a wide range of frequencies and the dominant Strouhal number is hard to distinguish. However, the LES results capture the broadband spectral roll-off levels with an acceptable agreement with the measurements. On the other hand, SAS and URANS predict almost the same dominant frequency ($St=0.23$) which is in acceptable range. However, for $y/d = 1.6$ and $y/d = 3$ the amplitude of the peaks is again highly overestimated by these two turbulence models. Similar to Fig. 8, additional tonal fluctuations are predicted by the SAS computation. The low level of these makes it difficult to determine whether they are spurious or physical and simply masked by broadband fluctuations in the experimental data.

IV. CONCLUSION

In this paper the accuracy of three numerical modeling approaches were assessed for the generation of aerodynamic fluctuations as a result of a rod wake interaction with an airfoil. A quasi-2D domain was used for the computations. The comparisons with experimental data were made for mean and root-mean-squared velocity fields as well as velocity spectra. It was demonstrated that a time-dependent description of turbulent eddies is necessary, not only for the prediction of broadband type fluctuations, but also for the accurate estimation of the mean flow field. The mean and RMS velocity profiles from the LES approach yield the best agreement with the measured data, particularly in the wake region. In addition, the comparison of these three models to experiment illustrates that URANS as well as SAS overestimated the strength of the rod vortex shedding (about 200% more than experiment) which is responsible for the high intensity tonal fluctuations. Conversely, the LES approach mainly captured the contribution of small vortical structures which correspond to broadband spectral contents. Utilizing a quasi-2D computational domain seems to be the primary reason for the inability of the LES computations to predict tonal fluctuations (i.e., those from vortex shedding). The key finding of the paper is that following Kato's approach, it is possible to correct the near-field data even in the limit of a quasi-2D computational domain. Further, the magnitude of the correction factor is four orders of magnitude smaller than in Kato's far-field correction,

so less overall amplification (compared to Kato’s expression) of the localized fluctuations is required. This is due to the imposition of two-dimensionality on the flow field. The two-dimensionality also leads to the lack of strong tonal fluctuations in LES, since the size of the coherent structures is restricted in the quasi-2D approach.

V. ACKNOWLEDGMENTS

This work is funded by the NSERC Discovery Grants program. Computational resources are provided by Compute/Calcul Canada.

REFERENCES

- [1] J. Boudet, N. Grosjean, and M.C. Jacob, “Wake-airfoil interaction as broadband noise source: a large-eddy simulation study,” *International Journal of Aeroacoustics*, 2005, 4(1), pp.93-115.
- [2] A. ELTaweel, and M. Wang, “Numerical simulation of broadband noise from airfoil-wake interaction,” 17th AIAA/CEAS Aeroacoustics Conference (32nd AIAA Aeroacoustics Conference), 2011, p. 2802.
- [3] M.C. Jacob, J. Boudet, D. Casalino, and M.A. Michard, “A rod-airfoil experiment as a benchmark for broadband noise modeling,” *Theoretical and Computational Fluid Dynamics*, Vol. 19, 2005, pp. 171-196.
- [4] D. Casalino, M.C. Jacob, and M. Roger, “Prediction of rod-airfoil interaction noise using the Ffowcs-Williams and Hawkings Analogy,” *AIAA Journal*, Vol. 41, No. 2, 2003, pp. 182-191.
- [5] B. Greschner, F. Thiele, M.C. Jacob, and D. Casalino, “Prediction of sound generated by a rod-airfoil configuration using EASM DES and the generalised Lighthill/FW-H analogy,” *Computers & fluids*, 37(4), 2008, pp.402-413.
- [6] J. Berland, P. Lafon, F. Crouzet, F. Daude, and C. Bailly, “Numerical insight into sound sources of a rod-airfoil flow configuration using direct noise calculation,” 16th AIAA/CEAS Aeroacoustics Conference, AIAA, 2010.
- [7] J.C. Giret, S. Moreau, and J.F. Bousuge, “Uncertainty quantification of the far-field noise from a rod-airfoil configuration,” In *Proceedings of the Summer Program*, 2012, pp. 261-270.
- [8] C. Kato, A. Iida, Y. Takano, H.A.J.I.M.E. Fujita, and M. Ikegawa, “Numerical prediction of aerodynamic noise radiated from low Mach number turbulent wake,” 31th Aerospace Sciences Meeting, 1993, p. 145.
- [9] C. Kato, Y. Yamade, H. Wang, Y. Guo, M. Miyazawa, T. Takaishi, S. Yoshimura, and Y. Takano, “Numerical prediction of sound generated from flows with a low Mach number,” *Computers & Fluids*, 2007, 36(1), pp. 53-68.
- [10] F.R. Menter, and Y. Egorov, “The scale-adaptive simulation method for unsteady turbulent flow predictions. Part 1: theory and model description,” *Flow, Turbulence and Combustion*, 2010, 85(1), pp.113-138.
- [11] F.R. Menter, J. Schutze, K. Kurbatskii, R. Lechner, M. Gritskevich, and A. Garbaruk, “Scale-resolving simulation techniques in industrial CFD,” 6th AIAA Theoretical Fluid Mechanics Conference, 2011, pp. 3474.
- [12] K.S. Brentner, “Numerical algorithms for acoustic integrals with examples for rotor noise prediction,” *AIAA journal*, 1997, 35(4), pp. 625-630.
- [13] B.R. Agrawal, and A. Sharma, “Aerodynamic noise prediction for a rod-airfoil configuration using large eddy simulations,” 20th AIAA/CEAS Aeroacoustics Conference, 2014, p. 3295.
- [14] F. Mathey, D. Cokljat, J.P. Bertoglio, and E., Sergent, “Assessment of the vortex method for large eddy simulation inlet conditions,” *Progress in Computational Fluid Dynamics, An International Journal*, 2006, 6(1-3), pp.58-67.
- [15] L. Davidson, “Fluid mechanics, turbulent flow and turbulence modeling,” *Div. of Fluid Dynamics, Dep. of Applied Mechanics, Chalmers University of Technology, Goteborg, Sweden*, 2015.
- [16] H.K. Versteeg, and W. Malalasekera, “An Introduction to Computational Fluid Dynamics: The Finite Volume Method,” Harlow: Pearson Education, 2007.
- [17] U. Piomelli, and J.R. Chasnov, “Large-eddy simulations: theory and applications,” In *Turbulence and transition modelling*, Springer, Dordrecht, 1996, pp. 269-336.
- [18] P. Sagaut, “Large eddy simulation for incompressible flows: an introduction,” Springer Science & Business Media, 2006.
- [19] F.R. Menter, “Best Practice: Scale-Resolving Simulations in ANSYS CFD”, Version 1, Ansys Germany GmbH, 2012.
- [20] L. Davidson, “Large eddy simulations: how to evaluate resolution,” *International Journal of Heat and Fluid Flow*, 2009, 30(5), pp.1016-1025.
- [21] W. Chen, W. Qiao, L. Wang, F. Tong, and X. Wang, “Rod-airfoil interaction noise reduction using leading edge serrations,” 21st AIAA/CEAS aeroacoustics conference, 2015, p. 3264.
- [22] B. Greschner, S. Peth, Y.J. Moon, J.H. Seo, M.C. Jacob, and F. Thiele, “Three-dimensional predictions of the rod wake-airfoil interaction noise by hybrid methods,” 14th International Congress on Sound and Vibration, ICSV, 2007.

Numerical study of turbulent heat transfer of a radially-rotating circular pipe flow

Zhao-Ping Zhang
Dept. of Mechanical Engineering
Univ. of Manitoba
Winnipeg, Canada
umzha258@myumanitoba.ca

Bing-Chen Wang*
Dept. of Mechanical Engineering
Univ. of Manitoba
Winnipeg, Canada
BingChen.Wang@umanitoba.ca

Dao-Qi Liu
College of Science
Inner Mongolia Univ. of Tech.
Hohhot, China
Liudaoqi123@163.com

Abstract—Turbulent heat transfer of a radially-rotating circular pipe flow has been studied using direct numerical simulation (DNS) for a wide range of rotation numbers. In response to the radial system rotation, large-scale secondary flows appear as streamwise counter-rotating roll cells in the cross-stream plane, which significantly impact the transport of momentum and thermal energy. The flow becomes increasingly laminarized on the suction side of the pipe as rotation number increases, reaches a full laminarization state at the highest rotation number tested. The influence of Coriolis forces on turbulence convective heat transfer has been investigated by comparing temperature statistics of rotating pipe flows against those of a non-rotating flow.

Keywords—direct numerical simulation, pipe flow, rotating flow, turbulence, heat transfer

I. INTRODUCTION

Turbulent flows confined within a circular pipe subjected to radial system rotation is considered as an interesting topic in engineering applications, such as rotating machinery, centrifugal separators and turbo-machinery. In response to the system rotation imposed, Coriolis forces are induced, which has a significant impact on the flow field and coherent structures. As a result, large-scale secondary flows occur in the cross-stream direction.

In literature, turbulent heat transfer in spanwise-rotating 2D plane channel or square duct flows has been studied extensively. Liu and Lu [1] conducted direct numerical simulation (DNS) of spanwise-rotating turbulent plane channel flows with heat transfer at different rotation numbers. In their observation, Liu and Lu indicated that the Nusselt number (Nu) increases and decreases on the pressure and suction sides, respectively, in response to the Coriolis forces. Furthermore, they also investigated the the impact of Taylor-Görtler-

like (TGL) vortices, associated with the system rotation, on the thermal statistics. Xun *et al.* [2] performed large-eddy simulation (LES) of turbulent heat transfer in a similar configuration at different rotation numbers. They showed that TGL vortices as streamwise counter-rotating roll cells appear in the cross-stream plane. They also demonstrated that the wall-normal heat flux corresponding to the turbulent motions is strengthened and reduced near the pressure and suction sides, respectively, by the imposed spanwise system rotation. Pallares and Davidson [3] performed a series of LES to study the turbulent heat transfer in stationary and rotating square ducts with respect to constant peripheral wall temperature and uniform peripheral wall heat flux boundary conditions. They indicated that the Nu value and turbulent level of flows are not strongly influenced by different thermal boundary conditions when the imposed rotation number is relative high. In addition, they found that the temperature fluctuation intensities are larger under the uniform peripheral heat flux condition than under the constant peripheral temperature condition. More recently, Fang and Wang [4] performed DNS of turbulent heat transfer confined within a square duct subjected to spanwise system rotation. They systematically studied the impacts of Coriolis forces on different turbulence thermal statistics, and observed that the analogy between the molecular diffusion processes of the momentum and thermal energy in the viscous sublayer is only verified in non-rotating flows and disappears with an increasing rotation number. Fang and Wang [4] also analyzed the budget balance of turbulent heat flux, and concluded that the Coriolis production term, associated with the streamwise turbulent heat flux, tends to strengthen the wall-normal turbulent heat flux in response to the spanwise system rotation.

In the current literature, numerical simulation of fully-developed incompressible turbulent heat flows through a radially-rotating pipe is still lacking in detail. Ishigaki [5] conducted DNS of forced laminar heat transfer in both curved

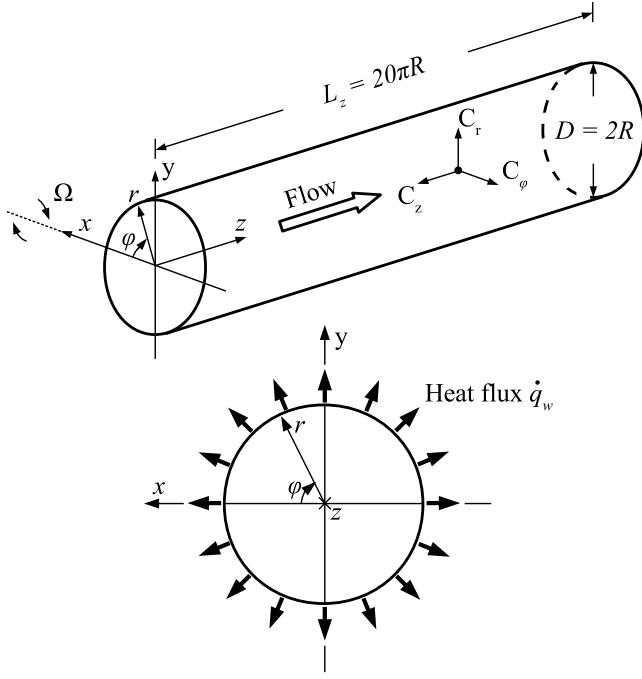


Fig. 1. Cross-sectional view and configuration of a radially-rotating circular pipe in both cylindrical and Cartesian coordinate systems. The symbols of C_r , C_φ and C_z represent three components of Coriolis forces, and the arrows indicate their directions. The flow is cooled along the axial direction by imposing a constant wall heat flux (\dot{q}_w) on the circular wall.

pipes and radially rotating pipes within boundary conditions of uniform peripheral wall heat flux and temperature, respectively, to investigate a similarity of those flows through mean Nusselt number. In view of this, the objective of this paper is to perform a DNS study of turbulent heat transfer for flow in a circular pipe subjected to radial system rotations. In order to investigate the Coriolis effects, a wide range of rotation number will be tested, varying from $Ro_\tau = 0.0$ to 1.0. The mean and turbulent statistics of the temperature field of rotating flows will be compared against those of a non-rotating flow.

II. METHODOLOGY

Figure 1 shows the cross-sectional view and configuration of circular pipe subjected to radial system rotation where r , φ and z represent the radial, azimuthal and axial coordinates of the cylindrical coordinate system, and the three corresponding velocity components are denoted by u_r , u_φ and u_z , respectively. The axial length of the pipe is set to $20\pi R$ where R is the pipe radius. The current domain length is the longest in the literature of DNS of radially-rotating circular pipe flows for fully capturing the most energetic turbulence flow structures in the streamwise direction. In DNS, both pipe flow and temperature fields are fully developed, and periodic boundary condition is applied along the axial direction. No-slip boundary condition is enforced at the circular wall for velocity field. As shown in Fig. 1, the flow is cooled down along the streamwise direction through a uniform peripheral wall heat

flux boundary condition for the temperature field. Therefore, the local mean peripheral wall temperature T_w varies linearly along the streamwise direction. The Reynolds and Prandtl numbers of the flow are fixed to $Re_\tau = u_\tau R/\nu = 180$ and $Pr = 1.0$, respectively. To ensure that the effects of Coriolis forces can be completely investigated, a wide range of rotation numbers ($Ro_\tau = 2\Omega R/u_\tau$) have been tested, varying from $Ro_\tau = 0.0$ to 1.0.

In the radially-rotating reference frame, the governing equations of an incompressible flow regarding to continuity, momentum and thermal energy read as

$$\nabla \cdot \vec{u} = 0, \quad (1)$$

$$\frac{\partial \vec{u}}{\partial t} + \vec{u} \cdot \nabla \vec{u} = -\Pi \hat{e}_z - \frac{1}{\rho} \nabla p + \nu \nabla^2 \vec{u} + \vec{C}, \quad (2)$$

and

$$\frac{\partial \theta}{\partial t} + \nabla \cdot (\vec{u} \theta) = -\Psi + \alpha \nabla^2 \theta, \quad (3)$$

respectively. Here, \vec{u} , θ , ρ , p and α represent the velocity, temperature (defined as $\theta = T - T_w$), density, pressure and thermal diffusivity of the fluid, respectively. Π (defined as $\Pi = (dP/dz)/\rho$) is the constant mean axial pressure gradient, Ψ (defined as $\Psi = u_z(dT_w/dz)$) is the mean axial driving temperature gradient, and \hat{e}_z is the base unit vector of the z -direction, with $|\hat{e}_z| \equiv 1$. Due to a counterclockwise rotation at a constant angular velocity (Ω) acting along the x -direction of the pipe, three Coriolis force components are developed and denoted as $C_r = 2\Omega u_z \sin\varphi$, $C_\varphi = 2\Omega u_z \cos\varphi$ and $C_z = -2\Omega(u_r \sin\varphi + u_\varphi \cos\varphi)$ in the radial, azimuthal and axial directions, respectively. It should be indicated that the pipe flow is cooled along the axial direction under the uniform peripheral heat flux boundary condition so the exchange of thermal energy between the flow and ambient environment maintain steadily along the axial direction. Therefore, both bulk mean temperature (T_b) and local mean peripheral temperature (T_w) decreases linearly along the axial direction, i.e. $dT_b/dz = dT_w/dz = 2\dot{q}_w/(\rho C_p U_b R)$ where \dot{q}_w represent uniform peripheral heat flux, C_p is specific heat of the fluid, and U_b is the bulk mean velocity.

In this paper, an instantaneous quantity Φ can be decomposed as $\Phi = \langle \Phi \rangle + \Phi'$, where $\langle \Phi \rangle$ represents averaged value over both time and homogeneous axial direction, and Φ' denotes a fluctuation of the quantity. In order to express all quantities in wall coordinates, a superscript '+' is imported in here. The overall wall friction velocity ($u_\tau = \sqrt{-\Pi R/2}$) and wall friction temperature ($T_\tau = \dot{q}_w/\rho C_p u_\tau$) is used for non-dimensionalization, such as $\theta^+ = \theta/T_\tau = (T - T_w)/T_\tau$.

All simulations were performed with a spectral-element method (SEM) code so-called "Semtex" developed by Blackburn and Sherwin [6]. The code is based on C++ and FORTRAN programming language, and parallelized using message passing interface (MPI) libraries. Fang and Wang [4] implemented the thermal energy equation into SEM code in order to simulate the heat transfer under a system rotation. The cross

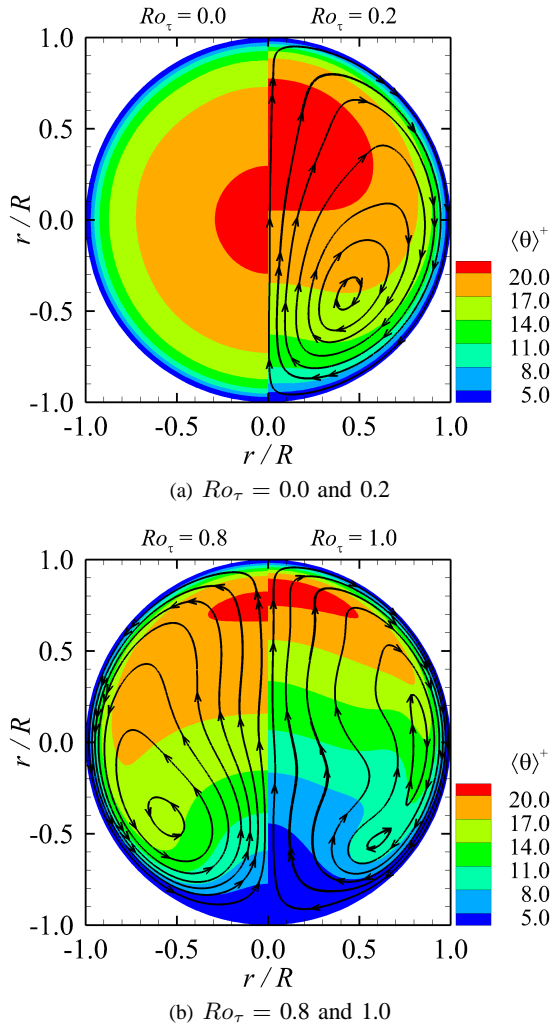


Fig. 2. Contours of mean temperature $\langle \theta \rangle^+$ superimposed with mean streamlines in the cross-stream plane at different rotation numbers.

section of the pipe was discretized with 352 quadrilateral-structural elements. Each element was interpolated using 8th-order Gauss-Lobatto-Legendre (GLL) Lagrange interpolant. All quantities were conducted with Fourier expansion of 960 modes along the axial direction. In total, the pipe domain contains 21.8 million grid points. Therefore, the grid resolution, measured in wall coordinates, is uniform in the axial direction with $\Delta z^+ = 11.78$, and varies in the azimuthal and radial directions with $R\Delta\phi^+ = 1.78\text{-}6.40$, $\Delta r^+ = 0.25$ at the first node off the wall and $\Delta r^+ = 1.03$ at the pipe center. Each simulation was conducted on the WestGrid (Western Canada Research Grid) supercomputer with 300 instantaneous flow and temperature fields (approximately 310 GB data) over 80 large-eddy turnover times (LETOTs, defined as R/u_τ)

III. RESULTS

In this section, statistical moments of the velocity and temperature fields obtained from the DNS are analyzed. In order to understand the effects of the Coriolis forces on

thermal convection, in total 11 rotation numbers are compared, varying from 0.0 to 1.0). We first investigate the mean temperature fields, followed by analyses of the friction velocity, Nusselt number, first- and second-order turbulence statistics, and turbulence structures.

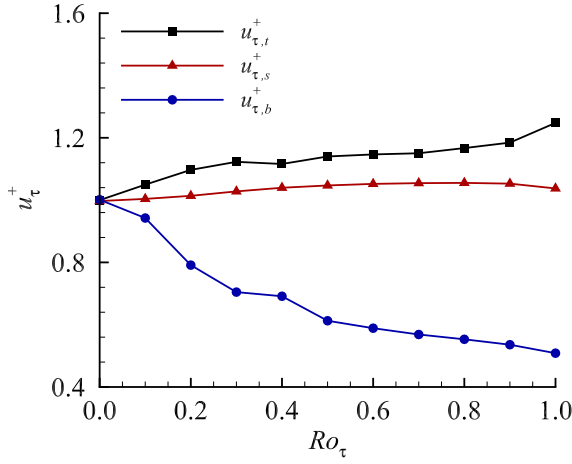
A. Mean Flow and Temperature Fields

Figure 2 displays the mean temperature field $\langle \theta \rangle^+$ and mean streamlines in the cross-stream plane of the pipe at four different rotation numbers. Given the axial symmetry of the mean temperature, only one half of the domain is plotted for each rotation number. In Fig. 2(a), at $Ro_\tau = 0.0$, it is clear that the mean temperature field exhibits a concentric pattern characteristic of a non-rotating Poiseuille pipe flow. At $Ro_\tau = 0.2$, large-scale secondary flows appear as a pair of streamwise counter-rotating vortices near the suction side of the pipe in response to imposed radial rotation. As is evident in Fig. 2, the peak values of $\langle \theta \rangle^+$ (shown with red color region) are pushed toward the pressure side by Coriolis forces as rotation number increases. Eventually, at $Ro_\tau = 1.0$ as shown in Fig. 2(b), the flow becomes fully laminarized. Two pairs of streamwise counter-rotating vortices are observed in the cross-stream plane of the pipe.

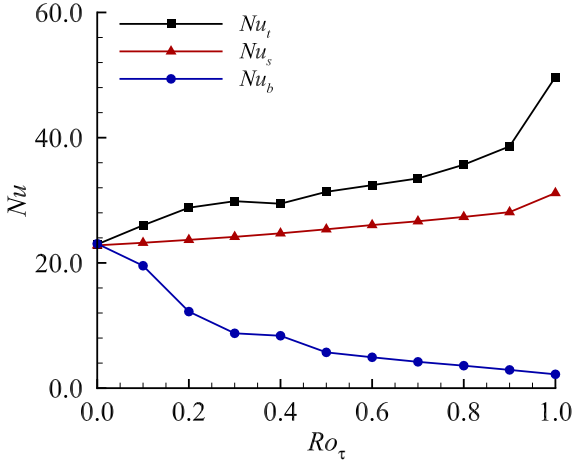
In order to compare the heat transfer performance under the effect of radial system rotation, the Nusselt number averaged along homogeneous axial direction at different position of wall is calculated as

$$Nu = \frac{hD}{k_f} = \frac{2R}{\langle \theta \rangle_b} \left. \frac{\partial \langle \theta \rangle}{\partial n} \right|_{n=0}, \quad (4)$$

where h represents the convective heat transfer coefficient, $D = 2R$ is the hydraulic diameter of the pipe, k_f is the thermal conductivity of the fluid, $\langle \theta \rangle_b$ is the bulk mean temperature, and n denotes the wall-normal distance in the cross-stream plane of the pipe. Figure 3 compares the friction velocities u_τ^+ and Nusselt number Nu under the effect of radial system rotation with respect to 11 rotation numbers. In the figure, the subscript ‘t’, ‘s’ and ‘b’ represent the top (or pressure side, at $\varphi = 90^\circ$), lateral sides (at $\varphi = 0^\circ$ or 180°), and bottom (or suction side, at $\varphi = 270^\circ$) of the pipe, respectively. As is known for a zero-pressure-gradient heated turbulent flow in a stationary pipe, an analogy between velocity and temperature distributions is held in the viscous sublayer, i.e. $u^+ = n^+$ versus $\theta^+ = Pr \cdot n^+$. It demonstrates that the magnitude of the Nusselt number is linearly proportional to that of the skin friction coefficient associated with the friction velocity in a non-rotating turbulent pipe flow. As a result, in response to the imposed radial system rotation, the Coriolis forces significantly impact the transportation of momentum and thermal energy, and are expected to break such analogy between friction velocity and Nusselt number as rotation number increases. As is evident in Fig. 3, the magnitudes of both $u_{\tau,t}^+$ and Nu_t increase monotonically on the pressure side of the pipe with an increasing rotation number. In contrast, the values of $u_{\tau,b}^+$ and Nu_b decrease monotonically on the suction side of the pipe. Those sharp contrast in tends of



(a) Friction velocities u_{τ}^{+}

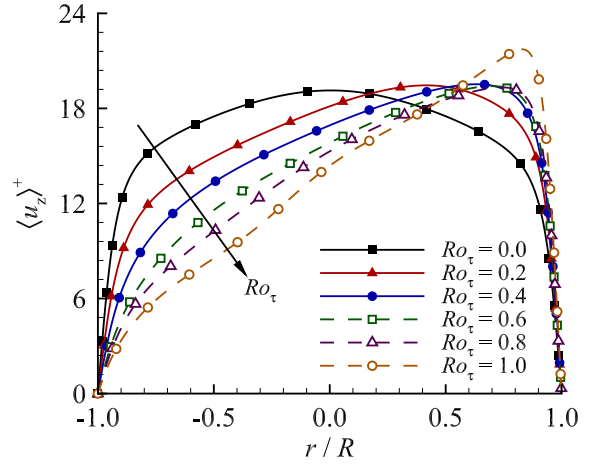


(b) Nusselt number Nu

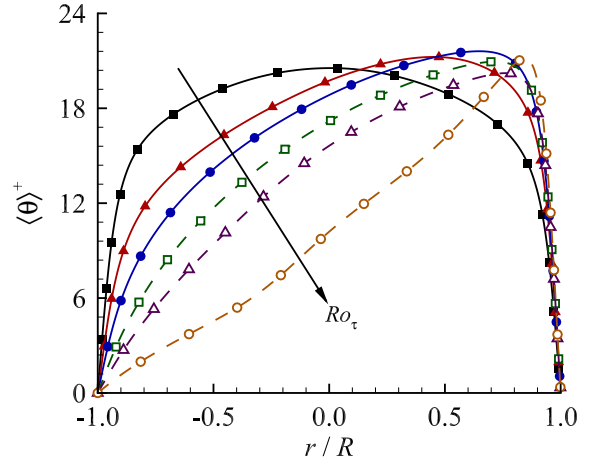
Fig. 3. Comparison of the friction velocity u_{τ}^{+} and Nusselt number Nu with respect to rotation number.

both u_{τ}^{+} and Nu can be well explained by the secondary flow patterns shown in Fig. 2. So far, the analogy between friction velocity and Nusselt number is still verified on both pressure and suction sides, and the effect of Coriolis force from radial system rotation can be negligible. However, from Fig. 3(a)-(b), it is interesting that the variation of $u_{\tau,s}^{+}$ is non-monotonic on the lateral-sides wall of the pipe as rotation number increases, which is different from slowly-increasing Nu_s . It indicates that the analogy between friction velocity and Nusselt number is broken by Coriolis forces on the lateral sides wall of the pipe, which occurs at $Ro_{\tau} = 0.6$.

Figure 4 compares the profiles of the mean axial velocity $\langle u_z \rangle^{+}$ and mean temperature $\langle \theta \rangle^{+}$ at six different rotation numbers in the central vertical plane ($\varphi = 90^{\circ}$). As is evident in Fig. 4, the profiles of both $\langle u_z \rangle^{+}$ and $\langle \theta \rangle^{+}$ are perfectly symmetrical for the non-rotating case ($Ro_{\tau} = 0.0$). Once Ro_{τ} starts to increase, this symmetrical pattern in both $\langle u_z \rangle^{+}$ and $\langle \theta \rangle^{+}$ breaks in response to the radial system rotation, and the peak value of $\langle u_z \rangle^{+}$ and $\langle \theta \rangle^{+}$ is shifted from the pipe center



(a) Mean axial velocity $\langle u_z \rangle^{+}$

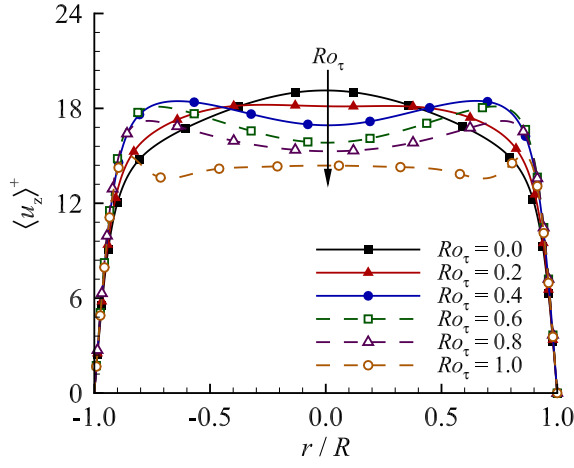


(b) Mean temperature $\langle \theta \rangle^{+}$

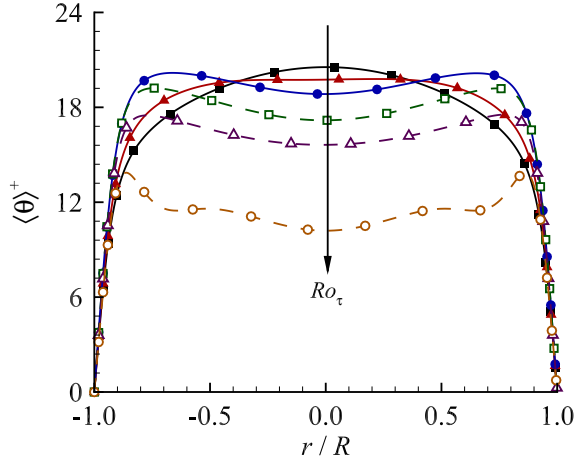
Fig. 4. Profiles of mean axial velocity $\langle u_z \rangle^{+}$ and mean temperature $\langle \theta \rangle^{+}$ at six different rotation numbers in the central vertical plane at $\varphi = 90^{\circ}$. Arrow points to the direction of monotonic variation of the rotation number.

to the pressure side of the pipe owing to the secondary flows in the cross-stream plane (shown in Fig. 2). Meanwhile, the magnitudes decreases as rotation number increases near the suction side of the pipe. It is interesting that the amplitude of $\langle \theta \rangle^{+}$ on decrease is much faster than that of $\langle u_z \rangle^{+}$.

Figure 5 compares the profiles of mean axial velocity $\langle u_z \rangle^{+}$ and mean temperature $\langle \theta \rangle^{+}$ at six different rotation numbers in the central horizontal plane ($\varphi = 0^{\circ}$). It is clear from Fig. 5(a), a quasi Taylor-Proudman (TP) region (the mean axial velocity is insensitive to the rotating x -direction) occurs at $Ro_{\tau} = 0.2$ and the magnitude of $\langle u_z \rangle^{+}$ decreases monotonically in the pipe center as rotation number increases from 0.0 to 1.0. In comparison with $Ro_{\tau} = 0.2$, the value of $\langle \theta \rangle^{+}$, shown in Fig. 5(b), also suppressed at the similar position with an increasing rotation number. Meanwhile, the distribution of $\langle \theta \rangle^{+}$ under the TP effect tends to be even, and the strongest TP effect occurs at $Ro_{\tau} = 1.0$ where the flow field becomes fully laminarized.



(a) Mean axial velocity $\langle u_z \rangle^+$

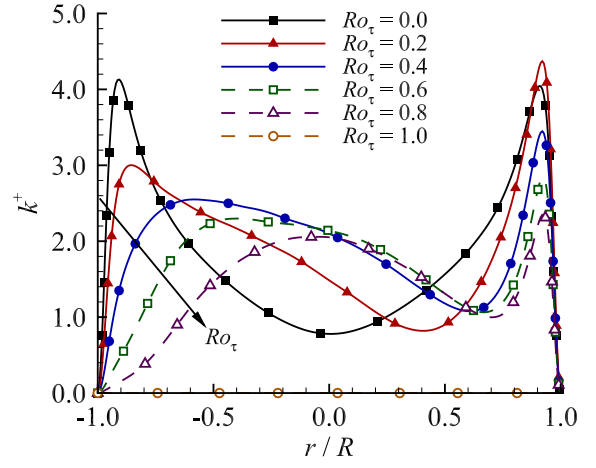


(b) Mean temperature $\langle \theta \rangle^+$

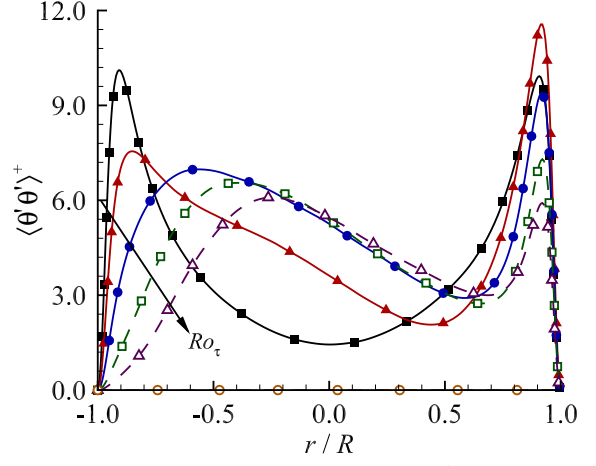
Fig. 5. Profiles of mean axial velocity $\langle u_z \rangle^+$ and mean temperature $\langle \theta \rangle^+$ at six different rotation numbers in the central horizontal plane at $\varphi = 0^\circ$. Arrow points to the direction of monotonic variation of the rotation number.

B. Temperature Fluctuations and Turbulent Heat Fluxes

Figure 6 shows the profiles of TKE $k = \langle u_i' u_i' \rangle / 2$ and temperature variance $\langle \theta' \theta' \rangle^+$ at six different rotation numbers in the central vertical plane ($\varphi = 90^\circ$). It is clear in Fig. 6 that both k^+ and $\langle \theta' \theta' \rangle^+$ exhibit a characteristic dual-peak pattern to reflect wall-anisotropic effects. In response to radial system rotation, the magnitudes decrease monotonically on the suction side as rotation number increases. It indicates that the radial system rotation throughout suppresses velocity and temperature fluctuations on the suction side of the pipe. In other words, the flow is expected to be laminarized on the suction of the pipe under the Coriolis effect. In contrast, the variation of both k^+ and $\langle \theta' \theta' \rangle^+$ is non-monotonic on the pressure side of the pipe. The peak value of k^+ and $\langle \theta' \theta' \rangle^+$ occurs at $Ro_\tau = 0.2$ at $r/R = 0.921$, indicating that the radial system rotation enhances the turbulent level in both flow and heat convection at relatively low rotation number ($Ro_\tau \leq 0.2$). At $Ro_\tau = 1.0$, k^+ becomes zero, implying that the flow is fully laminarized. Meanwhile, the temperature variation also



(a) TKE k^+

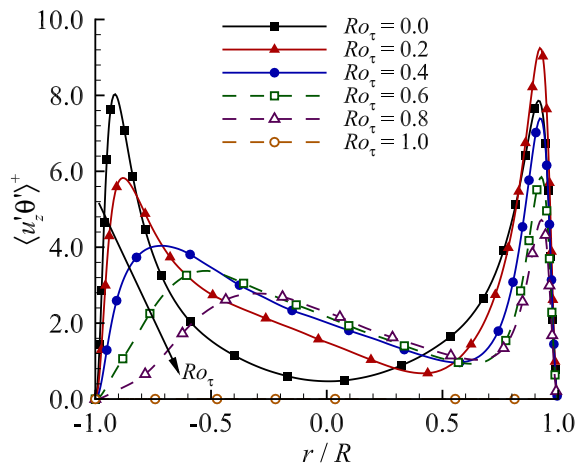


(b) Temperature variance $\langle \theta' \theta' \rangle^+$

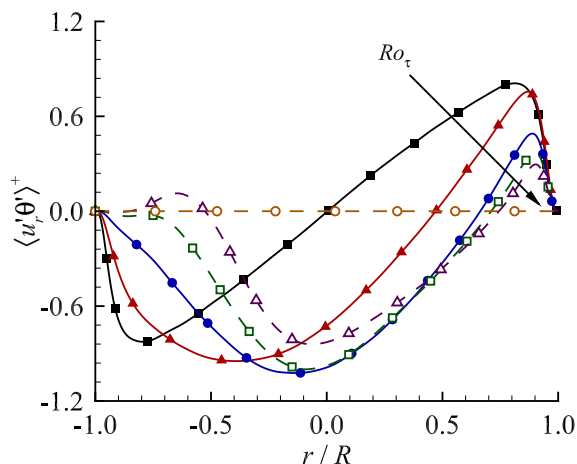
Fig. 6. Profiles of TKE k^+ and temperature variance $\langle \theta' \theta' \rangle^+$ at six different rotation numbers in the central vertical plane at $\varphi = 90^\circ$. Arrow points to the direction of monotonic variation of the rotation number.

becomes zero in the entire cross-stream plane of pipe.

Figure 7 compares the profiles of turbulent heat flux $\langle u_z' \theta' \rangle^+$ and $\langle u_r' \theta' \rangle^+$ at six different rotation numbers in the central vertical plane ($\varphi = 90^\circ$). As is shown in Fig. 7(a), $\langle u_z' \theta' \rangle^+$ decreases monotonically near the suction side of the pipe as rotation number increases. However, a peak value of $\langle u_z' \theta' \rangle^+$ occurs at $Ro_\tau = 0.2$ and $r/R = 0.921$. In contrast, it is interesting to observe from Fig. 7(b) that the well-recognized linear distribution of $\langle u_r' \theta' \rangle^+$ of a non-rotating flow starts to lose effect as soon as the radial system rotation is imposed. As Ro_τ increases, the magnitude of $\langle u_r' \theta' \rangle^+$ on the pressure side decreases monotonically; however, the variation of $\langle u_r' \theta' \rangle^+$ on the suction side is non-monotonic. Specifically, the magnitude of $\langle u_r' \theta' \rangle^+$ increases with an increasing the rotation number from 0.0 to 0.4. As the rotation number continues to increase up to 1.0, the peak value of $\langle u_r' \theta' \rangle^+$ is decreased. In this non-monotonic process, the position of peak value of $\langle u_r' \theta' \rangle^+$ is consistently shifted toward the pipe center. Finally, at $Ro_\tau = 1.0$, both $\langle u_z' \theta' \rangle^+$ and $\langle u_r' \theta' \rangle^+$ becomes trivial, indicating that



(a) Axial turbulent heat flux $\langle u'_z \theta' \rangle^+$



(b) Radial turbulent heat flux $\langle u'_r \theta' \rangle^+$

Fig. 7. Profiles of turbulent heat flux $\langle u'_z \theta' \rangle^+$ and $\langle u'_r \theta' \rangle^+$ at six different rotation numbers in the central vertical plane at $\varphi = 90^\circ$. Arrow points to the direction of monotonic variation of the rotation number.

the flow becomes fully laminarized by the Coriolis force.

IV. CONCLUSIONS

Direct numerical simulation of turbulent heat transfer has been investigated in a circular pipe subjected to radial system rotation. In order to study the Coriolis force effects on heat convection, a wide range of rotation numbers varying from $Ro_\tau = 0.0$ to 1.0 has been tested. The large axial domain tested in here is the largest in the current literature of turbulent pipe flow. The radial system rotation on the thermal convection has been examined in terms of mean temperature field, friction velocity, Nusselt number, flow structures, and the first- and second-order turbulence statistics.

In response to the radial system rotation, large-scale secondary flow vortical structures appear in the cross-stream plane of the pipe as the counter-rotating roll cells, a pattern that is in sharp contrast to the concentric pattern characteristic of a non-rotating pipe flow. As a result, the peak magnitudes of $\langle \theta \rangle^+$ are pushed toward to the pressure side of the pipe.

As rotation number increases, a quasi Taylor-Proudman region has been observed, and velocity and temperature fields under the Coriolis effects tend to be even. At $Ro_\tau = 1.0$, the turbulent circular pipe flow becomes laminarized. An analogy between friction velocity and Nusselt number in a non-rotating pipe flow appears on the pressure and suction sides of the circular wall with an increasing rotation number. However, such analogy disappears on the lateral sides wall once the rotation number increases over 0.6.

Both the velocity and temperature fluctuations, indicated by k^+ and $\langle \theta' \theta' \rangle^+$, have a dual-peak pattern in the non-rotating pipe flow. As rotation number increases, their magnitudes decrease monotonically on the suction side of the pipe. In contrast, the variation of k^+ and $\langle \theta' \theta' \rangle^+$ is non-monotonical on the pressure side, and peaks at $Ro_\tau = 0.2$ and $r/R = 0.921$. At $Ro_\tau = 1.0$, both k^+ and $\langle \theta' \theta' \rangle^+$ become trivial. It is interesting to observe that the well-recognized linear distribution in the radial heat flux $\langle u'_r \theta' \rangle^+$ breaks as soon as rotation number is imposed. The magnitude of $\langle u'_r \theta' \rangle^+$ decreases monotonically on the pressure side and varies non-monotonically on the suction side with an increasing rotation number. The peak position of $\langle u'_r \theta' \rangle^+$ near the suction side consistently shifted toward the pipe center as rotation number increases. Finally, the axial and radial heat fluxes become zero at $Ro_\tau = 1.0$, implying that the flow is fully laminarized.

ACKNOWLEDGMENT

The authors appreciate Blackburn and Sherwin [6] for making their spectral-element code available to the research community. The authors are also thankful to Western Canada Research Grid (WestGrid) for providing the computational and data storage resources. The financial support from Natural Sciences and Engineering Research Council (NSERC) is gratefully acknowledged.

REFERENCES

- [1] N.-S. Liu and X.-Y. Lu, "Direct numerical simulation of spanwise rotating turbulent channel flow with heat transfer," *Int. J. Numer. Meth. Fluids*, vol. 53, no. 11, pp. 1689–1706, 2007.
- [2] Q.-Q. Xun, B.-C. Wang, and E. Yee, "Large-eddy simulation of turbulent heat convection in a spanwise rotating channel flow," *Int. J. Heat Mass Trans.*, vol. 54, no. 1-3, pp. 698–716, 2011.
- [3] J. Pallares and L. Davidson, "Large-eddy simulations of turbulent heat transfer in stationary and rotating square ducts," *Phys. Fluids*, vol. 14, no. 8, pp. 2804–2816, 2002.
- [4] X.-J. Fang and B.-C. Wang, "On the turbulent heat transfer in a square duct subjected to spanwise system rotation," *Int. J. Heat Fluid Flow*, vol. 71, pp. 220–230, 2018.
- [5] H. Ishigaki, "Analogy of Forced Convective Heat Transfer between Laminar Flows in Curved Pipes and Orthogonally Rotating Pipes," *JSME International Journal Series B*, vol. 42, no. 1, pp. 48–55, 1999.
- [6] H. M. Blackburn and S. J. Sherwin, "Formulation of a galerkin spectral element-Fourier method for three-dimensional incompressible flows in cylindrical geometries," *J. Comp. Phys.*, vol. 197, pp. 759–778, 2004.

Large Eddy Simulation of Turbulent Flow in Ice-covered Channels

Rui Zeng, S. Samuel Li

Department of Building, Civil and Environmental Engineering
Concordia University
Montreal, Canada
sam.li@concordia.ca

Abstract—In winter ice covers the surface of water channels in cold regions, having significant impacts in many hydraulic applications. Open-channel hydraulic principles are no longer effective in predicting flow velocity distribution and local boundary shear stress under ice-covered conditions. The flowing water in a channel exerts significant boundary shear stress (BSS) on its wetted perimeter. Knowledge of this BSS has important applications such as channel stabilization, the restoration of fish habitats, and the prevention of contaminated materials from resuspension from the channel-bed. However, the knowledge is incomplete, partly because of technical and practical difficulties in measuring BSS in ice-covered channels. This paper aims to compute BSS distributions in ice-covered channels by means of large eddy simulation. Detailed structures of near-boundary flow and BSS distributions in both rectangular and trapezoidal ice-covered channel sections are predicted. The model results are validated using analytical solutions. The results capture typical features of BSS distributions at the channel sections. These include the occurrence of inflection points by bottom vortices. BSS values are relatively high in the central portion of the bed width and drop rapidly toward the corners. The sidewall shear stress has a similar shape as the bed shear stress. In the corners, the normalized BSS is always larger in the trapezoidal than the rectangular section. Secondary flow causes BSS fluctuations in the central portion of the bed width. The maximum BSS is not necessary to occur at the same location as the maximum primary velocity. The successful predictions are attributed to implementing proper conditions at the solid boundaries and resolving the viscous sublayer. For the first time, this paper has explored LES strategies for accurate and efficient BSS predictions in ice-covered channels.

Keywords: *River ice engineering; large eddy simulation; channel hydraulics; boundary shear stress*

I. INTRODUCTION

It is common that ice covers the surface of flowing water in northern river channels in winter. Winter ice covers can develop as far south as 33°N in North America and 26°N in Eurasia, which affect seven of the world's 15 largest rivers [1]. In Canada, winter ice covers have a thickness of more than 0.6 m for at least four months of the year [2]. They have significant impacts.

Breakup ice jams have interrupted commercial navigation [3]. They have caused the worst flood of the century in Canada in Manitoba's Red River in 2009. Frazil ice can cause blockages at water intakes, accumulate against the trash racks, and constrain flow passages [4]. Moreover, the existence of ice covers can lead to substantial losses of hydropower production, because the progression and maintenance of a stable ice cover consumes river flow. Ice-induced additional resistance reduces water level at the power dam [5]. Ice formation, development and melt change the channel roughness continuously. Good control should be taken to reach flat freeze-up mode and form a stable ice cap for large hydraulic projects [6].

The principles for open-channel flow are no longer effective in predicting velocity distribution, discharge, local boundary shear stress (BSS), and sediment load under ice-covered conditions. Predictions of such quantities are of practical and scientific interest. This paper focuses on BSS distribution in ice-covered channels.

BSS occurs as the pull of water acts on the wetted area in the direction of flow. The mean BSS, $\bar{\tau}_0$, can be estimated using the formula, $\bar{\tau}_0 = \gamma RS$, where γ is the specific weight of water, R is the hydraulic radius, and S is the bed slope [7]. However, the local BSS along the channel wetted perimeter is difficult to obtain because of its non-uniform characteristics. Distributions of local BSS along the channel-bed, sidewalls and ice underside affects channel stability and fish habitats. Knowledge of BSS distributions is needed for river engineering projects.

Previously, numerical simulations using the k- ϵ model for turbulence closure were carried out to calculate shear stress distributions in straight compound open channels. BSS at the corners of the main channel was not well predicted due to significant secondary flow effects [8], improper nodes [9] and the essential deficiency of the linear model [10]. Simulations of turbulent flow in a compound open channel were also performed using nonlinear k- ϵ turbulence closure models of Low-Reynolds type [11], Algebraic Stress Model (ASM) [12, 13] and Reynolds Stress Models (RSM) [14, 15]. All these simulations are based on the Reynolds-averaged Navier-Stokes (RANS) equations, which neglect some turbulent transient characteristics.

Direct Numerical Simulation (DNS) was used to study mean flow properties and turbulent statistics for square duct flow [16, 17]. DNS is recognized to be the most precise simulation tool for the analysis of turbulence structures and wall effects, but it incurs enormous computing costs, and thus can only be applied to simple flows at low Reynolds number [18].

Large Eddy Simulation (LES) is a compromise between RANS and DNS models. In LES, large-scale motions of flow are solved. Only small-scale motions are modeled. As a result, the number of grids is much smaller in LES than DNS, and the accuracy of LES can be kept to a satisfactory extent [19].

Previous numerical studies of BSS in open channel using LES have deficiencies. In some studies, the wall distance, y^+ , is usually not small enough to apply no-slip wall condition on the channel boundaries [20, 21]. Coarse resolutions adjacent to the channel-bed and sidewalls impede resolving the viscous sublayer. Some researchers resorted to using less accurate boundary conditions, such as the modified power law [22, 23] or the stress wall boundary condition [24]. Moreover, most of the previous studies used uniform mesh [22]. Uniform mesh is not desirable because of low computation efficiency. Other LES applications reported in the literature include studies like turbulence characteristics in flow over dunes [25], sediment transport in open channel [26, 27], and bedform evolution in turbulent flows [28, 29]. In summary, previous applications of LES have been limited to open channel flow.

The presence of an ice cover makes flow structures more complex. The two-power law is widely used to describe the vertical distribution of streamwise velocity in ice-covered flows [30]. Suitable exponents and coefficient of a two-power law for ice-covered flows were determined by previous researchers [31]. The mean discharge in ice-covered flows is usually estimated by measuring only a few points using the velocity-area approach. The BSS in ice-covered flows is poorly understood. Numerous attempts have been made to obtain the mean bed shear stress and mean ice cover shear stress [32, 33, 34]. The work of Yamashita, Shimizu and Hohjo [35] is perhaps the only study dealing with BSS distribution under the ice-covered condition, but the local BSS was only measured at three locations.

Harsh working conditions make field measurements of BSS extremely difficult in ice-covered channels. Numerical results will be helpful. The purpose of this paper is to investigate distributions of BSS in both rectangular and trapezoidal ice-covered channels by means of LES. LES techniques avoid inaccurate estimates of roughness on the boundary surfaces. They predict instantaneous BSS. This paper uses advanced meshing strategies and realistic wall conditions. The results will be compared with analytical solutions.

II. METHODOLOGIES

A. Model channels

The geometry of a rectangular and a trapezoidal model channel used in this paper is shown in Fig. 1a and Fig. 1b. Simulations of flow in the channels are referred to as Run 1 and Run 2, respectively. The flow field is considered to be symmetrical about the vertical plane OPMN (Fig. 1a) through the channel centerline. Accordingly, computations need to be

performed for only one half of the model channels. The symmetry assumption reduces computing costs. Run 2 matches Knight et al.'s [36] experiments in channel dimensions, inlet velocity and discharge.

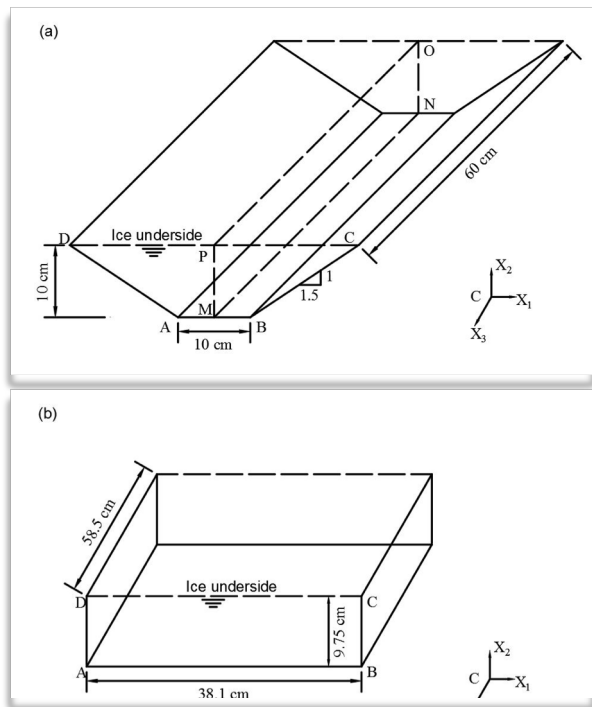


Figure 1 LES model channels: (a) an ice-covered trapezoidal channel; (b) an ice-covered rectangular channel

The setup of two runs are summarized in Table 1. The lengths of the channels are multiple times the depth of flow. The idea is to minimize possible end effects caused by the upstream and downstream lateral open boundaries. The Reynolds number is estimated based on the characteristic velocity and characteristic length. The conditions imposed at the upstream boundary are prescribed functions.

Table 1 Summary of LES channel geometry and setup.

Run	Channel shape	Length-to-depth ratio	Inlet velocity (cm/s)	Discharge (L/s)	Reynolds number
1	trapezoidal	6	5.0	1.25	10^4
2	rectangular	6	49.5	13.30	10^5

B. Model Equations

The flow of water is governed by the Navier-Stokes equations. Numerical solutions to them are obtained using LES techniques. Motions of large eddies are computed, whereas subgrid-scale eddies are modelled. The finite-volume discretization itself implicitly provides the filtering operation. The filtered Navier-Stokes equations are given by

$$\frac{\partial \bar{u}_i}{\partial x_i} = 0, \quad (1)$$

$$\frac{\partial \bar{u}_i}{\partial t} + \frac{\partial}{\partial x_j} (\bar{u}_i \bar{u}_j) = -\frac{1}{\rho} \frac{\partial \bar{p}}{\partial x_i} + \nu \frac{\partial}{\partial x_j} \left(\frac{\partial \bar{u}_i}{\partial x_j} \right) + \rho g_i, \quad (2)$$

where \bar{u}_i denotes the resolvable-scale filtered velocity; x_i represents coordinates; t is the time; \bar{p} is the resolvable pressure; and g_i is the gravitational acceleration.

The effect of the unresolved fluctuations on the resolved motion is expressed as

$$\tau_{ij} = \bar{u}_i \bar{u}_j - \overline{u_i u_j}, \quad (3)$$

Eq. (2) can be rewritten as

$$\frac{\partial \bar{u}_i}{\partial t} + \frac{\partial}{\partial x_j} (\bar{u}_i \bar{u}_j) = -\frac{1}{\rho} \frac{\partial P}{\partial x_i} + \frac{\partial}{\partial x_j} \left(\nu \frac{\partial \bar{u}_i}{\partial x_j} + \tau_{ij} \right). \quad (4)$$

It is important to establish a satisfactory model for the subgrid scale stress τ_{ij} . This paper uses the Smagorinsky-Lilly model [37, 38] for estimates τ_{ij} . It is assumed that τ_{ij} follows a gradient-diffusion process similar to molecular motion. τ_{ij} is approximated by relating it to the resolved strain rate, S_{ij} , via an artificial eddy viscosity ν_τ , as

$$\tau_{ij} = 2\nu_\tau S_{ij}, \quad (5)$$

where $S_{ij} = \frac{1}{2} \left(\frac{\partial \bar{u}_i}{\partial x_j} + \frac{\partial \bar{u}_j}{\partial x_i} \right)$, and ν_τ is expressed as

$$\nu_\tau = L_s^2 \sqrt{2S_{ij}S_{ij}}. \quad (6)$$

In this equation, L_s is the mixing length, given by

$$L_s = \min(C_s V^{1/3}, \kappa d), \quad (7)$$

where C_s is the Smagorinsky coefficient; V is the volume of the computational cell; κ is Von Kaman constant; d is the distance to the closest wall. Lilly [38] suggested a C_s value of 0.17. A value of 0.1 for C_s has been found to yield the best results for a wide range of flows. This value is used in this paper.

C. Numerical Solutions

The model equations and model domains are discretized in both space and time. Spatial discretization uses the finite volume method, which divides the domain into a number of control volumes or cells. As an example, the discretization of the model channel plotted in Fig. 1a is shown in Fig. 2a. The cells are non-staggered, or co-located grids, meaning that variables of interest like pressure and velocity components are stored at the centroid of each control volume. Equations (1) to (4) of differential form are integrated over each cell to yield algebraic equations for the discrete dependent variables. Then, interpolation profiles are

applied to describe the variation of variable between cell centroids. The resulting solution must satisfy the conservation of mass and momentum.

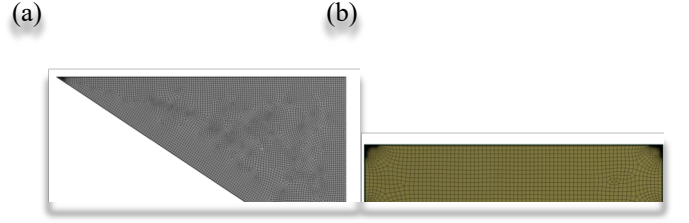


Figure 2 Cross-sectional view of mesh for: (a) Run 1; (b) Run 2.

Temporal discretization integrates every term in the model equations over a time step Δt . A time step small enough is used to achieve numerical stability and to enhance prediction accuracy. Estimates of the appropriate time step are based on the Courant number, $C = U_3 \Delta t / \Delta$, where U_3 is the streamwise bulk mean velocity; Δ is the spacing of the grid parallel to the direction of flow. For all the simulations, the time step used satisfies the restriction that C is smaller than unity.

The solution procedures require estimates of interfacial values of the involved variables from their cell central values. The gradients are used to construct values of a scalar at cell faces and to compute secondary diffusion terms (e.g. the second last term in (4)) and velocity derivatives (e.g. the first term in (1)). The least squares cell based method is chosen to calculate the gradients in this study because of its high accuracy and less computational cost. We use the 2nd order scheme to reconstruct the face pressure accurately, which is needed for the calculation of convection terms (e.g. the second term in (4)). The bounded central differencing scheme is used to solve the momentum equations (4) and it produces face values for all the variables except the pressure field in the equations. For the temporal development, we use the unsteady solver. The bounded 2nd-order implicit method is used to integrate the differential equations over time (e.g. the first term in (4)). This method has the advantage of maintaining unconditional stability with respect to time step. We use the SIMPLE algorithm, a pressure-velocity coupling method, to solve the equations simultaneously in a coupled manner. It is possible to adjust under-relaxation factors to facilitate convergence using this method [39]. The solution methods discussed above are summarised in Table 2.

Table 2 Solution methods of LES computations

Solution methods		
Pressure-velocity coupling method	Simple algorithm	
Spatial discretization scheme	Gradient	Least squares cell based method
	Pressure	Second order scheme
	Momentum	Bounded central difference scheme
Transient formulation scheme	Bounded second-order implicit method	

The solution to these nonlinear coupled equations involves iterations until the convergence criterion is met. The solution is considered converged when residuals are very small (Table 3).

Table 3 A summary of model parameters

Parameter	Run 1	Run 2
Total nodes	1129005	1352736
Elements	1232934	1296100
Mesh type	Structured, Hexahedron	
Time step size (s)	0.02	0.01
Criterion for convergence	10^{-6}	
Number of time steps	2100	360
Model time period (s)	42	3.6
Max iterations per time step	120	

D. Boundary Conditions

At the channel boundaries (Fig. 1), flow conditions must be specified. These boundaries include the channel-bed, sidewalls, the underside of ice, the inlet at upstream, and the outlet at downstream.

The channel-bed, sidewalls and the underside of ice are solid walls. For the two runs (Table 1), the no-slip wall condition (or $\bar{u}_i = 0$) is applied on these boundaries. The wall distance of the first node off the wall is small such that $y^+ \leq 1$, where $y^+ = y' U^*/\nu$ is the wall distance, y' is the distance of the first node off a wall, and U^* is the shear velocity. The mesh used resolves the viscous sublayer. The wall shear stress τ_w in the streamwise direction is equal to $\mu \bar{u}_3 / y'$, where μ is the dynamic viscosity of water.

At the inlet (Fig. 1), the inflow normal to the inlet is given in terms of velocity profiles, which are specified using a two-power law for ice-covered flow (Fig. 3) as

$$\frac{\bar{u}_3}{U_3} = k_0 \left(\frac{y}{H} \right)^{1/m_i} \left(1 - \frac{y}{H} \right)^{1/m_b}, \quad (8)$$

where U_3 is the bulk mean velocity in the streamwise direction, y is the flow depth, and H is the total depth of flow; k_0 is a parameter related to per-unit-width discharge; m_i and m_b are parameters associated with the frictional effect of ice and bed, respectively. According to Attar and Li [31], for a smooth ice cover, m_i is equal to 7, and m_b is equal to 4.

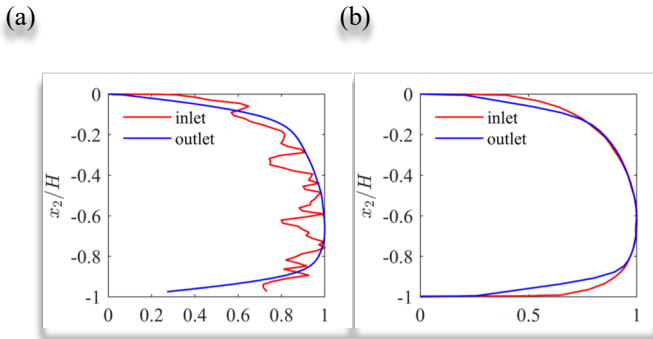


Figure 3 Vertical profiles of the streamwise velocity at the inlet

(the red curve) and outlet (the blue curve) as the initial condition for: (a) Run 1; (b) Run 2

The condition of turbulence at the inlet is specified in terms of fluctuations in velocity components. The spectral synthesizer is used to generate fluctuating velocity components. The intensity of turbulence and the turbulent viscosity ratio are both set to 10%.

At the outlet, the gradients of all variables (except pressure) are zero in the flow direction. Pressure outlet boundary condition is applied at the outlet. This requires the specification of a static (gauge) pressure equal to zero, which means that the pressure distribution is hydrostatic at the outlet.

E. Initial Condition

At model time $t = 0$, initial values of flow variables are specified for the entire channel. The specification of proper initial values can accelerate the simulation considerably. In this paper, the initial values are taken from the inlet velocity profiles (8). Initial velocity profiles at the inlet and outlet at the centerline in the channels are plotted in Fig. 3a and Fig. 3b for Run 1 and Run 2, respectively.

The gauge pressure is zero and the turbulence kinetic energy and the turbulence dissipation rate are estimated from the initial velocity and boundary conditions.

F. Meshing strategies

1) Face Sizing and Sweep

Face sizing is applied to the inlet plane (Fig. 2) in order to construct structured mesh in relatively regular geometries. The mesh configuration on the inlet plane is swept consistently in the X_3 -direction, generating 3D elements between the upstream and downstream boundaries. The cell length of the hexahedrons is set to three times the width to reduce computing nodes.

The mesh size on the inlet is 1.5×10^{-3} , and 3×10^{-3} m for Runs 1 and Run 2, respectively. The mesh is fine enough to determine turbulent features.

2) Inflation

For the model channels, an inflation of five layers was applied adjacent to the channel-bed, sidewalls, and ice cover underside. The first layer off a solid wall had a thickness of 3.14×10^{-4} m for the trapezoidal channels (Fig. 3a), and 3.76×10^{-5} m for the rectangular channels (Fig. 3b). The use of these fine resolutions ensures that the dimensionless wall distance y^+ of the first node off a wall does not exceed unity. The growth rate of the layer thickness was 1.1 for a smooth transition. The mesh used resolves the viscous sublayer.

3) Body of Influence

The Body of Influence technique is applied to the corner regions in order to refine the mesh. For Run 1, only one arc is specified at each corner region (Fig. 3a). The radius of the arc is 0.5 cm. The mesh sizes refined within the arcs are 3.14×10^{-4} m. Four arcs of different radius are specified at each corner for Run 2 (Fig. 3b). The radius of the four arcs are, respectively, 0.2, 0.5, 0.9, and 1.4 cm. The radius gradually increases in 0.2, 0.3, 0.4, and 0.5 cm increments. The refined mesh sizes within the sub-regions are, respectively, shown in Table 4.

Table 4 Parameters used in mesh generation

Run	Arc radius (cm)	Mesh size between arcs (m)	First layer thickness (m)	Face sizing (m)	Cell length (m)
1	0.5	3.14×10^{-4}	3.14×10^{-4}	1.5×10^{-3}	4.5×10^{-3}
2	0.2 0.5 0.9 1.4	7.52×10^{-5} 1.32×10^{-4} 1.9×10^{-4} 2.74×10^{-4}	3.76×10^{-5}	3×10^{-3}	9×10^{-3}

The mesh is a structured mesh. The time step varies between the runs because the cell sizes are different. The simulation periods exceed three times the flow-through time for both runs. The results presented are for the last time step of the simulation.

III. RESULTS

A. Velocity Profiles

Vertical profiles of the streamwise velocity for Run 1 and Run 2 are shown in Fig. 4a and 4b, respectively. The profiles from cross sectional centerline at a distance of 75% of the total channel length or $x_3 = -0.450$ and -0.439 m, respectively, measured from the inlet plane. The vertical axis shows the normalized distance (across the sidewall from the ice cover to channel-bed) by the flow depth. The horizontal axis shows the normalized streamwise velocity by the maximum velocity.

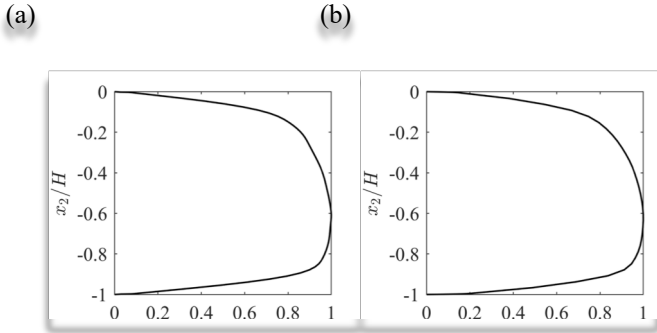


Figure 2 Streamwise velocity profiles at a selected vertical line for (a) Run 1 and (b) Run 2

In Fig. 4a (Run 1) and Fig. 4b (Run 2), the vertical distributions of streamwise velocities are characterised by a parabolic shape. This is the same pattern as the two-power law reported in the literature [31]. The velocity profile in an ice-covered channel can be considered two velocity profiles: one associated with the ice cover, and the other associated with the channel-bed. The two profiles meet at a certain point in the water column, where the shear stress is zero. For both Run 1 and Run 2, the velocity profiles show a core of relatively strong flow between the 15 and 85% flow depths. The flow velocities drop quickly above the core because of the ice underside influence and below because of the bed influence. Within the core of high velocities, there are only gradual changes in flow velocity, in comparison to the regions outside. In other words, the velocity

profiles have large spatial gradients in the vicinity of the upper and lower boundaries. The maximum velocity has a value of 6.39×10^{-2} m/s for Run 1, and 5.82×10^{-1} m/s for Run 2 (Table 5), and they occur at a depth of about 40% the total flow depth above the channel-bed for both runs.

Table 5 Maximum and mean boundary shear stresses and velocities for Run 1 and Run 2

Run	1	2
Max. bed shear stress (Pa)	9.71×10^{-3}	5.78×10^{-1}
Mean bed shear stress (Pa)	9.17×10^{-3}	5.24×10^{-1}
Max. sidewall shear stress (Pa)	1.14×10^{-2}	8.23×10^{-1}
Mean bed sidewall stress (Pa)	8.99×10^{-3}	5.27×10^{-1}
Max. velocity (m/s)	6.39×10^{-2}	5.82×10^{-1}
Mean velocity (m/s)	5.00×10^{-2}	4.95×10^{-1}

B. Velocity Contours

Contours of the predicted streamwise velocity, \bar{u}_3 , are shown in Fig. 5a and Fig. 5b for Run 1 and Run 2, respectively. The corresponding longitudinal positions are $x_3 = -0.450$ and -0.439 m. The contour plots show 100 contour levels. The horizontal axis shows the normalized distance by the channel-bed width \overline{AB} . The vertical axis shows the normalized distance (across the sidewall from the ice cover to the channel-bed) by the flow depth. The contour value is normalized by the maximum velocity. For Run 1 and Run 2, the channel-bed width is equal to 10.0 and 38.1 cm, respectively.

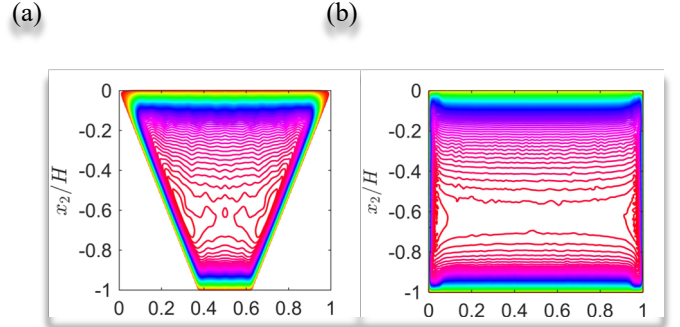


Figure 3 Contours of streamwise velocity, \bar{u}_3 , at a selected cross section for (a) Run 1 and (b) Run 2

The ice underside is treated as a no-slip boundary. For both channel sections (Fig. 5a and Fig. 5b), the contours of flow velocity reflect boundary layer dynamics near the channel boundaries and ice underside. There is a significant difference in velocity magnitude between the flow in the central region of the cross section and the flow in the boundary layer. The densely distributed contours near the channel boundaries correspond to a sharp decrease in velocity magnitude. There is a core of relatively high velocities surrounding the maximum velocity in the central region of the channel cross section (away from the solid boundaries). The velocity contour values decrease slowly in this region. Small fluctuations of velocity contours occur near the boundaries as a result of turbulent effects (Fig. 5b).

C. Bed shear stress

The wall shear stress is obtained from the linear stress-strain relationship discussed in the section of boundary condition. The cross-channel distributions of bed shear stresses τ_w are plotted in Fig 6a and 6b for Run 1 and Run 2, respectively. The corresponding longitudinal positions of the plots are $x_3 = -0.450, -0.439$ m. In each of the plots, the local bed shear stresses τ_w have been normalised by the mean bed shear stress $\bar{\tau}_{cb}$. The horizontal axis shows the normalized distance (across the channel-bed from the left corner A) by the channel-bed width \overline{AB} . For Run 1 and Run 2, the channel-bed width (Fig. 1) is equal to 10.0 and 38.1 cm, respectively. Table 5 gives a summary of the mean and maximum bed shear stresses.

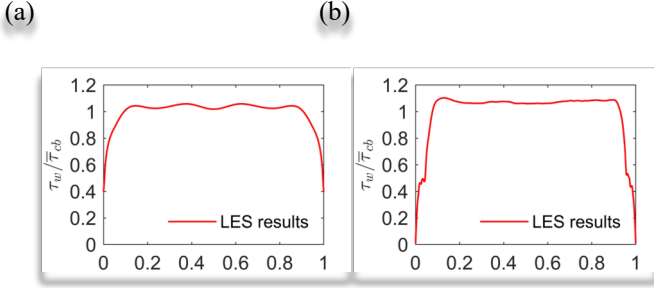


Figure 4 Predicted BBS distributions for: (a) Run 1; (b) Run 2

The BSS refers to the tractive force exerted by the flowing water on the boundary in question. From this paper, values of local BSS, τ_w , are relatively high within the largest central portion of the channel-bed and drop rapidly to zero toward the corners. This is in consistence with the results about open channel studies reported in [7]. Chow's results are partly based experimental data and membrane analogy analysis. It can be argued that the shear stresses at the corners must be equal to zero. Non-zero shear stresses at the corners will lead to the unphysical condition that the local shear forces approach infinity.

The normalized bed shear stresses in the corner regions have different distributions between the trapezoidal channel section (Run 1, Fig. 6a) and the rectangular channel section (Run 2, Fig. 6b). The distributions of bed shear stress have two inflection points in the rectangular channel section (Run 2). From these points toward the corners, the bed shear stresses decrease dramatically (Fig. 6b). The inflection points are symmetrical about the central line of the channel. They are located at a horizontal distance of 5% the bed width from each sidewall corner. At the inflection points, the bed shear stresses have a value of around 50% the mean bed shear stress. According to Tominaga & Nezu [40], secondary flow plays an important role in generating inflection points. For Run 2 (Fig. 6b), the distributions of bed shear stresses show small local peaks before their dramatic drop to lowest values toward the corners. These local peaks are located at a horizontal distance of approximately 20% the total channel width from the sidewall corners. For Run 1, the distribution of bed shear stress (Fig. 6c) has strong spatial fluctuations, making it difficult to identify any peaks.

D. Sidewall shear stress

Similar to the bed shear stress, the sidewall shear stress is also obtained from stress-strain relationship discussed in the boundary condition section. Distributions of the sidewall shear stresses, τ_s , are plotted in Fig. 7a and Fig. 7b for Run 1 and Run 2, respectively. The corresponding longitudinal positions are $x_3 = -0.450$ and -0.439 m. In each of the plots, the local sidewall shear stresses have been normalized by the mean sidewall shear stress value. The vertical axis shows the normalized distance (across the sidewall from the ice cover to the channel-bed) by the flow depth. Run 1 and Run 2 have a flow depth of 10.0 and 9.75 cm, respectively (Fig. 1). Table 5 gives a summary of the mean and maximum sidewall shear stresses.

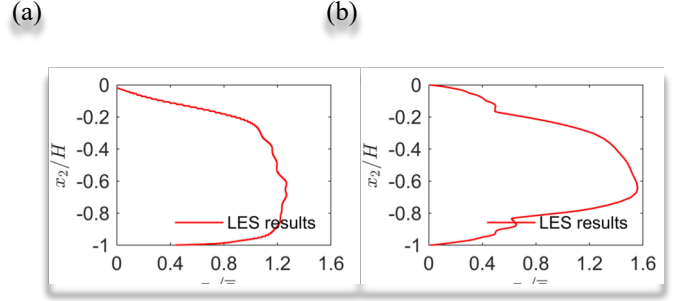


Figure 5 Distribution of predicted sidewall shear stress for (a) Run 1 and (b) Run 2

For Run 1 (Fig. 7a) and Run 2 (Fig. 7b), the distributions of sidewall shear stresses τ_s under open water condition show a similar trend as the bed shear stresses (Run 1, Fig. 6a; Run 2, Fig. 6b). The sidewall shear stresses at the middle depth are much larger than near the top and bottom boundaries. The sidewall shear stresses decrease dramatically toward zero at the ice cover and the channel-bed. The normalized sidewall shear stresses in the corner regions have different distributions in the trapezoidal channel (Run 1, Fig. 7a) and the rectangular channel section (Run 2, Fig. 7b). For Run 2, the distributions of sidewall shear stresses have two inflection points, one being near the ice cover, and the other near the channel-bed (Fig. 7b). These inflection points are symmetrically about the middle depth, located at 15 and 85% the flow depth below the ice cover. The sidewall shear stresses at the inflection points have a value of approximately 60% the mean sidewall shear stress. For Run 1, there are moderate spatial fluctuations around the middle depth (Fig. 7a), but there is no inflection point. For Run 1 and Run 2, the distributions of sidewall shear stress are not symmetrical about the middle depth (Fig. 7a and Fig. 7b). The sidewall shear stresses (Table 5) have a maximum value of $1.25 \bar{\tau}_{cs}$ and $1.55 \bar{\tau}_{cs}$, located at a vertical distance (above the channel-bed) of 30 and 35% the flow depth (Fig. 7a and Fig. 7b), respectively. These locations are closer to the bed than to the ice cover. For both Run 1 and Run 2, the sidewall shear stresses have a maximum value of 1.18 and 1.42 times larger than the maximum bed shear stresses, respectively. However, the mean shear stress value on the sidewalls and channel-bed are almost the same for each of the two runs (Table 5).

IV. DISCUSSION

Einstein's [41] hydraulic radius separation theory is widely used in laboratory studies and engineering practice. Guo and Julien [42] used this theory to develop an analytical model for estimating mean BSSs in rectangular open channels. Chen et al. [33] extended the model to rectangular ice-covered channels, which shows reliable results in comparison to the collected data from literature. Therefore, Chen et al.'s model is adopted in this paper to validate the results of Run 2 obtained from LES.

At the plane of zero shear stress, the cross-sectional area of the ice-covered channel is divided into a lower bed layer and an upper ice layer. Two-power law (8) describes the vertical distribution of mean streamwise velocity in the ice-covered channel. The parameters m_i and m_b associated with ice and channel bed frictional effects herein are estimated using the Tsai and Ettema [30] method, which are 8.77 and 8.93, respectively. In this method, Darcy-Weisbach resistance coefficients are resolved from the coupled equations of Parthasarathy and Muste [43], where the roughness height of channel bed and ice-cover underside are set to 127 mm and 0, respectively. Proportionality constants are selected from the recommended range as 0.42 and 0.4 for channel bed and ice cover, respectively.

The value of maximum Reynolds stress near the channel boundaries is approximately equal to the BSS. The elevation of maximum Reynolds stresses in the channel cross-section are determined using parameters m_i and m_b . Using the Boussinesq approximation involving eddy viscosity concept, together with the two-power law and Prandtl's mixing length theory, we can obtain the maximum Reynolds stress near channel bed and ice cover. With the calculations implemented, the position of zero shear stress plane can then be calculated using Tsai and Ettema's [30] modified eddy viscosity model, which is 0.0564 m above the channel bed for Run 2.

In the bed layer and the ice layer, each cross-sectional area is divided into two subsections [41]. As a result, the shear force on the bed or ice cover could be separated from the lateral boundaries. The conformal mapping method determines the functional relationships for the division curves. Based on the force balance in each flow subsection, together with the second-order approximation method, we can calculate the mean BSSs on the channel bed, sidewalls and ice cover. The mean bed shear stress over the selected line (described in results) and the mean ice cover shear stress over the projection line of the selected line on the ice cover are 5.24×10^{-1} and 3.54×10^{-1} Pa obtained from LES in comparison to 4.36×10^{-1} and 3.37×10^{-1} Pa obtained from this analytical method, with energy slope $S = 9.66 \times 10^{-4}$. The comparison proves the results from LES is satisfactory, though the results of LES is relatively larger than those of the analytical model.

V. CONCLUSION

This paper reports LES results of BSS distributions along the wetted perimeters of channel sections. These include a trapezoidal ice-covered channel (Run 1) and a rectangular ice-covered channel (Run 2). In LES, it is appropriate to treat ice cover as a no-slip boundary, being added to the top of an open channel. The presence of ice cover causes significant changes in flow structure and shear stress in comparison to open water

condition. An examination of the LES results has led to the following conclusions:

LES gives acceptable BSS predictions in ice-covered channels. The predicted BSS varies across the channel-bed, true for the trapezoidal and rectangular channel sections. BSS values are relatively high within the largest central portion of the bed and sidewall widths, and drop rapidly toward the corners of the channel sections. The predicted BSS is in reasonable agreement with available analytical model. The BSS distribution across its sidewalls shows a maximum value at a location closer to the channel bed than to the ice cover.

Predicted turbulent flows in the channel sections show features consistent with literature reports. The normalised bed shear stresses (normalising the local bed and sidewall shear stresses by the spatially averaged values for the bed and sidewalls, respectively) in the corner regions have different distributions between the trapezoidal channel and the rectangular channel section. The BSS distributions in the rectangular channels show symmetrical inflection points in the corner regions (Run 2). In the central region of trapezoidal channel sections, BSS has small spatial fluctuations probably caused by secondary flow (Run 1). The peak BSS does not necessarily need to be in the same location as the maximum primary velocity. The maximum sidewall shear stress values are generally larger than their corresponding bed shear stress values.

Velocity profiles show a maximum value at more or less the middle depth, closer to the bed than to the ice cover. The frictional effects of ice cover force the maximum velocity to occur at a lower depth, instead of the water surface under open water condition.

The use of a proper setup and mesh configurations has been demonstrated as important in LES. In particular, it is crucial to implement mesh refinements adjacent to the channel-bed, sidewalls, and corner regions. The wall distance of the first node off a solid surface should not exceed unity. This means that reliable BSS predictions require to resolve the viscous sublayer. This is not the case in most of the existing LES applications to channel flow. For given hydraulic conditions and channel geometry, it is necessary to test the sensitivity of LES predictions to slight changes in mesh size and configurations.

In general, LES incurs high computing costs. The costs can effectively be reduced by using User Defined Functions and symmetrical conditions, and by adjusting the ratio of grid length. Given the high costs and often technical difficulties in obtaining BSS measurements, LES offers an attractive complement to physical models, laboratory experiments, and field measurements.

ACKNOWLEDGMENT

This study received financial support from NSERC Discovery Grant held by S. Li.

REFERENCES

- [1] S. Beltaos and T. Prowse, "River-ice hydrology in a shrinking cryosphere," *Hydrological Processes: An International Journal*, vol. 23, (1), pp. 122-144, 2009.

- [2] A. Robert and T. Tran, "Mean and turbulent flow fields in a simulated ice-covered channel with a gravel bed: some laboratory observations," *Earth Surf. Process. Landforms*, vol. 37, (9), pp. 951-956, 2012.
- [3] B. Morse, "Winter navigation on the St. Lawrence river," in *Proceedings of the International Conference on Port and Ocean Engineering Under Arctic Conditions*, 2001, .
- [4] M. Richard and B. Morse, "Multiple frazil ice blockages at a water intake in the St. Lawrence River," *Cold Reg. Sci. Technol.*, vol. 53, (2), pp. 131-149, 2008.
- [5] P. D. Yapa and H. T. Shen, "Effect of ice cover on hydropower production," *J. Energy Eng.*, vol. 110, (3), pp. 231-234, 1984.
- [6] G. Liu, G. Guan and C. Wang, "Transition mode of the middle route of south-to-north water transfer project before freezing," in *2011 International Conference on Networking, Sensing and Control*, 2011, .
- [7] V. Chow, "1959, Open channel hydraulics, McGraw-Hill, New York," .
- [8] B. G. Krishnappan and Y. L. Lau, "Turbulence modeling of flood plain flows," *J. Hydraul. Eng.*, vol. 112, (4), pp. 251-266, 1986.
- [9] P. Rameshwaran and P. S. Naden, "Three-dimensional numerical simulation of compound channel flows," *J. Hydraul. Eng.*, vol. 129, (8), pp. 645-652, 2003.
- [10] F. Jazizadeh and A. Zarrati, "Development of a three-dimensional numerical model to solve shallow-water equations in compound channels," *Canadian Journal of Civil Engineering*, vol. 35, (9), pp. 963-974, 2008.
- [11] D. Sofialidis and P. Prinos, "Compound open-channel flow modeling with nonlinear low-Reynolds $k-\epsilon$ models," *J. Hydraul. Eng.*, vol. 124, (3), pp. 253-262, 1998.
- [12] D. Naot, I. Nezu and H. Nakagawa, "Hydrodynamic behavior of compound rectangular open channels," *J. Hydraul. Eng.*, vol. 119, (3), pp. 390-408, 1993.
- [13] X. Shao, H. Wang and Z. Chen, "Numerical modeling of turbulent flow in curved channels of compound cross-section," *Adv. Water Resour.*, vol. 26, (5), pp. 525-539, 2003.
- [14] D. Cokljat and B. Younis, "Second-order closure study of open-channel flows," *J. Hydraul. Eng.*, vol. 121, (2), pp. 94-107, 1995.
- [15] H. Kang and S. Choi, "Reynolds stress modelling of rectangular open-channel flow," *Int. J. Numer. Methods Fluids*, vol. 51, (11), pp. 1319-1334, 2006.
- [16] S. Gavrilakis, "Numerical simulation of low-Reynolds-number turbulent flow through a straight square duct," *J. Fluid Mech.*, vol. 244, pp. 101-129, 1992.
- [17] A. Huser and S. Biringen, "Direct numerical simulation of turbulent flow in a square duct," *J. Fluid Mech.*, vol. 257, pp. 65-95, 1993.
- [18] B. E. Launder, "Phenomenological modelling: Present.... and future?" in *Whither Turbulence? Turbulence at the Crossroads* Anonymous 1990, .
- [19] Y. Joung, S. Choi and J. Choi, "Direct numerical simulation of turbulent flow in a square duct: analysis of secondary flows," *J. Eng. Mech.*, vol. 133, (2), pp. 213-221, 2007.
- [20] M. Sterling et al, "Bed-shear stress characteristics of a simple, prismatic, rectangular channel," *J. Eng. Mech.*, vol. 134, (12), pp. 1085-1094, 2008.
- [21] S. Kara, T. Stoesser and T. W. Sturm, "Turbulence statistics in compound channels with deep and shallow overbank flows," *Journal of Hydraulic Research*, vol. 50, (5), pp. 482-493, 2012.
- [22] J. Shi, T. Thomas and J. Williams, "Large-eddy simulation of flow in a rectangular open channel," *Journal of Hydraulic Research*, vol. 37, (3), pp. 345-361, 1999.
- [23] Z. Xie, B. Lin and R. A. Falconer, "Large-eddy simulation of the turbulent structure in compound open-channel flows," *Adv. Water Resour.*, vol. 53, pp. 66-75, 2013.
- [24] T. Thomas and J. Williams, "Large Eddy Simulation of a symmetric trapezoidal channel at a Reynolds number of 430,000," *Journal of Hydraulic Research*, vol. 33, (6), pp. 825-842, 1995.
- [25] Z. Xie, B. Lin and R. A. Falconer, "Turbulence characteristics in free-surface flow over two-dimensional dunes," *Journal of Hydro-Environment Research*, vol. 8, (3), pp. 200-209, 2014.
- [26] P. Widera, E. Toorman and C. Lacor, "Large eddy simulation of sediment transport in open-channel flow," *Journal of Hydraulic Research*, vol. 47, (3), pp. 291-298, 2009.
- [27] E. A. Zedler and R. L. Street, "Sediment transport over ripples in oscillatory flow," *J. Hydraul. Eng.*, vol. 132, (2), pp. 180-193, 2006.
- [28] Y. Chou and O. B. Fringer, "A model for the simulation of coupled flow-bed form evolution in turbulent flows," *Journal of Geophysical Research: Oceans*, vol. 115, (C10), 2010.
- [29] S. Kraft, Y. Wang and M. Oberlack, "Large eddy simulation of sediment deformation in a turbulent flow by means of level-set method," *J. Hydraul. Eng.*, vol. 137, (11), pp. 1394-1405, 2011.
- [30] W. Tsai and R. Ettema, "Ice cover influence on transverse bed slopes in a curved alluvial channel," *Journal of Hydraulic Research*, vol. 32, (4), pp. 561-581, 1994.
- [31] S. Attar and S. Li, "Data-fitted velocity profiles for ice-covered rivers," *Canadian Journal of Civil Engineering*, vol. 39, (3), pp. 334-338, 2012.
- [32] Y. L. Lau and B. G. Krishnappan, "Sediment transport under ice cover," *J. Hydraul. Eng.*, vol. 111, (6), pp. 934-950, 1985.
- [33] G. Chen et al, "Boundary Shear Stress in Rectangular Ice-Covered Channels," *J. Hydraul. Eng.*, vol. 141, (6), pp. 06015005, 2015.
- [34] S. G. Aghaji Zare et al, "Boundary Shear Stress in an Ice-Covered River during Breakup," *J. Hydraul. Eng.*, vol. 142, (4), pp. 04015065, 2015.
- [35] S. Yamashita, Y. Shimizu and K. Hohjo, "Characteristics of shear stress in the ice-covered river," in *Proceedings of the International Symposium on Ice*. Banff, Canada, 1992, .
- [36] D. W. Knight, J. D. Demetriou and M. E. Hamed, "Boundary shear in smooth rectangular channels," *J. Hydraul. Eng.*, vol. 110, (4), pp. 405-422, 1984.
- [37] J. Smagorinsky, "General circulation experiments with the primitive equations: I. the basic experiment*," *Mon. Weather Rev.*, vol. 91, (3), pp. 99-164, 1963.
- [38] D. K. Lilly, *On the Application of the Eddy Viscosity Concept in the Inertial Sub-Range of Turbulence*. 1966.
- [39] A. Fluent, "14.5 User's Guide," Fluent Inc., Lebanon, NH, 2012.
- [40] A. Tominaga and I. Nezu, "Turbulent structure in compound open-channel flows," *J. Hydraul. Eng.*, vol. 117, (1), pp. 21-41, 1991.
- [41] H. A. Einstein, "Formulas for the transportation of bed load," *Trans. ASCE Paper*, vol. 2140, pp. 561-597, 1942.
- [42] J. Guo and P. Y. Julien, "Shear stress in smooth rectangular open-channel flows," *J. Hydraul. Eng.*, vol. 131, (1), pp. 30-37, 2005.
- [43] R. Parthasarathy and M. Muste, "Velocity measurements in asymmetric turbulent channel flows," *J. Hydraul. Eng.*, vol. 120, (9), pp. 1000-1020, 1994.